Advanced Materials and Engineering

Edited by
Taufiq Yap Yun Hin

TRANS TECH PUBLICATIONS

Advanced Materials and Engineering

Edited by
Taufiq Yap Yun Hin

Advanced Materials and Engineering

Selected, peer reviewed papers from the
Annual International Conference on
Intelligent Materials and Nanomaterials
(AIMN 14),
April 18-19, 2014, Seoul, South Korea

Edited by

Taufiq Yap Yun Hin

Trans Tech Publications Ltd
Churerstrasse 20
CH-8808 Pfaffikon
Switzerland
http://www.ttp.net

Volume 983 of
Advanced Materials Research
ISSN print 1022-6680
ISSN cd 1022-6680
ISSN web 1662-8985

Full text available online at *http://www.scientific.net*

***Distributed** worldwide by*

Trans Tech Publications Ltd
Churerstrasse 20
CH-8808 Pfaffikon
Switzerland

Fax: +41 (44) 922 10 33
e-mail: sales@ttp.net

and in the Americas by

Trans Tech Publications Inc.
PO Box 699, May Street
Enfield, NH 03748
USA

Phone: +1 (603) 632-7377
Fax: +1 (603) 632-5611
e-mail: sales-usa@ttp.net

Preface

In order to be organized as a leading annual international conference of IAMR for researchers, scientists to participate all over the world, Annual International Conference on Intelligent Materials and Nanomaterials (AIMN14) is successfully held on April 18-19, 2014 in Seoul, South Korea.

AIMN14 serves as the important and influential platform for authors to publish manuscripts in excellent international proceedings and exchange new ideas face to face. AIMN14 is the unique conference with its strong organization team, dependable reputation and wide sponsors all around the world.

All accepted papers of AIMN14 have been strictly selected for the quality and the relevance to the conference. We sincerely hope that the current selected papers provide a good overview of the research activities related to advanced materials and engineering. These new materials includes, intelligent materials, nanomaterials synthesis and properties, nano devices and system, nano materials, technologies for applications, materials/nanufacturing processes, etc.

The volume of AIMN14 is expected to boast future research activities within the new actions, meetings and conferences and this volume is provided not only for the readers abroad overview of the latest research results on material science and related fields, but also for those who wish to have a valuable summary and reference in these fields.

We would like to express our sincere appreciations to all the authors for their contributions to this volume. We are indebted to all the referees for their constructive comments on the papers. Many thanks are also warmly given to Trans Tech Publications, the distinguished publisher of AIMN14.

All staffs of AIMN14 Organizing Committees from IAMR look forward to your continuous attention and support to this Annual International Conference in the future.

AIMN14 Organizing Committees

Committees

Honorary Chairs

Prof. Vikas Tomar, Purdue University, USA

Editorial Chairs

Prof. Taufiq Yap Yun Hin, Universiti Pertanian Malaysia (UPM), Malaysia

PC Co-Chairs

Prof. Elias Saion, Universiti Pertanian Malaysia (UPM), Malaysia

Prof. Razali Ismail, Universiti Teknologi Malaysia (UTM), Malaysia

Prof. Jeonghoon Yoo, Yonsei University, South Korea

Prof. Min Chen, Aalborg University, Denmark

Dr. Xufeng Dong, Dalian University of Technology, China

Prof. Mohd Sapuan Salit, Universiti Pertanian Malaysia (UPM), Malaysia

Prof. Kurapati Srinivas, GMR institute of technology, India

Prof. Jayabalan M, Biomaterials Subject Group of MRSI, India

Prof. Avishai Yshai, Ben-Gurion University of the Negev, Israel

Dr. Othman Inayatullah, Universiti Pertanian Malaysia (UPM), Malaysia

Steering Committee Chairs

Prof. Choi Changhwan, Hanyang University, South Korea

Prof. Kun Zhao, China University of Petroleum (Beijing)

Table of Contents

Chapter 3: Composites and Alloys

Chapter 4: Manufacturing Processes, Materials Forming and Machining

Chapter 5: Power Systems, Energy and Environmental Engineering

Chapter 6: Applied Mechanics and Engineering

CHAPTER 1:

Advanced Materials, Technologies and Applications

Advanced Materials Research Vol. 983 (2014) pp 3-6

doi:10.4028/www.scientific.net/AMR.983.3

Gangue as Flame Retardants for Flexible Poly (Vinyl Chloride) [1]

Ming Gao[1,a], Chun-guang Song [1,b] ,Dan Rong[1,c],Yu-wen Ji[1,d]

[1] School of Environmental Engineering, North China University of Science and Technology, Box 206,Yanjiao Beijing 101601, China

[a] gaoming@ncist.edu.cn, [b] 1114149912@qq.com, [c] 2235697702@qq.com, [d] 1633910613@qq.com

Key words: Gangue, flame retardant, aluminum hydroxide ,PVC

Abstract: Gangue as flame retardant was used to PVC, the mechanical properties and flame retardance of the samples were studied. The resultant data show that gangue little effect on the mechanical properties of the sample, especially tensile strength, yield stress, and 10% of gangue obtained good flame retardance. PVC treated with flame-retardants showed a high limiting oxygen index, char yield, which indicated that the flame retardance of the treated PVC was improved.

Introduction

PVC materials or products tend to have excellent fire performance. But to make it easy to process, semirigid and flexible PVC compound always contains a large volume of plasticizer such as DOP [di(2-ethylhexyl)phthalate], which can deteriorate the flame retardation and smoke suppression properties. When the PVC products contain 45 parts DOP, the limiting oxygen index (LOI) would decrease to about 24 and the PVC would thus become a high-flammability material. However, plasticized PVC products can still have good fire performance, particularly if additionally fire-retarded [1,2].

In recent years, the use of metal hydroxide flame retardant and smoke suppressant in PVC has been reported [3,4].These flame-retardants, e.g., $Mg(OH)_2$, $Al(OH)_3$ are required at high concentrations (40–60%) for imparting a good degree of flame retardancy. Because of the high loading it is essential that good degree of flame retardancy be obtained, but mechanical properties decrease obviously. Using coupling agents and synergists are good ways to solving this problem [5–7]. Many elements, such as alloys, organic substances and inorganic compounds including antimony, tin, zinc, copper, iron and molybdenum, have been used in the flame retardation and smoke suppression of PVC. Gangue contains many kinds of metal oxides, which may have the similar effective.

The purpose of our present study is to study mechanical properties, flame retardant of the samples treated with combinations of $Al(OH)_3$ and gangue.

Experimental

Materials

PVC, S G Type 2, dioctyl phthalate (DOP); Tribasic lead sulfate, Dibasic lead phosphate, commercially available; Stearic acid, industrial grade; $Mg(OH)_2$, industrial grade; $Al(OH)_3$, ZX-131 type.

Instrumentation

LOI values were determined in accordance with ASTM D2863-70 by means of a General Model HC-1 LOI apparatus. The vertical burning test was conducted by a CZF-II horizontal and vertical burning tester (Jiang Ning Analysis Instrument Company, China). The mechanical properties were

tested according to GB/T 1040.2-2006 standard with a LJ-5000 tensile testing machine (Chengde Experimental Factory).

Preparation of Flame Retardant PVC Samples

Formulation according to predetermined material (including PVC, three salts, salts of stearic acid, DOP, hydroxide, chloride, coal) are mixed in a mixer 3 to 5 minutes at 35 - 45 °C. Then the mixture was plastified on the two-roll mill at 165°C for 6-8 min, compressed at 180°C to form sheets of 100mm×10mm×3mm. The test specimens were cut from the molded sheets.

Table 1 The composition of the samples

Sample	PVC (g)	DOP (g)	Tribasic lead sulfate (g)	Dibasic lead phosphate (g)	Stearic acid (g)	$Al(OH)_3$ (g)	Gangue (g)	Oxygen index (%)
A	500.0	150.0	7.5	7.5	5.0	0.0	0.0	24.5
B	500.0	150.0	7.5	7.5	5.0	5 0.0	0.0	26.6
C	500.0	150.0	7.5	7.5	5.0	75.0	0.0	28.4
D	500.0	150.0	7.5	7.5	5.0	100.0	0.0	29.5
E	500.0	150.0	7.5	7.5	5.0	125.0	0.0	29.4
F	500.0	150.0	7.5	7.5	5.0	125.0	5.0	29.7
G	500.0	150.0	7.5	7.5	5.0	125.0	10.0	29.8
H	500.0	150.0	7.5	7.5	5.0	125.0	15.0	29.2
I	500.0	150.0	7.5	7.5	5.0	125.0	20.0	27.9

RESULTS AND DISCUSSION

Flame retardancy of $Al(OH)_3$ and gangue

$Al(OH)_3$ as one halogen-free, flame-retardant additives, inorganic acid, used in plastics and rubber industry, attracted widespread attention. From the oxygen index values in Table 1, the flexible PVC added $Al(OH)_3$ has good flame retardancy, whose LOI increase from 24.5% to 29.4%. The flame-retardant effect of $Al(OH)_3$ in soft PVC is mainly based on their dehydration endothermic effect, thus inhibiting soft PVC temperature from rising. When addition of $Al(OH)_3$ reaches 100g, the best effect is obtained.

To get better flame retardancy for PVC, gangue was added. The data were shown in Table 1, LOI of samples (F,G) increase with the addition of gangue. When more gangue was added, the LOI of samples decrease, 10g gangue is optimal. Gangue and Al $(OH)_3$ can be a good flame retardant for flexible PVC.

Effect of $Al(OH)_3$ and gangue on the Mechanical Properties

Mechanical properties such as tensile strength, breaking strain, yield stress and tensile modulus of samples were measured, and shown in Figs.1-4.

Fig.1 shows the effect of the gangue on tensile strain of samples (TS), which shows that the TS increase when the added gangue's weight is less than 5g, when it is more than 5g and less than 10g, the TS decrease. When it is more than 10g and less than 15g, the TS second increase but slowly, while more than 15g, the TS decrease.

Fig.2 shows the effect of the gangue on breaking strain of samples (BS). We can see that the BS increase when the added gangue's weight is less than 7g, the BS start decreasing when the weight is more than 7g. Obviously, the highest value of BS is obtained when the gangue's weight is 7g.

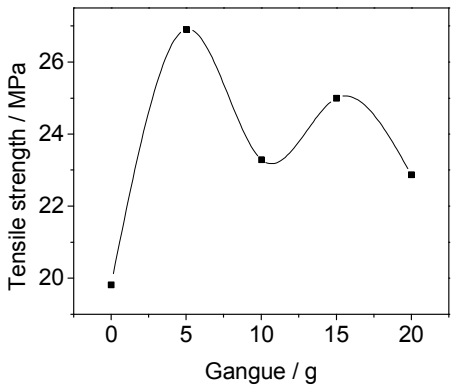

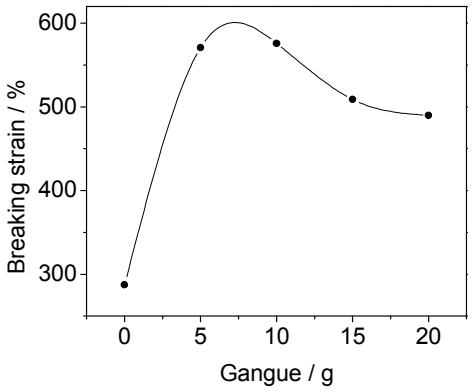

Fig.1 Tensile strength of samples **Fig.2** Breaking strain of samples

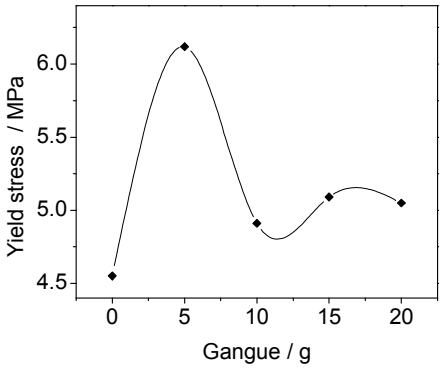

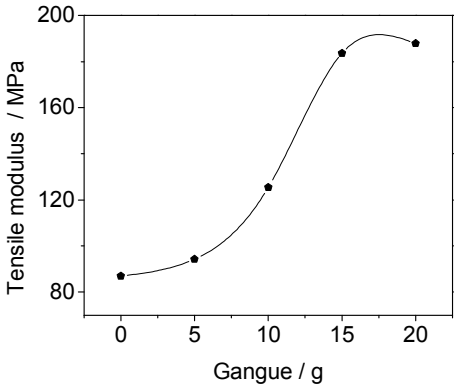

Fig.3 Yield stress of samples **Fig.4** Tensile modulus of samples

Fig.3 shows the effect of the gangue on yield stress of samples (YS). When the added gangue's weight is less than 5g, the YS keep increasing, then the YS decreases, sometimes it also has slightly increase, when the gangue's weight is 5g, the YS has its highest value.

Fig.4 shows the effect of the gangue on tensile modulus of samples (TM). The TM constantly increases. However, the TM is much greater in the range of 5-10g of gangue.

Similar to other additives, the gangue can reduce some mechanical properties. This is because the interactions among the polymer molecules were decreased and the movement of the polymer chains was limited when the flame-retardants reached at 15g.

Analysis of Char Yield

Fig.5, 6 present the SEM photographs of the surface of char of the samples (sample A, sample G). From Figure 5, it can be observed that the char is very slight, loose and soft, which could not protect the underlying material from fire. Contrarily, Figure 6 shows that the char is compact, tough and hard though there are some holes on the surface. It is possible that the gangue could promote the formation of effective charring layer. The structure of the intumescent charring layer may increase the efficiency of the flame retardancy, act as heat insulation, and protect inner matrix materials.

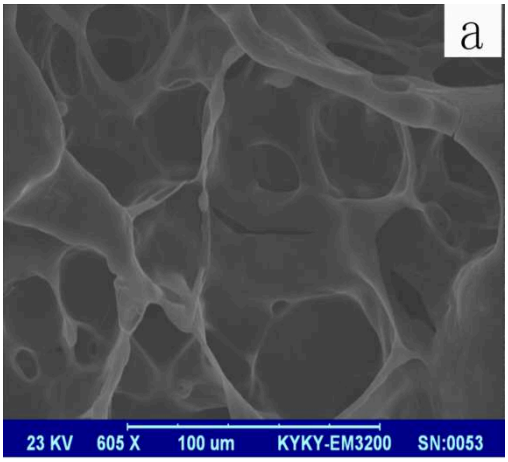

Fig.5 SEM photographs of sample A

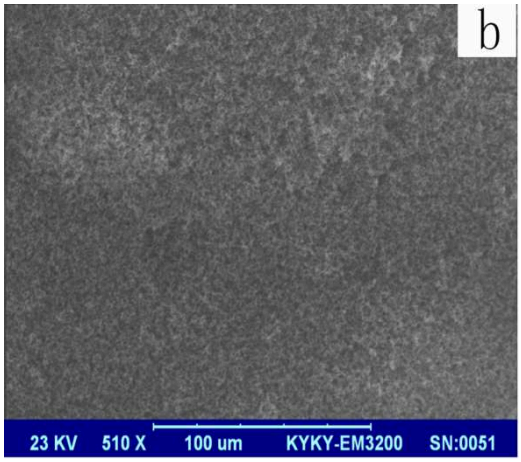

Fig.6 SEM photographs of sample G

Conclusions

10g gangue and 100g Al (OH) $_3$ were added can obtain a good flame retardant for flexible PVC, whose LOI reached 29.8%. Gangue has little effect on the mechanical properties of the sample, especially tensile strength, yield stress. The flame-retardant effect of $Al(OH)_3$ in soft PVC is mainly based on their dehydration endothermic effect, thus inhibiting soft PVC temperature from rising. Gangue could promote the formation of effective charring layer. The structure of the intumescent charring layer may increase the efficiency of the flame retardancy, act as heat insulation, and protect inner matrix materials.

[1] Contract grant sponsor: Fundamental research funds for the Central Universities: 3142013102.

References

[1] Hirschler, M.M. (1998). Fire Performance of Poly (Vinyl Chloride) Updated and Recent Developments, Flame Retardants, 98: 103.

[2] Hirschler, M.M. (1982). Recent Developments in Flame-Retardant Mechanisms, Development in Polymer Stabilisation, Vol. 5, p. 107, Applied Science Publ, London.

[3] Tong, N. and Shaoyun, G. (2000). Flame-Retardant and Smoke-Suppression Properties of Zinc Borate and Aluminum Trihydrate-Filled Rigid PVC, J. Appl. Polym. Sci., 77: 3119.

[4] Hornsby, P.R. and Watson. C.L. (1990). A Study of the Mechanism of Flame Retardance and Smoke Suppression in Polymers Filled with Magnesium Hydroxide, Polymer Degradation and Stability, 30: 73.

[5] Jha, N.K., Misra, A.C. and Bajaj, P. (1984). Flame-Retardant Additives for Polypropylene, J. Macromol Sci., Rev. Macromol. Chem. Phys., C24: 1: 69.

[6] Pearce, E.M. (1986). Flame Retardants for Polymer Systems, Pure & Appl. Chem., 58: 925.

[7] Shigco, M., Takeshi, I. and Hitoshi, A. (1980). Fire-Retarding Polypropylene with Magnesium Hydroxide, J. Appl. Polym. Sci., 25: 415.

Advanced Materials Research Vol. 983 (2014) pp 7-10

doi:10.4028/www.scientific.net/AMR.983.7

Novel Thermo Thickening Smart Gel with Interpenetrating Polymer and Surfactant Network

Jiang Yang[1,2,a], Yining Zhou[2], Yongjun Lu[1], Weixiang Cui[1], Xiaohui Qiu[1], Baoshan Guan[1], Yunhong Ding[1]

[1]Research Institute of Petroleum Exploration & Development-Langfang, PetroChina, Hebei, China

[2]Department of Petroleum Engineering, Xi'an Petroleum University, Xi'an, Shaanxi, China

[a] Corresponding author email: jyang98@126.com

Keywords: Thermo gel, Surfactant, Polymer, Wormlike Micelle

Abstract

A novel smart gel based on interpenetrating network of anionic polymer and surfactant was investigated. A supramolecular assembly structured gel is formed by associating polymer side chain with wormlike micelle of surfactant. The physical interaction of val der vaal and hydrogen bonding force between surfactant and polymer gives a strong viscoelastic gel at evaluated temperature. The viscoelastic properties and gel structure were characterized by dynamic rheometer and cryo-TEM. The polymer and VES complex gel is highly elastic, which elastic moduli G' is higher than loss moduli G'' at low angular frequency, 0.1 rad/s, in high temperature. The total concentration of surfactant and polymer is low which is economically to use in industries.

Introduction

The smart intelligent materials which properties can be controlled by environmental changes are much interested research areas around the world. The environmental change can be electrical, magnetic, light, thermal and pH etc. Among these materials, the polymer could be designed from molecular structure and form smart materials in response different environmental changes [1-4]. The small molecules such as surfactant can also form different aggregates which respond to environmental changes [5-8]. The microstructure changes can induce major changes in the macroscopic properties such as viscoelasticity and solid-liquid transition. The intelligent materials have been used in pharmaceutical [9], automobile [10], drag reduction [11] and oil industry [12,13] etc.

Thermo thickening gel is interested for application in oil and pharmaceutical industries, where fluid has lower viscosity at low temperature and form gel at higher temperature. In oil and gas stimulation operation, fluid is preferred to have low viscosity at low temperature for easy of pumping with low friction pressure, and form viscoelastic gel to suspend proppant particles at high temperature at reservoir. For example, sodium erucate as surfactant can transform from fluid to elastic gel at high temperature above its Kraft temperature [7]. Polymer and surfactant could have synergistic interaction at certain condition. For examples, associating polymer can interact with spherical micelle and formed the network [14]. We hereby study a new class of surfactant with wormlike micelle structure in combination of associating polymer. The new system forms viscoelastic fluid at broader range of concentration and forms stronger gel at higher temperature. The complex gel can be used in oil and gas stimulation.

Experiment

Materials

Amphoteric surfactant with C18 chain length and hydrophobically modified polyacrylamide polymer with anionic group (AP) were made by our lab. Anionic surfactant, sodium lauryl sulfate, was received from Sinopharm Chemcial Co, China. Conventional polyacrylamide with anionic group (CP) was obtained from Beijing Henju Co. Water was deionized.

Methods

Rheological properties were measured by a Haake Mars II Rheometer Pressured Cell. Dynamic properties were measured by cone and plate geometry on rheometer.

Cryo-transimission electron microscopy (Cryo-TEM) observation of surfactant solution was carried out in a controlled-environment vitrification system. Samples were prepared at 25 °C and 100% RH on a Quantifoil holey carbon grid (Electron Microscopy Sciences). The grid was quenched rapidly in liquid ethane at -180 °C and then transferred to liquid nitrogen (-196 °C) for storage. Imageing of the samples was performed using JEM2010 cryo-microscope with a Gatan 626 cryoholder. The acceleration voltage was 200 keV, and the working temperature was kept below -170 °C. Digital images were recorded using a charge-coupled device camera (Gatan 832).

Results and Discussions

The surfactant studied is a mixture of amphoteric and anionic surfactant (MS) similar to system studied previously [6]. The surfactant system showed viscoelastic behavior itself above certain concentration which forms entangled wormlike micelle structure. The viscosity of surfactant and polymer with variation of temperature is shown in Fig. 1. It can be seen that viscosity of fluid with single surfactant or polymer all decreases as temperature increases. The viscosity in mixture of conventional polymer (CP) and surfactant (MS) also decreases with increasing temperature. However, the viscosity in mixture of hydrophobically modified polymer (AP) and surfactant (MS) increases with increasing temperature. The overall concentration of mixed AP and MS is also higher than their individual combined. Hence, there is positive synergism interaction between these two materials at increasing temperature. It can be seen that viscosity starts to increase above 50 °C. This behavior could be due to the increase of solubility of longer chain surfactant at higher temperature. The complex fluid formed between associating polymer (AP) and surfactant (MS) is a highly elastic gel as shown in Table 1, which the storage modulus, G', is larger than loss modulus, G'' at frequency 0.1-100 rad/s.

At further higher temperature above 80 °C, formation of branches along the micelles leading to a multionconnected rather than an entangled network. Branch junction points increase the number of possible configurations, enabling percolation, and the formation of extended micellar networks, which leads to a multiconnected rather than an entangled network of cylindrical micelles. Hence the visocosity decreases for branched worm-like micelles.

The driving force for this increased viscosity in mixed polymer and surfactant system is due to physical crosslinking of polymer and surfactant through intermolecular val der vaal interaction of hydrophobic side chain in associating polymer and surfactant micelle. In addition, hydrogen bonding between the polymer hydrophilic and surfactant head group could also reinforce their interaction and crosslinking. The interpenetrating network of wormlike micelle from surfactant and hydrophobic modified polymer is graphically shown in Fig. 2a.

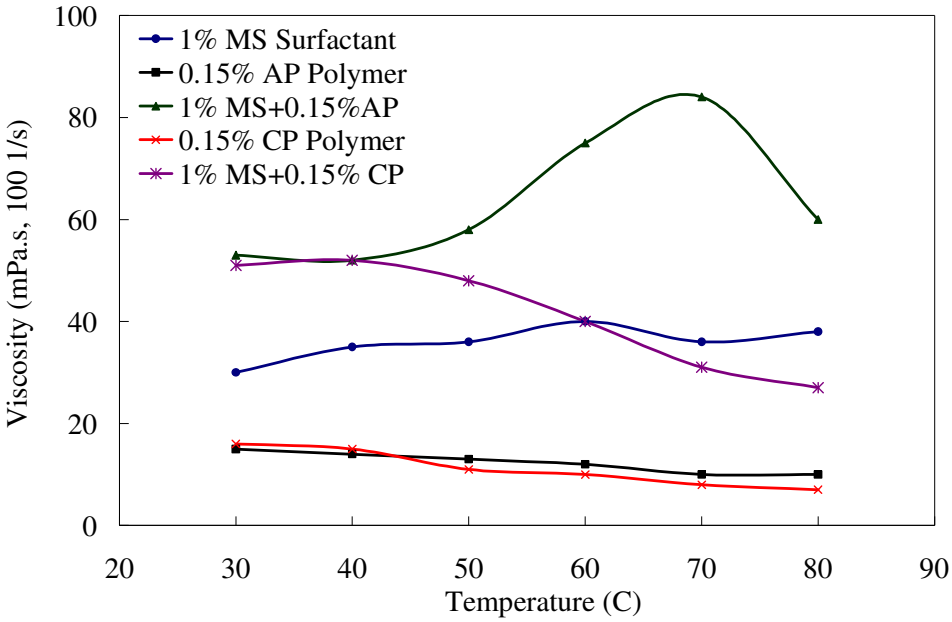

Figure 1. Viscosity versus temperature for polymer, surfactant and their mixture.

Table 1. Storage modulus (G') and loss modulus (G'') versus angular frequency for 1% mixed surfactant (MS) and 0.15% associating polymer (AP) at 70 °C.

Augular Frequency [rad/s]	0.10	0.40	1.58	6.31	25.10	100.00
G' [Pa]	5.45	6.36	7.78	9.37	11.20	11.90
G'' [Pa]	1.37	1.48	1.69	2.10	2.80	4.16

The presence of wormlike micelle structure in surfactant studied is directly confirmed by Cyro-TEM observation as shown in Fig. 2b. It can be seen that threadlike structure with about 10nm in diameter and >1 μm in length exists. The wormlike micelles entangle with each other as well as polymer gives highly elastic gel.

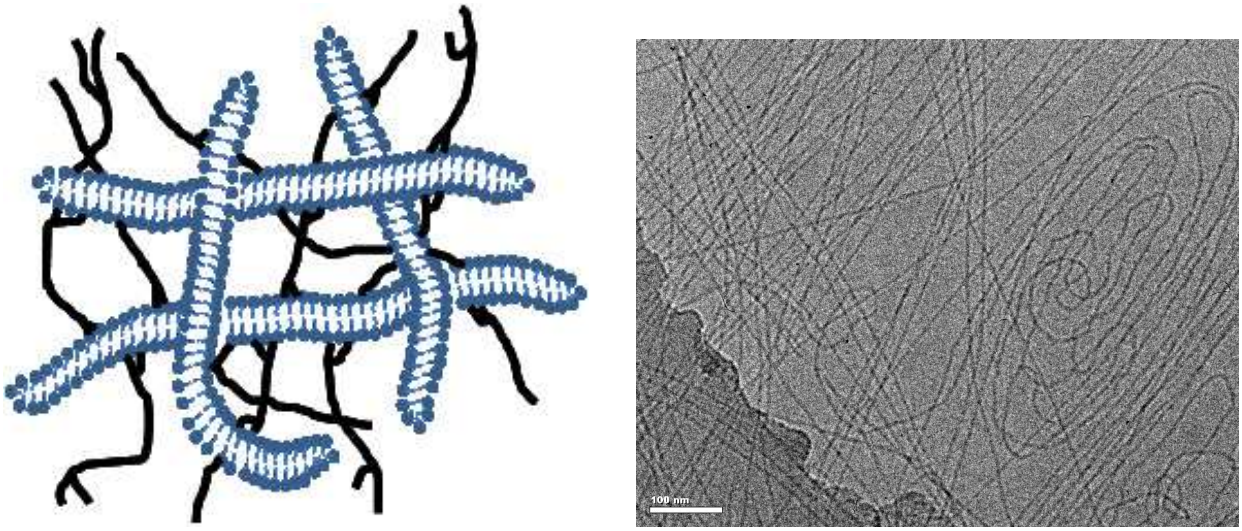

(a) **(b)**

Figure 2. **(a)** Illustrated crosslink model of wormlike micelle and associating polymer. **(b)** Cryo-TEM micrographs of wormlike micelle in mixed ampheteric and anionic surfactant (1%, wt) at 25 °C.

Conclusions

A novel smart gel based on interpenetrating network of anionic polymer and surfactants was formed through physical crosslink. The val der vaal and hydrogen bonding interaction between wormlike micelle and polymer network gives strong viscoelastic gel. The gel strength is stronger at evaluated temperature. The smart gel is useful as stimulation fluids in oil and gas industry, hydraulic fluid, household and personal care products.

Acknowledgement

The authors acknowledgement the supports from the National Hi-Tech Development (863) Plan Project (2013AA064801) and National Natural Science Foundation of China (Grant No 51174163).

References

[1] J. Zhang, R.D.K. Misra, Magnetic drug-targeting carrier encapsulated with thermosensitive smart polymer: Core–shell nanoparticle carrier and drug release response, Acta Biomaterialia, 3 (2007) 838-850.
[2] G. Filipcsei, I. Csetneki, A. Szilágyi, M. Zrínyi, Magnetic field-responsive smart polymer composites, Advances in Polymer Science, 206(2007)137-189.
[3] M. S. Yavuz, Y. Cheng, J. Chen et al, Gold nanocages covered by smart polymers for controlled release with near-infrared light, Nature Materials, 8 (2009)935-939.
[4] K. Al-Tahami, J. Singh, Smart polymer based delivery systems for peptides and proteins, Recent Patents on Drug Delivery & Formulation, 1(2007) 65-71.
[5] J. Yang, Cur. Viscoelastic wormlike micelles and their applications, Opin. Colloid Interface Sci., 7(2002) 276-281.
[6] J. Yang, Z. Yang, Y. Lu et al, Rheological properties of zwitterionic wormlike micelle in presence of solvents and cosurfactant at high temperature， J. Dispersion Sci. Tech. 34 (2013) 1124-1129.
[7] Y. Zhang, Y. Han, Z. Chu, S. He, J. Zhang, Y. Feng, Thermally induced structural transitions from fluids to hydrogels with pH-switchable anionic wormlike micelles, J. Col. Interf Sci, 394 (2013) 319–328.
[8] R. Kumar , A. M. Ketner, S. R. Raghavan, Nonaqueous photorheological fluids based on light-responsive reverse wormlike micelles, Langmuir, 26 (2010) 5405–5411.
[9] A.S. Hoffman, “Intelligent” polymers in medicine and biotechnology, Macromolecular Symposia, 98 (1995) 645–664.
[10] A.G. Olabi, A. Grunwald, Design and application of magneto-rheological fluid, Materials & Design, 28(2007) 2658-2664.
[11] Y. Qi, J.L. Zakin, Chemical and rheological characterization of drag-reducing cationic surfactant systems, Ind. Eng. Chem. Res., 41(2002) 6326-6336.
[12] L. Li, H.A.Nasr-El-Din, K.E. Cawiezel. Rheological properties of a new class of viscoelastic surfactant, SPE Prod. Oper, 25(2010) 355-366.
[13] Y.J. Lu, B. Fang, D. Y. Fang et al, Viscoelastic surfactant micelle systems and their rheological properties, Oilfield Chemistry, 20(2003)291-294.
[14] N. Gaillard, A.Thomas, C. Favero, Novel associative acrylamide-based polymers for proppant transport in hydraulic fracturing fluids, SPE International Symposium on Oilfield Chemistry, SPE-164072, 8-10 April, The Woodlands, Texas, 2013.

Advanced Materials Research Vol. 983 (2014) pp 11-15

doi:10.4028/www.scientific.net/AMR.983.11

Smart and Robust Composite Tube Columns Frames for Offshore Sub-Structure Construction

Thar M. Badri Albarody[a,*], Zahiraniza Bt Mustaffa[b] and Mohd Shahir Liew[c]

Civil Engineering Department, Universiti Teknologi PETRONAS, Bandar Seri Iskandar,

31750 Tronoh, Perak, Malaysia

[a]t.albarody@ymail.com, [b]zahiraniza@petronas.com.my, [c]shahir_liew@petronas.com.my

Keywords: Offshore Structure; Steel-encased Composite; Nano-Hyprid Composite; FGM; Laminated Shell theory.

Abstract. Offshore industry has been welcoming to composite material for its saliences. Features such as corrosion and temperature resistance, construction cost reduction, and superb fatigue performance are some of the reasons for this choice. Steel tube-encased composite is an appropriate found composite replacement for traditional offshore construction. Regardless of all its advantages, they suffer from the interfacing problem between composite and steel layers; however, magnetostrictive nanofillers are proposed to increase the integration between the layers. Therefore, current effort is discussed the vibrational behavior of the proposed robust steel tube column as well as the actuation characteristics of the magnetostrictive nanofillers in encased composite. The result reveals that, the steel tube-encased composite columns exhibit greater stiffness in compare with traditional steel tube. Furthermore, magnetostrictive nanofillers have shown higher actuation capability of vibration at seismic mode.

Introduction

Composites have found extensive applications in the oil & gas industry since last two decades. Significant advances have been made in the areas of composite pipe work and fluid handling [1, 2]. The high cost to replace steel elements in retrofit applications and increased longevity in new construction are driving the use of composites, which withstand severe conditions as experienced in offshore environment [3, 4]. In the offshore oil and gas industry, the cost of manufacturing and erecting oil rigs could be reduced significantly if heavy metal column could be replaced with lighter ones made of composites. Composite column also could be used for:

1. Replace steel components to eliminate corrosion
2. Exhibit excellent fatigue performance, good resistance to temperature extremes and wear, especially in offshore industrial sectors.
3. Build lighter structures to increase platform performance.
4. Improved combat survivability.
5. Produce complex structural parts at reduced cost, especially in quantity
6. The tailorability of composites to suit specific applications has been one of its greater advantages such as imparting low thermal conductivity, low coefficient of thermal expansion, high axial strength and stiffness etc.

Therefore, offshore engineering center in Universiti Teknologi PETRONAS (OECU) has shifted attention to the development of composite structures of carbon and/or glasses fiber reinforced epoxy and steel for offshore jacket sub-structure construction with the aim of becoming a medium-scale contractor with leading-edge technology. Steel Tube-Encased Composite (STEC) column is developed essentially as weldable tubular structural element expected to be good replacement of traditionally steel tubes in offshore industrial facilities constructions. However, still the interfacing problem between composite and steel layers in STEC represent a challenge to be work out.

Therefore, a Nano-Hyprid-functionally graded composite (NHFG) proposed to increase the integration between the layers and grading the structural properties across tube thickness using magnetic nanoparticles as fillers. Furthermore, such functional composites could utilize the magnetostrictive properties to actuate the vibration inside the composite tubes. Several models have been found in the literature dealt with functional composite [5, 6]. Some of them could specialize to demonstrate the vibrational behavior of multilayered and functionally graded magnetostrictive composite. Albarody, et.al., [5] derived the exact solution for linearly constitutive properties, simply supported, functional composite shell subjected to static and dynamic loadings. The authors were investigated and analyzed the effects of the material properties, lay-ups of the constituent layers, and shell parameters under the free vibration behavior.

In this paper, a STEC columns filled with magnetic nanoparticles is modeled and the vibrational characteristic is discussed. Also, some of NHFG composite are examined.

Theoretical Formulation

Based on Hamilton's variational principle linked with Gibbs free energy functions, the steel tube-encased composite model is casted according to the first-order shear deformation shell theory. The exact solution is derived for linearly magnetostrictive constitutive properties, simply supported, and thick shell having rectangular plane-form. Expressed in the (meter–kilogram–second) system of units, the generation procedure of thick composite shell model, written in curvilinear coordinates and provides the much-needed materials in state of the smart or adaptive materials are as follows;

1. **Constitutive Relations:** In a system gather mechanical, magnetic, and thermal influences, the constitutive relations are expressed formally as:

$$S_{ij} = [\varsigma^{G,T}_{ijkl}\varepsilon_{ij} - \kappa^{T}_{pkl}\chi_p - \lambda^{G}_{kl}\tau], \tag{1}$$

2. **Kinematic Relations:** According to the FOSD shell theory, the following representation of the 3D displacement and magnetic potentials is postulated:

$$u(\alpha,\beta,\zeta,t) = u_o(\alpha,\beta,t) + \zeta\psi_\alpha(\alpha,\beta,t), \qquad v(\alpha,\beta,\zeta,t) = v_o(\alpha,\beta,t) + \zeta\psi_\beta(\alpha,\beta,t),$$

$$w(\alpha,\beta,\zeta,t) = w_o(\alpha,\beta,t), \quad \text{and} \quad \vartheta(\alpha,\beta,\zeta,t) = -\big(\vartheta_o(\alpha,\beta,t) + \zeta\vartheta_1(\alpha,\beta,t)\big), \tag{2}$$

where u_o, v_o, and w_o are referred to as the mid-surface displacement functions, and ψ_α and ψ_β are the midsurface rotation functions of the shell, and ϑ is the magnetic potential function. The strains at any point in the shell can be written in terms of mid-surface strains and curvature changes as:

$$\begin{aligned} &\varepsilon_\alpha = (\varepsilon_{o\alpha} + \zeta\varepsilon_{1\alpha}), \qquad \varepsilon_{\alpha\beta} = \big(\varepsilon_{o\alpha\beta} + \zeta\varepsilon_{1\alpha\beta}\big), \quad \varepsilon_{\alpha\zeta} = \big(\varepsilon_{o\alpha\zeta} + \zeta\,\psi_\alpha/R_\alpha\big),\\ &\varepsilon_\beta = \big(\varepsilon_{o\beta} + \zeta\varepsilon_{1\beta}\big), \qquad \varepsilon_{\beta\alpha} = \big(\varepsilon_{o\beta\alpha} + \zeta\varepsilon_{1\beta\alpha}\big), \quad \varepsilon_{\beta\zeta} = \big(\varepsilon_{o\beta\zeta} + \zeta\,\psi_\beta/R_\beta\big). \end{aligned} \tag{3}$$

However, the mid-surface strains as well as the curvature and twist changes are extended by Codazzi-Gauss geometric relations, as [6]. The distributions of magnetic fields at any point in the composite shell are assumed as:

$$\chi_\alpha = (\chi_{o\alpha} + \zeta\chi_{1\alpha}), \qquad \chi_\beta = \big(\chi_{o\beta} + \zeta\chi_{1\beta}\big). \tag{4}$$

and the magnetic field changes are

$$\chi_{o\alpha} = -\frac{1}{A}\frac{\partial\vartheta_o}{\partial\alpha}, \quad \chi_{1\alpha} = -\frac{1}{A}\frac{\partial\vartheta_1}{\partial\alpha}, \quad \chi_{o\beta} = -\frac{1}{B}\frac{\partial\vartheta_o}{\partial\beta}, \quad \chi_{1\beta} = -\frac{1}{B}\frac{\partial\vartheta_1}{\partial\beta}. \tag{5}$$

3. **Kinetic Relations:** The elastic, electric, and magnetic force and moment resultants are obtained by integrating the constitutive relations (1) over the shell thickness as below:

$$\{N_n\ ,\ M_n\} = \int_{-\frac{h}{2}}^{\frac{h}{2}} (1, \zeta)\{S_{ij}\}\gamma_n d\zeta + \{N_n^T,\ M_n^T\}, \tag{6}$$

where $\gamma_n = (1 + \zeta/R_n)$, the subscripts n denote either of α, β or $\alpha\beta$, and h is the shell thickness. In order to gain a numerical stability and pursue a possible integration of Eq. (6) in absence of thermal forces, the term $(1 + \zeta/R_n)$ should be expanded in a geometric series as in [7, 8].

4. **Variational Principle:** The variational energy method via the Hamiltonian axiom has been used by [9, 10] for coupling of the energy phenomena and to derive a consistent set of equations of motion coupled with the free charge equation. In summary, the total energy of a shell element can be defined as:

$$\delta \int_{t_o}^{t_1} (K - P)\, dt = 0, \tag{7}$$

where P is the total potential energy induced in the system given by:

$$P = \iiint_V \left[\varsigma_{ijkl}^{G,T}\varepsilon_{ij} - \kappa_{pkl}^{T}\chi_p - \lambda_{kl}^{G}\tau\right]dV \ - \iint_{\Omega_o} \left(t(S_i, G_{l,}) + W(S_i, G_{l,})\right), \tag{8}$$

where $Q(S_i, G_l, T)$ is the thermodynamic potential. $t(S_i, G_{l,})$ and $W(S_i, G_l)$ are the tractions and the work done by body force, and magnetic charge, respectively. The kinetic energy is given as:

$$K = \frac{I}{2}\iint_{\Omega_o} \int_{-\frac{h}{2}}^{\frac{h}{2}} \left((\dot{u}_o^2 + \dot{v}_o^2 + \dot{w}_o^2) + \zeta^2(\dot{\psi}_\alpha^2 + \dot{\psi}_\beta^2) + 2\zeta(\dot{u}_o^2\dot{\psi}_\alpha^2 + \dot{v}_o^2\dot{\psi}_\beta^2)\right)\gamma_\alpha\gamma_\beta\, ABd\zeta dA. \tag{9}$$

The traction is

$$t(S_i, G_l) = \left(\tilde{S}_{nn}\delta u_n + \tilde{S}_{nt}\delta v_t + \tilde{S}_{n\zeta}\delta w_r\right) + \left(\tilde{G}_{nn}\delta\vartheta + \tilde{G}_{nt}\delta\vartheta\right) \tag{10}$$

and the external work is

$$W(S_i, G_l) = \left(F_\alpha^S u_o + F_\beta^S v_o + F_n^S w_o + C_\alpha^S\psi_\alpha + C_\beta^S\psi_\beta\right) - \left(F^G\,\vartheta_o + C^G\,\vartheta_1\right), \tag{11}$$

where F_α^S, F_β^S, and F_n^S are the distributed forces in α, β and ζ directions, respectively, while C_α^S and C_β^S are the distributed couples about the middle surface of the shell. F^G and C^G are the distributed forces and couples due to the magnetic charge. Hence, the temperature, τ is a known function of position and enter the formulation only through the constitutive equations. Substituting Eqs. (1, 10, and 11) into Eq. (8) and equating the resulting equation with Eq. (9), yields after expanding the terms:

$$\delta\int_{t_o}^{t_1}\iint_{\Omega_o}\begin{pmatrix}\frac{\bar{I}_1}{2}(\dot{u}_o^2 + \dot{v}_o^2 + \dot{w}_o^2) + \frac{\bar{I}_3}{2}(\dot{\psi}_\alpha^2 + \dot{\psi}_\beta^2)\\ +\bar{I}_2(\dot{u}_o^2\dot{\psi}_\alpha^2 + \dot{v}_o^2\dot{\psi}_\beta^2)\end{pmatrix}ABdAdt - \int_{t_o}^{t_1}\iiint_V (\varsigma_{ij}\varepsilon - \kappa_{ij}\chi - \lambda_i\tau\delta\varepsilon)\, dVdt$$

$$+\int_{t_o}^{t_1}\iint_{\Omega_o}\left(\tilde{S}_{nn}\delta u_n + \tilde{S}_{nt}\delta v_t + \tilde{S}_{n\zeta}\delta w_r + \tilde{G}_{nn}\delta\vartheta + \tilde{G}_{nt}\delta\vartheta\right)ABdAdt$$

$$+\int_{t_o}^{t_1}\iint_{\Omega_o}\left(F_\alpha^S u_o + F_\beta^S v_o + F_n^S w_o + C_\alpha^S\psi_\alpha + C_\beta^S\psi_\beta - F^G\,\vartheta_o - C^G\,\vartheta_1\right)ABdAdt = 0. \tag{12}$$

Replacing the constitutive terms in Eq. (12) by the kinetic relations (6), then integrating the displacement gradients by parts to obtain only the virtual displacements, we can set the coefficients of δu_o, δv_o, δw_o, $\delta\psi_\alpha$, $\delta\psi_\beta$, $\delta\vartheta_0$ and $\delta\vartheta_1$ to zero, individually. The equations of motion and the charge equilibrium equation for isothermal case are

$$\frac{\partial}{\partial\alpha}BN_\alpha + \frac{\partial}{\partial\beta}AN_{\beta\alpha} + \frac{\partial A}{\partial\beta}N_{\alpha\beta} - \frac{\partial B}{\partial\alpha}N_\beta + \frac{AB}{R_\alpha}Q_\alpha + \frac{AB}{R_{\alpha\beta}}Q_\beta + ABF_\alpha = AB\left(\bar{I}_1\frac{\partial^2 u_o}{\partial t^2} + \bar{I}_2\frac{\partial^2\psi_\alpha}{\partial t^2}\right),$$

$$\frac{\partial}{\partial\beta}AN_\beta + \frac{\partial}{\partial\alpha}BN_{\alpha\beta} + \frac{\partial B}{\partial\alpha}N_{\beta\alpha} - \frac{\partial A}{\partial\beta}N_\alpha + \frac{AB}{R_{\alpha\beta}}Q_\alpha + \frac{AB}{R_\beta}Q_\beta + ABF_\beta = AB\left(\bar{I}_1\frac{\partial^2 v_o}{\partial t^2} + \bar{I}_2\frac{\partial^2\psi_\beta}{\partial t^2}\right),$$

$$-AB\left(\frac{N_\alpha}{R_\alpha} + \frac{N_\beta}{R_\beta} + \frac{N_{\alpha\beta}+N_{\beta\alpha}}{R_{\alpha\beta}}\right) + \frac{\partial}{\partial\alpha}BQ_\alpha + \frac{\partial}{\partial\beta}AQ_\beta + ABF_n = AB\left(\bar{I}_1\frac{\partial^2 w_o}{\partial t^2}\right),$$

$$\frac{\partial}{\partial\alpha}BM_\alpha + \frac{\partial}{\partial\beta}AM_{\beta\alpha} + \frac{\partial A}{\partial\beta}M_{\alpha\beta} - \frac{\partial B}{\partial\alpha}M_\beta - ABQ_\alpha + \frac{AB}{R_\alpha}P_\alpha + ABC_\alpha = AB\left(\bar{I}_2\frac{\partial^2 u_o}{\partial t^2} + \bar{I}_3\frac{\partial^2\psi_\alpha}{\partial t^2}\right)$$

$$\frac{\partial}{\partial\beta}AM_\beta + \frac{\partial}{\partial\alpha}BM_{\alpha\beta} + \frac{\partial B}{\partial\alpha}M_{\beta\alpha} - \frac{\partial A}{\partial\beta}M_\alpha - ABQ_\beta + \frac{AB}{R_\beta}P_\beta + ABC_\beta = AB\left(\bar{I}_2\frac{\partial^2 u_o}{\partial t^2} + \bar{I}_3\frac{\partial^2\psi_\beta}{\partial t^2}\right). \quad (13)$$

here $\bar{I}_1$, $\bar{I}_2$, and $\bar{I}_3$ are the inertia terms defined as:

$$\bar{I}_j = \left[I_j + I_{j+1}\left(\frac{R_\alpha + R_\beta}{R_\alpha R_\beta}\right) + \frac{I_{j+2}}{R_\alpha R_\beta}\right]_{j=1,2,3}, \ [I_1, I_2, I_3, I_4, I_5]$$
$$= \sum_{k=1}^{N}\int_{h_{k-1}}^{h_k} I^k\,(1, \zeta, \zeta^2, \zeta^3, \zeta^4, \zeta^5)d\zeta,$$

where I^k is the mass density of the k^{th} layer of the shell per unit mid-surface area. Eqs. (13) can be written in a matrix form as $\left(K_{ij} + \partial^2/\partial t^2\ M_{ij}\right)\{\Delta\} = \{F - F^T\}$, where K and M are stiffness and mass matrices, respectively, and F^T is the thermal forces. Thus, the forced method will apply satisfying SS boundary conditions and admit specially-orthotropic rectangular laminates, to determine the governing equations that satisfied everywhere in the domain of the shell.

Thus far, the accurate treatment of thermal, magnetic and elastic energies that are taken into account in this smart composite shell that encased a steel tube column, expect yields rather sophisticated equations interlink the magnetic inductions and stress resultants.

Parametric Analysis

As deepwater structures for the future developments are expected to be floating structures. Structural systems that can adapt to the environment automatically offer new vistas for designers and lead to novel efficient developments. An offshore structure that form from the proposed steel tube-encased composite is defined smart due to the actuation capability of the magnetostrictive materials that integrated into structural.

The challenging part of the offshore structural adaption is that the structure is subjected to highly uncertain environmental forces. Thus, the effects of the material properties, and lay-ups of the constituent layers of the encased composite and the steel tube parameters on the vibration behavior are required to be dissected. In Fig. 1, a $CoFe_2O_4$ Nano particle material is scrutinized and the mechanical properties of the encased shell are found to be varied in a very orderly manner across the tube thickness. The STEC tubes that encased with shell made of composite filled with $CoFe_2O_4$ appear with higher stiffness as compared to traditional steel tube and exhibit possible actuations when a magnetic field propagate along the tube.

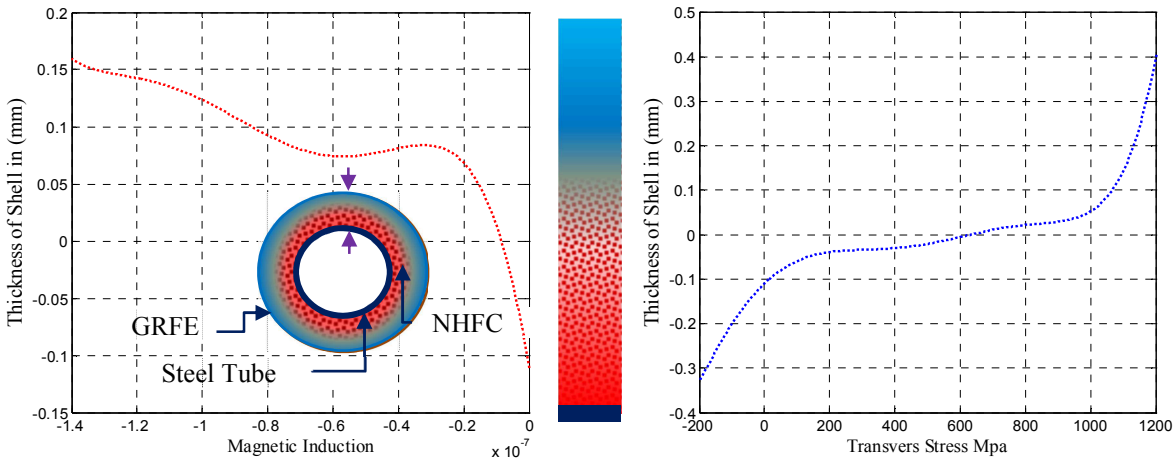

Fig 1. The transvers stresses and magnetic induction across the composite tube thickness, at unity load. GRFE properties are (E_1/ E_2=15, G_{12}/ E_2=0.5, G_{13}/ E_2=0.5, υ_{12}=0.3, a/b=1, a/h=10, and the lamination scheme is $(0/09)_S$), while $CoFe_2O_4$ properties and the grading material properties model can be found in [5].

Conclusions

The evolutionary process of development of adaptive steel tube-encased composite for tubular constructions has opened up new vistas for the several interdisciplinary applications. The benefits of these composite tubes are expected to be enormous. The concept of a structure with capability of automatically responding to the environment by change in the self-configuration, or by changing the interface with the environment is one which offers the potential of extremely attractive advantages in the design, development and operation of offshore structures. The STEC columns comprising magnetostrictive materials have been modeled and scrutinized. The present model may serve as a reference in developing a prototype of STEC columns for further experimentations.

Acknowledgment

Authors would like to acknowledge Universiti Teknologi PETRONAS for sponsoring this work.

References

[1] Z. Mustaffa, M. B. Taufiq, T. M. Badri, Applied Mechanics and Materials 353, 3316 (2013).

[2] T. M. Badri, M. Zahiraniza, M. B. Taufiq, Applied Mechanics and Materials 376, 181 (2013).

[3] Z. Mustaffa, M. B. Taufiq, T. M. Badri, Applied Mechanics and Materials 353, 3280 (2013).

[4] T. M. Badri, M. Zahiraniza, M. Badri Taufiq, Applied Mechanics and Materials 376, 185 (2013).

[5] T. M. B. Albarody, H. H. Al-Kayiem, in Shell Structures: Theory and Application. (CRC Press, Taylor & Francis, ISBN: 978-1-138-00082-7, London, 2013), vol. 3, pp. 49.

[6] T. M. B. Albarody, H. H. Al-Kayiem, M. B. Taufiq, The Theory of Functional and Adaptive Shell Structures. Mschmoeltz, Ed., (LAP LAMBERT Academic Publishing GmbH & Co., ISBN: 978-3-8465-2175-5, Saarbrücken, Germany., 2013), pp. 212 Pages.

[7] Leissa A.W., Chang J., Compos. Struct. 35, 53 (1996).

[8] T. M. Badri, H. H. Al-Kayiem, Asian Journal of Scientific Research 6, 236 (2013).

[9] Y. Bao, University of Kentucky (1996).

[10] T. M. Badri, H. H. Al-Kayiem, Journal of Applied Sciences 12, 2541 (2012).

Advanced Materials Research Vol. 983 (2014) pp 16-19

doi:10.4028/www.scientific.net/AMR.983.16

The research process and application prospect of the smart piezoelectric materials

Xiaoliang Fang[1, a], Weifang Zhang[1, b], Hongxun Wang [1, c]

[1]BeiHang University, School of Reliability and Systems Engineering, Science & Technology Laboratory on Reliability & Environment Engineering, XueYuan Road No.37,HaiDian District, Beijing, China.

[a]bit20092110@live.cn, [b]08590@buaa.edu.cn, [c]wanghongxun1990@163.com

Keywords: Smart piezoelectric materials; Preparation process; Application status and prospects

Abstract: Piezoelectric material which can be used as both sensor and drive is an important kind of smart material. Studies on piezoelectric materials are now the research focus and hotspots of smart materials which have achieved fruitful results. This article describes the working principle of smart piezoelectric materials, provides an overview of the preparation progresses and application status, based on which the research and development trends are discussed.

1. Introduction

The performance requirement of the smart materials is that the perceptions, drive and information processing should be integrated in one system, which is similar to biological materials that have intellectual properties [1]. Smart materials system can get the outside world information by its own perception, make judgment and processing, emit instruction, and then adjust own state and structure to adapt to the changes in the extemal environment. Consequently, the smart materials system fulfill various special functions, such as self-detection, self-diagnosis, self-regulation, self-adaptive and self-repair, which are similar to biological system [2].

The smart materials are based on the function materials which can be divided into two categories according to their different roles playing at work. These can be made into various types of sensors are known perception materials, which are used to sense the signal of stimulation and changes from the outside or internal, such as stress, heat, light and electricity etc. The common perception materials include photosensitive materials, heat-sensitive materials, moisture-sensitive materials, acoustic emission material, inductor material, shape memory materials, magnetostrictive materials, piezoelectric materials etc. These can be made into drivers are known as actuating materials, which can change the shape, size, location, stiffness and structure of their own according to the changes of temperature, electric field and magnetic field etc. The common actuating materials include shape-memory materials, electrostrictive materials, electrorheological fluids, magnetostrictive material, magnetorheological fluid and piezoelectric materials [2, 3, 4].

With the progress of the research of the smart materials, the piezoelectric materials which can be made into both driver and sensor drive more and more attention. Piezoelectric materials are able to achieve mutual transformation between mechanical energy and electric energy. Transforming the changes of the outside pressure into appropriate electric signal, piezoelectric materials fulfill the function of being a sensor, meanwhile piezoelectric materials meet the requirement of being a driver while transforming the electric signal of the excitation source into corresponding mechanical signal, such as the vibration signal and deformation signal [5, 6, 7].

With the rapid development of the materials science, microelectronics and computer technology, the piezoelectric materials show broad prospect of application which catches the interests of the global scientists. Based on the background above, the working principle of smart piezoelectric materials are described; an overview of the preparation progresses and application status are provided and the research and development trends are discussed in this article [5.8].

2. Working principle of the smart piezoelectric materials

The working principle of the smart piezoelectric materials is based on piezoelectric effect. The piezoelectric effect is that when there is a deformation of the materials by external forces, positive and negative electric charges will arise in the relative two surfaces of the material due to an internal polarization at the same time. There are direct piezoelectric effect when mechanical energy is transformed into electrical energy and inverse piezoelectric effect electrical energy is transformed into mechanical energy [3, 5].

3. New preparation technology of the smart piezoelectric materials

3.1 The piezoelectric coatings prepared by plasma spraying method

W Haessler et al. investigated the structure and piezoelectric properties of the PZT coatings prepared by plasma spraying method. They found out that the heat treatment and polarization process after spraying have a significant effect on the piezoelectric properties of the PZT coatings [9].

Songlin Gu, Guolu Li et al. fabricated PZT coatings on the surface of 45 steel by supersonic plasma spraying method. The research results showed that the PZT coatings with a typical layered structure had dense microstructure, of which the surface was flat and the air hole rate was 1.6%. The PZT coating was well bonded to the substrate, which met the requirement of application at actual work [10].

3.2 Piezoelectric ceramic materials prepared by sol-gel method

Piezoelectric ceramic materials fabricated by sol-gel method have high purity, well-distributed chemical constituents and low temperature of reaction compared with these prepared by the traditional solid state reaction.

Minglei Zhao et al. prepared $Na_{0.5}Bi_{0.5}TiO_3$ ceramic by sol-gel method. The piezoelectric constant $d_{33}=173\times10^{-12}$pC/N increased by 40% compared with that fabricated by traditional method. Meanwhile the piezoelectric ceramic in this study had small coercive field and large residual polarization [11].

Y. D. Hou et al. investigated the fabrication of $(Na_{0.8}K_{0.2})_{0.5}Bi_{0.5}TiO_3$ (NKBT) prepared by sol-gel –hydrothermal method and its densification. The analysis of the morphology and structure showed that NKBT nanowire with pure perovskite structure could be prepared by sol-gel-hydrothermal method with the synthetic temperature of 160 ℃, of which the diameter was 50-80nm, and the length was 1.5-2.0μm. The theoretical density of the flake made of NKBT nanowire was more than 98% [12].

3.3 Fabrication of piezoelectric composites

Lei Dai, Shan Hu et al. prepared PZN-PZT/PVDF piezoelectric composite material by solid phase sintering combined with solution blending method, and investigated the properties of the materials. The results revealed that the generation of pyrochlore phase could be restrained by appropriately excessive Pb, but too much Pb would reduce the degree of crystallization of the main crystal phase and the piezoelectric properties of the piezoelectric composite material [13].

4. Application prospect of the smart piezoelectric materials

4.1 Application in structural health monitoring

Due to chemical corrosion, stress effect, tiny impact and influence and other factors, local damage and micro-cracks may appear on the surface of the structure of large aircraft, nuclear

reactors, bridges, and large pipes. On the structure of local damage, especially micro - cracks on the surface of monitoring it is a very important part of structural health monitoring system to monitor the local damage and micro-cracks on the surface of the vital structure [14].

A damage detection method based on an innovative 2D phased sensor array made of piezoelectric paint is proposed for in situ damage detection of a thin isotropic panel using guided Lamb waves. In this study, a 2D phased sensor array with a spiral configuration is fabricated using a piezoelectric composite patch and used for detecting damages in an aluminum panel. Steered array responses are generated from the raw sensor signals using a directional filtering algorithm based on phased array signal processing. To enhance the proposed analysis technique, empirical mode decomposition (EMD) and a Hilbert–Huang transform (HHT) are applied. A new damage detection algorithm including threshold setting and damage index (DI) calculation is developed and implemented for detecting damages in the form of holes and a simulated crack. The characteristic damage indices consistently increase as damage size grows [15].

4.2 Application in energy converter

In order to optimize the deformation and brittleness of the piezoelectric materials, the Langley research center of the NASA fabricated a new kind of smart piezoelectric macro fiber composite (MFC). Tungpimoluryt K, Hatti N et.al designed an energy collection device based on MFC materials. The main structure of the device is cantilever structure with the MFC fixed on the surface of the cantilever. When sinusoidal excitation is applied, capacitor of the energy collection device is used to collect the electric current generated by MFC, so that the function of collecting energy is fulfilled. The study results showed that this device can produce up to 45. 6v voltage [16].

4.3 Application in adaptive wing

Based on the inverse piezoelectric effect, Paradies et al. designed and made an active control wing model of which the wingspan was 500mm.The key parts of the model were seven set of MFC modules. The wings would be controlled to auto-deform while the MFC parts were applied with voltage. The study results showed that the deformation value of the wing end was 4.3mm when the voltage applied was 1.5kV [17].

5. Research prospect of the smart piezoelectric materials

In this paper, new fabrication methods and application of the smart piezoelectric materials are introduced. Although the smart piezoelectric materials have been used in many fields owing to the big driving force and fast response speed, it should be noted that the effects to decrease the brittleness and improve the deformation degree of the smart piezoelectric materials are still needed. The key focus of the study of smart piezoelectric materials are to compound the structures and increase the serviceability. As the synthesis and integration of various materials and high technology, the research of smart piezoelectric materials is bound to have a good and broad prospects.

References

[1] Y. Liu, K. Gall, M.L. Dunn: Mech. of Mater. Vol.36 (2004), p.929.

[2] C. Lin, F. Chen, L. Yuan, G.Z. Liang: FRP/Compo. Vol. 2 (2012), p. 74.

[3] X.M. Zhang: FRP/Compo. Vol. 6 (2013), p. 57.

[4] J.H. Xie, W.G. Zhang, D.K. Liang: Mater. Review. Vol. 20 (2006), p. 6.

[5] C. He, W.G. Chen: Jour. Fun. Mater. Vol. S1 (2010), p. 11.

[6] S.R. Platt, S. Farritor, H. Haider: IEEE/ ASME Transactions on Techtronic. Vol. 10 (2005), p. 240.

[7] Y.X. Bian, C.H. Yang: Piezoelectrics & Acoustooptics, Vol. 33 (2011), p. 612.

[8] H. Takahashi, Y. Numamoto et al: Appl. Phys. Vol. 47 (2008), p. 8468.

[9] W. Haessler et al: Mater. Lett. Vol. 24 (1995), p. 387.

[10] S.L. Gu, G.L. Li et al: Mater. Sci. Eng. Powder Metall. Vol. 18 (2013), p. 560.

[11] M.L. Zhao et al: Acta. Phys. Sin. Vol. 52 (2003), p. 229.

[12] Y. D. Hou et al: J Am Ceram Soc. Vol. 90 (2007), p. 1738.

[13] L. Dai, S. Hu et al: CHN Ceram. Vol. 43 (2007), p. 47.

[14] F. Zhang et al: Chinese Journal Sensors and Actuators. Vol. 18 (2005), p. 215.

[15] B. Yoo, A.S. Purekar, Y. Zhang: Smart Mater. Struct. Vol. 19 (2010), p. 17

[16] K. Tungpimoluryt et al: IEEE International Symposium on Applications of Ferroelectrics, 2011.

[17] R. Paradies, P. Ciresa: Smart Mater. Struct. Vol. 18 (2009), p. 1.

Advanced Materials Research Vol. 983 (2014) pp 20-25
© (2014) Trans Tech Publications, Switzerland
doi:10.4028/www.scientific.net/AMR.983.20

Reusable and efficient polystryrene-supported acidic ionic liquid catalyst for the synthesis of n-butyl acetate

Yuhe Cheng [a], Biao Zhang [b], Shangjiang Dai [c], Hanlin Tong [d], Lixia Li [e *]

[1]School of environment and safety engineering, Jiangsu University, Zhenjiang 212013, PR China

[a] chengyuhe@126.com, [b] 851974763@qq.com, [c] 584119471@qq.com, [d] tonghanlin1@163.com, [e]*qingpipa@163.com

Keywords: Polystyrene-supported acidic ionic liquid. Esterification. n-Butyl acetate.

Abstract. A series of polystyrene-supported 1-(propyl-3-sulfonate)-3-methy-imidazolium hydrosulfate acidic ionic liquid (PS-[SO_3H-PMIM][HSO_4]) catalysts with different [SO_3H-PMIM][HSO_4] contents were prepared and tested for esterification of n-butyl alcohol with acetic acid. It was found that the reactivity of the catalyst increased with increasing [SO_3H-PMIM][HSO_4] content, and best yield of n-Butyl acetate of 98% was obtained using PS-[SO_3H-PMIM][HSO_4]1 within 1.5h. The catalytic activity of this catalyst decreased slightly after fifth using.

Introduction

Caboxylic esters is a important intermediates. Traditionally, they were synthesized by Fischer esterification of carboxylic acids and alcohols under the catalyst of hydrochloric acid or sulfuric acid [1]. Although much success has been achieved with these inorganic liquid-phase acids, some problems still remain, for example, tedious purification procedure of the product, needing of a lot of inorganic acids, corrosion of equipments[2,3]. Various novel catalysts have therefore been explored in order to avoid these insufficient. Since the end of last century, with more and more recognition of room temperature ionic liquids (TSILs), there are growing interests in using ionic liquids as solvents or catalysts for esterification [4,5], but high costs and unendurable viscosities limited their further applications [6].

In recent years, some researches were reported about supported acidic ionic liquid catalyst for organic reactions [7-9]. These researches showed that the supported ionic liquid catalysts had many advantages over their unsupported counterparts, such as separation, reusability, and the ability to provide practical conveniences in a continuous system. Recently, Xu[10] reported a new approach of synthesis of PS-supported acidic ionic liquid (PS-CH_2-[SO_3H-pIM][HSO_4]) catalyst and its catalytic performance for Fischer esterification. In the previous work, we supported a imidazole type Brønsted-acidic TSILs, 1-(propyl-3-sulfonate)-3-methy-imidazolium hydrosulfate acidic ionic liquid ([SO_3H-PMIM][HSO_4]), onto three kind of chloromethylated polystyrene beads prepared in lab to prepare a series of PS-[SO_3H-PMIM][HSO_4] catalysts, and studied their catalytic capability in nitration of aromatic compounds [11, 12]. As part of our continuing interests, here, we tested for esterification of n-butyl alcohol with acetic acid. The catalysts were characterized by FT-IR, SEM/TEM, elements analysis, TG/DSC and acid base titration.

Experimental

Catalyst preparation. Scheme 1 showed the synthetic process of PS-[SO_3H-PMIM][HSO_4] [10, 13]. First, sodium methylate (0.1mol) in methanol (10mL) was added dropwise into the mixture of imidazole (0.1mol), KI (0.1g) and toluene (5mL) at 40 ℃. Then, PS-CH_2Cl beads (0.01mol, –CH_2Cl), prepared according to the previous report [14], in acetonitrile (15mL) was added to the formed imidazole sodium salt solution, the reaction was carried out at 65 ℃ for 48 h. The PS-CH_2-imidazole product was filtered off and washed by soxhlet extraction using ethanol as solvent and dried under vacuum. Second, PS-CH_2-imidazole and equiv (relative to -imidazole) 1,3-propane sultone were

added in anhydrous toluene and reacted at 75 ℃ for 14h. Then product named as the PS-[SO_3H-PMIM] was filtered off, washed with toluene and dried under vacuum. Last, dried PS-[SO_3H-PMIM] was soaked in dichloromethane at 0 ℃, and acidified with equiv concentrated sulfuric acid or hydrochloric acid. The mixture were heated to 75 ℃ for 4h under stirring. The target catalyst PS-[SO_3H-PMIM][HSO_4] or PS-[SO_3H-PMIM][Cl] were collected by filtration, washed with diethyl ether and dried under vacuum.

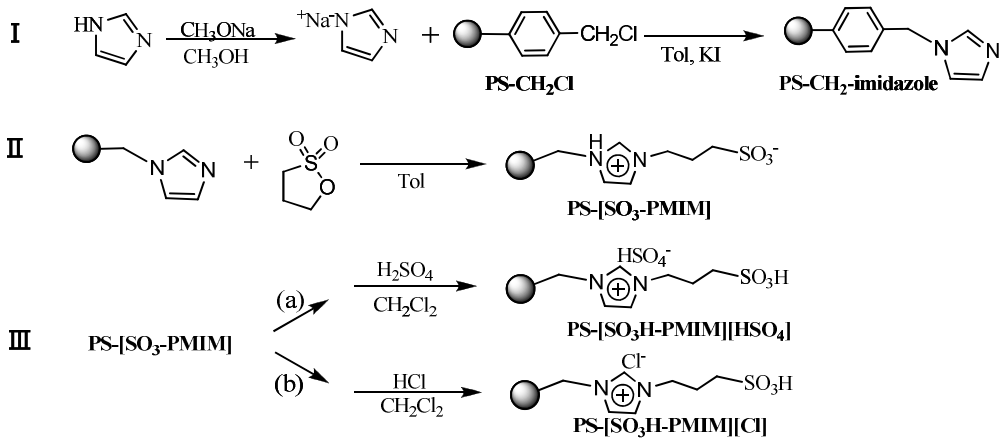

Scheme 1 Synthesis of PS-[SO_3H-PMIM][HSO_4] catalyst

Catalyst characterizations. IR spectroscopy was recorded using a Nicolet IS10 FTIR spectrometer. TG/DSC studies were carried out using METTLER TOLEDO SDTA851e/DSC823e instrument. Elemental analysis was determined by Vario MICRO EL. Average particle sizes and surface morphologies were characterized by a SEM Leica S440i. GC spectra were recorded using Agilent GC-6820 spectrometer. Acidic sites was confirmed by titration of PS-[SO_3H-PMIM][HSO_4] catalyst with 2.08×10^{-2} M aq. NaOH, using phenolphthalein as indicator.

Catalyst for aromatics esterification reactions. PS-[SO_3H-PMIM][HSO_4] (0.95g), n-butyl alcohol (96mmol), acetic acid (80mmol) and cyclohexane (8mL) were charged successively into a three-neck flack with a water segregator, and stirred at 92℃ for length of time. The resultant mixture was cooled. The catalyst was filtered off, washed with ethanol, and dried for the recycling experiments. The filtrate was analyzed using GC.

Results and discussion

FT-IR. As shown in Fig.1, for PS-CH_2Cl, the characteristic peaks of polystyrene exhibited the C–H stretching vibration of aromatic ring at 3016 cm^{-1}, and C–H asymmetric and symmetric stretching vibrations of methylene at 2920 cm^{-1} and 2855 cm^{-1}. The peaks at 1609 cm^{-1} and 1507 cm^{-1} were due to the C–C skeleton vibration of aromatic ring of polystyrene. Moreover, a typical peak at 1265 cm^{-1} was attributed to stretching vibrations of the functional group –CH_2Cl, and another peak at 672cm^{-1} was due to stretching vibrations of C-Cl[15]. The two typical peaks were practically omitted after introduction of imidazole. Meanwhile, a peak assigned to the C=N stretching vibration of imidazole ring at 1560 cm^{-1} appeared[16], which was indicated the imidazole anchored on the polystyrene by covalent bond. In the IR spectrum of PS-[SO_3-PMIM], several strong peaks, i.e. 1039 cm^{-1}, 1160 cm^{-1} and 1209 cm^{-1}, appeared which were attributed to the absorb of –SO_3^-. When PS-[SO_3-PMIM] was acidified with concentrated sulfuric acid, there were no obvious change in IR spectrum but two peaks, 1039 cm^{-1} and 1209 cm^{-1} became stronger, which were attributed to the S=O asymmetric and symmetric stretching vibrations of –SO_3– group.

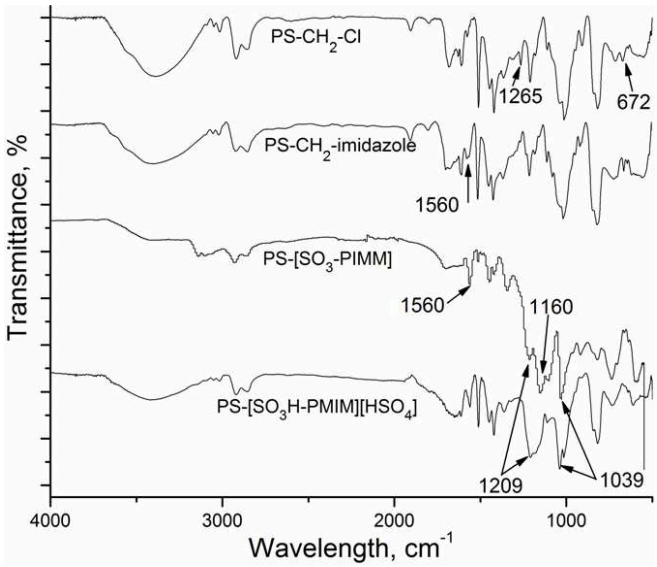

Fig. 1 IR-spectra of PS-CH_2Cl, PS-CH_2-imidazole, PS-[SO_3-PMIM] and PS-[SO_3H-PMIM][HSO_4].

Elements analysis of PS-CH_2-imidazole and acidic sites of PS-[SO_3H-PMIM][HSO_4]. Table 1 showed the elemental analysis for PS-CH_2-imidazole. It can be seen that the imidazole contents increased with the increasing of VBC in feed composition of PS-CH_2Cl. Acid sites of the PS-[SO_3H-PMIM][HSO_4] catalyst was confirmed by acid base titration. The loading amounts of [SO_3H-PMIM][HSO_4] in PS-[SO_3H-PMIM][HSO_4]1 and PS-[SO_3H-PMIM][HSO_4]2, PS-[SO_3H-PMIM][HSO_4]3 were 2.22, 2.03 and 1.69mmol/g respectively.

Table 1 Elemental analysis of PS-CH_2-imidazole

Sample	VBC:St:DVB, vol%	% C	% H	% N	Imidazole, mmol/g
PS-CH_2-imidazole1	98:0:2	73.88	6.84	12.77	4.56
PS-CH_2-imidazole2	74:24:2	74.11	6.88	11.58	4.14
PS-CH_2-imidazole3	49:49:2	77.50	7.09	9.24	3.30

"VBC:St:DVB, vol%"was the feed composition of PS-CH_2Cl beads. "VBC, St and DVB" are the abbreviation of "4-vinylbenzyl chloride, styrene and divinyl benzene" respectively.

SEM/TEM and TG-DSC. It can be seen that PS-CH_2Cl (Fig. 2 A and C) was uniform globular in the size of ~600 nm. After the introduction of [SO_3H-PMIM][HSO_4], the catalyst became big a little, about ~700nm and the surface became smooth (Fig. 2 B and D), which is in accord with other report [10].

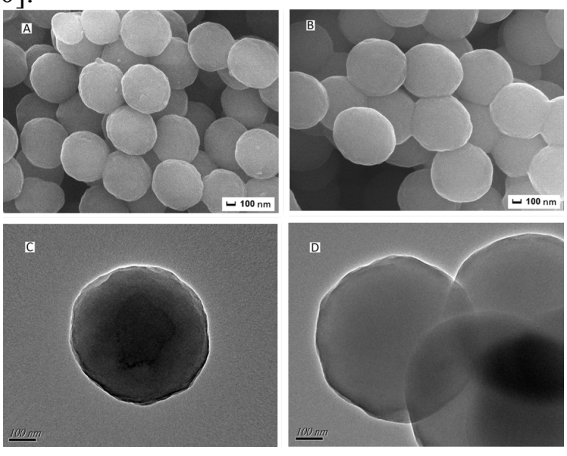

Fig. 2 SEM and TEM of PS-CH_2Cl (A and C) and PS-[SO_3H-PMIM][HSO_4] (B and D).

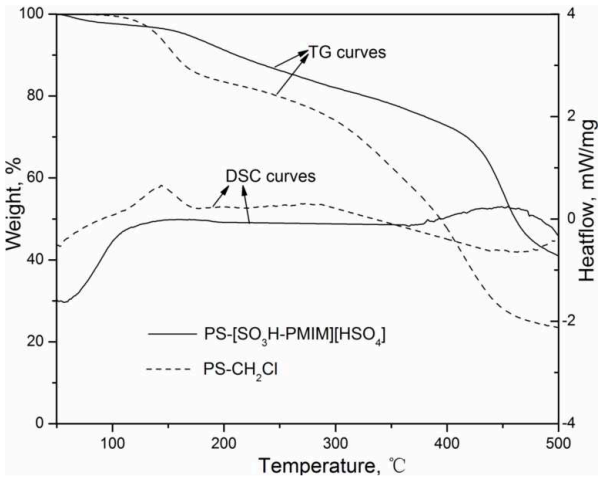

Fig. 3 TG/DSC curves of PS-CH_2Cl and PS-[SO_3H-PMIM][HSO_4] catalyst.

TG/DSC analysis was carried out in N_2 with heating rate of 10 ℃/min. As shown in Fig. 3, no significant weight loss was observed from both PS-CH_2Cl and PS-[SO_3H-PMIM][HSO_4] at beginning. Above 120℃, weight loss was accelerated for both the two particles and weight loss speed of PS-CH_2Cl was quicker than that of PS-[SO_3H-PMIM][HSO_4]. There was a obvious weight loss

from PS-CH_2Cl nearby 150 ℃. Correspondingly, for the DSC curve of PS-CH_2Cl, a small exothermic peak appeared, however it didn't appear in the DSC curve of PS-[SO_3H-PMIM][HSO_4]. The weight loss and the exothermic peak of PS-CH_2Cl were possibly ascribed to the water inside the porous PS-CH_2Cl particles. When the [SO_3-PMIM] was immobilized onto PS-CH_2Cl in organic solvent, the water was droved and the holes were jammed. When the temperature further increased up to higher than 300 ℃ for PS-CH_2Cl and 410 ℃ for PS-[SO_3H-PMIM][HSO_4], weight loss accelerated heavily. A possible reason is that their structures were destroyed or the chloromethyl groups and the [SO_3H-PMIM][HSO_4] separated from PS. The residue weight of PS-[SO_3H-PMIM][HSO_4] and PS-CH_2Cl was about 56.5% and 27.2% at 450 ℃, respectively. These observations indicated that the immobilization of [SO_3H-PMIM][HSO_4] onto polystyrene could improve the thermal stability of PS-CH_2Cl.

Catalytic reaction. The esterification of n-butyl alcohol with acetic acid is showed in Scheme 2.

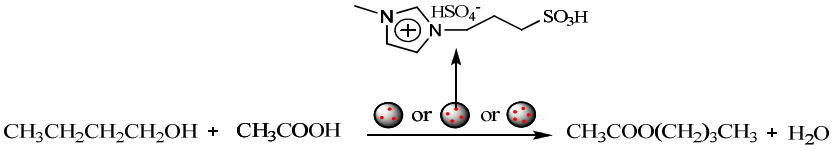

Scheme 2 Esterification of n-butyl alcohol with acetic acid.

To evaluate the PS-[SO_3H-PMIM][HSO_4] catalyst described here, the catalytic activities of various catalyst for the esterification reaction of n-butyl alcohol and acetic acid were examined under the same reaction conditions (Table 2). Obviously, the yields of n-butyl acetate over PS-[SO_3H-PMIM][HSO_4] (Table 2, entry1-3) were much higher than that over the support (Table 2, entry 5) and no catalyst(Table 2, entry 6). This meant that the reaction hardly carried out without catalyst and the support almost had no influence on the yield. It was worth noting that the PS-[SO_3-PMIM]1 had no influence on the reaction evidenced the scheme of the synthesis of PS-[SO_3H-PMIM][HSO_4] catalyst at a certain extent. In addition, it easy to see that both the PS-[SO_3H-PMIM][HSO_4] catalysts and PS-[SO_3H-PMIM][Cl] (Table 2, entry 4) catalyst were effective for the reaction of n-butyl alcohol and acetic acid although the catalytic activity of the latter was far lower than that of the former. The reason was that both the two kinds of solid catalysts could provide proton H^+, which could make the acetic acid protonated and then was attacked by nucleophilic n-butyl alcohol to form n-Butyl acetate. Which analysis was based on the classical two key steps esterfication [17-19]. Compared to PS-[SO_3H-PMIM][HSO_4] catalysts, there are two groups, i.e. HSO_4^- anions and SO^3H- group, could supply proton H^+, the providing proton H^+ ability of PS-[SO_3H-PMIM][Cl] is limited, which contributed lower catalytic capability.

It can be seen that all of the PS-[SO_3H-PMIM][HSO_4] catalysts exhibited high catalytic activity. The yield of n-Butyl acetate increased with the increasing of [SO_3H-PMIM][HSO_4] content at same reaction time, which was attributed to the gradually increasing amount of acid sites in the catalyst. When using the PS-[SO_3H-PMIM][HSO_4]1 as catalyst, 98% yield was obtained at 92℃, within 1.5h, which was better than the similar study reported by Xu[10].

Table 2 Result of n-Butyl acetate over various catalyst and reaction time[a]

Entry	Catalyst	Yield, %		
		0.75, h[b]	1.5, h[b]	3, h[b]
1	PS-[SO_3H-PMIM][HSO_4]1	94	98	98
2	PS-[SO_3H-PMIM][HSO_4]2	90	96	98
3	PS-[SO_3H-PMIM][HSO_4]3	90	93	98
4	PS-[SO_3H-PMIM][Cl]1	57	68	74
5	PS-[SO_3-PMIM]1 (or PS-CH_2Cl1)	34	47	52
6	Blank	33	48	50

[a] By quantitative GC based on crude product

[b] Reaction time, h

Catalyst recycle study. The reusability of PS-[SO_3H-PMIM][HSO_4] catalyst was evaluated in esterification of n-butyl alcohol with acetic acid catalyzed by PS-[SO_3H-PMIM][HSO_4]1. As shown in Table 3, PS-[SO_3H-PMIM][HSO_4]1 still showed very high activity after third runs and the catalytic activity decreased only 3% for 5 runs, which indicated that PS-[SO_3H-PMIM][HSO_4] catalyst was efficient and reusable.

Table 3 The reusability of PS-[SO_3H-PMIM][HSO_4]1 for n-Butyl acetate[a]

Runs time	1	2	3	4	5
Yield, %	98	98	97	96	95

[a] By quantitative GC based on crude product, reaction time 1.5h.

Conclusion

A series PS-[SO_3H-PMIM][HSO_4] catalysts were prepared by grafting [SO_3H-PMIM][HSO_4] onto the highly chloromethylated polystyrene beads, and showed a better thermal stability than that of PS-CH_2Cl resins. These catalysts were efficiencies for esterification of n-butyl alcohol with acetic acid. The yield of n-Butyl acetate generally increased with increasing of the [SO_3H-PMIM][HSO_4] content. The best yield of 98% was obtained under 92℃ within 1.5h over PS-[SO_3H-PMIM][HSO_4]1 catalyst. The catalyst could be recovered by simple filtration, and the yield only decreased 3% after reusing for 5 times. In conclusion, the PS-[SO_3H-PMIM][HSO_4] catalyst prepared in this paper was an excellent recyclable catalyst for the synthesis of n-Butyl acetate, and it showed potential application for carboxylic esters in industry.

This work was supported by the grant (No. 1281370046) from the Scientific Research Foundation for the high-ranking talent of Jiangsu university.

References

[1] S. Kaewta, L. Edgar, G.G. James, Solid bronsted acid catalysis in the gas-phase esterification of acetic acid, Ind. Eng. Chem. Res. 46 (2007) 7050–7056.

[2] X.Z. Li, W.J. Eli, A green approach for the synthesis of long chain aliphatic acid esters at room temperature, J. Mol. Catal. A: Chem. 279 (2008) 159–164.

[3] V.R. Vamsi, V.R. Modukuri, A. Ratnamala, et. al. A Simple, Efficient, Green, Cost Effective and Chemoselective Process for the Esterification of Carboxylic Acids, Org. Process Res. Dev. 13 (2009) 769-773.

[4] J.F. Dubreuil, K. Bourahla, M. Rahmouni, et. al. Catalysed esterifications in room temperature ionic liquids with acidic counteranion as recyclable reaction media, Catal. Commun. 3 (2002) 185-190.

[5] T. Joseph, S. Sahoo, S.B. Halligudi, Brönsted acidic ionic liquids: A green, efficient and reusable catalyst system and reaction medium for Fischer esterification, J. Mol. Catal. A: Chem. 234 (2005) 107-110.

[6] P.M. Christian, A.C. Raymond, C.D. Nicholas, et. al. Supported Ionic Liquid Catalysis − A New Concept for Homogeneous Hydroformylation Catalysis, J. Am. Chem. Soc. 124 (2002) 12932-12933.

[7] C. DeCastro, E. Sauvage, M.H. Valkenberg, et. al. Immobilised Ionic Liquids as Lewis Acid Catalysts for the Alkylation of Aromatic Compounds with Dodecene, J. Catal. 196 (2000) 86-94.

[8] H.L. Shim, S. Udayakumar, J.I. Yu, et.al. Synthesis of cyclic carbonate from allyl glycidyl ether and carbon dioxide using ionic liquid-functionalized amorphous silica, Catal. Today 148 (2009) 350-354.

[9] D.W. Kim, D.J. Hong, K.S. Jang, et. al. Structural modification of polymer-supported ionic liquids as catalysts for nucleophilic substitution reactions including fluorination, Adv. Synth. Catal. 348 (2006) 1719-1727.

[10] Z.J. Xu, H. Wan, J.M. Miao, et. al. Reusable and efficient polystyrene-supported acidic ionic liquid catalyst for esterifications, J. Mol. Catal. A: Chem 332 (2010) 152-157.

[11] X.L. Li, Q. L. Ling, Z. L. Liu, et. al. Reusable and Efficient Polystryrene-supported Acidic Ionic Liquid Catalyst for Mononitration of Aromatic Compounds, Bull. Korean Chem. Soc. 2012, 33(2012) 3373-3377.
[12] L.X. Li, Q.L. Ling**,** X.D. Xing, et. al. Reusable and Efficient PS-supported Acidic Ionic Liquid Catalyst for Mononitration of Toluene, Advanced Materials Research, 581-582(2012) 252-257.
[13] A.S. Amarasekara, O.S. Owereh, Synthesis of a sulfonic acid functionalized acidic ionic liquid modified silica catalyst and applications in the hydrolysis of cellulose, Catal. Commun. 11 (2010) 1072-1075.
[14] F.S. Macintyre, D.C. Sherrington, L. Tetley, Synthesis of Ultrahigh Surface Area Monodisperse Porous Polymer Nanospheres, Macromolecules 39 (2006) 5381-5384.
[15] Q. Wu, H. Chen, M.H. Han, et. al. Transesterification of Cottonseed oil catalyzed by bronsted acidic ionic liquids, Ind. Eng. Chem. Res. 46 (2007) 7955-7906.
[16] M.J. Earl, S. Haas, C.B. Carl, et. al. Catalystic nitration of aromatics by ionic liquid, CN1469859A, 2004.
[17] F. Xu, H.Y. Chen, H.B. Zhang, et. al. Protophilic amide ionic liquid assisted esterification and catalysis mechanism, J. Mol. Catal. A: Chem. 307 (2009) 9-12.
[18] S.R. Kirumakki, N. Nagaraju, S. Narayanan, A comparative esterification of benzyl alcohol with acetic acid over zeolites Hβ, HY and HZSM5, Appl. Catal. A 273 (2004) 1-9.
[19] J.Z. Gui, H.Y. Ban, X.H. Cong, et.al. Selective alkylation of phenol with tert-butyl alcohol catalyzed by Brönsted acidic imidazolium salts, J. Mol. Catal. A: Chem. 225 (2005) 27-31.

Advanced Materials Research Vol. 983 (2014) pp 26-29

doi:10.4028/www.scientific.net/AMR.983.26

An exploration of factors affecting the preparation of SiO_2-coated α-Al_2O_3 pearlescent pigment

Nan Wu[1,a], Qinghua Chen[1,b*], Weiming Zhou[2,c], Meizhen Ke[2,d], Qingrong Qian[1,e*], Zhanhui Yuan[1,f]

[1] College of Environmental Science and Engineering, Fujian Normal University, Fuzhou, China
[2] College of Materials Science and Engineering, Fujian Normal University, Fuzhou, China
[a] 270732913@qq.com, [b] cqhuar@126.com, [c] zhouweiming721@126.com, [d] 757412608@qq.com, [e] qrqian@fjnu.edu.cn, [f] zhanhui.yuan@fzkuncai.com

Keywords: SiO_2-coated α-Al_2O_3; pearlescent pigment; liquid phase deposition

Abstract: The SiO_2-coated α-Al_2O_3 pearlescent pigment was prepared by liquid phase deposition (LPD). The effects of concentration of sodium silicate solution, reaction temperature and pH value of the aluminum oxide suspending liquid were systemically studied in this paper. The obtained samples were characterized by scanning electron microscopy (SEM). The results showed that when the process parameters are the concentration of sodium silicate solution of 0.1 mol/L, the reaction temperature of 80 ^oC and the pH value of 9.0, the high quality of SiO_2-coated α-Al_2O_3 pearlescent pigment could be obtained.

Introduction

Pearlescent pigment is one of the color effect materials which composed of a highly reflective platelet-shaped substrate encapsulated with a low index of refraction material [1]. It is widely applied in plastics, printing ink, cosmetic and ceramic materials due to its unique decorative optical color effects and weather-resistance effects [2].

The common substrates of traditional pearlescent pigment were mica or synthetic mica [3]. The defect of the mica or synthetic mica based pearlescent pigment are these: 1. the mica or synthetic mica is difficult to delamination; 2. the pearlescent pigment made by mica or synthetic mica has a poor dispersion.

α-Al_2O_3 based pearlescent pigment[4] is a newly emerging material which overcome the defect of the mica or synthetic mica based pearlescent pigment. In this paper, the factors affecting the preparation of SiO_2-coated α-Al_2O_3 pearlescent pigment was studied in order to find a easy and fast way of preparing the SiO_2-coated α-Al_2O_3 pearlescent pigment.

Experimental

Raw materials and reagents. The platelet-shaped α-Al_2O_3 was supplied by Xiamen ZF Co., Ltd. The morphology of α-Al_2O_3 was shown in Fig.1. The sodium hydroxide and sodium silicate were provided by Tianjin Fuchen chemical reagents factory, both of them are analytical-reagent. And the chemically-pure sulphuric acid was obtained from Fuzhou chemical engineering research institute.

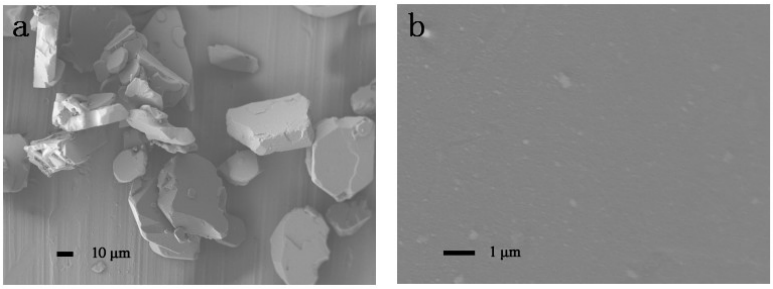

Fig.1 The morphology of α-Al_2O_3 (a:×500; b:×10000)

Preparation process. Measured 25 g α-Al_2O_3 and added it to 100 mL distilled water as the reaction mother liquor. The suspending liquid was heated and stirred in certain temperature. The pH value was adjusted by sodium hydroxide. Then injected Na_2SiO_3 dropwisely (about 0.75 mL/min) into the suspending liquid and added H_2SO_4 (0.1 mol/L) at the same time to kept the pH value constant (The H_2SO_4 was added by ProMinent Dulcometer D1Cb, a pH controller). After that, the product was filtered and washed for several time to move the free SiO_2. In the end, the precipitate was dried at 102 ^oC for 12 h.

Characterizations. The morphologies of SiO_2-coated α-Al_2O_3 were tested by the scanning electron microscope (JSM 7500F).

Results and discussion

Influence of concentration of sodium silicate solution. Elevated the concentration of sodium silicate solution could accelerate the hydrolysis of sodium silicate, so the $H_2SiO_3.nH_2O$ would generate massly and rapidly. The crystal particles would be small, because they didn't have enough time to grow up, as shown in Fig.2-b and Fig.2-c. But if the generation rate of $H_2SiO_3.nH_2O$ was far faster than its deposition rate, the $H_2SiO_3.nH_2O$ would be more likely to formed free SiO_2 or large grain of SiO_2 on the surface of α-Al_2O_3, as shown in Fig.2-d. Therefore the optimum concentration is 0.10 mol/L.

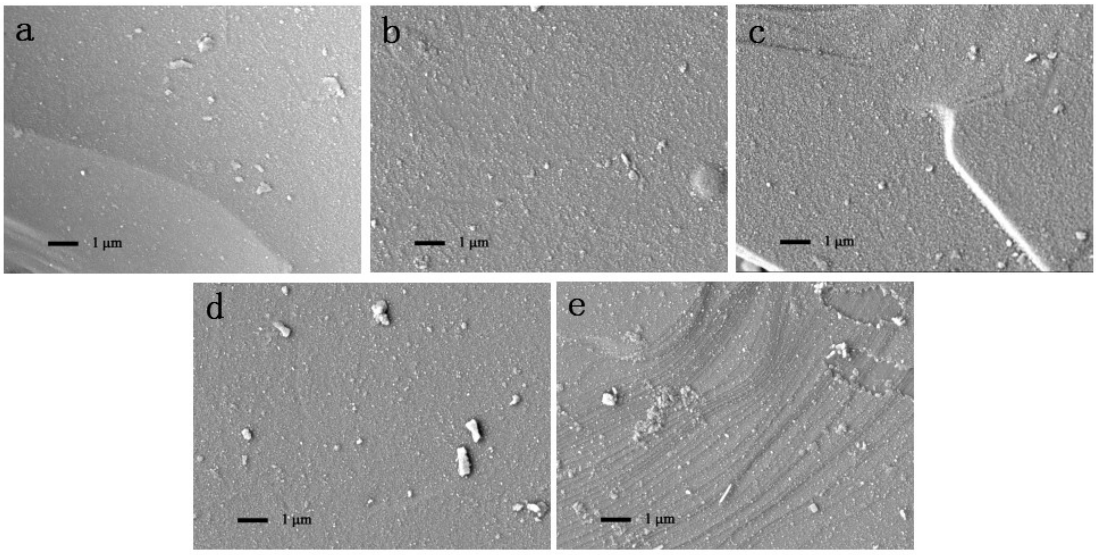

Fig.2 The morphology of SiO_2-coated α-Al_2O_3 prepared by different concentration of sodium silicate solution (a: 0.05 mol/L ; b: 0.10 mol/L; c: 0.15 mol/L; d: 0.20 mol/L; e: 0.25 mol/L), all the sample above were prepared in 80 ^oC, with the pH 9.0

Influence of the reaction temperature. Heating properly could promote the growth of SiO_2 crystal particles as well as accelerate the hydrolysis of sodium silicate. With the increase of temperature, the crystal particles that formed in the surface of α-Al_2O_3 would be larger and larger, as shown from Fig.3-a to Fig.3-d. But when the temperature was too high, the crystal might also fail to form, as shown in Fig.3-e. Therefore the optimum reaction temperature is 80 ^oC.

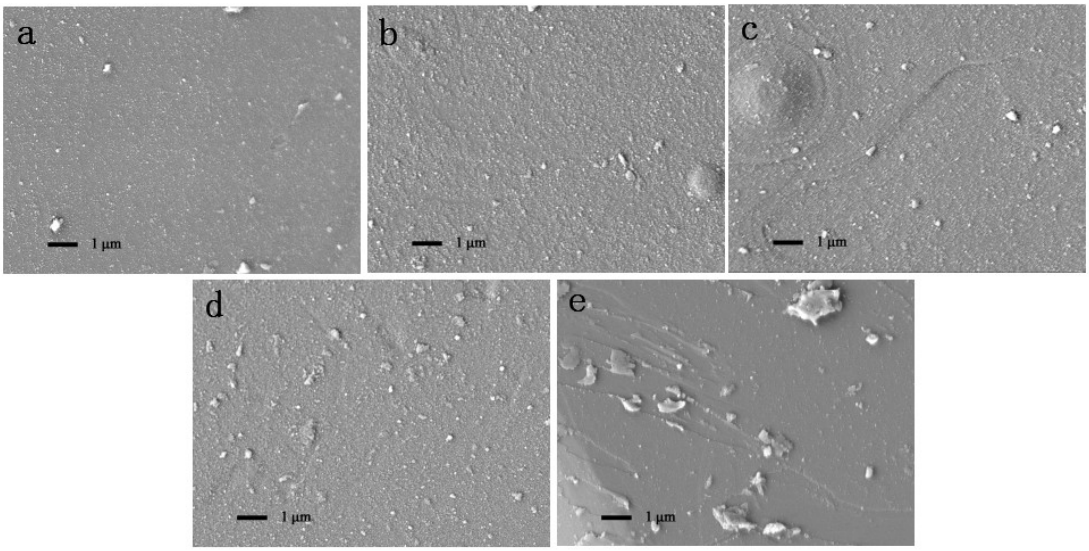

Fig.3 The morphology of SiO_2-coated α-Al_2O_3 prepared in different temperature (a: 75 ^oC; b: 80 ^oC; c: 85 ^oC; d: 90 ^oC; e: 95 ^oC), all the sample above were prepared by 0.10 mol/L sodium silicate solution, with the pH 9.0

Influence of the pH value. The pH value could affect both the hydrolysis and gelling of silicate. The sodium silicate would hydrolyze rapidly at a low pH value, which might lead to self-nucleation of silicate. We could learn from the pre-experiment that the hydrolysis rate of sodium silicate would be appropriate when the pH value was 8.0~10.0. The relationship of gelling time with pH was following N curve [5]. The pH 8.0~8.5 was nearly at the bottom of the N curve, at that range, the gelling rate would be high, and the large grain of SiO_2 would be formed before it deposited on the surface of α-Al_2O_3, as shown in Fig.4-a and Fig.4-b. When the pH value was 9.0, the gelling rate was moderate and close to the deposition rate, the SiO_2 on the surface of α-Al_2O_3 would be well-distributed, as shown in Fig.4-c. Therefore the optimum pH is 9.0.

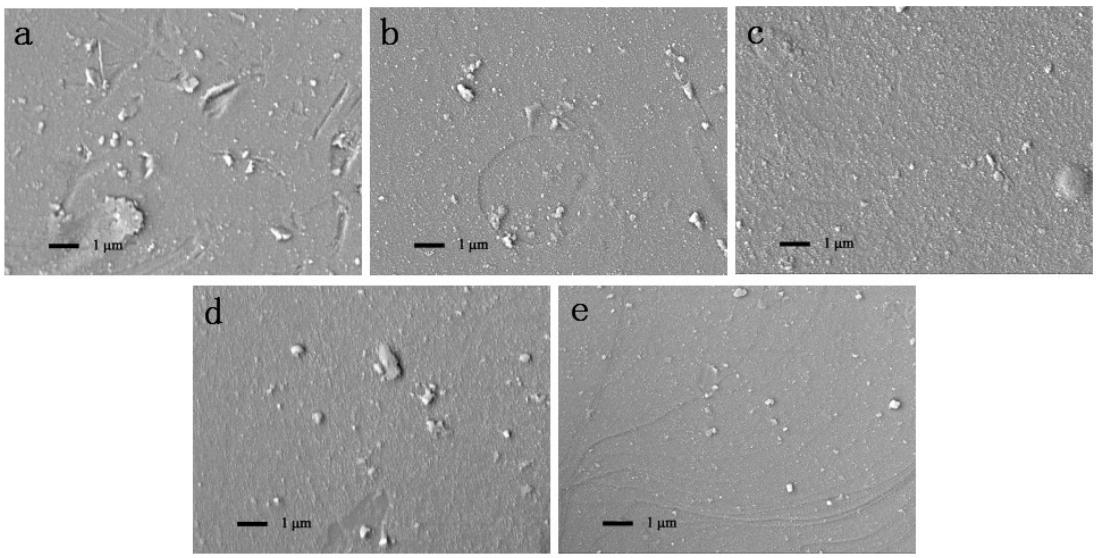

Fig.4 The morphology of SiO_2-coated α-Al_2O_3 prepared in different pH (a: 8.0; b: 8.5; c: 9.0; d: 9.5; e: 10.0), all the sample above were prepared by 0.10 mol/L sodium silicate solution, in 80 ^oC

Conclusions

The SiO_2-coated α-Al_2O_3 pearlescent pigment was prepared by liquid phase deposition (LPD). The result of SEM showed that when the process parameters are concentration of sodium silicate solution of 0.1 mol/L, reaction temperature of 80 ^oC and pH value of 9.0, the SiO_2 on the surface of α-Al_2O_3 would be dense, fine and well-distributed.

Acknowledgements

This work is supported by Program for the Fujian Provincial Science and Technology and the Provincial Financial Department (2011H6005), and the Scientific Research Foundation for the Returned Overseas Chinese Scholars, State Education Ministry (2011-1568).

The corresponding authors are Qinghua Chen and Qingrong Qian.

References

[1] Curtis J. Zimmermann, James D. Christie, Vivian K. Doxey and Daniel Stevenson Fuller, U.S. Patent 6,821,333. (2004)

[2] Deborah Cacace, Carolyn Lavallee, Michael T. Venturini, U.S. Patent 5,759,255. (1998)

[3] Frank J. Maile, Gerhard Pfaff, Peter Reynders, Effect pigments—past, present and future, Progress in Organic Coatings. 54 (2005) 150-163.

[4] Jung Min Lee, Jeong Kwon Suh, Byung Ki Park, Dong Uk Choe, Gil Wan Chang, Kwang Su Lim, Sung Yun Jo, Kwang Choong Kang, U.S. Patent 8,287,636. (2012)

[5] Cui Aili, Wang Tingjie, Jin Yong, Xiao Shuaigang, Ge Xudong, Mechanism and Structure Analysis of TiO_2 surface coated with SiO_2 and Al_2O_3, Chemical journal of Chinese universities. 19 (1998) 1727-1729.

Advanced Materials Research Vol. 983 (2014) pp 30-38

doi:10.4028/www.scientific.net/AMR.983.30

Assessment of Engineering Properties of Geosynthetics with Seaming Methods

Han-Yong Jeon

Department of Applied Organic Materials Engineering, Inha University, Incheon, Korea(Rep.)

hyjeon@inha.ac.kr

Keywords: geosynthetics, seaming method, transmissivity, strength retention, chemical resistance, seam strength, reduction factor

Abstract. 8 Geotextiles (; 4 woven and 4 nonwoven types), 4 geogrids and 2 geocomposites of [nonwoven/fibers/nonwoven] structure were used as raw materials and the different seaming methods were applied to compare the seam properties of 3 geosynthetics and transmissivity of geocomposites. Tensile strength retentions of these geosynthetics were evaluated as the degree of damage by chemical degradation. Woven geotextiles showed the higher seam strength in the order (SSd-1 < SSd-2) > (SSa-1 < SSa-2) > geospacer without regard to the design strength. For nonwoven geotextiles, the order of seam strength is geospacer > (SSa-1 < SSa-2). Geogrids showed the higher seam strength in the order of band > geospacers but reduction factors were increased in the order of band > geospacer without regard to the geogrid's compositions. Finally, geocomposites showed the higher seam strength in the order of geospacer > (SSa-1 < SSa-2) but showed the transmissivity in the order of geospacer > (SSa-1 > SSa-2) without regard to the kinds of filled fibers and weight of geocomposite.

Introduction

Geosynthetics have their seaming methods such as mechanical or chemical seaming techniques due to their own structures, physical, chemical and thermal properties. Furthermore, the seam strength of geosynthetics must be influenced by seaming methods and for reinforcement/protection applications with geosynthetics, the seaming is typically the weak connection to applied load transfer in the reinforcement/protection system [1]. For filtration or drainage applications, this phenomena on geosynthetics could affect the vertical or horizontal hydraulic flow. Seaming can have a significant impact on the performance of geosynthetic systems whether their intended function is reinforcement/protection, separation or filtration and drainage. When reinforcement/ protection is the function, the seaming must be considered as a limiting strength factor and assessed by the same performance standards as the reinforcement/protection geosynthetic only [2, 3, 4]. Besides this, the seaming of geosynthetics should be evaluated for durability limitations such as installation damage, creep deformation, chemical and biological degradations etc. Seaming of geotextiles by traditional sewing methods necessarily causes needle damage to fibers and yarns as well as creating stress concentrations where the sewing threads reverse direction for their return stroke. These effects are relatively small for light-weight geotextiles and the resulting seam strength are generally quite high. For geogrids, the connection techniques require a high level of dimensional

stability within the geogrid structure to withstand the stress concentrations imposed by connection techniques. Filtration or drainage performance of geocomposites could be also influenced by the seam strength with different seaming methods. In this study, geotextiles - 4 woven and 4 nonwoven types, 4 geogrids and 2 geocomposites of [nonwoven/fibers/nonwoven] structure were used as raw materials and the different seaming methods were applied to compare the seam properties of 3 geosynthetics and transmissivities of geocomposites.

Experimental

Preparation of Samples and Seaming

8 Geotextiles(; 4 woven and 4 nonwoven types), 4 geogrids and 2 geocomposites of [nonwoven/fibers/nonwoven] structure were used as raw materials. Geocomposites of 3-layer structure which have the excellent drainage function under confined loading condition were manufactured by needle punching method. Three different punching patterns were applied to manufacture these geotextiles as ↑, ↑ and ↓ punching pattern.

Assessments of Performance of Geosynthetics

Seaming methods that applied to geosynthetics were as following: (1) geotextiles - sewing methods : flat seam(; SSa-1, -2), butterfly seam(; SSd-1, -2), geospacer, (2) geogrids - band and geospacer, (3) geocomposites – flat seam(; SSa-1, -2) and geospacer. Table 1 shows the specifications and seaming methods of these geosynthetics and Figure 1 shows the various seam types and geospacer. Seam properties of geotextiles and geocomposites were examined by ASTM D 4884(; test method for seam strength of sewn geotextiles) and those of geogrids were investigated through ASTM D 4884. Chemical resistance of geosynthetics were tested in the condition of pH 3 and 8, 25°C and 50°C during 360 days. These solutions were adopted to compare the chemical resistance by considering the waste leachates. The degree of chemical resistance of geosynthetics were estimated by comparing the tensile strength retention ratio after 360 days with ASTM D 5322. Especially for geogrids, creep deformation tests were done to determine the reduction factor of geogrids to affect the long-term performance by ASTM D 5262 and GRI GG 3(b). Transmissivities of geocomposites were tested by ASTM D 4716. 2 types of geonet composites – GNC-1, -2 - having the same thickness as smart geotextiles were used as comparison materials for drainage function and Figure 2 showed the cross sectional morphology of geocomposites and geonet composites.

Table 1. Specifications and seaming methods of geosynthetics

Geosynthetics			Fibers	Design Strength(kN/m)	Weight (g/m^2)	Seaming Methods
Geotextile	Woven	WGT-1	Polyester	50		Flat Seam, Butterfly Seam, Geospacer
		WGT-2		100		
		WGT-3		150		
		WGT-4		200		
	Non-woven	NWGT-1	Polypropylene		712	
		NWGT-2			1,024	
		NWGT-3			1,532	
		NWGT-4			2,156	
Geogrid		GG-1	High tenacity Polyester	80		Band, Geospacer
		GG-2		150		
		GG-3		200		
		GG-4		250		
Geocomposite [Nonwoven/Fibers* /Nonwoven]		GC-1	*Polypropylene Waste Fiber		1,306	Flat Seam, Geospacer
		GC-2			2,084	

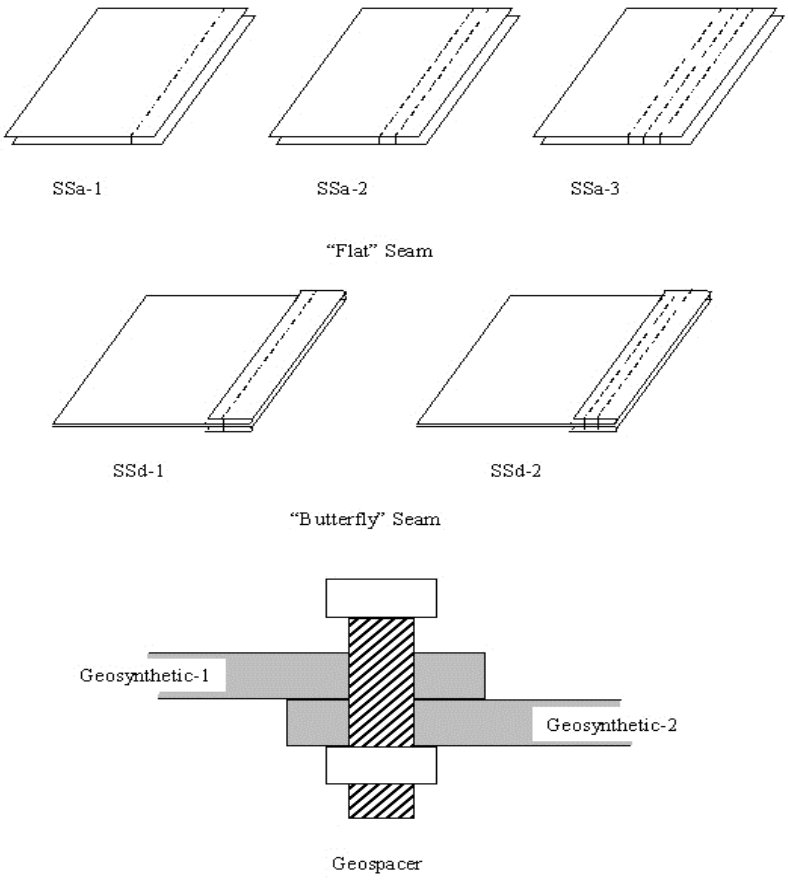

Fig 1. Schematic diagrams of various seam types and special geospacer

(a) Smart geotextiles (b) Geonet composite

Fig 2. Photographs of cross section areas of geosynthetics

Result and Discussion

Seamed geosynthetics by geospacers

Fig. 2 shows the seamed geosynthetics, e.g., nonwoven geotextile, geogrid and geocomposite by the geospacer. In this Figure, it was seen that this seaming method has no problem to be used in the bonded area instead of the overlapping the geosynthetics, especially the thick geotextiles which have the weight more than 1,000g/m2.

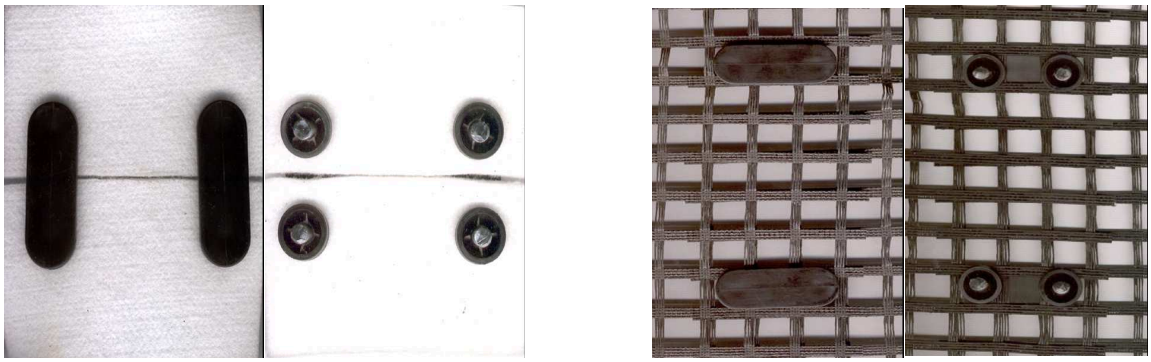

(a) Nonwoven geotextile (b) Geogrid

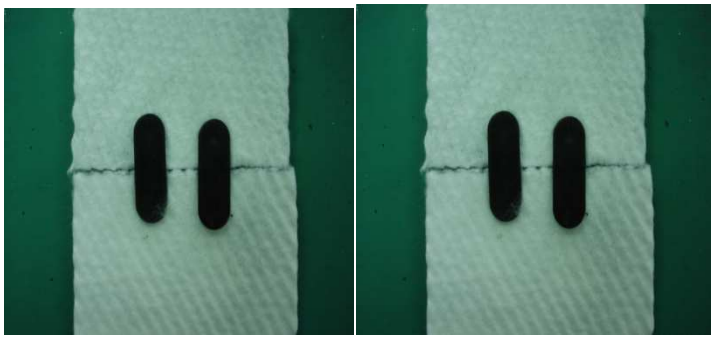

(c) Geocomposite

Fig 3. Photographs of seamed geosynthetics by geospacer

Seam Strength

Table 2 shows the seam strength of the seamed geosynthetics with the seam type. For woven geotextiles, the butterfly seam(SSd-1 and SSd-2) shows the excellent seam strength than the flat seam(SSa-1 and SSa-2) but the geospacer seam shows the lower seam strength than the flat and butterfly seams. From this, it was seen that the geospacer seam is not optimum for the woven geotrextiles. For nonwoven geotextiles, the geospacer seam shows the excellent seam strength than the flat and butterfly seams with the increase of weight. It is thought that geospacer makes more

compact seam than the flat and butterfly seams for thicker nonwoven geotextiles. For geogrids and geocomposites, the geospacer seam shows the excellent seam strength than the band seam without regard to the design strength and geogrid's composition.

Table 2. Seam strength of geosynthetics with seam type

Seam Type / Geosynthetics	SSa-1	SSa-2	SSd-1	SSd-2	Band	Geospacer
WGT-1	116	120	127	134	-	86
WGT-2	118	123	134	138	-	92
WGT-3	121	127	138	143	-	101
WGT-4	124	131	141	148	-	118
NWGT-1	78	85	-	-	-	92
NWGT-2	80	87	-	-	-	98
NWGT-3	81	89	-	-	-	106
NWGT-4	83	92	-	-	-	113
GG-1	-	-	-	-	66	76
GG-2	-	-	-	-	68	84
GG-3	-	-	-	-	72	78
GG-4	-	-	-	-	76	86
GC-1	64	78	-	-	-	154
GC-2	81	94	-	-	-	158

Chemical Resistance

The degree of chemical resistance of geosynthetics in the acidic and alkaline solutions were represented in Table 3~6. Nonwoven geotextiles showed the excellent chemical resistance than the woven geotextiles. The tensile strength retentions of woven geotextiles was decreased with high pH value and temperature. This is the typical phenomena of polyester fibers which were unstable against the high pH value and temperature. However, the geospacer seam showed the excellent chemical resistance for all geosynthetics. For geogrids, chemical resistance is not dependent on the seam type and the design strength. Geocomposites showed the same tendency of chemical resistance as the nonwoven geotextiles but smaller change than nonwoven geotextiles.

Table 3. Tensile strength retention of geosynthetics with seam type at pH 3, 25°C

Seam type / Geosynthetics	SSa-1	SSa-2	SSd-1	SSd-2	Band	Geospacer
WGT-1	82	84	84	86	-	86
WGT-2	84	85	86	87	-	86
WGT-3	84	85	86	88	-	87
WGT-4	85	86	86	88	-	88
NWGT-1	78	80	-	-	-	83
NWGT-2	80	83	-	-	-	85
NWGT-3	82	83	-	-	-	87

NWGT-4	83	85	-	-	-	88
GG-1	-	-	-	-	92	92
GG-2	-	-	-	-	92	92
GG-3	-	-	-	-	92	92
GG-4	-	-	-	-	92	92
GC-1	84	86	-	-	-	88
GC-2	84	86		-	-	88

Table 4. Tensile strength retention of geosynthetics with seam type at pH 3, 50°C

Seam type / Geosynthetics	SSa-1	SSa-2	SSd-1	SSd-2	Band	Geospacer
WGT-1	80	82	83	85	-	85
WGT-2	82	83	84	86	-	85
WGT-3	82	84	85	86	-	86
WGT-4	82	84	84	87	-	86
NWGT-1	78	80	-	-	-	83
NWGT-2	81	82	-	-	-	84
NWGT-3	82	82	-	-	-	86
NWGT-4	82	84	-	-	-	86
GG-1	-	-	-	-	92	92
GG-2	-	-	-	-	92	93
GG-3	-	-	-	-	93	92
GG-4	-	-	-	-	92	92
GC-1	83	86	-	-	-	88
GC-2	84	86	-		-	88

Table 5. Tensile strength retention of geosynthetics with seam type at pH 8, 25°C

Seam type / Geosynthetics	SSa-1	SSa-2	SSd-1	SSd-2	Band	Geospacer
WGT-1	74	76	78	80	-	82
WGT-2	76	76	78	82	-	82
WGT-3	76	78	80	82	-	83
WGT-4	78	79	80	83	-	83
NWGT-1	78	80	-	-	-	82
NWGT-2	80	81	-	-	-	83
NWGT-3	80	81	-	-	-	83
NWGT-4	82	83	-	-	-	84
GG-1	-	-	-	-	91	92
GG-2	-	-	-	-	91	92
GG-3	-	-	-	-	91	93
GG-4	-	-	-	-	92	92
GC-1	82	84	-	-	-	86
GC-2	82	85		-	-	86

Table 6. Tensile strength retention of geosynthetics with seam type at pH 8, 50°C

Seam type / Geosynthetics	SSa-1	SSa-2	SSd-1	SSd-2	Band	Geospacer
WGT-1	74	75	78	81	-	78
WGT-2	76	75	78	82	-	78
WGT-3	76	77	80	83	-	80
WGT-4	78	78	80	84	-	80
NWGT-1	74	78	-	-	-	81
NWGT-2	75	80	-	-	-	82
NWGT-3	77	80	-	-	-	82
NWGT-4	78	81	-	-	-	83
GG-1	-	-	-	-	91	91

GG-2	-	-	-	-	90	91
GG-3	-	-	-	-	90	91
GG-4	-	-	-	-	91	92
GC-1	82	83	-	-	-	86
GC-2	82	84	-	-	-	86

Long-Term Design Strength of Geogrid by Creep Reduction Factor

From GRI Standard Test Method GG4, the allowable strength of geogrid could be written in the following equation to be taken into consideration of the ultimate strength, reduction factors for application of geogrids. The long-term design strength of geogrid should be used in the following equation. The reference document can be found in the GRI Standard Test Method GG4(b) "Determination of the Long-term Design Strength of Flexible Geogrids".

$$T_{design} = T_{ultimate}\left[\frac{1}{RF_{id} \times RF_{cr} \times RF_{cd} \times RF_{bd}}\right] \quad (1)$$

where, T_{design} = long-term design strength of geogrid

$T_{ultimate}$ = ultimate strength of geogrid

RF_{id} = reduction factor for installation damage

RF_{cr} = reduction factor for creep deformation

RF_{cd} = reduction factor for chemical degradation

RF_{bd} = reduction factor for biological degradation

Table 7 shows the longterm design strength of geogrids by the reduction factor of the above mentioned conditions. We used the default values of each reduction factor to be written in the reference, [1]. In here, reduction factors of the geospacer seam are smaller than those of the band seam and this means geospacer seam is more effective than the band seam. Therefore, the long-term design strength values of geospacer showed higher than those of the band seam.

Table 7. Long-Term design strength by reduction factor of geogrids with seam type.

Geogrid	Reduction Factor		Long-Term Design Strength (KN/m)	
	Band	Geospacer	Band	Geospacer
GG-1	2.4	2.0	33.3	40.0
GG-2	2.4	1.9	62.5	78.9
GG-3	2.4	1.8	83.3	111.1
GG-4	2.3	1.8	108.7	138.9

Transmissivities of Geocomposite

Table 8 shows the transmissivities of geocomposites by seam type. Geospacer seam showed higher transmissivity than the flat seam(; SSa-1 > SSa-2) without regard to the kinds of filled fibers and weight of geocomposite. For the similar specification, geocomposites showed the better transmissivities than the typical drainage materials, geonet composites.

Table 8. Transmissivities of geocomposites and geonet composites

Seam Type / Geogrid	SSa-1	SSa-2	Geospacer
GC-1	1.581	1.224	0.983
GC-2	1.218	1.057	0.915
GNC-1	-	-	0.699
GNC-2	-	-	0.485

Conclusion

Woven geotextiles showed the higher seam strength in the order of butterfly seam(; SSd-1 < SSd-2) > flat seam(; SSa-1 < SSa-2) > geospacer without regard to the design strength. For nonwoven geotextiles of 1,000g/m2~, the order of seam strength is geospacer > flat seam(; SSa-1 < SSa-2). Geogrids showed the higher seam strength in the order of band > geospacer but creep deformation were increased in the order of band > geospacer without regard to the design strength and geogrid's compositions. Geocomposites showed the higher seam strength in the order of geospacer > flat seam(; SSa-1 < SSa-2) but showed the transmissivity in the order of geospacer > flat seam(; SSa-1 > SSa-2) without regard to the kinds of filled fibers and weight of geocomposite.

References

[1] R. M. Koerner, 1998, "Designing with Geosynthetics", 4th Ed., Prentice-Hall, New Jersey, U.S., Chapter 4.

[2] R. D. Holtzs, B. R. Christopher and R. R. Berg, 1995, "Geosynthetic Design and Construction Guidelines", U.S. Dept. of Transportation Federal Highway Administration, Publication No. FHWA HI-95-038, 27-105.

[3] FHWA, 1989, "Geotextile Design & Construction Guidelines", U.S. Dept. of Transportation Federal Highway Administration, Publication No. FHWA HI-90-001, 24-46.

[4] Jewell R. A., 1996, Soil Reinforcement with Geotextiles, CIRLA Special Publication, Thomas Telford, Westminster, Chapter 5.

Advanced Materials Research Vol. 983 (2014) pp 39-43
© (2014) Trans Tech Publications, Switzerland
doi:10.4028/www.scientific.net/AMR.983.39

Comparative study of physico-chemical properties of pure Polyurethane and Polyurethane based on Castor Oil

M. A. ALAA[1, a*], KAMAL YUSOH[2, b], S.F.HASANY[3, c]

[1]Faculty of Chemical & Natural Resources Engineering, University Malaysia Pahang, Malaysia

[2]Department of Chemical Engineering, University of Technology, Baghdad, Iraq

Allavip63@yahoo.com, hjkamal@gmail.com, hasany_@live.co.uk

Keywords: PPG based PUs and Castor oil mixed PUs, In Situ polymerization, Physico- chemical properties, comparison

Abstract. Petroleum based polyurethanes are contributing major portions in the world requirement. To overcome the environmental issues and price adaptability, there is always a massive demand of utilization of renewable resources for polyurethane synthesis with comparable physico-chemical properties. Castor oil is the only major natural vegetable oil that contains a hydroxyl group (-OH) and unsaturated double bonds (C=C) in its organic chain and therefore can be employed with or without modification due to the excellent properties derived from the hydrophobic nature of triglycerides. In this study, physico-chemical properties of high performance polyurethane synthesized from Poly propylene glycol (PPG) in comparison with a combination of PPG and Castor oil (a renewable source), by in situ polymerization technique has been studied. The variations in properties of both types of polyurethanes are evaluated by Fourier Transform Infrared Spectroscopy (FTIR), Scanning Electron Microscopy (SEM) and Thermogravimetric analysis technique (TGA). Tensile strength properties were investigated by Film Tensile testing equipment. Results indicated the presence of large -CH stretching in castor oil mixed polyurethane with a larger oxidative thermal stability, over a pure PPG polyurethanes. Tensile properties were found almost comparable in pure and mixed polymers, which signify the usage of mixed polymer in coming future, to overcome the environmental and economical crisis in polyurethanes synthesis.

Introduction

Polyurethanes (PU) have been extensively used due to excellent physical properties (e.g. low flexibility, high tensile strength, tear and abrasion resistance, solvent resistance, etc.) and high versatility in chemical structures [1-2]. Polyurethane is generally synthesized from the isocyanate reaction with polyol. Polypropylene glycol (PPG) is a polyol, is basically derived from the petrochemical industry [3]. High rising costs of petrochemical feedstock's and enhanced public desire for environmentally friendly green products, utilization of renewable resources to manufacture the rigid polyurethane is a work necessary at the present time [4-6].

Polyurethane based on polyols derived from different vegetable oils, like castor [7-8], sunflower and rapeseed oils [9].Castor oil is one of the major natural vegetable oil that contains a hydroxyl group and so it is widely used in many chemical industries, especially in the production of polyurethanes [10]. Krushna Chandra Pradhan and P. L. Nayak investigated the synthesis of polyurethane nanocomposites prepared from natural oil like castor oil using HMDI and organically modified clay and covalently linked PU/n-HMDI composite, which was later collected successfully by the electro spinning process [7]. D.J. dos Santos et al., study preparation ,diagnosis from castor oil exhibited increasing of diisocyanate groups, in relation to polyol amount, has increasing of

diisocyanate groups, in relation to polyol amount, has increased the strength at rupture of the obtained polymers and has decreased the polymers elongation, which has resulted into a modulus increasing [11]. Anupama Kaushik et al., examines a series of 1,4-butane diol chain extended polyurethane nanocomposites based on castor oil, and 4,40-diphenylmethane diisocyanate (MDI) were synthesized with modified clay (Cloisite 30B) as filler [12].

1. Experimental

2.1 Materials

Commercial grade Castor oil was purchased from the local market. It was dehydrated at 80ºC in in a vacuum oven and characterized for hydroxyl value (148), acid value (2) and moisture content (0.379%). Polypropylene glycol (PPG) (Mn=4000) was supplied by SIGMA- Aldrich Company. Chain extender, 1, 4-butane diol was procured from Himedia, India. The toluene diisocyanate (TDI), which were used as received, were supplied from SIGMA- Aldrich Company. The catalyst used in this research is DABCO-33LV which is the mixture of triethylenediamine and di (propylene glycol) and it was supplied by Air Products and Chemicals (United Kingdom).

2.2 Characterization Technique

Fourier transform infrared spectroscopy (FTIR) analysis of polyurethanes was done using A Vector-22 FT-IR spectrometer (Nicolet 5DX FT-IR) with a resolution of 1 cm^{-1} from 4000 to 400 cm^{-1}. Thermal stability (TGA) of polyurethanes was carried out using a Universal V4.5A, TA instruments under a nitrogen atmosphere. Scanning electron microscopy (SEM) was carried out on a JEOL 6300F machine at an acceleration voltage of 5KV. Tensile testing of the nanocomposites film was carried out on an instron model 4505 universal testing machine at 25ºC, with a load cell of 5 KN and following ASTM D 638. The crosshead speed was set to 2 mm/min. Samples were cut in a dumbbell shape with an ASTM D 638 (type V).

3. Result and Discussion

3.1 FTIR Analysis

The micro-domain structures of the pure PU and castor oil based PU were analyzed by FTIR as shown in **Figure 1**. A small broad band in the range 4000–3500 cm^{-1}, was observed in both samples relating to the O-H stretching vibrations from either water or hydroxyl terminated compounds, and N-H stretching vibrations from either urea or amine group [13-14]. The $CH - CH_3$ peaks stretching are more prominent in castor oil based PU, then pure PU which may be due to larger organic chain present in castor oil based PU. Peaks at 1727 cm^{-1} represents (C=O) non bonded urethanes [12] which are likely to be present in larger number, in castor oil based PU synthesis.

2.2 TGA Analysis

The result of the thermo gravimetric analysis (Figure 2) shows that thermal stability of pure PU and castor oil PU based under identical conditions and a comparison of the weight losses occurred. The thermal stability of these polymers is starting generally above 200 °C [15-16]. It is

seen from Fig. 2 that onset decomposition temperature starts from 250°C and 235°C for pure PU and castor oil based PU, respectively. At 400 °C almost 85% of pure PU decomposed while castor

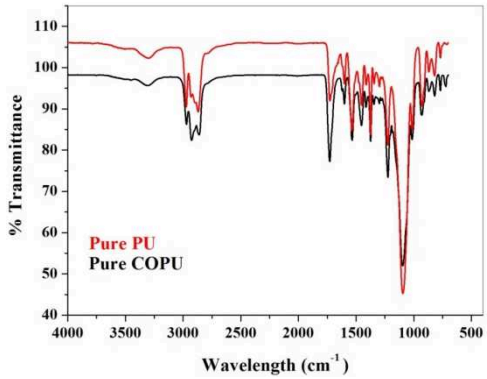

Fig. 1 Comparative FTIR spectra for PU (pure PPG & PPG and castor oil)

based PUs showed less than 80% decomposition, which may be due to the different polyol conditions, when PPG is mixed with castor oil. It may be due to the presence of low hydroxyl content polyols in the formulation which improved the thermal resistance of the castor oil based PU samples [15]. Overall thermal stability of PUs showed a slight decreasing trend as the rigid segments content increased which supports the literature samples [16]. They concluded that PU based on vegetable oils has a better oxidative thermal stability than PU based on poly (propylene glycol) [18].

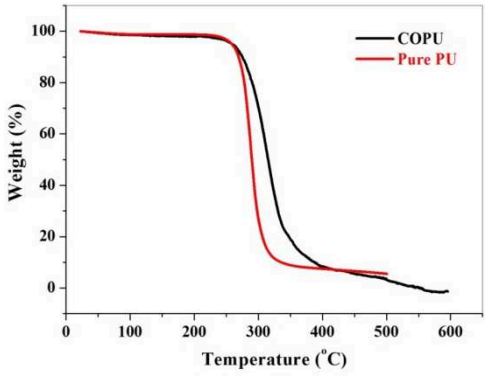

Fig. 2 Comparative TGA graph for PU (pure PPG & PPG and castor oil)

3.3 Scanning electron microscope

In pure PU, during the polymerization reaction isocyanates reacted with the polyol gelation, resulting in the formation of the cell wall of the polyurethanes, as shown in figure 3.a. When castor oil was mixed with PPG as a polyol, cell wall formation is slower and larger cells formed due to the low reactivity of castor oil [3], which exhibited the controlled cell formation by addition of castor

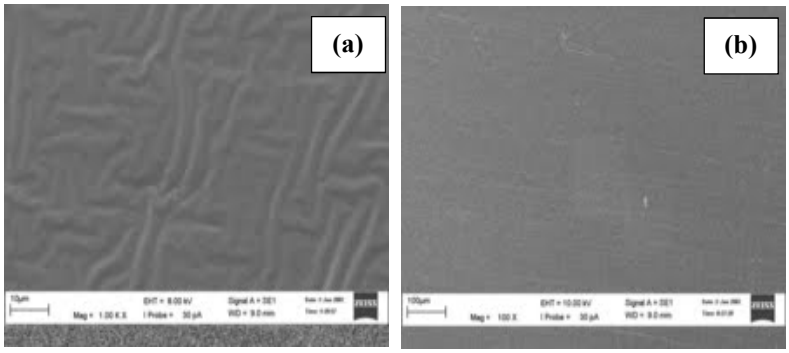

Fig. 3 SEM for PU with (3a) and without (3b) Castor Oil

oil in PPG glycol, as shown in Figure 3.b. Due to the difference in the chemical structure of the soft and hard segment, microphase separation takes easily arising from the incompatibility in PU [19].

3.4 Tensile and Mechanical properties

Figure 4 and 5 showed stress strain curves of the effect of the castor oil content in elongation at break increases, while stress decreases compared with pure PUs. The COPUs depicted an improvement of a ~21% in elongation time while stress decreases to ~58% in comparative stress–strain study of pure PUs and with COPUs 15wt% of castor oil. The improved elongation time of the COPUs may be due to the presence of the CH – CH_3 peaks stretching are more prominent in COPUs, then pure PUs which may be due to larger double bonds and bigger organic chain [20] present in COPUs. Presence the monoglyceride in castor oil helps to control such reaction due to low reactivity of secondary hydroxyl group present in the fatty acid chain [21].

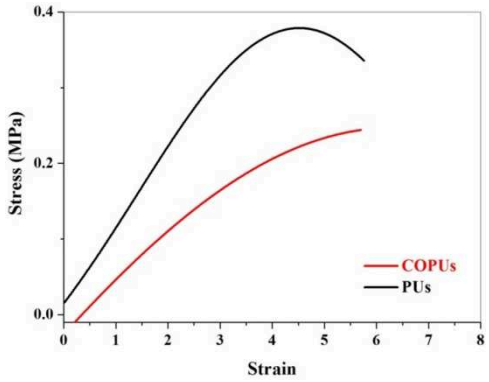

Fig. 4 Stress strain curves for pure COPUs and PUs

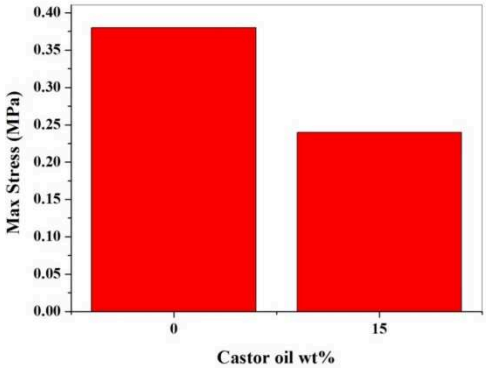

Fig. 5 Tensile strength of pure PUs and COPUs with 0 and 15wt% of castor oil.

4. Conclusion

The results depicted enhanced physico-chemical properties of castor oil mixed PUs, over pure PPG originated PUs. The presence of larger organic chains in castor oil mixed polyurethanes resulted in a larger oxidative thermal stability, over pure PPG polyurethanes. A slower cell formation was also observed in mixed polyurethanes, exhibiting a controlled synthesis. Further studies will be done to enhance the mechanical properties by applying nanofillers.

5. Acknowledgement

Authors are thankful to Universiti Malaysia Pahang, for research grant RDU 130329, for the financial support.

6. References

[1] Q.W. Lu and C.W. Macosko, J. of Polymer.45 (2004) 1981-1991.
[2] X. Caoa, L. J. Leea, T. Widyab and C. Macosko, J. of Polymer. 46 (2004) 775-783.
[3] E. Pratondo, A. W. Hanggoro, E. O. Ningrum and Sumarno, Conference on Chemical and Material Engineering. ISBN: 978-602-097-281-7 (2012) 1- 5.
[4] M.A. Meier, J.O. Metzger and U.S. Schubert, J. of Chem Soc Rev. 36 (11) (2007) 788-802.
[5] S. Gaidukov, U. Cabulis, K. Gromilova, V. Tupureina, and A. Grigalovica, International Journal of Polymer Science. 2013 (2013) Article ID 834595, 1-8.
[6] G. Lligadas, J.C. Ronda, M. Galia and V. Cadiz, J. Materials today. 16 (2013) 337-343.
[7] K. C. Pradhan and P. L. Nayak, J. Advances in Applied Science Research. 3 (5) (2012) 3045-3052.
[8] L.T. Yang, C.S. Zhao, C.L. Dai, F.U. LY and S.Q. Lin, J. of polymers and the environment. 20 (1) (2012) 230.
[9] P. Rojek and A. Prociak., J. of Applied Polymer Science. 125 (4) (2012) 2936-2945.
[10] O. Saravari and S. Praditvatanakit, J. of Progress in Organic Coatings. POC-3031, (2013) 1-7.
[11] D.J. Santos, L.B. Tavares and G.F. Batalha, J. of Achievements in Materials and Manufacturing Engineering. 54 (2) (2012) 211- 217.
[12] A. Kaushik, D. Ahuja, V. Salwani, J. of Composites. 42 (2011) 1534-1541.
[13] M. Jose, U. J. Cervantes, C. J. Rodrguez, V. H. Torres, G. L. Mesas and D. Paul: J. Thermochim Acta. 457(1-2) (2007) 92-102.
[14] U. J. Cervantes, J.I. M. Espinosa, J.V. C. Rodrıguez, A. A. Ortega, H. V. Torres, A. M. Fernandez and J. S. Roman, J. Polym Degrad Stabil. 94 (10) (2009) 1666-1677.
[15] M. Fernanda, Coutinho, C. Marcia, J. Polymer Degradation and Stability. 70 (2000) 49-57.
[16] S. M. Cakic, I. S. Ristic and O. Z. Ristic, J. Open Science (INTECH). Additional information is available at the end of the chapter 5. (2012) 80-100
[17] Gite, P.P. Mahulikar and D.G. Hundiwale, J. Progress in Organic Coatings. 68 (2010) 307-312.
[18] I. Javni, Z.S. Petrovic, A. Guo, R. Fuller, J. Appl Polym Sci. 77 (2000) 1723-1734.
[19] X. Gao, B. Zhou, Y. Guo, Y. Zhu, X. Chen, Y. Zheng, W. Gao, M. Xiaoyu and Z. Wang, J. Physicochem. Eng. Aspects. 371 (2010) 1-7.
[19] Z. S. Petrovic, J. Applications and Technology I-1 (2010) 366 - 386
[20] S. Thakur and N. Karak, J. Progress in Organic Coatings (2013) Accepted 2 September 2012 Available online.

Advanced Materials Research Vol. 983 (2014) pp 44-51

doi:10.4028/www.scientific.net/AMR.983.44

Temperature Effects and pH Value on Free Swell Behaviors of Bentonite Solutions

Han-Yong Jeon

Department of Applied Organic Materials Engineering, Inha University, Incheon, Korea(Rep.)

hyjeon@inha.ac.kr

Keywords: swelling behavior, powder and granular, sodium bentonite, permeate solutions, swell volume, pH values

Abstract. Swelling behaviors of powder and granular type sodium bentonites in permeate solutions such as NaCl, KCl, MgCl2, CaCl2, distilled water and in HCl and NaOH (with different pH values) under different temperatures were investigated. Swelling behaviors of these bentonites were dependent on strength, reactivity power and physical form of ion, and temperature and pH value of permeate solution. +1 ion solution showed higher swell volumes than +2 ion solution. Distilled water showed highest swell volumes among these tested solutions. Powder type sodium bentonite showed higher swells volume than granular type bentonite. Higher temperatures brought quickly the bentonite to a stable swell volume state. The pH value also affected on swelling volumes of bentonite as lower pH values (pH<3) increased and higher pH values (11<pH<12) decreased the swell volume of powder and granular type sodium bentonite.

Introduction

Geosynthetic clay liners (GCL) have been used as a barrier to migrating liquids in civil engineering works over 30 years. For these clay liners, sodium bentonite-montmorillonite (reactive clay) is widely used, because it gives the excellent expand and sealant property at wet stage [1]. Swelling procedure of sodium bentonite happens due to the sodium carbonate through ion exchange equilibrium process. Then, due to the flow of water, the micro structure is changed from smaller, finely distributed clay mineral flakes to larger clay mineral crystals with giving lesser permeability [2]. Swelling of montmorillonite particles is generally attributed to the volume of water molecules that are bound to the clay surface, size and valence of cation and pH values of permeate liquids [2, 3]. Swelling of bentonite decreases with increasing valence Thus, it was reported that increasing hydrated cation size for mono-valent cation(; +1 ion) gives swelling to bentonite structure and no difference results for bi-valent cation(; +2 ions) regardless of hydrated cation size. The cases of pH<3 and pH>12 showed a greater influence on swelling of bentonite, whereas pH value in between them reported a constant swell volume [3-5]. In this study, we analyzed the swelling of sodium bentonites of powder and granular types in mono-valent cation solutions such as NaCl and KCl, bi-valent cation solutions such as MgCl2 and CaCl2, distilled water and also in HCl and NaOH solutions (with different pH values) under different temperatures such as room temperature (16°C), 30°C, 40°C, 50°C and 60°C, respectively.

Experimental

Preparation of bentonites

Sodium bentonites of powder and granular types were used in this study. Chemical composition of these bentonites in chemical structure was shown in Table 1. NaCl, KCl, CaCl2 and MgCl2 were used as permeate liquids. The pH values of these solutions were shown in Table 2.

Table 1. Chemical composition of used bentonite

Chemical component	Chemical composition [%]
SiO_2	61.59
Al_2O_3	20.43
Fe_2O_3	2.78
Na_2O	3.05
T_iO_2	0.22
CaO	0.66
MgO	2.03
K_2O	0.31
L.O.I	2.38
H_2O	5.50
others	1.05

Table 2. pH values of permeate solutions

Solution	NaCl	KCl	$CaCl_2$	$MgCl_2$
PH	6.94	6.70	6.54	8.28

Free swell test

Free swell tests were carried out in accordance with ASTM. D5890. Approximately 90ml of 0.1 mol/L solution (NaCl, KCl, CaCl2 or MgCl2) or distilled water was poured into a clean 100 ml graduated cylinder. Two grams of powder or granular bentonite was added in each solution in the graduated cylinder in 0.1g increments after that, cylinder inner surface was rinsed down by solution to remove any particles adhering to the sides of it. Then, the cylinder was filled up to 100 ml mark. We prepared 5 cylinders for each permeate medium to observe the effect of temperature. And then, it was placed the cylinders in water baths under room temperature (approximately 16°C), 30°C, 40°C, 50°C and 60°C. After this, swollen volume of bentonite was measured by direct reading the cylinder scale (in ml) in every 24 hours. In order to observe the effect of pH on bentonite swelling, HCl and NaOH solutions with different pH values were used. In addition, the effect of pH on bentonite swelling was investigated in HCl ($1<pH<6$) and NaOH ($8<pH<12$) solutions were used under mentioned temperatures and swelling volume was measured in every 24 hours till come to a stable volume.

Result and Discussion

The swelling behavior of bentonite in types of powder and granular in NaCl solutions under different temperatures were shown in Fig. 1. From this, it is clearly seen that swelling volume is depend on the bath temperature till 7th experimental day. After that, swelling of bentonite lies at a

constant level of 14 ml. Thus, higher temperatures rapidly bring the bentonite to a stable swelling volume. According to Fig. 1, dependency of granular bentonite swelling on temperature exists till 15th day, which is longer than powder bentonite. After that, swelling volume does not change and stays at 13ml, which is lesser than powder form of bentonite. Thus, as in Fig. 1, powder bentonoite rapidly comes to a stable swelling volume at higher temperatures. Another feature of Fig. 1 is that during swelling, bentonite stays at constant level/s for certain period before come to a stable volume, but powder bentonite at 60°C is an exceptional case. Fig. 2 shows the selling behavior of granular and powder bentonite in KCl solution under different temperatures. In both cases, swelling volume is higher than the bentonite in NaCl solution. The pH doesn't give any effect for this, because, both solutions had approximately equal pH values. Only the possible reason is that higher reactivity of K+ ions, which raise the chemical reaction to give higher swell volume. Thus, powder bentonite gives higher swell volume than their granular form in all experimented temperatures. Hence, powder form shows a shorter period of temperature dependency to achieve a constant level of swelling than granular form. In addition, two stage of swelling behavior was observed in all cases of powder and granular bentonite as in NaCl solution.

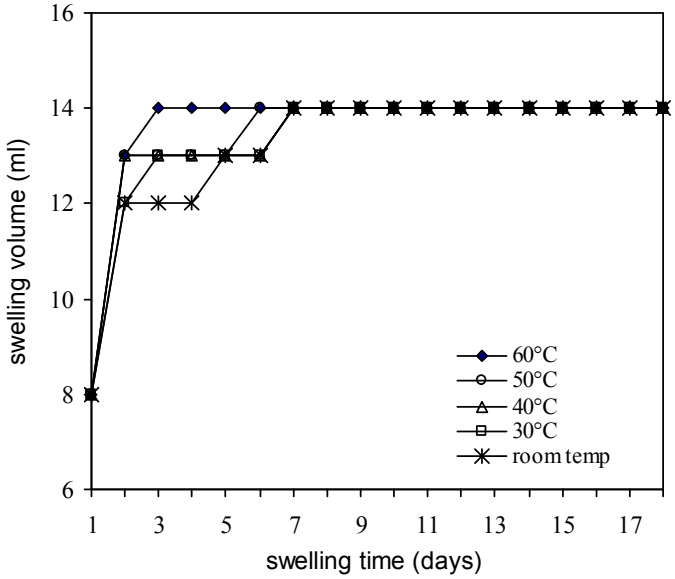

(a) Powder bentonite

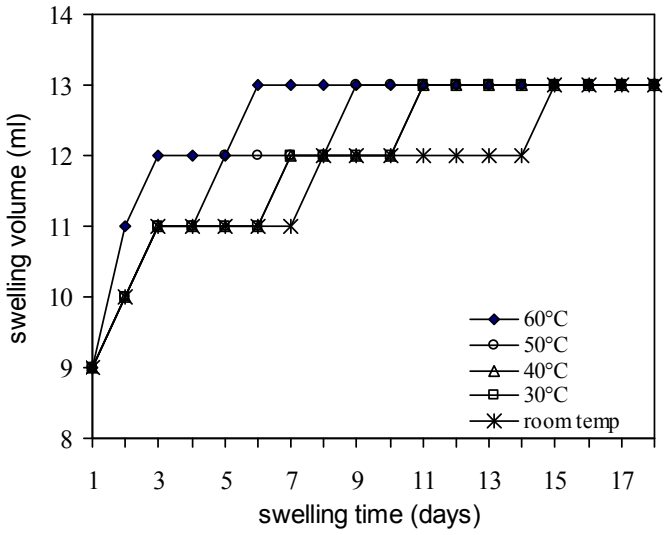

(b) Granular bentonite

Fig 1. Swelling behavior of bentonite in NaCl (0.1mol/L) solution under different temperatures

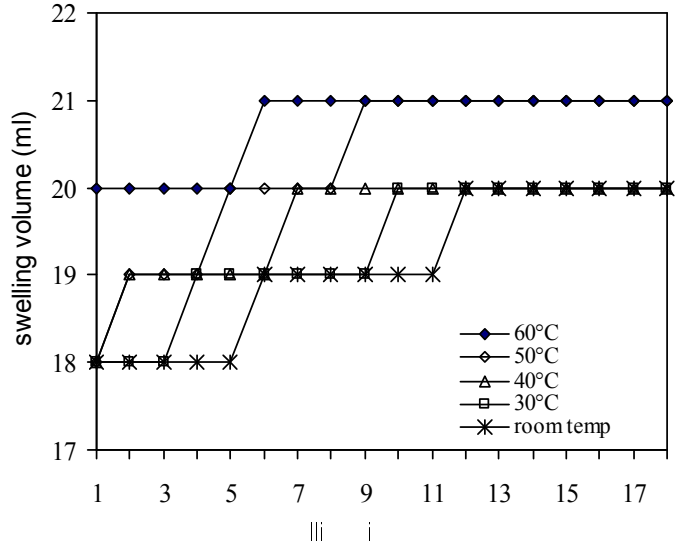

(a) Powder bentonite

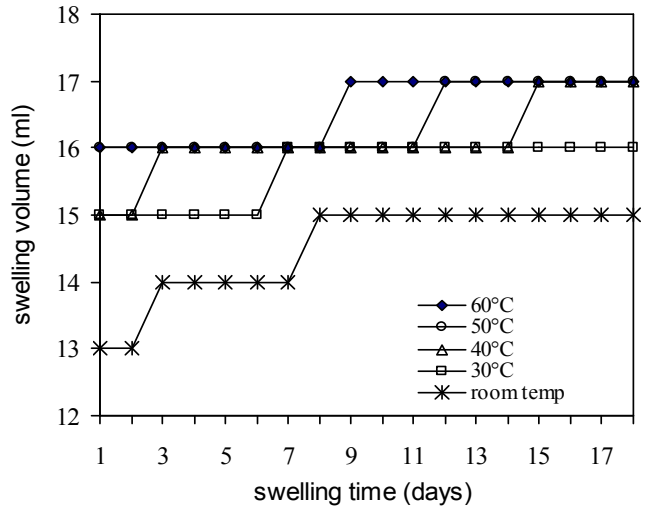

(b) Granular bentonite

Fig 2. Swelling of bentonite in KCl (0.1 mol/L) solution under different temperatures

Fig. 3 illustrates the swelling volumes of powder and granular bentonite in $CaCl_2$ solution under applied temperatures. According to that, $CaCl_2$ (+2 ions) solution gave lower swelling volumes to powder and granular bentonite compared to the swelling volumes given by NaCl and KCl (monovalent cations) solutions. Reason would be the lower reactivity power of Ca^{2+} than K^+ and Na^+, which effect on ion exchange process in swelling mechanism of bentonite to change the its micro from smaller, finely distributed clay mineral flakes to larger clay mineral crystals. The pH value cannot be affected on this change, because, we maintained the pH values approximately in same range (about 7) in all above mentioned solutions. Thus, they also show the temperature dependency of bentonite swelling. Hence, higher temperature gives higher swell volumes and quickly came to a highest state. Meanwhile, powder benonite indicate higher swell volumes than with granular bentonite.

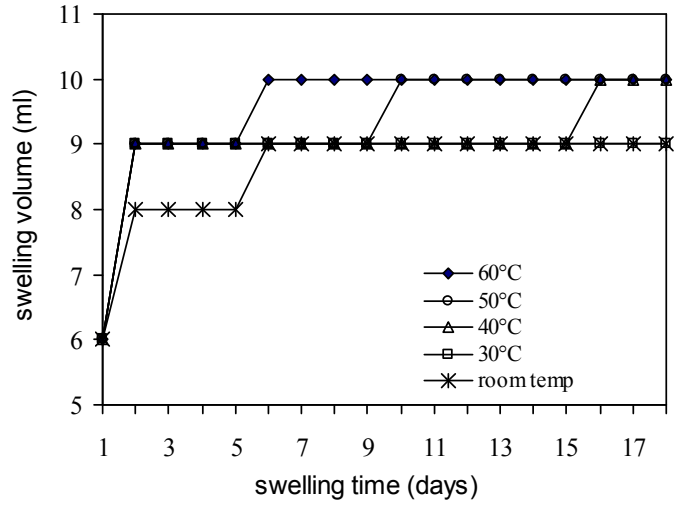

(a) Powder bentonite

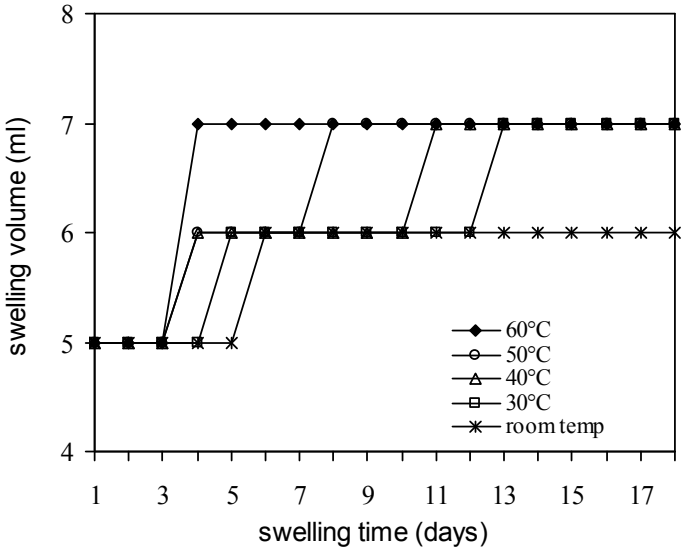

(b) Granular bentonite

Fig 3. Swelling of bentonite in $CaCl_2$ solution (0.1mol/L) under different temperatures

Fig. 4 illustrates the swelling behavior of powder and granular bentonite in $MgCl_2$ (+2 ions) solution under different temperatures. It gives lowest swelling volumes under all temperatures tested. Reason can be the lowest reactivity power of Mg^{2+} than Na^+, K^+ and Ca^{2+}. Even though

solution pH value is slightly higher than other cases, it is hard to think its' significant effect on the lowest swell volume. Fig. 4 clearly demonstrates the temperature dependency of swelling of powder bentonite. However, higher temperatures bring the bentonite rapidly to a constant level. Till 8 days, temperature dependency of powder bentonite can be observed, but that is for granular form is more longer (11 days). That implies that powder bentonite can swell rapidly to a constant level than their granular form. According to the illustrations made above, we have understood that bivalent cations gave lower swell volumes than mono-valent cation(; +1 ion). Reason would be that increase of inner-crystalline attraction by bivalent cations leads to certain reduction of structural volume of bentonite compared to mono-valent(; +1 ion) cations.

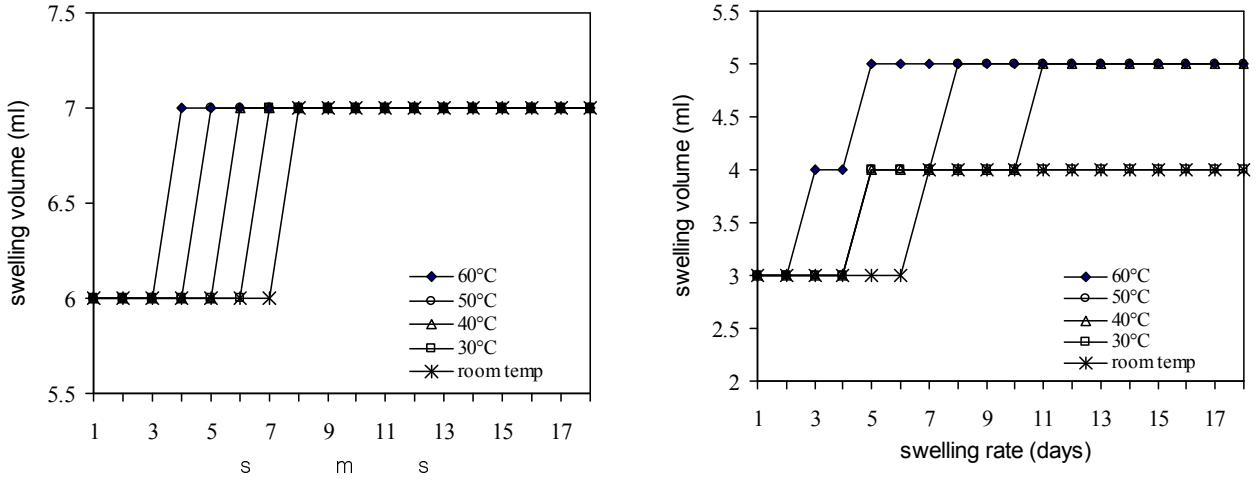

(a) Powder bentonite (b) Granular bentonite

Fig 4. Swelling of bentonite in $MgCl_2$ solution (0.1mol/L) under different temperatures

Fig. 5 shows the variations of bentonite swelling volume in distilled water under different temperatures. Distilled water gives highest swelling volumes to both powder and granular bentonite with experimented temperatures, compared with other solutions. We hypothesized the reason for this as that distilled water does not possess any valent ions to attract inner–crystalline layers of bentonite compared to mono-valent(; +1 ion) or bi-valent(; +2 ions) solutions. Thus, powder form gave slightly higher swell volume than granular form of bentonite. Thus, bentonite swells in distilled water is also temperature dependence reaction and higher temperatures bring bentonite (both forms) quickly come to a stable swell volume.

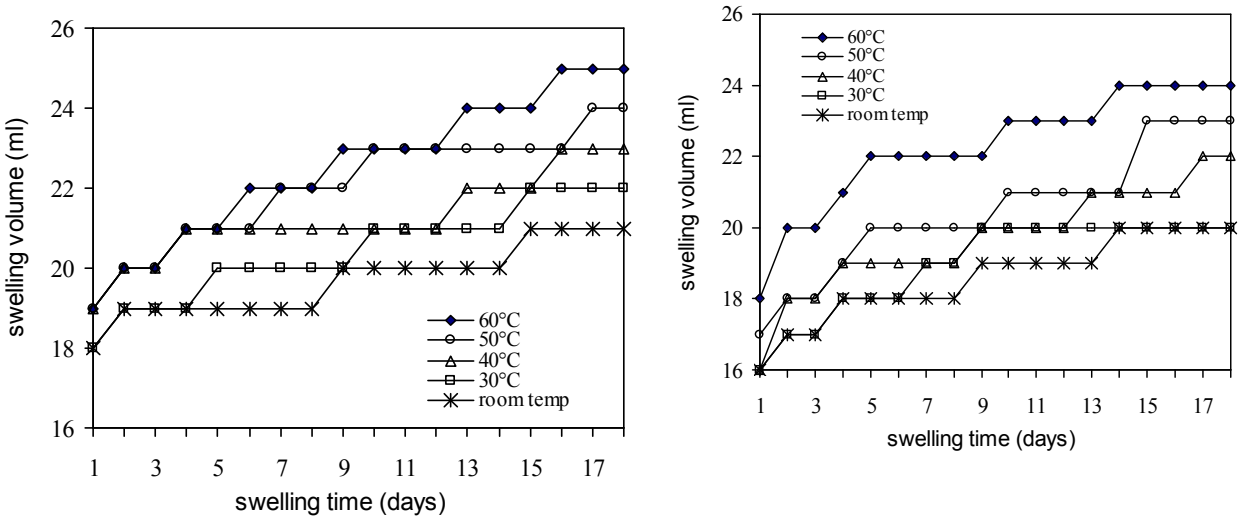

(a) Powder bentonite (b) Granular bentonite

Fig. 5. Swelling behavior of bentonite in distilled water under different temperatures

Fig. 6 illustrates the swelling behavior of Sodium bentonite powder and granular forms with differe nt pH values (using HCl and NaOH solutions) under different temperatures. We changed the pH val ues from 1 to 12, without considering 13 and 14, because these pH values were not familiar to leach ate. It is clearly shown that pH<3 and 11<pH<12 show a greater influence on swelling of bentonite. Specially, with lower pH values increase and higher pH values decrease the swell volume, in concer n of active pH ranges. Usually, a higher temperature and powder bentonite (compared to granular fo rm) leads to higher swell volumes.

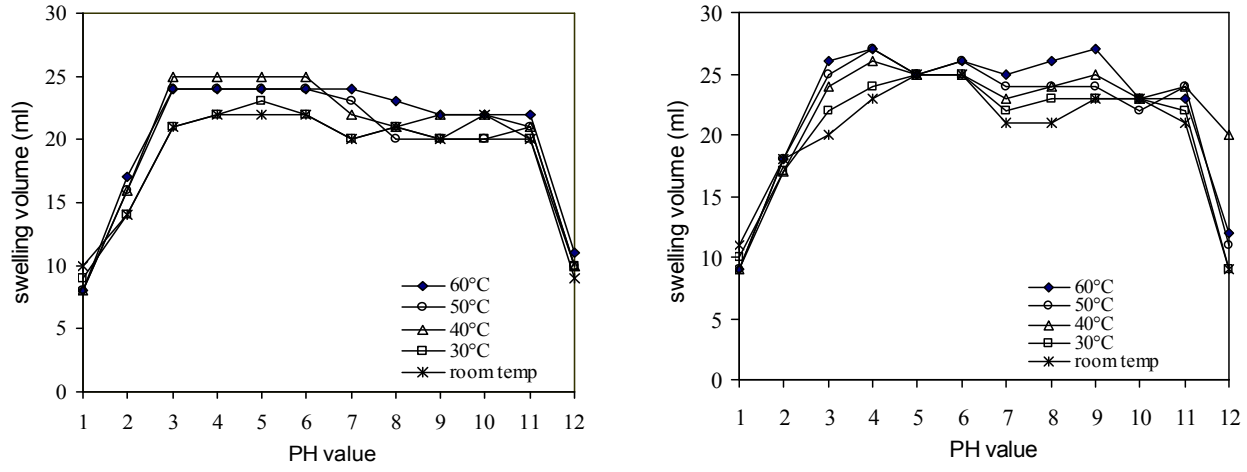

(a) Powder bentonite (b) Granular bentonite

Fig 6. Swelling of bentonite under different pH values

Conclusion

Sodium bentonite swelling behavior depends on permeate liquids. Solutions with mono-valent(; +1 ion) cations swell the bentonite highly than bi-valent(; +2 ions) cation solutions. Thus, swell volume also depends on the reactive power of these cations. Distilled water gave highest swell volumes among all tested solutions. Hence, swell volume depends also on the temperature of solutions as higher the temperature higher the swelling rate. Powder bentonite showed

comparatively higher swell volumes than their granular form. The pH value also effect on swelling volumes of bentonite as lower pH values (pH<3) increased and higher pH values (11<pH<12) decreased the swell volume of powder and granular sodium bentonite.

References

[1] R.M. Koerner, Designing with Geosynthetics, 5th ed., Prentice-Hall, Englewood Cliffs, NJ, 2005 (Chapter 5).

[2] T.A. Egloffstein, Natural bentonites-influence of the ion exchange and partial desiccation on permeability and self-healing capacity of bentonites used in GCLs", Geotextiles and Geomembranes, vol.19, 2001, pp.427-444.

[3] H.Y. Jo, T. Katsiumi, C.H. Benson, T.B. Edil, Hydraulic conductivity and swelling of nonprehydrated GCLs permeated with single-species aslt solutions, Journal of Geotechnical and Geoenvironmental Engineering, ASCE, vol.127, No.4, 2001, pp.557-567.

[4] C.D. Shackelford, C.H. Benson, T. Katsumi, T.B. Edil, L. Lin, Evaluating the hydraulic conductivity of GCLs permeated with non-standard liquids, Geotextiles and Geomembranes, vol.18, 2000, pp.133-161.

[5] C.D. Shackelford, M.J. Majeski, R.T. Stern, Electrical conductivity breakthrough curves, Journal of Geotechnical and Geoenvironmental Engineering, ASCE, Vol.125, No.4, 1999, pp 260-270.

Advanced Materials Research Vol. 983 (2014) pp 52-55

doi:10.4028/www.scientific.net/AMR.983.52

The thermal properties of unsaturated polyester resin treated with intumescent flame retardants*

Ming Gao[1,a] Dan Rong[1,b], Chunguang Song[1,c], Yuwen Ji[1,d]

[1] School of Environmental Engineering, North China University of Science and Technology, Box 206,Yanjiao Beijing 101601, China

[a] gaoming@ncist.edu.cn, [b] 2235697702@qq.com, [c] 1114149912@qq.com , [d] 1633910613@qq.com

Key words: Unsaturated Polyester Resin, degradation, flame retardant, synthesis, TG

Abstract A novel cheap macromolecular intumescent flame retardant (IFR), was synthesized. Unsaturated polyester resin (UPR) was modified with IFR to get the flame retardant UPR, whose flammability and burning behavior were characterized by limiting oxygen index (LOI). 22.7% of weight of IFR was doped into UPR to get 28.5 of LOI. The thermal properties of epoxy resins containing IFR were investigated with thermogravimetry (TG). Activation energy for the decomposition of samples was obtained using Kissinger equation. The resultant data show that for UPR containing IFR, compared with UPR, IFR decreased weight loss, thermal stability, increased the char yield, which shows that IFR can catalyze decomposition and carbonization of UPR.

Introduction

Recently halogen-free intumescent flame retardant (IFR) are attracting more and more attention from both academic and industrial communities for their multifold advantages including low toxic, low smoke, low corrosion, no corrosive gas, and so on[1,2]. Three ingredients are necessary for IFR: acid source, carbon source and gas source. Phosphorus-containing compounds are often used as an acid source while nitrogen-containing compounds are used as a blowing agent. The greatest benefit to be obtained in this way is a dramatic decrease in the heat generated due to the exothermic combustion of polymers. Other advantages include the conservation of the structural integrity of polymer as a result of the residue of solid carbon and a decrease of formation of flammable gaseous product [3]. In the former work of our group, a novel macromolecular IFR which contains an acid source, a gas source and a char source simultaneously had been synthesized. Thermal degradation and flame retardancy of EP were improved after blending with the IFR [4,5].

On the other hand, unsaturated polyester resin (UPR) is widely used as thermal insulators and mechanical shock absorbers in transport overpacks and in air conditioning. They are also used as structural materials because of their light weight, greater strength to weight ratio, and energy-absorbing capabilities [6]. UPR, like other organic polymeric materials, tends to be flammable.

So in this work, IFR synthesized was applied to UPR get flame retardancy, and the degradation behavior of UPR modified with the IFR was investigated.

Experimental

Materials

Pentaerythritol, 85% of phosphoric acid, Ethanolamine, 37.0%~40.0% of formalin as formaldehyde were received from Tianjin Fuchen Chemical Reagent Factory. Melamine was obtained from Beijing Chemical Reagent Company. Urea was received from Tianjin Yongda Chemical Reagent Company, Acetone was obtain from Beijing Chemical Factory.191 Accelerator for Unsaturated Polyester Resin and 191 Unsaturated Polyester Resin Curing Agent.

Instrumentation

Thermogravimetry (TG) was carried out on a HCT-2 thermal analyzer (Beijing Hengjiu Scientific Instrument Factory) under a dynamic nitrogen (dried) atmosphere at a heating rate of 10°C min^{-1}. LOI was tested by JF-3 LOI Apparatus (Jiang Ning Analysis Instrument Company, China) and KYKY2800B SEM (KEYI Technology Development Ltd).

Synthesis of IFR

MIFR was synthesized as reference [4], the structure is to see Scheme 1. 37% formalin as formaldehyde [F] 1 mol was brought to PH 8-8.5 with ethanolamine and heated. Then melamine [M] 0.2mol and urea [U] 0.5mol were added to the above solution, stirred until dissolved and heated under reflux for 50 min. Heating was stopped and the solution was allowed to cool to get MUF prepolymer A. 85% phosphoric acid 1 mol and pentaerythritol 0.5mol were mixed, heated to 120°C, stirred for 4h until without water distilled to get caged bicyclic pentaerythritol diphosphonate to get B. B was added slowly into A under stirring to obtain MIFR.

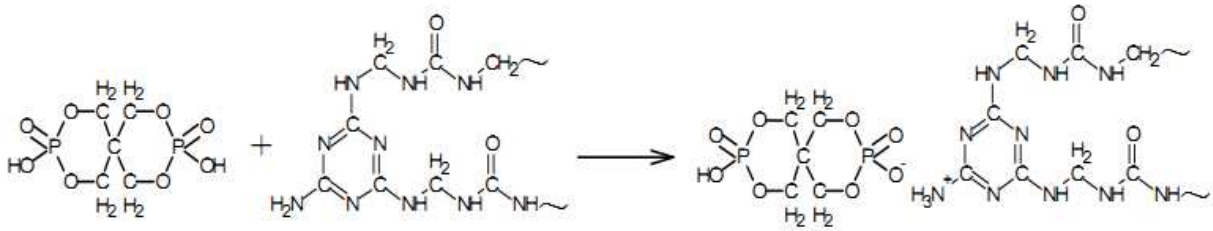

A B MIFR

Scheme 1 Synthesis of MIFR

Preparation of flame retardant UPR

The 191 Accelerator for Unsaturated Polyester Resin and the 191 Unsaturated Polyester Resin Curing Agents homogeneously were mixed followed the Table 1. After 3~5 minutes, the intumescent flame retardant (IFR) was added into the solution and stirred. Then added the bicyclic pentaerythritol diphosphonate, stirred homogeneously and transferred them into a 2500ml beaker. Kept it in an oven at 50 ℃ for five hours. Scoured the samples with acetone after them were solidified and dried it. The samples were obtained.

Table 1 The composition of the samples

Sample	Accelerator /g	Curing Agent /g	A /g	B/g	IFR/%	LOI/%
A	102.9	2.5	0	0	0	20
B	99.9	2.7	10.1	15.2	19.5%	24.8
C	100.3	2.7	11.5	16.5	21.5%	27.5
D	101.5	2.7	12.4	18.4	22.7%	28.5
E	99.2	2.7	13.5	20.2	24.6%	30.5
F	101.8	2.8	16.1	24.3	28.3%	31.5

RESULTS AND DISCUSSION

Flame retardancy of intumescent flame retardant (IFR)

Flame retardant properties of UPR containing different IFR were list in Table 1. From the Table 1, we can see the good flame retardancy of the IFR. With the increases of IFR, the LOI values increase. 28.3% weight of IFR was doped into UPR to get 31.5% of LOI.

Degradation of Unsaturated Polyester Resin

The TG curves of sample A and sample D were carried out in dynamic nitrogen from ambient temperature to 650°C and are shown in Figs 1-2. The initial decomposition temperature (IDT) determined by 5% of weight loss, integral procedure decomposition temperature (IPDT) determined by 50% of weight loss, char yield at 600°C were measured, list in Table 2.

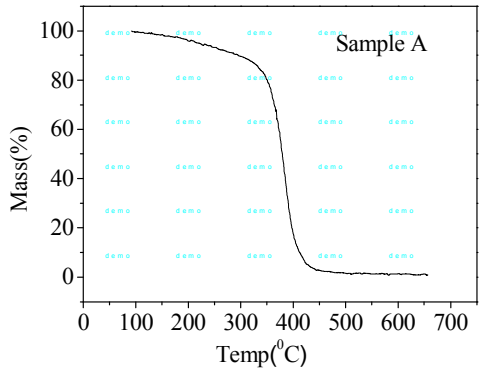

Fig. 1 TG curves of Sample A

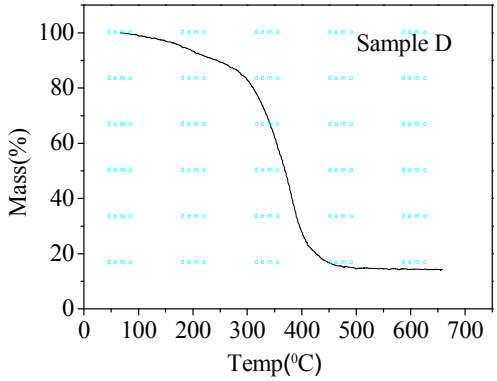

Fig. 2 TG curves of Sample D

Table 2 Thermal data of UPR from thermogravimetrtic analysis in nitrogen

No.	MIFR (%)	IDT (°C)	IPDT (°C)	Char yield (%)
A	-	221	379	1.4
D	22.7	179	369	14.4

When the flame retardant elements are incorporated into polymeric materials, the weight loss pattern of the polymers is altered. Phosphorus groups decompose at relatively low temperature to form a heat-resistant char, to retard the weight loss rate of the polymers at high temperatures [7]. Nitrogen-containing compounds produce incombustible gases when they degrade. The heat gases can swell the just formed char. The swollen char can isolate the transfer of mass and heat between the materials and the flame in a fire. That protects the unburned materials. The actions play some critical roles in flame retarding polymeric materials through condensed-phase mechanisms as well as gas-phase mechanism.

From the Figs. 1-2, it can be seen that there is a main and quick decomposition stage, and the weight loss behavior of UPR containing IFR is found to follow the patterns discussed above. From Table 2, For UPR containing IFR (Sample D), compared with Sample A, char yields (14.4%) are increased. The decrease significantly of weight loss rates is lowers the amount and rate of release of combustible products from the UPR' decomposition, consequently depressing the resins' flammability. The increase of char yields agrees with mechanism of flame retardant [8]. Introduction of flame-retardants leads to more char formed at the expense of flammable volatile products of thermal degradation, thus suppressing combustion and increasing the LOI.

Thermal stability of intumescent flame retardant (IFR)

The thermal stability of the intumescent flame retardant is assessed with two parameters: andante decomposition temperature and main decomposition temperature as well as char temperature. Andante decomposition temperature indicates the apparent thermal stability of the unsaturated Polyester Resin, i.e., the failure temperatures of the resins in processing and moulding. On the other hand, main decomposition temperature and char temperature exhibits the resins' inherent thermal stability, i.e. the decomposition characteristics of the resins' volatile composition. From Table 2, phosphorus-containing intumescent flame retardant (Sample D) show relatively lower andante

decomposition temperature than do the phosphorus-free resin (Sample A), since phosphorus-groups decompose at low temperatures. On the other hand, the existence of IFR (Sample D) exhibits higher main decomposition temperature and char temperature than the Sample A, retarding the weight loss rate of the polymers at high temperatures. The high main decomposition temperature and char temperature (325~425 and 425~650) implies the UPR' potential application in highly anti-thermal coatings and thermal insulating materials.

Analysis of the images from the SEM

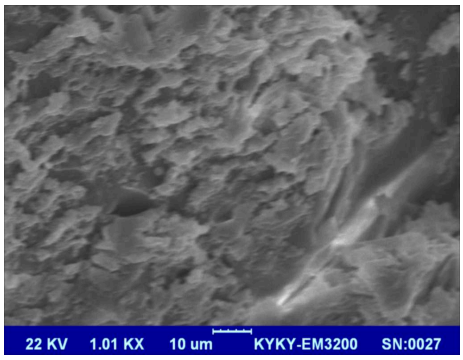

Fig.3 SEM of the char of sample A

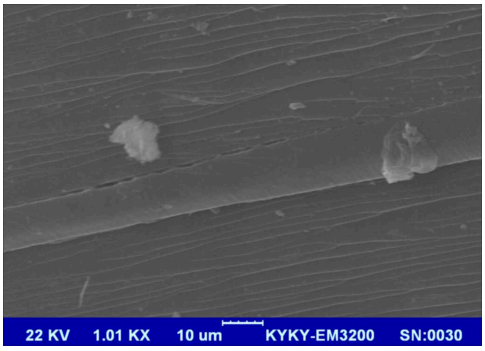

Fig.4 SEM of the char of sample D

From Figs3-4, we can find easily that there is a great different between the images. The Sample A hardly formed char level after burned, but formed alveolate floccule .That can not retard the volatile gas getting out. But the Sample D formed char level with higher density. It's effective to isolate to be burned.

Conclusions

We succeed in synthesizing a novel cheap macromolecular IFR with a structure of a caged bicyclic pentaerythritol diphosphonate. 22.7% weight of the IFR are doped into UPR to get 28.5 of LOI. For UPR containing IFR, compared with UPR, incorporating IFR into unsaturated polyester resin alters degradation characteristics, which decreases weight loss, increases the char yield. However, for UPR containing IFR, the andante decomposition temperature decreased, which shows the stability was decreased. In the thermal degradation of UPR containing IFR, phosphorus groups decompose at relatively low temperature, then catalyzing decomposition and carbonization of UPR to form a heat-resistant char, retarding the weight loss rate of the UPR at high temperatures. Nitrogen serving as blowing agents and char-reinforcing components, leads to the production of intumescent chars which protects the underlying combustible substrate to get good flame retardancy.

*Contract grant sponsor: Fundamental research funds for the Central Universities: 3142013102.

References

[1] S Bourbigot, M Le Rras, S Duquesne, M Rochery: Macromolecular Materials and Engineering, Vol. 289(2004), p.499.
[2] Q Wu, B Qu: Polymer Degradation and Stability, Vol. 74(2001), p.255.
[3] C. F. Cullis, M. M. Hirschler: Eur. Polym. J. Vol. 20(1984), p.53.
[4] M Gao, W Wu, Y Yan: J. Therm. Anal. Cal. Vol. 95(2009), p.605
[5] M Gao, S S Yang: J. Appl. Polymer Sci. Vol. 115(2010), p.2346
[6] Oertel, G. Polyurethane Handbook; Hanser: New York, 1994.
[7] B. Youssef, B. Mortaigne, M. Soulard and J. M. Saiter, Therm. Anal. Cal., 90 (2007), 489
[8] B. K. Kandola, A. R. Horrocks, D. Price, and G. V. Coleman, J. Macromal. Sci., Rev. Macromol. Chem. Phys. C36 (4) (1996), 721

CHAPTER 2:

Nanomaterials and Nanotechnologies

Advanced Materials Research Vol. 983 (2014) pp 59-62

doi:10.4028/www.scientific.net/AMR.983.59

Microstructure of gold nano-cystals from nanometer to micrometer lengthscale in gold bulk metallic glass

Nirut Boonchu[1, a] , Anan Lawan[2], Kamolchanok Thipayarat[3], Suphakit Pintasiri[4], Worasit Kanjanakijkasem[5], Surasak Kuimalee[6,b] and Boonrat Lohwongwatana[3,c,*]

[1, 2,3,7]Innovation Metal Research Unit, Department of Metallurgical Engineering,

Faculty of Engineering, Chulalongkorn University, Bangkok, Thailand. 10330

[4]Western Digital (Thailand) Co.Ltd., Phra Nakhon Si Ayutthaya, Thailand, 13160

[5]Department of Mechanical Engineering,

Faculty of Engineering, Burapha University, Chonburi, Thailand, 20131

[6]Department of Industrial Chemistry and Textile Technology,

Faculty of Science, Maejo University, Chiang Mai, Thailand, 50290

[a] nirutb@mtec.or.th, [b]kuimalee.s@gmail.com, [c]boonrat@gmail.coml

Keywords: Gold based metallic glass, Gold BMG, TEM study, Nucleation and Growth.

Abstract. Gold based bulk metallic glass was synthesized at with different quenching rates. $Au_{54}Ag_5Pd_2Cu_{24.3}Si_{14.7}$ alloy ingots were cast into wedge shape and cone shape samples. The critical casting thickness of this alloy composition was found to be 4 mm when cast in copper mold. Completely amorphous structure as found in sections thinner than 4 mm when considering a infinite copper plate geometry. In locations with slower cooling rates, there are small fractions of transformed nano-crystals. The transmission electron microscope (TEM) study of $Au_{54}Ag_5Pd_2Cu_{24.3}Si_{14.7}$ solidified microstructure could offer snap shots of nucleation and growth of crystals from nanometer to micrometer length-scale as evolved with different cooling rates. The phase evolution was recorded by transmission electron microscope study, electron diffraction and metallography using scanning electron microscope. The specimens comprised of both fully amorphous solid and nano-composites which were the combination of nano-crystals of controlled sizes in amorphous matrix. Vickers hardness values increased to 350-450 Hv, when compared to sub 100-150 Hv level of conventional 18-k gold alloys as cast. The study offers a revolutionary way to create ultrahigh strength bulk metals that comprise of large percentage of nano-crystals in amorphous matrix.

Introduction

Recent development of robust and stable glass forming alloy compositions [1-4] has enabled materials scientists to study the nucleation and growth theory during solidification at various snapshots in time. Due to sluggish kinetics, as the molten metal is cooled from liquid state, there is a tendency for the system to bypass the crystallization events. Crystals that form in the nanometer length-scale would slowly grow as functions of cooling rate and time allowed. By casting into wedge shape or cone shape specimens, the cooling rate could be varied significantly. We explored the possibility to process metals with various cooling rates in the region near the critical cooling rates of bulk metallic glass.

Materials and methods

Methodology. Two series of processing pathways were selected as to vary cooling rates. The first technique involved a rapid quenching of the molten liquid into a wedge-shape cavity inside a copper mold which acted as a large thermal reservoir. The second technique utilized quartz tube which was drawn into cone shape. The metal alloy was melted and poured inside the cone. The cone was then

quenched a large water bath. As shown in fig.1, the two samples had different dimensionality, boundary conditions, thermal diffusivity at the interface and therefore, different cooling rates. The samples were cast into wedge and cone shapes so that cooling rates could also be varied within the same specimen as shown in fig. 1.

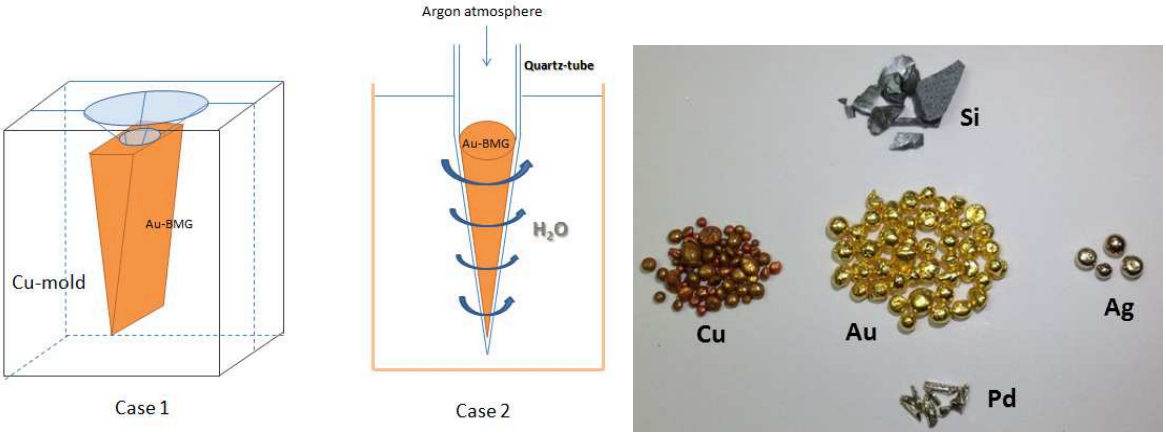

Fig. 1. (Left) Two material preparation methods. Case 1 represents copper mold casting of wedge shape sample, and case 2 represents quartz mold casting of cone shape sample.
Fig. 2. (Right) Raw metals of 99.9% or higher purity was synthesized to make alloy ingots.

Materials preparation

The $Au_{54}Ag_5Pd_2Cu_{24.3}Si_{14.7}$ gold alloy ingots were prepared by arc-melting 99.9% or higher pure metals together on a water-cooled copper plate, under titanium-gettered atmosphere (fig. 2). The mixed ingots were then cast into copper mold (wedge shape specimen) and quartz mold (cone shape specimen). For the latter case, the quartz was subsequently stirred inside water reservoir as to cool down the heated metal. The samples were prepared by both polishing, twin-jetting and focus ion beam and lift off in the case of TEM study.

Cooling rate calculation

The cooling rates were determined at the central of the cast specimen of different values of thicknesses (wedge shape) and diameters (cone shape) (Fig.1). For the case of copper mold wedge sample, the results were excerpted from [5] and [6]. For the case of cone sample as cast in quartz tube, cooling rate was approximated using implicit unsteady scheme. The initial condition was set at 800 °C before the apparatus is dropped and stirred in water (h = 2000 W/m^2.K) for 12 seconds.

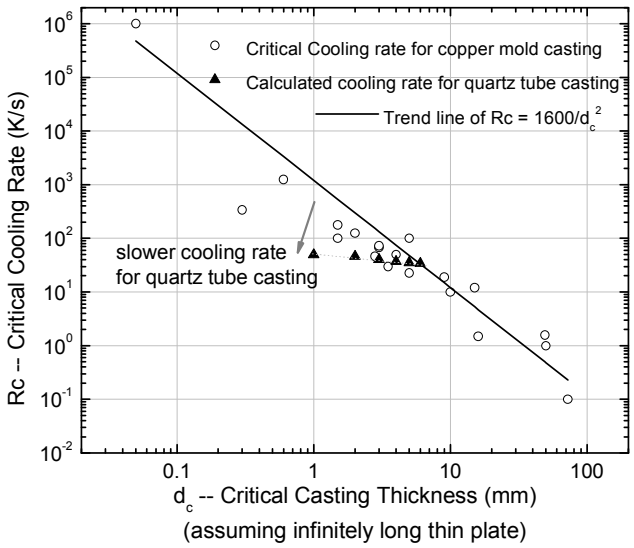

Fig. 3. Cooling rates in copper mold casting is represented by the trend line. For the case of quartz tube casting, the quartz itself acts as an insulator and prevents the metals from quenching sufficiently.

Microstructure study and sample preparation

Because the effective cooling rates are relatively slower in the case of quartz tube casting, the samples were found to have many nano-crystals starting at 1mm- to 2mm- thick portions. Back-scattered elections (BSE) imaging in scanning electron microscope (SEM) was used to study the microstructure of crystals with dendritic growth as embedded in amorphous matrix. As shown in fig. 4, cross sections of gold BMG at 1 mm was found to have crystals in sub 10-microns level and 2 mm diameter sections reveal 10-microns level dendritic microstructure.

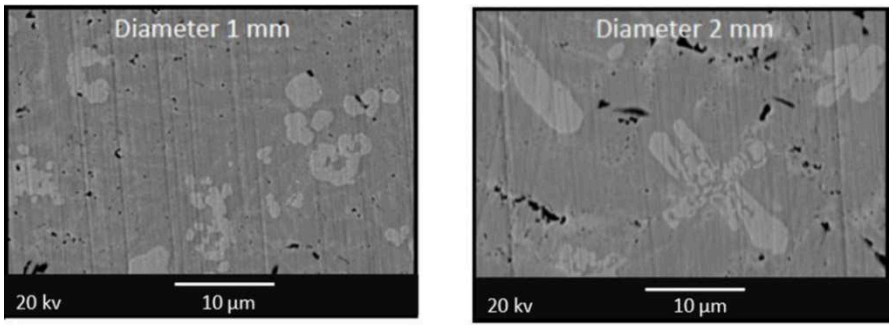

Fig. 4. BSE images reveal gold dendrites embedded in gold BMG background. The microstructure features were in the 10 microns level for cast portions that were 1-2 mm thick.

Results and Discussion

BSE SEMs, TEM, selected area electron diffraction (SAED) and x-ray diffraction were the four main techniques used to identify microstructures of the samples. TEM study shown in fig. 5 and fig. 6 are examples from cross-sections of wedge shape sample as cast in copper mold at 3 mm and 4.5 mm. Drastic difference could be found in the two materials. For the case of 3 mm, there was a small evidence of coarsening that could be the origins of nucleation and growth of crystalline phases. However, for the 4.5 mm thick cast, the samples were full of nano-crystals. SAED patterns also revealed diffused rings which are the signature of amorphous material.

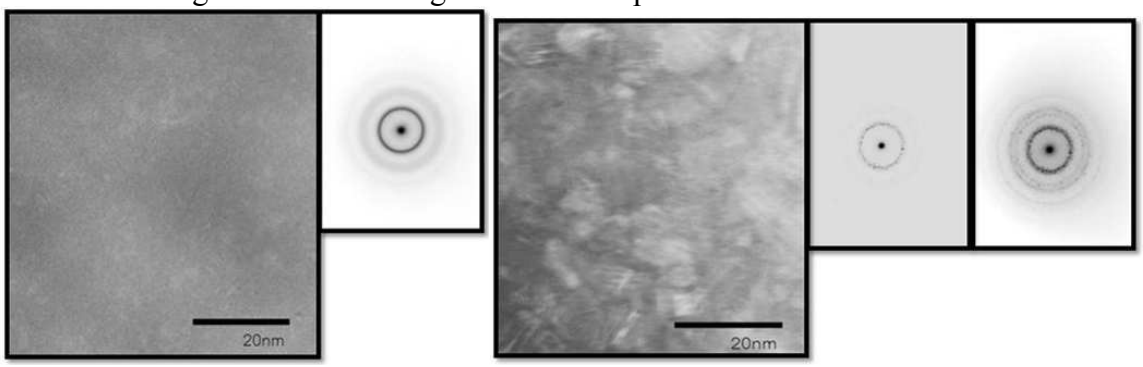

Fig. 5 and fig. 6. The two images are TEM micrographs obtained copper mold cast samples. The cross sections were at 3 mm thick portion (left) and 4.5 mm thick portion (right). SAED patterns reveal large amorphous background as evidenced by diffused ring pattern. For 4.5 mm thick sample, nano-crystals of less than 10 nanometer diameter were found.

Conclusion

Two types of nano-composites were created by two casting techniques – copper mold casting (wedge shape) and quartz tube casting (cone shape). The cooling rates were heavily controlled by the interface of the melt. Particularly for the case of quartz, the cooling has been restricted by the interface which is an insulator itself. By carefully selecting the cooling rates, sizes of nano-crystals could be designed and controlled. The hardness values of 350 Hv and desired properties suggest that BMG is an interest class of materials in which theoretical strengths of materials are being challenged.

Acknowlegement

Researchers acknowledge financial funding supports from (1) The 90th Anniversary of Chulalongkorn University Fund (Ratchadaphiseksomphot Endowment Fund), Chulalongkorn University, (2) Neuroscience of Headache Research Unit, (3) The Gem and Jewelry Institute of Thailand, and (4) Thailand Research Fund (Grant number MRG5180201). This research would not be accomplished without kind supports of Mr. Anan Lawan, Mr. Suphakit Pintasiri, and Ms. Budsabong Kuntalue.

References

[1] Schroers J, Lohwongwatana B, Johnson WL, Peker A. Gold based bulk metallic glass. Applied Physics Letters 2005;87:061912.

[2] Wei BC, Loser W, Xia L, Roth S, Pan M, Wang WH, et al. Anomalous thermal stability of Nd-Fe-Co-Al bulk metallic glass. Acta Materialia 2002;50:4357-67.

[3] Wang WH, Lewandowski JJ, Greer AL. Understanding the glass-forming ability of Cu50Zr50 alloys in terms of a metastable eutectic. Journal of Materials Research 2005;20:2307-13.

[4] Schroers J, Lohwongwatana B, Johnson WL, Peker A. Precious bulk metallic glasses for jewelry applications. Materials Science and Engineering a-Structural Materials Properties Microstructure and Processing 2007;449:235-8.

[5] Lohwongwatana B, Schroers J, Johnson WL. Strain rate induced crystallization in bulk metallic glass-forming liquid. Phys Rev Lett 2006;96:075503.

[6] Lohwongwatana B. Development, characterization, and applications of gold and platinum bulk metallic glasses. 2007.

Advanced Materials Research Vol. 983 (2014) pp 63-66

doi:10.4028/www.scientific.net/AMR.983.63

Nanotechnology and earth construction: the mechanical properties of *adobe* brick stabilized by *Laponite* nanoparticles

Francesca Scalisi [1, a]

[1]Department of Architettura, University of Palermo - Viale delle Scienze, Italy

[a] francesca.scalisi@unipa.it

Keywords: adobe, laponite, earth, construction.

Abstract. The contribution describes the experimental analysis for the improvement of the mechanical properties of samples of earth with the addition of Laponite nanoparticles. Were made two types of samples: the first consisting of soil, sand and water; the second consisting of soil, water, sand and Laponite nanoparticles. The operations performed were: chemical analysis of soil and sand; preparation of samples; Scanning Electron Microscope (SEM) observation of samples for the distribution of the elements, especially the Laponite nanoparticles; testing of compression strength and flexural strength of two types of samples; comparisons of the resulted of the mechanical tests. The improvement of the mechanical characteristics of the earth material using nanotechnology, will increase the use of eco-friendly, non-toxic, cost effective, available materials in architecture.

Introduction

The mineral component of earth is made of a fine granulometry fraction composed mainly by clay minerals belonging to the class of phyllosilicates (which dimension is below 4 μm) and by a coarse granulometry fraction (silt, sand and gravel fractions) composed by quarts, feldspars, carbonate, iron idroxides, roch fragments. The soil is a composite natural material, is made up of two types of components: the binder or matrix and the reinforcements. The research program PRIN 2008 entitled *Nanotechnologies for clay bricks: tradition, innovation and sustainability* aims at designing new nanocomposites, a new class of materials characterized by a dispersion of ultra-fine phases, typically of the order of a few nanometers; such a dispersion confers to the nanocomposites unique properties not shared with the conventional composites or micro-composites [1]. The sample realized is of the *adobe* type, an earthen brick shaped by hand in a mould, without being compressed, and left to dry under natural conditions. The mixture used to produce traditional *adobe* is: soil and water with sand as a stabilizer. *Stabilizing* earth means basically modifying the properties of an earth/water system in order to improve its physical-chemical and mechanical characteristics. There are various stabilizers used in earthen bricks, ranging from cement to natural stabilizers such as straw [2] [3]. As well as soil, water and sand, the nanocomposite envisages the utilization of a stabilizer in the shape of a small percentage of Laponite nanoparticles (clay nanodiscs with a diameter of 25 nm and a thickness of 1 nm). Both types of *adobe* were subjected to tests of compression and flexion resistance and the results were compared in order to verify whether the addition of Laponite nanoparticles had improved the mechanical resistance of the *adobe*.

Materials

The materials used to make the samples are: soil, sand, water and Laponite nanoparticles. Soil was taken from the Roccasieli quarry, situated in the municipality of Motta S. Anastasia in Sicily. The sand utilized was lavic and of basaltic origin from Nicolosi in Sicily. The Laponite RD is a synthetic layered silicate, was supplied by Rockwood Additives Ltd. as a white powder and used without further purification. It is composed of rigid disk-shaped crystals with a well defined

thickness of 1 nm and an diameter of 25 nm. The results of the chemical analyzes of soil, sand and Laponite nanoparticles are shown in Tables 1, 2 and 3. The results of the grain size distribution analyzes of sand is shown in Table 4. After chemical analysis it was noted that SiO2 was the element with the greatest presence percentagewise of all the materials.

Table 1 - Chemical composition of soil

	[%]
SiO_2	48,88
Na2O	1,33
K2O	0,56
MgO	5,05
$Fe2O_3$	8,08
$Al\ 2O_3$	11,80
MnO_2	0,05
TiO_2	0,05
Organic matter	2,03
Cl	0,013
F	0,001

Table 2 - Chemical composition of sand

	[%]
SiO_2	92,00
Al_2O_3	4,00
Fe_2O_3	0,040
TiO_2	0,01
CaO	0,30
MgO	0,02
K_2O	3,20
Na_2O	0,20

Table 3 - Chemical composition of Laponite

	[%]
SiO_2	59.5
MgO	27.5
Li_2O	0.8
Na_2O	2.8
Loss on Ignition	8.2

Table 4 - Grain size distribution of sand

mm	[%]
>1.00<1.50	3
1.00 - 0.80	8
0.80 -0.60	37
0.60 - 0.40	37
0.40 - 0.30	8
<0.30	5

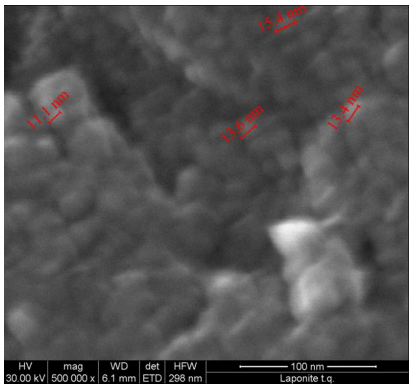

Fig. 1 - SEM 500.000x of Laponite.

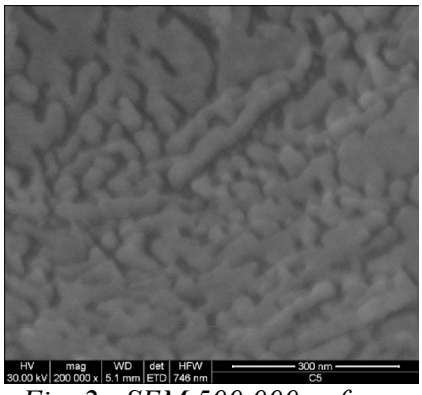

Fig. 2 - SEM 500.000x of sample ASN.

Preparing samples

The samples produced were of two types: the type indicated with the initials AS, made up of 30% sand, 38.46% water and 31.54% soil; the type indicated ad ASN comprised 25% sand, 38.46% water, 31.54% soil and 5% Laponite nanoparticles. The materials were mixed dry and the water was added subsequently. The mixture was poured into the moulds and the following day the *adobe* was ready to be extracted. The *adobe* were placed on a shelf in a dry and ventilated ambience until they had dried completely. The sizes of the samples were 40x40x160 mm, for the flexion tests and 50x50x50 mm for the compression test. The specimens were scrutinized on the *Scanning Electron Microscope* (*SEM*), which consented verification of the uniform distribution of the elements making up the samples (Fig. 2). The main problem to emerge during the preparation of these test-samples

was that of determining the percentage of Laponite nanoparticles to be inserted in the compound. To this end two types of test-sample were produced: the first, comprising soil, water, sand and 8% Laponite nanoparticles (Fig. 3); the second comprised soil, water, sand and 5% Laponite nanoparticles (Fig. 4). The test-samples produced during the drying-out phase presented several cracks, occasionally splitting up completely; this drawback arose because the Laponite nanoparticles absorbs a lot of water and does not allow the correct drying-out of the test-sample. On the other hand, the samples produced with 5% Laponite nanoparticles did not present any cracks.


Figs. 3, 4 - Samples produced with 8% (left) and 5% of Laponite nanoparticles (rigth).

Testing of compression strength and flexural strength

The AS and ASN samples were subjected to compression and flexion tests (Figs. 5, 6). In the absence of regulations regarding earthen bricks, for the administration of the compression and flexion tests, reference was made to the following norms: for compression, NORMA UNI EN 772-1:2011 the title being *Testing methods for masonry elements - Part 1: Determining compression resistance;* and for flexion, NORMA 12372:2007 with the title *Testing methods for natural stone - Determining flexion resistance under concentrated load.* Before carrying out the tests the samples were compacted to constant mass, at a temperature of 20±2 °C and relative humidity of 65±5%. *Compression strength*. The results of the compression resistance tests are shown in Table 5. The samples made up of soil, water and sand (*AS*) showed an average compression resistance of 3.6 MPa, whilst those composed of soil, water, sand and Laponite nanoparticles (*ASN*) showed an average compression resistance of 4.7 MPa.

Table 5 - Test results of compression strength of the samples AS and ASN

Sample	Compression strength [MPa]	Sample	Compression strength [MPa]
AS/1	4,0	ASN/1	4,1
AS/2	3,0	ASN/2	5,0
AS/3	3,2	ASN/3	4,4
AS/4	3,4	ASN/4	4,7
AS/5	4,6	ASN/5	5,3
AS/6	3,4	ASN/6	4,7
Average compression strength 3,6 MPa		Average compression strength 4,7 MPa	

If we bear in mind that the compression resistance demanded for an *adobe* is about 2 then the results obtained can be deemed satisfactory. The ASN samples present an average compression resistance of 4.7 MPa; this is higher than the compression resistance of the extruded blocks, which goes from 1.7 MPa to 4.5 MPa, whilst it is higher than the minimum compression resistance of the compressed blocks (which is 4 MPa). *Flexural strength.* The results of the tests for flexion resistance under concentrated load are shown in Table 6. The samples composed of clay, sand and water (AS) present an average flexion resistance of 1.7 MPa, whilst those composed of clay, sand,

water and Laponite nanoparticles (*ASN*) present an average flexion resistance of 2.32 MPa. If we consider that the minimum flexion resistance demanded for an *adobe* is 0.4 MPa, then an average flexion resistance of 2.42 MPa represents a notable result.

Figs. 5, 6 - The samples AS to be tested for compression strength (left) and flexural strength (rigth).

Table 6 - Test results of flexural strength of the samples AS and ASN

Sample	Flexural strength [MPa]	Sample	Flexural strength [MPa]
AS/1	1,8	ASN/1	1,9
AS/2	1,8	ASN/2	2,2
AS/3	1,6	ASN/3	2,3
AS/4	1,6	ASN/4	2,4
AS/5	1,7	ASN/5	2,8
Average flexural strength 1,7 MPa		Average flexural strength 2,42 MPa	

Conclusions

The use of Laponite nanoparticles in earthen bricks has brought about a 30% increase in mechanical compression and flexion resistance when compared to traditional bricks. Improving the mechanical resistance of *adobe* is very important for its utilization in construction. In fact, *adobe* can be used on both existing buildings and newly-built ones, and can be employed for supporting structures or internal partitions. The greater difficulty encountered by using earthen bricks in construction is due precisely to its mechanical resistance, a limitation that, if it can be overcome, will contribute to the diffusion of a material offering countless advantages. The main advantages of the building system using unfired clay are the following: 1) minimal use of fossil fuels for the cooking; 2) reduction of the CO_2; 3) reduction of pollutants emissions; 4) optimal indoor climate, generated by a good hydrometric regulation in the indoor, due to the large mass and high capacity to adjust the humidity; 5) large resistance to the fire; 6) neutrality of electrostatic charges; 7) full recyclability.

References

[1] M.F. Ashby, P.J. Ferreira, D.L. Schodek, Nanomaterials, Nanotechnologies and Design, Elsevier, Oxford, 2009.

[2] L. Fontaine, R. Anger, Batir en terre. Du grain de sable à l'architecture, Belin, Paris, 2009.

[3] R. Rael, Earth Architecture, Princeton Architectural Press, New York, 2008.

Advanced Materials Research Vol. 983 (2014) pp 67-70

doi:10.4028/www.scientific.net/AMR.983.67

On Optimal Planning for DNA Nanomechanical Robots

Vladimir Popov[1,a]

[1] Ural Federal University, 620083, Ekaterinburg, Russia

[a]Vladimir.Popov@usu.ru

Keywords: robot, reconfiguration planning, DNA nanomechanical device, Runge Kutta neural network, artificial physics optimization.

Abstract. In this paper, we consider the optimal reconfiguration planning problem of finding the least number of reconfiguration steps to transform between two configurations for chain-type modular robots. We propose an intelligent algorithm for solution of the problem. In particular, we use the set of parameterized k-covers problem and the approximate period problem to detect periodic regularities in genetic sequences of DNA nanomechanical robots. We try to use similar reconfiguration actions for similar parts of genetic sequences. We consider an artificial physics optimization algorithm. We use Runge Kutta neural networks for the prediction of virtual force law.

Introduction

DNA has established itself as an important building block for self-assembly in nanotechnology (see e.g. [1]). Recent successes in the investigation of DNA nanostructures and DNA nanomechanical devices provide a foundation for designing autonomous DNA nanomechanical devices capable of complex behaviors (see e.g. [1-3]). However, many of traditional principles of control can not be applied to such devices. These devices require the development of essentially new control systems. It should be noted that nearly all structures in DNA nanotechnology make use of branched DNA structures containing different junctions, as opposed to most biological DNA which exists in a linear double helix form. Therefore, we can consider DNA nanomechanical devices as modular robots (see e.g. [4]). Current DNA nanomechanical devices are self-assembly systems. So, we can consider such devices as self-reconfigurable robots (see e.g. [5-7]). Therefore, we can use reconfiguration planning for control systems of DNA nanomechanical robots.

It should be noted that problems of planning of self-reconfigurations received considerable attention. In particular, the optimal reconfiguration planning problem of finding the least number of reconfiguration steps to transform between two configurations for chain-type modular robots was proposed in [8]. The problem is NP-complete (see [8]). An approach to solve the problem was proposed in [9]. This approach is based an explicit reduction from the problem to the satisfiability problem. Note that encoding hard problems as instances of the satisfiability problem has caused considerable interest. In particular, there are a number of efficient satisfiability algorithms. However, satisfiability algorithms are not applicable for real time solution of the optimal reconfiguration planning problem. In this paper, we consider an intelligent algorithm for the problem.

Preliminaries and the Problem Definition

Self-reconfiguration process consists in changing connectivity of the system of modules aimed at transformation of the robot from the current configuration to a goal configuration subject to restrictions of physical implementation. As for many other robotics problems (see e.g. [10]), we can use a graph model for this process. In particular, a special graph has been introduced for representing robot's configurations (see [8]). It is called C-graph (see [8]). The C-graph is an extension of a graph with connection points. In particular, each node has a finite number of connection points corresponding to connectors of different types. A connection between connector i

of module u and connector j of module v is made to correspond to edge (i, j) between nodes u and v. In general, there are two types of elementary reconfiguration actions: creation of a new connection and disconnection of a current connection between modules to rearrange the modules. In case of DNA nanomechanical devices, we can assume that branched DNA structures are represented by nodes of C-graph. Given two connected C-graphs H = (V, E[1]) and G =(V, E[2]), we say that there exists a reconfiguration plan with at most k reconfiguration steps if and only if there exists a sequence of elementary reconfiguration actions of length r < k+1 such that, starting from H, we obtain G.

Optimal reconfiguration planning problem (ORP):

Instance: Two C-graphs H = (V, E[1]) and G = (V, E[2]) and an integer k.

Question: Find out whether there exists a reconfiguration plan for H and G with at most k reconfiguration steps?

Periodic Regularities in Genetic Sequences

Since we consider only DNA nanomechanical robots, it is natural to pay attention to the nature of the structure of these robots. In particular, it is well-known that there are a large number of different periodic regularities in genetic sequences. Some of them are well-studied (see e.g. [11-14]).

In this paper, we consider parameterized k-covers [11] and approximate periods [14]. We find such periodic regularities and try to use similar reconfiguration actions for similar parts of genetic sequences. We use a simple genetic algorithm for the detection of periodic regularities. We use a recurrent neural network to predict sequences of reconfiguration actions.

An Artificial Physics Optimization Algorithm

It should be noted that different heuristics have proven very effective for solving global optimization problems. In particular, the artificial physics optimization can be used for such purposes (see [15, 16]). Artificial physics optimization algorithms use three procedures: initialization, calculation force and motion (see [16]). A swarm of individuals is sampled randomly from a problem space in the initialization. Masses of individuals of the swarm should be calculated in the procedure of calculation force. The procedure of motion uses the total force to calculate the velocity of individuals. Note that different virtual forces are considered (see e.g. [16]). In particular, we can use negative exponential force law, unimodal force law, linear force law [16].

Runge Kutta neural networks

The main advantage of artificial physics optimization algorithms consists in the proper design of force law. In particular, proper designed force law can drive individuals in the problem search space intelligently and efficiently. Runge Kutta neural networks can be used for the prediction of different nonlinear systems [17]. Therefore, we can try to use Runge Kutta neural networks for the design of a general force law. We consider 4-order Runge Kutta neural networks with multilayer perceptron networks. To create a training set, we consider an explicit reduction from the problem to the satisfiability problem [9] and use different satisfiability algorithms. We use a gradient learning algorithm for 4-order Runge Kutta neural networks.

Experimental Setup

Note that many structures in DNA nanotechnology make use of branched DNA structures containing different junctions. One of the simplest branched structures is a four-arm junction. It can be made using four individual DNA strands which are complementary to each other in the correct pattern. It should be noted that unlike in natural Holliday junctions, in the artificial immobile four-arm junction, the base sequence of each arm is different, meaning that the junction point is fixed in

a certain position [2, 18]. It is clear that DNA nanostructures must be designed so that they will assemble into the desired structures. Based on this idea, we have analyzed real world data from EMBL - EBI database [19] and created a test set. In particular, we have considered eukaryotic DNA sequences. We have used substrings of 10^6 - 2×10^6 base pairs of DNA sequences of 2×10^7 - 21×10^7 base pairs (e.g. *Anopheles gambiae*, *Callithrix jacchus*) and substrings of 10^5 - 2×10^5 base pairs of DNA sequences of 10^6 - 10^7 base pairs (e.g. *Candida dubliniensis*, *Dictyostelium discoideum*).

Experimental Results

In our experiments, we consider the artificial physics optimization with negative exponential force law (NEFL), unimodal force law (UFL), linear force law (LFL), and general force law predicted by a Runge Kutta neural network (RKFL). Let T be the average number of reconfiguration steps for solutions obtained by a satisfiability algorithm. Let T[X] be the average number of reconfiguration steps for solutions obtained by an artificial physics optimization with force law X. It is easy to see that we can consider N[X]=T[X]/T as a measure of the quality of the artificial physics optimization with force law X. Selected experimental results for different force laws are given in Table 1.

Table 1. Experimental results for different force laws

X	NEFL	UFL	LFL	RKFL
N[X] for 10^5 - 2×10^5 base pairs *Candida dubliniensis*	3.2384	7.5221	8.0043	1.5211
N[X] for 10^5 - 2×10^5 base pairs *Dictyostelium discoideum*	3.2226	7.5236	8.0152	1.5104
N[X] for 10^6 - 2×10^6 base pairs *Anopheles gambiae*	3.6711	7.9218	8.3792	1.2061
N[X] for 10^6 - 2×10^6 base pairs *Callithrix jacchus*	3.7004	7.9203	8.3727	1.1843

It is clear that we have obtained the best results for the artificial physics optimization with general force law predicted by a Runge Kutta neural network. It should be noted that the performance of the algorithm depends essentially from the length of DNA sequences. At same time, there is no essential dependence from the type of sequences.

Summary

We have considered the optimal reconfiguration planning problem of finding the least number of reconfiguration steps to transform between two configurations for chain-type modular robots. We have considered the problem for DNA nanomechanical robots. We have proposed an intelligent algorithm for solution of the problem. In particular, we have used the set of parameterized k-covers problem and the approximate period problem to detect periodic regularities in genetic sequences of DNA nanomechanical robots. We have used a simple genetic algorithm for the detection of periodic regularities and a recurrent neural network to predict sequences of reconfiguration actions. We have considered an artificial physics optimization algorithm for different force laws. In particular, we have used Runge Kutta neural networks for the prediction of virtual force law. We have presented experimental results for genetic sequences of different length.

Acknowledgement

This research was partially financially supported by RFBR, research project No. 13-01-00048 a, and under the Agreement 02.A03.21.0006 of 27.08.2013 between the Ministry of Education and Science of the Russian Federation and Ural Federal University.

References

[1] S. Murata and M. Stojanovic, DNA-based nanosystems, New Gener. Comput. 26 (2008) 297-312.

[2] N. Seeman, Nanotechnology and the double helix, Sci. Am. 290 (2004) 64-75.

[3] P. Yin, A. Turberfield, S. Sahu and J. Reif, Design of an autonomous DNA nanomechanical device capable of universal computation and universal translational motion, LNCS 3384 (2005) 426-444.

[4] N. Brener, F. Ben Amar and P. Bidaud, Characterization of lattice modular robots by discrete displacement groups, in: IROS 2010, 1133-1139.

[5] T. Fukuda and S. Nakagawa, A dynamically reconfigurable robotic system (Concept of a system and optimal configurations), in: Proc. of the 1987 IEEE Int. Conf. on Industrial Electronics, Control, and Instrumentation, 1987, 588-595.

[6] M. Yim, W. Shen, B. Salemi, D. Rus, M. Moll, H. Lipson, E. Klavins, and G. Chirikjian, Modular self-reconfigurable robot systems: challenges and opportunities for the future, IEEE Robotics & Automation Magazine 14 (2007) 43-52.

[7] S. Murata and H. Kurokawa, Self-reconfigurable robot: shape-changing cellular robots can exceed conventional robot flexibility, IEEE Robotics & Automation Magazine 14 (2007) 71-78.

[8] F. Hou and W. Shen, On the complexity of optimal reconfiguration planning for modular reconfigurable robots, in: ICRA 2010, 2791-2796.

[9] A. Gorbenko and V. Popov, Programming for modular reconfigurable robots, Programming and Computer Software 38 (2012) 13-23.

[10] A. Gorbenko and V. Popov, Self-learning of robots and the model of Hamiltonian path with fixed number of color repetitions for systems of scenarios creation, Advanced Materials Research 683 (2013) 909-912.

[11] A. Gorbenko and V. Popov, The set of parameterized k-covers problem, Theoretical Computer Science 423 (2012) 19-24.

[12] V. Popov, Multiple genome rearrangement by swaps and by element duplications, Theoretical Computer Science 385 (2007) 115-126.

[13] V. Popov, Computational complexity of problems related to DNA sequencing by hybridization, Doklady Mathematics 72 (2005) 642-644.

[14] V. Popov, The approximate period problem for DNA alphabet, Theoretical Computer Science 304 (2003) 443-447.

[15] W.M. Spears, D.F. Spears, J. Hamann and R. Heil, Distributed, physics-based control of swarms of vehicles, Auton. Robot. 17 (2004), 137-162.

[16] L. Xie and J. Zeng, The performance analysis of artificial physics optimization algorithm driven by different virtual forces, ICIC Express Lett. 4 (2010) 239-244.

[17] Y.-J. Wang and C.-T. Lin, Runge Kutta neural network for identification of continuous systems, in: ICSMC 1998, 3277-3282.

[18] P. Rothemund, Folding DNA to create nanoscale shapes and patterns, Nature 440 (2006) 297-302.

[19] Genomes Pages - Eukaryota. Information on http://www.ebi.ac.uk/genomes/eukaryota.html

Advanced Materials Research Vol. 983 (2014) pp 71-74

doi:10.4028/www.scientific.net/AMR.983.71

Preparation of nano Ni_2P/TiO_2-Al_2O_3 catalyst and catalytic activity for hydrodesulfurization

Hua Song[1,a], Zi-Dong Wang[1,b], Zai-Shun Jin[2, c], Feng li[1,d], Huai-Yuan Wang[1,e], Hua-Lin Song*[,3, f]

[1]Provincial Key Laboratory of Oil & Gas Chemical Technology, College of Chemistry & Chemical Engineering, Northeast Petroleum University, Daqing, Heilongjiang 163318, China

[2]Key Laboratory of Cancer Prevention and Treatment of Heilongjiang Province, Mudanjiang Medical University, Mudanjiang, Heilongjiang 157011, China

[3]Department of Image College, Mudanjiang Medical University, Mudanjiang, Heilongjiang 157011, China

[a]songhua2004@sina.com, [b]wzd001@126.com, [c]zaishun5@126.com, [d]lifeng_dqpi@sina.com, [e]wanghyjiji@163.com, [f]songhualin401@126.com

*Corresponding Author：Hua-Lin Song, Tel: 0453-6892892, songhualin401@126.com

Keywords: Nickel phosphide; TiO_2-Al_2O_3 binary oxides; Hydrodesulfurization; Preparation

Abstract. Nano nickel phosphide Ni_2P catalysts supported on TiO_2-Al_2O_3 support were prepared by impregnation. The catalysts were characterized by XRD, BET, and XPS. The effects of impregnation method，Ni_2P loading on catalyst structure and HDS activity were studied. The results indicated that co-impregnation method is beneficial to the formation of Ni_2P and can avoid the formation of $Ni_{12}P_5$. The catalyst prepared with co-impregnation method, Ni_2P loading of 30% exhibited the best performance. At a reaction temperature of 606 K, a pressure of 3.0 MPa, a hydrogen/oil ratio of 500 (V/V), and a weight hourly space velocity (WHSV) of 2.0 h^{-1}, the conversion of DBT HDS was 96.0%.

Introduction

Driven by the need to meet the stringent environmental regulations and the continuing decline in the quality of petroleum feedstocks, reduction of the sulfur content in transportation fuels is an area which has aroused great interest in the refining industry [1]. Among the sulfur removal methods, hydrodesulfurization (HDS) probably is one of the most paramount hydrotreating processes in petroleum refining industry to produce the clean fuels.

Transition metal phosphides have attracted great attention because of their high activity for the HDS of fuels [2]. Among the phosphides, Ni_2P shows an excellent activity for hydrodesulfurization.In this work, a number of TiO_2-Al_2O_3 supported nano nickel phosphide catalysts were prepared and the effect of preparation conditions, such as impregnation method, Ni_2P loading on the catalyst structure and HDS activity for DBT was studied.

Experimental

Preparation of support and catalysts The composite TiO_2-Al_2O_3 supports (denoted as TA) with TiO_2 mass fraction of 50% were prepared by sol–gel methods described in the literature [2]. The supported Ni_2P catalyst precursors were prepared by a standard incipient wetness impregnation of an ammonium dihydrogen phosphate [$NH_4H_2PO_4$] and nickel nitrate hexahydrate [$Ni(NO_3)_2 \cdot 6H_2O$] solution with TA support simultaneously [2]. In a typical experiment, the impregnated solids were dried at 393 K for 10 h and calcined at 773 K for 3 h. Finally, a temperature programmed reduction was used to convert the phosphite into phosphide in a H_2 flow (200 mL/min). Different catalysts were prepared by changing one variable at the other conditions remain unchanged. The supported Ni_2P

catalysts with different Ni_2P loading (10 wt%, 20 wt%, 30 wt% and 40 wt%) were prepared with initial Ni/P molar ratio of 1/2.

The obtained catalysts were denoted as Ni_2P/TA (W-M), where W represented the Ni_2P loading, M represented impregnation method. Five different impregnation methods used here are method *a*, *b*, *c*, *d* and *e*, respectively, in which M=*a* represented co-impregnation of P and Ni, M=*b* represented impregnation of support with P first then with Ni after dried, M=*c* represented impregnation of support with Ni first then with P after dried, M=*d* represented impregnation of support with P first then with Ni after dried and calcined, M=*e* represented impregnation of support with Ni first then with P after dried and calcined.

Characterization methods X-ray diffraction (XRD) performed on a D/max-2200 polycrystalline X-ray instrument operating with Cu Kα radiation. Surface area and pore volume were obtained on a Micromeritics ASAP 2400 by using the BET method.

Catalytic activities Catalytic hydrotreating performances of the prepared catalysts were conducted in a high-pressure fixed-bed reactor with 2 g of catalyst at reaction temperature of 603 K, pressure of 3.0 MPa, hydrogen/oil ratio of 500 (V/V), WHSV=2 h^{-1}. The feedstock was a blend of cyclohexane (96 wt%), DBT (2 wt%), and dodecane (2 wt%). The feed and reaction product was analyzed by FID gas chromatography with a GC-14C-60 column. Tests showed that the cyclohexane solvent and dodecane internal standard were un-reactive at these experimental conditions.

Results and Discussion

X-ray diffraction for catalysts with different impregnation method XRD patterns of five Ni_2P/TA samples with different impregnation treatment are presented in Fig. 1 For all samples the peaks observed at 2θ=25.2°, 37.8°, 48.0°, 54.0° and 55.0° correspond to the characteristic peaks of anatase TiO_2 (PDF:21–1272), indicating that most of the TiO_2 has the anatase TiO_2 structure. For samples (1) (co-impregnation) and (2) (impregnate Ni after P) show peaks at 2θ=40.7°, 44.6°, 47.3° and 54.1°.They correspond to the characteristic peaks of Ni_2P (PDF: 3–953), indicating that the main reductive product is the Ni_2P phase. While for sample (3) (impregnate P after Ni), both Ni_2P and $Ni_{12}P_5$ (2θ=41.7°, 44.4°, 46.9° and 48.9°, PDF: 74-1381) were observed. The possible reason may be lack of P for sample (3) compared with sample (1) and (2), because the Ni/P molar ratio over support plays an important role on the formation of Ni_2P [1]. When impregnate P after Ni, the large fraction of the support surface were covered by Ni before introducing P, which makes P more difficult to be loaded over the support. However, for samples (1) and (2), this effect of loaded Ni to P was weaker, making more P species accessible to react with Ni species to form Ni_2P due to the "ensemble effect" of P [3]. Oyama et al. [4] concluded that excess phosphorus was needed to prepare Ni_2P catalysts, meaning that sufficient P was beneficial to form Ni_2P, which in accordance with our results. Moreover, for sample (4), $Ni_{12}P_5$ phase was observed besides Ni_2P phase. This can be ascribed to the calcination of P loaded sample before introducing Ni, leading to partial loss of P and causing high Ni/P molar ratio compared with sample (2). Thus the formation of $Ni_{12}P_5$ is understandable.

X-ray diffraction for catalysts with different Ni_2P loading The XRD patterns of Ni_2P/TA with various Ni_2P loading are shown in Fig. 2 Samples (1)-(4) show anatase TiO_2 peaks at 2θ=25.2°, 37.8°, 48.0° and 55.0°, whose intensities decrease successively as the Ni_2P loading increases. While the peaks at 2θ=40.7°, 44.6°, 47.3° were corresponding to the main reductive product is the Ni_2P phase. The Ni_2P peak intensity of samples are in the sequence: Ni_2P/TA(40%-*a*) > Ni_2P/TA(30%-*a*) > Ni_2P/TA(20%-*a*) > Ni_2P/TA(10%-*a*), showing the Ni_2P peaks grow as the Ni_2P loading increases.

Textual characterization It can be seen that the surface area of the support TA is up to 177.5 m^2/g, and shows a significant decrease in surface area by addition of Ni_2P(Table 1). The changes in the surface area are accompanied by a decrease in the pore volume. The higher the loading of Ni_2P, the lower surface area is observed. For samples prepared with different methods, the surface areas follow the order: TA > Ni_2P/TA(30%-*a*) > Ni_2P/TA(30%-*b*) > Ni_2P/TA(30%-*c*) > Ni_2P/TA(30%-*d*) > Ni_2P/TA(30%-*e*). The sample prepared with method *a* has the highest surface area, indicating that

co-impregnation method is beneficial to obtain large catalyst surface. The twice calcination during preparation (methods *d* and *e*) led a further decrease in surface area and pore volume compared with the corresponding methods *b* and *c* which were calcined once.

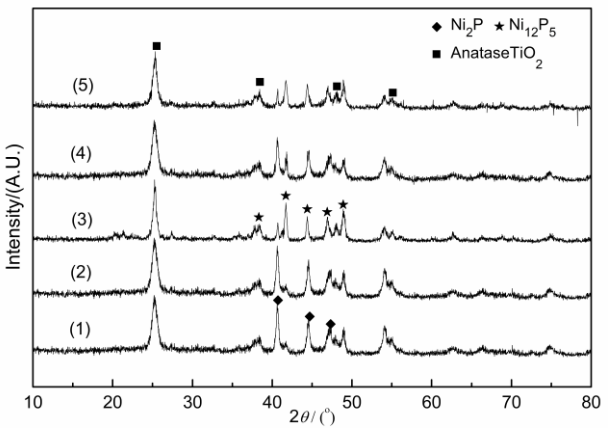

Fig. 1 XRD patterns of Ni_2P/TA catalyst obtained from various impregnation methods: (1) Ni_2P/TA(30%-a); (2) Ni_2P/TA(30%-b); (3) Ni_2P/TA(30%-c); (4) Ni_2P/TA(30%-d); (5)Ni_2P/TA(30%-e).

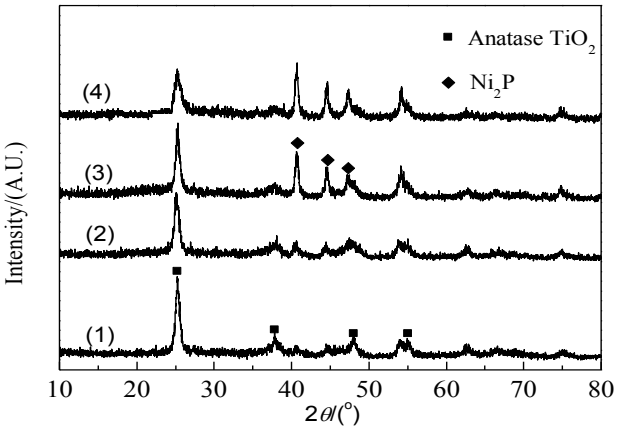

Fig. 2 XRD patterns of Ni_2P/TA with various Ni_2P loading: (1) Ni_2P/TA(10%-a); (2) Ni_2P/TA(20%-a); (3) Ni_2P/TA(30%-a); (4) Ni_2P/TA(40%-a).

Table. 1 Textual properties of support and catalysts

Support and catalysts		S_{BET}/$m^2 \cdot g^{-1}$	d_p/nm	V_p/$cm^3 \cdot g^{-1}$	catalysts		S_{BET}/$m^2 \cdot g^{-1}$	d_p/nm	V_p/$cm^3 \cdot g^{-1}$
TA		177.5	10.6	0.472		10%	97.3	8.8	0.215
	a	75.2	11.5	0.215		20%	83.5	10.1	0.211
	b	66.1	13.4	0.221	Ni_2P	30%	69.7	12.3	0.208
Impregnation methods	*c*	62.9	9.3	0.146	loadings	40%	58.1	14.1	0.205
	d	51.8	11.3	0.147					
	e	46.9	7.2	0.085					

The effect of impregnation method on activity of catalyst The DBT conversions for Ni_2P/TA catalysts prepared by five different impregnation methods are presented in Fig. 3 The DBT conversion follow the order: Ni_2P/TA(30%-*a*) > Ni_2P/TA(30%-*b*) > Ni_2P/TA(30%-*c*) > Ni_2P/TA(30%-*d*) > Ni_2P/TA(30%-*e*). Compared to other samples, Ni_2P/TA(30%-*a*) exhibited the best DBT HDS activity. Oyama et al. [5] confirmed the presence of two types of sites in Ni_2P phase, tetrahedral Ni(1) site (lower coordination) and square pyramidal Ni(2) site (higher coordination). Both Ni(1) and Ni(2) sites are present on large crystallites but that the Ni(2) sites are more numerous on the more highly dispersed samples. The lower coordination Ni(1) sites are responsible for desulfurization by the DDS pathway by taking on a sulfur atom while the Ni(2) sites are the high-activity sites that carry out HDS by the hydrogenation (HYD) route. Hence, we conclude that the high DBT HDS activity over the sample prepared by method *a* must be associated with the dispersion of active phase. It has the highest surface area (Table 1), which is beneficial to better dispersion of active phase over support and formation of high-activity Ni(2) sites. Furthermore, a pure Ni_2P phase was observed with sample prepared by method *a* (Fig.2), which have been found to be higher active in HDS reaction compared with $Ni_{12}P_5$ phase [4]. For sample (3), (4) and (5), the low HDS activities of DBT could be assigned to the lower surface areas and formation of a certain fraction of $Ni_{12}P_5$ phase, which have been found to be less active in HDS reaction than Ni_2P phase [4].

The effect of Ni_2P loading on the HDS activity As shown in Fig. 4, only 57.0% DBT conversion was obtained on the Ni_2P/TA(10%-*a*). This is understandable, because lower loading of Ni_2P results

in less active Ni_2P over catalyst. The DBT conversion increased with increasing the Ni_2P loading, and the best HDS activity was observed with Ni_2P loading of 30%. With a further increase of Ni_2P loading, the DBT conversion decreased, possibly because excessive Ni_2P loading on the support leads to a bad dispersion of active Ni_2P phase and a significant reduction in surface area (Table 1). This result is in accordance with those results reported by Wang et al. [6].

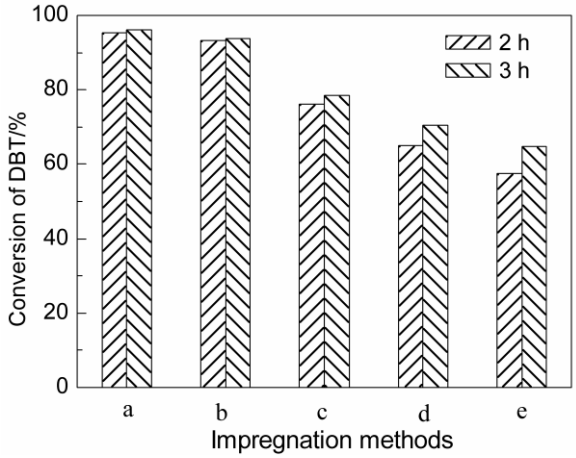

Fig. 3 Effect of impregnation methods on the activity of Ni_2P/TA(30%-M) catalysts: T= 603 K, p= 3.0 MPa, H_2/oil= 500 (V/V), WHSV=2 h^{-1}

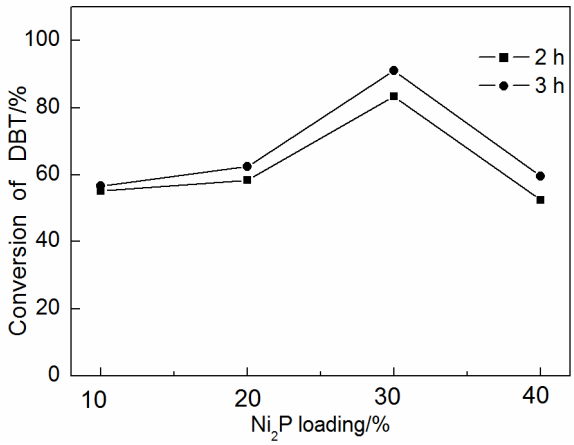

Fig. 4 Effect of Ni_2P loading on the activity of the Ni_2P/TA(W-a): T= 603 K, p= 3.0 MPa, H_2/oil= 500 (V/V), WHSV=2 h^{-1}

Conclusion

The nickel phosphide Ni_2P catalysts supported on TiO_2-Al_2O_3 supports were prepared by a standard incipient impregnation and the effect of preparation conditions, such as impregnation method, Ni_2P loading on the catalyst structure and HDS activity for DBT were studied. The co-impregnation method is preferable, as it is beneficial to the formation of Ni_2P and can avoid the formation of $Ni_{12}P_5$. Higher loading of the active Ni_2P results in higher HDS activity, however, excessive Ni_2P loading on the TA support results in a reduction in catalytic activity.

Acknowledgments

The authors acknowledge the financial supports from the National Natural Science Foundation of China (NSFC No21276048).

References

[1] H. Song, Y.T. Guo, F. Li, H.J. Wu, Petrochem. Techno. 39 (2010) 944-951.

[2] H. Song, M. Dai, Y.T. Guo, Y.J. Zhang, Fuel Process. Technol. 96 (2012) 228-236.

[3] P. Liu, J.A. Rodriguez, T. Asakura, J. Gomes, K.J. Nakamura, Phys. Chem: B. 109 (2005) 4575-4583.

[4] S.T. Oyama, X. Wang, Y. Lee, K. Bando, F.G. Requejo, J. Catal. 210 (2002) 207-217.

[5] S.T. Oyama, Y.K. Lee, J. Catal. 258 (2008) 393-400.

[6] K.L. Wang, B.L. Yang, Y. Liu, C.H. Yi, Energy Fuels. 23 (2009) 4209-4214.

Advanced Materials Research Vol. 983 (2014) pp 75-78

doi:10.4028/www.scientific.net/AMR.983.75

Study on the nanoemulsion formulation of piceatannol and in vitro release

Yue Zhang[1,2,3,a], Yifeng Yu[1,2,b], Zhenhua Shang[1,c*], Man Du[1,d], Chunfang Wang[1,e]

[1]School of Chemical and Pharmaceutical Engineering, Hebei University of Science and Technology, Shijiazhuang 050018, CHINA

[2]Hebei research center of pharmaceutical and chemical engineering, Shijiazhuang, 050018, CHINA

[3]State Key Laboratory Breeding Base-Hebei Province Key Laboratory of Molecular Chemistry for Drug, Shijiazhuang, 050018, CHINA

[a]yuezhang@hebust.edu.cn, [b]kdyyf@163.com, [c]zhenhuashang@126.com, [d]dumanpgy@163.com, [e] Wangcf1960@hebust.edu.cn

*Correspondance

Keywords: nanoemulsion; piceatannol; in vitro release

Abstract. In this paper, a novel stable piceatannol nanoemulsion is established. The piceatannol nanoemulsion formulation was screened based on the pseudo ternary phase diagrams. An optimized prescription was given as piceatannol 0.54%, EL-40 25.6%, ethanol 3.87%, castor oil 10.30%, water 60.23% (mass ratio), with the mean particle size 87.3 nm. The morphology of piceatannol nanoemulsion was characterized by TEM. The test results demonstrate that the nanoemulsion has dramatically improved the the solubility and release performance of piceatannol in ABS and PBS.

Introduction

Piceatannol (Fig. 1), with chemical name of *E*-3,3',4,5'-tetrahydroxystilbene, is a derivative of polyhydroxystilbene which attracts a lot of attentions due to its potential applications in medical and nutrition fields [1]. Recently reports on the physiological effects of piceatannol were focused on the anti-inflammatory, antiviral, antioxiditive and antiapoptosis activities [2-5]. As a typical stilbene derivative, piceatannol exhibits very poor stability and water solubility leading to the poor release in vivo and bioavailability. Therefore, it is necessary to seek for a new vehicle to elevate the stability and solubility of piceatannol to promote the absorption in body. Nanoemulsion always possesses high solubility and thermodynamic stability [6]. The nanoemulsion system is spontaneously formed from water, oil, surfactant and cosurfactant in an appropriate proportion and it can improve not only the bioavailability of the poorly water-soluble drugs, but also the stability [7]. The aim of the present work is to screen an optimal binding of surfactant and cosurfactant to obtain an ideal nanoemulsion of piceatannol with a better particle size distribution at low concentrations of surfactant and cosurfactant for improving the solubility and stability of piceatannol. Formulation optimization is based on the ternary phase diagrams and the particle size distributions studies. The particles formed by optimized formulation are verified by transmission electron microscopic (TEM) analysis. The tests of stability and in vitro release of the prepared piceatannol nanoemulsion have been also investigated.

Experimental section

General. Solvents and reagents were commercially available and used without further purification. Piceatannol (98%) was synthesized according to the literature [8]. Isopropyl myristate (IPM) was bought from Shanghai LEASUN chemical Co.LTD. Polyoxyethylene sorbitan fatty acid esters

(Tween80) and Polyoxyethylenated castor oil (EL-40) were purchased from Tianjin Yongda Chemical Reagent Development Center. 1, 2-Propylene glycol used as cosurfactant was purchased from Kangkede Com., Tianjin, China. Olive oil, castor oil and soybean oil were made in COFCO, Tianjin, China. Here used water was twice distilled. Morphology of piceatannol nanoemulsion was determined using transmission electron microscopy. Droplet size of the prepared nanoemulsion was determined using dynamic light scattering. Samples were diluted for 400 times by distilled water and observed the droplet size distribution on Nano-S90 (Malvern Instruments, UK).

The solubility of piceatannol in different components was tested as follows. The excess amount of piceatannol and 1 mL of each selected component were mixed at 37±1 ^{o}C for 36 h respectively in a stoppered vial. Then the vials were centrifuged at 3600 rpm for 10 min. The content of piceatannol in the supernatant was determined by HPLC.

The aqueous titration method was used to construct the pseudo ternary phase diagram. Single phase, bluish and transparent mixture was designated as nanoemulsions, the opaque mixture was designated as normal emulsions [9]. Surfactant and cosurfactant were mixed at two specific mass ratios (Km) from 9:1, 8:2... to 1:9 respectively and the nanoemulsion regions formed under these circumstances were compared. The ratio of oil to the combination of surfactant and cosurfactant (Smix) at specific Km was varied from 1:9 to 9:1. Surfactant and cosurfactant were mixed in different mass ratios such as 6:1, 5:1, 4:1 and 3:1, to each group, oil and the mixture of surfactant-cosurfactant with specific Km were mixed well at mass ratios ranging from 1:9 to 9:1. Region of the nanoemulsion was used to screen the optimal formulation.

To prepare the O/W nanoemulsion, piceatannol was dissolved in cosurfactant, surfactant and oil were added to the above mixture. The distilled water was added drop-wise to the oily phase with constant stirring to form the O/W nanoemulsion.

The stability test of the prepared nanoemulsion was conducted based on the regulations of Chinese Pharmacopoeia (Edition 2010) [10]. The hard conditions include high temperature, humidity and the strong light irradiation. Samples were withdrawn after specified time intervals (0, 5 and 10 days) and examined for physical change, droplet size distribution and the content of piceatannol.

The dynamic dialysis method was applied in vitro release test of piceatannol nanoemulsion. The release performance of prepared nanoemulsion was observed under the buffer solution (pH 3.6 or pH 7.4) simulating the physiological conditions in a dialysis bag. Release behavior of nanoemulsion was compared with that of control piceatannol suspension in pH 3.6 ABS or pH 7.4 PBS. Data obtained here were managed by calibration curve method to acquire content corresponding to each time interval. The accumulated amount was obtained as follows:

$$Q_t=C_t\times50+C_{0.5}\times5+C_{0.5}\times5+\ldots+C_{t-1}\times5 \quad (1)$$

Where *Ct* is defined as the concentration of (*E*)-piceatannol at *t* (time) in nanoemulsion or control piceatannol suspension in buffers, *Qt* stands for the accumulated amount of piceatannol released from the dialysis bag.

Results and Discussions

The solubility studies of piceatannol in various kinds of components including surfactants, cosurfactants, oils, water, buffers and the nanoemulsion system were shown in Fig.2. Preliminary selections of the oil phase and the surfactant would be depended on the solubility of piceatannol. Seen from Fig.2, piceatannol has good solubility in EL-40 and Tween-80, of all the oil, castor oil has the biggest solibility. Comparatively, piceatannol shows very poor dissoving performance in water and buffers, hence, it further illustrates the necessity of finding new delivery system. Therefore, castor oil was selected as the oil phase.

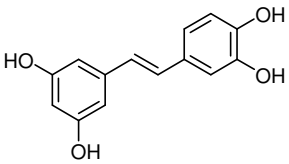

Figure 1 Structure of piceatannol

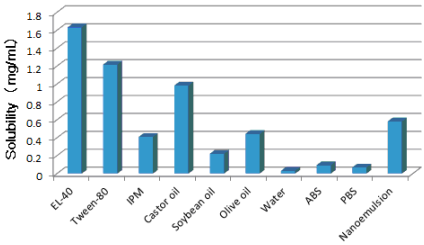

Figure 2 Solubilities of piceatannol in various components

An ideal surfactant is non toxic with appropriate hydrophile-lipophile balance (HLB) value and has good dissoving ability for piceatannol. Based on the solubility studies, EL-40 and Tween-80 who presented considerable solubilities of piceatannol were used as candidate surfactants. In addition, a binding of surfactants and cosurfactant possessing an appropriate HLB value contributes to adjusting the interfacial tension to acquire a favorable emulsifier. Surfactant and cosurfactant were mixed at different ratios that were 9:1 or 8:2 respectively to observe if the nanoemulsionand was formed (shown in Fig. 3). Obviously, nanoemulsions formed by EL-40 along with four kinds of cosurfactants (ethanol, ethylene glycol, 1,2-propylene glycol and n-butyl alcohol) possessed a better result compared to Tween-80. In addition, the maximum amount of oil emulsifies by EL-40 was higher at the two specific ratios. Because ethanol is a preferred solvent in oral agent, EL-40 is chosen in pairs with ethanol for the formulation.

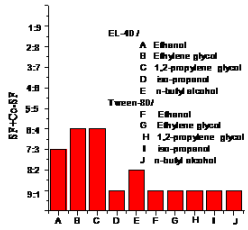

Figure 3 Impacts of surfactants and co-surfactants

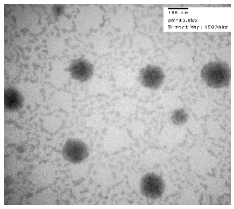

Figure 4 TEM of nanoemulsion

The optimal nanoemulsion has a narrow droplet size distribution with the mean particle size of 87.3 nm and the particle of nanoemulsion is spherical shape (Fig. 4) with a dark core of piceatannol. The nanoemulsion formulation was selected as: piceatannol 0.54%, EL-40 25.6%, ethanol 3.87%, castor oil 10.30%, water 60.23% (mass ratio). In stability test, no phase separation appeared and nanoemulsion keeps a appropriate stability under all hard conditions (Tab. 1).

The release performance is an important factor for evaluating the delivery system. The release performance of the prepared nanoemulsion was observed by with the release of the same quantity of control piceatannol suspension. As seen from Fig. 5, nanoemulsion in ABS provides the highest release of 74.1% after 12 h in comparison to 19.1% of the control piceatannol suspension. The release of nanoemulsion in PBS is not satisfactory but still 28.0% of piceatannol is released with comparing with 2.8% of control suspension. It is obvious that as a delivery system, nanoemulsion greatly enhances the solubility of piceatannol and shows a satisfactory releasing result.

Table 1 Stability test, n=3

Condition	Clarity	Average diameter/nm	Content/%
0 d	Yes	87.89±0.12	98.00±0.02
60 °C, 5 d	Yes	87.19±0.32	97.70±0.08
60 °C, 10 d	Yes	87.35±0.21	97.31±0.05
4500 ± 500 lx, 5 d	Yes	87.65±0.17	97.89±0.03
4500 ± 500 lx, 10 d	Yes	87.48±0.22	96.65±0.02

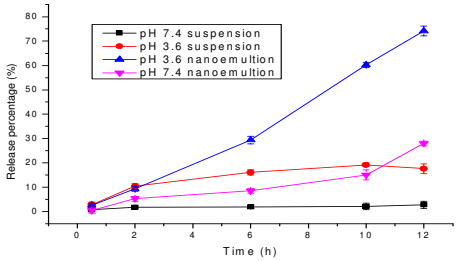

Figure 5 Release behavior of piceatannol nanoemulsion

Acknowledgements

We express our gratitude for the Innovation Team Funding of Hebei University of Science and Technology, Hebei Research Center of Pharmaceutical and Chemical Engineering, Pharmaceutical Molecular Chemistry Key Labouratory of Ministry Technology and Hebei Province Key Laboratory of Molecular Chemistry for Drug.

References

[1] A.M. Brinker, D.S. Seigler, Isolation and identification of piceatannol as a phytoalexin from sugarcane, Phytochemistry. 30 (1991) 3229-3232.

[2] J. Zheng, V.D. Ramirez, Piceatannol, a stilbene phytochemical, inhibits mitochondrial F0F1-ATPase activity by targeting the F1 complex, Biochem. Biophys. Res. Commun.. 261 (1999) 499-503.

[3] M. Takei, A. Umeyama, S. Arihara, H. Matsumoto, Effect of piceatannol in human monocyte-derived dendritic cells in vitro, J. Pharm. Sci.. 94 (2005) 974-982.

[4] R. Amorati, M. Lucarini, V. Mugnaini, G.F. Pedulli, M. Roberti, D. Pizzirani, Antioxidant Activity of Hydroxystilbene Derivatives in Homogeneous Solution, J. Org.Chem.. 69 (2004) 7101-7107.

[5] K. Likhitwitayawuid, B. Sritularak, K. Benchanak, V. Lipipun, J. Mathew, R.F. Schinazi, Phenolics with antiviral activity from Millettia erythrocalyx and Artocarpus lakoocha, Nat. Prod. Res. 19 (2005) 177-182.

[6] J. Gutiérrez, C. González, A. Maestro, I. Sole, C. Pey, J. Nolla, Nano-emulsions: New applications and optimization of their preparation, Current Opinion in Colloid & Interface Science. 13 (2008) 245-251.

[7] J. Szebeni, C. Alving, S. Savay, Formation of complement-activating particles in aqueous solutions of Taxol: possible role in hypersensitivity reactions, Int J Immunopharmacol. 1 (2001) 721-735.

[8] H.Y. Sun, C.F. Xiao, W. Wei, Y. Chen, Z.L. Lv, Y. Zhou, Synthesis of Piceatannol, Chinese Journal of Organic Chemistry. 30 (2010) 1574-1579.

[9] Y. Zhang, J. Gao, H. Zheng, R. Zhang, Y. Han, The preparation of 3,5-dihydroxy-4-isopropylstilbene nanoemulsion and in vitro release, International Journal of Nanomedicine. 6 (2011) 649–657.

[10] Chinese State food and drug adminastration. Chinese Pharmacopoeia, 2010 ed. Appendix XIX c, Material medicine and pharmaceutical preparations stability Experiment principle; Appendix V C, HPLC method, 2010.

Advanced Materials Research Vol. 983 (2014) pp 79-83

doi:10.4028/www.scientific.net/AMR.983.79

The green preparation of nano-silver particle by reductive polysaccharide

Mingshan Yang[1,a], Xinpin Wen[1], Linkai Li[2]

[1.] Department of Material Science and Engineering, Beijing Key Lab of Special Elastomer Composites Materials, Beijing Institute of Petrochemical Technology, Beijing 102617,P.R.China;

[2.] Guangdong Rongtai Industry Co., Ltd., Jieyang Guangdong 522000, P.R.China

[a]yangms001@126.com

Keywords: nano silver particle; reductive polysaccharide; green preparation

Abstract: Silver nanoparticles have been prepared using reductive polysaccharides (glucan) as protecting agents and silver nitrate as precursor via a facile green approach, and possible formation mechanism of silver nano-particle was proposed in this paper. Silver nanoparticles appearance, size and size distribution were controlled by different synthesis technologies and reaction conditions. By changing the reaction conditions such as $AgNO_3$ solution concentration, glucan dosage, reaction temperature, reaction time, the parameters affecting the product shape, particle size and size distribution were investigated. The samples synthesized were characterized by scanning electron microscopy(SEM), transmission electron microscopy (TEM), UV-vis spectrophotometer (UV-vis) methods. The results have showed that nano-silver particle with different shapes such as rod-like, sheet-like or flake and tree-like etc. can be prepared by reductive polysaccharides, and it is a green preparation technology.

Introduction

In present, the fast development of electric information such as communication, computer, etc. put forward much strict demands for electromagnetic shielding materials. So the development trends of electromagnetic shielding materials are focused in green, environmentally friendship and low cost. One of the electromagnetic shielding materials, polymer conducting coatings which are used in mobile phones, laptops, weapons and information security, have been rapidly developed during the past 20 years, and the market amount has been larger and larger. The conducting medias used in polymer conducting coating are mainly silver particles with varied shapes and varied particle size. It is very important for silver particles to be dispersed better in conducting coating, and the particle size, shape also severely affect the electromagnetic shielding effect. Smaller silver particle can improve the close stacking and so can improve the conductivity of coating, decrease the using amount and so decrease the cost of conducting coating. Therefore, nano or ultra-fine silver powder was actively studied all over the world and many achievements of synthesis of ultra-fine silver powder were obtained in the several past years[1]-[2].

The most widely used method for preparing nano or ultra-fine silver powder was chemical deoxidization which has many excellences such as simple technology, simple and low-price equipments, high productivity and easy to large-scale produce, but it can generate a large amount of waste water containing poison and contaminate the environment. So many researchers developed some green methods for preparing nano or ultra-fine silver powder, and one of the methods was

using reductive polysaccharides[4]. Ma et al prepared nano silver particles using β-D- glucan as reductive, water soluble starch as modular. Sun et al synthesized nano-silver particle with core-shell structure by water thermal method using glucan as precursor. So it is urgent to study deeply the green preparation technology of nano silver particle. The reactive conditions and parameters for preparing nano silver particle by glucan were investigated, and the technology for controlling the size and shape of nano silver was explored in this paper.

Experimentals

Materials. Silver nitrate, $AgNO_3$, analytical grade, was supplied by Beijing Beihua Fine Chemicals Co., Ltd., China; β-D- glucan, molecular weight 40000, was supplied by Beijing Chemistry Regent Co., National Medicine Group Co., China. Anhydrous alcohol was supplied by Beijing Chemical Plant, China.

Preparation of nano/ultra-fine silver powder. First, weighed 50mg glucan, put it into distilled water, and the glucan solution was prepared. Then, prepared $AgNO_3$ solution with different concentration of 1, 5, 10 $mmol \cdot L^{-1}$, respectively, put it into glucan solution above and reacted for 24hours under stirring. Afterwards, the product was separated by high-speed centrifugal, and the solid product was dried in oven for 8hours at 80℃, and nano/ultra-fine silver powder was obtained.

Measurements. UV-vis spectrophotometer (UV-vis) was determined by UV 2450(Shimazhu Co., Ltd., Japan). SEM was measured by SSX-550 Scanning Electronic Microscope(Shimazhu Co., Japan). TEM was measured by JEM-1200EX Transmission Electronic Microscope(JEOL Co., Japan).

Results and Discussions

The synthesis route of nanosilver particle in reductive polysaccharides. Polysaccharides are the very important organic compounds which exist in animal, botanic and microbe. Polysaccharides are divided into reductive and non-reductive, and gelose, malt dust, lactose and glucose are the reductive polysaccharides. Compared with starch and cellulose, Glucan has higher water solubility, and the reductive aldehyde group attached on glucan molecules is the site in which the metal ion is reduced and forms the nuclei of metal cluster. The reaction equation of nanosilver particle in reductive glucan is as following:

$$2AgNO_3 + \begin{matrix} CH & CH \\ OH & OH \end{matrix} \quad 2Ag + 2NO_3^{-1} + 2 \quad CH{=}{=}O$$

Preparation technology, particle size and distribution of nanosilver particle. In order to research the effects of experimental parameters on the size and distribution of nanosilver particle, the experimental formula were designed as Table 1. The nanosilver particle size and distribution were determinated by UV-vis.

Table 1 The preparation parameters, particle size and distribution of nanosilver particles

Sample No.	Dosage of glucan	Dosage of $AgNO_3$	Reaction temperature	Reaction time	Average particle size, nm	Particle size distribution
1	0.0506g 20mL, distilled water	1 mmol•L^{-1} 10mL, distilled water	60	24h		
2	0.0508mg 20mL, distilled water	5 mmol•L^{-1} 10mL, distilled water	60	24h	267.50	narrow
3	0.0505mg 20mL, distilled water	100 mmol•L^{-1} 10mL, distilled water	60	24h	220 240	clutter
4	0.5005g 200mL, distilled water	1 mmol•L^{-1} 100mL, distilled water	60	24h	406.50	wide
5	0.2503g 100mL, distilled water	1 mmol•L^{-1} 100mL, distilled water	60	24h	449.50	wide
6	0.1250g 50mL, distilled water	1 mmol•L^{-1} 100mL, distilled water	60	24h	441.50	wide
7	0.5002g 200mL, distilled water	1 mmol•L^{-1} 100mL, distilled water	80	24h	408.00	very wide
8	0.5008g 200mL, distilled water	1 mmol•L^{-1} 100mL, distilled water	100	24h	419.50	wide
9	0.5006g 200mL, distilled water	1 mmol•L^{-1} 100mL, distilled water	40	24h		

From Table 1, it can be seen that the nanosilver particle size was smaller and particle size distribution was narrow in sample 2 colloid solution, which shows that the nanosilver particle preparation parameter of sample 2 was better than those of other samples and can be used for synthesizing nanosilver powder.

The TEM analysis of nanosilver particles. The particle size and distribution were characterized by TEM and the results were as in Figure 1.

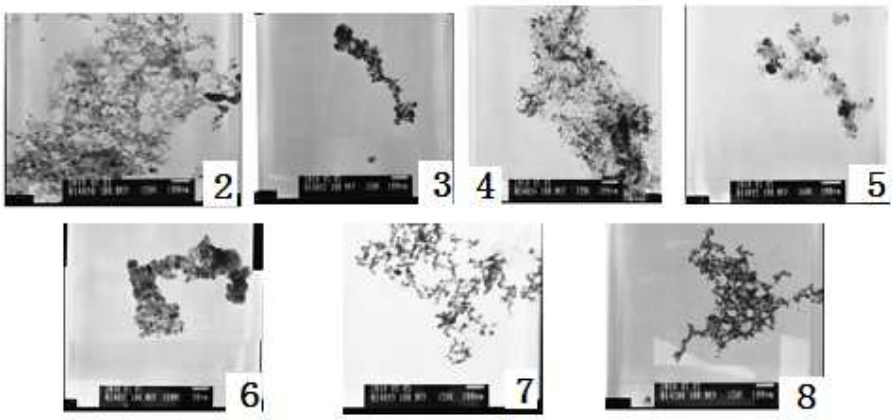

Figure 1 The TEMs of nanosilver particles of varied samples

From Figure 1, it is seen that the average nanosilver particle size of sample 2, sample 3 and sample 4 were 160nm, 330nm and 400nm respectively, which showed that the nanosilver particle size became larger with the higher concentration of $AgNO_3$. Also, the average nanosilver particle size of sample 4, sample 5 and sample 6 were 100nm, 80nm and 50nm respectively, which showed that the

nanosilver particle size became larger with the larger dosage of glucan. Meanwhile, the average nanosilver particle size of sample 4, sample 7 and sample 8 were 100nm, 160nm and 250nm respectively, which showed that the nanosilver particle size became larger with the higher reactive temperature. The results obtained above can be referenced for the nanosilver powder preparation.

The SEM Characterization of nano silver particles. The particle size and shape were characterized by SEM and the results were as in Figure 2.

Figure 2 showed that sample 1 appeared large sheet-like shape with the square area of 0.2μm^2; sample 2 appeared short rod-like shape with the length of 80μm and the diameter of 200μm and

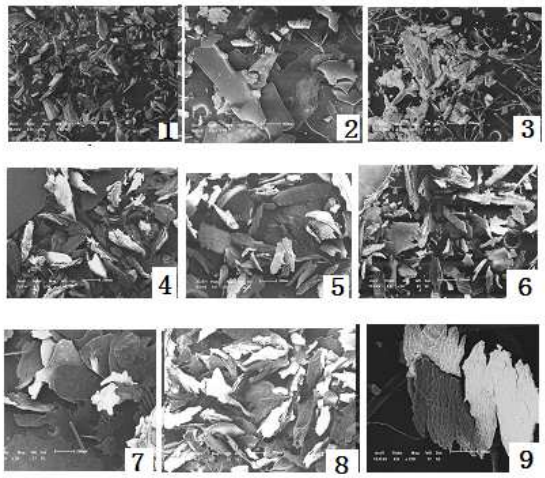

Figure 2 The SEM of nano or ultra-fine silver particles of varied samples

their dispersion were good; sample 3 appeared short rod-like with the length of 80μm and the diameter of 240μm and their dispersion were poor; sample 4 appeared short rod-like with the length of 100μm and the diameter of 400μm and their size were large; sample 5 appeared hybrid shape of short rod with the length of 100μm and the diameter of 400μm and big sheet with the square area of 0.12μm^2; sample 6 appeared small flake shape with the square area of 0.04μm^2; sample 7 appeared large sheet-like shape with the square area of 0.14μm^2; sample 8 appeared tree-like shape; sample 9 appeared large sheet shape with the square area of 0.4μm^2 and their dispersion were poor. Therefore, the technology of sample 2 was suitable for preparing nanosilver particles with rod-like shape, the technologies of sample 5 and sample 6 were suitful for preparing nanosilver particles with sheet-like or flake shape, and the technology of sample 8 was suitable for preparing nanosilver particles with tree-like shape, which showed that it was a green technology for preparing nano or ultra-fine silver powder..

Conclusions

Nano or ultra-fine silver particles with varied size and shapes were synthesized by using reductive polysaccharides(for example, glucan) and the products were characterized by UV-vis, SEM and TEM. The results showed that the synthesis method using reductive polysaccharides is the better “green” method to prepare nano or ultra-fine silver powder.

Acknowledgements

This work was sponsored by the All-round Strategic Cooperation Plan of Guangdong Province with Chinese Academy of Sciences (project No.: 2009B091300084).

References

[1] M. Xie, Y.C. Yang, L.L. Chen, et al. The study on silver powder materials used for electromanetic shielding[J]. J. of Rare Metals(in Chinese), Vol.30, No.4(2009), p. 5-8.

[2] Y.H. Song. Study on the prepararion of spherical nano silver powder[J]. J. of Rare Metal Materials and Engineering(in Chinese), Vol.36, No.4 (2007) , p.709 -712.

[3] Y. Ma, N. Li, C. Yang, X. Yang. One-step synthesis of amino-dextran-protected gold and silver nanoparticles and its application in biosensors[J]. J. Chem. Eng. Data, Vol.382(2005), p.1044-1048.

Advanced Materials Research Vol. 983 (2014) pp 84-89

doi:10.4028/www.scientific.net/AMR.983.84

Hybrid Microstructures on Si Surface Formed by Nanosecond Pulse Laser for Broadband Antireflection

Lantian Yang

Institute of Electronics and Communication Engineering, Guiyang Universty, Guizhou Guiyang 550005, China

Email: 510022925@qq.com

Keywords: hybrid laser Broadband Antireflection.

Abstract. In this paper, a hybrid quasi-micro-pyramid structure is fabricated via nanosecond pulse laser micro-processing, which demonstrates a 15% drop in average reflectance as compared to the uniform quasi-micro-pyramid structures. The influences of laser fluence, pulse number, and designed pitch are also studied experimentally and systematically. The results show that reflection increases with the pattern pitch, decreases with pulse number, and a minimum in reflection is reached at a laser fluence of 4.83 J/cm2. The method here demonstrated provides an alternative and low-cost solution for broadband anti-reflection by hybrid structures with normal aspect ratio rather than uniform structures with high aspect ratio. Higher antireflection performance can be expected by optimizing the laser processing parameters.

1. Introduction

Broadband anti-reflection surfaces are widely studied because of its extensive applications in flat panel displays, solar cells, and electro-optical sensors.1-4)To date, the ways to create broadband anti-reflection surfaces are mainly based on either coating multi-layer thin films or texturing the substrate surfaces with sub-wavelength structures. Both ways aim to properly match refractive indices between the air and substrate. While the former one is based on multilayer material designs for gradient refractive indices, the latter one is attributed to a single layer material but gradient morphology for the refractive index gradient. Due to the scarcity of optical materials existing in nature with the refractive index close to air, multi-layer thin films for broadband anti-reflection surfaces were not realizable until recently when a SiO2 nanorod film with the refractive index of n=1.05 was achieved via oblique-angle deposition by Schubert and his co-workers.4,5)However, there is one technical challenge, which hinders the multi-layer thin film applications, i.e. the mismatch in thermal properties of different materials.1,6)On the other hand, sub-wavelength structures fabricated on the substrate surfaces are explored for broadband anti-reflection property, including many bio-mimetic quasi-moth-eye structures from the inspiration of the cornea and the wings of some species of moths, 7,8) such as pyramids, cones, nipples and tips.9-13)Among them, the pyramid structure was often selected as antireflection structure because it is easier to be fabricated by low-cost and mass production method of wet etching and reactive ion etching (RIE). Compare to this conventional fabrication method, pulse la-ser micro-processing14-17)is more flexible and repeatable due to its high precision engineering capability. In the presence of elemental sulfur gas, femto-second pulsed laser has been used to form a black silicon surface which exhibits near-unity absorption over a broad wavelength range. 18) However, this technique is high production cost with potential environment pollution because of using the expensive femto-second laser and poisonous gas. Here, in this paper, nanosecond pulse laser was used to fabricate hybrid quasi-micro-pyramidal structures on Si substrate as broadband anti-reflection surface. After hybrid laser processing with two different scan speed, the formed hybrid structure presents a drop of 15% in average reflectance over the wavelength of 300~800 nm, and a reduction of 35% in Si characteristic peak reflectance, when compared to the uniform quasi-micro-pyramid structures formed by the non-hybrid processing with one scan speed. Meanwhile, the influences of laser flounce, pulse number and designed pattern pitch on the reflection property are studied experimentally. The better broad anti-reflection property held by hybrid pyramid structure can be used to photovoltaic and flat display devices.

2. Experimental

Laser micro-processing is versatile for texturing surfaces, because laser flounce, repetition rate and scanning speed can be controlled flexibly. Typical patterns made by pulsed laser have an aspect ratio of 1:2 and presents uniform structures on the substrate surface in micrometer scale. By multiple laser scans, the uniformity of patterns can be changed. As can be seen from Fig. 1, by laser irradiation along horizontal, vertical and two diagonal directions, the surface patterns tend to be uneven (hybrid) structures: many small structures formed on a big pattern structure. This is due to dynamic laser ablation process.

The influence of laser fluence, pulse number and designed pattern pitch on reflection properties was investigated. A fiber laser (IPG photonics FM-18-C, pulse duration 1.5ns, wavelength 1060 nm) was used to texture the Si substrate by focusing the spot size at 35μm. Optical measurement was carried out by a UV-VIS-NIR spectrophotometer (Shimadzu, UV-3600). The total reflection spectrum was recorded at an incident angle of 8˚ in the integration sphere system.

The initial experimental conditions are: a laser fluence of 4.78 J/cm2, a scan speed of 100 mm/s, a repetition rate of 100 KHz, and a design pitch of 25μm. When consider the influence of individual parameter on the antireflection property, other parameters are fixed and only the considered parameter varies.

As can be seen in Fig.2a, with the laser fluence increasing from 2.69 to 4.83 J/cm2, the average and peak reflection over the wavelength of 300~800 nm reduce. However, the peak and average reflectance increase when the laser fluence continues to increase. For example, when the laser fluence increases up to 8.51 J/cm2, the average and peak reflectance increases up to 10.06% and 13.37%, respectively. The minimum average and peak reflectance, 5.25% and 5.34%, are obtained by laser radiation at laser fluence of 4.83 J/cm2. Furthermore, at this fluence, the average and peak reflectance are close to each other, meaning that the reflection spectrum had a low reflection value over a broad range of wavelengths.

The influence of pulse number on the reflection is also studied, which is performed by fixing spot size and repetition rate, but varying scan speed from 30 to 160 mm/s. As depicted in Fig. 2b, with the increase of pulse number, both the average and peak reflectance over the wave-length range of 300~800 nm decrease. Meanwhile, the difference in the values between the average reflectance and peak reflectance tends to reduce with increasing pulse number, which means a flat spectral curve and better broadband anti-reflection property. As the pulse number increases to 117, the average and peak reflectance drop to 8.28% and 12.14%, respectively. It can be deduced that lower average reflection may be obtained by increasing the pulse number. In the laser micro-processing, the designed pitch of the texture is an important factor to tune reflection property, because it affects the pulse number applied. Here the design pitch varies from 10 to 45μm at a step of 5μm. As can be seen from Fig. 2c, when the pitch decreases, the average and peak reflectance over the wavelength range drop. However, when the pitch de-creases down to 20μm, the average reflectance tends to remain constant but the peak reflectance keeps reducing, which means that a pattern with smaller pitch has a flat reflection spectrum. As a conclusion, reflection increases with the pattern pitch, decreases with pulse number, and a minimum in reflection is reached at a laser fluence of 4.83 J/cm2. It can be deduced that lower average reflection can be obtained by further optimizing these processing parameters.

Figure 2d shows the surface structures varies with scan speed, since the morphology and antireflection property of patterns made by laser irradiation can be tuned by the scan speed, a hybrid texture for enhanced anti-reflection performance was made by laser ablation at two different scan speeds. The samples were textured along both horizontal and vertical directions, at a laser fluence of 4.78 J/cm2, but at a scan speed of 75 and 90 mm/s. Figure 3 illustrates the measured reflection spectra of uniform textures made with one scan speed and hybrid structures made with two scans. It shows that the structures made by hybrid micro-processing hold better anti-reflection property than the uniform structures in the wavelength range below 662 nm, while it presents higher reflection in the wavelength range above 760 nm. In the wavelength range of 662~760 nm, however, the reflection of the hybrid structure is between the two uniform structures. The characteristic peak of silicon materials remains at 367 nm, but the value of the characteristic peak drops to 3.97% after the hybrid

microprocessing. The average reflections of three structures are 5.18%, 5.64% and 4.79% over the wavelength range of 300~800 nm, respectively. There is a reduction of 15% (4.79% VS 5.64%) and 35% (3.97% VS 6.11%) in average and peak reflectance as compared to the uniform patterns, respectively. The property of lower reflection in the range below 662 nm held by the hybrid structure benefits to photovoltaic devices, because the solar light is the strongest around 500 nm. Reducing reflection over a broader spectral range can be achieved by further optimization the laser processing parameters.

3. Approximate Simulation for hybrid pyramids

Approximate simulation is performed to further investigate the antireflection property of hybrid pyramids by using 3D FDTD method (Numerical, Inc.). Periodic boundary conditions are defined along x- and y- boundaries, while the perfect matched layer (PML) boundary condition is applied along z-boundary. A plane wave light source with normalized intensity and polarization along x-axis is normally incident on the silicon substrate with its dielectric constant taken from reference 19)for the numerical simulation.

As shown in Fig.4, the x- and y- axes are defined in the plane and z-axis along the out-of-plane direction. The hybrid pyramid is approximate as many smaller pyramidal structures closely packed over a big pyramid. The big pyramids are with a height of 200 nm, packed closely with the period same as the side length of 300 nm, while the small pyramid has a height 6 of 20 nm and a side length of 30 nm. As depicted in Fig.4c, the hybrid pyramid has the lower average and maximum reflectance of 7.55% and 18.65%, as compared to the uniform pyramids of 10.60% and 28.12%. There is a drop of 29% and 33% in average and peak reflectance, respectively. This simulation result is in accordance with the experiments where the hybrid quasi-micro-pyramids demonstrate a better suppression of the reflection over a broadband spectrum than uniform structures. The enhanced anti-reflection capability of the hybrid structure is attributed to the fact that the small pyramids break down the sharp change in refractive index when the light rays travel from air into silicon and cause a reduction of the Fresnel reflection of the surface.

4. Conclusions

In this paper, a hybrid structure was fabricated by nanosecond pulse laser with multiple scanning, which demonstrates a lower reflection with a decrease of 7% and 35% in average and peak reflectance than its corresponding uniform structures. The approximate simulation for hybrid quasi-pyramids was performed and the conclusion is in accordance with the experiments. The enhanced anti-reflection capability of the hybrid structure is attributed to that the small pyramids provides a slower change in the refractive index from air to silicon and brings out a reduction in the Fresnel reflection of the surface. Meanwhile, several factors during the laser micro-fabrication, including laser fluence, scan speed (pulse number) and pitch of the pattern were investigated to optimize the reflection property of the surface patterns. The experimental results show that better broadband anti-reflection performance appears at the laser fluence of 4.83 J/cm2, while the average reflectance and peak reflectance decrease with increasing pulse number. With the decrease of pitch, average reflectance drops sharply and then remains constant, while peak reflectance keeps reducing. It is expected that higher broadband antireflection performance can be obtained by optimizing the laser processing parameters.

Figure Captions:

FIG.1. SEM images of (a) cross section and (b) top view of laser textured silicon surface by multiple scans.

FIG.2. (a) Reflection spectra of surfaces vary with the laser fluence for texturing, (b-c) Average and peak reflectance as functions of pulse number (b) and pitch (c), and (d) SEM images of textured surface by different laser scan speed (from top to bottom, the speed is 0.26,0.35 and 0.525 mm/s).

FIG.3. (a) Reflection spectra (Curves: 1. One scan with 90 mm/s, 2. One scan with 75mm/s, 3. Two scans with 75 and 90 mm/s), and (b-c) 3D microscope images of uniform and hybrid textured structures fabricated by laser texturing (b. uniform structure, c. hybrid structure).

FIG.4. Schematic drawings (3D view) of (a) uniform and (b) hybrid pyramid structures, and (c) their reflection spectra.

Figures:

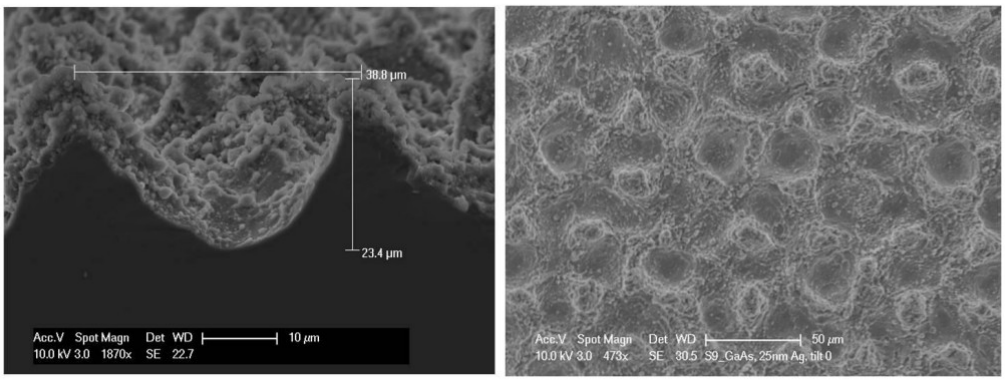

FIG.1

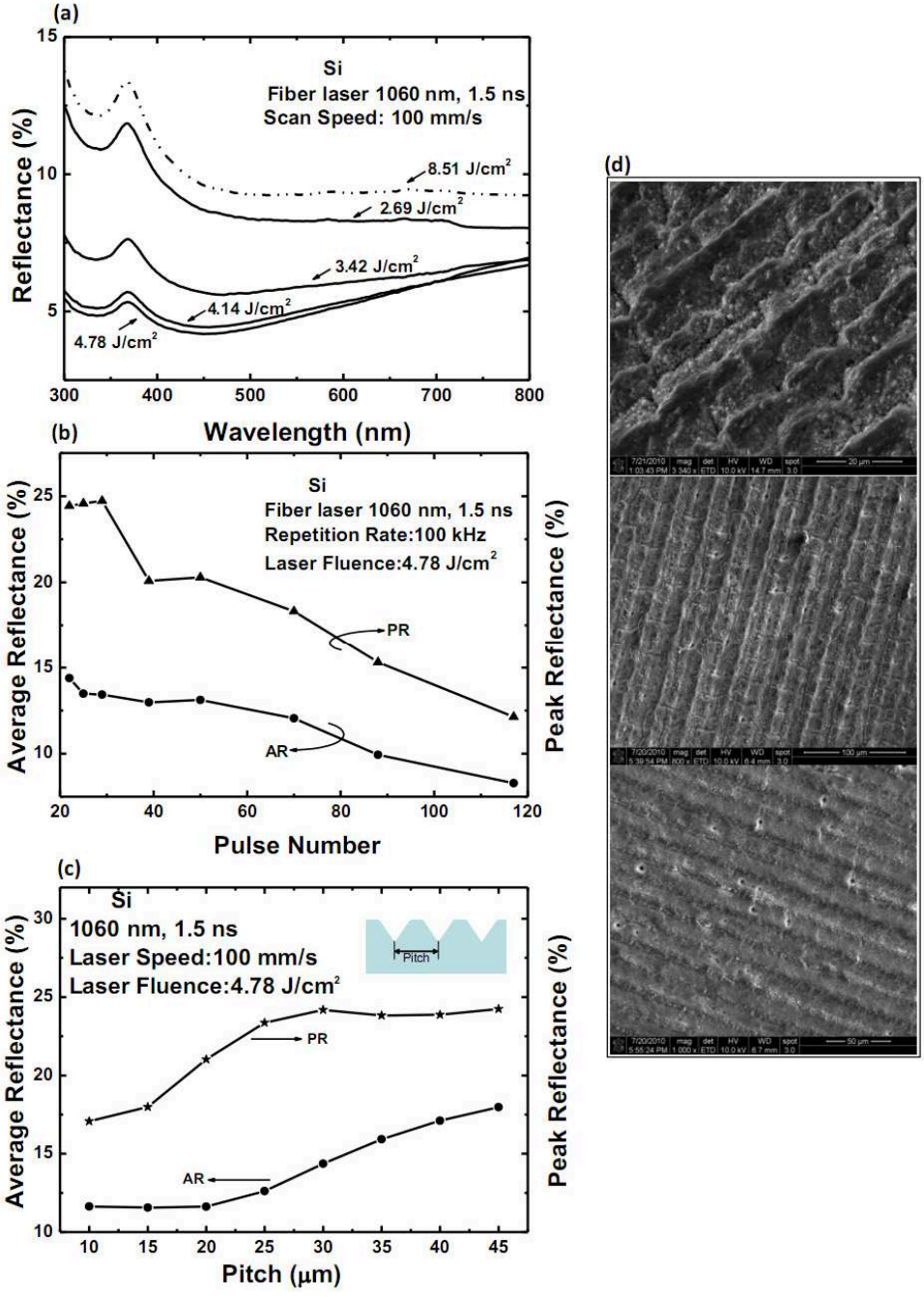

FIG.2

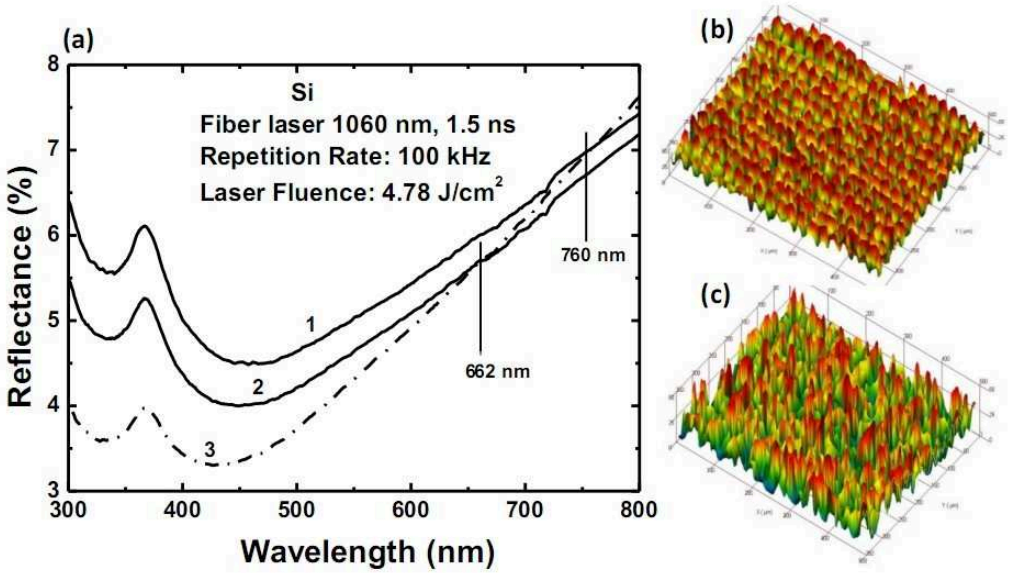
(a)
Si
Fiber laser 1060 nm, 1.5 ns
Repetition Rate: 100 kHz
Laser Fluence: 4.78 J/cm²
760 nm
662 nm
1
2
3
Reflectance (%)
Wavelength (nm)
(b)
(c)

FIG.3

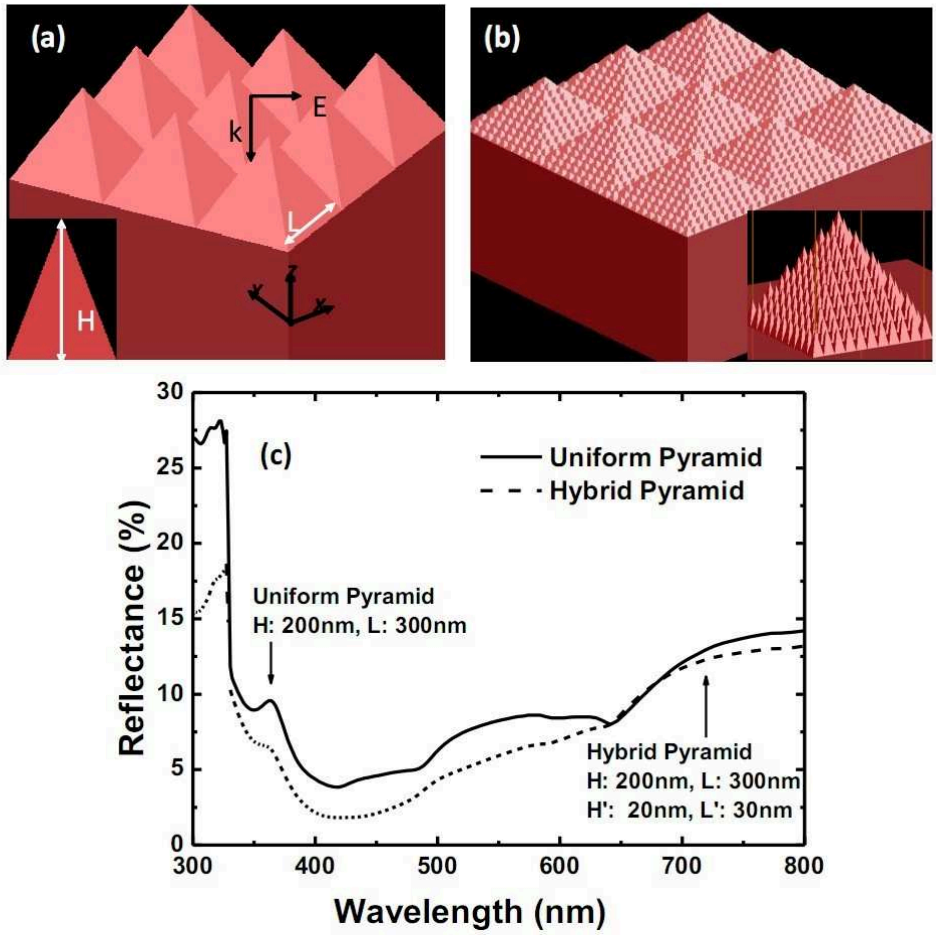
(a)
k
E
L
H
(b)
(c)
Uniform Pyramid
Hybrid Pyramid
Uniform Pyramid
H: 200nm, L: 300nm
Hybrid Pyramid
H: 200nm, L: 300nm
H': 20nm, L': 30nm
Reflectance (%)
Wavelength (nm)

FIG.4

References

[1] Y. Li, J. Zhang, S. Zhu, H. Dong, F. Jia, Z. Wang, Z. Sun, L. Zhang, and H. Li: Adv. Mater. 21 (2009) 4731.

[2] Y. Huang, S. Chattopadhyay, Y. Jen, C. Peng, T. Liu, Y. Hsu, C. Pan, H. Lo, C. Hsu, and Y. Chang: Nat. Nanotechnology 2 (2007) 770.

[3] L. Ma, Y. Zhou, N. Jiang, X. Lu, J. Shao, W. Lu, J. Ge, X. Ding, and X. Hou: Appl. Phys. Lett. 88 (2006) 171907.

[4] J. Xi, M. Schubert, J. Kim, E. Schubert, M. Chen, S. Lin, W. Liu, and J. Smart: Nat. Pho-tonics 1 (2007) 176.

[5] S. Chhajed, M. Schubert, J. Kim, and E. Schubert: Appl. Phys. Lett. 93 (2008) 251108.

[6] S. Boden and D. Bagnall: Appl. Phys. Lett. 93 (2008) 133108.

[7] O. Deparis, N. Khuzayim, A. Parker, and J. Vigneron: Phys. Rev. E 79 (2009) 41910.

[8] J. Huang, X. Wang, and Z. Wang: Nanotechnology 19 (2008) 025602.

[9] Y. Lin, H. Wang, C. Lin, and J. He: J. Appl. Phys. 106 (2009) 114310.

[10] B. Päivänranta, T. Saastamoinen, and M. Kuittinen: Nanotechnology 20 (2009) 375301.

[11] Q. Chen, G. Hubbard, P. Shields, C. Liu, D. Allsopp, W. Wang, and S. Abbott: Appl. Phys. Lett. 94 (2009) 263118.

[12] Y. Chang, G. Mei, T. Chang, T. Wang, D. Lin, and C. Lee: Nanotechnology 18 (2007) 285303.

[13] Y. Chen, P. Han, and X. Zhang: Appl. Phys. Lett. 94 (2009) 041106.

[14] D. Edwards: in Handbook of Optical Constants of Solids, ed. E. Palik (Academic Press, New York, 1985) p. 547.

[15] M. Halbwax, T. Sarnet, P. Delaporte, M. Sentis, H. Etienne, F. Torregrosa, V. Vervisch, I. Perichaud, and S. Martinuzzi: Thin Solid Films 516 (2008) 6791.

[16] W. Liang, F. Chen, H. Bian, Q. Yang, H. Liu, X. Wang, J. Si, and X. Hou: Opt. Commun., 283 (2010) 2385.

[17] A. Zoubir, L. Shah, K. Richardson, and M. Richardson: Appl. Phys. A 77 (2003) 311.

[18] C.H.Crouch, J.E.Carey, M.Shen, E.Mazur, and F.Y.Gé nin, Appl. Phys. A 79 (2004) 1635.

[19] E. Palik, and G. Ghosh: “Handbook of optical constants of solids” (Academic Press, Or-lando, 1985).

Advanced Materials Research Vol. 983 (2014) pp 90-93

doi:10.4028/www.scientific.net/AMR.983.90

Computer Aided Simulation and Prototype Experiment on Nanocoated Products

Jeremy (Zheng) Li [1,a]

[1]University of Bridgeport, 221 University Ave., Bridgeport, CT 06604, USA

[a] zhengli@bridgeport.edu

Keywords: Nanotechnology, computer-aided analysis, nanocoating control, anti-corrosion, simulation modeling

Abstract

The material damages in aerospace industry caused by correction can be detected in many different products including welded and bolted areas in aircraft and jet engines. The corrosion occurs when different conducted materials contact to each other in electrolyte media and different conducted materials present potential difference that causes rusting. The rusting problems in products lead both safety issues and billions of dollar loss in different businesses including aerospace industry. This paper studies the rusting mechanism and anti-corrosive coatings by applying computational simulation and prototype experiment. Both computer-aided analysis and sample testing demonstrated similar results which confirm the feasibility of analytic methodology introduced in this research paper.

Introduction

The corrosive potential difference moves galvanic current in metallic materials. To slow down rusting process, several traditional methods used are adjusting geometrical surface contacts, maintaining good bridge conditions, keeping proper material composition, and decreasing material potential among different materials [1, 2, and 3]. Also the geometrical area ratio of materials should be controlled for dissolution current density to slow down the rusting process [4 and 5]. In order to efficiently solve corrosion problems, nanocoating technology has been applied recently due to its strong anti-corrosion property [6 and 7]. Nanomaterial displays excellent physical and mechanical properties due to its tiny grain size and enlarged grain boundary ratio [8 and 9]. Nanocoating is a very thin film that is strongly adhesive to material substrate and demonstrates excellent water-proof property to prevent metallic materials from rusting [10, 11, and 12]. Compared to regular coating processes which will cause air pollution, nanocoating process is an environmentally-friendly manufacturing process [13, 14, and 15]. This paper focuses on the study of material nanocoating on aerospace products such as jet engine blades by introducing computer-aided simulation and sample testing and all the results show much better anti-rusting performance in nanocoated materials than in regular coated materials.

Computer-aided simulation on coating performance

Control of nanocoating grain size can improve material mechanical and physical properties. The sampled nanocoating has been used in this research to compare its anti-rusting performance with regular coating techniques.

The computational model has been built up to simulate coating anti-rusting performance and help to understand corrosive-resistant mechanism. Fig. 1 shows corrosion speed in galvanized coating and nanocoating.

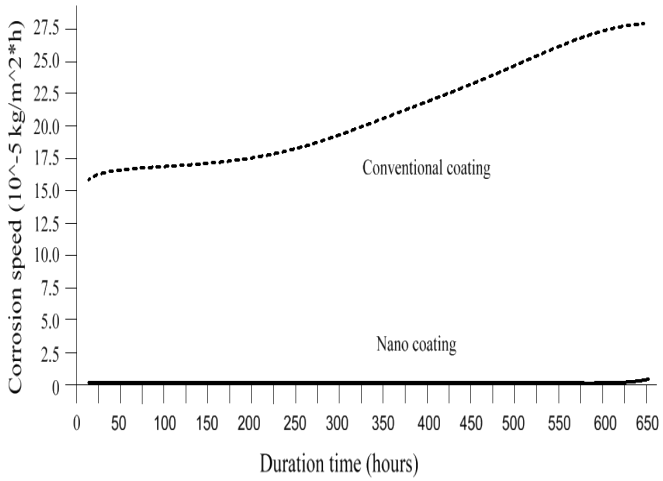

Fig. 1 Corrosion speed in regular coating and nanocoating vs. duration time

This simulation result shows that the nanocoating has much lower corrosion speed than regular coating due to its enlarged corrosion barrier inside nanocoating. The increased element Cr composition in nanocoating can well control molecular diffusion in internal material phase boundary and the intensified grain boundary in nanocoating structure can compensate the oxide loss to keep nanocoating material more durable and reliable in corrosive prevention.

Fig. 2 depicts the current density vs. potential in material anodic polarization.

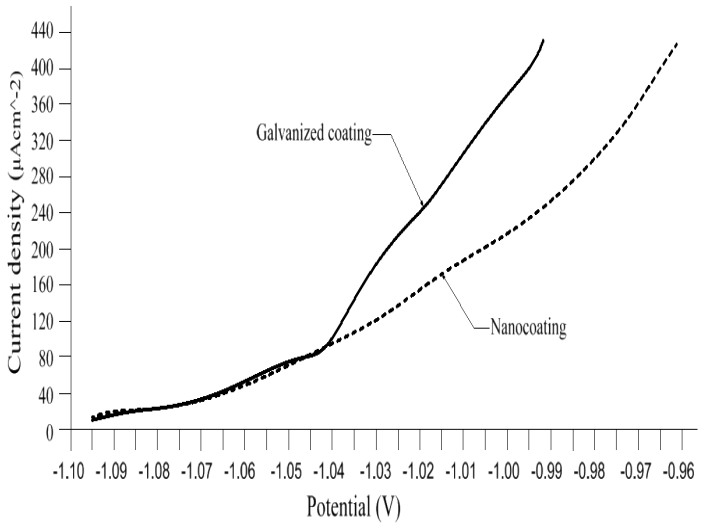

Fig. 2 Current density vs. potential in material anodic polarization

Fig. 2 displays the current density vs. potential of anodic polarization in regular coating and nanocoating materials. Since the graph shows more sharp change of current density in regular coating than in nanocoating, the anti-rusting performance in nanocoating is more stable and durable than in regular coating.

Sample testing

The prototyped samples were tested for nanocoated and galvanized materials in 3.85 % NaCl solution to compare computer-aided simulation results. The experimental results of material corrosion speed and material current density vs. potential are shown in Tables 1 and 2 respectively.

Table 1 Corrosion speed vs. testing time in 3.85 % NaCl solution

Duration of testing (hours)	Corrosion speed (10^{-5} kg/m^2 h)	
	Nanocoating	Galvanized coating
50	0.00	15.80
100	0.00	16.38
150	0.00	16.98
200	0.00	17.44
250	0.00	17.78
300	0.00	18.48
350	0.00	18.78
400	0.00	21.35
450	0.00	21.85
500	0.00	23.68
550	0.02	25.46
600	0.05	26.78
650	0.12	27.38
700	0.18	29.44

Table 2 Current density vs. potential of material anodic polarization in experiment

Potential (V)	Current density (μAcm^{-2})	
	Nanocoating	Galvanized coating
-1.10	7.56	7.62
-1.09	15.68	16.06
-1.08	18.33	18.34
-1.07	32.48	32.12
-1.06	45.42	45.32
-1.05	62.44	60.88
-1.04	75.43	76.55
-1.03	96.54	175.45
-1.02	126.43	230.48
-1.01	162.41	318.38
-1.00	188.48	365.78
-0.99	260.22	454.33
-0.98	278.45	488.38

Table 1 indicates very low corrosion speed in nanocoating than in regular coatings and nanocoated material displays more stable and durable coating performance than regular coatings shown in Table 2. These testing results are very close to the results determined by computer-aided simulation. Both results confirm lower corrosion speed in nanocoated material than in galvanic coated material.

Conclusion

This research paper introduces a feasible analytic method to simulate coating corrosion-resistant performance by computer-aided simulation and sample experiment. It helps to understand the fundamentals of rust-resistant mechanism. The computer-aided simulation model is used to study and analyze the nanocoating performance and prototyping samples have also been tested to verify results from computer-aided simulation. Both results show close results and superior performance in nanocoating than in regular coating because of strong corrosive-resistant in nanocoated material structure.

References

[1] Kizuka, T., Miyazawa, K. and Matsuura, D., 2012, “Synthesis of Carbon Nanocapsules and Nanotubes Using Fe-Doped Fullerene Nanowhiskers”, Journal of Nanotechnology, Vol. 1, pp.10-16.

[2] Jeremy (Zheng) Li, 2013, "Computational Analysis and Prototype Experiment of Nanomaterial for Aircraft Wing Inboard Flap in Aerospace Industry", Journal of Mechatronics, Vol. 1, pp. 1-4, published in December, 2013.

[3] Jeremy (Zheng) Li, 2013, "Computational Simulation and Prototype Testing of Nanocoated Materials for Jet Engine Blades in Aerospace Industry", Journal of Applied and Industrial Science, Vol. 1, pp.36-38, published in November, 2013.

[4] Yoon, W., Jung, K. and Liu, J., 2010, “Plasmon-enhanced optical absorption and photocurrent in organic bulk heterojunction photovoltaic devices using self-assembled layer of silver nanoparticles”, Journal of Solar Energy Materials and Solar Cells, Vol. 94, pp.128–132.

[5] Jeremy (Zheng) Li, 2013, "Study of Nanocoating Technology of Control Product Corrosion in Aerospace Industry", Journal of Advanced Materials Research, Vols. 785-786, pp. 967-969, published in October, 2013.

[6] Jeremy (Zheng) Li, 2013, "Computational Simulation and Prototype Testing of Nanocoating on Products in Aerospace Industry", Journal of Advanced Materials Research, Vols. 750-752, pp. 2088-2091, published in May, 2013.

[7] Wang, Y., Limb, S., Luob, J. and Xub, Z., 2006, “Tribological and corrosion behaviors of Al_2O_3 polymer nanocomposite coatings”, Journal of Wear, Vol. 2, pp.976-983.

[8] Jeremy (Zheng) Li, 2012, “Computer-Aided Modeling of Nanochrystalline Coating to Reduce the Galvanic Corrosion”, Journal of Nanoscience and Nanotechnology, Vol.1, pp.13-15, published in November, 2012.

[9] Jeremy (Zheng) Li, 2012, “Computational Simulation and Testing of Nano Particle Coating in Material Anti-Corrosion”, International Journal of Materials Engineering, Vol.2, pp.18-22, published in July, 2012.

[10] Jaqueline, S. and Jorio, A., 2012, “Study of Carbon Nanotube-Substrate”, Journal of Nanotechnology, Vol. 2, pp.56-66.

[11] Jeremy (Zheng) Li, 2012, “Study and Computational Simulation of Nanomaterial Coating to Reduce Crevice Corrosion”, Journal of Nanoscience and Nanotechnology, Vol.2, pp.1-4, published in June, 2012.

[12] Akiyama, T., Aiba, K., Hoashi, K., Wang, M., Sugawa, K. and Yamada, S., 2010, “Enormous enhancement in photocurrent generation using electrochemically fabricated gold nanostructures”, Journal of Chemical Communications, Vol. 46, pp.306–308.

[13] Jeremy (Zheng) Li, 2012, “Study and Computational Modeling of Nano Coating to Protect Products from Atmospheric Corrosion”, American Journal of Material Science, Vol. 1, pp.38-40, published in March, 2012.

[14] Jeremy (Zheng) Li, 2012, “Computer Modeling and Experimental Study of Material Surface Improvement by Nano Coating Technology”, International Journal of Materials and Chemistry, Vol. 1, pp.48-50, published in February, 2012.

[15] Cai, R., Van, G., Aw, P. and Itoh, K., 2006, “Solar-driven self-cleaning coating for a painted surface”, Journal of Chemistry, Vol. 9, pp.829-835.

Advanced Materials Research Vol. 983 (2014) pp 94-98

doi:10.4028/www.scientific.net/AMR.983.94

Influence of Injection Conditions on the Mechanical Property of MWCNTs/ PC Nanocomposites

Lijun Wang[1, a], Jianhui Qiu[1, b] and Eiichi Sakai[1, c]

[1] Akita Prefectural University, Tsuchiya-Ebinokuchi 84-4, Yurihonjo, Akita, Japan

[a]d15s001@akita-pu.ac.jp, [b]qiu@akita-pu.ac.jp, [c] e_sakai@akita-pu.ac.jp

Keywords: Multiwalled carbon nanotubes/Polycarbonate, Nanocomposites, Injection speed, Injection temperature, Mechanical property

Abstract. The melting mixing was applied in the preparation of Multiwalled carbon nanotubes/Polycarbonate (MWCNTs/PC) nanocomposites. MWCNTs/PC nanocomposites with different MWCNTs contents were prepared under different injection conditions. The mechanical property of nanocomposites was comparatively investigated. The results demonstrated that: the tensile property of the nanocomposites was slightly improved by MWCNTs content increasing; but as the MWCNTs contents went on to increase to 10wt%, the tensile strength and bending strength were obviously decreased about 35% and 47%, respectively, but the impact strength and hardness were increased. The center hardness of MWCNTs/PC nanocomposites was greater than the surface hardness. Besides, the changes on the mechanical properties of the nanocomposites were studies by changing the injection conditions. By Scanning Electron Microscopy (SEM) observation, the microstructure and morphology of nanocomposites were analyzed, revealing that the center of the nanocomposite distributed more MWNTs, and the injection conditions would affect the MWNTs' dispersion in the matrix and the interfacial interaction between MWCNTs and PC.

Introduction

Polycarbonate (PC) is non-crystalline thermoplastic plastic. As general plastic, it is known for its large yield and wide range of applications. PC is widely used in packaging, automotive, medical apparatus and instruments, construction industry and other industries. Since the discovery of carbon nanotubes (CNTs) by Iijima in 1991[1], CNTs have received much attention for their many characteristics, such as unique structure, excellent mechanical properties, thermodynamic properties, conductive properties and high aspect ratio features, which has been as a typical one-dimensional material[2]. In recent years, Carbon nanotubes/Polymer nanocomposites have attracted much attention for their many potential applications [3-4], such as nanoelectronic devices, electrostatic recording paper, electromagnetic shielding, electromechanical actuators, electrochemical capacitors, nanowires and superconductors [5-7]. However, owing to some disadvantageous of CNTs, such as inherent large specific surface area [8], higher surface activation energy and easy to be aggregate, there is still a great challenge in achieving alignment of CNTs in a polymer matrix. If CNTs disperse evenly in the polymer matrix, the mechanical property of nanocomposites will be reinforced. So the major problem is to overcome the dispersion of CNTs in a polymer matrix and the interfacial interaction between CNTs and polymer.

In our recent work, we successfully prepared MWCNTs/PC nanocomposites by melting mixing. With the injection speed and injection temperature changed, the mechanical properties of MWCNTs/PC nanocomposites were compared. The effects of the injection speed and temperature

changed and the contents of MWCNTs were tested via kinds of characterisitics. Expectedly, the mechanical properties of the nanocomposites have a degree improvement.

Experiment

Materials. Carbon nanotubes (CNTs), (Shouwa Denko Company in Japan), with an average diameter of 10～15nm and a mean length of 3μm, were used without any purification process as the filler. Polycarbonate (PC) from Teijin Chemicals Company in Japan with a melt flow index of 18cm^3/10min was used as the matrix.

Preparation of composites. Because PC was very easy to absorb water in the air, a vacuum drying at 100℃ for 8 hours had to be done. First, added the mass fraction of MWCNTs as 5wt% and 10wt% into PC to mix, then put them into the dry mixing machine to mix uniformly (two times). Second, carried out the melt blending (the mixing temperature is 290℃, the speed is 100rpm), then get the MWCNTs/PC composites master batch. Third, through drying treatment at 120℃ for 5 hours, did the injection molding, then get the Standard specimen of PC/MWNTs composites.

Mechanical property tests. Values of the mechanical properties of each group were decided by the means of five samples. All of the mechanical property tests were carried out at room temperature about 23 ± 2℃.

(1) Tensile test. The tensile properties of nanocomposites were measured by using a universal testing machine (Shenzhen Xinsansi Metering Technology Co., Ltd, China). The experiment samples were Dumbbell shape specimen (JIS K 7113 1(1/2)). Measurement of the tensile strength and elongation at break were performed with an electrical extensometer. The tests were carried out at the tensile rate of 10mm/min.

(2) Bending test. The bending properties of nanocomposites were tested by using the same universal testing machine (Shenzhen Xinsansi Metering Technology Co., Ltd, China) as in tensile tests. The experiment samples were rectangular shape specimen (JIS K 7171 1(1/2)). Measurement of the bending strength and bending strain were performed with the same electrical extensometer as in tensile tests. The tests were carried out at the speed of 2mm/min.

(3) Impact tests. The impact properties of nanocomposites were tested by a pendulum impact tester (SHANGAI JIMING MEASURING EQUIPMENT Co., LTD, China). The experiment samples were rectangular shape specimen (JIS K 7171 1(1/2)), and a 2mm deep standard V-notch was carved on each sample. The maximum impact energy was set to be 7.5J and the impact speed was 3.5m/s.

(4) Hardness test. The hardness of nanocomposites was tested by a computer display manual turret microscopic hardness meter (GOTECH TESTING MACHINES Co., Ltd, China). The test was performed at the load of 10g and the load holding time of 15s. The hardness of nanocomposites from surface to inner was tested by using the same machine. The test sample was showed in Fig.1. In addition, because the sample surface roughness might affect the test results, the sample surface was polished firstly before testing.

Microstructure analysis. The microstructure of MWCNTs/PC nanocomposites was analyzed by Scanning electron microscope (SEM, Hitachi Ltd S-4300) observation. Through gold-coated and observed under an acceleration voltage of 15KV, SEM micrographs of the fractured surfaces of composites after tensile testing were obtained at room temperature.

Results and Discussion

Tensile properties. The tensile properties of the nanocomposites at room temperature were determined. The tensile strength and elongation at break were listed in Table 1. In general, the tensile strength of the nanocomposites with MWCNTs content of 5wt% were slightly higher than that of pure PC, showing the reinforcing effect of MWCNTs; however, with further increasing MWCNTs content, the tensile strength of the nanocomposites with MWCNTs content of 10wt% were decreased about 35% than that of pure PC. The total elongation of composites was decreased significantly and showed brittleness to some degrees. At MWCNTs content of 5wt%, partial tensile strain could be transferred to MWCNTs embedded in PC matrix under tensile stress that leaded to the increase in the tensile strength of nanocomposites. However, MWCNTs maintained the strength of the nanocomposites, but brittleness became strong, so the elongation at break was decreased obviously.

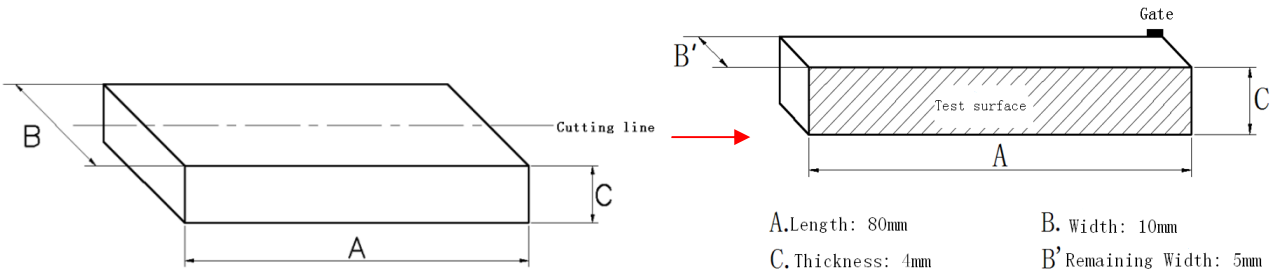

Fig.1 The shape of samples for hardness test

Table 1 Influence of MWCNTs content on the tensile properties of MWCNTs/PC nanocomposites

MWCNTs content	Injection speed(mm/s)	Injection temperature( )	Yield strength MPa)	Tensile strength MPa)	Elongation at break (%)
Pure PC	80	280	57.33	57.44	193.17
5wt%	80	280	60.03	60.04	21.04
10wt%	80	280	37.41	38.84	11.15
Pure PC	40	305	56.72	56.73	196.80
5wt%	40	305	59.64	59.71	23.68
10wt%	40	305	41.76	41.87	11.88
Pure PC	10	330	57.97	57.98	205.00
5wt%	10	330	59.11	59.17	20.02
10wt%	10	330	34.63	35.82	10.93

Fig.2 shows the influence of injection speed on the tensile strength and fracture strain of nanocomposites with MWCNTs content of 5wt% for different injection temperatures. It could be obviously seen that the injection temperature and injection speed affected the tensile strength and fracture strain of the nanocomposites. The injection conditions would affect the fluidity of MWCNTs/PC composites which leaded to changing the viscosity of the composites and forming the different internal subtle structures of MWCNTs/PC composites samples (three layers with different thickness) in injection molding. Meanwhile the orientation of MWCNTs in PC matrix was changed, thus affected the mechanical properties of the composites.

Bending properties. The bending properties of the nanocomposites at room temperature were investigated. Fig.3 shows the influence of injection speed on bending strength and bending strain with MWCNTs content of 5wt%. It could be seen that the injection speed affected the bending

strength and bending strain of the nanocomposites obviously. This might be because of the formation mechanism of the internal microstructure of the samples in injection molding.

Impact properties. The impact properties of the nanocomposites at room temperature were studied. The influence of MWCNTs content on impact strength is shown in Fig.4. The impact strength was monotonously decreased as MWCNTs content increased to 5wt%. Besides, at a higher injection temperature and a lower injection speed or at a lower injection temperature and a higher injection speed, the impact strength was almost changed in the same trend. The reason might be attributed to that the injection conditions affect the orientation of the nanocomposites and form different surface structures of MWCNTs/PC nanocomposites samples (formed three layers with different thickness) in injection molding.

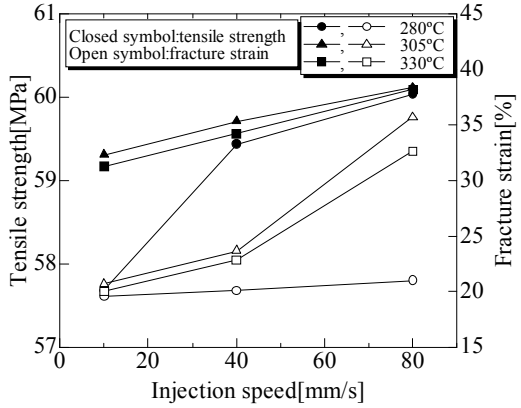

Fig.2 Influence of injection speed on tensile strength and fracture strain (5wt%MWCNTs)

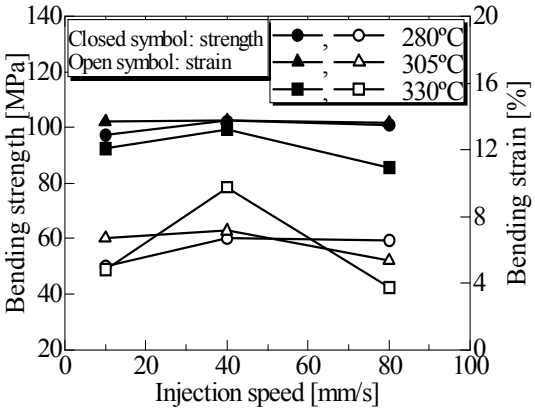

Fig.3 Influence of injection speed on bending strength and strain (5wt% MWCNTs)

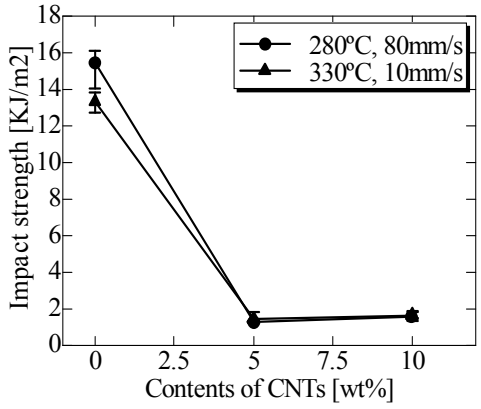

Fig.4 Influence of MWCNTs content on impact strength

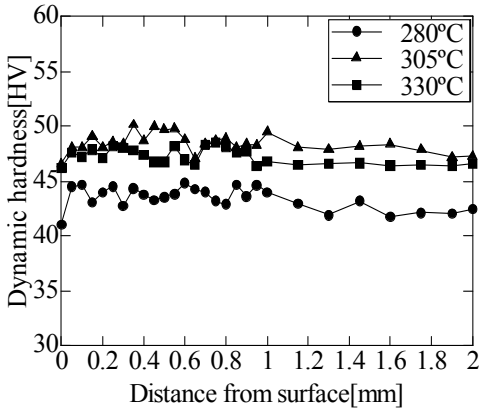

Fig.5 Influence of injection temperature on distribution of hardness in cross (5wt%, 10mm/s)

Hardness properties. In order to prove the influence of injection conditions on mechanical properties, the distribution of the nanocomposites hardness in cross were investigated at room temperature. Fig.5 shows that as injection temperature increasing, the hardness of the nanocomposites with MWCNTs content of 5wt% increased at different degree. Besides, the closer to the inner of nanocomposites, the hardness of nanocomposites was more stable. This might be because of the formation mechanism of the internal microstructure of the samples in injection molding, and MWCNTs showed excellent mechanical property.

Microstructure structure. Fig.6 shows the SEM images of MWCNTs/PC nanocomposites obtained at injection temperature of 280℃ and injection speed of 10mm/s. In Fig.6 (a), it was

obviously seen that MWCNTs were dispersed evenly and the orientation of nanocomposites with MWCNTs content of 5wt% was very good, so as to increase the mechanical properties of MWCNTs/PC nanocomposites. Therefore, the strong interaction between MWCNTs and PC matrix greatly enhanced the dispersion as well as the interfacial adhesion, thus strengthening the overall mechanical properties of the nanocomposites. However, when MWCNTs content went to increasing (reach to 10wt%, in Fig.6 (b)), the dispersion of MWCNTs in PC matrix was poor, easy to be aggregated, resulting in showing the brittleness be strong, leading to more brittle fracture.

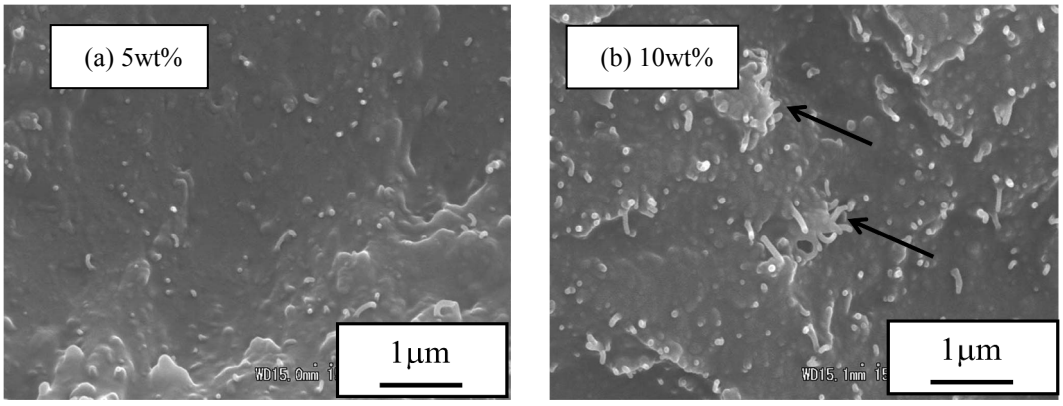

Fig. 6 SEM images for fracture surface of MWCNTs/PC composites 280 , 10mm/s)

Summary

In summary, we successfully prepared the MWCNTs/PC nanocomposites by the melt blending method. From the above results, the influence of MWCNTs on the mechanical properties of the MWCNTs/PC nanocomposites could clearly be seen in all cases. The MWCNTs content was the most dominant factor which would enhance the mechanical property of MWCNTs/PC nanocomposites. However, when MWCNTs content was increased to 10wt%, the brittleness of MWCNTs was performed strongly, lead to more brittle fracture of MWCNTs/PC nanocomposites, so as to the tensile property and bending property of the nanocomposites be decreased. Besides, the mechanical properties and SEM analysis showed that the injection conditions were also one of major factors which would obviously affect the mechanical properties of MWCNTs/PC nanocomposites. In addition, the SEM images showed good interactions between MWCNTs and PC. This resulted in a denser microstructure and higher strength when compared to the injection conditions.

Reference

[1] Iijima S. Helical microtubules of graphitic carbon [J]. Nature,1991,354:56-58.
[2] D. Tasis, et al., Chemistry of carbon nanotubes, Chem. Rev. 2006,106:1105–1136.
[3] Hornbostela B, Potschke P, Kotza J, et al.Mechanical properties of triple composites of polycarbonate,single-walled carbon nanotubes and carbon fibres. Physica E 2008,40:2434- 2439.
[4]Ramasubramaniam R, Chen J, Liu H. Homogeneous carbon nanotube/polymer composites for electrical applications[J]. Appl Phys Lett, 2003,83(14):2928-2930.
[5] Andrews R, et al. Carbon nanotube polymer composites. Curr Opin Solid State Mater Sci 2004;8:31-37.
[6]Bachtold A, et al. Logic circuits with carbon nanotube transistors. Science 2001;294:1317-1320.
[7] L. A. Nagahara, et al. Applied Physics Letters, 2002,80(20):3826–3829.
[8]JC Kearns,R L Shambaugh.J.Appl.Polym.Sci,2002,86(8):2079-2084.

Advanced Materials Research Vol. 983 (2014) pp 99-102
© (2014) Trans Tech Publications, Switzerland
doi:10.4028/www.scientific.net/AMR.983.99

Nanomechanical properties of core-shell structured Ni@NiO nanoparticles reinforced epoxy nanocomposites

Huai-Yuan Wang[1, a *], Lei Yan[1, b], Yan-Ji Zhu [1, c], Hua Song[1, d], Jia-Hua Zhu[2, e]

[1]College of Chemistry and Chemical Engineering, Northeast Petroleum University, Daqing, 163318, China

[2] Chemical and Biomolecular Engineering,The University of Akron, USA

[a]corresponding author, email: wanghyjiji@163.com, [b]email: yanlei.0821@163.com,

[c]email: jsipt@163.com, [d]email: songhua2004@sina.com, [e]email: jzhu1@uakron.edu

Keywords: Polymer nanocomposites; Nanomechanical properties; Epoxy; Nanoparticles

Abstract. Epoxy resin (EP) nanocomposites reinforced with different contents of core-shell structured Ni@NiO nanoparticles (NPs) were fabricated by using a surface wetting method. The nanoindentation and nanoscratch properties of Ni@NiO/EP nanocomposites were comparatively studied based on nanoindentation technique. Results revealed that 5 wt.% content of Ni@NiO NPs was the optimal concentration for Ni@NiO/EP composites to obtain the best improvement of nanomechanical properties. In comparison with pristine EP, the highest enhancements of hardness and elastic modulus of 5 wt.% Ni@NiO/EP nanocomposites were increased by 37.8% and 16.3%, respectively.

Introduction

Epoxy resin (EP), as an advanced thermosetting matrix of polymeric nanocomposites (PNCs), exhibits a sequence of excellent properties such as favorable dimensional stability, high chemical corrosion resistance and low curing shrinkage [1,2]. When it is cross-linked with appropriate curing agents, outstanding chemical resistance and adhesive properties can be gained [3,4]. Nevertheless, cured EP is inherently brittle owing to its high crosslinking density, hence posing a constraint on many engineering applications. In order to further improve the mechanical properties of pure EP to meet more demanding applications, one effective and promising method is to add reinforcing fillers into the EP matrix [5].

Nanoparticles (NPs) are promising candidates serving as reinforcing materials due to their quantum size effect, surface effect and volume effect [6-8], which make nanocomposites possess favorable corrosive resistance and excellent mechanical properties, such as high toughness, high stiffness and high hardness [9]. Among a variety of nanoparticles, iron group Ni metallic NPs are of great interest because of their superior mechanical and magnetic properties [10]. However, these exposed Ni metallic NPs are easily oxidized and flammable in air [11]. To stable the Ni NPs, one effective approach is to introduce a stable shell (NiO) to protect the NPs from oxidation or self-ignition in harsh environments.

Up to now, to our best aware, the nanomechanical properties of core-shell structured Ni@NiO nanoparticles reinforced epoxy nanocomposites have been rarely studied in literatures. In this work, the Ni@NiO/EP nanocomposites with different contents of Ni@NiO NPs are fabricated by using a surface wetting method. Then the nanomechanical properties of Ni@NiO/EP nanocomposites are mainly investigated by both nanoindentation and nanoscratch tests.

Experimental details

Materials and Preparation of Ni@NiO/EP nanocomposites

862 bisphenol F epoxy and epicure curing agent W were purchased from Miller-Stephenson Chemical Company, Inc. Core-shell structured Ni@NiO NPs (average diameter of 20 nm, shell thickness of 4 nm) were provided by QuantumSphere, Inc. The Ni@NiO/EP nanocomposites with 0,

1, 3, 5, 8 and 12 wt.% contents of Ni@NiO NPs were fabricated, respectively. Different contents of Ni@NiO NPs were weighted accurately and then epoxy 862 was added, keeping the mixture overnight until the the surfaces of Ni@NiO NPs were wetted absolutely. Then the mixture was stirred (400 rpm) at room temperature for 60 min. After that, epicure curing agent W was added. The weight ratio of epoxy 862 and epicure curing agent W was 100:26.5 according to the recommendation of the company. The mixture was further mechanical stirred for 240 min in a 75 ^{o}C water bath. Then removing the bubbles in the mixture under ultrasonication at room temperature for 20 min. Finally, the mixture was transferred to silicon-rubber molds and put into an oven at 120 ^{o}C about 8 h for curing.

Nanoindentation and nanoscratch tests

Nanoindentation was taken to study the nano-mechanical behaviors (including hardness and elastic modulus) of the Ni@NiO/EP nanocomposites with different contents of Ni@NiO NPs. The nanoindentation and nanoscratch tests were conducted on a nanotriboindenter (Hysitron Inc., USA) using a conical diamond indenter at room temperature (25 ^{o}C, humidity 50-55%). Before each test, the surface of specimen was polished to adequately smooth, and the average roughness was no more than 50 nm. For all the nanoindentation tests, the holding time at the Fmax was 24 seconds for indentation to minimize the time-dependent plastic effect. For each indentation test, at least 12 tests were repeated. In the nanoscratch tests, the conical diamond indenter pressed vertically into the specimen and moved horizontally on the specimen surface under designed load.

Results and discussion

A. Morphology of Ni@NiO/EP nanocomposites

Figure 1 shows the optical and TEM images of 5 wt.% Ni@NiO/EP nanocomposites, respectively. In Figure 1a, the 5 wt.% Ni@NiO/EP nanocomposites exhibits homogeneous black color, suggesting that 5 wt.% Ni@NiO can be well dispersed in matrix. And TEM image further reveal that the Ni@NiO NPs are dispersed uniformly and well separated in the epoxy matrix (Figure 1b).

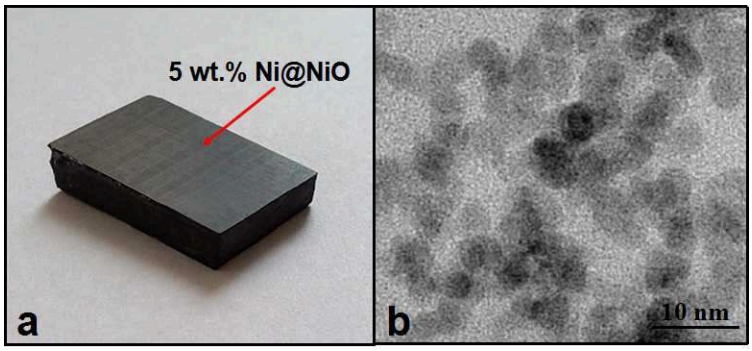

Fig. 1 (a) Optical image and (b) TEM micrograph of 5 wt.% Ni@NiO NPs nanocomposites.

B. Nanoindentation results

The hardness and elastic modulus of Ni@NiO/EP nanocomposites with different contents of Ni@NiO NPs are displayed in Figure 2 and Figure 3. From the figures, it can be seen that both hardness and elastic modulus of Ni@NiO/EP nanocomposites are enhanced by adding various contents of Ni@NiO NPs into the EP matrix. In particular, the mechanical properties of Ni@NiO/EP nanocomposites are obviously improved with the addition of 5 wt.% Ni@NiO NPs. In comparison with pure EP, the hardness and elastic modulus of 5 wt.% Ni@NiO/EP nanocomposites are increased by 37.8% and 16.3%, respectively. Nevertheless, when the content of Ni@NiO NPs further increases, the hardness and elastic modulus of the Ni@NiO/EP nanocomposites are decreased. The main reason may be because of the poor dispersion and agglomeration of Ni@NiO NPs in the matrix.

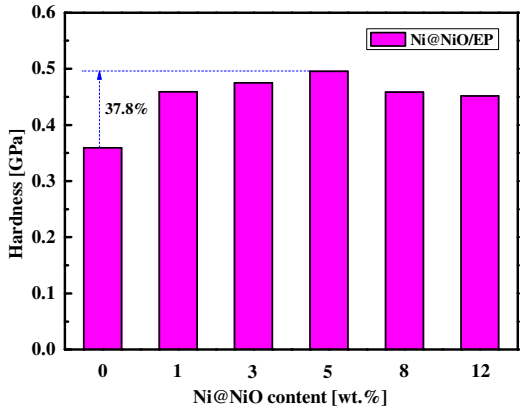

Fig. 2 Hardness of Ni@NiO/EP nanocomposites with different contents of Ni@NiO.

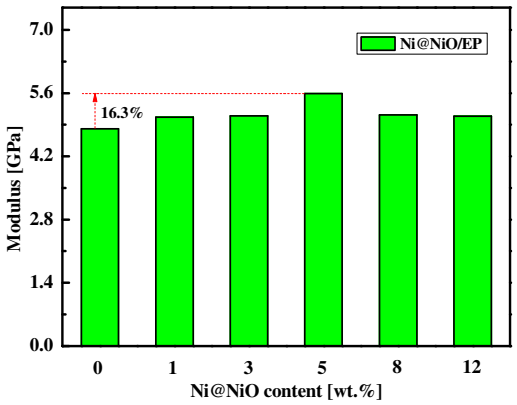

Fig. 3 Elastic modulus of Ni@NiO/EP nanocomposites with different contents of Ni@NiO.

Figure 4 shows the depth-time nanoindentation curves of Ni@NiO/EP nanocomposites at a peak load of 0.5 mN. As shown in the figure, pure EP exhibits the highest indentation depth, suggesting that it possesses the lowest resistance to indentation force. For the Ni@NiO/EP nanocomposites, all the depth-time curves are shifted down. In particular, 5 wt.% Ni@NiO/EP nanocomposites shows the minimum indentation depth. It indicates that 5 wt.% content of Ni@NiO NPs is the optimal concentration for Ni@NiO/EP nanocomposites to obtain the best improvement of the indentation resistance. The results are consistent with those of hardness and elastic modulus of Ni@NiO/EP nanocomposites as shown in Figure 2 and 3. Besides, no discontinuities on the depth-time curves, revealing an uniform dispersion of Ni@NiO NPs and no cracks formed during the indentation.

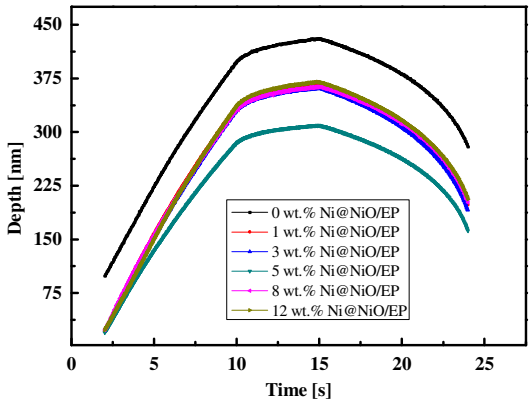

Fig. 4 Depth-time curves of Ni@NiO/EP nanocomposites under 0.5 mN load in the nanoindentation tests.

C. Nanoscratch results

The displacement-time nanoscratch curves of Ni@NiO/EP nanocomposites at the peak load of 0.5 mN are demonstrated in Figure 5. It is apparent that pure EP possesses the highest scratch depth. However, all the scratch depths of the Ni@NiO/EP nanocomposites with different contents of Ni@NiO NPs are decreased compared with pure EP. Especially, the Ni@NiO/EP nanocomposites with 5 wt.% content of Ni@NiO NPs obtain the lowest scratch depth, indicating that 5 wt.%Ni@NiO/EP nanocomposites show the highest resistance to scratch force. The above improvement of 5 wt.% Ni@NiO/EP nanocomposites can be ascribed to the uniform dispersion of Ni@NiO NPs in the EP matrix and the highest reinforced mechanical properties (hardness and modulus) of 5 wt.% Ni@NiO/EP nanocomposites. In addition, it can be found that Ni@NiO/EP nanocomposites with the lowest (1 wt.%) and the highest (12 wt.%) concentration of Ni@NiO NPs display unstable scratch depths during the nanoscratch tests. The main reason may be due to the poor dispersion and agglomeration of Ni@NiO NPs in the EP matrix.

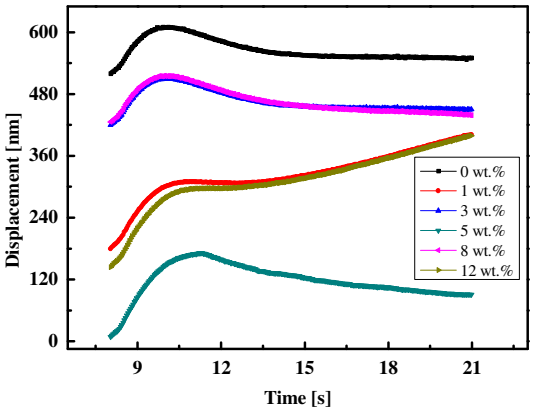

Fig. 5 Displacement-time curves of Ni@NiO/EP nanocomposites under 0.5 mN load in the nanoscratch tests.

Summary

5 wt.% content of Ni@NiO NPs is the optimal concentration for Ni@NiO/EP nanocomposites to obtain the best improvement of mechanical properties, scratch and indentation resistance. In comparison with pristine EP, the highest enhancements of hardness and elastic modulus of 5 wt.% Ni@NiO/EP nanocomposites increase by 37.8% and 16.3%, respectively.

References

[1] J. Sandler, M.S.P. Shaffer, T. Prasse, W. Bauhofer, K. Schutle, A.H. Windle, Development of a dispersion process for carbon nanotubes in an epoxy matrix and the resulting electrical properties, Polymer 40 (1999) 5967-5971.

[2] O. Jacobs, H.Y. Chen, W. WuG. RüdigerB. Schäel, Effect of dispersion method on tribological properties of carbon nanotube reinforced epoxy resin composites, Polym.Test 26 (2007) 351–360.

[3] Kuang-Ting Hsiao, Justin Alms and Suresh G Advani, Use of epoxy/multiwalled carbon nanotubes as adhesives to join graphite fibre reinforced polymer composites, Nanotechnology 14 (2003) 791–793.

[4] M. K. Abdullah, M. Z. Abdullah, M. A. Mujeebu, S. Kamaruddin, Z. M. Ariff, A study on the effect of epoxy moulding compound (EMC) rheology during encapsulation of stacked-chip scale packages (S-CSP), J. Reinf. Plast. Compos. 28 (2009) 2527–2538.

[5] Lei Yan, Huaiyuan Wang, Chao Wang, Liyuan Sun, Dujuan Liu, Yanji Zhu, Friction and wear properties of aligned carbon nanotubes reinforced epoxy composites under water lubricated condition, Wear 308 (2013) 105-112.

[6] Prashant V. Kamat, Nada M. Dimitrijević, Colloidal semiconductors as photocatalysts for solar energy conversion, Solar Energy 44 (1990) 83-98.

[7] Philip Ball, Laura Garwin, Science at the atomic scale, Nature 355 (1992) 761-766.

[8] R. E. Cavicchi and R. H. Silsbee, Coulomb suppression of tunneling rate from small metal particles, Phys. Rev. Lett. 52 (1984) 1453.

[9] Jimei Mou, Lide Zhang, The development tendency of nanocomposites, Phys 25 (1996) 31-36.

[10] Jiahua Zhu, Suying Wei, Dan Rutman, Neel Haldolaarachchige, David P. Young, Zhanhu Guo, Magnetic polyacrylonitrile-Fe@FeO nanocomposite fibers-electrospinning, stabilization and carbonization, Polymer 52 (2011) 2947–2955.

[11] Di Zhang, Ruby Chung, Amar B. Karki, Feng Li, David P. Young and Zhanhu Guo, Magnetic and magnetoresistance behaviors of solvent extracted particulate iron/polyacrylonitrile nanocomposites, J. Phys. Chem. C 114 (2009) 212–219.

CHAPTER 3:

Composites and Alloys

Advanced Materials Research Vol. 983 (2014) pp 105-109

doi:10.4028/www.scientific.net/AMR.983.105

Effect of Injection Conditions on the Electrical Conductivity of MWCNTs/ PC Conductive Composites

Lijun Wang[1, a], Jianhui Qiu[1, b], Eiichi Sakai[1, c] and Xiaowei Wei[2, d]

[1] Akita Prefectural University, Tsuchiya-Ebinokuchi 84-4, Yurihonjo, Akita, Japan

[2,]Xihua University, Tuqiao Jinzhou road 999, Chengdu, Sichuan, China

[a]d15s001@akita-pu.ac.jp, [b]qiu@akita-pu.ac.jp, [c] e_sakai@akita-pu.ac.jp,

[d]weixiaowei190@yeah.net

Keywords: Multiwalled carbon nanotubes/Polycarbonate, Nanocomposites, Injection speed, Injection temperature, Electrical conductivity

Abstract. Multiwalled carbon nanotubes/Polycarbonate (MWCNTs/PC) nanocomposites were successfully prepared by melting mixing. With the injection speed and temperature changed, different MWCNTs contents MWCNTs/ PC composites were prepared. The electrical conductivity of nanocomposites was compared with different injection speeds and injection temperatures. It was found that the electrical conductivity of the MWCNTs/PC nanocomposites was decreased with MWNTs content increasing, and were both affected by the injection speed and temperature. Besides, at the vicinity of the surface of samples, the resistivity of MWCNTs/PC nanocomposites was the maximum; the closer to the samples inner, the resistivity was smaller and more stabilized. The microstructure and morphology of composites were analyzed by Scanning Electron Microscopy (SEM) techniques, and the MWCNTs' dispersion in PC matrix and the interfacial interaction between MWCNTs and PC were analyzed.

Introduction

Carbon nanotubes (CNTs) have attracted great interest since they were found in 1991 [1]. Because of their unique structure, excellent mechanical, thermodynamic, conductive properties and high aspect ratio features, it has been as a typical one-dimensional material [2, 3]. There exhibiting ballistic transport along the tubes, and sustaining current density as high as 10^9 ～10^{10}A/cm^2 [4]. CNTs, which have outstanding high aspect ratio and electrical property, are potential candidates for nanoelectronic applications [5], and regarded as promising conductive additives for composites, since they can provide electric percolation at lower concentrations than other fillers [6,7]. Considering effective realization of excellent properties of carbon nanotubes (CNTs) in CNTs reinforced polymer composites [8-10], there is still a great challenge in achieving alignment of CNTs in polymer matrix. However, CNTs have inherent large specific surface area [11], higher surface activation energy and are easy to form agglomerates, which lead to be difficultly dispersed evenly in the polymer matrix, therefore it sets off the focus on researching CNTs filling polymer matrix composites. If CNTs disperse evenly in the polymer matrix, it will reinforce the conductivity of composites. So it is a focus of the present study that how can make CNTs disperse evenly in polymer matrix.

In this work, we prepared MWCNTs/PC nanocomposites by the melting mixing. With the injection speed and injection temperature changed, the electrical conductivity of MWCNTs/PC nanocomposites was compared. The effects of the injection speed and temperature changed and the contents of MWCNTs were tested via kinds of characteristics.

Experiment

Materials. Multiwalled carbon nanotubes(MWCNTs), (Shouwa Denko Company in Japan) were used without any purification process, with an average diameter of 10～15nm and a mean length of 3μm, and its density is evaluated as $\rho c = 1.86 g/cm^3$ (Fig.1). Polycarbonate (PC), (Teijin Chemicals Company in Japan), its density is evaluated as $\rho p = 1.2 g/cm^3$.

Preparation of nanocomposites. Because PC is very easy to absorb water in the air, must do a vacuum drying at 100°C for 8 hours. First, the mass fraction of MWCNTs as 5wt% and 10wt% added into PC to mix, then put them into the dry mixing machine to mix uniformly by two times, because MWCNTs was easy to be aggregated. Second, did the melt blending (the mixing temperature is 290°C, the speed is 100rpm), then got the PC/MWNTs composites master batch. Third, through drying treatment at 120°C for 5 hours, did the injection molding, then got the standard specimen of MWCNTs/PC nanocomposites.

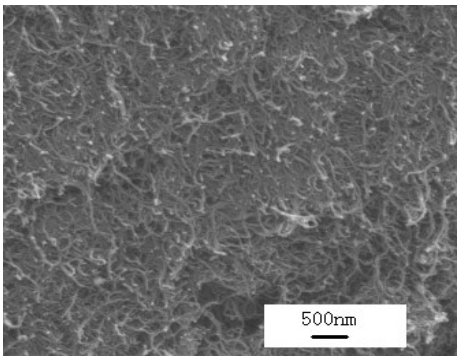

Fig.1 SEM image of MWCNTs

Electrical property test. The electrical property of MWCNTs/PC nanocomposites was tested by Four Probe Resistivity Tester (RTS-2, Guangzhou Four Probe Electronic Technology Co., Ltd.). (Fig.2) The electrical property of MWCNTs/PC nanocomposites from surface to inner was tested by the same machine. The surface of samples was ground in the same direction with the 800# sandpaper, (the grinding distance: about 250mm, load: 2.5kg). (Fig.3)

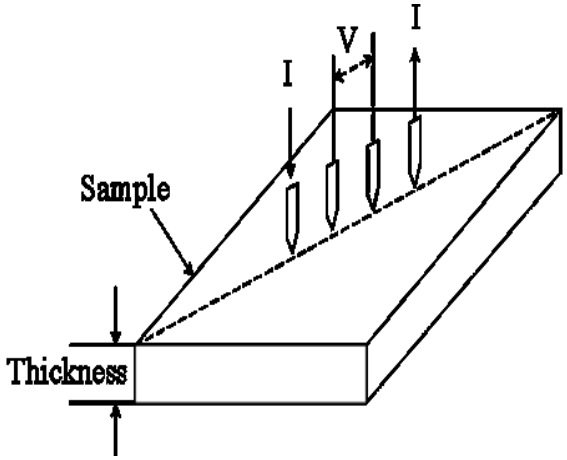

Fig.2 Method of four probe test

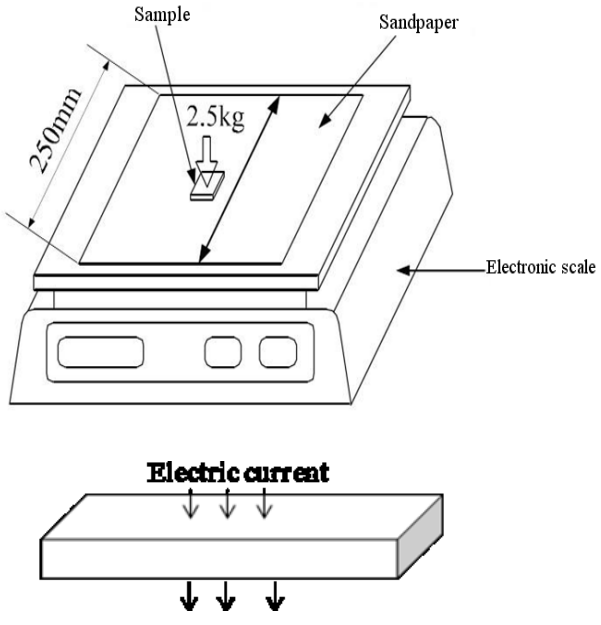

Fig.3 Samples shape for grinding method

Microstructure analysis. The microstructure of MWCNTs/PC nanocomposites was analyzed by Scanning electron microscope (SEM, Hitachi Ltd S-4300). The freshly broken surfaces by tensile test were sputtered with gold and then were observed by SEM under an acceleration voltage of 15KV.

Results and Discussion

In the present work, PC was mixed with MWCNTs by different contents. With the injection conditions changed, the samples were produced for electrical conductivity test. The electrical conductivity of MWCNTs/PC nanocomposites was much higher than that of the pure PC. Fig.4 shows the conductivity characteristics of MWCNTs/PC nanocomposites with different contents of MWCNTs under various injection temperatures. Compared with the test results, the volume resistivity of the composites were decreased with MWCNTs contents increasing. To investigate the influence of the injection conditions on the surface and volume resistivity of composites, the test results of 10wt% MWCNTs nanocomposites were listed in Table 1. Compared with the results at the same injection temperature, the surface and volume resistivity (i.e. SR and VR) of nanocomposites were increased with the injection speed increasing; at the same injection speed, the surface and volume resistivity of composites were decreased with the injection temperature increasing. The influence of injection conditions was very evident.

Table 1 The surface and volume resistance of MWCNTs/PC nanocomposites (MWCNTs: 10wt%)

No.	Injection speed[mm/s]	Injection temperature[^{o}C]	SR[Ω/sq]	VR[Ω·cm^{-1}]
1	10	280	97.1	13.4
2	40	280	193.9	28.0
3	80	280	248.5	33.5
4	10	305	60.4	10.6
5	40	305	99.2	16.1
6	80	305	102.3	16.9
7	10	330	37.7	5.2
8	40	330	64.0	8.3
9	80	330	65.6	8.6

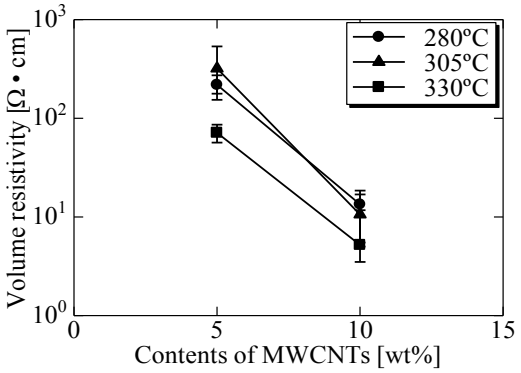

Fig.4 Effect of MWCNTs content on volume resistivity (10mm/s)

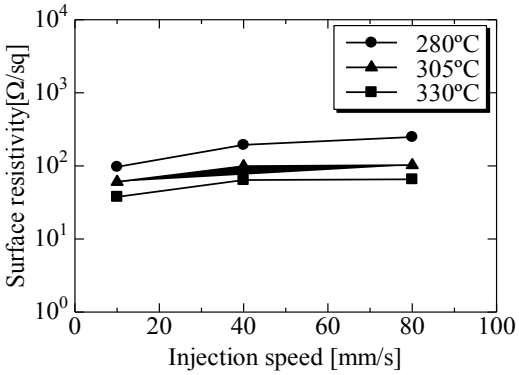

Fig.5 Effect of injection speed on surface resistivity (10wt%MWCNTs)

Fig.5 shows effect of injection speed on surface resistivity of MWCNTs/PC nanocomposites. It is obviously seen that with the injection speed increased the surface resistivity of MWCNTs/PC nanocomposites was increased, with the injection temperature increased the surface resistivity of

MWCNTs/PC nanocomposites was decreased. This might be because of the formation mechanism of the internal microstructure of the samples in the injection molding process. The injection conditions would affect the flow rate and viscosity of the nanocomposites, so as to affect the orientation of MWCNTs in PC matrix, consequently formed different internal microstructure of the nanocomposites. Then the orientation and internal microstructure would affect the probability of the formation of conductive network, and directly affected the conductivity of MWCNTs/PC nanocomposites.

Fig.6 and Fig.7 show the distribution of the surface resistivity of MWCNTs/PC nanocomposites (from surface to inner) with different MWCNTs contents and under different injection temperature, respectively. As exhibited in Fig.6, when the injection temperature was 330°C and injection speed was 10mm/s, with the MWCNTs content increased, the surface resistivity was decreased about one magnitude. When MWCNTs contents was 10wt%, the surface resistivity was about $10^2\Omega$/sq at the most outer surface (i.e. Sanding thickness is zero). It was also evident from Fig.6 and Fig.7 that the surface resistivity of the inner of MWCNTs/PC nanocomposites was lower than that of surface. This was basically caused by the formation mechanism of the internal subtle structure in the injection molding. Under the injection conditions, the surface of sample was high orientation, difficultly formed conductive path, so the resistivity was greater; however, the inner of sample was low orientation, easily formed conductive path, so the resistivity was lower. The closer to the inner of nanocomposites, the surface resistivity was to be stability. This might because that there were more MWCNTs in the inner and the dispersion of MWCNTs was better.

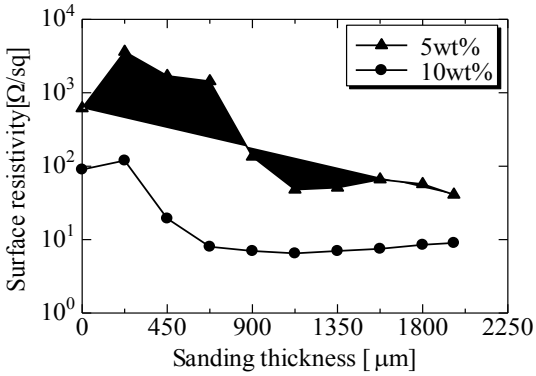

Fig.6 Effect of MWCNTs content on surface resistivity (330°C, 10mm/s)

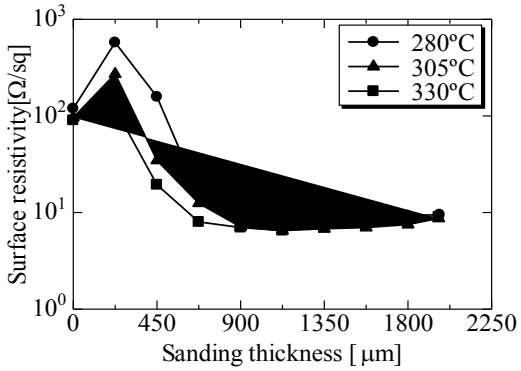

Fig.7 Distribution of surface resistivity from surface to inner (10wt%, 10mm/s)

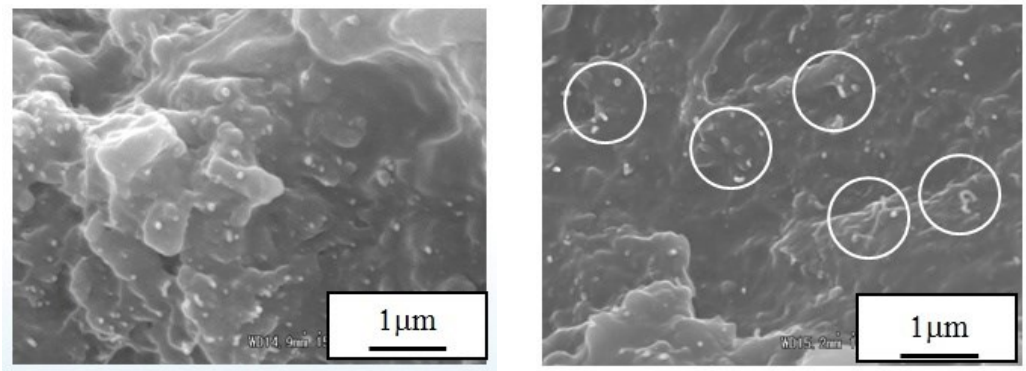

(a) (b)

Fig.8 SEM images of MWCNTs/PC nanocomposites (5wt%). (a) injection temperature:280°C, injection speed:80mm/s, (b) injection temperature:330°C, injection speed:10mm/s

Fig.8 shows the SEM images of MWCNTs/PC nanocomposites. It is obviously seen that when the injection temperature was 280^{o}C and injection speed was 80mm/s, MWCNTs were pulled out to be visible distinctly and dispersed unevenly in the matrix and thus the conductive paths weren't formed, resulting in the lower resistivity of MWCNTs/PC nanocomposites. However, when the injection temperature was 330^{o}C and injection speed was 10mm/s, MWCNTs weren't pulled out and dispersed evenly, playing a key role to form the conductive paths in the matrix, and hence the resistivity of MWCNTs/PC nanocomposites was higher, reached to about $10^{3}\Omega$/sq.

Summary

The MWCNTs/PC nanocomposites were prepared by the melt blending method. The electrical conductivity and SEM analysis showed that both the MWCNTs content and the injection conditions both would affect the electrical conductivity of MWCNTs/PC nanocomposites. The MWCNTs content was the main factor which would affect the resistivity. But when the MWCNTs contents reached a certain value, carbon nanotubes had little effect on the conductivity of the MWCNTs/PC nanocomposites. Besides, the injection conditions were also very important to affect the conductivity of the nanocomposites. The electrical conductivity of the inner of MWCNTs/PC nanocomposites was greater than that of surface. Especially, at a higher injection temperature and a lower injection speed, the electrical conductivity of MWCNTs/PC nanocomposites was better than other injection conditions, increased about 6 times.

Reference

[1] Iijima S. Helical microtubules of graphitic carbon [J]. Nature,1991,354,56-58.

[2] Moniruzzaman M, Winey KI. Polymer nanocomposites containing carbon nanotubes. Macromolecules 2006; 39: 5194-205.

[3] D. Tasis, N. Tagmatarchis, A. Bianco, and M. Prato, Chemistry of carbon nanotubes, Chem. Rev. 2006,106:1105–1136.

[4] Y.T. Peng, Y.Z. Hu and W.B. Lu. Journal of Nanomaterials, 2011, 2011:1-5.

[5] L.A. Nagahara, I. Amlani, J. Lewenstein, and R. K. Tsui. Applied Physics Letters, 2002, 80 (20):3826–3829.

[6] Y.e. Mamunya, A. Boudenne, N. Lebovka, L. Ibos, Y. Candau, M. Lisunova, Compos. Sci. Technol. 68 (2008) 1981.

[7] Jie-Feng Gao, Ding-Xiang Yan, Bo Yuan, et al. Large-scale fabrication and electrical properties of an anisotropic conductive polymer composite utilizing preferable location of carbon nanotubes in a polymer blend. Compos. Sci. Technol.70 (2010) 1973-1979.

[8] McNally T, Pvtschke P, Halley P, Murphy M, Martin D, Bell SEJ, et al. Polymer 2006; 45:8222.

[9] Kong H, Gao C, Yan D. Controlled functionalization of multiwalled carbon nanotubes by in situ atom transfer radical polymerization. J Am Chem Soc 2004; 126(2):412–3.

[10] Sha-Ni Li, Bo Li, Zhong-Ming Li, et.al. Morphological manipulation of carbon nanotube / polycarbonate/polyethylene composites by dynamic injection packing molding. Polymer 47(2006) 4497-4500.

[11] JC Kearns,R L Shambaugh.J.Appl.Polym.Sci,2002,86(8):2079-2084.

Advanced Materials Research Vol. 983 (2014) pp 110-115

doi:10.4028/www.scientific.net/AMR.983.110

Influence of casting method and heat treatment for corrosion resistance of magnesium alloy AZ91D

DOBKOWSKA Anna[1,a], ADAMCZYK – CIESLAK Bogusława[1,b], ZDUNEK Joanna[1,c], MIZERA Jaroslaw[1,d], KURZYDŁOWSKI Krzysztof Jan[1,e]

[1] Warsaw Univeristy of Technology, Faculty of Materials Science and Engineering, Woloska 141, 02-507 Warsaw, Poland

[a] anna.dobkowska@inmat.pw.edu.pl, [b] badamczyk@inmat.pw.edu.pl, [c] jzdunek@inmat.pw.edu.pl, [d] jmizera@inmat.pw.edu.pl, [e] kjk@inmat.pw.edu.pl

Keywords: magnesium alloys, corrosion resistance, permanent mould casting, pressure die casting, heat treatment

Abstract. In this paper the effect of production method and heat treatment of magnesium alloys to their corrosion resistance is presented. The study was carried out on the AZ91D alloy obtained by permanent mould casting, pressure die casting and pressure die casting with the subsequent heat treatment. Studies of the microstructure were carried out using a light microscope. The corrosion resistance was examined using the Potentiodynamic Test. The surface observations after corrosion tests were carried out using the Scanning Electron Microscope (SEM). It was stated that the best corrosion resistance is typical for AZ91D alloy produced by pressure die casting method with heat treatment. The alloy after permanent mould casting has got the worst corrosive properties.

Introduction

Magnesium alloys, because of the low density and good mechanical properties, are the most popular materials in modern industry. This group of light metals is common in automotive, electrical, aircraft and armaments industry. New technologies of making use of magnesium alloys follow from progress of winning of metals and from possibilities in improving their microstructure [1-2]. The strength to density ratio of magnesium alloys exceeds the others common materials. This is important issue in motorization where the reducing weight is necessary. The magnesium alloys, in spite of low density, are characteristic because of the vibration damping capability and good weldability [3-5].

There are two groups of magnesium alloys: to wrought and cast alloys. The cast alloys vary in properties with the method of processing which they are cast by. The MgAl9Zn1 is the most popular cast alloy (AZ91D) [6]. This material is characterized by good casting properties, attractive mechanical and physical properties. It should be noted that a considerable reduction of the use of this materials is its corrosion susceptibility in many environments [7-8].

The aim of this work was to characterize the corrosion resistance of AZ91D alloys according to the method of their manufacture.

Material and research methodology

The material used in the investigations was an AZ91D alloy prepared by different methods: permanent mould casting, pressure die – casting, pressure die – casting and heat treated in 416° C by 16 hours [9]. The chemical composition of AZ91D alloy is given in Table 1 (according to PN-EN 1753:2002 norm) [10].

Table 1 Chemical composition of the AZ91D alloy (in wt%)

Mg	Al	Zn	Mn	Si	Fe	Cu	Ni	other
balance	8,3- 9,7	0,35 - 1,0	min. 0,1	max 0,1	max 0,005	max 0,03	max 0,002	max 0,01

Metallographic specimens were etched by picrinian acid etching substrate. The metallographic observations were carried out using the optical microscope.). Corrosion resistance was investigated by Potentiodynamic Polarization Test followed by a SEM surface analysis. The electrochemical tests were conducted in a 0,01 M Na_2SO_4 with 0,01% chloride ions at room temperature. The Autolab potentiostat were used equipped with three electrodes: the platinum was a counter electrode (CE), the saturated calomel electrode was a reference electrode (RE) and the measured sample was a working electrode (WE). All the samples were left 3 hours in the solution in open circuit potential. The potentiodynamic tests were conducted with a scan rate 0.02 mV/s.

Results and discussion

Microstructure

Fig. 1 shows the microstructure of AZ91D alloy produced by permanent mould casting. It is a typical dendritic structure consisting of α – Mg solid solution with numerous areas of the secondary phase separation β. The entire volume of the analyzed material revealed pores formed during the permanent mould casting. The microstructure of AZ91D pressure die – cast alloy is presented at Fig. 2. The pictures show the characteristic dendritic structure of cast materials. The microstructure also includes pores. The matrix is a α – Mg solid solution. The microstructure of this alloy includes also a numerous of β phase precipitations ($Mg_{17}Al_{12}$) and areas of the mixture of phases α + β located at the grain boundaries [11-12]. Fig. 3 shows the microstructure of AZ91D pressure die – cast alloy subjected to supersaturation process. As a result of this process a granular structure formed. The matrix, as in the previous two cases, is a solution of α – Mg with the β – phase at the grain boundaries [13-15].

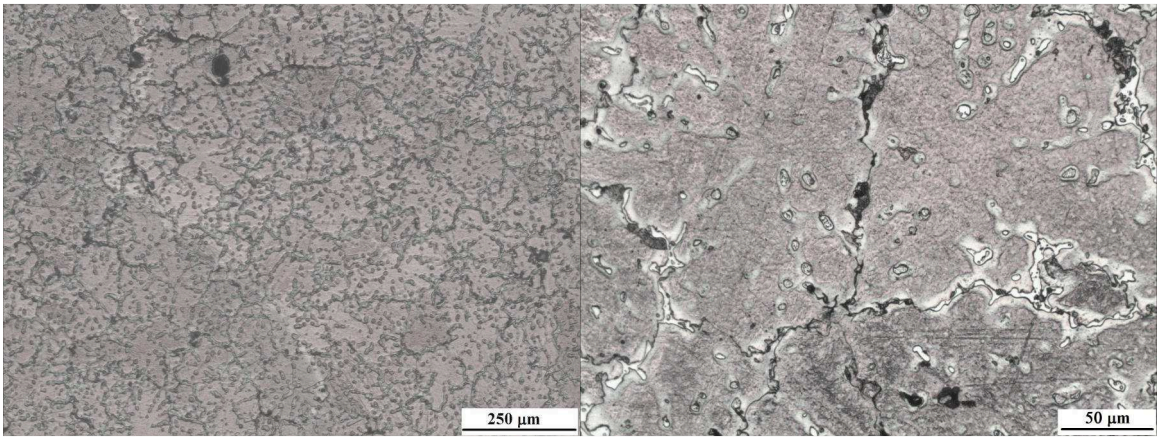

Fig. 1. SEM photographs of microstructure of AZ91D obtained by permanent mould casting

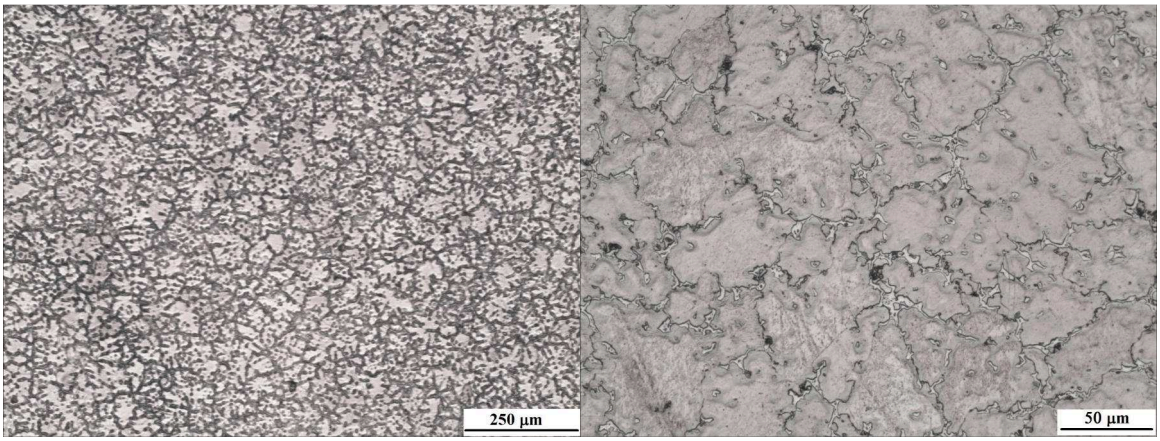

Fig. 2. SEM photographs of microstructure of AZ91D obtained by pressure die casting.

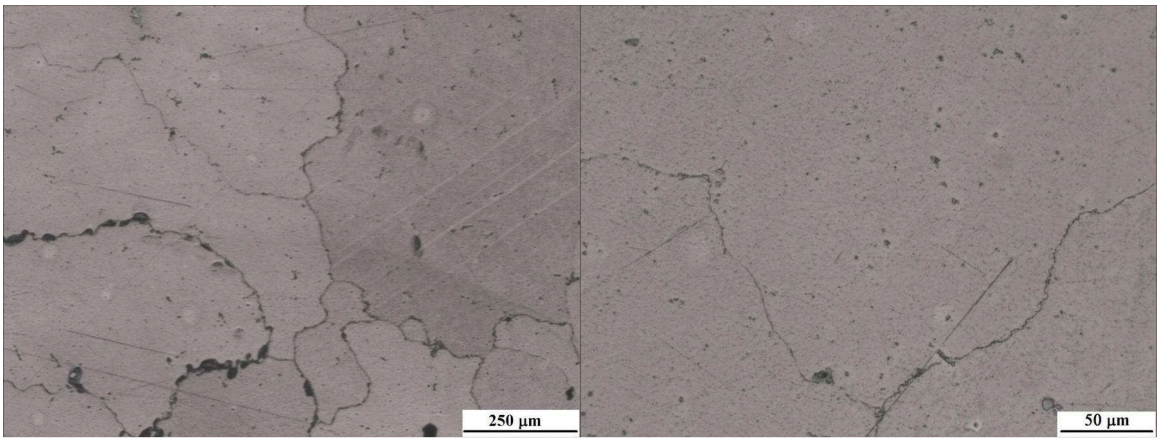

Fig. 2. SEM photographs of microstructure of AZ91D obtained by pressure die casting and heat treated

Corrosion resistance

Fig. 3 shows the results from Electrochemical Potentiodynamic Test. The shape of curves obtained during the test indicates that methods of production and heat treatment have got meaningful influence on course of corrosion processes.

The potentiodynamic anodic curves show that analyzed materials is in passive state and undergoes the pitting corrosion. The growths of current density in passive state and small differences between corrosion and breakthrough potentials (Table 2) speak volumes for insignificant stabilization of passive layer. This effect is well observable in the case of AZ91D obtained by die casting, where the received values of potentials (E_{cor} and E_{np}) are similar. This result is caused by considerable account of places in the microstructure where the pits were initiated (f.e. pores indicated after permanent mould casting and pressure die casting processes). The heat treatment influences for corrosion resistance of analyzed materials, also. The alloy produced by pressure die casting and heat treated characterizes better corrosion resistance than alloy without heat treatment. It is confirmed by higher value of corrosion potential ((E_{kor} = -1490 mV) and almost twice lower corrosion current density (i_{kor} = 5,4 µA/cm^2) in comparison with AZ91D without heat treatment where the E_{kor}= -1510 mV and i_{kor} = 12,5 µA/cm^2.

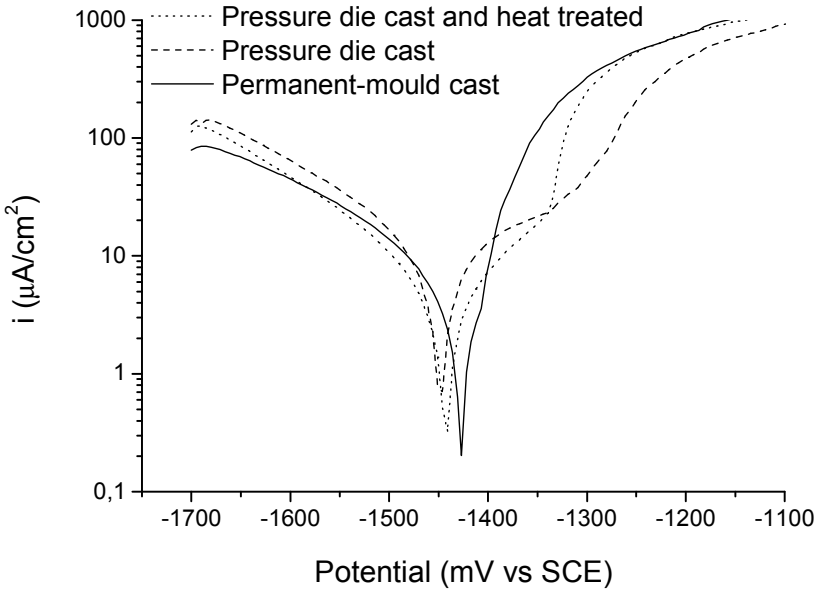

Fig. 3. Potentiodynamic anodic polarization curves (0,02 mV/s) of AZ91D

Table 2 Polarization curve parameteres of AZ91D

AZ91D	E_{cor} [mV]	E_{np}[mV]	I_{cor} [μA/cm^2]
Pressure die cast	-1510	-1380	12.5
Permanent-mould cast	-1430	-1400	3.0
Pressure die cast and heat treated	-1490	-1380	5.4

Surface observations

The corrosion morphology of examined samples is shown at Fig. 4. As the G. Song et al. wrote the corrosion mechanism of AZ91D alloy consists of few aspects. The strong influence on the corrosion properties has got the composition of alloy and grain size (formation of eutectic α and β strongly determined the micro-galvanic corrosion processes, which were explained in [[14]]). The porosity plays the meaningful role in corrosion processes of AZ91D, also. It is well known that pores are the active points for corrosion reaction. Pits which were observed at AZ91D after pressure die casting formed just in the places where the eutectic phase were observed. The surface observations after potentiodynamic tests showed that in the case of AZ91D produced by permanent-mould casting the pits were formed uniformly at whole analyzed surface. These pits were deeper as in previous case. It is caused by more porous in the microstructure which was the privileged places to initiate the pits.

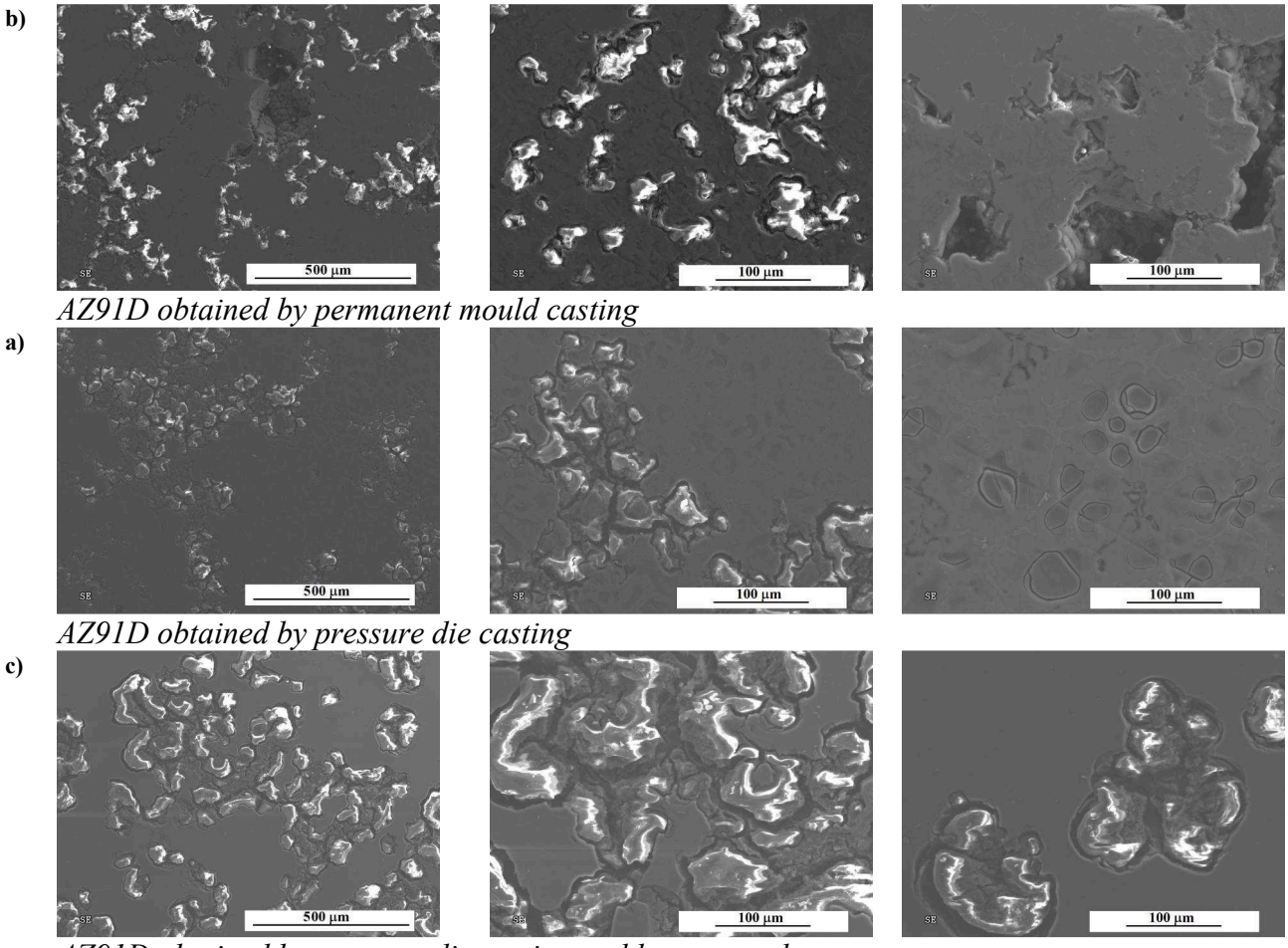

Fig. 4. Surface observations of AZ91D after corrosion tests a) permanent-mould cast alloy b) pressure die cast alloy, c) pressure die cast and heat treated

The AZ91D after solutioning is characterized by less account of pits. It could be explain by the mechanism of solutioning, which caused the reducing of pores in the microstructure of AZ91D obtained by pressure die casting.

The previous studies conducted on the AZ91D alloy produced by these three methods indicate that the casting method and heat treatment of this investigated material has a strong effect on the mechanical properties and corrosion resistance by changing the porosity and microstructure of the alloy during the manufacturing [16-17].

References

[1] Jufu Jiang, Ying Wang, Gang Chen, Jun Liu, Yuanfa Li, Shoujing Luo, Comparison of mechanical properties and microstructure of motorcycle wheels formed by die casting and double control forming, Materials & Design, Vol. 40, 2012, pp. 541 - 549

[2] K.N. Braszczyńska – Malik, Discontinuous and continuous precipitation in magnesium – aluminium type alloys, J. Alloys Compd., 477 (2009), pp. 870–876

[3] T. Blawer, N. Hort, K.U.Kainer, Automotive applications of magnesium and its alloys, Center for Magnesium Technology, Institute for Materials Research, 2004

[4] Kainer KU, Kaiuser F., Eds. Magnesium alloys and technology, Weinheim: Wiley – VCH GmbH, 2003

[5] Mordike B.L., Kainer KU, Eds. Magnesium alloys and their applications, Frankfurt: Werkstoff-Informationsgesellschaft 1998

[6] Mao-liang, HU, Ze-sheng JI, Xiao-yu CHEN, Effect of extrusion ratio on microstructure and mechanical properties of AZ91D magnesium alloy recycled from scraps by hot extrusion, Transaction of Nonferrous Metals Society of China, Vol. 20, Issue 6, 2010, pp. 987 - 991

[7] Kelvii Wei Guo, A review of Magnesium Alloys Corrosion and its Protection, Recent Patents on Corrosion Science, 2010

[8] Zeng Rong-chang, Zhang Jim, Guang Wei – jiu, Dietzel W., Kainer K.U., Blawert C., KE Wei, Review of studies on corrosion of magnesium, Transactions of Nonferrous Metals Society, China 16(2006), s. 763-771

[9] Reguła T., Bronicki M., Lech-Grega M., Czekaj E., Ocena możliwości kształtowania właściwości mechanicznych odlewniczego stopu magnezu AZ91 przez zastosowanie odpowiedniej obróbki cieplnej, Prace Instytutu Odlewnictwa tom XLVIII, zeszyt 1 (2008), s. 39-45 – in polish

[10] PN – EN 1753:2002 Magnez i stopy magnezu – Gąski i odlewy ze stopów magnezu - in polish

[11] Cheng Yuan – Sheng, Chen Qiang, Huang Zhe-qun, Huang Shu – hai, Microstructure evolution and thixoextrusion of AZ91D magnesium alloy produced by SSTT, Trans. Nonferrous Met. Soc. China 20 (2010), 739-743

[12] A. Oniszczuk, S. Rzadkosz, Wpływ parametrów odlewania ciśnieniowego stopu AZ91D na jego mikrostrukturę, Akademia Górniczo – Hutnicza, 2006 – in polish

[13] R. Ambat, Naing Naing Aung, W. Zhou, Evaluation of microstructural effects on corrosion behavior of AZ91D mahnesium alloy, Corrosion Science 42 (2000) 1433-1455

[14] G. Song, A. Atrens, M. Dargusch, Influence of microstructure on the corrosion of diecast AZ91D, Corrosion Science 41 (1999) 249 – 273

[15] Wang Y., Liu G., Fan Z., Microstructural evolution of rheo – diecast AZ91D magnesium alloy during heat treatment, Acta Materialia 54 (2006), 689 – 699

[16] S. Tzamtzis, H. Zhang, Hari Babu, Z.Fan, Microstructural refinement of AZ91D die-cast alloy by intensive shearing – article in press

[17] J. Adamiec, S. Roskosz, T. Garncarczyk, Influence of the macro – and microstructure of AZ91D alloy after thermal treatment on its mechanical properties, Inżynieria Materiałowa, 3-4/2007, 120-123

Advanced Materials Research Vol. 983 (2014) pp 116-120

doi:10.4028/www.scientific.net/AMR.983.116

Low Temperature Oxidation Behaviors of CNTs/$MoSi_2$ Composites

Houan Zhang [1,a,*],Hejian Wu[1,b], Jia Lin[1,c] ,Siyong Gu[1,d],Lei Yu[2,e]

[1]School of Materials Science and Engineering, Xiamen University of Technology, Xiamen 361024, China

[2] Quality Management Center of Luoyang Copper Co., Ltd., Luoyang 471039, Henan, PR China

[a]ha_zhang@163.com,[b]wu_hejian@163.com,[c]jiajia10182003@163.com,[d]gu-siyong@163.com, [e]leiyu207@163.com

Keywords: $MoSi_2$ matrix composite; Oxidation; Carbon nanotubes; Low temperature

Abstract

Molybdenum disilicide ($MoSi_2$) matrix composites with various contents of carbon nanotubes (CNTs) were fabricated by sintering in vacuum at 1550 °C for 1 h. The oxidation behaviors of CNTs/$MoSi_2$ composites at 400 °C and 500 °C for 200 h in air were studied. Results showed that the weight loss of CNTs/$MoSi_2$ composites increased with the increase of CNTs content. "Pest" phenomenon happened at 400 °C but not at 500 °C. Phase identification and microstructure of the samples were analyzed by X-ray diffraction (XRD) and scanning electron microscopy (SEM). It was found that many MoO_3 whiskers and microcracks only occurred on the surface of CNTs/$MoSi_2$ composites when oxidized at 400 °C in air, which leaded to the catastrophic disintegration of CNTs/$MoSi_2$ composites.

1 Introduction

$MoSi_2$ is a promising high-temperature material with low density (6.23 g/cm^3), high melting point (2030 °C), and good oxidation resistance at high temperatures of about 1900 °C. However, it is susceptible to a "pest" reaction in the low temperature range of 400 °C to 600 °C, which would cause catastrophic disintegration by a combination of oxidation and fracture [1]. Many researchers have reported the investigation about the "pest" and found that "pest" is caused by simultaneous oxidation of Mo and Si. However, the mechanism of "pest" has not been satisfactorily clarified yet [2-4]. This is because there are many factors in the accelerated oxidation, such as pores, cracks, composition, oxidation temperature and atmosphere [5].

Many researchers [6-9] have done a lot of studies about the oxidation behaviors of $MoSi_2$ matrix composites at low temperature. As known, the addition or the third element has significant influence not only on the oxidation mechanism but also on the densification and pre-existing defects in the process of preparation. Our previous work [10] has shown that the addition of carbon nanotubes (CNTs) to the $MoSi_2$ matrix results in the improvement in both hardness and fracture toughness. In this paper, the main purpose is to investigate the effect of CNTs content on the oxidation behaviors of $MoSi_2$ matrix composites at 400 °C and 500 °C in air.

2 Experimental

Commercially available Mo powder (2–4 μm, purity > 99.9%), Si powder (43 μm, purity >99.9%) and multi-walled CNTs were used as the elemental materials in this study. According to the Ref. [10], CNTs/$MoSi_2$ composites with contents of 1.5 %, 3.0 %, 4.5 %, 6.0 % and 8.0 % in volume were prepared by sintering in vacuum at 1550 °C for 1 h. For comparison, pure $MoSi_2$ sample was also made using the same technique.

Prior to oxidation, the samples were polished and ultrasonically cleaned. The isothermal static oxidation tests were conducted in a box furnace at the temperature of at 400°C and 500°C for 200 h

in air. Samples were took out in order to measure weight (to an accuracy of 0.1 mg) change at different intermittent times. A minimum number of five specimens were tested for each experimental condition.

Phase identification and microstructure of the samples were analyzed by X'pert PRO X-ray diffraction (XRD) and S-4800 scanning electron microscopy (SEM), respectively.

3 Results and discussion

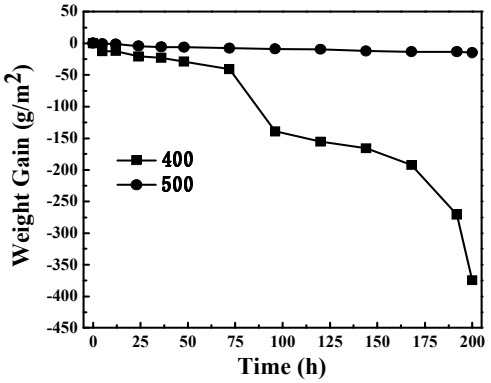

Fig.1 The weight change of 1.5 %CNTs/$MoSi_2$ at 400°C and 500°C in air as a function of times

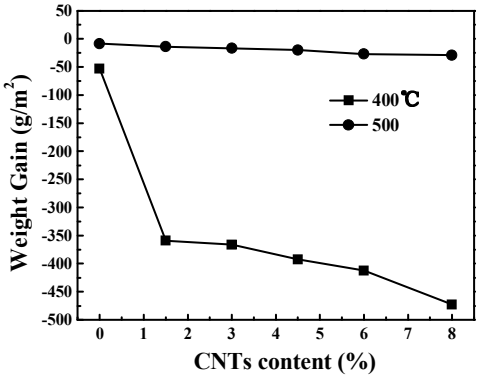

Fig.2 The weight change of CNTs/$MoSi_2$ composites at 400 °C and 500 °C as a function of CNTs contents

The weight change of $MoSi_2$ matrix composites with 1.5% CNTs during the long exposure in air at 400 °C and 500 °C is presented in Fig.1. It can be seen that the weight gain of CNTs/$MoSi_2$ composite oxidized at 400 °C and 500 °C decreases as the oxidation time increases, meanwhile, the weight loss of the composite at 400 °C is much larger than that at 500 °C. And "pest" happens at 400 °C. Fig.2 shows the weight gain of CNTs/$MoSi_2$ composites oxidized at 400 °C and 500 °C for 200 h as a function of CNTs contents. It is found that the weight gain of CNTs/$MoSi_2$ composites decreases as the increase of the CNTs content. This means the low temperature oxidation resistance of $MoSi_2$ matrix composites oxidized at 400 °C and 500 °C in air is reduced when the addition of CNTs increases. Especially, when the content of CNTs increases, the weight loss increases at 400 °C, which indicates "pest" phenomenon occurs in all of CNTs/composites when oxidized at 400 °C.

The XRD spectra of CNTs/$MoSi_2$ composites oxidized at 400 °C and 500 °C exposure for 200 h are shown in Fig.3 and Fig.4. As presented in Fig.3, new phases of MoO_3 and Mo_3Si are detected. And the diffraction peak intensity of MoO_3 is enhanced as the CNTs content increases. This means that the "pest" of CNTs/$MoSi_2$ composites becomes easier as the addition of CNTs increases. This is agreed with the results as shown in Fig.2. It is also found that the diffraction peak intensity of $MoSi_2$ phase decreases with the increasing CNTs content. However when the composites are oxidized at the temperature of 500°C, phases of Mo_5Si_3 and SiO_2 are detected in Fig.4, the diffraction peak of SiC still existed when the addition of CNTs are up to 8.0 % and the residual $MoSi_2$ is the main phase. Therefore, these possible reactions of low temperature oxidation of $MoSi_2$ matrix composites can be listed as follows [11]:

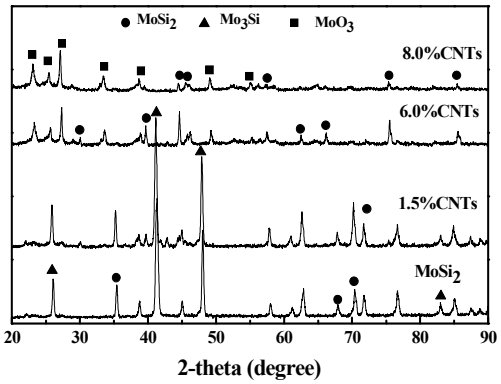

Fig.3 XRD patterns of CNTs/$MoSi_2$ composites oxidized in air at 400 °C for 200 h

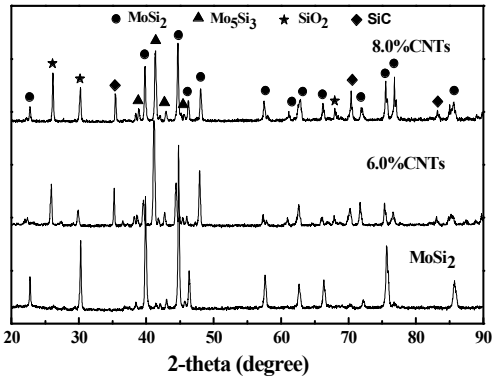

Fig.4 XRD patterns of CNTs/$MoSi_2$ composites oxidized in air at 500°C for 200 h

$2MoSi_2(s)+7O_2(g)\rightarrow 2MoO_3(g)+4SiO_2(s)$ (1)

$5MoSi_2(s)+7O_2(g)\rightarrow Mo_5Si_3(s)+7SiO_2(s)$ (2)

$2Mo_5Si_3(s)+21O_2(g)\rightarrow 10MoO_3(g)+6SiO_2(s)$ (3)

$3Mo_5Si_3(s)+30O_2(g)\rightarrow 5Mo_3Si(s)+30SiO_2(s)$ (4)

$2Mo_3Si(s)+11O_2(g)\rightarrow 6MoO_3(g)+2SiO_2(s)$ (5)

Fig.5 shows micrographs of surface of CNTS/$MoSi_2$ composites after oxidized at 400 °C for 200 h in air. It can be seen that MoO_3 whiskers and microcracks are found on the surface of $MoSi_2$ matrix composites with 1.5%, 6.0% and 8.0% CNTs. The formation of the volatile MoO_3 phase destroys the compactness of SiO_2 film on the surface, and causes the formation of microcracks because of volume expansion resulting in the internal stresses. This accelerates oxidation process of CNTs/$MoSi_2$ composites and leads to the "pest" phenomenon [3, 4]. Protective silica is broken and SiC in the CNTs/$MoSi_2$ composite [10] is oxidized.According to the Ref. [12], the oxidation reaction of SiC to SiO_2 is speculated to be as follows:

$SiC(s) + 1.5\ O_2(g) \rightarrow SiO_2(s) + CO(g)$ (6)

$SiC(s) + 2\ O_2(g) \rightarrow SiO_2(s) + CO_2(g)$ (7)

And this experience with applications to the waste treatment of toxic substances, the dominant by-product gas at 400 °C is CO [13]. Thus, the oxidation reaction of SiC at 400 °C is speculated to be reaction (6). Therefore SiC phase is not detected in Fig.3. The gaseous product, CO, offers channels for the more oxygen soaking into the composites. The content of SiC phase in CNTs/$MoSi_2$ composites increases with the increases of CNTs contents [10], which means that the higher content of CNTs will cause more serious oxidation at 400 °C in air and result in higher weight loss in Fig.2. From Fig.5 (d), it can be seen that there are no MoO_3 whiskers and microcracks on the surface of $MoSi_2$ matix composite with 8.0% CNTs. This is agreed with the results as shown in Fig.4. The oxidation reaction of CNTs/$MoSi_2$ composites at 500 °C is speculated to be reaction (2). The formation of SiO_2 layer on the surface during oxidation process provides an effective protection, which reduces obviously the weight loss and $MoSi_2$ and SiC phases still exist in CNTs/$MoSi_2$ composites. According to the Ref. [14], the reason that "pest" occurs when CNTs/$MoSi_2$ composites oxidized at 400 °C but not at 500 °C in air, may be attributed to the oxidation reaction constant reaching the maximum at 400°C.

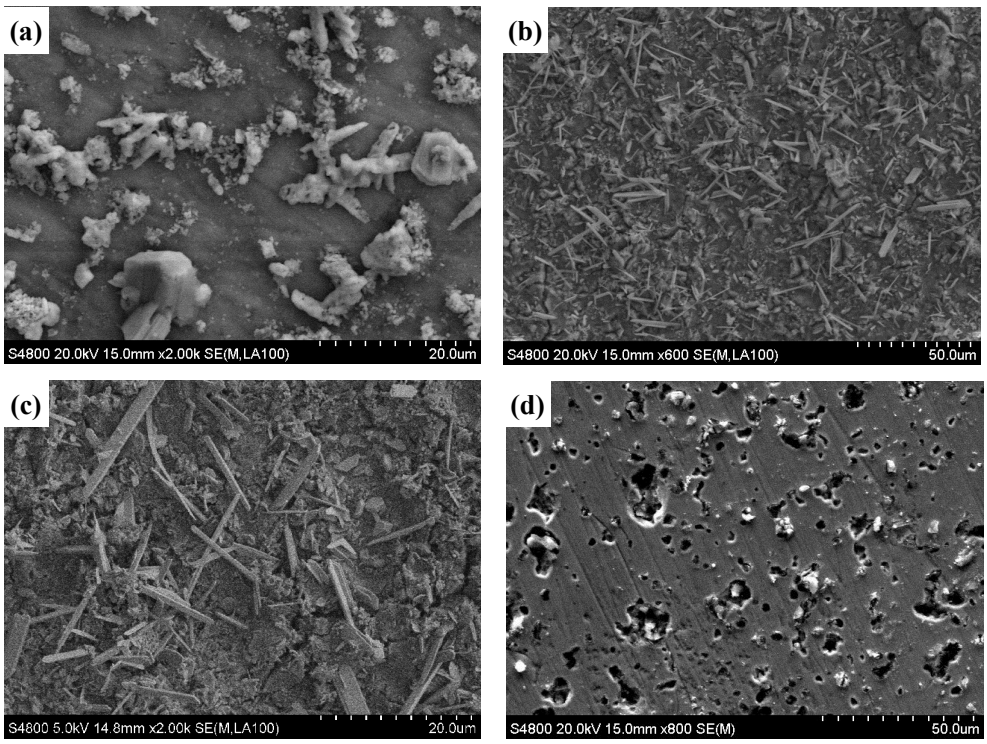

Fig.5 SEM micrographs of surface of CNTs/$MoSi_2$ composites after oxidized in air at 400 °Cand 500 °C for 200 h in air. (a) 1.5 % CNTs/$MoSi_2$, 400 °C; (b) 6.0 % CNTs/$MoSi_2$, 400 °C; (c) 8.0 % CNTs/$MoSi_2$, 400 °C; (d) 8.0 % CNTs/$MoSi_2$, 500 °C

4 Conclusions

Oxidation behaviors of $MoSi_2$ matrix composites with different CNTs contents oxidized at 400 °C and 500 °C for 200 h in air were investigated. For CNTs/$MoSi_2$ composites, "pest" phenomenon happened at 400 °C but not at 500 °C. Based on XRD and SEM results, it was found that many MoO_3 whiskers and microcracks only occurred on the surface of CNTs/$MoSi_2$ composites when oxidized at 400 °C. Whether oxidized at 400 °C or 500 °C, the weight loss of CNTs/$MoSi_2$ composites increased with the increase of CNTs content.

Acknowledgments

This work was financially supported by the National Natural Science Foundation of China (No. 51071133 and 51371155), the Natural Science Foundation of Fujian Provincial (No. 2010J01313), and the Opening Project of State Key Laboratory of High Performance Ceramics and Superfine Microstructure (No. SKL201113SIC).

* Corresponding author.School of Materials Science and Engineering, Xiamen University of Technology, Xiamen 361024, Fujian, P.R.China. Tel: +86 592 6291045, Fax: +86 592 6291045

E-mail address: ha_zhang@163.com (H. Zhang)

References

[1] C.G. McKamey, P.F. Tortorelli, J.H. DeVan, and C.A. Carmichael, A study of pest oxidation in polycrystalline $MoSi_2$, J. Mater. Res. 7(1992) 2747–2755.

[2] A.A. Sharift, A. Misra, J. J. Petrovic, A. Misra, T.E. Mitchell, Alloying of $MoSi_2$ for improved mechanical properties, Intermetallics. 9(2001) 869–873.

[3] P.J. Meschter, Low temperature oxidation of molybdenum disilicide, Metallurgical Transaction. 23(1991) 1763–1722.

[4] T.C. Chou, T.G. Nieh, Kinetics of $MoSi_2$ pest during low-temperature oxidation, J. Mater. Res. 8(1993) 1605–1610.

[5] K. Kurokawa, H. Houzumi, I. Saeki, H. Takahashi, Low temperature oxidation of fully dense and porous $MoSi_2$, Materials Science and Engineering. 261(1999) 292–299.

[6] K. Ramasesha, K. Shobu, Oxidation of $MoSi_2$ and $MoSi_2$-based materials, Bull. Mater. Sci. 22(1999) 769–773.

[7] P.Z. Feng, X.H. Qu, I.S. Humail, X.L. Du, Low-temperature oxidation behavior of $MoSi_2$ powder, J. Univ. Sci. Techno. 14(2007) 558–561.

[8] D.B. Lee, Oxidation features of SiOC/$MoSi_2$ composite at low temperatures, METALS AND MATERIALS International. 10(2004) 413–147.

[9] H.M. Hong, G.Q. Liu, L.R. Xiao, D.Q. Yi, L. Zeng, Low temperature oxidation behavior of $MoSi_2$ composites strengthened and toughened by Si_3N_4 particles and SiC whiskers, Journal of Inorganic Materials. 24(2009) 929–933.

[10] H.A. Zhang, H.J. Wu, S.Y. Gu, Preparation and properties of $MoSi_2$ based composites reinforced by carbon nanotubes, Ceramics International.39(2013) 7401–7405.

[11] Y.Q. Liu, G. Shao, P. Tsakiropoulos, On the oxidation behaviour of MoSi2, Intermetallics, 2001, 9:125-136.

[12]T. Futatsuki, T. Oe, H. Aoki, N. Komatsu, C. Kimura, T. Sugino, Low-temperature oxidation of SiC surfaces by supercritical water oxidation, Applied Surface Science. 256(2010) 6512–6517.

[13] S. Kawasaki, T. Oe, N. Anjoh, T. Nakamori, A. Suzuki, K. Arai, Practical Supercritical Water Reactor for Destruction of High Concentration Polychlorinated Biphenyls (PCB) and Dioxin Waste Streams, Process Safety and Environmental Protection. 84(2006) 317-324.

[14] H.A. Zhang, S.Y. Gu, On the oxidation behaviors of MoSi2 at 673– 873 K, Advanced Materials Research. 284–286(2011) 1630–1634.

Advanced Materials Research Vol. 983 (2014) pp 121-126
© (2014) Trans Tech Publications, Switzerland
doi:10.4028/www.scientific.net/AMR.983.121

Microsegregation behavior of single crystal superalloy

Yu Zhuhuan*, [a], Qiang Junfeng[b],

Material Science and Engineering Department, Xi'an University of Science and Technology, Xi'an 710054, PR China

[a] yzh0709qyy@163.com

Key words: Carbon, Electron probe microanalysis (EPMA), Segregation behavior

Abstract. The major advancements in some mechanical properties of single crystal superalloys can be attributed to the carbon addition. The present study investigated the effect of carbon addition levels on the microsegregation behavior of single crystal superalloys. Quantitatative partitioning results indicated that typical single crystal superalloy segregation behavior for some elements such as W, Ni, Co, are all towards the dendrite core regions, while for elements of Al, Mo, Ta, Ti, Cr, partition towards the interdendrite regions. For all the alloys studied, the baseline alloy showed the most severe segregation degree, while the no carbon alloy the slightest. Furthermore, the segregation behavior of Ti and Ta were affected by the carbon additions, and that of W was greatly affected by the carbon levels.

Introduction

The origins of nickel-based superalloys can be traced back to the need for structural materials with high temperature stability and strength and ultimately to the development of gas turbine engines. The compositions of nickel based superalloys have evolved substantially due to constant need for higher temperature capabilities, in which designing goals for newer and higher performance engines need to be met[1-3]. Recent studies have shown that carbon additions is useful for optimizing solidification microstructure for many of single crystal superalloys, [4-6], but no clear connections have been built on the effect of carbon addition on the microsegregation behaviors. The goal of this study is to try to understand the role of carbon in the microsegregation behavior of single crystal superalloys.

A segregation coefficient, k′, which is usually defined as the ratio of the concentration of the element in the dendrite core to the concentration of the element in the interdendritic region, or $k' = \frac{x_{i,Dendrite}}{x_{i,Interdendritic}}$, where x_i is the concentration of each specific element in wt% [7,8]. k′ values of less than 1 indicate the element solute segregate to the interdendritic region. While k′ values of greater than 1 indicate the element solute are enrichment in the dendrite core.

Refractory elements have also been shown to affect the segregation of superalloy [9-12], in particular, numerous studies have shown rhenium additions to be useful for optimizing thermal-mechanical properties of superalloys [13-15]. However, the effect of carbon addition on the microsegregation behavior has not yet been clearly and systematic reported. Since the degree of segregation is a function of composition, it is necessary to understand the effect of carbon additions on the segregation behavior of the elements. A better understanding of the effects of the carbon additions on the segregation of all of the elements is helpful to process of currents alloys and design new alloys. Therefore, the main objective of this study is to investigate the different carbon additions on the chemical segregation. A short explanation of the composition and casting process is

presented. The main characterization methods used to measure the severity of microsegregation are presented; specifically, the EPMA quantitative analysis.

Materials and Experimental Procedure

A first generation Ni-based alloy AM3 was selected as a baseline material, and the carbon level of the baseline alloy was 0.006 %. Various carbon modifications were made to the base alloy composition, and totally five alloys (Table 1) were presented for further studying the effects of alloying additions on the segregation behaviors.

Table 1 Nominal compositions of the test alloys (wt.%)

Sample\Element	C(act)	C (aim)	Cr	Co	Mo	W	Al	Ti	Ta	Ni
1	0.001	0.00	7.87	5.50	2.31	5.10	6.06	2.12	3.55	Balance
2	0.006	0.006	7.82	5.34	2.25	4.88	6.02	1.94	3.49	Balance
3	0.045	0.05	7.82	5.34	2.25	4.88	6.02	1.94	3.49	Balance
4	0.085	0.10	7.85	5.47	2.30	5.03	6.00	2.09	3.56	Balance
5	0.150	0.15	7.85	5.47	2.30	5.03	6.00	2.09	3.56	Balance

Single crystal samples were processed using seed crystal with <001> orientation and high gradient processing techniques in a Bridgeman-type furnace. The thermal gradient during solidification was estimated to be about 300-400K/cm and withdraw rate 50 um/s was used. The orientation of each single crystal sample with a misorientation of greater than 7° , was considered defective and was not utilized in this study. In addition, any samples with defects, such as high angle boundaries (HAB), low angle boundaries (LAB), sliver, freckles and multi-grains were also considered defective and not used in this study.

In order to determine the degree of microsegregation presented in the dendrite core and interdendrite regions, an accurate compositional analysis was carried out for each alloy. Electron probe microanalysis (EPMA) was performed on all of the 5 as cast specimens in the as-polished condition, using a JEOL Model Super probe JXA-8100. The instrument was operated at an accelerating voltage of 15 KeV, a EMI 21uA, and a pot size about 1um.

The microstructure of the as-cast alloys was examined using standard metallographic sample preparation. This was accomplished by analyzing a number of low-magnification optical images for each alloy. Samples were prepared using traditional metallographic techniques and etched to reveal the dendritic/eutectic solidification structure.

Results and Discussion

The microstructures of all of the five different carbon level alloys were characterized to evaluate the as-solidified structures and to determine the locations for the compositional analysis using optical microscopy (Fig.1). The as-cast single crystal Ni-base superalloys at 50 um/s exhibited a dendrite microstructure. The segregation of each of the elements is discussed individually below for clarity.

It can be concluded that with the increasing of carbon level, more carbides networks were found in the interdendritic region, and few carbide formed in the dendrite core. With the increasing carbon content, secondary and tertiary arms became coarse [Fig.1c, 1d], which indicated the segregation behavior of alloying elements was different in different carbon level alloys. The as-cast microstructure of all of the alloys were clearly inhomogeneous due to the severe elemental segregation that occurred during solidification. Certain elements preferentially partition to the dendritic core and others to interdendritic regions. The elements that tended to partition to the interdendritic region were the γ′-formers, I ncluding Ti, Ta, and Al .

Although the general trends for the elemental segregation in Ni-base superalloy single crystal are already known, no systematic study was found on minor carbon addition on the elements of specific segregation degree. To determine the effects of carbon changes on the segregation behavior, as-cast microstructures were characterized by microprobe techniques to calculate the segregation coefficient, k′. Once the segregation coefficients were determined for all elements, some general trends for segregation were apparent.

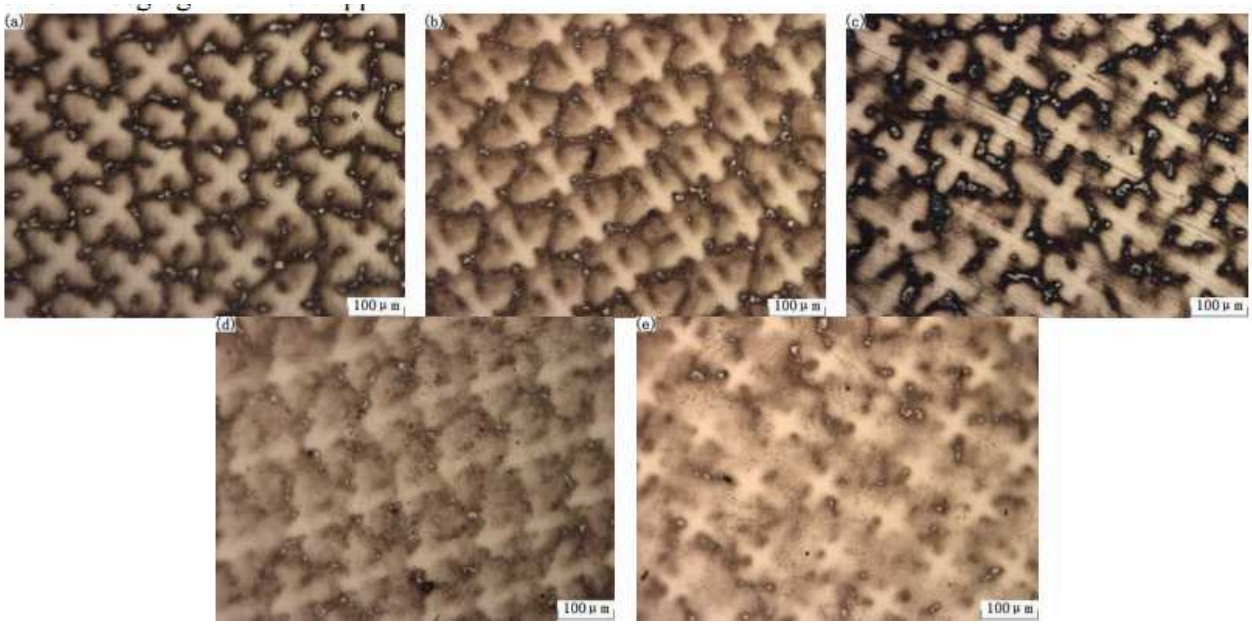

Fig. 1 Microstructure of different carbon level alloys (a) 0.001 % C; (b) 0.006 t% C; (c) 0.045 % C; (d) 0.085t% C; (e) 0.15 % C

The effect of the carbon content on segregation of all elements in the alloy was examined by comparing the individual segregation coefficients for each element in all alloys. Figure 2 illustrated the effect of carbon level on the segregation of all the alloying elements, it can be seen that except W, the segregation degree of baseline alloy was the most server, it can be concluded that modifying the carbon content resulted in changes to the segregation behavior of all of the elements in the alloy, this results disagrees with previous report [16]. However, the greatest effect was observed on the segregation behavior of W. The following degree of segregation were W, Ti and Ta. This may be because these elements were carbide forming elements (Figure 3), and the carbides depleting part of these elements.

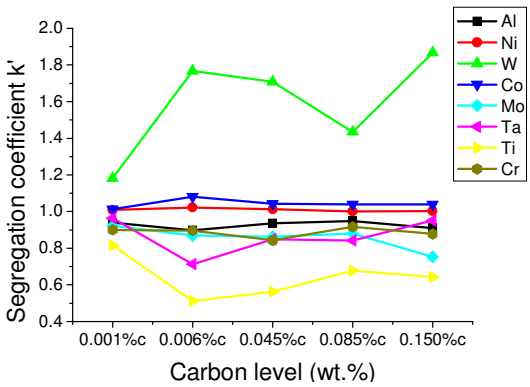

Fig. 2 The effect of carbon level on the segregation of all elements

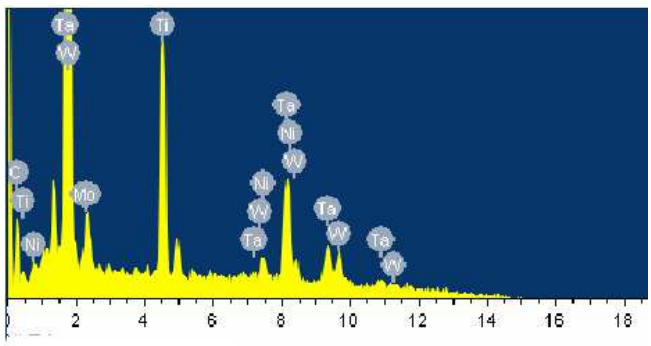

Fig. 3 EDS analysis of carbide

Figure 4 illustrated the effect of carbon level on the segregation of those elements that segregate to the dendrite core, and the segregation behavior of the elements that segregated to the interdendritic region was shown in Figure 5. W was the element that was most affected, of all of the elements that segregated to the dendrite core, by increasing the carbon level of the alloy. The segregation behavior of Co was also affected by the Cr content, but to a lesser degree. Ni exhibited only a weak tendency to partition to the dendrite core, and the segregation behavior of Ni showed no obvious change with the increasing of carbon level. Except the baseline alloy, the segregation degree of Mo did also affected by the carbon modifications. For the interdendritic segregation elements, except Ta, the segregation behavior of other elements had the same change tendency, in all of the five different carbon level alloys, the segregation behavior of baseline alloy (0.006 wt% C) was the most severe, and the segregation degree of no carbon alloy (0.001 wt% C) was the most slightest. the segregation degree of 3# alloy (0.085 wt% C) was the most slightest In all of the carbon containing modification alloys. The segregation behavior of Ta and W had the same tendency, which was the segregation degree of no carbon alloy (0.001 wt% C) was the most slightest, and in the carbon containing alloys, with the increasing of carbon level, the segregation degree change to slight and when the carbon addition was 0.15 wt% , then the segregation degree was the most severest.

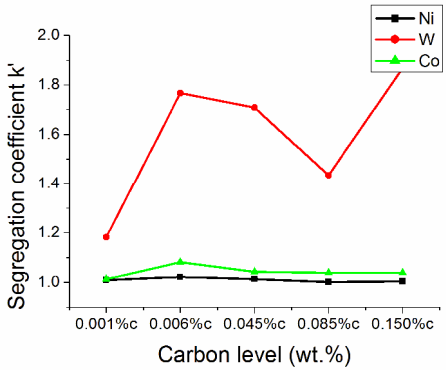

Fig. 4 The effect of carbon level on the segregation of elements that segregate to the dendrite core

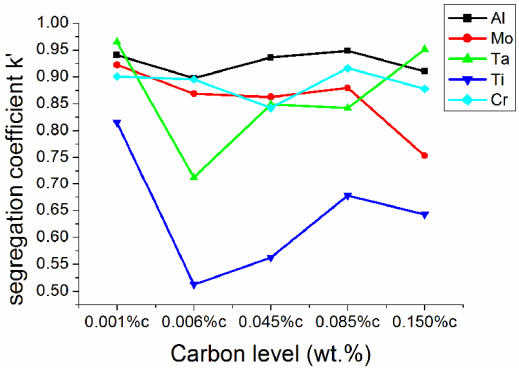

Fig.5 The effect of carbon level on the segregation of elements that segregate to the interdendrite region

It is known that the precipitation of Ta-rich MC carbides suppresses the formation of convective instabilities, since it would deplete tantalum from the liquid in beneficial with respect to stabilizing against convective instabilities. Since tungsten partition strongly to the primary γ dendrites during solidification, a density inversion develops between the solute and the bulk due to the depletion of W. The accumulation of tantalum in the solute assists in reducing the forces by compensating for the depleted levels of W.

Conclusions

In all of the different carbon level alloys, segregation degree of the baseline alloy was the most severe. and with increasing of carbon level, the segregation degree firstly decreased, and when the carbon level was added to 0.15 wt%, then the segregation degree increased. In other words, in all of the carbon containing modifications alloys (3#, 4#, 5#), the segregation degree of 0.085 wt % C alloy was the most slight. For all of the elements, W was the element that was the most affected, and then the segregation behavior of Ti and Ta also was affected by the carbon level. This may be because these elements were the major carbide forming elements. Apparently, the carbon additions alter the activity of the refractory element W in solution. And the potent refractoyr carbide formers, such as tungsten and tantalum, were found to interact most strongly with the carbon additions.

Associated with this change in solute composition is a change in the driving force the convective instabilities.

The authors would like to acknowledge the financial support of The National Natural Science Funds （51201130, 51101120）, Natural Science Basic Research Plan in ShaanXi Province of China （2012JQ6005）,the fund of the State Key Laboratory of Solidification Processing in NWPU (SKLSP201226), Scientific Research Program Funded by Shaanxi Provincial Education Department（11JK0805）, the National Basic Research Program of China (2011CB610406).

References

[1] Z. H. Yu, L. Liu, X. B. Zhao. Effect of solidification rate on MC carbide morphology in single crystal Ni-base superalloy AM3. Transactions of Nonferrous Metals Society of China. 2010, 20（10）：1835-1840

[1] Mihalisin, J R. Some Effects of Carbon in the Production of Single Crystal Superalloy Castings. Superalloys, TMS. 2004: 795-799.

[3] Z. H. Yu, L. Liu, X. B. Zhao. Effect of carbon additions on the microstructure of a single crystal Ni-base superalloy AM3. China Foundry. 2010, 7（4）：352-356

[4] K.A. Al-Jarba and G.E. Fuchs, Effect of Carbon Additions on the As-Cast Microstructure and Defect Formation of a Single Crystal Ni-Based Superalloy, Mat. Sci. and Eng. A, 373 (2004), 255-267.

[5] K A. Al-Garba. Effect of Carbon Additions on the Microstructure and the Mechanical Properties of Model Single Crystal Ni-base Superalloy, Ph. D. Thesis, 2003, University of Florida:12-14

[6] S.Tin, P. D. Lee, A. Kermanpur. Integrated modeling for the manufacture of Ni-based superalloy discs from solidification to final heat treatment. Metallurgical and materials transactions. 36A, 9, (2005):2493-2504.

[7] E.C. Caldwell, F.J. Fela, G.E. Fuchs. Segregation of Elements in High Refractory Content Single Crystal Nickel Based Superalloys. K.A. Green, T.M. Pollock, H. Harada, et al. Superalloys 2004, Pennsylvania, 2004. Warrendale, PA, TMS, 2004: 811-818

[8] E.C. Caldwell, F.J. Fela, G.E. Fuchs. The Segregation of Elements in High Refractory Content Single Crystal Nickei-based Superalloys. Journal of the Minerals, Metals and Materials Society. 2004, 56(9): 44-48

[9] Gang Liu, Lin Liu, Cheng Ai. Influence of withdrawal rates on the microstructures of Ni-base single-crystal superalloys containing Re and Ru. Jounal of Alloy and Compounds. 2011, 509(19): 5866-5872.

[10] Gang Liu, Lin Liu, Xinbao Zhao. Effects of Re and Ru on the solidification characteristics of nickel-base single-crystal superalloys. Metallurgical and Materials Transactions A. 2011, 42A: 2733-2741.

[11] E. C. Caldwell, F. J. Fela, G. E. Fuchs. Segregation of Elements in High Refractory Content Single Crystal Nickel Based Superalloys. Superalloys 2004. The Minerals, Metals & Materials Society. 2004: 801-810.

[12] R.M. Kearsey, J.C. Beddoes, K.M. Jaansalu, W.T. Thompson, P.Au1. The Effects of Re, W and Ru on Microsegregation Behavior in Single Crystal Superalloy Systems, Superalloys 2004, TMS, 2004: 801-810.

[13] R.A. Hobbs, L. Zhang, C.M.F. Rae, S. Tin. The effects of ruthenium on the intermediate to high temperature creep response of high refractory content single crystal nickel-base superalloys. Mater. Sci. Eng. A. 2008, 489: 65-76

[14] A. Mottura, N. Warnken, M.K. Miller, M.W. Finnis. R.C. Reed. Atom probe tomography analysis of the distribution of rhenium in nickel alloys. Acta Mater. 2010, 58(3): 931-942

[15] B.H. Ge, Y.S. Luo, J.R. Li, J. Zhu. Distribution of rhenium in a single crystal nickel-based superalloy. Scripta Mater. 2010, 63: 969-972

[16] L.R. Liu, T. Jin, N.R. Zhao. Effect of Carbon Additions on the Microstructure in a Ni-base Single Crystal Superalloy. Materials Letters. 2004, 58: 2290-2294.

Advanced Materials Research Vol. 983 (2014) pp 127-130

doi:10.4028/www.scientific.net/AMR.983.127

Modeling the correlation between microstructure and tensile properties of Ti-17 alloy using artificial neural network

Zhiqiang Jia[1, a], Weidong Zeng[1, b]

[1]State Key Laboratory of Solidification Processing, Northwestern Polytechnical University, Xi'an 710072, China

[a]jzq19841102@163.com, [b]zengwd@nwpu.edu.cn*

Keywords: Ti-17 alloy; BP neural network; tensile properties; microstructure

Abstract. In this work, a relational model was established correlating microstructure and tensile properties for the Ti-17 alloy using a back-propagation (BP) neural network technique. In the proposed model, the input data consisted of quantitative microstructural feature parameters, including the volume fraction, thickness and Ferret ratio of α phase. Meanwhile, the tensile properties are the outputs of the model, such as ultimate tensile strength, yield strength, elongation and reduction in area. The coefficient of determination is more than 0.900, which indicates that the developed model possesses the excellent ability to predict the internal relationship of the microstructure and tensile properties of Ti-17 alloy.

Introduction

Titanium alloys have been extensively used in the field of aerospace because of its excellent combination of high strength-to-weight ratio, fracture resistant characteristics and exceptional resistance to corrosion [1]. It is well-known that the mechanical properties of titanium alloys are quite sensitive to their microstructure characteristics, such as morphology, volume fraction and distribution of phases. Therefore, there have been some reports on the relationship between the microstructural features and mechanical properties. Boyer [2] claimed that the ductility increases and the toughness decreases duo to the globularization of α phase for the Ti-10V-2Fe-3Al alloy. G. Lütjering [3] found that the yield stress, the ductility, the crack nucleation resistance and the microcrack propagation resistance are improved with decreasing α colony size for α + β titanium alloys because of decreased slip length. However, the effect of the microstructure characteristics on the mechanical properties is generally non-linear and complex. Therefore, it is extremely difficult to establish the accurate quantitative relation between them by traditional method.

In recent years, with the fast development of the computing technique, artificial neural network (ANN) is increasingly applied in term of materials processing. The artificial neural network is an information treatment system with the characteristics of adaptive learning, and is especially suitable for treating non-linear phenomena and complex relationships without needing explicit mathematical [4]. Nowadays, the ANN technique has become one of the most powerful tools in the field of materials science, such as optimization of processing parameters [5] and development of constitutive relationships [6].But little research has concerned on the correlation of microstructure and mechanical properties of titanium alloys based on the artificial neural network.

In this study, as the most widely used ANN model, a back-propagation (BP) neural network model has been built to characterize the relationship between microstructures and tensile properties of the Ti-17 alloy, which was developed primarily for gas turbine engine components [7,8].

Experimental procedure

The 20kg Ti-17 cakes with diameter of 20mm, which produced by Baoshan Iron & Steel Co., Ltd., PR China, were employed in this study. The cakes have been forged above β-transus temperature. Then isothermal forging was conducted on Ti-17 alloy cakes for obtaining different microstructures. The cakes were forged at 840°C with deformation rate about 2mm/s, and a height reduction range 15-75% at an interval of 15%. After the forging, the alloy cakes were subjected to a series of heat treatments. In order to assess the effect of microstructure on performance, the tensile properties of Ti-17 alloy were tested. The testing specimens cut from different locations of the cakes were machined into standard size. Meanwhile, specimens for microstructural observation were prepared and observed by Olympus/PMG3 optical microscopy.

Development of BP neural network model

The architecture of BP neural network model is shown in Fig. 1. The BP neural network consists of an input layer, one hidden layer and an output layer. The input layer is used to receive data from outside, while the output layer sends the information out to users. So, analyzing and choosing appropriate parameters as input for reliable database is the first critical step for development the model. Firstly, Wang [9] considered that the tensile strength of titanium alloys is significantly affected by the volume fraction of α phase. Secondly, the increased thickness of α phase can decreases the yield strength and plasticity because the thickness is beneficial to the nucleation of an initial crack. Finally, the yield strength and plasticity would increase while the lamellar α phase turns to be globularized. As a consequence, the Feret ratio (Feret ratio= $Feret_{max}$/ $Feret_{min}$), must be taken into account. Meanwhile, other microstructural characteristics, such as the size and shape of β phase and secondary phase, are not considered in the present study duo to the hot working process. Hence, the important microstructural features, including volume fraction, the thickness and Feret ratio of α phase, are seen as the input of the developed model.

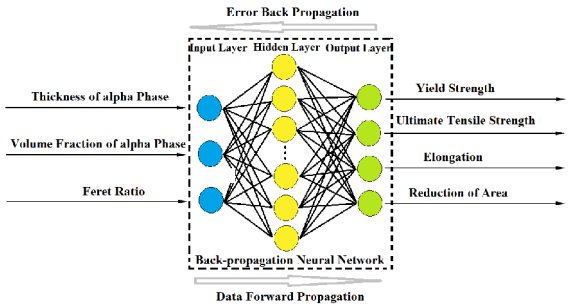

Fig. 1. The architecture of artificial neural network model

Subsequently, the prediction accuracy of the model is obviously influenced by the number of neurons in the hidden layer. It was found that the hidden layer has 10 neurons presented the most excellent performance. Meanwhile, for quantitative assessment the effect of tensile properties, the output layer must consist of four nodes of yield strength, ultimate tensile strength, elongation and reduction in area. Before training the network, both input and output variables were normalized within the range from 0 to 1 in order to obtain a usable form for the network to read [10]. The widely used unification method is

$$z_i = \frac{z - 0.95z_{\min}}{1.05z_{\max} - 0.95z_{\min}} \tag{1}$$

Where Z is the original data, Z_{min} and Z_{max} are the minimum and maximum value of Z, respectively. Z' is the unified data of the corresponding Z. Such pre-processing procedure can make the train of neural network more efficient. 45 data sets (as shown in Table 1) in total for the Ti-17 alloy have been used, in which 5 data sets were randomly selected to evaluate the predictive ability of the neural network and the remaining were used to train the model.

Table 1 Experiment result of tensile properties for Ti-17 alloy

No.	1	2	...	44	45
Micro-structure	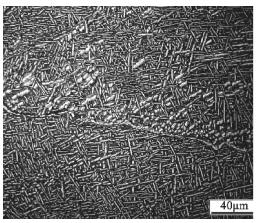	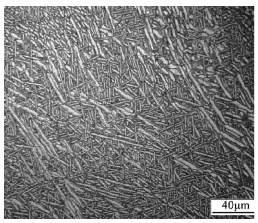	...	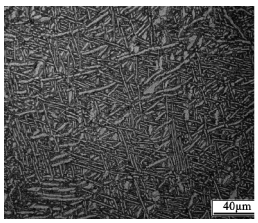	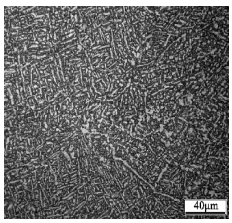
R_m (MPa)	1190	1200		1190	1210
$R_{p0.2}$ (MPa)	1150	1160		1150	1200
Z (%)	12	14		14	16
A (%)	23.5	19		33	28

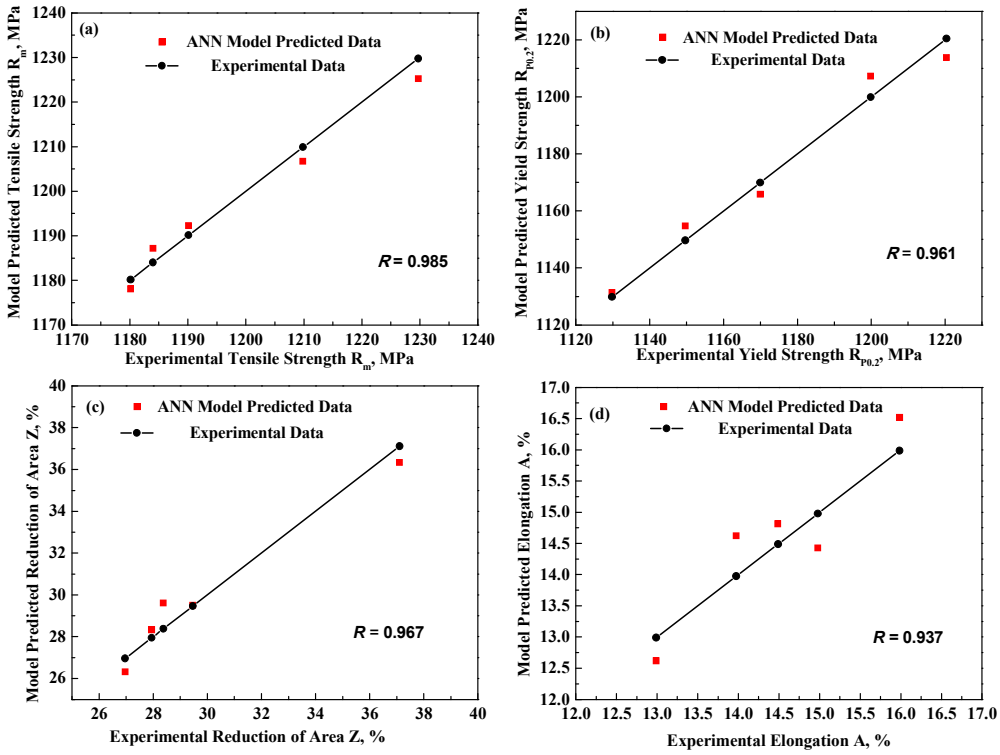

Fig. 2. Comparison of predications from BP neural network model and experimental data for mechanical properties at room temperature for Ti-17 alloy
(a) Tensile Strength; (b) Yield Strength; (c) Reduction of Area (d) Elongation

In addition, the hyperbolic tangent function was selected for training the model and the minimum error tolerance was set to 1.0%. The Levenberg-Marquardt algorithm was utilized as the optimization algorithm. Finally, the training and testing of the model has been completed.

Results and discussion

After the training, the model could be used to predict the correlation between microstructure and tensile properties of Ti-17 alloy. The compared results are shown in Fig. 2, and the coefficient of determination (R) is considered as the performance criteria. As shown in Fig. 2, all the coefficient of determination are more than 0.900, which means that the developed back-propagation (BP) neural network could successfully model the internal relationship of the microstructure and tensile properties of Ti-17 alloy.

Summary

Based on the technique of BP neural network, a prediction model which demonstrates the relationship of microstructure and tensile properties of Ti-17 alloy has been established successfully. Excellent agreement between the experimental and predicted results was obtained with the help of proposed model. It was found that the coefficient of determination is more than 0.900, which implies that it is a powerful and effective method to solve the multivariable and non-linear problem.

Acknowledgment

The authors thank the financial supports from Research Fund for the Doctoral Program of Higher Education of China (20116102110015).

References

[1] S. Mironov, M. Murzinova, S. Zherebtsov, G.A. Salishchev and S.L. Semiatin: Acta Mater Vol. 57 (2009), p. 2470.

[2] R.R. Boyer, G.W. Kuhlman: Metall. Mater. Trans. A Vol. 18 (1983), p. 2095.

[3] G. Lütjering: Mater. Sci. Eng. A Vol. 243 (1998), p. 32.

[4] D.E. Rumelhart, G. Hinfon, R. Williams: Nature Vol. 323 (1986), p. 533.

[5] Y. Sun, W.D. Zeng, Y.F. Han, X. Ma, Y.Q. Zhao: Comput. Mater. Sci. Vol. 50 (2011), p. 1064.

[6] Y.C. Zhu, W.D. Zeng, Y. Sun, F. Feng, Y.G. Zhou: Comput. Mater. Sci. Vol. 50 (2011), p. 1785.

[7] K.X. Wang, W.D. Zeng, Y.Q. Zhao, Y.T. Shao, Y.G. Zhou: Mater. Sci. Eng., A Vol. 527 (2010), p. 6193.

[8] S. Fréour, D. Gloaguen, M. François, R. Guillén: Scr. Mater. Vol. 54 (2006), p. 1475.

[9] K.X. Wang, W.D. Zeng, Y.T. Shao, Y.Q. Zhao, Y.G. Zhou: Rare Metal Mater. Eng. Vol. 3 (2009), p. 398.

[10] K. Swingler: *Applying Neural Networks: A Practical Guide* (Morgan Kaufman Publishers, Inc., America 1996).

Advanced Materials Research Vol. 983 (2014) pp 131-134

doi:10.4028/www.scientific.net/AMR.983.131

One step fabrication of core-shell structures in immiscible alloys for thermal energy storage

Fuming Xu [a], Mingbi Fu [b], Wei Dong* [c], Li Zhao[d], Dong Lu[e] and Yi Tan[f]

School of Materials Science and Engineering, Dalian University of Technology, Dalian 116024, Liaoning, China

[a)] fuminxu@dlut.edu.cn, [b)] mingbifu8724@163.com, [c)] w-dong@dlut.edu.cn,

[d)] xianrenqiu_xph1209@163.com, [e)] ludong-0531@163.com, [f)] tanyi@dlut.edu.cn

Keywords: Core-shell; Microstructure; Immiscible alloy; Phase transformation; Energy storage

Abstract: The microscopic morphologies of $Bi_{30}Ga_{70}$ immiscible alloy particles were investigated. Monosized microparticles with similar core-shell structures were fabricated for the first time by one step using the Pulsated Orifice Ejection Method. The EDS revels that the core and the shell consist of a Ga-rich phase (＞90 at. %) and a Bi-rich phase (＞80 at. %), respectively. The DSC testing at different temperatures is performed. Core-shell microstructures as well as endothermic peaks and exothermic peaks are observed after heating-cooling cycles when the working temperature is below the temperature of spinodal line, indicating good thermal stability after phase transformation. The thermal energy storage was preliminary tested, which is a good attempt for thermal energy storage. It is likely to use core-shell structures as microencapsulated phase change materials.

Introduction

Microencapsulated Phase Change Materials (MicroPCMs), composed of a capsule-core and a wall material, are newly-developing fields. They are likely to be used for energy storage because of various advantages, such as high thermal efficiency storage density and stability at available working temperature [1]. Traditionally, MicroPCMs are packaged in spherical capsule, through which the corrosion and consistency can be solved technically and the applications limit can be overcome effectively [2,3]. For long ages, studies on alloys-based core-shell structures, electroplated by containers, have been performed to make MicroPCMs for thermal energy storage due to their high energy densities but not been possible to make it. Further developments, however, are seriously restricted because of their multiple-step complex packaging technology such as chemical, physical-chemical and mechanical methods [4,5], leading to expensive producing cost. In recent years, core-shell micro particles based on self-assembly property of immiscible alloys have raised significant attention [6]. It is considered that the low melting point phase core can save and release latent heat of phase transformation and the high melting point phase shell can be used as wall materials [7,8]. Good combinations of consistency and corrosion resistance are easily understood because of the self-assembly property. Up to now, scarce works have been reported, it is therefore significantly important to fabricate core-shell composite structures with high melting point phase shell.

The Pulsated Orifice Ejection Method (POEM) can be a proper approach to achieve monosized core-shell structure of immiscible alloys by one step [9]. The Bi-Ga immiscible alloy probably

meets the target due to lower surface energy of Bi than Ga [10-12]. In this paper, Bi-Ga immiscible alloy was performed by the POEM. The morphologies and thermal storage property of the resultant micro particles were both investigated.

Experimental procedure

According to the phase diagram of Bi-Ga binary immiscible alloy [13], 10 g $Bi_{30}Ga_{70}$ alloy was prepared from high purity Bi and Ga (both 99.99 wt. %) and placed in a stainless steel crucible. The mixture was heated to 545 K (10 K above the critical temperature *Tc*=535 K) for 30 min to ensure sufficient mixing of the components under Ar atmosphere. A certain amount of droplets were ejected per pulse from an orifice (Φ300 μm). The micro particles were embedded in resin, ground down to the equatorial plane, polished with ice water and then vacuum dried. The micro particle morphology was analyzed using a SUPRA 55VP scanning electron microscope (SEM) with energy dispersive spectroscopy (EDS). The sectional microstructures were characterized using a MEF4A optical microscope. The energy storage property was tested using a DSC 822^e differential scanning calorimetry analyzer.

Results and discussion

Fig. 2 shows typical morphologies of $Bi_{30}Ga_{70}$ micro particles fabricated by the POEM. In Fig. 2(a), most micro particles are mono-sized with a mean diameter of about 300 μm. Similar core-shell microstructures are formed as shown in Fig. 2(b) indicating the microparticles experience consistent thermal history during free fall so that narrow size distributions can therefore be produced accurately. EDS analysis shows that the core consists of a Ga-rich phase (＞90 at. %), whereas the shell consists of a Bi-rich phase (＞80 at. %). Core-shell structures with higher melting point shell were obtained and are possible to use as microPCMs.

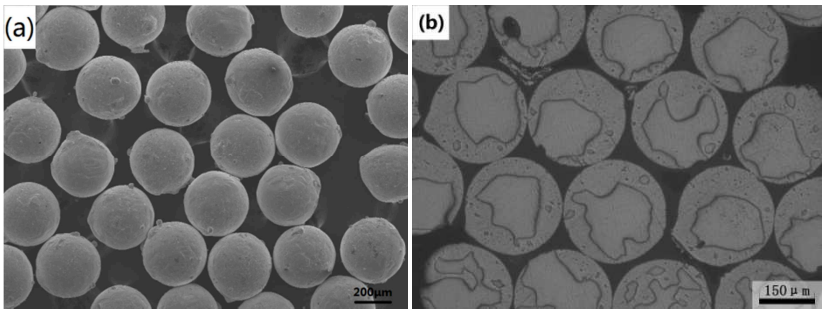

Fig. 2. (a) Overall morphologies and (b) sectional morphologies of $Bi_{30}Ga_{70}$ alloy micro particles.

Fig. 3 shows cross sectional morphologies of $Bi_{30}Ga_{70}$ alloy micro particles after DSC testing. Vigorous changes have been found at different heating-cooling cycle temperature. Comparing with the morphologies in Fig. 2 (b), when heating temperature is in point “a” (see in Fig. 1), there is little change in the morphology of the micro particle and the core-shell structure in Fig. 3 (a), which indicates a good stability of core-shell structure. In Fig. 3 (b), when heating temperature is up to point b, the core-shell structure is similar to Fig. 3 (a) while become eccentric and smaller than what it was. However, the core-shell structure disappears and is nearly dispersed in Fig. 3 (c). The above results show that the microparticles are possible to use for thermal energy storage when working temperature is between the melting temperatures of the shell and the core.

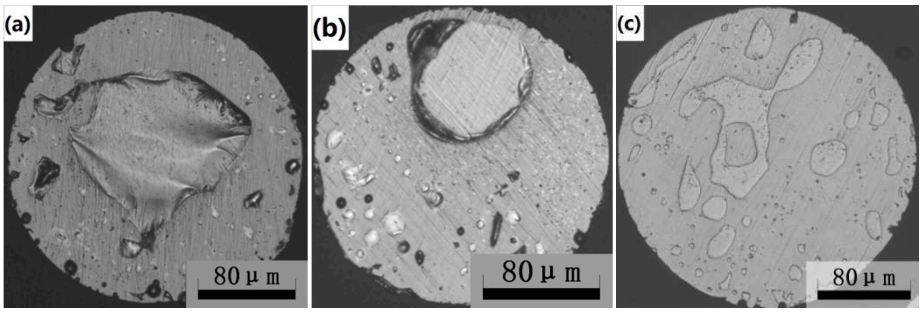

Fig. 3 Morphologies of $Bi_{30}Ga_{70}$ alloy micro particles after DSC tesing at different heating-cooling cycles: (a) -20~50~-20 ℃; (b) -20~240~-20℃; (c) -20~300~-20℃.

Fig. 4 shows the phase transformation behaviors of $Bi_{30}Ga_{70}$ alloy micro particles by DSC heating and cooling scans at a rate of 10 K/min. In Fig. 4 (a), the sample exhibits an endothermic peak in the heating scan trace. The onset temperature of the peak is around 30℃, which is quite close to the Bi-Ga eutectic reaction point of 29.8℃, and can be attributed to Bi-Ga eutectic reaction. Compared with Fig. 4(a), another more endothermic peak in the higher temperature is respectively observed in Fig. 4 (b) and (c) with the onset temperature of around 222 ℃, corresponding to a monotectic reaction. In DSC cooling scan traces, one or two exothermic peaks appear in the samples, indicative of monotectic reaction and eutectic reaction one after another. However, there exhibits a low peak or reflection before monotectic reaction in Fig. 4 (c), implying the occurrence of the liquid phase separation. It is consistent with the microstructural observation. The onset temperature in the cooling scan trace is lower than in the heating scan trace because of supercooling. The above analysis indicates endothermic and exothermic processes will occur during the heating-cooling cycle, which is a good attempt for thermal storage through phase transformation of core-shell structures.

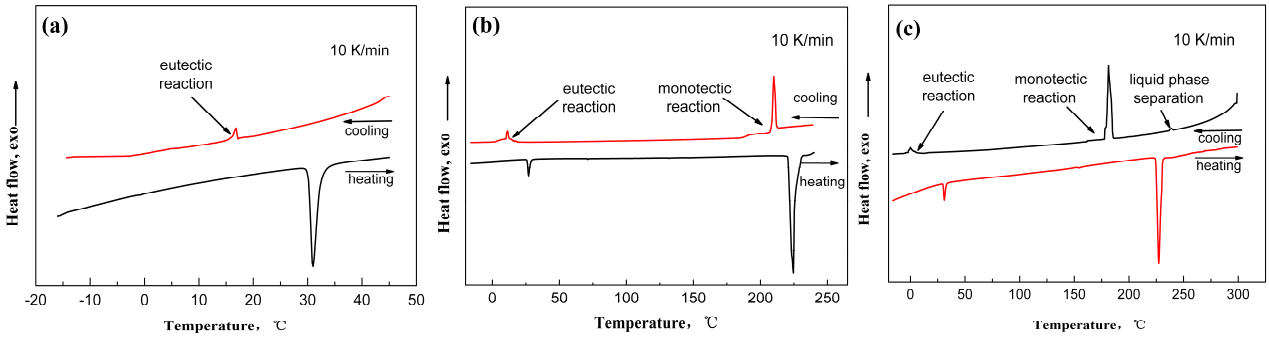

Fig. 4 DSC curves of heating-cooling cycles for $Bi_{30}Ga_{70}$ alloy micro particles at a rate of 10 K/min at different heating-cooling cycles: (a) -20~50~-20 ℃; (b) -20~240~-20℃; (c) -20~300~-20℃.

Summary

Mono-sized $Bi_{30}Ga_{70}$ immiscible alloy micro particles with similar core-shell structure were obtained by the POEM. The core and the shell consist of a Ga-rich phase and a Bi-rich phase, respectively. DSC heating-cooling cycle testing shows that the core-shell structures can maintain a good structural stability within the proper working temperature, indicating it is possible to save and release energy in the recovery of industrial waste heat through the phase changes the endothermic and exothermic processes. Further work is focused on the stability after several heating-cooling cycles. The POEM is effective to prepare mono-sized core-shell particles for industrial applications.

Acknowledgement

The support from Liaoning Provincial Natural Science Foundation of China (No. 2013020114) is gratefully acknowledged.

Corresponding Author

Wei Dong E-mail: w-dong@dlut.edu.cn, ceramictech@gmail.com
Tel & Fax: +86-411-84707455

References

[1] M.F. Mohammed, M.K. Amar, A.R. Siddique, A.H. Said, A review on phase change energy storage: materials and applications, Energy Convers. Manage. 45(2004)1597-1615.

[2] K. Murat, M. Khamid, Solar energy storage using phase change materials, Renew. Sust. Energ. Rev. 11(2007) 1913-1965.

[3] A.M. Khudhair, M.M. Farid, A review on energy conservation in building applications with thermal storage by latent heat using phase change materials, Energy Convers. Manage. 45(2004)263-275.

[4] M.H. Gtucho, Microcapsules and Microencapsulation Techniques, Noyes Date Corp Press, New York, 1976.

[5] C.P. Wang, X.J. Liu, I. Ohnuma, R. Kainuma, K. Ishida, Formation of immiscible alloy powders with egg-type microstructure, Science 297(2002)990-993.

[6] B.Q. Ma, J.Q. Li, Z.J. Peng, G.C. Zhang, Structural morphologies of Cu-Sn-Bi immiscible alloys with varied compositions, J. Alloys Compd. 535 (2012) 95-101.

[7] Z. Belen, M. Jose, F.C. Luisa, M. Harald, Review on thermal energy storage with phase change: materials, heat transfer analysis and applications, Appl. Therm. Eng. 23(2003) 251-283.

[8] M.K. Murat, High-temperature phase change materials for thermal energy storage, Renew. Sust. Energ. Rev. 14 (2010) 955-970.

[9] Y. Li, W. Dong, Y. F. Fu, Y. Tan, A. Miura, A. Kawasaki, The critical cooling rate of Fe-based mono-sized spherical particles with fully glassy phase, Adv. Mater. Res. 509(2012)185-191.

[10] A.H. Ayyad, W. Freyland, Wetting transition in liquid Ga–Bi alloys: light scattering study of surface energy and entropy, Surf. Sci. 506(2002)1-11.

[11] T. Qin, H.P. Wang, B.B. Wei, Simulated evolution process of core-shell microstructures, Sci. China. Ser. G 50(2007)546-552.

[12] R.P. Shi, C.P. Wang, D. Wheeler, X.J. Liu, Y. Wang, Formation mechanisms of self-organized core/shell and core/shell/corona microstructures in liquid droplets of immiscible alloys, Acta Mater. 61 (2013) 1229-1243.

[13] Information on http://www.factsage.cn/fact/phase diagram.

Advanced Materials Research Vol. 983 (2014) pp 135-140

doi:10.4028/www.scientific.net/AMR.983.135

Surface Modification of Titanium Alloys Using Alumina Particles Blasting for Biomedical Applications

Suparat Udomlertpreecha[1,a], Prasit Pavasant[2,b] and Boonrat Lohwongwatana[1,c]

[1] Innovative Metal Research Unit, Department of Metallurgical Engineering,

Faculty of Engineering, Chulalongkorn University, Bangkok, Thailand

[2] Mineralized Tissue Research Unit, Department of Anatomy,

Faculty of Dentistry, Chulalongkorn University, Bangkok, Thailand

[a] suparat.udomlertpreecha@gmail.com, [b] prasit215@gmail.com, [c]*boonrat@gmail.com

Keywords: Titanium, blasting, roughness, wettability and biomedical applications.

Abstract. Ti-based bulk metallic glass (BMG) is a new class of titanium alloys that exhibits excellent properties for biomedical applications. They have high strength, good corrosion resistance, low elastic modulus and satisfactory biocompatibility. Therefore, Ti-based BMG is an excellent alternative material to be used in biomedical application. Titanium alloy with a nominal composition of the $Ti_{40}Zr_{10}Co_{36}Pd_{14}$ was synthesized by replacing Cu with Co in a better-known bulk glass forming composition. Coin-shape samples with a diameter of 15 mm and thickness of 1 mm were prepared by arc-melting and casting into copper mold. The coin-shape samples were polished, then followed by blasting with 50 μm and 250 μm average particle sizes of alumina. Alumina blasting caused plastic deformation at the surface and induced change in surface roughness. The larger size of alumina particle, the higher the R_a, R_q and R_t with significant difference. Some abrasive alumina particles were found to be embedded onto the blasted surface. The blasted $Ti_{40}Zr_{10}Co_{36}Pd_{14}$ sample showed lower roughness values than those blasted Ti-6Al-4V samples. This may be because of the higher hardness values of $Ti_{40}Zr_{10}Co_{36}Pd_{14}$ sample, when compared to the softer Ti-6Al-4V samples. The contact angle measurement which demonstrated wettability of all samples did not show significant difference in a tested range of R_a (from 40 to 428 nm).

Introduction

Bulk metallic glass (BMG) has been widely studied and developed because of their attractive properties, when compared to conventional crystalline alloys, such as superior strength, low elastic modulus, high corrosion resistance, high wear resistance and unique processing capability [1-3]. Among various kinds of BMGs, Ti-based BMGs are one of the most investigated alloys for implant biomaterials [4, 5]. The influence of implant's surface properties (surface composition, hydrophilicity, topography and roughness) on biological response are investigated.

A number of methods for surface roughening of titanium have been divided into three main categories: physical, chemical-and-electrochemical and biochemical [6]. Particle blasting is an example of commonly used physical treatment based on high velocity bombardment of abrasive particle to the surface. The technique produces higher roughness and induces mechanical constraints on the metallic surface [6, 7], Many researchers [7-9] found relationship between cellular attachment and surface roughness of blasted titanium. However the influences of roughness on cellular behavior in the range of sub-micron to nanometer level are still poorly understood. The aim of this research was to study surface properties of titanium alloy with a nominal composition of $Ti_{40}Zr_{10}Co_{36}Pd_{14}$ which was blasted by alumina particles of various particle sizes. Ti-6Al-4V alloy was used as a reference material.

Materials and methods

Materials preparation

Ti alloy with a nominal composition of $Ti_{40}Zr_{10}Co_{36}Pd_{14}$ was synthesized by replacing Cu with Co in a better-known bulk glass forming composition. The alloy ingot was prepared by arc-melting four elements of 99.8% or better purity in a titanium–gettered argon atmosphere. In order to ensure the homogeneity of the composition, each ingot was re-melted 3 to 4 times. The ingot was then cast into a copper mold using Orotig Speedcast (Speedcast 220-M, Italy). The cast coin-shape samples had a diameter of 15 mm with 1 mm thickness. Meanwhile, Ti-6Al-4V with diameter of 15 mm rod was cut to thickness of 1 mm in order to repeat the same tests as reference material.

Surface preparation

The samples were ground with 400# to 2000# SiC sand paper as a control surface. Then some of them were blasted with alumina particles using laboratory blasting machine at the pressure of 3 bar for 1 min. The surfaces were blasted using 1) 240 grit alumina (with average particle size of 50 μm as shown in Fig.1 (a-b)) and 2) 60 grit alumina with average particle size of 250 μm (Fig.1 (c-d)), in order to obtain different roughness. Afterward, all samples were cleaned ultrasonically in acetone and ethanol for 5 min, and then finally dried in air. All samples were divided into 6 groups:
TiMG-untreated: $Ti_{40}Zr_{10}Co_{36}Pd_{14}$ sample with untreated surface, ground up to 2000# SiC paper
TiMG-50: $Ti_{40}Zr_{10}Co_{36}Pd_{14}$ sample blasted with alumina (average particle size of 50 μm)
TiMG-250: $Ti_{40}Zr_{10}Co_{36}Pd_{14}$ sample blasted with alumina (average particle size of 250 μm)
Ti64-untreated: Ti-6Al-4V sample with untreated surface, ground up to 2000# SiC paper
Ti64-50: Ti-6Al-4V sample blasted with alumina (average particle size of 50 μm)
Ti64-250: Ti-6Al-4V sample blasted with alumina (average particle size of 250 μm)

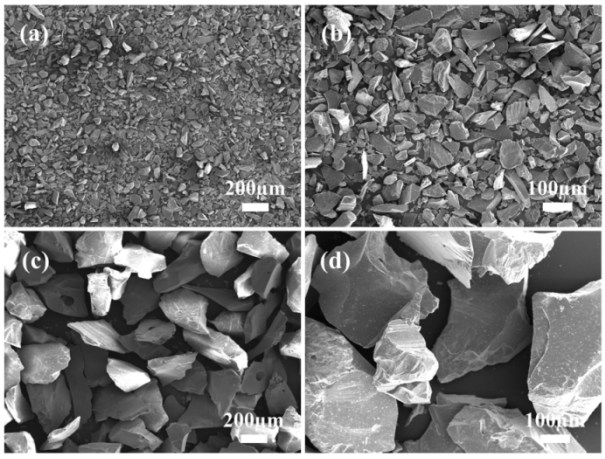

Fig.1 Alumina-average particle size of 50 μm (a) low magnification, (b) high magnification and alumina-average particle size of 250 μm (c) low magnification, (d) high magnification.

Surface characterization

Surface observation The surface morphology of samples was characterized by scanning electron microscope (SEM, JOEL JSM-6400, Japan). The backscattered electron imaging technique was used to investigate the remaining blasted particles on sample surfaces. The percentage of embedded particle (EP%) was also determined.

Surface roughness The surface roughness was measured by surface profilometer (Talyscan 150, Taylor Hobson, UK). Six measurements were scanned on the area of 500x500 μm^2 with 400 μm/s scan speed, spacing on X-axis was 0.5 μm and on Y-axis was 5 μm. Results were express as R_a (arithmetic average roughness), R_q (root mean square roughness) and R_t (absolute height) as the summation of R_p (maximum relative height) and R_v (maximum relative depth).

Micro-hardness Vicker's micro-hardness was measured using micro-hardness tester (FM-700e Type D, Future-Tech, Japan) under load of 500 g and 15 seconds dwell time. Each sample was measured 10 times and the hardness values were reported as mean ± standard deviation.

Wettability Water wettability of titanium surface was measured through the contact angle measurement using sessile drop method (DM-CE1, Kyowa, Japan). One μL of water was ejected using a micrometric syringe and deposited on the samples surface at room temperature. Five drops were deposited on each sample and the wettability was reported as mean contact angle ± standard deviation.

Results and Discussion

Fig.2 reveals surface morphologies of $Ti_{40}Zr_{10}Co_{36}Pd_{14}$ and Ti-6Al-4V samples in three conditions: 1) ground with SiC, untreated, 2) blasted with 50 μm alumina particles, and 3) blasted wth 250 μm alumina particles. Blasting process caused the plastic deformation of sample surface that created randomly distributed topography. Some abrasive alumina particles were embedded on the blasted sample even after ultrasonic cleansing. The quantification of embedded particle (EP%) was summarized in Table 1. There was significant EP% difference between two types of substrate blasted with the same particles size. $Ti_{40}Zr_{10}Co_{36}Pd_{14}$ samples had lower EP%-values than those of Ti-6Al-4V samples. Moreover, in the same material, the samples blasted with the larger size of alumina have higher EP%-values than those blasted with smaller-sized alumina. It can be clearly seen in Fig.3 through BSE imaging that there were remnants of blasted particles that remained on all blasted surface. In previous studies the particles adhered on the surface are clearly seen, obtaining up to an approximately 10% of surface covering with blasting particles [9]. Even though there were similar research previously reported on girt-blasting of titanium metals and alloys [8-10], there were very limited information on blasting effects of different size particles on titanium metallic glass (MG) composition. It must be emphasized that solid state amorphization through ball milling and shot peening had been the center of interests in early 1980's. It is proven as one possible method to subsequently transform our MG alloy surface into amorphous state [11].

The value of the roughness parameters, R_a, R_q and R_t, are shown in Table 1. The greater size of alumina particle, the higher the R_a, R_q and R_t values with significant difference were registered. Differences in surface roughness are due to the different size of the grit-blasting particles used. The significant difference between $Ti_{40}Zr_{10}Co_{36}Pd_{14}$ and Ti-6Al-4V samples blasted with same-sized alumina was also determined. Fig.4 shows comparison of R_a of $Ti_{40}Zr_{10}Co_{36}Pd_{14}$ and Ti-6Al-4V samples in three aforementioned conditions. The blasted $Ti_{40}Zr_{10}Co_{36}Pd_{14}$ sample showed lower roughness parameter values than those blasted Ti-6Al-4V samples. This result could be explained by the hardness difference in both samples. The hardness values for $Ti_{40}Zr_{10}Co_{36}Pd_{14}$ and Ti-6Al-4V samples were measured at 566.0 ± 29.7 HV0.5 and 292.7 ± 11.1 HV0.5, respectively. $Ti_{40}Zr_{10}Co_{36}Pd_{14}$ sample has twice the hardness values of the Ti-6Al-4V samples.

Table 1 Mean value ± standard deviation of the roughness parameter, percentage of embedded particle (EP%) and contact angle of all samples.

Material/surface	R_a (nm)	R_q (nm)	R_t (μm)	EP%	Contact angle (deg.)
TiMG-untreated	40±5	49±6	0.32±0.10	-	77.1±1.9
TiMG-50	133±35	139±18	1.59±0.49	8.5%±3%	72.6±4.7
TiMG-250	359±25	447±26	3.21±0.49	16.9%±2%	90.5±10.9
Ti64-untreated	66±5	83±6	0.56±0.06	-	59.4±1.3
Ti64-50	196±33	245±42	1.72±0.38	14.2%±1%	87.3±8.4
Ti64-250	428±50	529±61	3.72±0.47	19.8%±2%	68.3±1.6

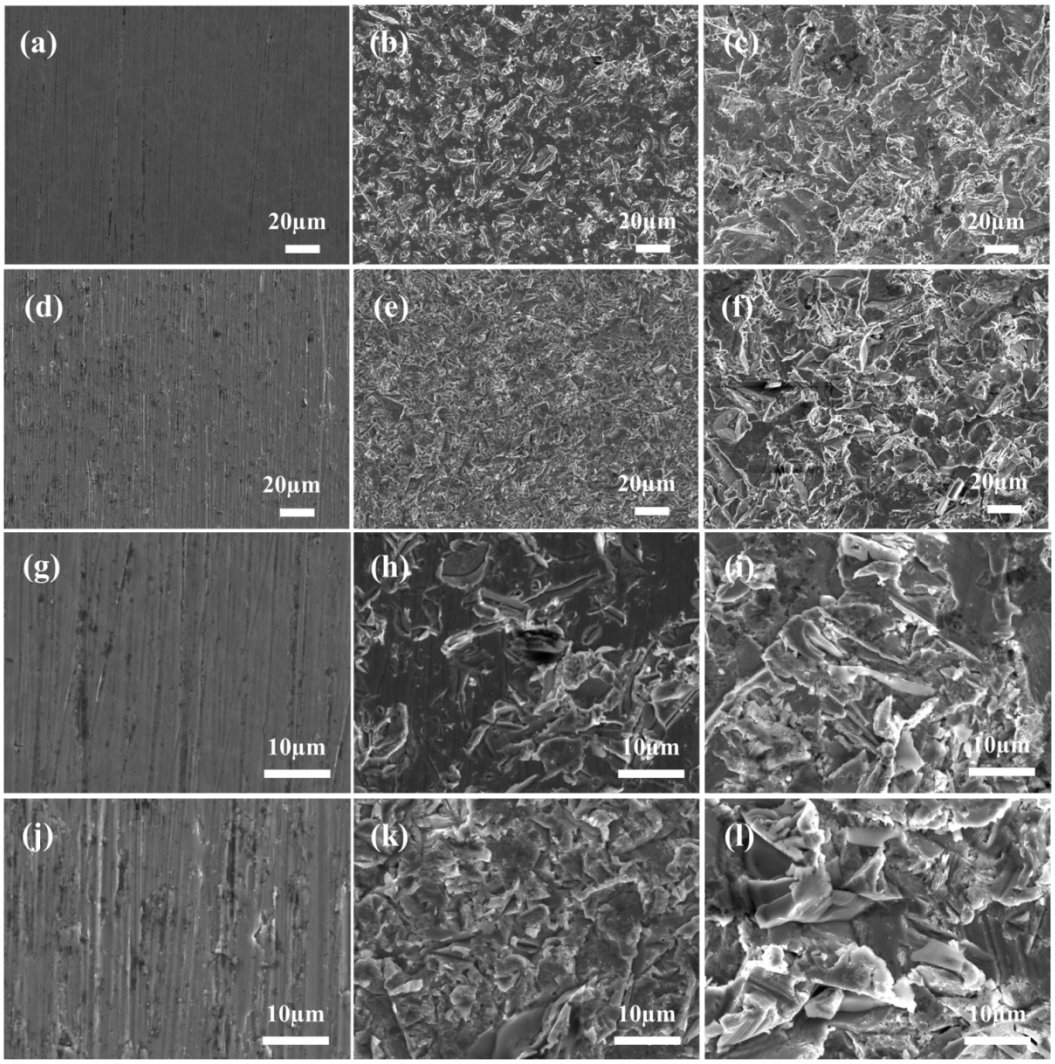

Fig.2 Low magnification SEM micrograph of (a) TiMG-untreated, (b) TiMG-50, (c) TiMG-250, (d) Ti64-untreated, (e) Ti64-50, (f) Ti64-250 and high magnification SEM micrograph of (g) TiMG-untreated, (h) TiMG-50, (i) TiMG-250, (j) Ti64-untreated, (k) Ti64-50, (l) Ti64-250.

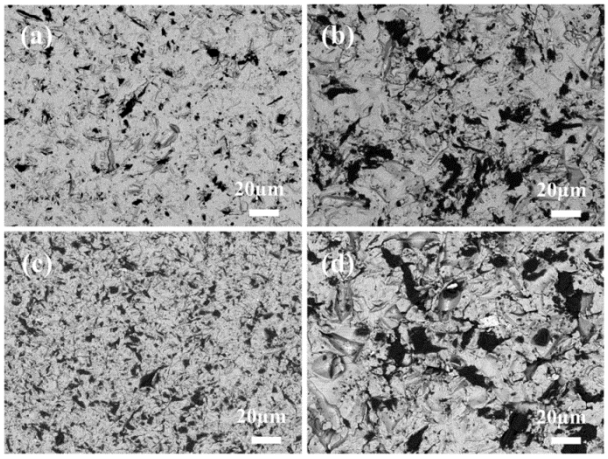

Fig.3 BSE imaging of (a) TiMG-50, (b) TiMG-250, (c) Ti64-50 and (d) Ti64-250.

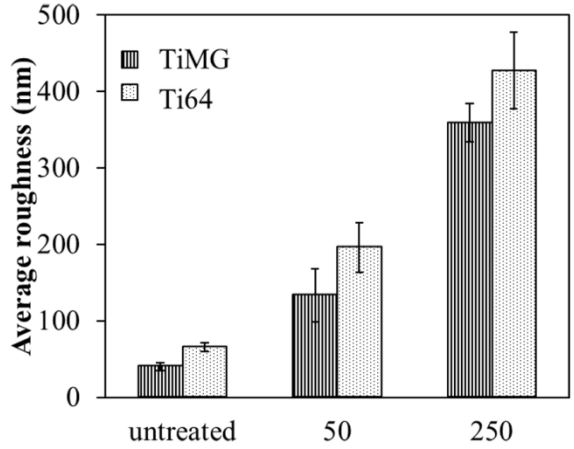

Fig.4 Arithmetic average roughness (R_a) of TiMG and Ti64 samples which untreated surface and blasted with alumina-average particle size of 50 μm and 250 μm. Error bar shows mean value ± standard deviation (n=6).

Wettability is one of the most important properties on biomaterial surface. The surface wettability is generally evaluated by the contact angle measurements [12]. The apparent contact angles of water drops on the ground and blasted samples were shown in Table 1. For the group of $Ti_{40}Zr_{10}Co_{36}Pd_{14}$ samples showed less hydrophilicity trend than the Ti-6Al-4V samples. Fig.5 demonstrated relationship between R_a and contact angle of $Ti_{40}Zr_{10}Co_{36}Pd_{14}$ and Ti-6Al-4V samples. The samples were less hydrophilic when R_a increased from 60 to 200 nm, but when R_a value was raised above 350 nm, the samples showed slight hydrophilicity. However, TiMG-untreated which had the lowest R_a showed less hydrophilicity when compared with Ti64-untreated which had similar R_a. On the other hand, many researchers [12-13] reported that rough surface could increase the wettability. However the range of our interest is narrower than the wide range of studied roughness effects. Nevertheless, in conclusion, the contact angle of all samples did not show significant different.

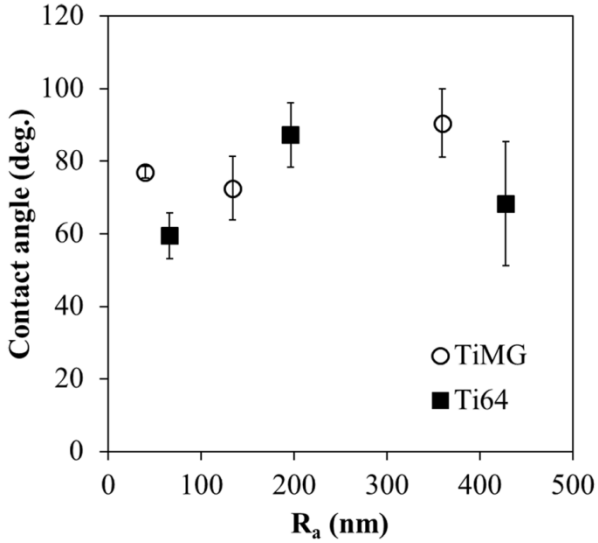

Fig.5 Relationship between Arithmetic average roughness (R_a) and contact angle of TiMG and Ti64 samples.

Conclusion

The present research investigated surface properties of $Ti_{40}Zr_{10}Co_{36}Pd_{14}$ alloy compared with Ti-6Al-4V which were blasted by alumina particles of various sizes. The greater-sized alumina particles resulted in the higher values of R_a, R_q and R_t with significant difference. Some abrasive alumina was embedded on the blasted sample. The blasted $Ti_{40}Zr_{10}Co_{36}Pd_{14}$ sample showed lower

roughness parameter values than the Ti-6Al-4V samples. This result could be explained by the hardness trend of both samples. $Ti_{40}Zr_{10}Co_{36}Pd_{14}$ sample had the hardness greater than those Ti-6Al-4V samples. The contact angle which demonstrated wettability of all samples did not show significant different in a range of R_a from 0.04 to 0.43 μm.

Acknowledgments

This research was financially supported by 2012 Overseas Reaearch Grants from The Asahi Glass Foundation, the 90th Anniversary of Chulalongkorn University Fund (Ratchadaphiseksomphot Endowment Fund) Chulalongkorn University, Government Research Budget 2014, Office of Higher Education Commission (WCU-008-HR-57) and Neuroscience of Headache Research Unit.

References

[1] Inoue, A., X.M. Wang, and W. Zhang, Developments and applications of bulk metallic glasses. Reviews on Advanced Materials Science 18 (2008) 1–9.

[2] Schroers, J., et al., Bulk Metallic Glasses for Biomedical Applications. Biomedical Materials and Devices Vol. 61 No. 9 (2009) 21–29.

[3] Kumar, G., A. Desai, and J. Schroers, Bulk Metallic Glass: The Smaller the Better. Advanced materials Vol.23 (2011) 461–476.

[4] Qin, F., et al., Ti-based Bulk Metallic Glasses for Biomedical Applications. in: Anthony N. Laskovski (Eds), Biomedical engineering – trends in materials science,. InTech., Rijeka, Croatia, 2011, 249–268.

[5] Zhu, S.L., et al., A new Ti-based bulk glassy alloy with potential for biomedical application. Materials Science and Engineering A 459 (2007) 233–237.

[6] Bagno, A. and C.D. Bello, Surface treatments and roughness properties of Ti-based biomaterials. Journal of materials science: Materials in medicine 15 (2004) 935–949.

[7] Koller, G., et al., Surface modification of titanium implants using bioactive glasses with air abrasion technologies. Journal of Materials Science: Materials in Medicine 18 (2007) 2291–2296.

[8] Aparicio, C., F.J. Gil, and J.A. Planell, Human – osteoblast proliferation and differentiation on grit - blasted and bioactive titanium for dental applications. Journal of materials science: Materials in medicine 13 (2002) 1105–1111.

[9] Aparicio, C., et al., Corrosion behaviour of commercially pure titanium shot blasted with different materials and sizes of shot particles for dental implant applications. Biomaterials 24 (2003) 263–273.

[10] Pegueroles, M., et al., The influence of blasting and sterilization on static and time-related wettability and surface-energy properties of titanium surfaces. Surface & Coatings Technology 202 (2008) 3470–3479.

[11] Suryanarayana, C., Solid-State Amorphization. in: Mechanical Alloying and Milling., Marcel Dekker., New York, 2004. 269-332.

[12] Li, H.F., et al., Osteoblast response on Ti- and Zr-based bulk metallic glass surfaces after sand blasting modification. Journal of Biomedical Materials Research Part B 100B (2012) 1721–1728.

[13] Rosales-Leal, et al., Effect of roughness, wettability and morphology of engineered titanium surfaces on osteoblast-like cell adhesion. Colloids and Surfaces A: Physicochem. Eng. Aspects 365 (2010) 222–229.

Advanced Materials Research Vol. 983 (2014) pp 141-147

doi:10.4028/www.scientific.net/AMR.983.141

Technique Research on High Strength Low Alloy Structural Steel Used in Semi-Rigid Guardrail

Yu Haixia[1, a], Zhou Zhiwei[1,b] and Zhang Hongsong[1,c]

[1]Research Institute of Highway, Ministry of Transport, No.8 Xitucheng Rd, Beijing, China, 100088

[a]hx.yu@rioh.cn, [b]zw.zhou@rioh.cn, [c]hs.zhang@rioh.cn

Key words: High strength low alloy structural steel, semi-rigid guardrail, finite element simulation, reduce guardrail penetrating, decrease steel consumption

Abstract: The technical and economic feasibility of high strength low alloy structural steel is analyzed used in highway semi-rigid guardrail. In principle of improving safety performance and reducing cost, a kind of high strength low alloy structural steel guardrail is designed. Through the finite element simulation method, the safety performance of this guardrail structure is validated to satisfy the grade-A conditions (160kJ kinetic energy). Compared with the guardrail of same protection level made of ordinary carbon structural steel, high strength low alloy structural steel guardrail can reduce the probability of penetrating when the accident vehicle impact the guardrail and decrease the accident damage, the steel consumption is above 20% lower and the construction cost can be saved as well, thus, remarkable economic and social benefits can be obtained.

1 Introduction

Highway Guardrail includes semi-rigid guardrail, rigid guardrail and flexible guardrail. Most of the structure forms of semi-rigid guardrail are W-beam barrier, thrie-beam barrier or beam-post barrier in China, the barrier material is commonly Q235 carbon structural steel. Semi-rigid guardrail is convenient to product in factory, the construction technology is simple, therefore, it is widely used in highway and plays an important role in road traffic safety protection.

With the rapid development of economy, the highway traffic characteristics have changed speedily in recent years in China, the traffic flow, vehicle speed and heavy vehicle percentage are all increased obviously, which puts forward higher demands on road safety protection level. The safety performance of some semi-rigid guardrail structures in used are limit, which are not match to the increasing protection demands. The accident that vehicle impact the guardrail and run out of the road or run into the opposite direction lane occurred frequently, the subsequent result is many injuries and fatalities, large property damages and serious social influence. To improve the protection capability of semi-rigid guardrail, the steel consumption must correspondingly be increased. So, considering the influence factors of security, economy, environmental protection, and resource saving comprehensively is the trend of sustainable development for semi-rigid guardrail.

Compared with the Q235 carbon structural steel widely used in semi-rigid guardrail material, high strength low alloy structural steel has good comprehensive mechanical properties, especially high impact toughness, superior weld ability and strong corrosion resistant capability [1]. If the key application techniques of high strength low alloy steel used in semi-rigid guardrail could be solved, and the guardrail structure could satisfy the collision protection demand, then high strength low alloy structural steel can replace ordinary carbon structural steel as guardrail material, so as to obtain higher protection performance, improved road security level, less steel consumption and lower construction cost.

2 Technical feasibility analysis for high strength low alloy structural steel used in highway semi-rigid guardrail

Mechanical properties of the material play a decisive role on safety performance of guardrail [2]. Select Q345 high strength low alloy structural steel which is common internationally as the research object.Q345 steel has well comprehensive mechanical properties, low temperature impact toughness, good welding performance and so on, it is widely used in the structure of dynamic loading [3].

For analyzing the technical feasibility that Q345 steel replace Q235 steel as the guardrail material, the static tensile experiments are completed to obtain basic performance parameters of these two kinds of material, thus to analyze their strength and ductility. The impact dynamics experiments are completed with Hopkinson bar equipment to analyze their resistance.

2.1 Static experiments The function of Semi-rigid guardrail to protect accident vehicle is mainly manifested in two aspects, on is protection and guidance function, the other is cushioning function. Protection performance depends on the intensity of guardrail material and cushioning effect depends on the ductility of guardrail material, therefore, semi-rigid guardrail material should have appropriate intensity and ductility.

Make static tensile experiments of Q235 steel and Q345 steel with a universal testing machine and analyze their intensity and ductility. The size of test specimen is shown in Fig. 1.

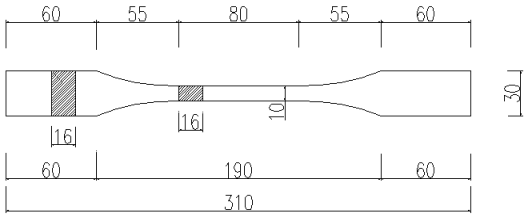

Fig. 1 Size of test specimen [mm]

The test results of static tensile experiments are shown in table 1.

Table 1 Test results of static tensile experiments

Material	Specimen number	Diameter	Tensile strength	Lower Yield strength	Elongation after fracture
		D/[mm]	R_m/[Mpa]	R_{eL}/[Mpa]	A/[%]
Q235 steel	1	5	393	237	26
	2	5	397	241	27
	3	5	402	239	27
	Average value	5	397.3	239	26.7
Q345 steel	4	5	514	346	24
	5	5	510	351	26
	6	5	513	353	25.2
	Average value	5	512.3	350	25.1

The experimental results show that the average elongation of Q235 steel is slightly higher than that of Q345 steel, both of the two materials have good ductility, but the intensity of Q235 steel is lower, the average tensile strength is 77.5% of that of Q345 steel, the average yield strength is 68.3% of that of Q345 steel. Applied to semi-rigid guardrail, the distinction of cushioning effect between the two materials is not obvious, but the capability of Q235 steel guardrail for protecting vehicle is markedly lower than that of the Q345 steel guardrail.

2.2 Impact dynamics experiments Metal material will appear strain hardening phenomenon under the action of impact load, deformation resistance ability of material will be enhanced [4]. In the collision processing of vehicle to the guardrail, the more strain hardening of guardrail material occurred, the higher ability to resist deformation obtained. Made impact dynamics experiments of Q235 steel and Q345 steel under three different impact speeds with Hopkinson bar equipment, the total counts of dynamic impact experiments is 18 times, analyze the ability to resist deformation of the two kinds of material under impact load.

The defining impact speed in Specification for Design of highway safety facilities (JTG D81-2006) consists of three kinds of speed: 60 km/h, 80 km/h and 100 km/h, converting to speed 16.7 m/s, respectively, 22.2 m/s, 27.8 m/s correspondingly. Selecting three kinds of impact loading speed as experiment speed, consists of slow speed (v_1 = 12 m/s), medium speed (v_2 = 20 m/s) and high speed (v_3 = 28 m/s), which cover the test collision speed range defined in specification mentioned above. The stress-strain curve of Q235 steel and Q345 steel under the impact load are shown respectively in Fig. 2 and the Fig. 3.

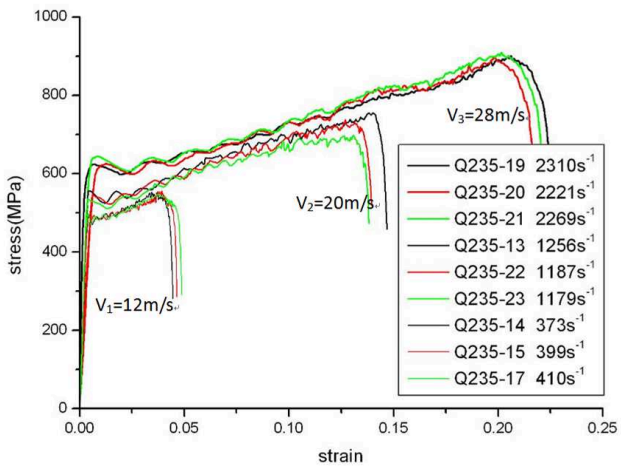

Fig. 2 Stress-strain curve of Q235 steel

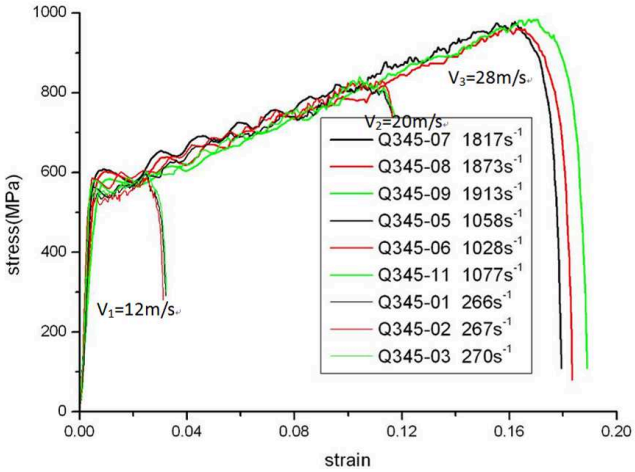

Fig. 3 Stress-strain curve of Q345 steel

The test results comparison between Q235 steel and Q345 steel are shown in table 2.

Table 2 Test results comparison between Q235 steel and Q345 steel

Material	Intensity (average) / [Mpa]	Static experiments	Impact dynamics experiments		
			v_1=12m/s	v_2=20m/s	v_3=28m/s
Q235 steel	Yield strength	239	480	550	630
	Tensile strength	397.3	530	700	880
Q345 steel	Yield strength	350	540	580	600
	Tensile strength	512.3	590	800	970

The experimental results show that the yield strength and tensile strength of the two materials are all increased obviously under impact dynamics experiments compared with the condition under static experiments. With the increase of impact loading speed, the yield strength and tensile strength of Q235 steel both grown, but for Q345 steel, there are some differences. The yield strength growth of Q345 steel is slightly, but the tensile strength growth of that is significantly. The tensile strength results of Q345 steel are all higher than that of Q235 steel obtained under three kinds of impact speed. That means the higher speed when vehicle impact guardrail, the more performance superiority for Q345 steel to prevent vehicle from penetrating guardrail compared with Q235 steel.

Above all, it is technologically feasible for using then high strength low alloy structural steel with superior material properties instead of ordinary carbon structural steel to be guardrail material,

it can improve the structure intensity of guardrail, reduce the probability of penetrating when the accident vehicle impact the guardrail.

3 Design of high strength low alloy structural steel guardrail

In order to compare with the existing guardrail structure expediently, the design of high strength low alloy structural steel guardrail retains the common post-beam structure. Considering the convenience of processing and construction, make the wave beam rail, pipe posts and hexagonal block to be the main components of new guardrail, and the structure will be optimized on size and material.

Select a kind of Q235 steel thrie- beam guardrail as a reference structure, which was validated to satisfy grade A (160kJ kinetic energy) [5]. The constructed contents of Q235 steel thrie-beam guardrail structure include:

(1) 3-mm thick thrie-beam rail made of Q235 steel.

(2) 4.5-mm thick pipe post made of Q235 steel, the diameter of post is 114 mm ,the distance of adjacent post is 2m and the depth of post under the ground is 1100mm.

(3) 4.5-mm thick hexagonal block made of Q235 steel with length of 400mm [6].

Design a new thrie-beam guardrail structure made of Q345 steel, the constructed contents of it include:

(1) 2.5-mm thick thrie-beam rail made of Q345 steel.

(2) 4.5-mm thick pipe post made of Q235 steel, the diameter of post is 140 mm ,the distance of adjacent posts is 4m and the depth of post under the ground is 1100mm.

(3) 4-mm thick hexagonal block made of Q345 steel with length of 400mm.

The new design make Q345 steel as material of thrie-beam rail and block and reduce the material thickness. For beam and block, the change of material thickness can be realized easily just by adjusting the existing mould space during new guardrail processing. But for the post, because of different processing craft, it will spend large cost to build a new mould to realize the change of material thickness. Considering this factor, the design of thickness and material for post did not changed. The diameter and distance of adjacent posts is increased.

The two guardrail structures are shown in Fig. 4 and Fig. 5.

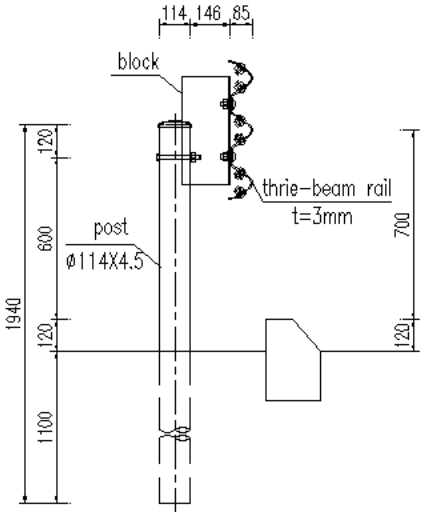

Fig. 4 Thrie-beam guardrail made of Q235 steel

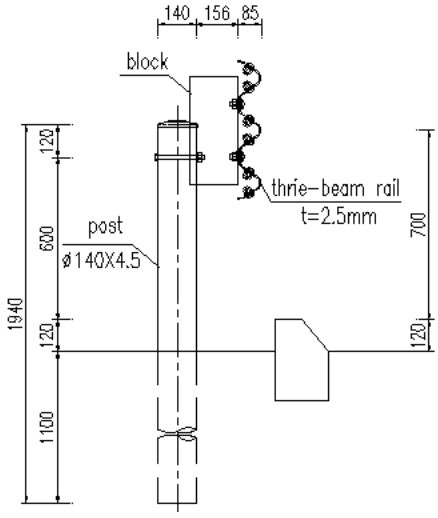

Fig. 5 Thrie-beam guardrail made of Q345 steel

4 Safety performance verification

The finite element simulation method is adopt to verify the safety performance of thrie-beam guardrail made of Q345 steel, the collision test conditions of grade-A is shown in table 3.

Table 3 Collision test conditions of grade-A

Vehicle Type	Vehicle Mass [t]	Impact Speed [km/h]	Impact Angle [°]	Kinetic Energy [kJ]
Car	1.5	100	20	-
Bus or truck	10	60	20	160

4.1 Collision test with car The vehicle trajectory of the car during impacting is shown in Fig. 6.

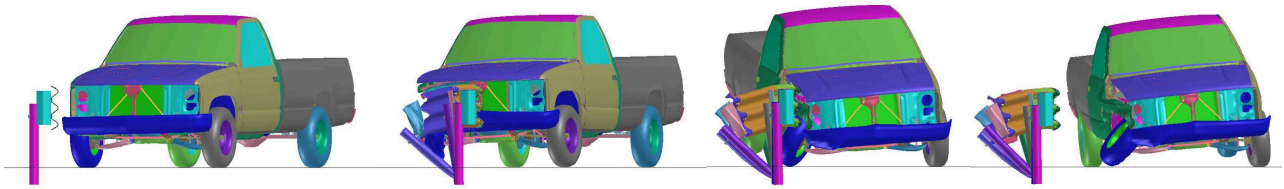

a) Initial time **b) Head impact** **c) End impact** **d) Run off**

Fig. 6 Vehicle trajectory of the car during impacting

Simulation results show that the thrie-beam guardrail made of Q345 steel has a good performance of protection and redirection. The test car doesn't penetrate, under-ride, or over-ride the test guardrail and remains normal driving posture. The maximum of occupant ride-down acceleration is 12.16g, the exit angle is 11.6°and the maximum of dynamic deflection is about 580mm. The guardrail deformation and stress nephogram crashed by car is shown in Fig. 7.

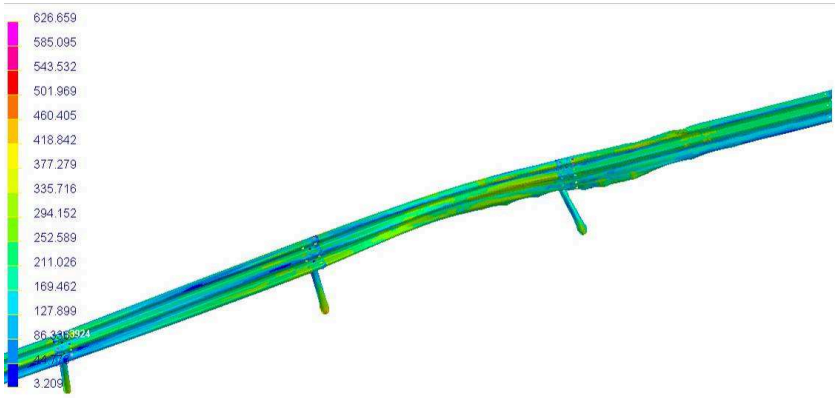

Fig. 7 Deformation and stress nephogram of guardrail crashed by car

4.2 Collision test with bus The vehicle trajectory of the bus during impacting is shown in Fig. 8.

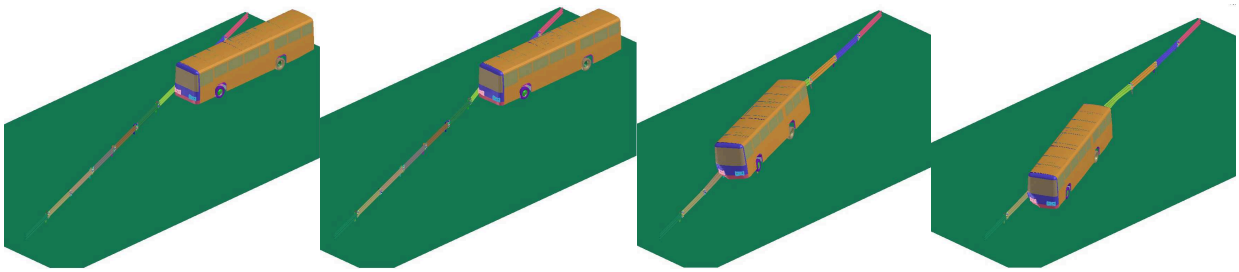

a) Initial time **b) Head impact** **c) End impact** **d) Run off**

Fig. 8 Vehicle trajectory of the bus during impacting

Simulation results show that the test bus doesn't penetrate, under-ride, or over-ride the test guardrail and remains normal driving posture. The exit angle is 5.3°and the maximum of dynamic

deflection is about 870mm. The guardrail deformation and stress nephogram crashed by bus is shown in Fig. 9.

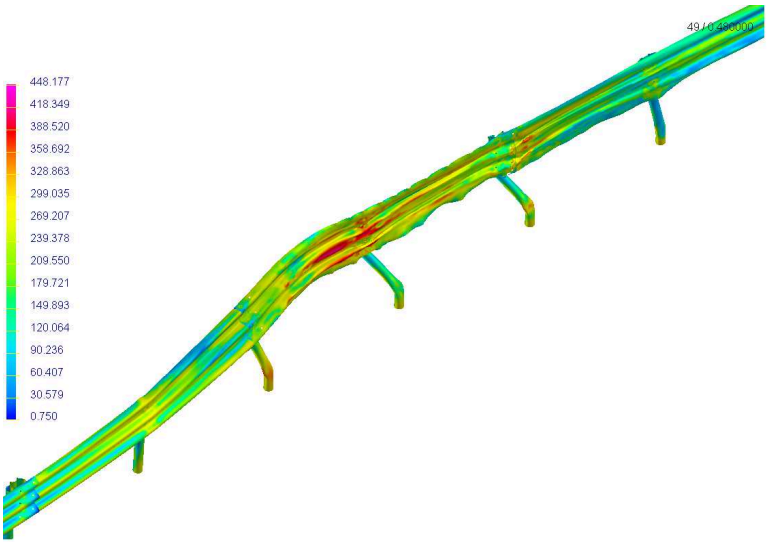

Fig. 9 Deformation and stress nephogram of guardrail crashed by bus

4.3 Simulation results analysis Simulation test results indicate that the thrie-beam guardrail made of Q345 steel can satisfy the protection demand of grade-A, all the evaluation index results meet the criteria limits of Evaluation Specification for Highway Safety Barriers (JTG/T F83-01-2004).

The comparison of simulation test results between thrie-beam guardrail made of Q345 steel and Q235 steel is shown in table 4.

Table 4 Comparison of simulation test results

		Q345 steel thrie-beam guardrail	Q235 steel thrie-beam guardrail
Kinetic Energy [kJ]		160	160
Car	Vehicle trajectory	normal	normal
	Maximum ride-down acceleration [g]	12.16	14.3
	Exit angle [°]	11.6	11.2
	Maximum dynamic deflection [mm]	580	592
Bus	Vehicle trajectory	normal	normal
	Exit angle [°]	5.3	7.4
	Maximum dynamic deflection [mm]	970	892

The maximum of occupant ride-down acceleration show that thrie-beam guardrail made of Q345 steel has an advantage of protecting occupant and reducing injuries. The deformation resistance capability of Q345 steel guardrail with 4m-distance post is similar to that of Q235 steel guardrail with 2m-distance post.

5 Economic analysis

The production process of high strength low alloy structural steel is similar to carbon structural steel, therefore, the price of the two materials is similar as well. The market price of Q345 steel is about CNY6400 /ton and the market price of Q235 steel is about CNY6000 /ton. The economic contrast of Q345 steel thrie-beam guardrail and Q235 steel thrie-beam guardrail is shown in table 5.

Table 5 Economic contrast of the two guardrails

	Q345 steel thrie-beam guardrail	Q235 steel thrie-beam guardrail
Q235 steel consumption [kg/m]	34.8	8.2
Q345 steel consumption [kg/m]	0	17.2
The total steel consumption [kg]	34.8	25.4
Cost of guardrail [CNY/m]	208.8	159.28

The economic contrast results show that, in condition of same kinetic energy, the Q345 steel thrie-beam guardrail can reduce steel consumption about 27.01% and decrease cost about 23.72% compared to Q235 steel thrie-beam guardrail.

6 Conclusion

Through static tensile experiments and impact dynamics experiments, the technical feasibility of high strength low alloy structural steel is analyzed used in highway semi-rigid guardrail. In principle of improving safety performance and reducing cost, a kind of thrie-beam guardrail made of Q345 steel is designed. Through the finite element simulation method, the safety performance of this guardrail structure is validated to satisfy the grade-A conditions (160kJ kinetic energy), which is defined in Specification for Design of highway safety facilities (JTG D81-2006). Compared with the guardrail of same protection level made of ordinary carbon structural steel, high strength low alloy structural steel guardrail can reduce the probability of penetrating when the accident vehicle impact the guardrail and decrease the accident damage, the steel consumption is above 20% lower and the construction cost can be saved as well, thus, remarkable economic and social benefits can be obtained.

References

[1] Standardization Administration of the People's Republic of China, High strength low alloy structural steels(GB/T 1591-2008), China Zhijian Publishing House, Beijing (2008).

[2] American Association of State Highway and Transportation Officials Executive Committee, Manual for Assessing Safety Hardware 2009, AASHTO, Washington DC (2009).

[3] Pocock G, High strength steel use in Australia, Japan and the US, The Structural Engineer, (2006), 84(21): p.27-30.

[4] Shi G, Bijlaard F S K, Finite element analysis on the buckling behaviour of high strength steel columns, Proceedings of the Fifth International Conference on Advances in Steel Structures, Singapore (2007).

[5] Ministry of Transport of the People’s Republic of China, Specification for Design of Highway Safety Facilities(JTG D81-2006), China Communications Press, Beijing (2006).

[6] Yang Manjuan, Zhang Hongsong, Crashworthiness Enhancing Technique for W-beam Barriers, The Fourth International Conference on Transportation Engineering, Cheng Du, China, (2013), p.476-481.

Advanced Materials Research Vol. 983 (2014) pp 148-151

doi:10.4028/www.scientific.net/AMR.983.148

The effect of Co/Pd MgO supported catalyst calcination temperature on the yield and morphology of CNTs via Methane decomposition

Ghazaleh Allaedini[1], Siti Masrinda Tasirin[1], Jaafar Sahari[2], Meor Zainal Meor Talib[2]

[1]Department of Chemical and Process Engineering, Universiti Kebangsaan Malaysia, 43600 Bangi, Selangor, Malaysia

[2]Fuel Cell Institute, Universiti Kebangsaan Malaysia, 43600 Bangi, Selangor, Malaysia

*Corresponding author email: jiny_ghazaleh@yahoo.com

Keywords: catalyst, Co/Pd bi metallic Nano particles, Nano carbon Tubes, yield.

Abstract

Co/Pd bi metallic catalyst supported on MgO has been prepared by sol gel method, at different calcination temperatures of 250 and 550 C. They were introduced in to the reactor for 5 hrs of reaction. The CNTs were collected. The obtained CNTs were characterized by XRD and SEM and the yield was observed. It has been concluded that the catalyst calcined at higher temperature will lead to higher yield and more uniform and smaller diameter CNTs.

Introduction

The discovery of CNT was in 1991 [1] since their discovery by Ijima, the CNT and the other structures of Carbon has attracted many researches for their research topic. Carbon can have various structures such as Graphite, Diamond, Fullerenes, Carbon Nano Tubes in form of Single wall, Multi wall and double wall, Graphene and also Carbon Nano fibers. [2]

CNT has many superior properties such as mechanical, electronics, optoelectronic and chemical, and that's the reason it has attracted many researches in industry and as well as academic purposes. They have so many superior applications in electronics , sensors , hydrogen storage, mechanical and field emission ,[3] super capacitates, semi conductors [4] and so many other commercial and industrial application review recently by Volder et al [5] .CNT can be produced by Arc discharge, laser ablation, electrolysis, from bulk polymer, low temperature solid pyrolysis, vertical/horizontal furnace, CVD (Chemical Vapor Deposition), PECVD (Plasma Enhanced Chemical Vapor Deposition) [6] .In the present paper the experiments are carried out in a CVD method since this method is better from the aspects of product purity and its large scale production [7]

Methodology:

In the literature there are so many reports of using metallic catalysts and Co and Pd have always been proven to be among active catalysts. Bethune et al used bi metallic catalysts with cobalt and they could grow SWCNTs and they concluded that cobalt plays an important role in formation of SWCNTs [8]. Rasesco et al also produced SWNTs by Co-Mo bi metallic catalysts. [9] We have used Co because Fe, Co, Ni have high solubility of carbon in these metals at high temperature and also high diffusion rate [10] They also have stronger adhesion with growing CNT [9] In addition to transition metals, the metals of other groups such as Au, Ag, Pt, Pd have been used to produce the CNT efficiently and with high yields. [11] Therefore because of these reasons the combination of Co and Pd have been used as a bi metallic catalyst in this paper. In the case of the support the Mgo has been used among other supports such as Al_2O_3, SiO_2, Zeolite etc, because it has been reported that MgO is easily dissolvable and easier to purify in CNT. [12]

But one of the factors which have been emphasized in the literature is the effect of temperature when preparing the catalyst [13-14].That is why in this paper the effect of catalyst calcination temperature has been investigated on morphology and yield of Carbon Nano Tubes.

Experiments

In this experiment $Co(No_3)_3.9H_2O$, $Pd(Br)_2(MeCN)_2$ which was heated were dissolved in distilled water , they were stirred while heating at 100 C, then they were sonificated for 1 hr, The metal contents was kept at 6 wt% and the molar ratio of co-pd was 1:2. They were dried at 100 C and calcined at 500. The Co-Pd catalysts then were impregnated at MgO with an aqueous solution. They were stirred followed by drying in oven at 100 C and Calcination at 250 and 550 C and were named as samples 1, and 2.In each experiment 200 mg of the catalysts were placed in a reactor, heated in Ar up to 50 C when purged and then up to 800 C and after the temperature was stabilized the methane was introduced with a flow rate of 100 cm/m3 for 5 hrs.

Results and discussion

As shown in Figure 1 , the particle size were determined by XRD and by an analysis of line broading at 2θ for the supported catalysts at sample1= 22,40,66,73 and for sample 2= 25,43,68, 75 respectively and it has found that the smaller uniform and more uniform Carbon Nano tubes have been grown from catalysts in sample 3 which were calcined at 550 , when comparing it with the 250C temperature ones which have a broader diameter and it shows that the growth had different structures and only few of them are regular in shape. The obtained diameter for the MWCNTs calcined catalyst at 550 C was 14.2 nm, however for the 250 C calcined catalyst was 18.6 nm.

The SEM result (Figure 2) shows that multi wall carbon nano tubes are presence and the size distribution is homogenous just for the higher calcined temperature catalysts and for the 250 C calcined catalysts the obtained CNTS there exists a different size distribution.

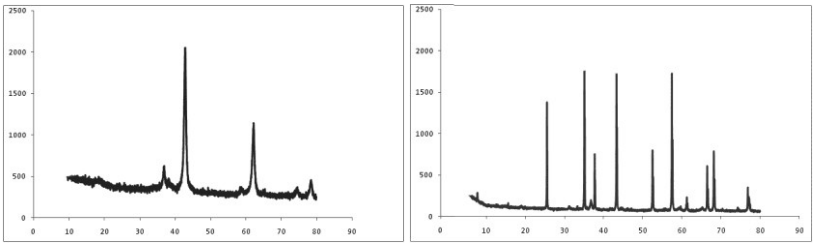

(a) (b)

Figure-1- SEM result of (a) CNT obtained by high temperature calcined catalyst (550 C) and (b) lower temperature catalyst(250 C)

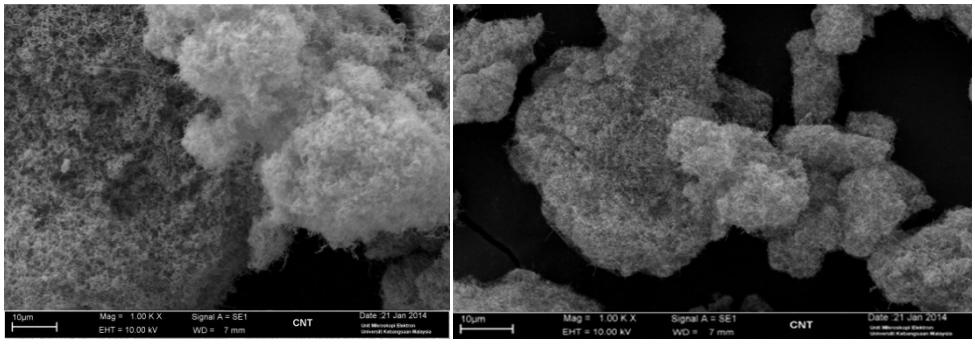

(a) (b)

Figure-2 SEM result of (a) CNT obtained by higher calcined temperature catalyst (550 C) and (b) lower temperature catalyst(250 C)

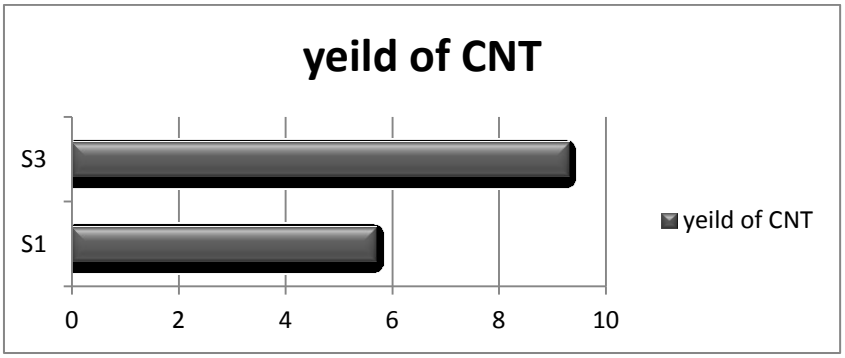

Figure- 3 - The yield of CNT obtained from 20 g of catalyst loading for samples 1(S1) at 250 C calcination temperature and sample 2(S2) at 550 C calcination temperature in a 5 hr reaction

Conclusion

Generally the CNTs obtained from the reaction which was carried out by sample 1 which was at lower calcined temperature of 250 C are a bit heterogeneous in diameter and size and the yield is so low .The bi metallic supported Co-Pd/MgO catalyst calcined at higher temperature of 550 C leads to the higher yield of CNT with a desired shape and structure and these facts are in accordance with the other researches done on the comparison of calcination temperature. [13]

References

[1] S. Iijima, Nature 354, 56 (1991)

[2] C. Liu, Y. Y. Fan, M. Liu, H. T. Cong, H. M. Cheng, M. S. Dresselhaus, Science 286, 1127 (1999) 404, 405

[3] Pulickel M. Ajayan1 and Otto Z. Zhou2, M. S. Dresselhaus, G. Dresselhaus, Ph. Avouris (Eds.): Carbon Nanotubes,Topics Appl. Phys. 80, 391–425 (2001) Applications of Carbon Nanotubes

[4] Z. Wu et al., Transparent, conductive carbon nanotube films. Science 305, 1273 (2004).

[5] Michael F. L. De Volder, ,Sameh H. Tawfick,,Ray H. Baughman,A. John Hart Carbon Nanotubes: Present and Future Commercial Applications ,SCIENCE VOL 339 ,2013

[6] B.Bhushan, Springer handbook of Carbon Nano tubes,introduction to nanotechnology, 3r edition, 2010 ,pp 62-68

[7] Manyamas S, Kojima R, Myanchi Y, Chiashi S, and Kohno M, 2002, low temperature synthesis of high purity SWCNTS from alcohol, chem. Phys let, 360, 229

[8] D. S. Bethune, C. H. Kiang, M. S. De Vries, G. Gorman,R. Savoy, J. Vazquez and R. Beyers, "Cobalt-CatalysedGrowth of Carbon Nanotubes with Single-Atomic-LayerWalls," Nature Vol. 363, 1993, pp. 605-607

[9] Irurzun Veronica M, Yongqiang Tan, and Daniel E. Resasco, Sol-Gel Synthesis and Characterization of Co-Mo/Silica Catalysts for Single-Walled Carbon Nanotube Production, Chem. Mater. 2009, 21, 2238–2246

[10] Kumar, M. &Ando, Y. (2010). Chemical Vapor Deposition of Carbon Nanotubes: A Review on Growth Mechanism and Mass Production. Journal of Nanoscience and Nanotechnology 10: 3739-3758.

[11] Ding F., Bolton K. and Rosen A. (2004). J. Chem. Phys. B 108, 17369-17377

[12] Hue P Wang, Liu Y, Wang B, Zhu . D, synthesis of SWNTs using MgO, Synthesis metal, 135-136, 833, 2003

[13] Siang-Piao Chai, Sharif Hussein Sharif Zein, Abdul Rahman Mohamed, he effect of catalyst calcination temperature on the diameter of carbon nanotubes synthesized by the decomposition of methane, Volume 45, Issue 7, June 2007, Pages 1535–1541

[14] Mukul Kumar,CVD of CNT A review on growth mechanism and mass production, J. Nanosci. Nanotechnol. 2010, Vol. 10, No. 6

Advanced Materials Research Vol. 983 (2014) pp 152-155

doi:10.4028/www.scientific.net/AMR.983.152

The structure and properties of NBR / Recycled Polytetrafluoroethylene(R-PTFE) composites

Wenwen Chen[1,a], Changlin Cao[2,b], Yi Zhang[1,c],Liren Xiao[2,d], Qingrong Qian[1,e*], Qinghua Chen[1,f*]

[1]College of Environmental Science and Engineering, Fujian Normal University, Fuzhou 350007, China.

[2] College of Materials Science and Engineering, Fujian Normal University, Fuzhou 350007, China.

[a]chenwenwen0723@sina.com, [b]charleycao2006@yahoo.com.cn, [c]zhangyi@slep.net.cn, [d]xlr1966@126.com, [e]qrqian@fjnu.edu.cn, [f]cqhuanr@fjnu.edu.cn

Key words: Waste PTFE, Recycling, NBR/R-PTFE composites

Abstract. The structure and properties of NBR and its composites coupled with different particle size of recycled polytetrafluoetylene（R-PTFE） are investigated. The results show that R-PTFE has a positive effect on NBR enhancing the curing properties of materials, mechanical properties, solvent resistance of NBR when the particle size of R-PTFE less than 200 mesh. However, when it is 200 mesh, R-PTFE is not easily dispersed in the NBR matrix, resulting in decreasing the properties of NBR/R-PTFE composites.

Introduction

Polytetrafluoroethylene (PTFE) is widely applied in the fields of chemical, mechanical, transportation, national defense due to its excellent chemical resistance, heat resistance, wear resistance, and self-lubricating properties[1]. The production of PTFE reached more than 30 million tons in 2012, and it will grow at an annual rate of 6% [2]. With increasing of PTFE dosage, it generates a lot of waste PTFE. However, the waste PTFE is difficult to be reprocessed, degraded, crushed, which is not beneficial for recycling. This not only causes a serious waste of resources, but also brings a heavy burden on the environment. What's more, the burning of waste PTFE will produce toxic gases such as hydrogen fluoride , which are harmful to the environment [3,4]. Therefore, developing the recycling techniques of waste PTFE has important concerning environmental and economic effects [5].

Nitrile rubber (NBR) prepared by acrylonitrile and butadiene is an elastomeric polymer [6]. With the rapid development of the oil industry and the automotive industry, ordinary NBR has been difficult to fully meet the requirements of the application .

In this paper, the recycled PTFE particle (R-PTFE) was added to NBR, and the effects of the different particle size of R-PTFE on the structure and properties of NBR / R-PTFE composites were investigated.

Experimental

Materials. The waste PTFE was supplied by Xiamen Borun Fluoride Materials Technology Co.,LTD. NBR, under trade name Perbunan, was supplied by Bayer AG (Germany) with acrylonitrile content of 34 + 1%, Moony viscosity (ML: 1 þ 4) at 100 ^{o}C, 4. Dicumyl peroxide (DCP) was offered by Aladdin Chemistry Co.,LTD.

The experimental formulations. The rubber formulations are shown in Tab.1.

Tab.1 Rubber formulations of NBR and NBR/R-PTFE composites.

Formulation	1	2	3	4	5	6
NBR3345(phr)	100	100	100	100	100	100
R_{PTFE}(mesh)	0	40	80	120	160	200
PTFE(phr)	0	5	5	5	5	5
DCP(phr)	1.5	1.5	1.5	1.5	1.5	1.5

Preparation of NBR / R-PTFE composites. The samples were carried out in an open two-roll mill at room temperature. Then the blends were left about 24 h before compression-molded under a pressure of about 4-10 MPa ,at 170 ^{o}C for about 2.0mm thick, T_{90} was set as curing time.

Characterization. An rheometer model (UC-2030,Taiwan) was used for measuring the curing characteristics of the blends at 170 ^{o}C. The morphology of the composites was investigated by scanning electron microscope (SEM) (JEOL JSM-7500F) at an accelerating voltage of 5 KV. All the samples were fractured in liquid nitrogen and then sputter-coated with gold before observation. The sheets were cut into dumbbell-shaped specimens for the evaluation of the mechanical properties according to Chinese Standard GB/T529-2009. Solvent resistance properties were tested through dichloromethane as the solvent, using the corresponding quality of two samples (Wa) about 40~50mg. After swelling 7 days in the solvent, weight the mass of two samples (Wb). Then, the swelling index(SI) was calculated by equation(1)

$$SI=W_b/W_a. \quad (1)$$

Results and Discussion

Curing characteristics. The curing characteristics of NBR/R-PTFE composites are shown in Tab. 2 and Fig.1. The difference between maximum and minimum torque (M_H-M_L) can be taken as a measure of the cross-link density[7]. It is shown that T_{90} reduces and ΔM increases with the addition of R-PTFE. This is because that R-PTFE has a reinforcing effect on NBR and the interaction between R-PTFE and NBR produces more physical cross-linking in the three dimensionally crosslinked networks. With the increasing particle size of R-PTFE, ΔM increases gradually, because the surface area and the interaction with NBR are increased. However, ΔM decreases when the particle size of PTFE is 200 mesh, which is probably due to the aggregation of R-PTFE in a high content.

Tab.2 Curing parameters of NBR/R-PTFE.

Formulation	T_1(s)	T_{90}(s)	M_L(dN.m)	M_H(dN.m)	ΔM(dN.m)
1）0 mesh	24	181	1.33	21.57	20.24
2）40 mesh	22	171	1.15	23.21	22.06
3）80 mesh	22	169	1.36	23.62	22.26
4）120mesh	21	167	1.58	24.62	23.04
5）160mesh	21	160	1.53	26.65	25.12
6）200mesh	21	167	1.43	23.98	22.55

CRI: M_L: minimum torque, M_H: maximum torque,T_1:scorch time,T_{90}:optimum cure time.

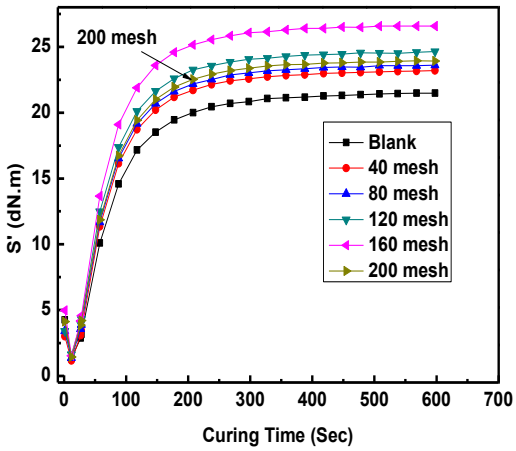

Fig.1. The curing characteristic curve of NBR and NBR/R-PTFE.

Morphology analysis. Fig.2 shows the SEM micrographs of NBR/R-PTFE composites with the different particle size of R-PTFE. It can be seen that R-PTFE particles disperse more uniformly with an increasing particle size. However, as the particle size of R-PTFE increases to 200 mesh, the R-PTFE particles agglomerate significantly in NBR matrix, which may be due to the increase of surface area and surface energy of R-PTFE particles.

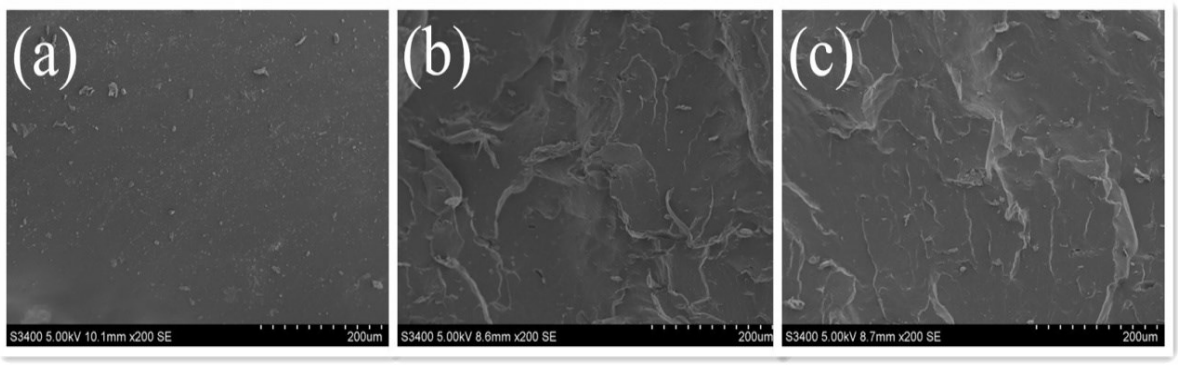

Fig.2 SEM micrographs of NBR/R-PTFE composites with the different particle size of PTFE: (a) 40mesh, (b) 160 mesh, (c) 200 mesh.

Mechanical properties. The mechanical properties of the NBR/R-PTFE composites are shown in Fig.3. It can be seen that the tensile strength of NBR/R-PTFE composites is less than that of pure NBR when the particle size of R-PTFE is 40 mesh. It is because that larger particle size of R-PTFE causes a decrease in the stress concentration and the tensile strength also decreases. In addition, with the increase of the particle size of R-PTFE, the tensile strength of NBR/R-PTFE composites increases, but the elongation at break changes inconspicuously. This is due to that the larger surface area of R-PTFE enhances the interaction with NBR. However, as the shown in Fig.3, the tensile strength of NBR/R-PTFE composites decline when the particle size is 200 mesh, which is due to the fact that R-PTFE is easy to reunite in NBR matrix.

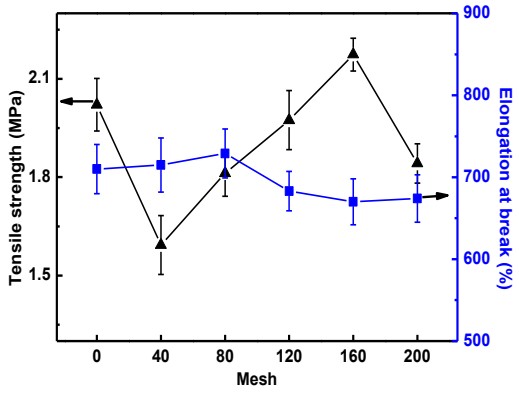

Fig.3 The mechanical properties of NBR and NBR/R-PTFE composites

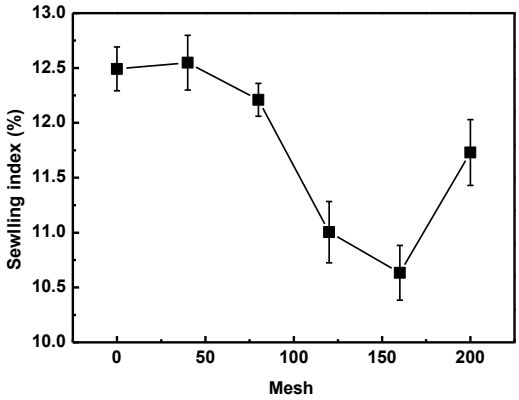

Fig.4 The swelling index of NBR and NBR/R-PTFE composites

Solvent resistance. Fig.4 shows the swelling index of NBR and NBR/R-PTFE composites. As it can be seen from Figure 4, the swelling index of NBR/R-PTFE composites gradually decreases with the increase of the particle size of R-PTFE. It is because that R-PTFE has excellent chemical resistance properties, leading to an improved resistance to erosion for NBR/R-PTFE composites. After adding R-PTFE with particle size of 200 mesh,the swelling index of NBR/R-PTFE increases, mainly because of the reunion of R-PTFE and the dcreasing of the specific surface area of NBR/R-PTFE composites.

Conclusion

The structure and properties of NBR/R-PTFE composites are investigated. It is found that R-PTFE can have a good modification effect on NBR, what's more the curing properties of materials, mechanical properties and solvent resistance are enhanced. The particle size of R-PTFE has a significant impact on the performance of NBR/R-PTFE composites. When it is less than 200 mesh, the properties of the composites increased gradually, but when it is 200 mesh, R-PTFE is easy to aggregate in the NBR matrix and the properties of NBR/R-PTFE composites decrease.

Reference

[1] Zhanxiong Li,Biaobing Wang , Xiang Ouyang. Heat Resistance Polymer, Chemical Industry Press, Beijing,2007.Reference to a chapter in an edited book: 215-247.
[2] YanwenDeng, Xiaoping Zhang ,BoYang. The recycling technology of PTFE[J].Plastic Industry, 2005, 33(6): 64-66.
[3] Fenghua Zhou.Plastic Recyling, Chemical Industry Press, Beijing,2005.Reference to a chapter in an edited book: 225.
[4] Jing Z, Baohe W, Dongzhi L. Synthesis of 1, 2-diiodotetrafluoroethane with pyrolysis gas of waste polytetrafluoroethylene as raw material[J]. Green Chem., 2013, 15(4): 1042-1047.
[5] Khan M S, Heinrich. PTFE-based rubber composites for tribological applications[J]. Advance polymer science, 2011, 239, 249-310.
[6] Suizhi Xie. Handbook of Rubber Industry(1): Raw rubber and reinforcing materials,Chemical Industry Press, Beijing,2001.Reference to a chapter in an edited book: 389.
[7] Arroyo M, Lopez-Monchado MA and Herrero B. Organo-montmorillonite as substitute of carbon black in natural rubber compounds. Polymer 2003; 44: 2447.

Advanced Materials Research Vol. 983 (2014) pp 156-160

doi:10.4028/www.scientific.net/AMR.983.156

Microstructure and Direct Measured Micro-strain by TEM of Hot Iso-static Pressed Alumina-Titanium Carbide (Al_2O_3-TiC) Composite

SineenartThumsoontorn[1,a], Surasak Kuimalee[2,b] , Budsabong Kuntalue[3,c]
Suphakit Pintasiri[4,d] and Boonrat Lohwongwatana[1,e*]

[1]Innovation Metal Research Unit, Department of Metallurgical Engineering,
Faculty of Engineering, Chulalongkorn University, Bangkok, Thailand. 10330

[2]Department of Industrial Chemistry and Textile Technology,
Faculty of Science, Maejo University, Chiang Mai, Thailand, 50290

[3]The Electron Microscopy Research and Service Center (EMRSc),
Faculty of Science, Chiang Mai University, Chiang Mai, Thailand, 50200

[4]Western Digital (Thailand) Co.,LTD, Ayutthaya, 13160

[a]sineenart.th@gmail.com, [b]skuimalee@gmail.com, [c]budsabong.em@gmail.com,
[d]suphakit.pintasiri@wdc.com, [e]boonrat@gmail.com

Keywords: HIP, Al_2O_3-TiC composite, AlTiC, Micro-strain, FIB-TEM sample preparation

Abstract. Alumina-titanium carbide composite (Al_2O_3-TiC) is one of advance ceramic matrix composites (CMC) that have been used in machining tool and tribology application because of its excellent mechanical properties. Powder processing is often a chosen method to produce this family of material, i.e. hot pressed (HP), hot iso-static pressed (HIP), and pressure-less sintering (PS). These manufacturing techniques convert sub-micron powder into dense bulk component. Al_2O_3-TiC composite has been prepared by HIP process, containing 65%vol Al_2O_3 and 35%vol TiC. The powders were pressured and sintered at temperature between 1250˚C - 1650˚C. Thermal residual stress from Al_2O_3-TiC manufacturing process is conventionally unavoidable. The aim of this study is to investigate the microstructure of HIPped Al_2O_3-TiC composite and its residual micro-strain using transmission electron microscopy (TEM) with selected area electron diffraction pattern (SADP) analysis. The Al_2O_3-TiC composite was prepared by high-precision machining/grinding processes then focus ion beam milling process was used to section the TEM lamella. Microstructures, grain size and phases were determined by TEM and X-ray diffractometry (XRD). Micro-strains of {200}TiC, {111}TiC , {220}TiC and {012}Al_2O_3 were investigated by SADP (Selected Area Diffraction Pattern). Our result revealed there is approximately 0.01 compressive strains distributed in Al_2O_3-TiC composite.

Introduction

In cutting tools and wear resistance application, alumina (Al_2O_3) ceramic with dispersed carbide composites, such as WC, SiC, NbC and TiC are used in many engineering applications. In hard disk drive, Al_2O_3-TiC composite (AlTiC) has been used as substrate in slider (reader-writer). Its hardness is ranked among the highest values for other engineering composite materials. The two materials are also known for small thermal coefficient of expansion mismatch. The outstanding properties are results from fine grained microstructure and fully dense density [1] as the AlTiC wafer was obtained from powder manufacturing technique such as hot pressed (HP), hot iso-static pressed (HIP) and pressure-less sintering (PS) [1-3].

Hot iso-static pressing (HIP) process enables the production of fully densed, near net shape components. HIPped Al_2O_3-TiC composite containing 35% volume fraction of TiC were produced at about 1250-1650 ˚C while 20-50 MPa of iso-static pressure was applied *in-situ* [3]. In our particular case, HIPped AlTiC process involved high temperature and high pressure. Our

investigation revealed the residual stress as found in AlTiC reader-writer which could be the result of built-in residual stress from HIP process. Additionally residual stresses could be induced in subsequent manufacturing processes. In particular, hard disk drive manufacturing requires high-precision machine/grinding processes that remove materials by applying pressure and deformation. In our investigation, the remaining residual stress inside the sample was a result of aggregate effects from both thermal and mechanical processes. However, it is possible to produce macro-stress free sample by performing thermal treatment process for stress releasing [4-7]. This work focused on investigation of microstructure and magnitude of aggreagte micro-strain in HIPped Al_2O_3-TiC composite with 35%TiC volume fraction in Al_2O_3 matrix by TEM and electron SADP analysis.

Material and Experiment

Material and sample preparation

As-received Al_2O_3-TiC wafers were prepared by cutting AlTiC wafer and slicing into bar shape. The bar dimension was 46 mm (length) x 0.85 mm (width) x 0.19 mm (thickness). Back and front side of 46 mm x 0.85mm surfaces of the bar were ground and lapped. Focus ion beam with lifted off technique was used to prepare samples for TEM investigation [8].

For sample preparation for the TEM, the lifted off technique was performed using focus ion beam (FEI Helios dual beam FIB/FESEM**)** with two beam systems, Ion beam (I-Beam) and Electron beam (E-beam). Lapped surface of the bar were coated with 2 layers of materials: the first layer was 0.8 μm Pt by E-beam and then the second layer was 1.2 μm Pt layer by I-beam as shown in Fig 1(a). Then FIB milling started to cut deep into lapped surface of the slider surface to form 3D thin films with 5 different thicknesses: 40, 60, 80, 100 , 120 nm. Thin film samples were then cut, lifted off, and then welded onto copper omniprobe grid. Finally, thin film specimen dimension was 10um (width) x 9um (height) x 40nm to 120nm (thickness) as illustrated in Fig 1(b).

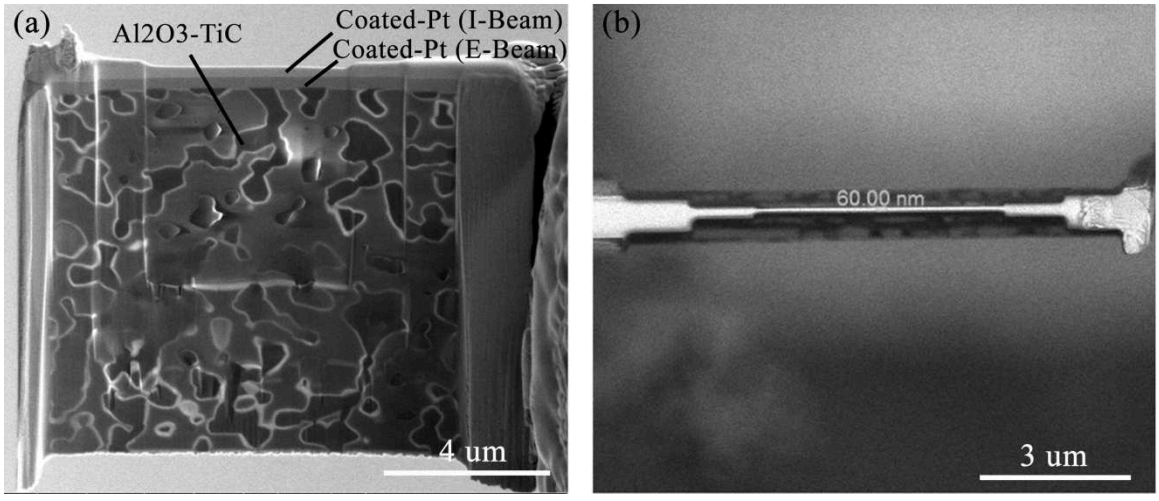

Fig 1. Focus ion beam etched Al_2O_3-TiC sample for TEM study (a) side view (b) top view.

Characterization

JOEL 2100 TEM operated at 200 keV was use to investigate the microstructure of The Al_2O_3-TiC composite. Bright field (BF) TEM image and spot energy dispersive x-ray spectroscopy (EDS) were used for phase identification. Lattice spacing of TiC and Al_2O_3 phases were determined using SADP with beam size diameter at approximately 3-5 nm. Image J software was used for measuring of distance and angles in reciprocal space. Additionally, X-ray diffraction technique with Cu-Kα source would be used to confirm crystal structure and composition.

Lattice strains in each phase were calculated from dissimilar between calculated lattice spacing and JCPDF database of interested planes. Diffraction patterns of major zone axis were

collected in order to quantify micro-strain in each plain. The Al_2O_3-TiC composite was found to have homogeneously distributed microstructure [3] with an average micro-strain of all samples. As an example, results of the sample with 60 nm thickness are discussed here for micro-strain analysis of specific planes.

Result and discussion

Microstructure

TEM image (fig.2) presented Al_2O_3-TiC composite with homogeneous submicron-level grain distribution. The microstructure consisted of two different grains types, namely TiC and α-alumina phases were confirmed using SADP as given in Fig. 3(a) and 3(b), respectively. TiC has a face center cubic (FCC) lattice type with space group $Fm\bar{3}m$ and α-alumina has a trigonal lattice type with space group $R\bar{3}c$, which corresponding to the JCPDF file number 32-1838 and 89-3072, respectively. TiC grains were usually located at Al_2O_3 grain boundary and triple junctions. It could be implied that TiC played an important role in pinning effect and inhibiting grain growth of alumina during HIP process [2].

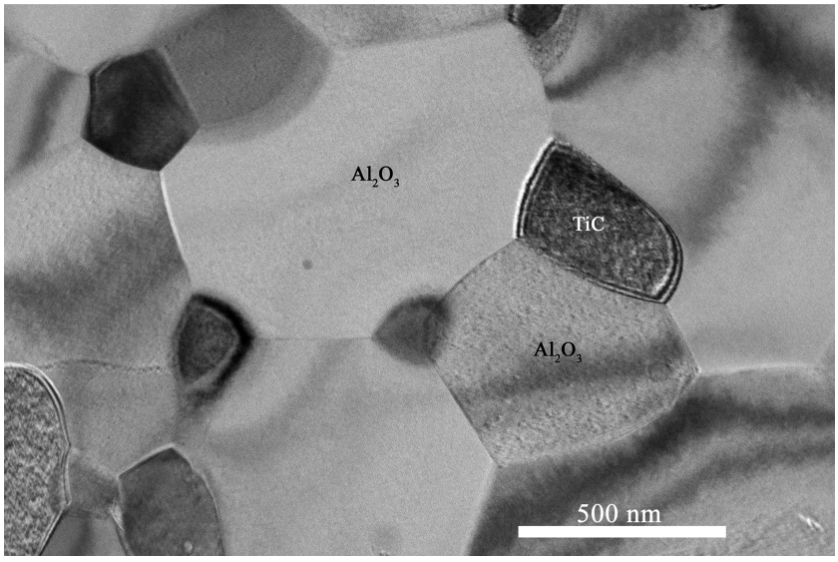

Fig 2. Microstructure of Al_2O_3-TiC composite materials (60 nm thin film sample)

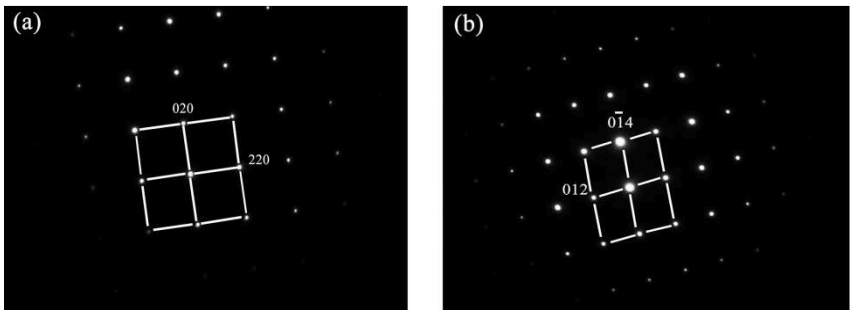

Fig 3. Diffraction patterns of (a) TiC at $[00\bar{1}]$ zone axis, and (b) Al_2O_3 $[\bar{1}00]$ zone axis (60 nm thin film sample)

EDX results confirmed the existence of Ti-rich phase and Al-rich phase, which is in good agreement with XRD analysis (Fig.4).

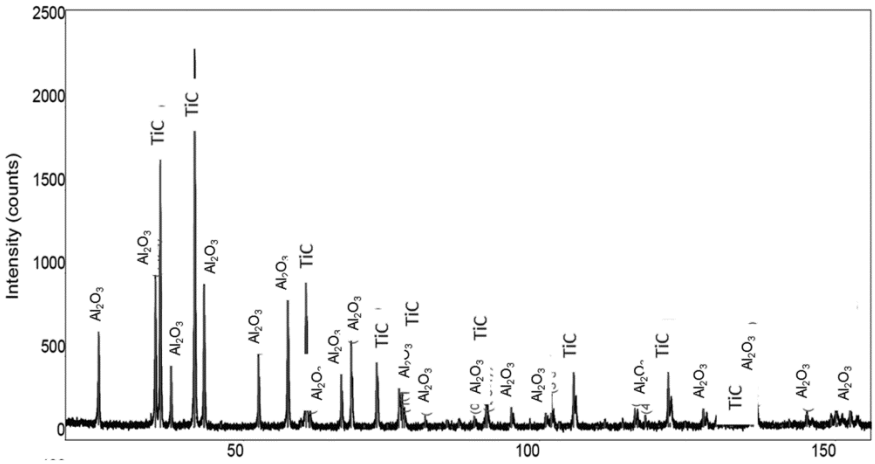

Fig 4. Diffraction Pattern (2θ scan) of Al_2O_3-TiC composite.

Lattice spacing and Micro-strains

Example of lattice spacing and micro-strain of TiC and Al_2O_3 were presented in table 1. Strain in lattice planes were mostly compressive micro-strain, however there were some tensile micro-strain observed. Average strain of {111}TiC is 0.005 in tensile, {200}TiC are 0.007 in compression, {222}TiC is 0.006 in compressive, and {012} Al_2O_3 is 0.008 in compression. The analysis revealed that there are about 0.01 elastic compressive strain distributed in Al_2O_3-TiC composite.

Table1. Example of indexing data of lattice spacing and calculated strain in TiC and Al_2O_3

Phase	Zone axis	Lattice plain	Lattice plane spacing (A)		Strain
			Indexing	Standard	
TiC	0 0 $\bar{1}$	2 0 0	2.1418	2.1637	-0.010
		0 2 0	2.1250	2.1637	-0.018
		2 2 0	1.5049	1.5302	-0.017
		$\bar{2}$ 2 0	1.5049	1.5302	-0.016
Al_2O_3	$\bar{1}$ 0 0	0 1 2	3.3987	3.4804	-0.024
		0 1 4	2.5104	2.5509	-0.016
		0 0 6	2.1346	2.1650	-0.014
		0 2 2	1.9641	1.9645	-0.000

Summary

Al_2O_3-TiC is a fully dense polycrystalline composite with submicron grain size microstructure. TiC contributed to pining effect in the composite. Micro strains of each lattice planes are different. Compressive and tensile strains are randomly found independent of any specific lattice plain. It is about 0.01 compressive strain distributed in Al_2O_3-TiC composite.

Acknowledgement

Researchers are thankful to the financial funding supports from 1) The 90th Anniversary of Chulalongkorn University Fund (Ratchadaphiseksomphot Endowment Fund), Chulalongkorn University,Bangkok,Thailand. 2) NSTDA University Industry Research Collaboration (NUI-RC),

National Science and Technology Development Agency, Pathum Thani, Thailand. 3) Western Digital (Thailand) co.th. 4) Government research budget 2014. 5) Office of Higher Education Commission (WCU-008-HR-57). This research would not be accomplished without always good supports from Mr. Chakkrit Supavasuthi and Mr. Theera Yaemglin.

References

[1] K.F. Caia, D.S.M., N. Axenb, R. Manyatsab, Preparation, microstructures and properties of Al2O3–TiC composites. Ceramics International, 2001. 28(2002): p. 7.

[2] Wilson Acchar, C.R., Ferreira da Cemara, et al., Mechanical performance of Alumina rainforced woth NbC, TiC, WC. Materials Research, 2012. 15(6): p. 4.

[3] J. Echeberria, J.T., J.Y. H, Butler, F. Castro, Sinter-HIP of alpha-alumina powders with sub-micron grain sizes. Journal of the European Ceramic Society 2002(22): p. 9.

[4] M.E.Fitzpatrick, M.T.Hutchings, and P.J.Withers, Separation of macroscopic, elastic mismatch and thermal expansion misfit stress in metal matrix composite quenched plates from nuetron diffraction. Acta metallurgica, 1997. 45(12): p. 9.

[5] Withers, P.J. and H.K.D.H. Bhadeshia, Overview Residual stress Part 2 Nature and origins. Materials Science and Technology, 2001. 17(10): p. 366.

[6] Schmid, H.K., et al., Microstructural Characterization of Al2O3-SiC Nanocomposites. Journayl of European Ceramic Societ, 1998. 18: p. 11.

[7] Guo, S., A. Limpichaipanit, and R.I. Todd, High resolution optical microprobe investigation of surface grinding stresses in Al2O3 and Al2O3/SiC nanocomposites. Journal of the European Ceramic Society, 2011. 31: p. 13.

[8] Yao, N. and A.K. Epstein, Surface nanofabrication using focused ion beam, in FORMATEX. 2010, Microscopy Science, Technology, Applications and Education. p. 10.

Advanced Materials Research Vol. 983 (2014) pp 161-165

doi:10.4028/www.scientific.net/AMR.983.161

Characterization and Parametric Study of Multilayered IPMC Actuator

M. F. Shaari[1,2,a] and Z. Samad[2,b]

[1]Faculty of Mechanical and Manufacturing Engineering, Universiti Tun Hussein Onn Malaysia, Parit Raja, 86400 Batu Pahat, Johor, Malaysia.

[2]School of Mechanical Engineering, Universiti Sains Malaysia, 14300 Nibong Tebal, Pulau Pinang, Malaysia.

[a]mdfarid@uthm.edu.my, [b]zahurin@eng.usm.my

Keywords: IPMC actuator, Actuation force, Displacement, Force-to-weight ratio

Abstract. Ionic Polymer-Metal Composite (IPMC) has been utilized as an actuator in several robotic applications such as the actuator for its locomotion and gripper of the end effector. However, due to its low actuation force which is normally less than 10gf (depend on dimension), the application has been limited to small scale robot. Hence, in this research we propose a multilayer structure of IPMC actuator and investigate the actuation force increment. Besides, parametric study was also conducted to determine the force-to-weight ratio and the bending displacement. The obtained results had been compared to single ply IPMC actuator at the same thickness. The result shows that the increment of IPMC layer had increased the actuating force up to 30% for two layers and 40% for three layers. In addition, utilizing multilayered IPMC had reduced the stiffness constraint for thicker IPMC. This finding would be useful in designing stage of a small scale robot that require higher actuation force at a higher bending displacement.

Introduction

Ionic Polymer-Metal Composite (IPMC) is regarded as one of the smart material that can be utilized either as actuator or sensing element. The key mechanism that contribute to this functions is the charge transduction within the membrane in two different conditions [1,2]. In the first condition, if the IPMC is supplied with voltage to its electrode, the free cation inside the IPMC attaches water molecules and attracted to the cathode [3,4]. As the consequence, the IPMC will physically bend towards the anode electrode (Fig. 1). Otherwise, if there is external force acts on the IPMC without external voltage, the transduction charge induces voltage at the electrode and become as a generator [4,5]. As a polymeric family member, the generated actuation force or the blocking force for IPMC is relatively small compared to metal-based smart material such as Shape-Memory Alloys (SMA). Few steps had been taken by researchers to increase IPMC performance such as enhancing the surface electrode, membrane composition as well as increasing the thickness of the IPMC actuator. Surface electrode enhancement requires additional layers on the IPMC surface such as gold, silver or silicate [6,7,8]. Membrane composition enhancement process involving polymeric molecule or ionomer molecule alterations in the membrane, for instance by adding lithium molecules to increase the strength of the osmotic pressure that cause the actuation [9,10]. Meanwhile, increasing the thickness of the IPMC is the simplest technique to increase the actuation force at lower cost compared to the previous enhancement process. However, by increasing the thickness of the actuator would reduce the curvature or bending degree [11,12]. Hence, we proposed a multilayered IPMC actuator to increase the actuation force performance. All IPMC actuators had been fabricated and the multilayered IPMC actuation had been characterized. Performance analysis had been conducted to compare the results with other enhancement techniques. There are two circuit models for the multilayered IPMC actuator which are the series circuit and parallel circuit. In this research, parallel circuit model had been selected to obtain a synchronized actuation for every IPMC strips (Fig. 2). The result showed that increment of the IPMC layer had increased the actuation force by 30%. The main difference with IPMC thickness increment is the displacement rate remains constant.

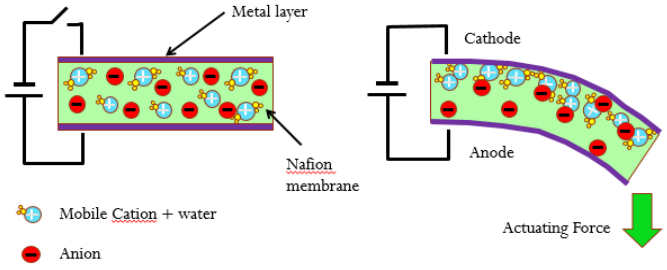

Figure 1: IPMC Actuation Mechanism

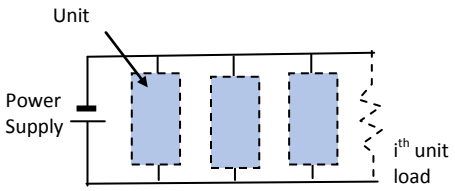

Figure 2: Model of parallel load circuit

Research Overview

IPMC is an ionic gel such as perflourinated alkenes which has embedded with noble metal particles under its opposite surface [1]. This noble metal layer which is normally 2 to 10 nm thick functions as electrode for this IPMC. The fundamental structure of this IPMC is depicted as in Fig. 1. Once the electrode is activated, the free cation that attached with water molecules in the membrane moves to the cathode [1,4,9]. The accumulation of cation and water molecules at the cathode side cause asymmetric built-in osmotic pressure in the membrane. As the result, the whole membrane would deform to the anode side. Analysis on geometrical morphology had revealed that during actuation, a beam shape IPMC would bend and round-flat shape IPMC would deforms into a hemispherical shape [13,14]. There are few factors that contribute to the actuation performance of the IPMC which are the supply voltage, membrane thickness, type of the alkaline metal in the ionomer, number of ionomer and type of the electrode materials. Electrode material would determine the surface resistivity of the IPMC and water permeability at the surface during actuation. The alkaline metal and ionomer structure influence the formation of the osmotic pressure in the IPMC which can be measured by current density. Membrane thickness determine the number of ionomer in volume basis. In order in to increase the performance of the IPMC, researchers had focused the enhancement works on specific factors. For instance, Preetichandra et al. and Shahinpoor et al. had enhanced the IPMC electrode by coating the platinum electrode with gold and silver layer to reduce surface resistivity and water permeability [6,7]. This process had increased the current density as well as reducing water leakage that weaken the blocking force. Nemat-Nasser et al. managed to improve IPMC performance by enhancing the ionomer microstructure with different alkaline elements [15]. In his research, the usage of Li^+-based ionomer had stronger effect compared to Na^+-IPMC and H^+-based IPMC. Vinh et al. targeted the membrane composition as well as surface enhancement by applying montmorillonite (MMT) to improved IPMC performance [8].

Materials and Method

Fabrication process. In this research, the IPMC actuator had been fabricated using chemically electroless plating. Nafion 1110 (Ion Power Inc.) had been selected as the base material and platinum (Sigma Aldrich) as the noble metal for the electrode. The platinum salt is deposited into the membrane using sodium borohydrate 98%(Sigma Aldrich) as the reducing agent. The electroless plating process was conducted in a water bath (Wood Yellow, WY-285). The reducing agent was added gradually at a controlled temperature into the solution to avoid any explosion risk from the reaction between the reducing agent and the water. The starting temperature is 40°C and end at 60°C. 0.2g sodium borohydrate will be added for every half an hour. The chemical reaction that occurred during this process is concluded in Eq.1.

$$NaBH_4 + 4[Pt(NH_3)_4]^{2+} + 8OH^- \Rightarrow 4Pt^+ + 16NH_3 + NaBO_2 + 6H_2O \quad (1)$$

The secondary plating process was carried out to increase the intensity of the deposited platinum layer by adding stronger reducing agent. Hydroxylamine hydrochloride 20%wt and Hydrazine

Hydrate 5%wt (both from Sigma Aldrich) had been utilized as the reducing agents. In this process, again the reducing agent had been added gradually for half an hour from 40°C to 60°C using the water bath. In the end of the process, a 400µm thick IPMC film had been fabricated. This film had been cut into four 45mm x 5mm samples. Active length of the IPMC was 40mm.

Characterization process. There were two observations were made in this research which are the actuation force and bending displacement. As discussed in the previous chapter, the multilayer IPMC is connected using parallel circuit model to ensure all actuators bend together (Fig. 3). There were three samples had been studied and recognized by number of the layer; 2 layer, 3 layer and 4 layer. The IPMC actuators obtained the supply voltage from a power supply (GW Instek PSM-3004). Mini digital scale (DS-11) with 0.01g resolution had been utilized to measure the actuating force. Investigation on supply voltage influence was conducted by supplying the multilayer IPMC actuator with 2V, 2.5V, 3V, 3.5V and 4V. Actuator displacement was measured using linear laser sensor (Microepsilon ILD-1402). Arduino microcontroller was utilized to provide square wave signal at predetermined frequency. The displacement data was recorded using Labview Signal Express via NI-USB 6009 data acquisition module (Fig. 4). This data was compared to the single ply IPMC actuator which has the thickness of 1.2mm.

Figure 3: Multilayer IPMC

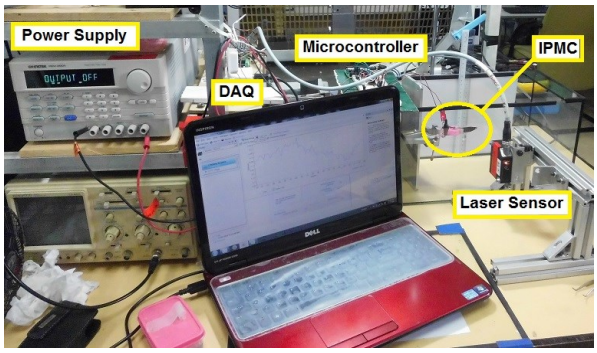

Figure 4: Characterization for displacement measurement

Results and Discussion

The result shows that the actuating force has linear relation to the supplied voltage. As depicted in Fig. 5, the increment of layer number had increased the magnitude of the actuation force. This constant increment was up to 30% for each additional layer. At 4 layers IPMC actuator, the recorded actuation force was approximately up to 9gf. Using the obtained data in actuation force characterization, the force-to-weight ratio for each samples of multilayered IPMC actuator was analyzed as depicted in Fig. 6. For a single layer, the force-to-weight ratio had reached near 10 but this ratio remains constant at 5 although the number of IPMC layer had been multiplied. Though the actuation force was increased as the result of the additional IPMC layer, the weight of the actuators was increased too. Each IPMC actuator has same weight and therefore the increment of any IPMC layer had increased the weight of the IPMC actuator in constant. This ratio might be changed if the actuation force increases exponentially. However, single ply IPMC actuator shows different force-to-weight ratio at different thickness. Thicker IPMC actuator results lower force-to-weight ratio. One reason that support the differentiation between multilayered and single ply IPMC actuator is the difference in weight of the noble metal electrode. Single ply IPMC has only two layers of electrode although the thickness of the membrane was increased but at the same thickness, multilayered IPMC has doubled the weight of its electrode.

In displacement characterization, two different IPMC actuator structures had been analyzed by supplying with square wave AC voltage. The frequency had been determined in the microcontroller program. The results shows that the multilayered IPMC actuator has better displacement compared to single ply IPMC actuator which has the same thickness (Fig. 7). The multilayered IPMC actuator was able to bend at 2cm in average for one side of actuation while the single ply IPMC actuator at

the same thickness managed to bend at 0.5cm per side. Single ply IPMC actuator had also shorter time response to the input frequency, compared to the multilayered IPMC actuator. These results conclude that single ply IPMC actuator has higher stiffness and more rigid compared to the multilayered IPMC. Besides, based on the Euler-Bernoulli beam bending theory, the increment of beam thickness would increase the internal shear resistance that reduce the bending capability. Hence, by slicing the beam into several layers, the shear resistance had been reduced and thus would create more moment to the bending beam.

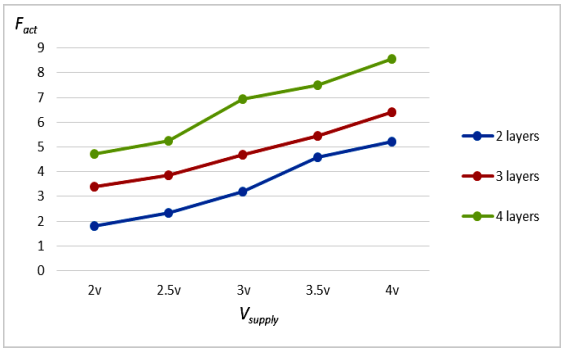

Figure 5: Actuating force at different drive

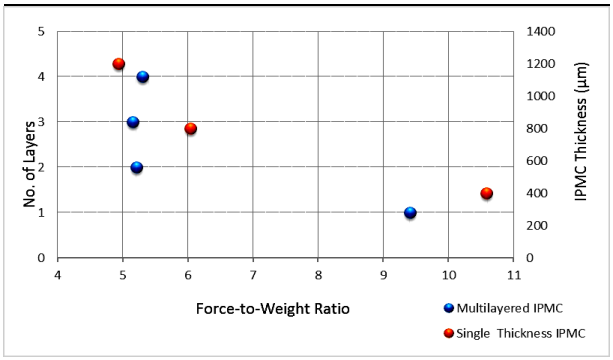

Figure 6: Force-to-weight ratio

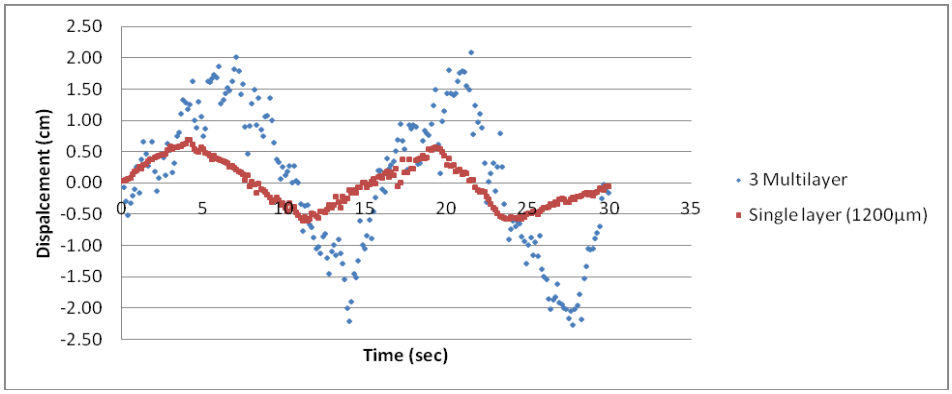

Figure 7: IPMC displacement over IPMC length

Conclusion

The additional layer of IPMC actuator increases the actuation force in constant. Each additional layer would increase the actuation force by 30% of the initial actuator. Although there is increment in thickness, multilayered IPMC actuator has better bending displacement relatively compared to the single ply IPMC. Generally, thicker IPMC is stiffer than thin IPMC. This is because of the beam bending concept where the thicker beam has higher shear stress resistance and bending moment that depend on the second moment of area. As proposed in the aim of this research, multilayered IPMC actuator has reduce the influence of the internal stress by reducing the second moment area. However, the multilayered IPMC actuator has lower time response compared to the single ply IPMC actuator. Multilayered IPMC actuator shows constant force-to-weight ratio while the single ply IPMC actuator presented different ratio at different thickness. These results is very important as a reference in order to utilize IPMC as an actuator for robot design. The developed multilayer IPMC actuator is suitable for higher actuation force at bigger deflection application.

Acknowledgment

The authors would like to address their compliment to the Ministry of Education Malaysia (MOE) for the FRGS grant sponsorship, Universiti Tun Hussein Onn Malaysia and Universiti Sains Malaysia for their technical and facilities support on this research.

References

[1] M. Shahinpoor, K. J. Kim, Ionic Polymer Metal Composite: I. Fundamentals, Smart Mater. Struct., 10, (2001), 819-833.

[2] J. Yip, L. S. Feng, C. W. Hang, Y. C. W. Marcus, and K. C. Wai, Experimentally validated improvement of IPMC performance through alternation of pretreatment and electroless plating processes, Smart Material Structures, 20, (2011), 1 – 8.

[3] M. Yu, H. Shen, D. Zhen-dong, Manufacture and Performance of Ionic Polymer-Metal Composites, Journal of Bionic Engineering 4, (2007), 143−149.

[4] S. Nemat-Nasser, Micromechanics of actuation of ionic polymer-metal composites, Journal of Applied Physics, 92, (2002), 2899-2915.

[5] E. Malone and H. Lipson, Freeform Fabrication of Ionomeric Polymer-Metal Composite Actuators, Rapid Prototyping Journal, 12/5, (2006), 244-253.

[6] M. Shahinpoor, K. J. Kim, Novel ionic metal-polymer composites equipped with physically loaded particulate electrode as biomimetic sensors, actuators and artificial muscles, Sensors and Actuators A, 96, (2002), 125 – 132.

[7] D.M.G. Preetichandra and Keechi Kaneto, An easy fabrication method for artificial muscles and bending curvature sensors using Ionic Polymer Metal Composites, First International Conference on Industrial and Information Systems (ICIIS), (2006), 227 – 230.

[8] V. K. Nguyen and Y. Yoo, A novel design and fabrication of multi-layered ionic polymer-metal composite actuators based on Nafion/layered silicate and Nafion/silica nanocomposites, Sensors and Actuators B, 123, (2007), 183 – 190.

[9] S.G. Lee, H. C. Park, Surya D. Pandita, and Y. Yoo, Performance improvement of IPMC (Ionic Polymer Metal Composites) for a flapping actuator, International Journal of Control, Automation, and Systems, 4, no. 6, (2006), 748-755.

[10] C. K. Chung, P. K. Fung, Y. Z. Hong, M. S. Ju, C.C.K. Lin, T.C. Wu, A novel fabrication of ionic polymer-metal composites (IPMC) actuator with silver nano-powders, Sensors and Actuators B, 117,(2006), 367–375.

[11] S. J. Lee, M. J. H., S. J. Kim, J. Y. Jho, H. Y. Lee and Y. H. Kim, A new fabrication method for IPMC actuators and application to artificial fingers, Smart Materials and Structure, 15, (2006), 1217 – 1224.

[12] J. W. Paquette, K. J. Kim, D. Kim and W. Yim, The behaviour of ionic polymer-metal composites in a multi-layer configuration, Smart Material Structures, 14, (2005), 881 – 888.

[13] Z. Chen, S. Shatara and X. Tan, Modelling of Biomimetic Robotic Fish Propelled by an Ionic Polymer-Metal Composite Caudal Fin, IEEE/ASME Transactions on Mechatronics, 15, no.3, (2010), 448-458.

[14] T. T. Nguyen, N. S. Goo, V. K. Nguyen, Y. Yoo and S. Park, Design, fabrication and experimental characterization of a flap valve IPMC micropump with flexibly supported diaphragm, Sensors and Actuators A, 141, (2008), 640 – 648.

[15] S. Nemat-Nasser and Y. Wu, Tailoring the Actuation of Ionic Polymer-Metal Composite, Smart Materials and Structure, 15, (2006), 909-923.

Advanced Materials Research Vol. 983 (2014) pp 166-170

doi:10.4028/www.scientific.net/AMR.983.166

A novel approach for determining critical fracture strain of a near alpha titanium alloy during hot compression deformation

Wenwen Peng[1, a], Weidong Zeng[1, b], Qingjiang Wang[2, c], Yanchun Zhu[1, d]

[1]State Key Laboratory of Solidification Processing, Northwestern Polytechnical University, Xi'an 710072, China

[2]Institute of Metal Research, Chinese Academy of Sciences, Shenyang 110016, China

[a]jxpengwenwen@163.com, [b]zengwd@nwpu.edu.cn, [c]qjwang@imr.ac.cn, [d]lzlzyc@163.com

Keywords: Titanium alloy, Compression test, High-speed photography, Fracture

Abstract. A novel high-speed photography is introduced to determine the critical fracture strain of a near alpha titanium ally during hot compression deformation. This method precisely captures the nucleation site and propagation process of cracking, and thus is an excellent method to represent dynamically the hot-deformation fracture. Compared with the traditional way, it can significantly decrease the number of trials and improve the accuracy. Based on this method, the critical fracture strain is measured, and a critical fracture model is developed.

Introduction

Ductile fracture is one of the major limiting factors in the forming processes of metal alloy with poor workability and should be avoided as far as possible in pursuit of desired quality of the products [1]. Over a period of nearly half a century, a large number of beneficial fracture criteria for the fracture prediction and prevention were extensively conducted and well documented [2-5]. It is well known that the most significant basis of establishing these helpful fracture criteria is the determination of critical fracture strain. In previous studies, the proposed critical fracture strain has been mostly used for predicting fracture in cold metal forming. Thus, after the appearance of a surface crack observable by the naked eye, the deformation was stopped and the critical fracture strain could be measured. For the hot deformation, however, it is very difficult to determine the critical fracture strain through the method as result of the bright red metal surface at elevated temperature. Additionally, it is also very difficult for the naked eye to observe the crack initiation when the forming is conducted at a high strain rate. Therefore, it is quite imperative to find a novel method to accurately determine the initial fracture strain during the hot deformation process.

At present, the traditional way to obtain the critical fracture strain of the metal alloys during the hot forming is the dichotomy [6]. However, it is necessary for the dichotomy to carry out a plenty of experiments to determine the critical fracture strain by means of differential method. Also, it is extremely difficult and time-consuming, and the result is rough. In addition, more attention needs to be paid to some new methods (acoustic emission [7], thermal infrared imager [8] and high-speed photography [9]), which may be employed to determine the critical fracture strain during hot forming. During high-temperature deformation process, however, it is difficult for acoustic emission to recognize the noise signals and to fix the sensor. The thermal infrared imager will be limited in high-strain-rate deformation of specimen. Besides, the dichotomy is also extremely difficult and time-consuming, and the result is rough. On the contrary, high-speed photography can catch the experimental process at tens of thousands or even hundreds of thousands of frames per second, and with the help of professional image-analysis software. It has been widely used in respect of propagation fracture [10], crack growth and expanding speed [11], the continuous formation of regions of localized shear in thin-walled tubular specimens and shear band propagation [12], and the chip formation area when machining steel in orthogonal turning tests, etc. [13]. Moreover, this technique can observe both the initial position of crack and the dynamic propagation of crack in

high-temperature deformation process. Hence, the high-speed photography will be adopted to determine the initial fracture reduction in this work

Recent years, the increasing attention has been received with respect to near-alpha titanium alloys, and they have been researched as the candidate of material for jet engines as compressor discs and blades because of their light weight and superior fatigue and creep properties at elevated temperatures up to 600 ℃ [14]. Ti60 alloy is a new near-alpha high-temperature titanium alloy developed on the basis of IMI834. Like other high-temperature titanium alloys, Ti60 alloy also possesses excellent heat resistant properties at high temperature. In industrial practice, however, most of surface cracking forge pieces were obtained by very costly trial-and-error, which is quite time-consuming and significantly decisive for the designers' empirical know-how [15]. Thus, it is quite essential to predict and prevent the occurrence of fracture for Ti60 alloy by precisely determining the critical fracture strain.

Therefore, in this work, a high-speed photography will be adopted to determine the initial fracture strain of Ti60 titanium alloy during hot compression deformation. Based on the initial fracture strains at different deformation conditions, a critical fracture model for Ti60 alloy is developed.

Materials and experimental procedures

The as-received alloy was supplied in form of an ingot with diameter of 155 mm. The β transformation temperature was measured to be approximately 1045 ℃ by metallographic observations. Its chemical composition was Ti-5.8Al-4.0Sn-3.5Zr-0.4Mo-0.4Nb-1.0Ta-0.4Si-0.06C (wt %). The cylindrical specimens for hot compression tests were electro-discharged machined from the bar with 10 mm in diameter and 15 mm in height, and the compression axis of specimens was parallel to the axial direction of the bar.

Hot compression tests were carried out in the temperature range of 970-1120 ℃ with 30 ℃ intervals and strain rate range of 0.01-10 s^{-1} and strain of 0.916 with an interval of 15% on a Gleeble-3500 simulator. Thermocouples were welded in the middle surface of the specimens to measure the actual temperature of the specimens. Specimens were heated to set test temperatures with a heating rate of 5℃/s, and then held for 6 min. In order to reduce the non-uniform deformation from friction between contact surface between specimen and machine, top and bottom end surfaces of the specimens were coated with graphite powder, and a foil tantalum was placed between these faces of the specimen and anvils. After compression, the specimens were cooled in the air to avoid cracking.

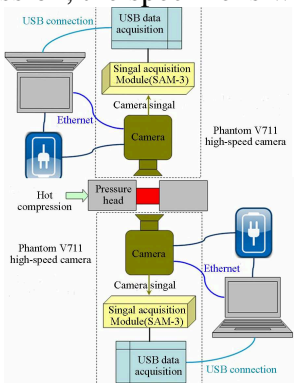

Fig. 1 Visual observation on the fracture initiation in hot compression of Ti60 titanium alloy using high-speed cameras.

For determining the precise critical fracture strain, two Phantom V711 high-speed cameras are fixed on opposite sides of the specimens to observe the whole crack surface of the alloy at the same time (Fig. 1). According to Fig. 1, the cameras are connected to portable laptops and power sources respectively, and subsequently check whether the image appears in the portable laptops and adjust the focus of cameras. Two Nikon AF-S Nikkor lens are attached to the high-speed cameras to get enlarged images near the fracture location. The lens apertures of cameras are adjusted to reduce the brightness of heated specimen so as to decrease the effect of brightness on the quality of image. A

series of images are photographically recorded at the rate of 1000 frames per second after the specimen forged to a true strain of 0.916.

Results and discussions

Critical fracture strain determined by high-speed cameras

Fig. 2 illustrates the crack initiation and propagation of the specimens determined through the time-series images by means of two high-speed cameras. From Fig. 2a, it can be seen that 45° crack at 970 ℃/0.01 s^{-1} initiates at one half side of the surface and is not observed at the other half side when strain reaches 0.426, indicating that the fracture occurs. Compared with that in α+β phase field, however, there is a significant difference in determining the initial crack signal for deformation in the β phase field. For deformation in the β phase field (1090 ℃/1 s^{-1}, Fig. 2b), it is difficult to distinguish clearly the appearance of a surface crack due to the bright red surface caused by deformation at elevated temperature. At the strain of 0.654, however, it is noted that a purple region appears on one half side of the surface and is not found on the other half side. It indicates that the specimen begins to fracture, and the strain of 0.654 can be deemed as the critical fracture strain at 1090 ℃/1 s^{-1}. Moreover, when the strain is up to 0.916, the observed cracking regions in the images are completely consistent with the practical situation, which manifests that the method for obtaining the critical fracture reduction is accurate and reliable.

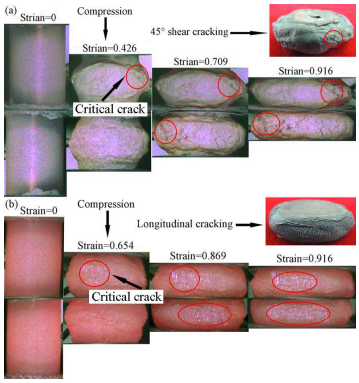

Fig. 2 Crack initiation and propagation under different deformation conditions observed by high-speed camera: (a) 970 ℃/0.01 s^{-1} and (b) 1090 ℃/1 s^{-1}.

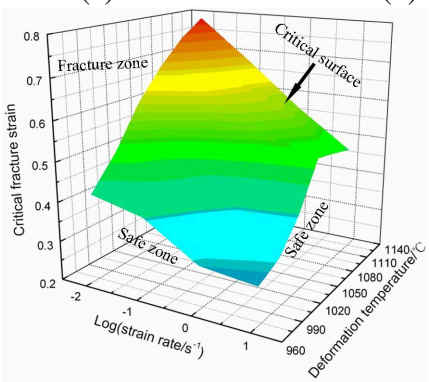

Fig. 3 Critical fracture strains obtained by high-speed photography plotted as a function of strain rate as well as temperature.

Fig. 3 shows the critical fracture strains obtained by high-speed photography plotted as a function of strain rate as well as temperature. As evidenced by Fig. 3, it is found that the critical fracture surface divides the deformation zone into two zones of above and below which are fracture zone and safe zone, respectively. In addition, it can be seen from Fig. 3 that the critical fracture strain decreases monotonically with increasing of strain rate, while it increases drastically with the increasing of temperature in most conditions of this experiment because diffusivity increases exponentially with temperature. On one hand, at relatively high temperature, dynamic softening takes place easily accompanying with a large amount of dislocations. On the other hand, at low strain rate, there is

sufficient time for dynamic recrystallization. It can provide stable flow and ideal workability to the material by simultaneously softening and making the microstructure reconstituted [16]. Thus, larger strain is needed to make the alloy fracture at high temperature and low strain rate. However, at high strain rate (≥1 s^{-1}) and high deformation temperature (≥1090 ℃), the critical fracture strain decreases with the increasing of deformation temperature, which indicates a degraded workability at higher temperature. This poor workability can be associated with the high-temperature oxidation and coarse grains [17]. Therefore, it can be concluded that the deformation temperature and strain rate have a significant effect on the critical fracture strain.

Critical fracture model

In general, the presented critical fracture strain in metal cold forming was mostly deemed as a constant. As mentioned above, however, the critical fracture strain of the present alloy during hot compression deformation can be plotted as a function of deformation temperature and strain rate. S. Alexandrov [18] studied a fracture criterion of aluminum alloys in hot metal forming, and claimed that the critical fracture strain is very sensitive to the temperature and strain rate. Similar result has been recorded in the hot forming of magnesium alloys [19]. Thus, for hot deformation of Ti60 titanium alloy, a new approach which incorporates the effects of temperature and strain rate into a critical fracture model needs to be developed. Zener-Holloman (Z) parameter ($Z=\dot{\varepsilon}\exp(Q/RT)$), in which $\dot{\varepsilon}$ is the strain rate, Q the activation energy, R the molar gas constant, and T the absolute temperature) accounts for a combined effect of strain rate and temperature. Hence, it is utilized to understand the effect of strain rate and temperature on crack of the near alpha titanium alloy.

Fig. 4 shows the critical fracture strain as a function of Z parameter. It is interesting to find from Fig. 4 that the critical fracture strain data of the present alloy is divided into two parts as result of different $\ln Z$ values caused by different Q values (574.8 kJ/mol in α+β phase field and 194.0 kJ/mol in β phase field) [16]. Furthermore, the critical fracture strain data both in α+β phase field and β phase field can be well correlated with Z parameter. According to fitting trial by regression, the critical fracture model of Ti60 alloy that describes critical fracture strain as a function of Zener-Holloman parameter for hot working of the near alpha alloy in the α+β two-phase and β single-phase region can be presented as:

$$970\text{-}1030\ ℃:\ \varepsilon_f = 2.241 - 0.031\ln Z \tag{1}$$

$$1060\text{-}1120\ ℃:\ \varepsilon_f = 0.822 - 0.026\ln Z \tag{2}$$

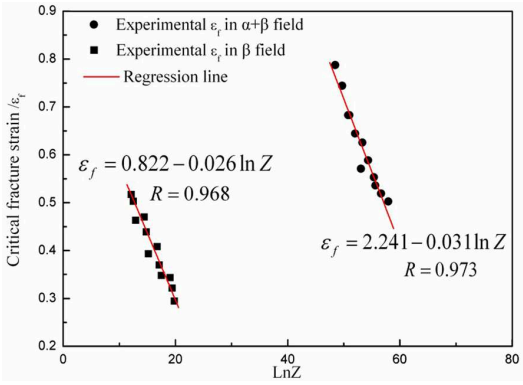

Fig. 4 Critical fracture strain as a function of Zener-Holloman parameter.

In addition, it can be clearly seen from Fig. 4 that the correlation coefficient (R) is as high as 0.973 in α+β phase field and 0.968 in β phase field respectively, demonstrating that the built relationship is highly linear. Similar linear relation between ε_f and $\ln Z$ was obtained in Ti-25V-15Cr-0.3Si alloy [6] and aluminum alloys [18]. It indicates that if critical fracture model for other metal alloys in hot forming were also a linear relationship, the critical fracture model would be developed after only limited experiment times, and further effectively decrease the number of trials and reduce the costs. Then the critical fracture model can be combined with FEM by inserting an in-house code using

FORTRAN language into the commercial FEM-based software DEFORM-3D. Based on the model, the critical fracture strain of the near alpha titanium alloy at different hot deformation conditions can be accurately predicted, and further the processing parameters during hot deformation can be optimized. These works have been accomplished and will be introduced in future papers.

Summary

In this work, the high-speed photography has been employed as a novel approach to determine the critical fracture strain of a near alpha titanium alloy during hot compression deformation, which precisely captures the nucleation site and propagation process of cracking. The critical fracture strain determined using this method is highly dependent upon temperature and strain rate. Moreover, a highly linear critical fracture model which combines the effects of temperature as well as strain rate is developed by regression analysis for critical fracture strain and Zener-Holloman parameter. Based on the linear model, the experimental time to determine the critical fracture strain of the near alpha titanium alloy during hot deformation can be effectively reduced. This is confirmed that the proposed model can be powerful tools in predicting the fracture strain of titanium alloys deforming at elevated temperatures. The model is anticipated to be also applicable in bulk forming such as forging.

References

[1] A.R. Rosenfield: Int. Mater. Rev. Vol. 13 (1968), p. 29-40.
[2] A.M. Freudenthal: The Inelastic Behavior of Solids, Wiley, New York (1950).
[3] M.G. Cockroft and D.J. Latham: J. Inst. Met. Vol. 96 (1968), p. 33-39.
[4] S.I. Oh, C.C. Chen and S. Kobayashi: J. Eng. Ind. Trans. ASME Vol. 101 (1976), p. 36-44.
[5] M. Oyane, T. Sato, K. Okimoto and S. Shima: J. Mech. Work. Technol. Vol. 4 (1980), p.65-81.
[6] W.D. Zeng, Y. Shu, X.M. Zhang, et al.: Mater. Sci. Technol. Vol. 24 (2008), p. 1222-1229.
[7] P. Fang, L.F. Cheng, L.T. Zhang, et al.: Nondestr. Test. Vol. 28 (2006), p. 358-361
[8] Y.F. Dong, Y.M. Lin, L.G. Wang, et al.: J. Liaoning Tech. Univ. Vol. 25 (2006), p. 848-850.
[9] Y.C. Zhu, W.D. Zeng, F.S. Zhang, Y.Q. Zhao, X.M. Zhang and K.X. Wang: Mater. Sci. Eng. A Vol.553 (2012), p. 112-118.
[10] S. Jin, T.G. Tang, Q.Z. Li, et al.: Chinese J. High Press. Phys. Vol. 20 (2006), p.434-438.
[11] C.E. Rousseau and H.V. Tippur: Mech. Mater. Vol. 33 (2001), p. 403-421.
[12] S.X. Song, X.L. Wang and T.G. Nieh: Scripta Mater. Vol. 62 (2010), p. 847-850.
[13] J. Pujana, P.J. Arrazola and J.A. Villar: J. Mater. Process. Technol. Vol. 202 (2008), p. 475-485.
[14] R.R. Boyer: Mater. Sci. Eng. A Vol. 213 (1996), p. 103-114.
[15] S.V.S. Narayana Murty, B. Nageswara Rao and B.P. Kashyap: J. Mater. Process. Technol. Vol. 147 (2004), p.94-101.
[16] W.W. Peng, W.D. Zeng, Q.J Wang and H.Q. Yu: Mater. Sci. Eng. A Vol. 571 (2013), p. 116-122.
[17] J. Unnam, R.N. Shenoy and R.K. Clark: Oxid. Met. Vol. 26 (1986), p.231-252.
[18] S. Alexandrov, P.T. Wang and R.E. Roadman: J. Mater. Process. Technol. Vol. 160 (2005), p. 257-265.
[19] W.J. Kim, H.K. Kim, W.Y. Kim and S.W. Han: Mater. Sci. Eng. A Vol. 488 (2008), p. 468-474.

Advanced Materials Research Vol. 983 (2014) pp 171-174

doi:10.4028/www.scientific.net/AMR.983.171

Thermal behavior of epoxy resins containing manganese compounds*

Fachao Wu[1, a],Shuang Tian[1, b], Song Liu[1, c]

[1] School of Environmental Engineering, North China University of Science and Technology, Box 206,Yanjiao Beijing 101601, China

[a]ahxmsw@ncist.edu.cn, [b]wfchljhnyj@163.com, [c]liusong715@ncist.edu.cn

Key words: epoxy resins, degradation, flame retardant, synthesis, manganese

Abstract A novel cheap macromolecular intumescent flame retardants (Mn-MIFR), was synthesized. Epoxy resins (EP) were modified with Mn-MIFR to get the flame retardant EP, whose flammability and burning behavior were characterized by UL 94, limiting oxygen index (LOI), dilatation, char yield, smoke density rating (SDR) and maximum smoke density (MSD). The epoxy resins were obtained for the UL 94 V-0 rating at low Mn contents of 4.0 % get a LOI of 26.5% and char yield of 18.2%. Dilatation, SDR and MSD of EP/Mn-MIFR decreased. The degradation behavior of the EP/Mn-MIFR was studied by TG and EDX analysis. The experimental results exhibited that the initial decomposition temperature (IDT) was decreased, integral procedure decomposition temperature (IPDT) and amounts of Mn and P at the residue were increased.

Introduction

Recently halogen-free intumescent flame retardant (IFR) are attracting more and more attention from both academic and industrial communities for their multifold advantages including low toxic, low smoke, low corrosion, no corrosive gas, and so on [1,2]. Three ingredients are necessary for IFR: acid source, carbon source and gas source. Phosphorus-containing compounds are often used as an acid source while nitrogen-containing compounds are used as a blowing agent. The greatest benefit to be obtained in this way is a dramatic decrease in the heat generated due to the exothermic combustion of polymers. Other advantages include the conservation of the structural integrity of polymer as a result of the residue of solid carbon and a decrease of formation of flammable gaseous products [3]. In the former work of our group, a novel macromolecular IFR (MIFR) which contains an acid source, a gas source and a char source simultaneously had been synthesized. Thermal degradation and flame retardancy of EP were improved after blending with the MIFR [4, 5].

However, the conventional IFR additives also have some disadvantages [6–8]. To achieve a certain flame retarding level, a higher loading of IFR additive is needed than that of some halogen-containing flame retardants, at the expense of the mechanical properties of the flame-retardant materials. The flame retardant efficiency of IFR needs to be further improved. Some research reports [9] have demonstrated that the presence of some metal-containing compounds with IFR seemed to enhance the flame-retardant action, and exhibit a synergistic effect on the flame retardancy of polymers.

So in this work, manganese element was incorporated into MIFR to get higher flame retardancy, and the degradation behavior of EP modified with the Mn-MIFR was investigated.

Experimental

Materials

Pentaerythritol, 85% of phosphoric acid, melamine, 37% of formalin as formaldehyde, urea and manganese oxide were received from Beijing Chemical Reagents Co.

Instrumentation

The IR spectra were measured on a NEXUS-470 FTIR (Nicolet) spectrophotometer using KBr. The elemental analysis was carried out using a Carlo Eroa 1102 Elemental Analyzer. LOI values were determined in accordance with ASTM D2863-70 by means of a General Model HC-1 LOI apparatus. The UL 94 vertical burning classification was obtained using an ATLAS HVUL 2 burning chamber according to FMVSS 302/ZSO3975. The sample was 127mm×12.7mm×3mm. Thermogravimetry (TG) was carried out on a DTA-2950 thermal analyzer (Dupont Co. USA) under a dynamic nitrogen (dried) atmosphere at a heating rate of 10°C min^{-1}. The energy dispersive x-ray spectroscopy (EDX) data were obtained using a EDS2100X system at 20.00keV.

Synthesis of MIFR

37% formalin as formaldehyde [F] 1 mol was brought to PH 8-8.5 with NaOH and heated. Then melamine [M] 0.2mol and urea [U] 0.5mol were added to the above solution, stirred until dissolved and heated under reflux for 50 min. Heating was stopped and the solution was allowed to cool to get MUF prepolymer A. 85% phosphoric acid 1 mol and pentaerythritol 0.5mol were mixed, heated to 120°C, stirred for 4h until without water distilled to get caged bicyclic pentaerythritol diphosphonate. Then manganese oxide was doped into under stirring, heated to 80°C, stirred for 1h to get B. B was added slowly into A under stirring to obtain Mn-MIFR.

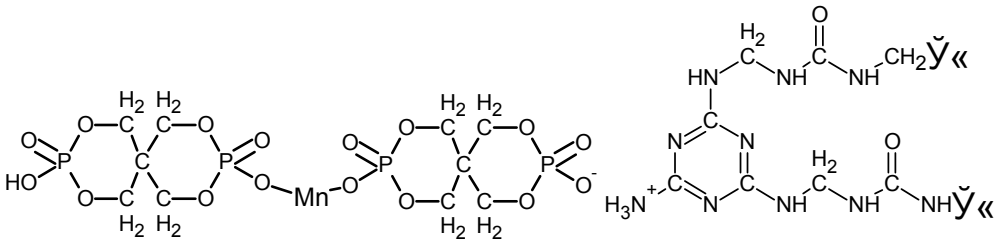

Scheme 1 Struture of Mn-MIFR

RESULTS AND DISCUSSION

Flame retardancy of epoxy resins

Table 1 Flame retardant properties of EP containing different content of Mn in Mn-MIFR

EP/Mn-MIFR	Mn content in Mn-MIFR (%)					
	0	2.0	3.0	4.0	5.0	6.0
LOI (%)	26.0	26.5	26.5	26.5	26.5	26.5
UL 94	V-1	V-1	V-1	V-0	V-0	V-1

Flame retardant properties of EP containing 20% Mn-MIFR were list in Table 1, and char and smoke suppression properties of EP samples were list in Table 2. From the Table 1 and Table 2, we can see the good flame retardancy of the IFR. With the increases of Mn content in Mn-MIFR at the same dosage, the LOI increases. 20% dosage is to get UL 94 V-0 when Mn content in Mn-MIFR exceeds 3.0%. The epoxy resins obtained for the UL 94 V-0 rating at low Mn contents of 4.0 % get a LOI of 26.5% and char yield of 18.2%. Such a large increase in the LOI value showed that the Mn provided a clearly synergistic effect on the LOI values of the EP/MIFR composites. Because metal ions can catalyze dehydration and oxidation reactions, it enhances char formation [10], the higher char yield (18.2%) for EP/Mn-MIFR supported this. Meanwhile, the dilatation of EP/ MIFR increases, more for Mn-MIFR, which shows the char is dense and compact, increasing the efficiency of the flame retardance, heat insulation, and protect inner matrix materials. The smoke density rating (SDR) and maximum smoke density (MSD) of EP samples decrease with the increases of Mn content in Mn-MIFR, which show its smoke suppression on EP.

Table 2 Char and smoke suppression properties of EP samples

FR	Addition (%)	Char yield(%)	Dilatation (cm^3/g)	SDR(%)	MSD(%)
-	0	9.1	6.4	74.35	99.63
MIFR	20	15.1	67.2	61.87	92.67
Mn-MIFR	20	18.2	51.4	64.72	94.25

Degradation of epoxy resins

The simultaneous DTG and TG curves of EP and EP/Mn-MIFR were carried out in dynamic nitrogen from ambient temperature to 800°C and are shown in Fig. 1. The initial decomposition temperature (IDT) is define as the temperature when the weight loss is 5%, integral procedure decomposition temperature (IPDT), char yield at 800°C, temperatures at the maximum weight loss rate (T_m) and the value of the maximum weight loss rate (R_{max}) were measured, list in Tab. 3.

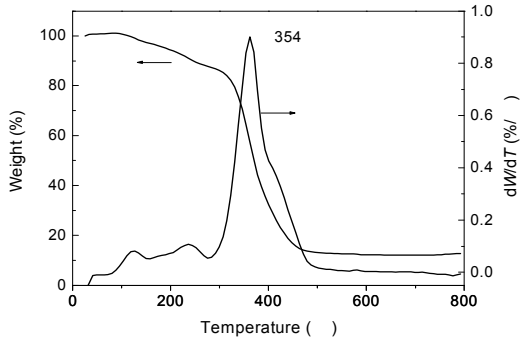

Fig. 1 TG and DTG curves of EP.

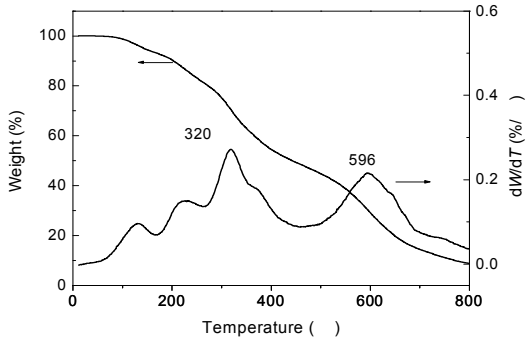

Fig. 2 TG and DTG curves of EP/Mn-MIFR.

Table 3 Thermal data of the epoxy resins from thermogravimetrtic analysis

No.	Mn-MIFR (%)	IDT (°C)	IPDT (°C)	Char yield (%)	Tm (°C)	R_{max}(%/°C)
EP-1	-	160	422	15.2	354	0.82
EP-2	20	146	436	8.8	320	0.28

From the Figs. 1, 2 and Table 3, For EP/Mn-MIFR, compared with EP, IDT are decreased. It is suggested that EP/Mn-MIFR was heated, the phosphoric groups were first decomposed, which can catalyze the decomposition of EP to form a carbonaceous char, which changed into heat-resistant intumescent char by gaseous products such as NH_3 to retard the weight loss rate of EP at high temperatures. Moreover, R_{max} (0.28%/°C) are decreased, and char yields (8.8%) are decreased.

The thermal stability of the epoxy resins is assessed with two parameters: IDT and IPDT. IDT indicates the apparent thermal stability of the epoxy resins, i.e., the failure temperatures of the resins in processing and moulding. On the other hand, IPDT exhibits the resins' inherent thermal stability, i.e. the decomposition characteristics of the resins' volatile composition. From Table 3, EP/Mn-MIFR show relatively lower IDT than do the phosphorus-free resin (EP), since phosphorus-groups decompose at low temperatures. On the other hand, the existence of flame retardants (EP/Mn-MIFR) exhibits higher IPDT than the EP, retarding the weight loss rate of the polymers at high temperatures. The high IPDT implies the epoxy resins' potential application in highly anti-thermal coatings and thermal insulating materials. The temperatures at the maximum weight loss rate (T_m) are also increased.

Characterization of the char structure

Table 4 EDX data of the residues of EP/Mn-MIFR

Elements	k	ZAF Correction	Weight (%)	Atom (%)
C --(Ka)	0.75919	16.9543	4.7670	6.7858
N --(Ka)	0.03338	0.2198	15.3448	18.7312
O --(Ka)	0.07402	0.0914	61.1707	65.3702
P --(Ka)	0.09248	0.6017	13.6533	7.5367
Mn --(Ka)	0.04093	0.7149	5.0642	1.5761

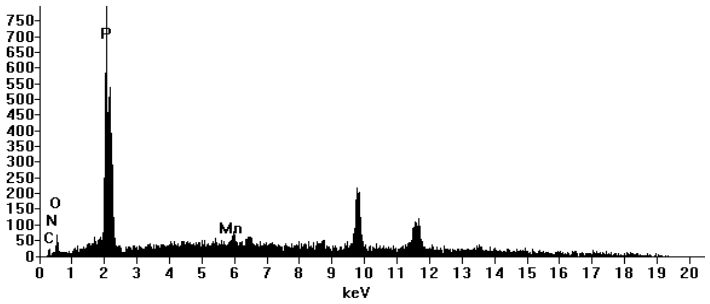

Fig. 3 EDX of the residues of EP/Mn-MIFR

EDX analysis of the residues of EP/Mn-MIFR is shown in Table 4. For EP/ Mn-MIFR, the percentage of carbon atom at the residue is low. It is noted that the amounts of Mn and P at the residue are high. These results imply that Mn and P can accumulate at the surface of char. Therefore, the presence of Mn-MIFR can improve the thermal-oxidative stability of the char layers and protect the matrix.

Conclusions

We succeed in synthesizing a novel cheap macromolecular Mn-MIFR with a structure of a caged bicyclic pentaerythritol diphosphonate. The epoxy resins obtained for the UL 94 V-0 rating at low Mn contents of 4.0 % get a LOI of 26.5% and char yield of 18.2%. Dilatation, smoke density rating (SDR) and maximum smoke density (MSD) of EP/Mn-MIFR decrease. In the thermal degradation of EP/Mn-MIFR, phosphorus groups decompose at relatively low temperature, then catalyzing dehydration, decomposition and carbonization of EP to form a heat-resistant char, retarding the weight loss rate of the EP at high temperatures. Mn and MIFR have a synergistic effect on flame retardancy of EP.

* Contract grant sponsor: [1]Fundamental research funds for the Central Universities: B09013; [2] Fundamental research funds for the Central Universities: 3142013102.

References

[1] S Bourbigot, M Le Rras, S Duquesne, M Rochery: Macromolecular Materials and Engineering, Vol. 289(2004), p.499.

[2] Q Wu, B Qu: Polymer Degradation and Stability, Vol. 74(2001), p.255.

[3] C. F. Cullis, M. M. Hirschler: Eur. Polym. J. Vol. 20(1984), p.53.

[4] M Gao, W Wu, Y Yan: J. Therm. Anal. Cal. Vol. 95(2009), p.605

[5] M Gao, S S Yang: J. Appl. Polymer Sci. Vol. 115(2010), p.2346

[6] Y. X. Ou: ‘‘Applied Flame-retarding Technology’’, Chemical Industrial Press, Beijing 2002.

[7] W. Y. Chiang, H. H. Hu: J. Appl. Polym. Sci., Vol. 82(2001), p.2399.

[8] Z. L. Ma, M. Zhao, H. F. Hu, H. T. Ding, J. Zhang: J. Appl. Polym. Sci., Vol. 83(2002), p.3128.

[9] M. Lewin, E. Makoto: Polym. Adv. Technol., Vol. 14(2003), p.3.

[10] N Wu and R Yang: Polymers for Advanced Technologies, Vol. 22(2011), p. 495

Advanced Materials Research Vol. 983 (2014) pp 175-178

doi:10.4028/www.scientific.net/AMR.983.175

Thermal degradation of Hemp Treated with guanidine dihydrogen phosphate*

Ying-juan SUN[1, a], Yong-li YANG [2, b], Ming GAO[1,c]

[1] School of Environmental Engineering, North China University of Science and Technology, Box 206,Yanjiao Beijing 101601, China

[2] School of Chemical and Environmental Engineering, China University of Mining and Technology, Beijing 100083, China

[a] syj040520@ncist.edu.cn, [b] yongli169@qq.com, [c] gaoming@ncist.edu.cn

Key words: degradation, DTA, flame retardant, hemp, TG

Abstract. Hemp was treated with guanidine dihydrogen phosphate [GDP] to impart flame retardance. The thermal degradation of the samples were studied by thermogravimetry (TG) and differential thermal analysis (DTA). The flame retardance was determined by LOI. Morphology of the char structure was studied by SEM to obtain information concerning the thermal degradation mechanism. For hemp treated with GDP, which has higher LOI and char yield values, the oxidative decomposition stages include a decomposition stage at lower temperatures (165-240°C) , leading to more carbonaceous residue and small amount of flammable products to get the good flame retardance. The SEM of the chars of hemp treated with GDP also indicate the structure of the charring layer may increase heat insulation, and protect inner matrix materials.

Introduction

Hemp, in which cellulose is a major component, is most frequently implicated in fire, causing injuries and fatalities [1]. Its use in house interiors, building or public transport constitutes a potential hazard for people in case of fire. The need for consumer protection, coupled with the new regulations and environmental concerns, increases the interest in flame retardant treatments. It is well known that some guanidine compounds are one of most effective and economical flame-retardants for hemp. Some authors suggested that these compounds could improve flame retardance of hemp and accelerate the formation of a carbonized layer on the materials [2,3]. It was reported that such additives could lead to a lowering of the decomposition temperature and a higher char yield [4]. However, the studies on the relationship between the flame retardance of hemp treated with compounds and their thermal degradation behavior have not been found.

The purpose of our present study is to observe thermal degradation behaviors more minutely to find any correlation between thermal degradation behavior and the different lever of flame retardance in order to characterize the flame retardant hemp. Hemp and treated hemp with compounds were subjected to thermal degradation using DTA and TG techniques. Further, Morphology of charred products was analyzed in an effort to obtain information concerning the thermal degradation mechanism. The degree of flame retardance was determined by LOI. We compared the thermal degradation behavior of these samples obtained from thermogravimetry with numerically determined flame retardance.

Experimental

Materials. The hemp sample was pulverized into particles passing 50 mesh. The flame retardant was GDP. The hemp was first heated for 1 hour in boiling water to remove the raw rosin, which can increase chemical penetration in the next procedure. Then the dried hemp was soaked at for 2 hours at 80°C under atmospheric pressure in each prescribed concentrated solution (10% in weight). Thereafter, the samples were air dried, then placed in a hot press and pressed at 160°C under 3 MPa for 15 min to get the samples with sizes (100mm L x 6mm W x 3mm T) for the LOI test. The pure and treated hemp with the aqueous solution of GDP were listed in Table 1.

Instrumentation. LOI values were determined in accordance with ASTM D2863-70 by means of a General Model HC-1 LOI apparatus. Hemp and hemp treated with GDP at 350°C were observed with a JSM-5600LV scanning electron microscopy (SEM) using 15 kV and 60mA of electric current. Differential thermal analysis (DTA) and thermogravimetry (TG) were carried out on a DT-40 thermal analyzer (Shimadzu, Japan). DTA and TG were performed under a dynamic air (dried) atmosphere at a heating rate of 10°C min^{-1}. α-Al_2O_3 was taken as the reference material. Phosphorus was estimated by the colorimetric method. Nitrogen was determined by the Kjeldahl method.

Results and Discussion

Thermal Degradation Behavior. The associated DTA and TG curves of hemp and hemp treated with GDP were carried out in dynamic air atmosphere from ambient temperature to 800°C and are shown in Figs 1-2. From Fig.1, it can be seen that the second stage is the main stage for the thermal degradation of hemp. It is also reported that the second stage in the thermal decomposition of samples plays a key role attributed to the combustibility [5,6]. Thermal degradation data of the second stage was shown in Table 1.

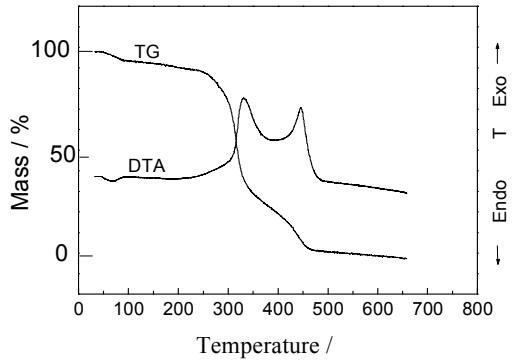

Fig.1 TG and DTA curves of sample 1

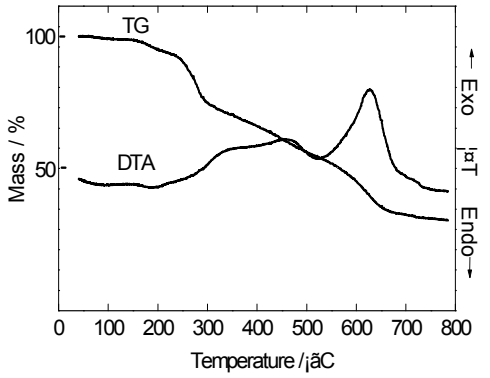

Fig. 2 TG and DTA curves of sample 2.

Table 1 Thermal degradation data of the second stage and analytical data of samples

Sample No.	Compounds	Mass Loss [%]	Temperature [°C]	LOI	Char yield [% Wt]	P [% Wt]	N [% Wt]
1	—	50.5	285-315	18	1.2	—	—
2	GDP	15.8	240-295	41.5	34.9	2.03	2.09

TG curve of hemp shows four stages of the thermal degradation (Fig.1). There is a mass loss of 4.8% in the temperature range 0-285°C in the first stage. Of the components in hemp, the thermal degradation of cellulose occurs while it rapidly decomposes at higher temperatures via the formation of laevoglucose which can be further decomposed into volatile and flammable products. For the second stage, a 50.5% rapid mass loss occurs in the temperature range 285-315°C. The large exotherm peaking at 326°C in the DTA curve is due to the flaming combustion of cellulose. After the main decomposition stage, mass losses of the residual materials of hemp are found to be slow in the temperature range 315-455°C. The TG curve shows a mass loss of 21.8%. There is an another exotherm in the DTA curve in this (third) stage where the less stable aliphatic groups are preferentially decomposed through homolytic cleavage of C-C and C-H bonds, and the resultant product is a highly condensed and cross linked carbonaceous materials [7]. For the fourth stage, the TG curve shows a mass loss of 2.6% in the temperature range 455-650°C.

For the thermal analysis curves of hemp, it is evident that the oxidative decomposition of hemp occurs at higher temperatures (>300°C), and the heat release is distributed between two sharp and closely spaced exotherms, which indicates a large rate of heat release. So the heat liberated is easily transferred back to hemp surfaces to continue hemp pyrolysis, maintaining a continuous supply of gaseous fuel for flame propagation, which makes hemp catch fire easily and burn vigorously with flame.

TG curve of treated hemp with guanidine dihydrogen phosphate still shows four stages of thermal degradation. There is a mass loss of 5.5% in the temperature range 165-240°C with a slight endotherm in DTA curve. It is suggested that the initial reactions are dephosphorylation and that the released acids then catalyze the dehydration of hemp [13]. For the oxidative decomposition (second) stage, 15.8% mass loss in the temperature range 240-295°C is due to acid-catalyzed decomposition of hemp. The exotherm of DTA peaking at 344°C is due to the oxidation of volatile products. The third stage is prolonged in the temperature range 295-570°C. TG curve shows a mass loss of 25.7%. The exotherm in the temperature range 396-524°C is due to the oxidation of intermediate chars which may be aromatic components [14]. For the fourth stage, TG curve shows a mass loss of 14.8% in the temperature range 570-660°C. The exotherm in this stage is due to the oxidation of charred residues.

For the thermal degradation of hemp treated with GDP, there are some differences related to flame retardancy as compared to hemp in the terms of following:

(a) Main decomposition stages are divided into three small stages, including a new thermal decomposition stage at higher temperatures.

(b) Increase in heat release in the beginning of pyrolytic degradation.

Characterization of the char structure.

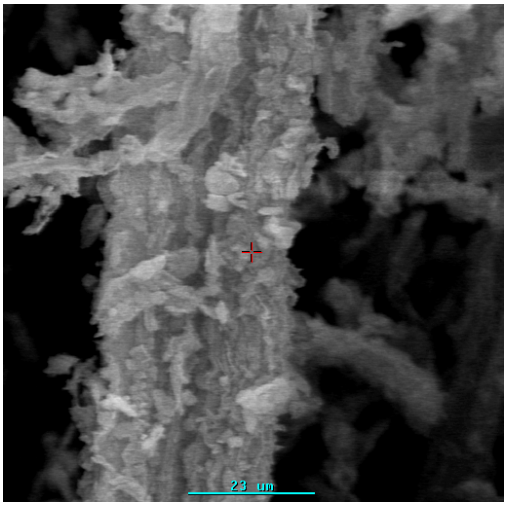

Fig. 3 Morphology of the char of sample 1.

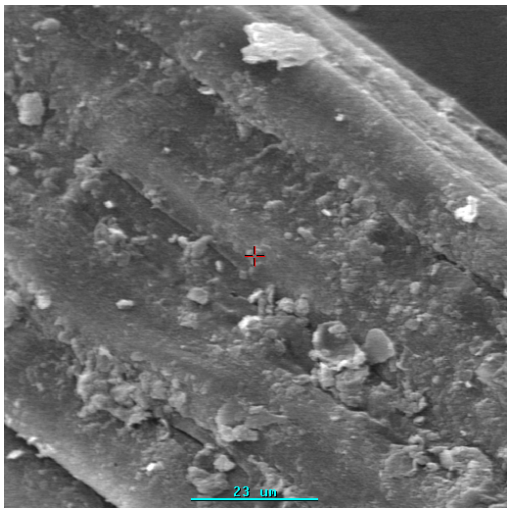

Fig. 4. Morphology of the char of sample 2.

Figs.3-4 present the SEM photographs of the surface of char of hemp and hemp treated with GDP at 350°C. From Figs. 3 and 4, it can be observed that hemp had been decomposed at 350°C, and the surface is very rough and irregular while it very different for hemp treated with GDP, which is dense and compact. The structure of the charring layer may increase the efficiency of the flame retardance, heat insulation, and protect inner matrix materials.

Flame Retardance of Samples and Mechanism. It is generally observed that the amount of char formed during thermal degradation of samples is related to the degree of flame resistance. In order to understand the flame retardant properties of these samples, the char yields (in mass %) determined at 700°C from TG curves are given in Table 1. From Table 1, it is evident that char yield and LOI values for hemp treated with GDP are high. These data suggest that the combustibility of the treated hemp is decreased. With the increases of char yields, the LOI values increase. This relation agrees with the mechanism of flame retardant. Thermal degradation mechanism of hemp in air has been review [8, 9]. At lower temperatures, the degradation of hemp involves dehydration, rearrangement and ultimate formation of carbonaceous residue and small amount of flammable products. At higher temperatures, the degradation of hemp includes a rapid volatilization via the formation of a tarry mixture which ultimately decomposes into flammable volatiles and leaves small amount of char. For hemp treated with GDP, the oxidative decomposition (second) stages include a decomposition stage at lower temperatures (165-240°C), which leads to more carbonaceous residue and small amount of flammable products. The higher LOI and char yield values in Table 1 show the good flame retardance. The SEM of the chars of hemp treated with

GDP also indicate the structure of the charring layer may increase heat insulation, and protect inner matrix materials.

Conclusions

The combustibility of the treated hemp is decreased, which has higher LOI and char yield values, For hemp treated with GDP, the oxidative decomposition stages include a decomposition stage at lower temperatures (165-240°C), leading to more carbonaceous residue and small amount of flammable products to get the good flame retardance. The SEM of the chars of hemp treated with GDP also indicate the structure of the charring layer may increase heat insulation, and protect inner matrix materials.

* Contract grant sponsor: [1] Fundamental research funds for the Central Universities: 3142013102

References

[1] Fire Statistics United Kingdom, Home Office, HMSO, 1992, p. 1994.

[2] J. K. Woo, and A. P. Schniewind, Holzforsch., 41 (1987) 305.

[3] H. Berndt, A. P. Schniewind and J. K. Woo, Holzforsch., 44 (1990) 439.

[4] T. P. Brady, and H. G. Langer, in W. Hemminger (Ed.) Thermal Analysis, Birkhauser Verlag, Basel, 2 (1980) 443.

[5] M. Gao, D. X. Pan and Y. C. Sun, J. Fire Sci., 21(3) (2003) 189.

[6] M. Gao, Y. C. Sun and K. Zhu, J. Therm. Anal. Cal., 75, (2004) 221.

[7] B. Kaur, I. S. Gur, and H. L. Bhatnagar, Angew. Makromol. Chem., 147 (1987) 157.

[8] M. Gao, K. Zhu and Y. C. Sun, J. Fire Sci., 22(6) (2004) 505.

[9] M. Gao, S. Y. Li and C. Y. Sun, Combustion Science and Technology, 176(12), (2004) 2057.

Advanced Materials Research Vol. 983 (2014) pp 179-182

doi:10.4028/www.scientific.net/AMR.983.179

Improving Mechanical Properties of Poly-β-Hydroxybutyrate-co-β-Hydroxyvalerate by Blending with Natural Rubber and Epoxidized Natural Rubber

CHUTAMAS Maneewong[1,a], JACKAPON Sunthornvarabhas[2,b], HYUN Joong Kim[3,c] and KLANARONG Sriroth[1,d *]

[1]Department of Biotechnology, Faculty of Agro-Industry, Kasetsart University, Chatuchak, Bangkok,Thailand. 10900.

[2]Cassava and Starch Technology Research Unit, National Center for Genetic Engineering and Biotechnology, Bangkok,Thailand. 10900.

[3]Laboratory of Adhesion and Biocomposite, Program in Environmental Materials Science, College of Agriculture and Life Science, Seoul National University, Seoul, Republic of Korea.151-921.

[a]chutamas_m@yahoo.com, [b]jackapon.sun@biotec.or.th, [c]hjokim@snu.ac.kr, [d]aapkrs@ku.ac.th

* Corespoding author

Keywords: Polyhydroxyalkanoates, Natural rubber, Epoxidized natural rubber, Blend, Toughness

Abstract. Poly-β-hydroxybutyrate-*co*-β-hydroxyvalerate (PHBV) is a bacterial-synthesized biopolymer. Moreover, PHBV is a biodegradable, it is an interesting biopolymer for disposable products. PHBV is difficult to process due to its low toughness, an elastic polymer such as natural rubber is introduced to develop toughness. In this experiment, PHBV mechanical properties were improved by blending with natural rubber (NR) and epoxidized natural rubber (ENR). The NR/PHBV and ENR/PHBV blends with the same ratio of 10/90 (wt/wt) could be extruded, whereas other conditions could not. This ratio was then used throughout this study to examine effect of maleic anhydride (MA) and benzoyl peroxide (BPO) to improve toughness of the blends. Result showed at composition where 1.0 % (wt/wt) MA and 0.05 % (wt/wt) BPO was mixed (coding EPMB2), several aspects of mechanical properties were improved. The blend, EPMB2 revealed the highest impact strength, significantly improved of elongation but drastically decreased of tensile strength. Storage modulus slightly decreased, tangent delta significantly increased when compared with neat PHBV.

Introduction

Polyhydroxyalkanoates (PHAs) is a biodegradable polymer. It has high crystallinity that makes it brittle. Blending PHBV with natural rubber (NR) could improve mechanical properties of PHBV. However, blending PHAs and NR is incompatible, NR is hydrophobic whereas PHAs is hydrophilic. Many attempts have been examined to develop compatibility of PHAs and NR by using compatibilizer and modifying of natural rubber such as epoxidized natural rubber (ENR).

Blending technology, many efforts attempted to improve mechanical properties of PHAs by blending PHAs with PLA [1-4] and propylene carbonate [5,6]. Using maleated polybutadiene as a compatibilizer for blending PHB with NR and ENR exhibited good compatibility and improved toughness [7]. This research focuses on improving toughness of poly-β-hydroxybutyrate-*co*-β-hydroxyvalerate (PHBV) which is a class of PHAs by blending with NR. The modified rubber such as ENR was also investigated. In order to enhance compatibility of PHBV and NR leading to improve mechanical properties of PHBV, the compatibilizer loading content such as maleic anhydride was examined.

Materials and Method

Materials. Poly-β-hydroxybutyrate-*co*-β-hydroxyvalerate (PHBV, ENMAT Y1000) was purchased from Ningbo Tianan Biologic Material Co. Ltd., China. NR bail grade STR 5L and ENR with 50% epoxidation level was purchased from Kij Paiboon Chemical Ltd., Thailand. Maleic anhydride (MA), was manufactured by Junsei Chemical Co. Ltd., Japan. Benzoyl peroxide (BPO), was manufactured by Alfa Aesar (A Johnson Matthey Company), South Korea.

Preparation of the Blends. The NR/PHBV blends were examined with following ratios (wt/wt): 10/90, 20/80 and 30/70, MA with 1.0 % (wt/wt) [8] was added in all blends. The ENR were examined with the same conditions. The formulation of the blends (Table 1) were mixed by a twin-screw extruder (Bautex, BA-19, Korea) with a screw diameter of 19 mm and L/D ratio of 40. Barrel temperature was in range of 140 to 172 °C. Screw speed was 50 rpm. After blending, strand extrudate was cut into pellets to use for examining morphological and mechanical properties.

Table 1 Formulation of the NR/PHBV and ENR/PHBV blends.

NR/PHBV	MA (% wt/wt)	BPO (% wt/wt)	ENR/PHBV	MA (% wt/wt)	BPO (% wt/wt)
NPMB1	0.5	0.05	EPMB1	0.5	0.05
NPMB2	1.0	0.05	EPMB2	1.0	0.05
NPMB3	5.0	0.05	EPMB3	5.0	0.05

Morphology. Morphology of neat PHBV and the blends were investigated with Scanning Electron Microscope (Mini SEM: nano eye, Korea).

Mechanical properties. The samples were prepared by injection molder (Bau Technology, Korea) with mixing speed 60 rpm at 175 ^{o}C for 5 min. Samples were then subjected to impact and tensile testing protocol and evaluated their behavior. Izod impact tests were performed according to ASTM D256 on a plastic impact tester (Daeyeong, Korea). Elongation at break, tensile strength and Young's modulus were examined according to ASTM D 638 on a Universal Testing Machine (Zwick).

Dynamic Mechanical Analysis. Storage modulus and tangent delta were determined on a Dynamic Mechanical Analyzer (DMA Q800, TA Instrument Korea). The DMA was run in the dual cantilever mode over a temperature range of -50 ^{o}C to 150 ^{o}C at a scanning rate of 5 ^{o}C per minute and using a frequency of 1Hz.

Results and discussion

Compatibility of the blends. During extrusion, NR/PHBV and ENR/PHBV blends with ratio 10/90 could be processed, whereas the others could not; 20/80 and 30/70. Figure 1 presents SEM micrograph of fractured surfaces. The SEM results of NR/PHBV and ENR/PHBV blends with ratio 10/90 (Figure 1A and 1D, respectively) exhibited small particles of rubber distributing in PHBV matrix. Therefore, this optimum ratio was used for studying to improve mechanical properties.

Mechanical Properties. Table 2 demonstrates mechanical properties of neat PHBV and the blends. EPMB2 exhibited the highest impact strength. In case of NR/PHBV blend, impact strength could not be improved.

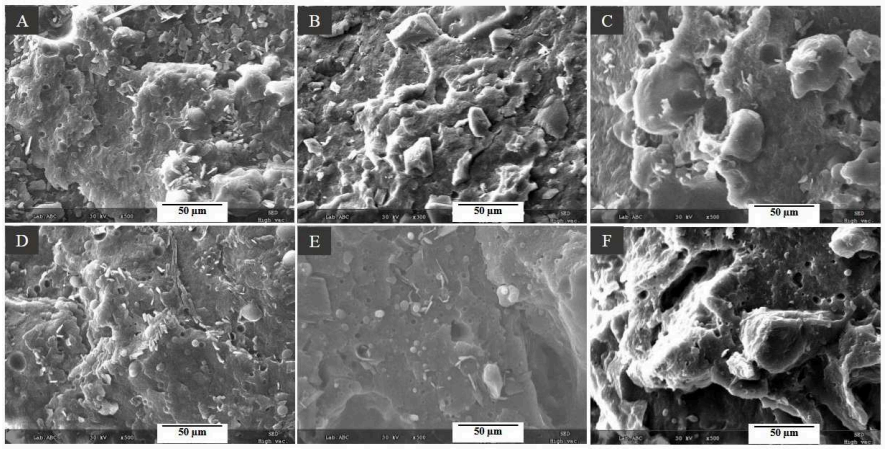

Fig 1 SEM micrographs of fractured surface of NPMB1 (A), NPMB2 (B), NPMB3 (C), EPMB1 (D), EPMB2 (E), and EPMB3 (F) (magnification × 500).

Dynamic Mechanical Analysis. Storage moduli and tangent delta of neat PHBV and ENR/PHBV blends were revealed in Figure 2. At below T_g, EPMB2 exhibited the highest storage modulus (Figure 2A). All blends presented higher tangent delta than neat PHBV (Figure 2B). High tangent delta revealed crosslinking between PHBV and NR/ENR. Therefore, addition of MA and BPO could promote reaction to enhance compatibility of ENR/PHBV.

Table 2 Mechanical properties of neat PHBV and the blends.

Samples	Impact Strength (kJ/m^2)	Elongation at Break (%)	Tensile Strength (MPa)	Young's Modulus (MPa)
PHBV	8.5^{a}	1.6	36.4	5778
NPMB1	2.47 ± 0.37	5.56 ± 0.65	7.95 ± 0.65^{f}	2387.98 ± 362.2^{i}
NPMB2	8.29 ± 0.67^{abc}	13.24 ± 1.02	8.75 ± 1.21^{fg}	2500.81 ± 211.5^{ij}
NPMB3	9.08 ± 0.46^{b}	22.95 ± 2.16^{e}	11.48 ± 1.86^{g}	2848.86 ± 101.2^{j}
EPMB1	4.48 ± 0.67	17.82 ± 1.75^{d}	11.41 ± 1.17^{h}	2732.65 ± 234.5^{j}
EPMB2	12.48 ± 0.84	19.88 ± 1.87^{de}	13.15 ± 1.87^{h}	2808.32 ± 257.8^{j}
EPMB3	7.71 ± 0.46^{c}	26.44 ± 1.64	18.68 ± 0.58	4775.99 ± 167.9

Note: different letters indicated statistically significant difference

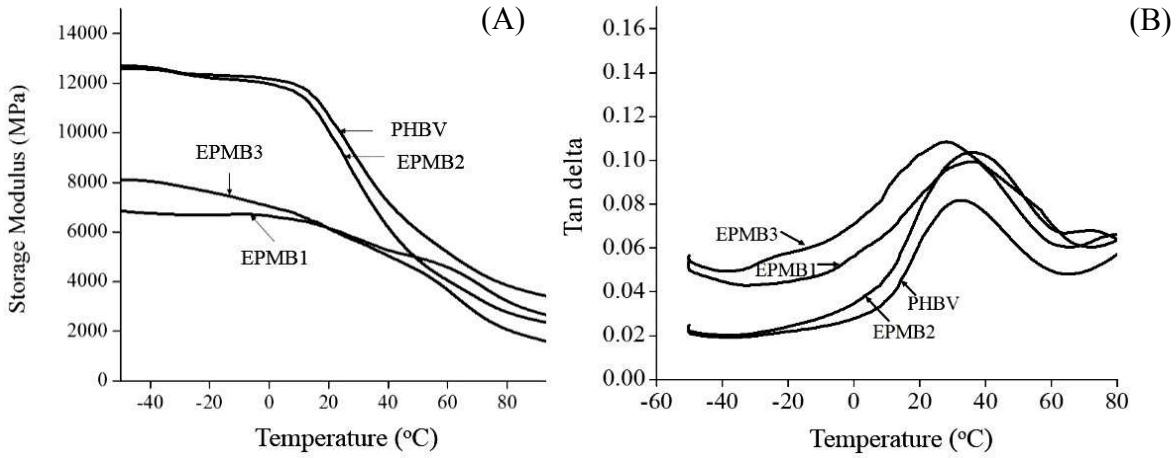

Fig 2 Storage modulus (A) and tangent delta (B) of the neat PHBV, EPMB1, EPMB2, and EPMB3.

Conclusion

In order to improve impact strength of PHBV by blending with NR or ENR, MA and BPO were needed to improve grafting. MA could improve compatibility by grafting onto the polymers backbone. Likewise, BPO generated free radical leading to an increasing grafting.

Addition MA with 1.0 % (wt/wt) and BPO with 0.05% (wt/wt) in ENR/PHBV blends (EPMB2) could improve impact strength and elongation at break. Storage modulus of EPMB2 slightly decreased, tangent delta significantly increased when compared with neat PHBV. Lower concentration of MA was required in ENR/PHBV blend comparing with NR/PHBV blends owing to an epoxy ring on ENR molecules reacting with PHBV directly.

Acknowledgment

The authors gratefully acknowledge financial support from Thailand Research Fund (TRF).

References

[1] Takagi, Y., R. Yasuda, M. Yamaoka, and T. Yamane, Morphologies and mechanical properties of polylactide blends with medium chain length poly(3-hydroxyalkanoate) and chemically modified poly(3-hydroxyalkanoate). J. Appl. Polym. Sci. 93 (2004) 2363-2369.

[2] Furukawa, T., H. Sato, R. Murakami, J. Zhang, I. Noda, S. Ochiai, and Y. Ozaki, Comparison of miscibility and structure of poly(3-hydroxybutyrate-*co*-3-hydroxyhexanoate)/poly(l-lactic acid) blends with those of poly(3-hydroxybutyrate)/poly(l-lactic acid) blends studied by wide angle X-ray diffraction, differential scanning calorimetry, and FTIR microspectroscopy. Polym. J. 48 (2007) 1749-1755.

[3] Gerard, T. and T. Budtova, Morphology and molten-state rheology of polylactide and polyhydroxyalkanoate blends. Eur. Polym. J. 48 (2012) 1110-1117.

[4] Zhao, Q., S. Wang, M. Kong, W. Geng, R.K.Y. Li, C. Song, and D. Kong, Phase morphology, physical properties, and biodegradation behavior of novel PLA/PHBHHx blends. J. Biomed. Mater. Res. Part B Appl. Biomater. 100B (2012) 23-31.

[5] Wang, X., S. Peng, and L. Dong, Effect of poly(vinyl acetate) (PVAc) on thermal behavior and mechanical properties of poly(3-hydroxybutyrate)/poly(propylene carbonate) (PHB/PPC) blends. Colloid. Polym. Sci. 284 (2005) 167-174.

[6] Corre, Y.-M., S. Bruzaud, and Y. Grohens, Poly(3-hydroxybutyrate-*co*-3-hydroxyvalerate) and poly(propylene carbonate) blends: an efficient method to finely adjust properties of functional materials. Macromol. Mater. Eng. 298 (2013) 1176-1183.

[7] Parulekar, Y. and A.K. Mohanty, Biodegradable toughened polymers from renewable resources: blends of polyhydroxybutyrate with epoxidized natural rubber and maleated polybutadiene. Green. Chem. 8 (2006) 206-213.

CHAPTER 4:

Manufacturing Processes, Materials Forming and Machining

Advanced Materials Research Vol. 983 (2014) pp 185-189

doi:10.4028/www.scientific.net/AMR.983.185

Application of calculus equation in solving thermal decomposition kinetics parameters of flame retardant epoxy resin [1]

Caiyun Sun [1, a], Yong-li Yang [2, b], Ming Gao[1,c]

[1] Department of Foundation, North China University of Science and Technology, Box 206, Yanjiao Beijing 101601, China

[2] School of Chemical and Environmental Engineering, China University of Mining and Technology, Beijing 100083, China

[a] yuncai@ncist.edu.cn, [b] yongli169@qq.com, [c]gaoming@ncist.edu.cn

Key words: Ozawa equation, Kissinger equation, activation energy, flame retardant

Abstract: The fire retardants were used in epoxy resin (EP) to get fire retardant EP, whose kinetic parameters activation energies (*Ea*) were calculated by Ozawa integral method and the Kissinger differential method. The results show that the correlation coefficient (R) is above 0.95, which shows good reliability of the two methods for solving *Ea*. E for the fire retardant foam is decreased by 40 $kJ \cdot mol^{-1}$, which shows that the fire retardant can catalyze decomposition and carbonization of EP.

Introduction

Epoxy resins are among the most important materials in modern polymer industries because of their balance of excellent heat, solvent, moisture, and chemical resistance, good mechanical and electrical properties, and satisfactory adherence to many substrates. Due to its structure containing flammable hydrocarbon chains, density, specific surface area, polyurethane is flammable, burn and decompose by fire, producing a large number of toxic smoke, bring fire hazards. Therefore, for aircraft, ships, railway cars, automobiles, and other important sites and facilities of EP, fire retardant requirements were made in China or abroad [1]. A series of fire retardants for EP are invented [2,3]. In recent years, Gao et al [4] invented an amino resinous fire retardant, which was added to the EP to get good fire retardancy.

On this basis, the kinetic parameters activation energies of the fire retardant EP were calculated by Ozawa integral method [5] and the Kissinger differential method [6], providing a theoretical basis for the study of the fire retardant mechanism.

1 Mathematical basis

For a solid state reaction, the reaction equation is

$$\mathrm{A}(s) \rightarrow \mathrm{B}(s) + \mathrm{C}(g) \tag{1}$$

The reaction rate can be expressed by two different forms:

Differential form: $$\frac{\mathrm{d}\alpha}{\mathrm{d}t} = k\, f(\alpha) \tag{2}$$

Integral form: $$G(\alpha) = k\, t \tag{3}$$

Where α is fraction of reacted A, t--- time, *k*--- reaction rate constant, f(α)--- differential form for reaction function, *G*(α)--- integral form for reaction function.

The relationship between f（α）an G（α）is:

$$f(\alpha)=\frac{1}{G'(\alpha)}=\frac{1}{\mathrm{d}[G(\alpha)]/\mathrm{d}\alpha} \tag{4}$$

The relationship between k and T can be well-known as Arrhenius equation:

$$k = A\exp(-E/RT) \tag{5}$$

Where A is Pre-exponential factor, E--apparent activation energy, R---gas constant, 8.3145 $J\cdot mol^{-1}\cdot K^{-1}$.

Equation (2) ~ (5) is under isothermal conditions, which are applied to non-isothermal conditions, the following relationship is:

$$T = T_0 + \beta\, t \tag{6}$$

Where $dT/dt = \beta$, T_0 is starting point temperature deviating from the baseline in DSC curve (K), β---heat rate (K/min).

The two commonly used kinetic equations in isothermal and non-isothermal conditions for heterogeneous systems are obtained:

$$d\alpha/dt = A\exp(-E/RT)f(\alpha) \qquad \text{(isothermal)} \tag{7}$$

$$\frac{\mathrm{d}\,\alpha}{\mathrm{d}\,T} = \frac{A}{\beta} f(\alpha)\exp(-E/RT) \qquad \text{(non-isothermal)} \tag{8}$$

2 Ozawa integral method

By integration and transform to equation (8), the Ozawa formula is obtained:

$$\log\beta = \log\left(\frac{AE}{RG(\alpha)}\right) - 2.315 - 0.4567\frac{E}{R}\cdot\frac{1}{T} \tag{9}$$

If α is constant, logβ and $1/T$ showed a linear relationship. For the TG curves in different β, logβ ~ $1/T$ diagram can be obtained, then E values obtained from the linear slope.

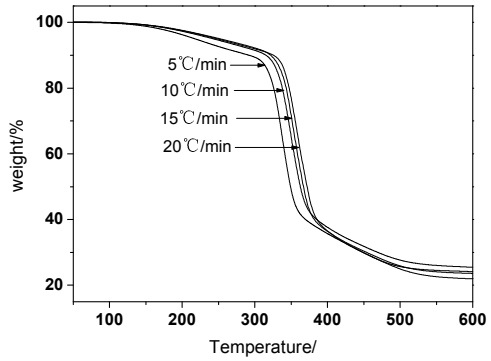

Figure 1 TG curves in different β

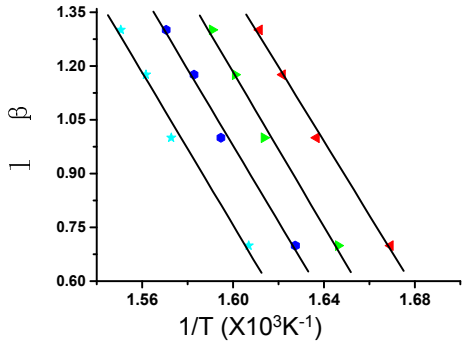

Figure 2 Relationship between logβ and $1/T$

From Fig1, it can be seen that the second stage in thermal decomposition of the fire retardant EP, decompose mainly and quickly, play a key role attributed to the combustibility. So we mainly discuss this stage. When β is 10, 20, 30 and 40 K/min, decompose fraction 50, 60, 70 and 80%, logβ, 1/T and correlation coefficient (R)are calculated as shown in Table 1. Based on Table 1, Figure 2 was obtained. It can be seen that logβ ~ 1 / T showed straight parallel lines, indicating that Ozawa method is applicable to the calculation of EP pyrolysis kinetic parameters. Then thermal decomposition activation energies of the second stage for fire-retardant EP were calculated

according to Figure 2. From Figure 2, it can be seen the good linear correlation, the correlation coefficient R above 0.95, which shows good reliability of the results.

Table 1 Data of logβ and 1/T in different α

logβ \ 1/T	50%	60%	70%	80%
	x10^{-3}/1·K^{-1}	x10^{-3}/1·K^{-1}	x10^{-3}/1·K^{-1}	x10^{-3}/1·K^{-1}
1	1.5150	1.4984	1.4823	1.4635
1.3	1.4865	1.4690	1.4542	1.4351
1.477	1.4787	1.4612	1.4438	1.4235
1.602	1.4588	1.4425	1.4393	1.4086
R	0.956	0.952	0.958	0.984

3 Kissinger differential method

Assumed reaction mechanism function is $f(\alpha)=(1-\alpha)^n$, corresponding kinetic equation can be expressed as:

$$\frac{\mathrm{d}\alpha}{\mathrm{d}t}=Ae^{-E/RT}(1-\alpha)^n \tag{10}$$

The equation describes a corresponding thermal analysis curve, differential form of equation (10) is:

$$\frac{\mathrm{d}}{\mathrm{d}t}\left[\frac{\mathrm{d}\alpha}{\mathrm{d}t}\right]=\left[A(1-\alpha)^n\frac{\mathrm{d}e^{-E/RT}}{\mathrm{d}t}+Ae^{-E/RT}\frac{\mathrm{d}(1-\alpha)^n}{\mathrm{d}t}\right]=\frac{\mathrm{d}\alpha}{\mathrm{d}t}\left[\frac{E\dfrac{\mathrm{d}T}{\mathrm{d}t}}{RT^2}-An(1-\alpha)^{n-1}e^{-E/RT}\right] \tag{11}$$

In the peak of the thermal analysis curve, its first derivative is zero, that is, the boundary conditions are:

$T=T_p$ $\qquad \dfrac{\mathrm{d}}{\mathrm{d}t}\left[\dfrac{\mathrm{d}\alpha}{\mathrm{d}t}\right]=0$

Putting it into equation (11):

$$\frac{E\dfrac{\mathrm{d}T}{\mathrm{d}t}}{RT_p^2}=An(1-\alpha_p)^{n-1}e^{-E/RT} \tag{12}$$

Kissinger proposed that $n(1-\alpha_p)^{n-1}$ is nothing to do with β, which is nearly equal to 1. So equation（12）is changed into :

$$\frac{E\beta}{RT_p^2}=Ae^{-E/RT_p} \tag{13}$$

Logarithm of the equation (13) is equation (14), namely the Kissinger equation:

$$\ln\left(\frac{\beta_i}{T_{pi}^2}\right)=\ln\frac{A\cdot R}{E}-\frac{E}{R}\cdot\frac{1}{T_{pi}} \qquad i=1\quad 2\quad \cdots \tag{14}$$

Where T_{Pi} is peak temperature in DTG curve.

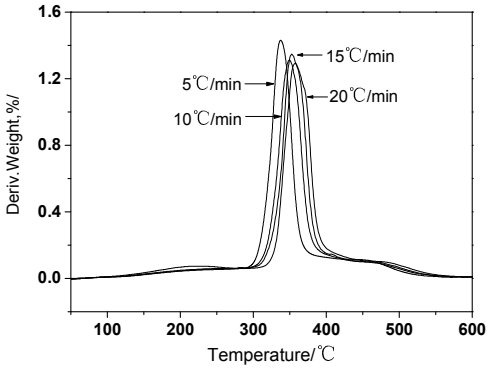

Figure 3 DTG curves in different β

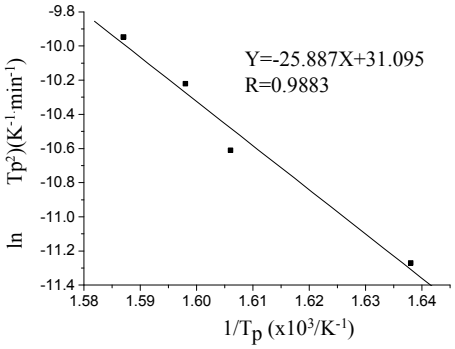

Figure 4 Relationship between $ln(\beta/T_P^2)$ and $1/T$

Differential of Figure 1 to get Figure 3, then T_{pi} are obtained. The linear in Kissinger equation is shown in Figure 4. From the slope of the plot, the activation energy can be calculated, i.e. *Ea*=R×slope while A can be gotten from intercept. Activation energies calculated by two methods are shown in Table 2. Figure 4 shows the good linear correlation, the correlation coefficient R with 0.962 shows the good reliability of the results.

Table 2 Activation energies of EP and fire retardant EP kJ/mol）

Methods	EP	fire retardant EP
Ozawa method	230.4	193.8
Kissinger method	246.2	215.2

From Table 2, it can be seen that the results calculated by the two methods are similar, a little lower by Ozawa method. Moreover, activation energies for EP is higher, that for fire retardant EP reduced by near 40 kJ/mol, which shows the fire retardant can catalyze decomposition of EP, producing more water and carbon residue, less of flammable gases, to achieve the purpose of fire retardancy.

4 Conclusions

The fire retardant foam, whose kinetic parameters activation energies of EP were obtained by Ozawa integral method and the Kissinger differential method. The results show that the correlation coefficient is above 0.95, which shows good reliability of the two methods for solving *Ea*. *Ea* for the fire retardant EP is decreased by 40 $kJ \cdot mol^{-1}$ compared with EP, which shows that the fire retardant can catalyze decomposition producing more water and carbon residue, less of flammable gases, to achieve the purpose of fire retardancy.

[1] Contract grant sponsor: Fundamental research funds for the Central Universities: 3142013102; Key project supported by North China Institute of Science and Technology: HKXJZD201402.

References

[1] M. M. Hirschler: Polymers for Advanced Technologies, Vol. 19 (2008), p. 521
[2] O. M. Putzeys, A. C. Fernandez-Pello, G. Rein and D. L. Urban: Fire and Materials, Vol. 32(2008), p. 485
[3] M. Zammarano and R. H. Krämer: Polymers for Advanced Technologies, Vol. 19(2008), p. 588
[4] M. Gao, T. Wang, F. C. Wu and R. J. Yang: Polymer Materials Science and Engineering, Vol. 25 (2008), p. 45
[5] T. Ozawa: Polymer, Vol. 12 (1971), p. 150
[6] H. E. Kissinger: J Research Natl Bur Standards, Vol. 57 (1956), p. 217

Advanced Materials Research Vol. 983 (2014) pp 190-193

doi:10.4028/www.scientific.net/AMR.983.190

Application of calculus equation in solving thermal decomposition kinetics parameters of flame retardant wood

Caiyun Sun [1, a], Yong-li Yang [2, b], Ming Gao[1,c]

[1] Department of Foundation, North China University of Science and Technology, Box 206, Yanjiao Beijing 101601, China

[2] School of Chemical and Environmental Engineering, China University of Mining and Technology, Beijing 100083, China

[a] yuncai@ncist.edu.cn, [b] yongli169@qq.com, [c]gaoming@ncist.edu.cn

Key words: Broido equation, activation energy, pyrolysis, wood.

Abstract: Wood has been treated with amino resins and amino resins modified with phosphoric acid to impart flame retardancy. The thermal degradation of samples has been studied by thermogravimetry (TG) in air. From the resulting data, kinetic parameters for different stages of thermal degradation are obtained following the method of Broido. For the decomposition of wood and flame retardant wood, the activation energy is found to decrease from 122 to 72 $kJmol^{-1}$.

Introduction

Because wood catches fire easily and burns vigorously with flame, it will be essential to make wood flame retardant as used for furniture, decorate and building materials. Some of most successful commercial flame-retardants for wood have been amino resins modified with phosphoric acid which are effective, stable, leach resistant and non-blooming flame-retardants [1,2]. The function of flame retardant in wood is to increase the char at the cost of flammable volatile products [3]. In the previous study, wood was treated with amino resins and modified amino resins with phosphoric acid [4,5]. In the present study, the values of different kinetic parameters of wood and modified wood were calculated by the Broido equation [6], providing a theoretical basis for the study of the fire retardant mechanism..

Experimental

Chemicals

Phosphate salt of the guanyl urea: 37% formalin as formaldehyde [F] 1 mol was brought to PH 8-8.5 with NaOH and heated. Then dicyandiamide [D] 1mol was added to the above solution, stirred until dissolved and heated under reflux for 10 min. Heating was stopped and the solution allowed to cool to 50-60℃. Then 85% phosphoric acid as phosphorus [P] 1 mol was added slowly. Then a solution of hydroxymethyl guanyl urea phosphoric acid was obtained [2].

The following procedures of preparation were similar to that of DFP. MFP was obtained with melamine, formaldehyde and phosphoric acid in the mole ratio 1:1:1. UDFP was obtained with urea, dicyandiamide, formaldehyde and phosphoric acid in the mole ratio 1:1:4:2. MF was produced by melamine and formaldehyde in the mole ratio 1:5. DF was produced by dicyandiamide and formaldehyde in the mole ratio 1:1. The reactants were diluted with water up to the prescribed concentration before use.

Regardless of the kinds of basic nitrogen compound, reaction between the nitrogen compound and formaldehyde forms a methylolated product. Methylolated products are polymerized by condensation reaction and develop a cross-linking structure by heat.

Sample preparation

Samples of white pine (*North of China*) were heated for 1 hour in boiling water. After this procedure, the wood was dried at 60℃. Then the wood was immersed in treating solution at 60℃ for 2 hours, and each sample was dried at 60℃. Samples milled passing 50 meshes were for thermal analysis. Sizes were 100mm L x 6mm W x 3mm T for LOI test. The samples1−6, pure and treated wood with the aqueous solution of DF, MF, DFP, MFP, and UDFP as flame retardants, respectively, were listed in Table 1-3.

Thermal analysis

Differential thermal analysis (DTA) and thermogravimetry (TG) were carried out on a DT-40 thermal analyzer (Shimadzu, Japan). DTA and TG were performed under a dynamic air (dried) atmosphere at a heating rate of 10℃min^{-1}.

Results and discussion

The simultaneous DTA and TG curves of samples (1−6) were carried out in a dynamic air from ambient temperature to 650℃ and are shown in Figure 1. The weight losses for various stages in TG curves are given in Table 1.

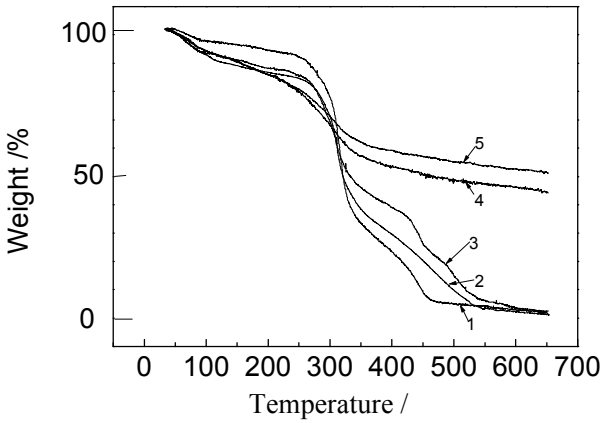

Fig.1. TG curves of sample (vi) in air.

TG curves of wood samples show three stages of the thermal degradation. There is a weight loss in the temperature range100-250℃ in the first stage, which is due to dehydration of wood. For the second stage, rapid weight loss occurs in the temperature range 250-350℃, which is due to the oxidative decomposition of wood. In this stage, the less stable aliphatic groups are preferentially decomposed through hemolytic cleavage of C-C and C-H bonds, and the resultant product is a highly condensed and cross linked carbonaceous which is a little more stable. After the oxidative decomposition stage, weight losses of the residual materials of wood are found to be slow in the temperature range 350-600℃, which is due to the oxidation of the carbonaceous.

For the various stages of thermal degradation of wood, the order of reaction is between 0 and 1. So the kinetic parameters for these stages were determined using the following equation, given by Broido [6]:

$$\ln(\ln\frac{1}{y}) = -\frac{Ea}{R}\cdot\frac{1}{T} + \ln(\frac{R}{Ea}\cdot\frac{Z}{\beta}\cdot T_m^2)$$

Where *y* is the fraction of initial molecules not yet decomposed. T_m is the temperature of maximum reaction rate, β is the rate of heating, Z is the frequency factor, and Ea is the activation energy.

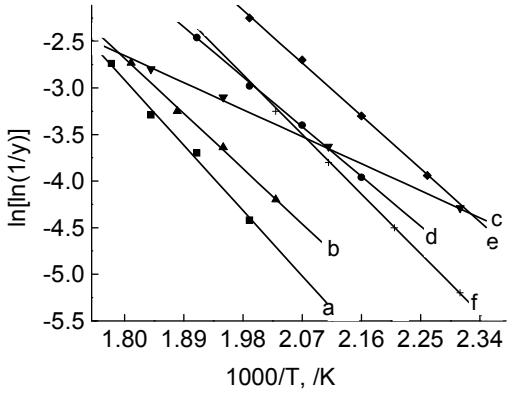

Fig.2 Plots of ln[ln(1/y)] versus 10^3/T using Broido equation for samples for first stage of thermal degradation in air.

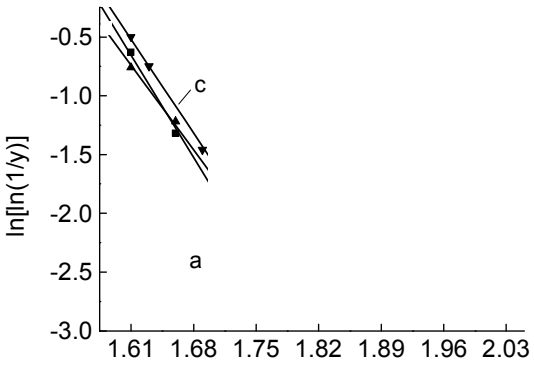

Fig.3 Plots of ln[ln(1/y)] versus 10^3/T using Broido equation for samples for second stage of thermal degradation in air.

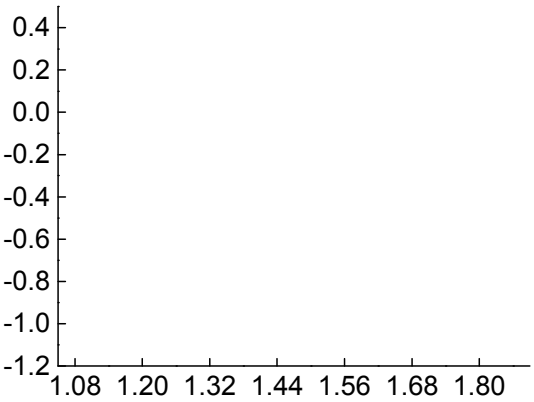

Fig.4 a, b, c, d, e, f are the plots of ln[ln(1/y)] versus 10^3/T using Broido equation for samples (i –vi) for third stage of thermal degradation in air.

From the slopes of the TG curves in Fig 1, plots of ln(ln1/*y*) versus 1/T for various stages of pyrolysis were drawn. Linear plots were obtained in each instance, and are shown in Figs 2-4. The activation energies, *Ea,* and the frequency factors, Z, determined from the slopes and intercepts, respectively, of these plots are given in Table 2. From Table 2, it is observed that for the first stage of thermal degradation of wood, mainly due to dehydration, the activation energy is 67 kJmol^{-1}; which for samples (4–6) reduce to 50, 52 and 59 kJmol^{-1}, respectively. This is mainly due to dephosphorylation and acid-catalyzed dehydration.

Generally, at lower temperatures, the degradation of wood involves dehydration, rearrangement and ultimate formation of carbonaceous residue and small amount of flammable products. At higher temperatures, the degradation of wood includes a rapid volatilization via the formation of a tarry mixture which ultimately decomposes into flammable volatiles and leaves small amount of char. For samples (4–6), the oxidative decomposition (second) stages occur at lower temperatures, which makes pyrolytic degradation of samples proceed through the first type of reaction. This factor will give a lower percent of flammable volatile products and correspondingly higher amount of char yield.

Table 1. The kinetic parameters of samples.

No.	Flame retardant	Stage	Weight loss (%)	Temperature range (℃)	Ea KJmol^{-1}	Z (s^{-1})
1	—	1st	7.2	230-290	67	$3.6\ 10^{2}$
		2nd	43.3	290-350	122	$8.1\ 10^{7}$
		3rd	36.2	350-540	19	$2.0\ 10^{-2}$
2	DF	1st	7.8	220-290	55	$3.1\ 10^{1}$
		2nd	30.2	290-348	87	$4.3\ 10^{4}$
		3rd	40.4	348-600	16	$8.0\ 10^{-3}$
3	MF	1st	7.0	150-290	27	$3.4\ 10^{-1}$
		2nd	31.0	290-350	96	$3.6\ 10^{5}$
		3rd	38.5	350-600	18	$2.0\ 10^{-2}$
4	DFP	1st	6.6	180-250	50	$2.5\ 10^{1}$
		2nd	27.4	250-296	92	$6.4\ 10^{5}$
		3rd	37.4	296-582	13	$5.6\ 10^{-3}$
5	MFP	1st	6.8	160-230	52	$1.1\ 10^{2}$
		2nd	26.7	230-285	72	$1.3\ 10^{4}$
		3rd	35.4	285-584	15	$1.2\ 10^{-2}$
6	UDFP	1st	4.5	160-232	59	$2.9\ 10^{2}$
		2nd	26.3	232-290	84	$1.2\ 10^{5}$
		3rd	35.0	290-577	13	$5.9\ 10^{-3}$

In the case of samples (4–6), the lowering of the decomposition temperatures is much great. Their activation energies for the second stage of pyrolysis, in a range of 72-92 kJmol^{-1}, decrease considerably as compared to wood. This is due to catalyzed decomposition of flame retardant. This shows that the flame-retardants change the mechanism of thermal degradation in such a way as to reduce the decomposition temperatures of wood, which can lead to less flammable volatile products and more char to get good flame retardancy.

Summary and conclusions

For the decomposition of wood and flame retardant wood, the activation energy is found to decrease from 122 to 72 kJmol^{-1}, the char yield is found to increase from 6.0 to 30.8%, LOI from 18 to 41.5, which indicates that the flame retardants catalyzed decomposition of wood, which makes the whole oxidative decomposition of wood occur at lower temperatures, resulting in formation of less flammable products and correspondingly more char. So the wood treated with amino resins modified with phosphoric acid has high flame retardant efficiency.

Acknowledgments

The work was supported by fundamental research funds for the central Universities(3142013102) and key project of North China Institute of Science and Technology (HKXJZD201402).

References

[1] Goldstein, I. S. and Dreher, W. A., 1964, U. S. 3,159,503.
[2] Juneja, S. C., 1975, U. S. 3,887,511.
[3] Bhagwan, J. and Lal, K., 1990, J. Polym. Mater. 7, 231.
[4] Gao, M. Zhu, K. and Sun, Y. C., J. Fire Sci., 22(6) (2004) 505.
[5] Gao, M. Li, S. Y. and Sun, Y. C., Combustion Science and Technology, 176(12), (2004) 2057
[6] Broido, A., 1969, J. Polym. Sci. Part A-2, 7, 1761.

Advanced Materials Research Vol. 983 (2014) pp 194-197

doi:10.4028/www.scientific.net/AMR.983.194

Dynamic analysis of stiffness part for a electromagnetic high frequency fatigue testing machine

Zheng yan [1, 2,a], Zhang yong [2] and Fan xiaowang [2]

[1.] Jilin university mechanical science and engineering college

[2.] Changchun mechanical science research institute co., LTD

[a]435562852@qq.com

Key words: Stiffness Fatigue; Testing Machine, The Mechanical Model

Abstract: Aiming at the problem that complex systems mechanical model is difficult to set up and analyze accurately, a certain type of electromagnetic high frequency fatigue tester as engineering background, setting up its mechanical model and carrying on the reasonable simplified. Through analyzing the effect of system mechanical properties causing by system main large stiffness parts, and determining the design principle of the engine's stiffness components, it provides scientific theoretical foundation for the design of this type host.

Introduction

Electromagnetic resonant high frequency fatigue tester is researched early in foreign countries, such as Switzerland and the UK's companies, it has high control precision, stability, and intelligent. But its structure is complex, and the price is expensive. At present, the domestic main research achievements include: Liu Jie[1], Li Jiansheng[2], Chen Haiming[3], its main work is main analyze the control and simulation, it has good theoretical level. It is not starting from the system mechanics model, so its guide for the practical design work is slightly insufficient. High-frequency fatigue tester has the dynamics characteristics of big quality, large elastic, large stiffness, its system dynamics model is very complex, and it maybe exist not decoupling elements. In this paper, through the establishment of the system simplified mechanical model, to solve the model system with damping cases, analyzing the effect of system mechanical properties causing by system main stiffness parts, and determining the design principle of large stiffness parts, it provides scientific theoretical foundation for the design work of this type host and it has a strong guiding role.

The Mechanics Model Establishment of a Certain Type of Electromagnetic Resonant High-Frequency Fatigue Tester

Figure 1 is high frequency fatigue tester host structure diagram, according to analysis, We can simplify the host physical structure, and assuming: The frame quality M6, The main vibration quality M4, Vibration quality M3, Additional dispelling code M5, Support spring K6, The main vibrating spring K4, Specimen K5, Vibration system spring K3.

To simplify host structure of tester，it simplify the physical structure that connected together to a whole mass block, Such simplification is reasonable, it will not affect the model accuracy. According to the principle of mechanics [4], the simplified model diagram as shown in Fig 2:

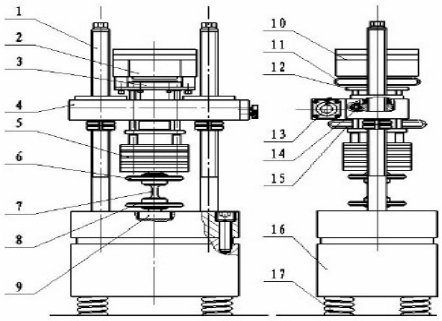

1.Screw 2.Magnet 3.Armature 4.The beam 5.Farmar 6.The up jig 7.Sample 8.The down jig 9.The sensor 10.Encourage quality 11.Incentive spring 12.The tray 13.The motor 14.The turbine worm 15.Arch ring 16.The base 17.Damping spring

Fig. 1 Host Structure Diagram

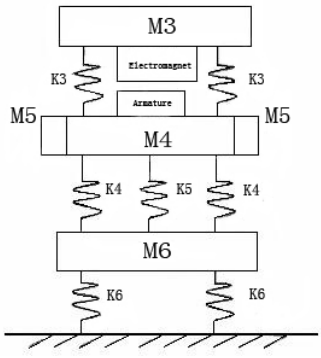

Fig.2 A Simplified Model

System mechanics model after simplified [5], by

$$\begin{Bmatrix} M_{dct}\ddot{x}_1 + 2k_{tjsg}(x_1 - x_2) = F \\ M_{xt}\ddot{x}_2 + 2k_{tjsg}(x_2 - x_1) + k_{jxg}(x_2 - x_3) = -F \\ (M_{dhl} + 2M_{lzs})\ddot{x}_3 + k_{jxg}(x_3 - x_2) + 2k_{tj}(x_3 - x_4) + 2k_{lz}(x_3 - x_5) = 0 \\ M_{fm}\ddot{x}_4 + 2k_{tj}(x_4 - x_3) + k_{sy}(x_4 - x_5) = 0 \\ (M_{dz} + 2M_{lzx})\ddot{x}_5 + k_{sy}(x_5 - x_4) + 2k_{lz}(x_5 - x_3) + 4k_{tjzct}x_5 = 0 \end{Bmatrix} \quad (1)$$

Have:

$$\mathbf{M}\ddot{\mathbf{x}} + \mathbf{K}\mathbf{x} = F_A \cos(\omega t)\mathbf{f} \quad (2)$$

Among them:

$$\mathbf{M} = \begin{bmatrix} M_{dct} & 0 & 0 & 0 & 0 \\ 0 & M_{xt} & 0 & 0 & 0 \\ 0 & 0 & M_{dhl} + 2M_{lzs} & 0 & 0 \\ 0 & 0 & 0 & M_{fm} & 0 \\ 0 & 0 & 0 & 0 & M_{dz} + 2M_{lzx} \end{bmatrix} \quad (3)$$

$$\begin{bmatrix} F \\ -F \\ 0 \\ 0 \\ 0 \end{bmatrix} = F\begin{bmatrix} 1 \\ -1 \\ 0 \\ 0 \\ 0 \end{bmatrix} = F_A\cos(\omega t)\begin{bmatrix} 1 \\ -1 \\ 0 \\ 0 \\ 0 \end{bmatrix} = F_A\cos(\omega t)\mathbf{f} \tag{4}$$

$$\mathbf{K} = \begin{bmatrix} 2k_{tjsg} & -2k_{tjsg} & 0 & 0 & 0 \\ -2k_{tjsg} & 2k_{tjsg}+k_{jxg} & -k_{jxg} & 0 & 0 \\ 0 & -k_{jxg} & k_{jxg}+2k_{tj}+2k_{lz} & -2k_{tj} & -2k_{lz} \\ 0 & 0 & -2k_{tj} & 2k_{tj}+k_{sy} & -k_{sy} \\ 0 & 0 & -2k_{lz} & -k_{sy} & k_{sy}+2k_{lz}+4k_{tjzct} \end{bmatrix} \tag{5}$$

The Influence Analysis for System of the Three Main Stiffness Components

According to the mechanical model established, applying MATLAB to simulate the model[6-7], changing parts' stiffness value within the range[1×10^8,1×10^9 N/m], analyzing the corresponding change rule of system fundamental frequency, getting three main stiffness parts corresponding relationship graphs between stiffness value and system fundamental frequency:

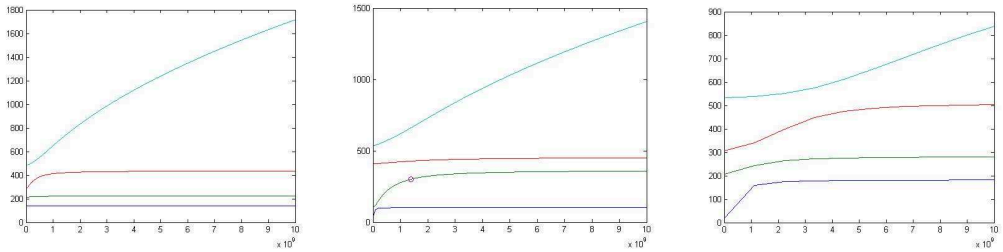

a）The up toxoplasma ring　b）The down toxoplasma ring　c）The base support spring

Fig.3 The Influence Analysis for System of Main Stiffness Components

It can be seen from the above Fig.3:

1 Stiffness change of up toxoplasma ring has little impact on first and second order fundamental frequency and towards stability, and first and second order fundamental frequency is in the work required security scope;

2 The stiffness of down toxoplasma ring in the greater than 3×10^9 N/m, the influence for first and second order fundamental frequency are towards stability, and firs order fundamental frequency is in the work required security scope, but second order fundamental frequency is beyond the scope of security;

3 The stiffness of the base support spring in the greater than 2×10^9 N/m, the influence for first and second order fundamental frequency are towards stability, and first and second order fundamental frequency is in the work required security scope;

It should be pointed out that, larger value of the base support spring will increased system 1 order frequency obviously, this will lead to the energy larger that resonance needs, it is beneficial to the actual design needs.

Conclusion

From the above work, when the engine is designed，when the stiffness of the up toxoplasma ring, the down toxoplasma ring and the base support spring are selected, it can be selected in the scope of $[1\times10^{8},1\times10^{9}]$N/m, the base support spring should be selected smaller as far as possible, while the stiffness value of down toxoplasma ring should not be too large, because larger value of down toxoplasma lead the system fundamental frequency significantly larger directly, and it will affect the system's security .

References

[1]Liu Jie, Wu Lin, Ji Shengqing, Wen Bangchun. Electric Vibration Amplitude Control Mathematical Model[J]. JOURNAL OF NORTHEASTERN UNIVERSITY,1996,01(22):23-26.
[2]Li Jiansheng. The Calculations and Analysis of the Vibration System of Pesonance Electro Magnetic Vibrator[J].JOURNAL OF GUIZHOU AGRICULTURAL COLLEGE,1997. 16,(2): 70-75.
[3]CHEN Hai-ming, HU Xin-hua, YANG Ji-long, JIANG Wei. The Simulation and Analysis of the Vibration System of Resonance Electromagnetism Vibrator[J]. Hydromechatronics Engineering, 2004,7(45):78-81.
[4]REN Xing-min,QIN Wei-yang. Engineering Vibration Foundation[M]. Beijing: Mechanical industry press,2005.
[5]SHI Han-min. vibration Systems - Analyzing. Testing. Modeling. Controlling(volume 1) [M]. Wuhan: Huazhong university of science and technology press, 2005.
[6]CHANG Zhi guo, LI Hong nan, WANG Hao. Structural Vibration Control Simulation Study[J]. Journal of Shenyang Architectural and Civil Engineering Institute, 2002,34(04):38-42.
[7]DU Chun-yan, LI Li-jun. Computer MTLAB Simulation Study Method Based on Vibration Theory[J].Journal of Jiamusi University(Natural Science Edition), 2002,57(04):60-63.

Advanced Materials Research Vol. 983 (2014) pp 198-203

doi:10.4028/www.scientific.net/AMR.983.198

New Upgrade Solution to Highway Concrete Barrier

Meng Li[1,a], Haixia Yu[1,b]

[1] Research Institute of Highway Ministry of Transport,

8 Xitucheng Rd, Beijing, China, 100088

[a]meng.li@rioh.cn, [b]hx.yu@rioh.cn

Keywords: guardrail, simulation, upgrade, Highway concrete barrier

Abstract: There are tens of thousands of highway miles with in-service concrete barriers all over the world. Many of them require upgrade to meet new collision protection level. In order to find a reliable and economical solution, authors of this paper develop three solutions in term of different materials and structures. Then, researchers use finite element to verify the effect of each solution and compare their expense. Advantages and disadvantages are discussed in the paper. Moreover, the paper explore the feasibility to adopt one of three solutions in the project in Guangdong province, China.

0.Introduction

Concrete barrier, such as the Jersey barrier, is one of the most common highway safety facilities. It offers protection for properties and passengers in vehicle accidents. There are numerous miles of concrete barriers serving in various countries. A lot of them were installed one or two decades ago. Both design and material of these old concrete barriers barely meet the new requirements of safety performance even though the quality of them still stays well. Highway agencies in different districts face the same dilemma that it is squander to replace these concrete barrier with brand new ones but the new safety standard demands higher safety performance level. Hence, it is a compromised scheme to upgrade old concrete barriers instead of whole replacement. Upgrade solutions adopts new material and design based on old concrete barriers so that the service period of concrete barriers can be extended. The upgrade project can save a lot of budget for new barrier purchase and diminish industrial pollution.

The research is based on a highway guardrail upgrade project in Highway Guangshen. which is a two-way six-lane freeway connecting Guangzhou and Shenzhen in China. The local highway management corporation plans to improve the anti-collision capacity of the highway median barrier, which is set in the median to prevent vehicle running into opposite lanes. The highway was open to traffic in 1994, and the design are for last century standards. The anti-collision performance cannot satisfy users and management agency since it has not been rehabilitated over the last two decades. The object of this project is to raise the anti-collision performance of in-service highway concrete barriers up to 280kj-level, which is new requirement for highway barrier in China.

1. Design of The Highway Barrier Before Upgrade

The in-service concrete median barrier before upgrade is similar to the Jersey barrier, which is the most common type in the world, though they are not exactly the same. TheFig.1 illustrate its cross section of original design and the photo of these barriers. The compressive strength of concrete originally is 30MPa, however, long-term corrosion greatly weakens the strength. Another issue is that the height of concrete barrier is only 800mm, while new standard requires a higher median barrier to offer better safety performance. The original design required 160kj-level impact protection. Finally, researchers expect to lift the impact kinetic energy of the highway barrier up to 280kj, which means the barrier can bear 280kj energy once vehicle-barrier crash occurs. [2]

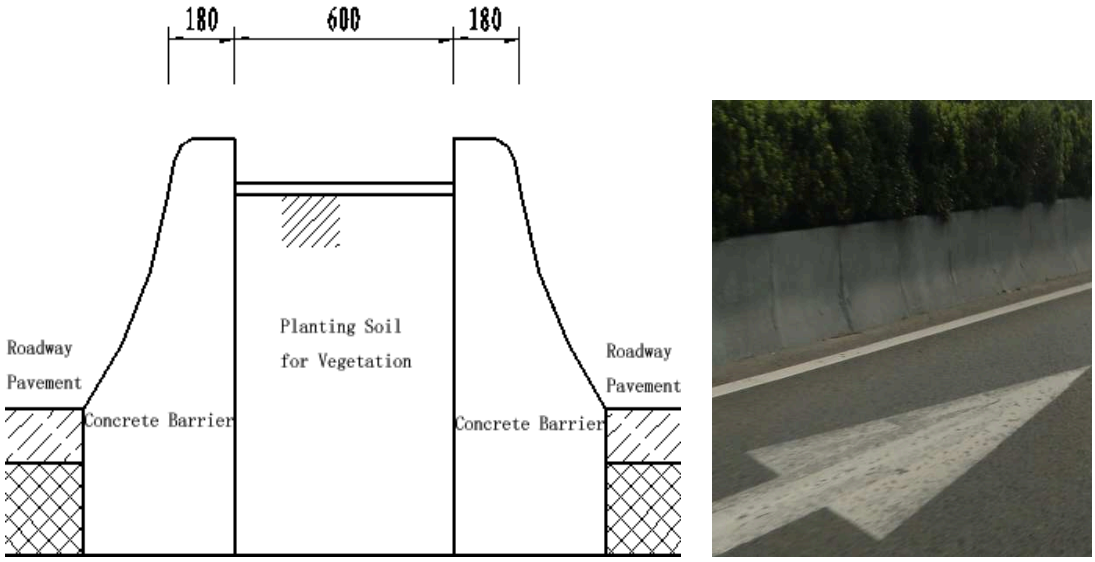

Fig.1 The original median concrete barrier before upgrade

2 Upgrade Solutions

The key point of the upgrade project is to increase the height and strength of the barrier at economical cost. The best method is to design a composite guardrail and keep the original concrete barrier. In order to accomplish the objective, researchers develop three different solutions for the upgrade project, and then study the feasibility of them.

2.1 Single-beam steel guardrail mounted on concrete barrier. The first solution combines the steel guardrail and original concrete barrier together. The cross-section is shown in Fig.2. The steel guardrail consists of mounts, high-strength bolts and cube steel beam. The function of mounts and bolts is to connect concrete components and steel components. The steel beam provides extra height and protection for vehicle impact. The total height above pavement surface rise from 800mm to 950mm. The anti-collision performance, especially for large vehicle like bus, is significantly improved by the composited design.

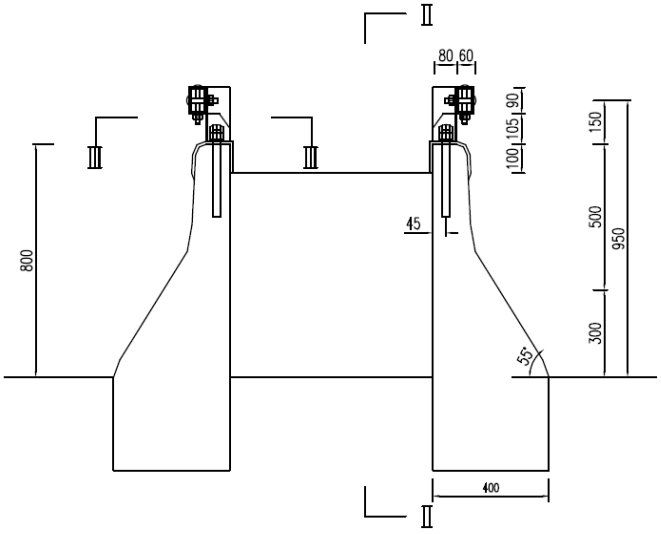

Fig.2 Solution 1 cross-section

2.2 Double-beam steel guardrail mounted on concrete barrier. The second solution is a Power-up edition of the first solution. There is a same thought in design. There are two differences between Solution 1 and 2. The burying depth of concrete barrier is deeper than Solution 1, the reason for this design is not that engineers plan to thrust barrier into soil but that the surface of pavement might rise due to pavement upgrade, which causes the height outside pavement maybe not enough. The second difference is there are two beams instead of a single-beam system. It can offer enough height and strength even when additional pavement is added. Fig.3 displays the cross section for solution 2.

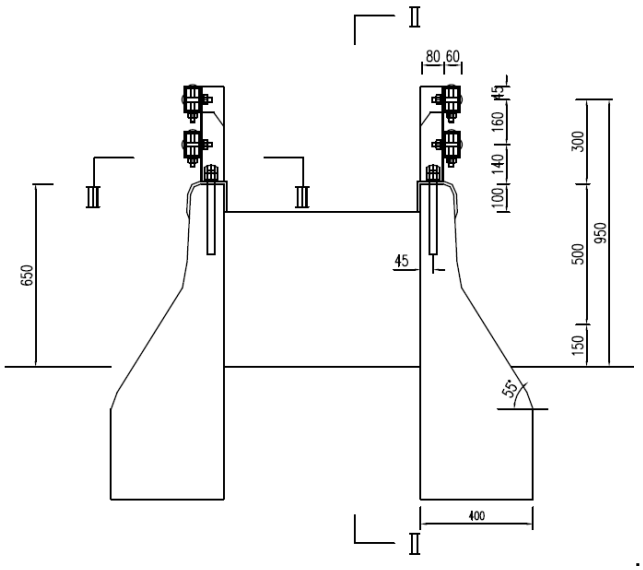

Fig.3 Solution 2 cross-section

2.3 Reinforced Concrete-lid. The third solution is to add a reinforced concrete lid over two rows of median barriers, connecting by 12mm-radius steel bar. The concrete lid increases height and strength for barriers. It is supported by original concrete components. Solution 3 is shown in Fig.4.

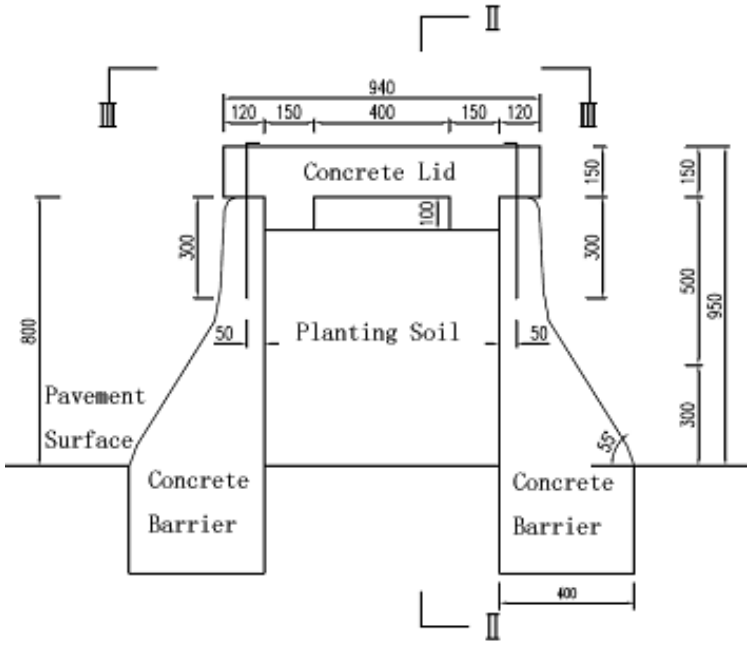

Fig.4 Solution 3 cross-section

3. Finite Element Simulation

There are three alternatives, while researchers have to assess the effect of each solution. Finite Element Simulation is a good way to accomplish the effect evaluation. It simulates the crash between vehicle and barrier by finite element calculation. This method has already been proved reliable and economical. LS-DYNA, a mature software of finite element analysis, is selected to conduct the simulation. Researchers set the impact conditions in accordance with Chinese current Standard for Safety Performance Evaluation of Highway Barriers, which requires one small-vehicle collision test and one large-vehicle collision test for each solution . The conditions for 280kj-Grade impact are 20° of impact angle, 1.5 ton of weight for small vehicle, 10 ton of weight for large vehicle, 100km/h of velocity for small vehicle and 80km/h of velocity for large vehicle.[1][3][4]

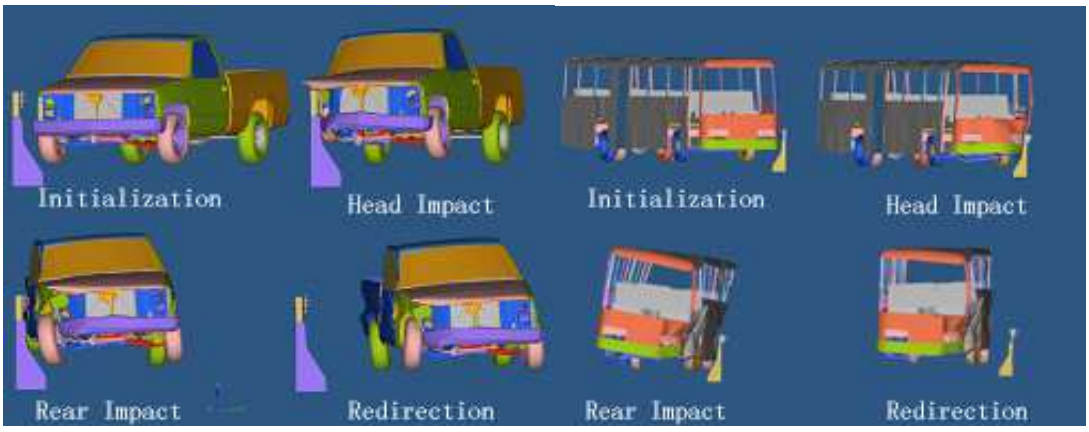

Fig.5 Simulation for single-beam steel guardrail mounted on concrete (Solution 1)

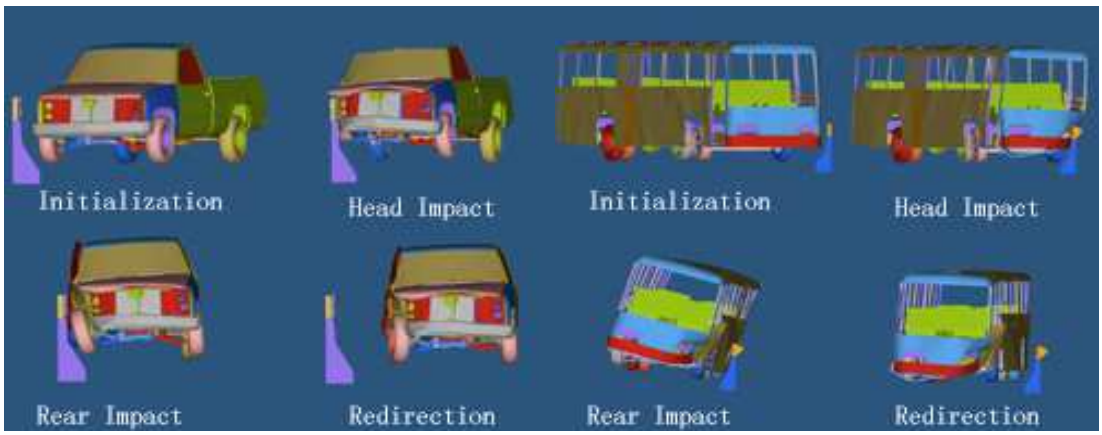

Fig.6 Simulation for double-beam steel guardrail mounted on concrete (Solution 2)

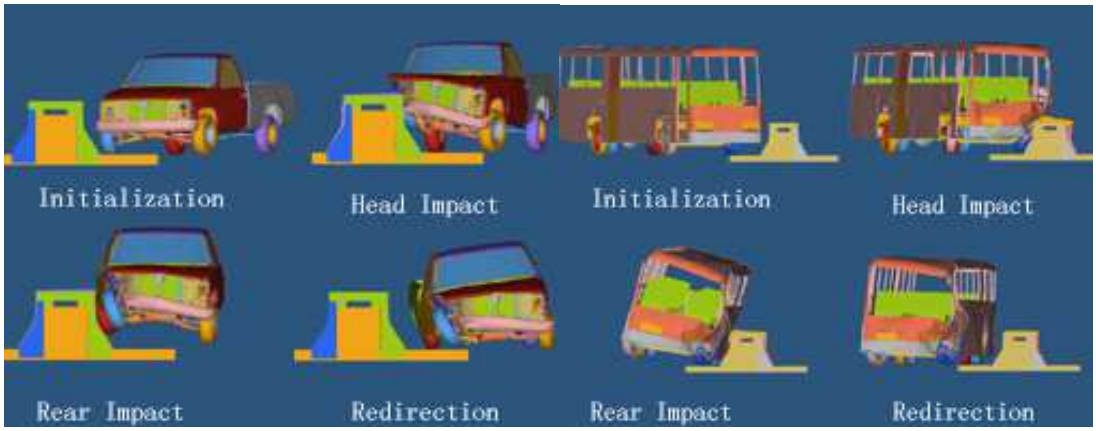

Fig.7 Simulation for Reinforced Concrete-lid (Solution 3)

Fig.5, Fig.6 and Fig. 7 respectively show the result of simulation for three solutions. For Solution 1 and Solution 2, researchers assume the concrete is rigid body, and there is no interaction between barriers on two sides of median. Therefore, only one side barrier guardrail is modeled to simplify the finite element analysis. However, the interaction between two-side barriers is not ignored in Solution 3 since the concrete lid can transmit energy from one side to the other. It is obvious that three solution both pass the finite element simulation test. They all can reach 280kj-grade anti-collision performance.[3]

4.Cost Assessment

All of three solutions can achieve 280kj-level protection, so there is necessity to rank them in price. The price for solutions is listed in Table.1.

Table 1. Cost of solutions

Solution	Description	Cost per meter ($)
Solution 1	Single-beam steel guardrail mounted on concrete	98
Solution 2	Double-beam steel guardrail mounted on concrete	138
Solution 3	Reinforced Concrete-lid	59

The budget above is general, including material, labor and other fees. From Table.1, the cheapest option is Solution 3, price of which is only 59$/meter. Solution 2 is the most expensive option:

138$/meter. It needs to be mentioned that researchers make the budget based on price in China, this price varies in different countries and districts. Nevertheless, the trend or the rank may keep the same in many developing countries. The specific cost depends on the market of each country.

5. Conclusion

Based on Simulation test and cost analysis, users can draw conclusion and make choice for their upgrade project. For Solution 1, there are three advantages: median cost, excellent protection and easy installation. But the greatest risk is the corruption issue, which makes the steel beam guardrail tough to maintain. The maintenance difficulty may increase the long-term cost. The Solution 2 is the least competitive one because of its cost. The two-beam system may offer better protection, but it also accompany higher price than one-beam system. The Solution 2 could be a better choice only if the solution 1, the one-beam guardrail, was barely effective to bear 280kj impact. However, the previous analysis has proved that all 3 solutions reach 280kj performance level. The high price lower the competitiveness of Solution 2. Solution 3 has the best cost-effect ratio. It is the cheapest solution as well as a effective one. In addition, it exclude most of corruption issues because concrete covers reinforcement. Another edge is its rigidity. It can keep intact in most collision unless the crash is extremely serious. It means the concrete-lid barrier does not often need repair or replacement. But the construction is very difficult. It demands some special equipments to transport, lift and install concrete lids, and the variation median results in various size of concrete lids, which may raise the price in Table.1.

Managers of highway guardrail upgrade project in Highway Guangshen prefer Solution 3, the concrete lid, for the reason that the environment around highway is so humid that corruption turn to be a big issue for maintenance. Plus, its price is the lowest. However, users in other area may have different decision. This research offers possible options for those who have demand to upgrade in-use concrete barrier. There are numerous factors influencing the final choice, such as the price of material, the construction capacity, temperature, humidity, traffic volume and so on. Basing on these factors, users can select the solution most suitable for them. This kind of upgrade plan instead of replacement will become more and more attractive for highway management agencies as sustainable development has been set as a global trend of economy.

6.References

[1]Highway Series Editorial Board, Highway Traffic Engineering and Roadside Facilities., China Communications Press, China, 1999.
[2]American Association of State Highway and Transportation Officials Executive Committee, Manual for Assessing Safety Hardware 2009., AASHTO, United States, 2009.
[3]The Road of Scientific Research Institute of the Ministry of Transport, JTG D81-2006 Specification for Design of Highway Safety Facilities., Ministry of Transport of the People's Republic of China, China, 2013.
[4]Beijing Shenhuada Traffic Engineering Detection Co Ltd, JTG B05-01-2013 Standard for Safety Performance Evaluation of Highway Barriers., Ministry of Transport of the People's Republic of China, China, 2013.

Advanced Materials Research Vol. 983 (2014) pp 204-207

doi:10.4028/www.scientific.net/AMR.983.204

The Research of Demarcating the Laser Ranging Sensor by Least Squares Method

Zheng yan [1, 2,a], Zhang yong [2] and Fan xiaowang [2]

[1.] Jilin university mechanical science and engineering college

[2.] Changchun mechanical science research institute co., LTD

[a]435562852@qq.com

Key words: the principle of triangulation; the laser ranging sensor, calibration, The least square method

Abstract: Basing on the laser range finder needs calibration used in non-contact measurement the, using the triangle range principle, through the experiment of design of different material, surface roughness, the under the different distance of under the different distance between 40 mm to 60 mm is achieved, the under the different distance, demarcated the laser ranging sensor by least squares method and analyzed the pricesion.

Introduction

Laser ranging sensor is a new type of sensor that do the non-contact measurement such as the change of location and displacement of the object by the photoelectric technology, is mainly used to measure the geometric quantities such as the displacement, thickness, vibration, distance, diameter of the object the measurement [1-3]. It has the unique advantage like high measuring speed, high precision, strong anti-interference ability, small measurement point, wide scope of, and it has got more and more attention in our country and abroad. But when the do the non-contact measurement, laser range finder needs calibration, to ensure the accuracy of the measurement result.

The work principle of the laser ranging sensor

The model of the laser ranging sensor is PT50 series, it is one of the Italian CASATI company's latest products, designed it based on the principle of triangulation, the appearance structure and size of laser ranging sensor of PT50 laser ranging sensor is shown as figure 1.

According to this perspective and known the distance between the laser and camera, digital signal processor can calculate the distance between the sensor and the object, as it's shown in figure 2. As shown in figure 3, it is the theoretical calculation of the laser ranging sensor model diagram, in the figure, l and l' is object distance and distance respectively; o', m', n' is the phase angle of the o, m, n respectively; θ is the incident Angle of diffuse light; φ is a phase Angle; f is receiving lens focal length. When the incident light spot with the measured surface by moving point o to point n, point of phase o' was moved to point n'.

Fig1. PT50 laser ranging sensor

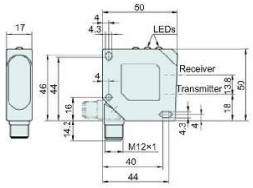

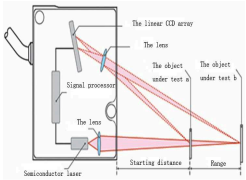

Figure2. Laser Displacement Sensor Principle Diagram

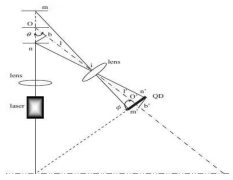

Figure3. Graph theory model of triangulation

The least squares fitting calibration

Laser ranging sensor measurement system is a direct type, its principle of triangulation formula is derived as follows [4]: it is shown by figure 2: the triangle nbi is similar to that $n'b'i'$, in the triangle nbi and triangle $n'b'i'$, $nb = on\sin\theta$, $n'b' = o'n'\sin\phi$.

Has made displacements be y and phase displacement is x, the relation between object and phase lag is,

$$\mathrm{y} = \frac{xl\sin\varphi}{l'\sin\theta - x\sin(\theta+\varphi)} \tag{1}$$

Rule of least squares: The sum of the squares δ_i then the fitting curve $f(x_i)$ and y_i then:

$$J(\mathrm{a}_1,\ \mathrm{a}_2 \ldots \mathrm{a}_m) = \sum_{i=1}^{n}\delta_i^2 = \sum_{i=1}^{n}[f(x_i)-y_i]^2 = \sum_{i=1}^{n}[\sum_{k=1}^{m}a_k r_k(x_i)-y_i]^2 \tag{2}$$

If there is $a_1, a_2, \ldots a_{\mathrm{m}}$ and $J(a_1, a_2, \ldots a_{\mathrm{m}})$ minimum, The necessary conditions for:

$$\frac{\partial J}{\partial a_k} = 0 \ (k = 1,\ldots,m).$$

Finally MATLAB programming for linear least squares fitting analysis can be fitted curv e in each point x The value of error fitting δ_i The stand or fall of fitting calculation, analysis the results.

Laser ranging sensor calibration experiment and data processing

Figure 4 measure the actual figure for experimental data, figure 5, 1 for laser range sen sor, 2 for the measured specimen. To many sets of data, the initial distance is transferred t o the 40 mm, The experiments, each move a fixed distance is γ_i, Note after moving distanc e L_i and The voltage value of the collected and the data acquisition card U_i, Until the dist ance moved beyond range (or data acquisition card to collect data to maintain a certain fix ed value without big change).

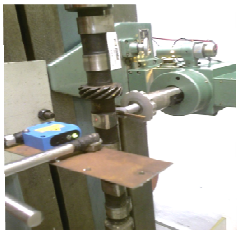

Figure 4 Measure the actual

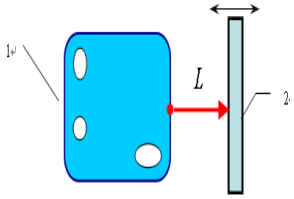

Figure 5 Static experimental data translation model for the calibration

With laser ranging sensor is used in the active optical measurement, measured by detecting the reflected beams, because of the influence of surface roughness and smooth the reflectivity of light, so the main consideration to the metal surface roughness on the result of measurement, respectively, to test the metal cuboid rough surface and smooth surface. In the experiment using the same specimen of the surface of the two different measurements, avoid the specimen material of different effects on the experimental results. Cuboid specimen with rough surface and smooth surface experiment data are shown in table 1.

Table 1 Cuboid specimen with rough surface and smooth surface calibration data

Cuboid specimen with rough surface	Ranging mm	40	40.5	41	41.5	42	42.5	43
	Voltag mv	-26780	-24950	-23100	-21430	-19660	-17980	-16280
	Ranging mm	43.5	44	44.5	45	45.5	46	46.5
	Voltag mv	-14510	-12690	-11100	-9470	-7710	-5970	-4330
	Ranging mm	47	47.5	48	48.5	49	49.5	50
	Voltag mv	-2560	-995	725	2350	4070	5740	7460
	Ranging mm	50.5	51	51.5	52	52.5	53	53.5
	Voltag mv	9090	10840	12500	14100	15780	16500	18000
	Ranging mm	54	54.5	55	55.5	56	56.5	57
	Voltag mv	19720	21540	23360	25090	26430	28390	29370
	Ranging mm	57.5	58	58.5	59	59.5	60	-
	Voltag mv	31020	32630	34230	35830	37580	39230	-
Cuboid specimen with smooth surface	Ranging mm	40	40.5	41	41.5	42	42.5	43
	Voltag mv	-23690	-22340	-20720	-18480	-16920	-15310	-13620
	Ranging mm	43.5	44	44.5	45	45.5	46	46.5
	Voltag mv	-11850	-10420	-8690	-7235	-5590	-3850	-2260
	Ranging mm	47	47.5	48	48.5	49	49.5	50
	Voltag mv	-620	925	2640	4220	5900	7510	9130
	Ranging mm	50.5	51	51.5	52	52.5	53	53.5
	Voltag mv	10750	12400	13900	15660	17140	18720	20400
	Ranging mm	54	54.5	55	55.5	56	56.5	57
	Voltag mv	22240	23830	25430	27050	28890	30570	32240
	Ranging mm	57.5	58	58.5	59	59.5	60	-
	Voltag mv	33810	35410	37150	38930	40350	41380	-

To software analysis of experimental data in table 1, by fitting the graphics and the fitting error as shown in figure 6,7.

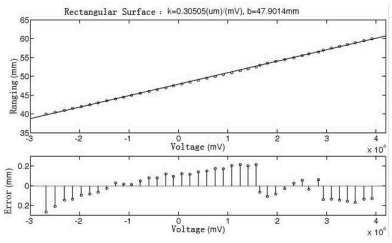

Figure 6 Cuboid rough surface

data fitting results

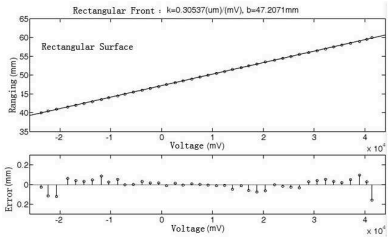

Figure 7 Cuboid smooth surface

data fitting results

The figure 6 shows that data fitting error is large, there is no regularity. Cuboid specimen with rough surface experimental calibration result is: $k = 3.0537\times10^{-4}$ mm/mv, b = 47.9014 mm. The figure 7 shows that the experimental data fitting error is small, in the middle of the laser ranging sensor measurement range around the experimental data fitting error is small, both sides is large, such analysis could be a measuring range measurement at the centre of the calibration. Experimental calibration results for $k = 3.0537\times10^{-4}$mm/mv, b = 47.2071. From the front two experimental data contrast can be obtained: smooth surface measurement result is better, the fitting error is small.

Conclusion

In the experiments we found that different surface roughness of specimens, light reflectivity of the object to be tested is different, have different effects on sensor output. In the calibration of the laser range finder, the smooth surface of the sample measurement result is better, the fitting error is small.

Reference

[1]Xing Wu, Wang Guotai Ge Yunjian.A Laser System for Distanee Measurement[J]. Instrument Technique and Sensor,1996,07,10-13.

[2]CAI Ze-su, HONG Bing-rong, ZHOU Pu-cheng. Navigating Simulation of House Pobot Based on Laserfinder[J]. Journal of Harbin Institute of Technology,2004,07,902-904.

[3]Chao Zhichao Fu Sihua Jiang Guangwen Yu Qifeng. Mono Camera and Laser Range finding Sensor Position-Pose Measurement System[J]. Acta Optica Sinica,2011,03,93-99.

[4]Wei Biao, Sheng Xinzhi. The Principle and Application of The Laser. Chongqing University Press,2007.

Advanced Materials Research Vol. 983 (2014) pp 208-213

doi:10.4028/www.scientific.net/AMR.983.208

A Fundamental Investigation on Ultrasonic Assisted Fixed Abrasive CMP (UF-CMP) of Silicon Wafer

Yongbo Wu[1, a] and Lijun Wang[2, b]

[1]Dept. Machine Intelligence and Systems Engineering, Akita Prefectural University, Tsuchiya-ebinokuchi 84-4, Urihonjo, Akita 015-0055, Japan

[2]Graduate School of Akita Prefectural University, Yurihonjo, Akita 015-0055, Japan

[a]wuyb@akita-pu.ac.jp, [b]d15s001@akita-pu.ac.jp

Keywords: Si wafer, CMP, CMG, Polishing, Fixed abrasive machining, Ultrasonic vibration, Surface roughness, Material removal

Abstract. Chemical mechanical polishing (CMP) is often employed to obtain a super smooth work-surface of a silicon wafer. However, as a conventional CMP is a loose abrasive process, it is hard to achieve the high profile accuracy and lots of slurry must be supplied during CMP operations. As an alternate solution, a fixed abrasive CMP process can offer better geometrical accuracy and discharges less waste disposal. In this paper, in order to enhance the polishing efficiency and improve the work-surface quality, a novel ultrasonic assisted fixed abrasive CMP (UF-CMP) is proposed and the fundamental machining characteristics of the UF-CMP of a silicon wafer is investigated experimentally. The results show that with the ultrasonic assistance, the material removal rate (MRR) is increased, and the surface quality is improved.

Introduction

Chemical mechanical polishing (CMP), a loose abrasive machining process, has been often employed to obtain a super smooth work-surface of a silicon wafer [1]. However, with the increase in the Si wafer size it becomes difficult more and more for this method to maintain the profile accuracy of Si wafer such as flatness. In order to simultaneously achieve superior surface quality and high profile accuracy, chemo-mechanical grinding (CMG) process, a kind of fixed abrasive CMP process and potentially an emerging defect-free machining process which combines the advantages of fixed abrasive process and CMP, was proposed [2]. So far, CMG has been successfully applied into machining of single crystal silicon wafers [3] and large-size quartz glass substrates used for photomask [4].

However, in this fixed abrasive CMP process, the abrasive tool contacts with the workpiece constantly during machining, and hence the formed chips are hardly dispelled from the machining zone, eventually leading to the significant decrease in the material removal rate (MRR) and the deterioration of surface quality. In response, the authors introduced elliptic ultrasonic vibration into the fixed-abrasive CMP process previously [5] in which the contact-free phenomenon periodically occurs between the workpiece and the tool for the sake of the ultrasonic vibration of the tool. Hereinafter, this process is referred to as UF-CMP (Ultrasonic-Assisted fixed-abrasive CMP). The results indicated UF-CMP produces a better work surface and higher MRR than those that can be attained without ultrasonic vibration.

In the current work, for the purpose of putting the UF-CMP technique to practical use in the high efficiency and ultra-fine quality machining of Si wafers, a new experimental apparatus attached with multi ultrasonic abrasive pellet holders was constructed and its performance was investigated. This paper describes the construction of the apparatus at first and then the fundamental machining characteristics are detailed.

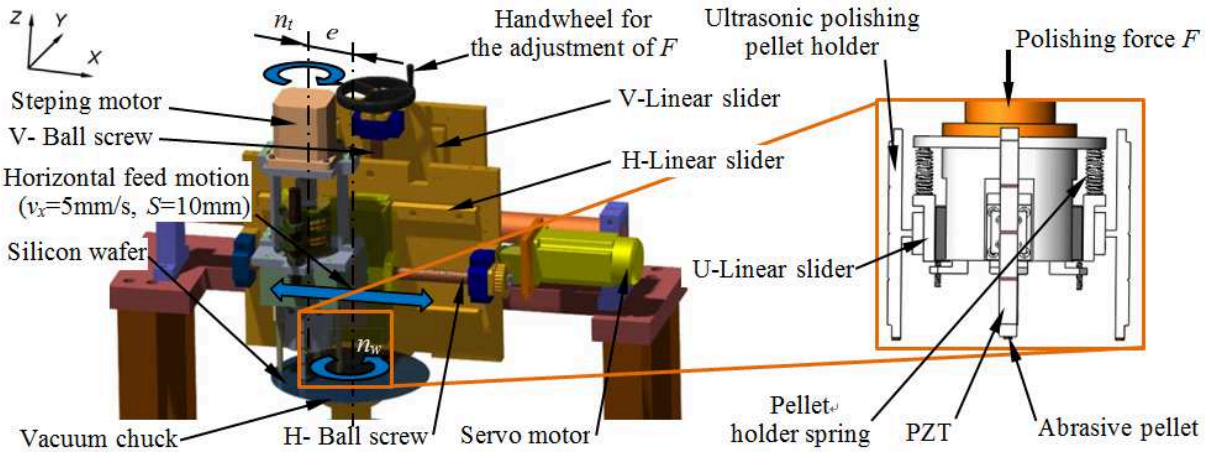

Fig. 1 Schematic illustrations of the experimental apparatus

Experimental Apparatus and Procedures

Figure 1 schematically illustrates the experimental apparatus constructed for the UF-CMP of silicon wafers. In the apparatus, as the workpiece a silicon wafer is mounted on a vacuum chuck that is fixed on an air spindle rotating at a speed of n_w around its axis. Four ultrasonic pellet holders are located along a circle at a regular interval and retained on a rotary head via their respective U-linear sliders. The ultrasonic holder was in practice constructed by bonding a piezoelectric ceramic device (PZT) having four separated electrodes onto a metal elastic body (SUS304). When two alternating current (AC) signals (over 20kHz) with a phase difference to each other generated by a wave function generator are applied to the PZT after being amplified by means of power amplifiers, the 1st longitudinal vibration (L1-mode) and 4th bending vibration (B4-mode) with their respective amplitudes of A_L and A_B are excited simultaneously, and the synthesis of vibration displacements in the two directions creates an elliptic motion on the end-face of ultrasonic holder.

In CMP of single crystal silicon materials, for breaking off those Si atoms which are located at the outmost surface, extra work is necessary to overcome their surface barrier potential energy [6]. Therefore, the abrasives need not only the mechanical action, but also a proper chemical reaction with Si material to weaken the Si atom bond strength to increase the material removal. By effective use of the solid-state reaction between CeO_2 abrasives and silicon, in which Si atoms are removed in the form of amorphous Ce-O-Si in a dry state [2], and considering a better machined surface and higher material removal can be achieved with ultrasonic vibration, each ultrasonic holder was attached with a disc-shaped pellet containing CeO_2 abrasives on its lower end face. Consequently, elliptical ultrasonic vibration can be generated on all of the abrasive pellets.

By handling the handwheel, the vertical position of the ultrasonic holder can be adjusted finely through the V-ball screw, and thus a polishing force F can be provided through coil springs between the workpiece and the abrasive pellets. The coil springs were installed in order to provide a flexible support for the ultrasonic holders and hence to reduce the risk of the occurrence of cracks on silicon wafers and/or others during polishing as the springs can absorb energy when the holder produces dull or excessive load. In the current work, coil springs with different spring constants of k=0.098, 0.29, 0.49 and 2.94N/mm were employed for investigating the effect of the holder support stiffness on the polishing characteristics. In addition, a servo motor was employed to provide the ultrasonic holders with a reciprocating feed motion in X-axis (horizontal direction) at a feed rate of v_x=5mm/s and a stroke of S=10mm, and a stepping motor for the rotational motion of rotary head at a speed of n_t around its axis. All experiments were conducted without adding any fluids during polishing. The detailed experimental parameters are listed in Table 1.

After polishing for every 15 minutes, silicon wafers were rinsed by alcohol and dried with an air blower. Then polished surface quality was characterized by measuring the surface roughness (Zygo Newview 600) followed by the calculation of the mean values of the roughness at four different

locations of A_i- A_i (i=1-4) (Fig. 2). Besides the surface roughness, it is also crucial to know how large the material removal is. In this paper, the depth of polishing trace obtained by polishing for 90 minutes was measured to indicate the material removal. Fig. 3 shows the cross section profile of a typical polishing trace, which was tested with a contact stylus profiler (Taylor Hobson Form Talysurf Intra 2). Depth H was obtained by calculating the average of four measurements (the cross-sectional area divided by the width B). In addition, the pellet surface topography and polishing chips were observed using a scanning electron microscope (SEM, ERA-8900S by Elionix Co., Ltd.).

Table 1 Experimental conditions

Applied AC voltage	Amplitude V_{p-p}	150 V
	Frequency f	25.4 kHz
	Phase difference ψ	90°
Ultrasonic vibration amplitudes of holder	A_L=2.2μm, A_B=1.3μm	
Abrasive pellet	CeO2(< 40 wt. %, #6000)	
Workpiece	Silicon wafer Φ200mm×t0.8 mm	
Polishing force F	5 N	
Ultrasonic holder rotational speed n_t	70 rpm	
Workpiece rotational speed n_w	200 rpm	
Offset distance e	5mm	
Reciprocating feed motion of holder	Feed stroke S	10 mm
	Feed rate v_x	10 mm/s
Polishing time	90 min	
Environment temperature	20°C	

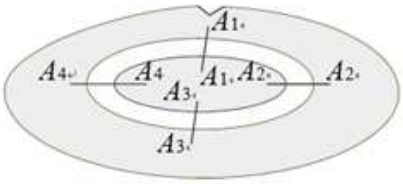

Fig. 2 Measurement locations on the Work-surface polished

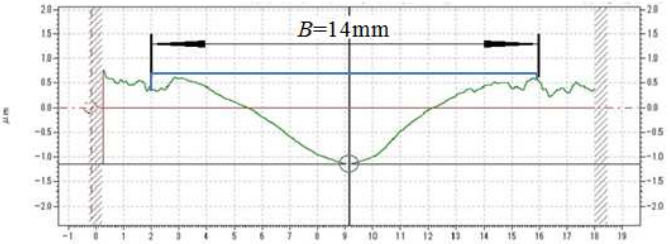

Fig. 3 The cross section profile of a typical polishing trace

Results and Discussion

Variations of the work-surface roughness with polishing time in UF-CMP (referred as with-UF) and CMG (referred as without-UF) are shown in Figs. 4(a)-(d) for coil springs with different constants of k, respectively. Figs. 5(a) and (b) show the material removal and the work-surface roughness vs. the spring constant k.

It is evident from Fig.4 that in UF-CMP with-UF when the value of k is less than 0.29N/mm, the Ra decreases monotonously during polishing, whereas in the case of k>0.29N/mm, the Ra decreases at beginning stage of polishing and turns to increase in the rest stage. This means the polishing operation becomes unstable as the k is more than 0.29N/mm in UF-CMP. By contrast, in conventional CMG without-UF, the unstable polishing operation occurs in smaller k compared with UF-CMP. It is worthy to note that regardless of the k, the Ra values in UF-CMP were smaller than those in CMG. As for the effects of the k on the material removal H (Fig.5(a)) and the minimum Ra (Fig.5(b)) either in UF-CMP or in CMG, with the increase in the k value, the H value tends to increase in CMG without-UF whilst in UF-CMP the H value reaches its peak at k=0.29N/mm. Comparing H value in

UF-CMP with that in CMG indicates the material removal in UF-CMP was larger than that in CMG by up to 26%. Similarly, the minimum Ra decreases by up to 19% once the ultrasonic vibration is applied.

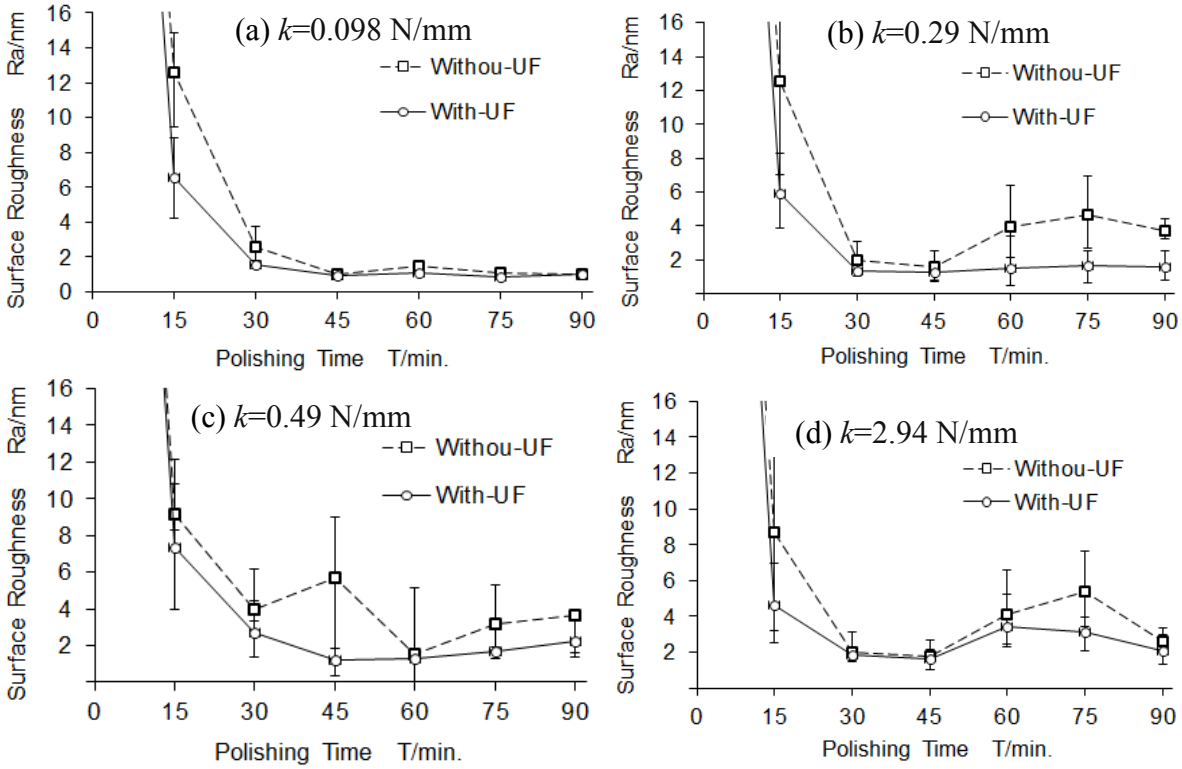

Fig. 4 Surface roughness vs. polishing time for different spring constants

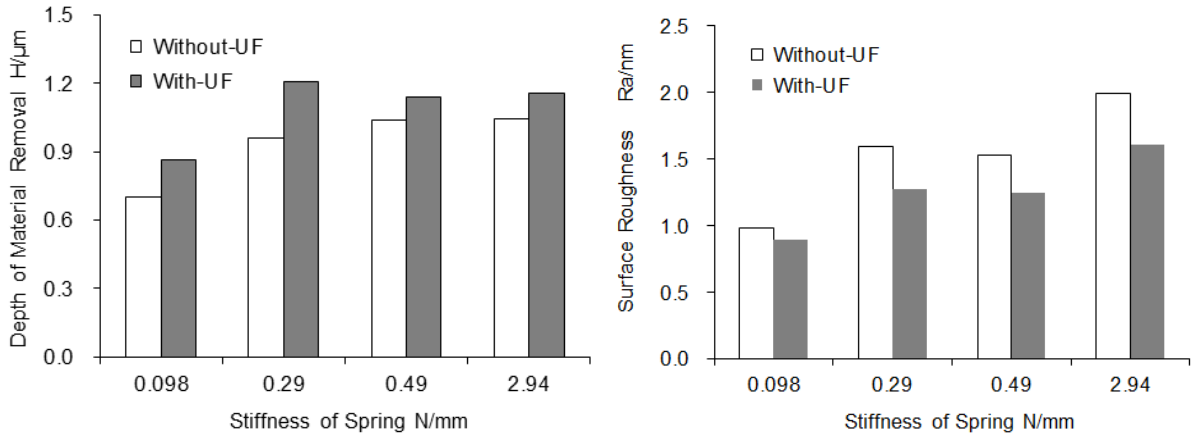

(a) Material removal (b) Surface roughness

Fig. 5 Material removal and surface roughness vs. spring constant

On the other hand, the morphologies of typical work-surfaces polished for 45 minutes with-UF and without-UF are as shown in Figs. 6(a) and (b), respectively. The scratches on the work-surface by CMG seem deeper and wider than that by UF-CMP, indicating that the ultrasonication of the abrasive pellet has a positive effect on the work-surface quality.

The reason for these phenomena can be considered: as the stiffness of coil spring increases, the mechanical action between the abrasives and the Si materials becomes more active. As being well known, material removal mechanism in CMP process is based on the combined chemical reaction and mechanical action. The material removal of Si wafer is affected by the formation rate of passivation which is controlled by the balance of chemical reaction and mechanical abrasive wear. The chemical reaction occurs between the solvent of the pellet and the Si wafer to change the mechanical properties

of the wafer surfaces. Thus, more solvent can produce in the polishing area to prompt the chemical reaction and eventually lead to the easier removal of material.

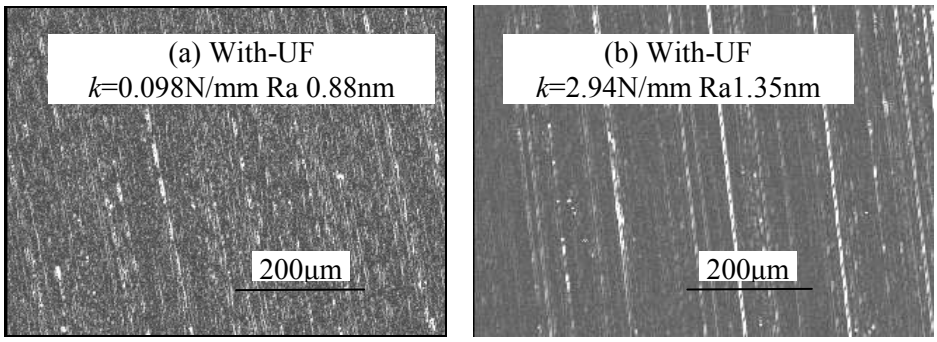

Fig. 6 Work-surface morphologies

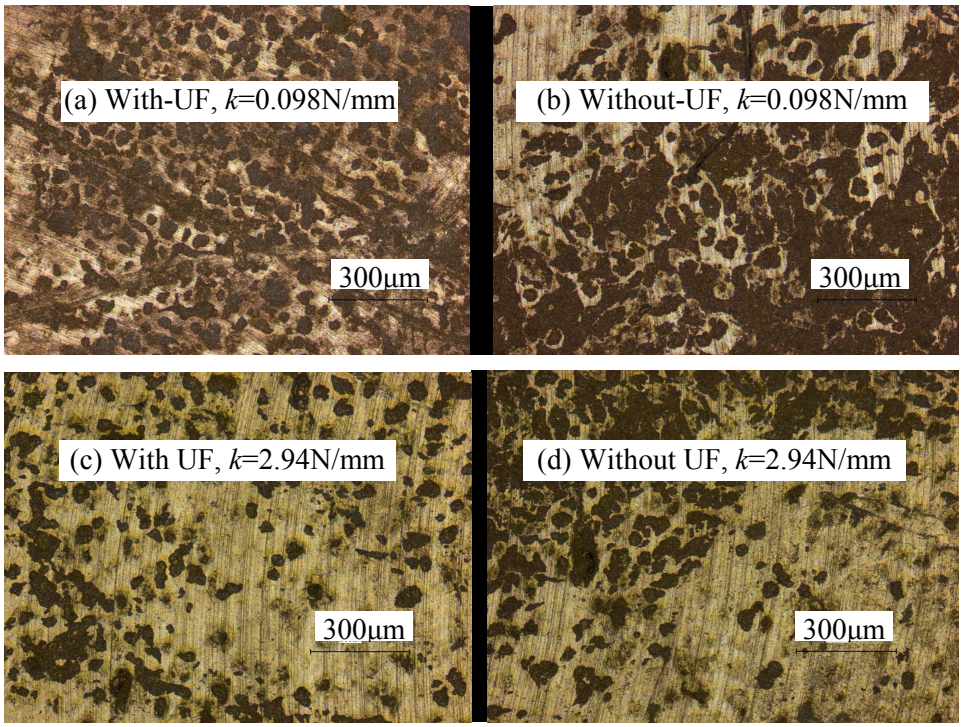

Fig. 7 Microscopic images of the working-surface of abrasive pellet used for 30min (Black dots indicate chip pores or craters)

Therefore, the working surface of abrasive pellets and chips for different spring stiffness in UF-CMP and CMG were carefully compared as shown in Fig. 7 and Fig. 8. It can be recognized without considerable difficulty from Fig. 7 that with a larger value of k, heavier wear of abrasive pellet occurred and hence more ceria abrasives were exposed to release additives. The ultrasonic vibration reduced the abrasive wear. On the other hand, Fig. 8 shows that the chips formed in UF-CMP were smaller than those in CMG, and the lower the spring stiffness is, the chip size becomes smaller.

Summary

The work-surface roughness, material removal and work-surface topography in UF-CMP with ultrasonic and CMG without ultrasonic of Si wafer were experimentally investigated for the different stiffness of coil spring used for supporting the ultrasonic pellet holder. The results obtained can be summarized as follows:

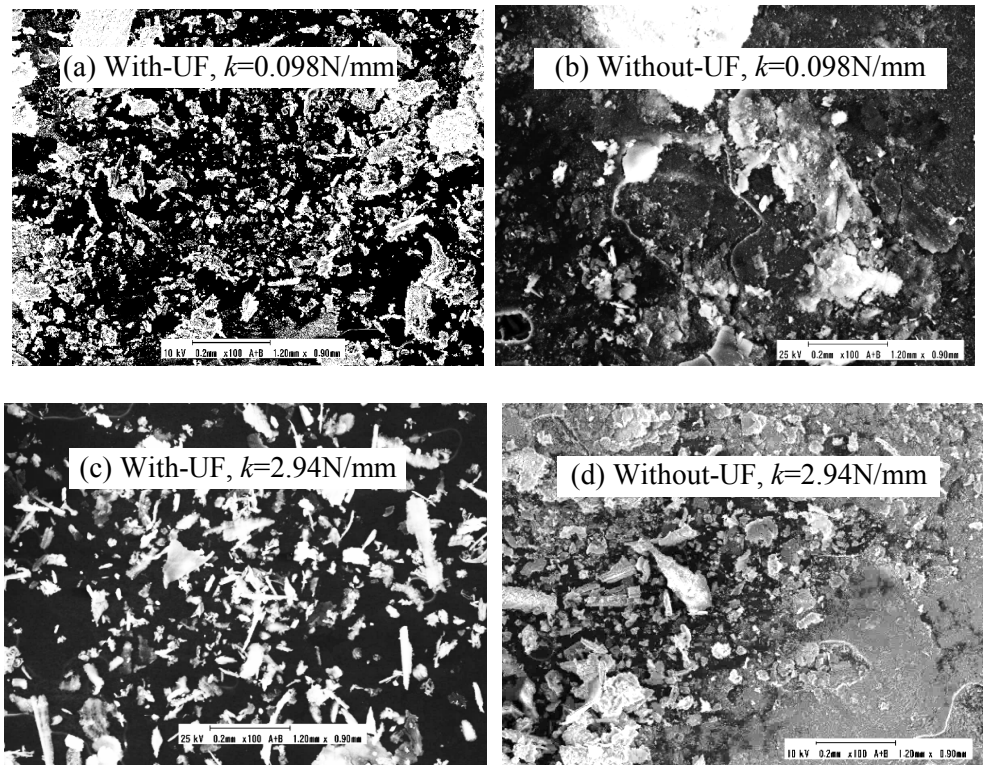

Fig. 8 SEM images of chips formed with pellet used for 30min

(1) At the same condition, UF-CMP process exhibited higher performance, a better silicon surface quality and a larger MRR are available under the ultrasonication of polishing pellet compared to that without.

(2) There is a certain spring stiffness at which the material removal is the largest.

(3) In the case of using coil spring with lower stiffness, not only a higher-quality surface can be obtained, but also the process performance becomes more stable.

The results obtained in the current work validated the UF-CMP in the silicon wafer surface machining, and confirmed the feasibility of UF-CMP in the high efficiency/ultra-fine machining of silicon wafer. As future works, detailed performances and material removal mechanism of UF-CMP of Si materials will be further investigated, in order to completely establish this proposed technique.

References

[1] TÖenshoff HK, et al. Abrasive Machining of Silicon [J]. Annals of the CIRP, 39, 2 (1990) 621–635.

[2] L. Zhou, et al. Development of Chemo Mechanical Grinding (CMG) Process, Proc of Int' Conf. on LEM21, (2003) 315-320.

[3] L. Zhou, et al. Defect-free Fabrication for Single Crystal Silicon Substrate by Chemo-Mechanical Grinding, Annals of the CIRP - Manufacturing Technology; 15 (2006) 313-316.

[4] L. Zhou, et al. Research on Chemo-Mechanical Grinding of Large Size Quartz Glass Substrate [J]. Precision Engineering, 33 (2009) 499-504.

[5] Y. Wu, et al. Performance improvement of chemo-mechanical grinding in single crystal silicon machining by the assistance of elliptical ultrasonic vibration [J]. Int. J. of Abrasive Tech., 4, 2 (2011) 117-131.

[6] S. Shimada, et al. Suppression of Tool Wear in Diamond Turning of Copper under Reduced Oxygen Atmosphere [J]. Annals of CIRP, 49, 1 (2000) 21-24.

Advanced Materials Research Vol. 983 (2014) pp 214-217

doi:10.4028/www.scientific.net/AMR.983.214

Study on slurry of SiC crystal substrate (0001) C surface in CMP based on silica sol (SiO_2 abrasive)

ZHANG zhuqing[1,a], CHENG Haifeng[1], SU Jianxiu[2]

[1] Henan University of Technology, Zhengzhou 450001, P. R. China

[2] Henan Institute of Science and Technology, Xinxiang 453003, P.R. China

[a]dlutsu2004@126.com

Keywords: SiC crystal substrate, CMP slurry, Material removal rate, Surface roughness, Chemical mechanical polishing.

Abstract. SiC single crystal substrate has been become an indispensable substrate material in the field of semiconductor lighting. But, there is no report on the commercial slurry of chemical mechanical polishing (CMP) SiC substrate. In this paper, according to orthogonal design, the composition selection and optimization of CMP slurry based on silica sol (SiO_2 abrasive) had been done in CMP SiC crystal substrate (0001) C surface by tests. The CMP slurry based on silica sol for SiC crystal substrate (0001) C surface had been obtained. According to the CMP test results, the material removal rate (MRR) is about 15nm/min and the surface roughness *Ra* is about 0.2nm.

Introduction

SiC crystal substrate has been widely applied in the field of semiconductor industry and optical components recently. It has been become the ideal substrate material of manufacturing the optoelectronic integrated devices, such as the components of high-temperature, high-frequency, high power, anti-radiation, short wavelength light-emitting, semiconductor lighting etc. and also the research focus on the field of semiconductor, microelectronics and optoelectronics [1]. Semiconductor lighting is one of the most promising high-tech fields in the 21st century. SiC single crystal substrate has been become an indispensable substrate material in the field of semiconductor lighting. LED based on SiC substrate takes the second place in LED market.

The literatures show that the device quality largely depends on surface quality of the substrate and the surface quality of the substrate has a great impact on epitaxial films. The high surface quality of SiC substrates is very difficulty to obtain due to its high hardness and high chemical stability. Chemical mechanical polishing (CMP) is one of the core technologies in the field of semiconductor manufacturing and has been become the most widely used technology in ULSI manufacturing. The schematic of CMP theory is shown in Fig.1[2].Therefore, CMP is the most effective technology to achieve ultra-smooth without damage surface in ultra-precision machining of SiC crystal substrate [3-6].

According to statistics, the 70% cost of CMP comes from the polishing slurry. The abrasives play an important role in polishing slurry in CMP. The hardness of the abrasive SiO_2 is lower than that of SiC substrate and abrasive diamond, but the price of the abrasive SiO_2 is much lower than that of abrasive diamond. Up to now, there is no report on the study of CMP SiC substrate based on abrasive SiO_2 by literatures.

In this paper, a series of tests of chemical mechanical polishing 6H-SiC (0001) C surface has been conducted by orthogonal design using slurry with abrasive SiO_2. The influences of the abrasive content and the slurry composition (pH, abrasive size, dispersion agent, oxidizing agent, active agent) on the material removal rate have been studied. Finally, the CMP slurry based on abrasive SiO_2 for SiC crystal substrate (0001) C surface had been obtained. It hopes to provide the reference for reducing the cost of CMP SiC crystal substrate.

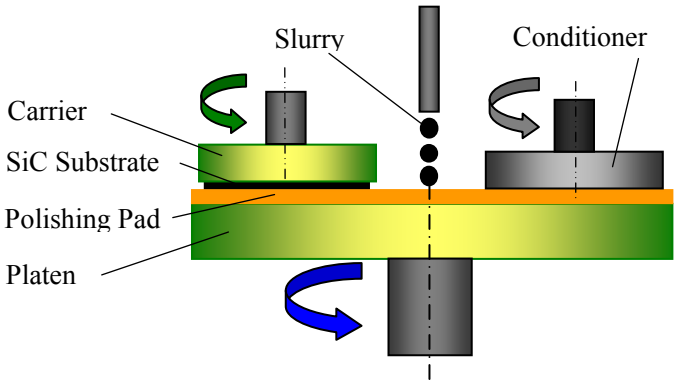

Fig.1 The schematic of CMP

Experiment.

Experimental conditions and experimental parameters. The CMP experiments were conducted under different parameters and slurry on the ZYP300 type CMP machine produced by Shenyan. All the experiments are done in a clean room with Grade 1000 at the constant temperature of 22°C. Many 6H-SiC wafers of 2 inches in diameter are used in the polishing experiments. Samples are bonded with paraffin on the carrier of stainless steel with Φ115mm in diameter. Each carrier sticks one SiC wafer. The roughness of the (0001) C surface before polishing is about *Ra* 40nm, which is tested by Talysurf CCI 3D surface profiler. In the CMP experiments, the polyurethane pad is applied and conditioned for 30min before every polishing experiment with a diamond conditioner, the slurry is supplied at the flow rate of 15ml/min. The slurry 500ml can be made before each test. During the CMP process, the carrier has a reciprocating motion with a stroke of 20mm at the frequency of 10s and the centre distance between the pad and the wafer is set 80mm, the polishing pressure P=2psi, the carrier rotational speed n_w=65r/min, the platen rotational speed n_p=60r/min, the polishing time is 30min for each test. The Deionized (DI) water with the electrical resistivity 18.24MΩ·cm is used in the CMP experiments. The MRR can be calculated by weighing the weight of the SiC wafer on the high precision balance with the accuracy 0.01mg before and after CMP.

Design of orthogonal table. MRR and surface roughness are the two important parameters to evaluate the performance of CMP slurry. In order to obtain the high MRR and low surface roughness in CMP SiC crystal substrate, the 5 factors, such as pH Value, oxidant content, dispersant content, abrasive size and abrasive content, were selected by former analysis and the condition of lab. Three levels were selected in each factor. The orthogonal table sees table 1.

Table 1 The factor-level table for the orthogonal experiment

Factor / Level	pH value	Abrasive size (nm)	Dispersant content ml/500ml）	Oxidant content ml/500ml）	Abrasive content g/500ml）
	A	B	C	D	E
1	9	60	3	10	30
2	11	90	6	20	60
3	13	120	9	30	90

The experimental results. According to the theory of orthogonal design experiment, the times of orthogonal design experiment are 18. Levels of each factor for each test are listed in table 2. The slurry 500ml can be made by each CMP before each test. The experimental results are also shown in table 2.

Analysis of test results

The range analysis method is the most common method used to analyze the results of orthogonal test. The meanings of these parameters calculated are as follows. K_{jm} is the sum of test results under factor j and level m, K_{jmp} is the average value of K_{jm} in all level, R_j is the range in factor j. Here,

j=A,B,C,D,E…, m=1,2,3….The best slurry is the optimization combination of factor j and level m by K_{jm}. R_j denotes the change range of factor j on test objective. The larger the R_j is, the more the influence of factor j on test objective is. The sequence of influence of factor j on test objective can be decided by the value of R_j.

Table 2 The experimental results of orthogonal experiment

Factor / Test number	A	B	C	D	E	MRR (nm/min)	Surface roughness, *Ra* (nm)
Test 1	1	1	1	1	1	5.24633	6.34
Test 2	1	2	2	2	2	3.90068	7.317
Test 3	1	3	3	3	3	3.64517	9.033
Test 4	2	1	1	2	2	2.72536	15.23
Test 5	2	2	2	3	3	2.35063	10.63
Test 6	2	3	3	1	1	1.02201	18.2
Test 7	3	1	2	1	3	2.31656	17.63
Test 8	3	2	3	2	1	3.64517	12.43
Test 9	3	3	1	3	2	2.72536	29.67
Test 10	1	1	3	3	2	0.64727	18.4
Test 11	1	2	1	1	3	1.44785	13.7
Test 12	1	3	2	2	1	1.73742	17.3
Test 13	2	1	2	3	1	1.39675	31.0
Test 14	2	2	3	1	2	0.54507	25.6
Test 15	2	3	1	2	3	0.39177	24.83
Test 16	3	1	3	2	3	0.78354	34.63
Test 17	3	2	1	3	1	1.97589	23.47
Test 18	3	3	2	1	2	3.83254	23.93

Numerical calculation. Take factor A for example. The sums of factor A are as follows.

K_{A1}=5.24633+3.90068+3.64517+0.64727+1.44785+1.73742=16.62472,

$k_{A1p}=K_{A1}/6$=2.770787,

K_{A2}=2.72536+2.35063+1.02201+1.35679+0.54507+0.39177=8.43159,

$k_{A2p}=K_{A2}/6$=1.405265,

K_{A3}=2.31656+3.64517+2.72536+0.78354+1.97589+3.83254=13.50758,

$k_{A3p}=K_{A3}/6$=2.251263,

$R_A= K_{A1p}-K_{A3p}$=2.770787-2.251263=0.519524

The calculation process for factors, B,C,D,E, are omitted. But the calculation results in detail are shown in table 3.

Result analysis. By the Table 3, the pH value has the largest influence on MRR, the next one is the dispersing agent. The abrasive size gives the lowest impact on MRR. According to the results of Orthogonal design experiment, the optimization combination is $A_1B_3C_2D_1E_2$. The basic slurry composition of CMP SiC (0001) C surface has been obtained, shown in Table 4.

Then, the test of CMP SiC (0001) C surface had been done using the basic slurry composition of the optimization combination,. The test results show that the MRR is 15nm/min and the surface roughness Ra is 0.2nm.

Conclusions

In this paper, according to orthogonal design theory, the table of orthogonal design with five factors and three levels was designed. The five factors were pH Value, oxidant content, dispersant content, abrasive size and abrasive content. Three levels were selected in each factor. By the table of orthogonal design, 18 type tests with different CMP slurry were conducted. According to the range analysis method, the optimal CMP slurry with based on abrasive SiO_2 for SiC crystal substrate (0001)

C surface had been obtained. According to the CMP test results using the optimization combination, the material removal rate (MRR) is about 15nm/min and the surface roughness *Ra* is about 0.2nm.

Table 3 The calculation results for range analysis method

Factor / Parameter	A	B	C	D	E
K_{j1}	16.62472	13.11581	14.51256	14.41036	13.25209
K_{j2}	8.43159	12.09381	15.53458	11.41246	14.37628
K_{j3}	13.50758	13.35427	8.51675	12.74107	10.93552
K_{jp1}	2.770787	2.185968	2.41876	2.401726667	2.208681667
K_{jp2}	1.405265	2.015635	2.58909667	1.902076667	2.396046667
K_{jp3}	2.251263	2.225712	1.41945833	2.123511667	1.822586667
R_j	1.365522	0.210077	1.16963833	0.49965	0.57346
The sequence of influence factors on MRR	A>C>E>D>B				
Optimal level	A1	B3	C1	D1	E2
Optimization combination	A1B3C2D1E2				

Table 4 The basic slurry composition from orthogonal design experiments

Ingredients	pH	Oxidant (ml/500ml)	Dispersant (ml/500ml)	Abrasive size (μm)	Abrasive content (g/500ml)	others
Number	9	10	6	120	60	DI water

Next, in order to further optimize the slurry composition, the influences of the polishing slurry composition, such as the pH value, the abrasive size and its concentration, the dispersant and the oxidants, the rotational speed of the polishing platen and the carrier and the polishing pressure, on the material removal rate of SiC crystal substrate (0001) C surface will be studied based on the abrasive SiO_2 in chemical mechanical polishing (CMP).

Acknowledgements

Supported by the National Natural Science Foundation of China (No.51075125).

Reference

[1] Su Jianxiu, Du Jiaxi, Ma Lijie, et al.. J. of Semi. Vol. 33,No. 10 (2012),p.106003-1~106003-7.

[2] H.Hara, Y.Sano, H.Mimura, et al. J. of Electro. Mater.,Vol.35,No.8(2006),p. L11-L14.

[3] SU Jianxiu, DU Jiaxi, LIU Xinglong, et al.. Adv. Mater. Research, Vol.497(2012), p. 250-255.

[4] Hojun Lee, Boumyoung Park, Sukhoon Jeong. J. of Ceramic Processing Research.Vol.10, No.3 (2009), p. 378~381

[5] Su Jianxiu, Zhang Zhuqing, Yao Jianguo, et al..Adv.Mater. Research, Vol. 797 (2013),p.261-265.

[6] Jianxiu Su, Zhuqing Zhang, Xinglong Liu, et al.. Adv. Mater. Research,Vol.703 (2013),p.90-93.

Advanced Materials Research Vol. 983 (2014) pp 218-221

doi:10.4028/www.scientific.net/AMR.983.218

Thermal stability of cotton cellulose modified with calcium complexes*

Ying-juan SUN[1, a], Yong-li YANG [2, b], Ming GAO[1,c]

[1] School of Environmental Engineering, North China University of Science and Technology, Box 206,Yanjiao Beijing 101601, China

[2] School of Chemical and Environmental Engineering, China University of Mining and Technology, Beijing 100083, China

[a] syj040520@ncist.edu.cn, [b] yongli169@qq.com, [c] gaoming@ncist.edu.cn

Key words: cotton cellulose, thermal stability, flame retardant, smoke suspension

Abstract. Complexes of cell-THPC-thiourea-ADP with Ca^{2+} have been prepared. The thermal stability and smoke suspension of the samples are determined by TG, DTA and cone calorimetry. The activation energies for the second stage of thermal degradation have been obtained by following Broido equation. Experimental data show that for the complexes of cell-THPC-thiourea-ADP with Ca^{2+}, the activation energies and thermal decomposition temperatures are higher than those of cell-THPC-thiourea-ADP, which shows these metal ions can increase the thermal stability of cell-THPC-thiourea-ADP.

Introduction

Cotton cellulose is used extensively to make life pleasant, comfortable and colorful. Unfortunately, it is flammable and causes a fire hazard. According to fire statistics, about 50% of fires are caused by textiles in the world [1], and the cotton cellulose is one of important components in textiles. So the emphasis on reducing combustibility has centered on its chemical modification. There are also many studies on thermal degradation of cotton cellulose treated with flame retardants [2]. However, with environmental sustainability required, the effects of flame-retardants on both smoke generation and the toxicity of combustion products have become special important, as flame retardant cellulose has been reported to produce denser smoke than pure cellulose [3].

In previous papers [4], compounds of transition metals have been found to be effective smoke retarders. However, there is no information about the effects of Ca^{2+} on smoke suspension and thermal degradation of cotton cellulose treated with flame retardants. So the main objective of the work reported here is to investigate the effects of Ca^{2+} on the thermal degradation and smoke suspension of cotton cellulose modified with flame retardant.

In this paper, complexes of cell-THPC-thiourea-ADP with Ca^{2+} were prepared. The thermal degradation of samples was studied from ambient temperature to 800°C by TG, DTA.

Experimental

Materials. Cotton cellulose of commercial grade (Hebei province, China) was selected for flame-retardant treatment. The cotton cellulose was immersed in 24% NaOH solution at room temperature for 24 h (mercerization process). The alkali was then filtered off and the sample was washed repeatedly with distilled water. The sample was dried in an oven at 60 °C and then stored in a desiccator.

Instrumentation. The elemental analysis was carried out using a Carlo Eroa 1102 Elemental Analyzer. LOI values were determined in accordance with ASTM D2863-70 by means of a General Model HC-1 LOI apparatus. Thermogravimetry (TG) was carried out on a DTA-2950 thermal analyzer (Dupont Co. USA) under a dynamic nitrogen (dried) atmosphere at a heating rate of 10°C min^{-1}.

Cotton cellulose treatment. The preparation of the samples is corresponded to references [4]. THPC (Shanghai, China) was neutralized with NaOH to give a pH value equal to 6.5 and its 45%

solution was mixed with 22.5% thiourea solution. The pH value was adjusted to 6.5 and a small amount of ADP was added. The resulting mixture was used as the treating solution. The mercerized cotton cellulose was immersed in the treating solution for 30 min at room temperature. The treated cotton cellulose was dried at 60 °C in an oven for 60 min. Curing of these treated cellulose was carried out by heating at 160 °C for 5 min in the oven. After cooling, the sample was thoroughly washed with distilled water for an hour and dried in an oven at 60 °C. Ca^{2+}complexes of cell-THPC-thiourea-ADP were prepared by treating 6g of cell-THPC-thiourea-ADP in each instance with 5% aqueous solutions of $CaCO_3$ at room temperature for 72 h under constant stirring. Each product was washed repeatedly with water until the filtrate was free from metal salt and dried overnight in an oven at 60 °C then stored in a desiccator.

Results and Discussion

The DTA, TG curves of (1) cotton cellulose, (2) cell-THPC-thiourea-ADP, (3) Ca^{2+} complexes of cell-THPC-thiourea-ADP were obtained in a dynamic air atmosphere from ambient temperature to 800 °C and are shown in Figure 1.

Differential thermal analysis. From the DTA curves of samples 1-3, the initiation temperatures (T_i), peak temperatures (T_p) and termination temperatures (T_t) of the various endotherms and exotherms were investigated and are given in Table1. The DTA curve of cotton cellulose shows two large exotherms with their respective peak maxima at 363 and 459°C. Before 350°C, decomposition and dehydration occur to form some flammable volatile products, and the first exotherm peaking at 363°C is due to the oxidation of these volatile products. Another exotherm, peaking at 459°C, represents oxidation of the charred residues. The dehydration process dominates at low temperatures and ultimately leads to a carbonaceous residue. At higher temperatures, cleavage of glycosyl units by intra-molecular transglycosylation starts, forming ultimately a tarry mixture with levoglucosan as the major constituent [5]. Levoglucosan decomposes into volatile and flammable products and therefore plays a key role in the flammability of cellulose.

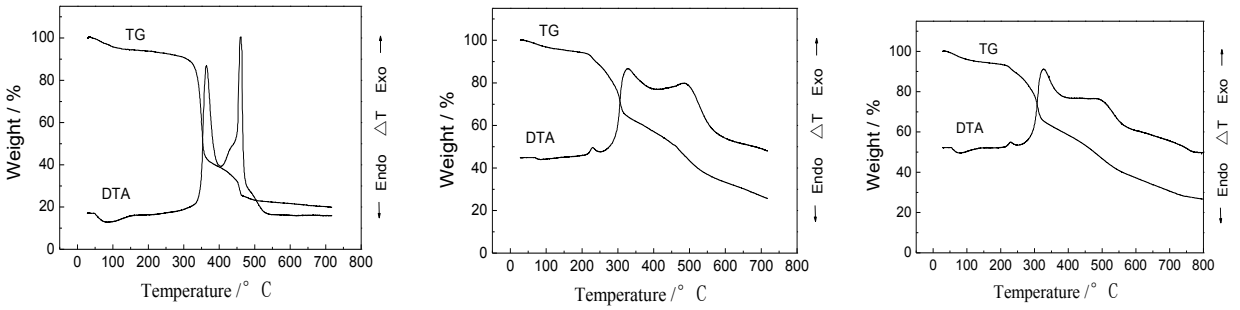

Fig. 1 Thermal analysis curves of samples1-3(1-left, 2-middle, 3-right)

The DTA curve of cell-THPC-thiourea-ADP is quite distinct from that of pure cotton cellulose. The treated cotton cellulose seemed to decompose in two steps [6]. A breakdown or depolymerization of the THPC-thiourea-ADP finish, a catalyzed dehydration of the cellulose, and some bond formation occurred during the first step. Two large exotherms with peak maxima at 326 and 485°C are shown in Fig.1, respectively. The second step involved a breakdown of the cellulose chain, evolution of gases from both the cellulose and the finish polymer, and continuation of bond formation. The bond formation was probably due to a phosphorylation reaction at the C-6 hydroxyl group of the anhydroglucose unit as suggested [7]. Phosphorylation at this position would inhibit the formation of levoglucosan and prevent further breakdown to flammable gases. This would account for the increased amount of char formed over that for untreated cotton cellulose. The last large exotherm peaking at 485°C is due to the combustion of the char [8].

Table 1 Peak temperatures in DTA curves of samples 1-3

No.	Compound	DTA curve			Nature of peak
		T_i	T_p	T_t	
1	Cellulose	320	363	403	Exo(large)
		403	459	539	Exo(large)
2	Cell-THPC-thiourea-ADP	255	326	414	Exo(large)
		414	485	614	Exo(large)
3	Ca^{2+} complex of cell-THPC-thiourea-ADP	230	254	280	Endo(small)
		280	326	418	Exo(large)
		418	500	560	Exo(large)

In the DTA curves of the metal complexes of cell-THPC-thiourea-ADP (sample 3), the first peak, a new endotherm with peak maxima in the range 230-280°C, represents depolymerization, a catalyzed dehydration of the cellulose and some bond formation. For the metal complexes (sample 3), there are also two large exotherms in each case. The decomposition stage, which is represented by the first exotherm, is very different in the decomposition temperature in the complexes. The peak temperature of the complexe is 326°C. The last exotherm, which is due to oxidative decomposition of the residual products, also shows considerable variation in the complexes.

For cotton cellulose, the two exotherms are sharp and narrow, which shows a large rate of heat release. For the samples 2-3, the two exotherms become small and broad. Heat release is distributed between two broad peaks covering a wide area, resulting in a major reduction in rate of heat release and flammable products which fuel the flaming combustion reaction. In the other hand, the second exotherms become much smaller for the samples 2-3, which indicates that oxidation of the charred residues becomes more difficult due to the existence of flame retardants.

Thermogravimetry. From Figure 1, it can be seen that the second stages in thermal decomposition of the samples, decompose mainly and quickly, play a key role attributed to the combustibility. So we mainly discuss this stage. Temperature Range (TR), Mass Loss (ML) at the second stage (quick mass loss rate) in TG are listed in Table 2. Generally, at lower temperatures, the thermal degradation of cellulose includes dehydration, depolymerization, oxidation, evolution of carbon monoxide, carbon dioxide, and formation of carbonyl and carboxyl groups and ultimately a carbonaceous residue; At higher temperatures, cellulose decomposes into a tarry mixture (mainly levoglucosan) which further decompose into volatile and flammable products. The main role of flame retardants containing phosphorus is to minimize the formation of levoglucosan by lowering the decomposition temperature of cellulose and enhancing char formation by catalyzing the dehydration and decomposition reaction. However, lowering the decomposition temperature of cellulose is to decrease its thermal stability, which is not favorable. So the two points must be considered simultaneously.

From Figure 1 and Table 2, it can be seen that for the cotton cellulose (sample-1), initial decomposition temperature is 326°C, the second stage is in a range 326-365°C, and the mass loss is 46%. For cell-THPC-thiourea-ADP, initial decomposition temperature is 214°C, the second stage is in a range 224-318°C, all these much decreased compared with those of cotton cellulose, which shows that the thermal stability of the cell-THPC-thiourea-ADP is much decreased because of the catalyzing dehydration and decomposition reaction. For sample 3, the decomposition temperature range is 225-320°C, higher than that of cell-THPC-thiourea-ADP, which shows that the thermal stability of samples is increased.

Table 2 Thermal degradation and analytical data of samples 1-3

No.	TR [°C]	ML [%]	Ea [kJ/mol]	CY [%]	LOI [%]	P [%]	N [%]	M [%]
1	326-365	46	198.3	20.2	18.0	-	-	-
2	214-318	28	78.1	26.5	29.6	1.69	3.78	-
3	225-320	25	85.1	33.4	28.1	1.45	3.00	0.71

In order to understand the flame retardant properties of these samples, LOI of samples is measured, given in Table 2. From Table 2, we can see that samples 2-3 show high values of LOI. This suggests that the combustibility of cotton cellulose treated with flame retardants decreases. Moreover, the sample-2 containing highest content of phosphorus and nitrogen shows highest value of LOI. The second stage of decomposition for sample-2 occurs at lower temperatures (224-318°C) and produces less flammable volatile products, resulting in higher flame retardancy.

The kinetic parameters for the second stage were determined using the following equation, given by Broido [9]:

$$\ln(\ln\frac{1}{y}) = -\frac{Ea}{R}\cdot\frac{1}{T} + \ln(\frac{R}{Ea}\cdot\frac{Z}{\beta}\cdot T_m^2) \quad (1)$$

Where y is the fraction of the number of initial molecules not yet decomposed, T_m the temperature of the maximum reaction rate, β the rate of heating and Z the frequency factor.

For the second stage, the major degradation and mass loss stage, the energy of activation for sample-2 is 78.1kJ/mol, is much decreased compared to cotton cellulose (198.3kJ/mol). The reason is that the flame retardant catalyzes decomposition reaction. The lower decomposition temperatures (224-318°C) also support this. The energy of activation for sample-3 is 85.1 kJ/mol, higher than that of sample-2, which shows the thermal stability of sample-3 is increased.

Conclusions

For complexes of cell-THPC-thiourea-ADP with metal ions, the activation energies and thermal decomposition temperatures are higher than those of cell-THPC-thiourea-ADP. The metal ions (Ca^{2+}) can increase the thermal stability of cell-THPC-thiourea-ADP. However, the two exotherms in DTA curves are very different in the decomposition temperature in all the complexes.

* Contract grant sponsor: [1]Fundamental research funds for the Central Universities: 3142013102.

References

[1] G. P. Nair, Colourage, 47(8) (2000) 27–34.

[2] J. Z. Xu and M. Gao, et al.,. J. Fire Sci. 20(3) (2002) 227-235.

[3] O. Grexa, H. Lubke,Polymer Degradation and Stability, 74 (2001) 427-432.

[4] B. Jai and L. Krishan, Indian J. Fibre Text. Res., 17 (1992) 32-38.

[5] B. K. Kandola, A. R. Horrocks, D. Price and G. V. Coleman, J. Macromal Sci, Rev Macromol Chem Phys., C36 (4) (1996) 721-794.

[6] S. M. Mostashari and S. Z. Mostashari. J. Therm. Anal. Cal. 91 (2008) 437-441.

[7] S. M. Mostashari and F. Fayyaz. J. Therm. Anal. Cal. 93 (2008) 933-936.

[8] G. Janowska, T. Mikołajczyk and M. Olejnik. J. Therm. Anal. Cal. 92 (2008) 495-503.

[9] M. Gao, W. Wu and Y. Yan, *J. Therm. Anal. Ca*l. 2009.1. 95(2), 605-608

Advanced Materials Research Vol. 983 (2014) pp 222-225

doi:10.4028/www.scientific.net/AMR.983.222

UV-radiation Curing Process of Cationic Epoxy Adhesive Materials

Weili Zhang[1, a,*], Jianjun Chen[2, b], Manlin Tan[3, c], Bo Li[1], Liqiang Ye[2], Dongju Fu[2], Qing Ma[3], Xiaowei Wang[1] and Dongshuang Li[3]

[1] Center for New Energy & Environmental Technology, Research Institute of Tsinghua University in Shenzhen, Shenzhen 518057, China

[2]Lithium Battery Electrode Active Materials Engineering Laboratory of Shenzhen, Research Institute of Tsinghua University in Shenzhen, Shenzhen 518057, China

[3]Energy Conversion and Storage Public Technology Service Platform of Shenzhen , Research Institute of Tsinghua University in Shenzhen, Shenzhen 518057, China

[a]zhangwl@tsinghua-sz.org, [b]chenjj@tsinghua-sz.org, [c]tangml@tsinghua-sz.org.

Keywords: Cycloaliphatic epoxy compounds, Cationic polymerization, Conversion rate

Abstract: The effect of photoinitiator content and species for adhesive liquid-solid conversion rate was studied. The infrared spectras of the alicyclic epoxy resin adhesives before and after the UV light curing were detected by FTIR. Thus light curing process for the alicyclic epoxy adhesive material was explored. The results showed that the UV light curing speed of Omnicat 550 was slower than that of Omnicat 650. Furthermore, the liquid-solid conversion rate was the maximum when the photoinitiator was added up to 3% with the same agent and coating thickness.

1. Introduction

UV-radiation curing systems has been widely used in coating, printing ink and adhesive industries [1-6]. Among which free-radical photopolymerization system has high curing speed and can accomplish within seconds. But the applications are limited because of oxygen inhibition in the solidifying process, monomer irritating to the skin and toxic. Compared with free-radical photopolymerization system, cationic photopolymerization system is free of these problems. Also, it exhibits smaller curing shrinkage, lower viscosity, better adhesion, optical properties, compressive strength, thermal stability and electrical properties[7-10]. Recently, it is industrial applied to optical fiber coatings and adhesives[11-14]. The first step of cationic photopolymerization process is stimulating the photoinitiator to an excited state via absorbing light energy. Then the photodissociation reaction occurs and generates superacid super proton acid or Lewis acid. Finally, the polymerization of these cationic oligomers and reactive diluents is catalyzed by these acids. The reaction rate and curing process can be influenced by initiator molecules structure, photoinitiator content, illumination time, coating thickness and light intensity [15-18]. Therefore, exploring UV-radiation curing process for the cationic epoxy adhesives is significant to achieve effective optical polymerization.

2. Experimental

2.1 Materials and equipments

The standard adhesive formulation contained 70 wt% of the epoxy resins including two different aicyclic epoxy resins, 27~29 wt % of curing agent, and 1~3 wt % of the photopolymerization initiator.The epoxy resins were the diglycidyl 1,2-cyclohexanedicarboxylate and the

3,4-Epoxycyclohexylmethyl 3,4-epoxycyclohexane carboxylate. The photopolymerization initiators (Omnicat 550 and 650) were used as received from IHT Group. The reactive diluent of Triethylene glycol two vinyl ether were obtained from Hubei Chu enterprise Chemical Co. Ltd..

FTIR spectroscopy of the samples was carried out under 400nm ~ 4000nm wavelength using a PerkinElmer Model Frontier. The UV Curing was carried out under 353nm wavelength using a Model HC-800 UV curing machine.The glue bubbles of adhsive was removed under 30 minutes and -0.1MPa using a Model SLED-1 Glue Defoaming Box equipped with vacuum system.

2.2 Preparation of samples and calculation

The adhesive film was prepared using the follwing procedure. All components were added in glass containers eparatelymix by stirring in at room temperature. After the mixture was distributing or enough to dissolve, we would removed bubble for the adhesive.The adhesive was coated on a glass and the film thickness was controlled by different kinds of spreaders before the UV-radiation under 13000 μw/cm2 light intensity for 360 seconds.The ethanol can separate the liquid organic molecules without curing from the solid membrane by the physical extraction methods. Then the conversion rates are calculated according to the weight changes before and after UV light irradiation.

3. Results and discussion

3.1 Effect of photoinitiator content on the conversion rate

The photoinitiator Omnicat 550 is used in liquid adhesives and the coating layer obtained is about 20μm thick. Infrared spectras is obtained by testing the liquid sample and light solid sample with the infrared spectrometer. The FTIR results are shown in Figure 1 and Figure 2. The conversion rate are shown inTable 1.

Table 1 Conversion rates in different 550 content

Initiator content (wt%)	1%	2%	3%	4%
Conversion rate (%)	98.15	98.47	98.69	98.27

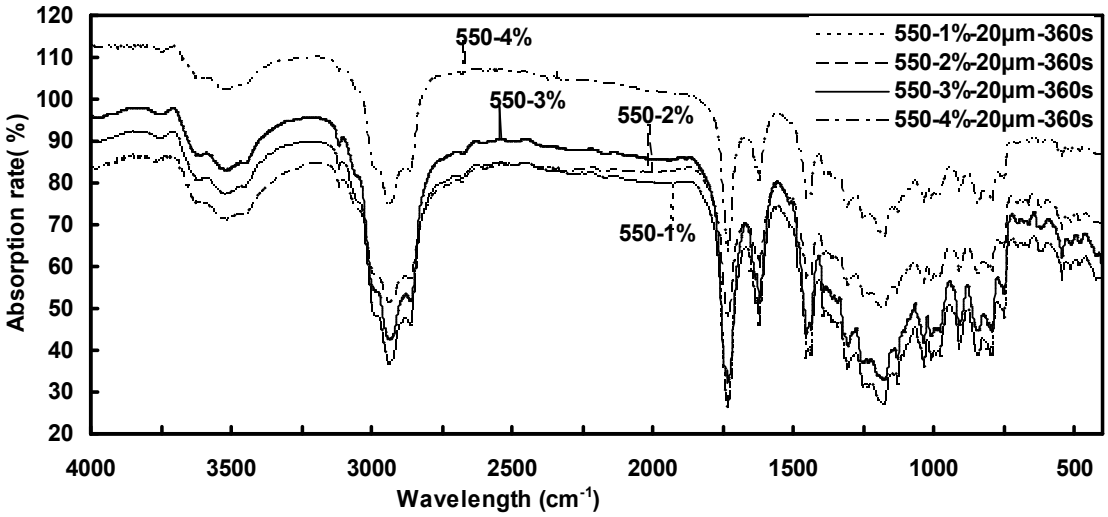

Figure 1 FTIR spectra of liquid sample before UV light light irradiation.

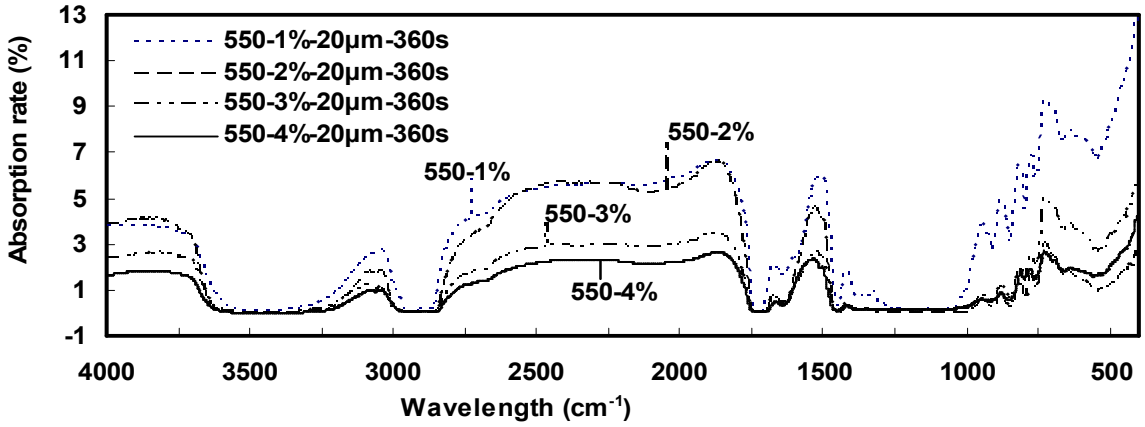

Figure 2 FTIR spectra of solid film after 360s UV light irradiation.

Figure 1 and Figure 2 shows the FTIR curves of liquid adhensive and solid film respectively. It has shown in Figure 2, the infrared spectrogram characteristic absorption peak of solid sample weakened gradually as the photoinitiator contents increased. In comparison of Figure 1 and Figure 2, it is obvious that the characteristic peaks within the wavelength range changed a lot for the liquid sample and solid sample. For example, the absorption peaks at 2937 cm^{-1},1738 cm^{-1} and 1621 cm^{-1} are stronger and sharper in figure 1 than the same position peaks in figure 2. Especially in the wavelength region 1400 ~ 1000 cm^{-1}, compared with absorption peaks of the liquid sample as shown in Figure 1, absorption peaks in Figure 2 is almost disappeared. Furthermore, in figure 2, with the increase of omincat550 initiator, the absorption peaks of solid sample are decreased quickly when omincat550 content is more than 3 wt %. It can be seen from Table 1 that liquid-solid conversion rate is first increased and then decreased with increasing omincat 550 content. The conversion rate is maximum when the content is 3 wt %.

3.2 Effect of the different photoinitiators on the conversion rates

The Omnicat550 and Omnicat650 cationic photoinitiator are compared with the same illumination time and radiation intensity. The relationship between photoinitiator species and conversion rates is studied, as shown in Table 2.

Table 2 The conversion rates in different photoinitiator content and coating thickness

Coating thickness (μm)	photoinitiator types	Photoinitiator content (wt%)			
		1%	2%	3%	4%
20	550	98.15	98.47	98.69	98.27
	650	98.62	98.86	98.97	98.67
40	550	98.28	98.74	98.85	98.54
	650	98.39	98.79	98.83	98.62

It can be seen from Table 2 that conversion rates with Omnicat650 are always higher than Omnicat550 while the coating thickness is the same. So it is sure that polymerization efficiency with Omnicat650 is higher than that with Omnicat 550. Because there is an alkoxy substituent and which is belong to a benzene ring linking anionic in the Omnicat650 molecular. But there is no such alkoxy substituent in Omnicat550. Maybe, the alkoxy substitute in the molecular chain of Omnicat650 has promoted and increased the UV absorption which may produces more super protonic acids and will accelerate the photo polymerization crosslinking reaction. Because lack of such alkoxy substitute, samples with Omnicat550 has limited light absorption and produces fewer super protonic acids so that there is a smaller decrease of the conversion rate.

4. Conclusions

For the cationic epoxy adhesive contains photoinitiator Omnicat550, the liquid-solid conversion first increases and then decreases with increasing Omnicat550 content. When Omnicat550 content is 3 wt %, the conversion rate reaches the maximum.Liquid-solid conversion rate of adhesive with Omnicat650 is higher than that with Omnicat550 under the same irradiation intensity, light illumination time and coating thickness. It may be because Omnicat650 has alkoxy substituent which can produce more super protonic acid and promote the adhesive's light polymerization crosslinking reaction.

References

[1] R.L. Sakaguchi, B.D. Wiltbank and C.F. Murchison. Dent. Mater. Vol. 21 (2005), p.43~46

[2] A.J. Hudson, S. C. Martin and M. Hubert. J. Electronic Packaging. Vol. 124(2002), p.352~354

[3] B. Yacobi, A. J. Hudson and S. C. Martin. Appl. Phys. Rev. Vol. 91(2002), p.6227~6262

[4] L.F. Francis, A.V. Mcormick and D.M. Vaessen. J. Mater. Sci. Vol. 37(2002), p.4897~4911

[5] Segurola J, Allen N and Edge M. Polym. Degrad. Stabil. Vol. 65 (1999), p.153~160

[6] Decker C., Viet TTN. and Thi, HP. Polym Int. Vol. 50(2001), p. 986~989

[7] Q.Q. Zhu and W. Schnabel. Polymer. Vol. 37 (1996), p.4129~4133

[8] S. Ye, N.B. Cramer and I.R. Smith. Macromolecules. Vol. 44 (2011), p.9084~9090

[9] Fuh JYH, Choo YS and Lu L. J Mater Process Technol Vol. 63 (1997), p.887~891

[10] J. V. Crivello, J. H. W. Lam. Macromolecules. Vol. 10(1977), p.1307~1315

[11] L. Valette, J.P. Pascault and B. Magny. Macromol Mater. Eng. Vol. 288(2003), p. 867~874

[12] Y. M. Kim, L. K. Kostanski and J.F. Polymer. Vol. 44(2003), p.5103~5109

[13] I. Czajlik, P. Hedvig and A. Ille. Radiat Phys Chem. Vol. 47(1996), p.453~455

[14] D. K. Chattopadhyay, Panda S. S. and N. Raju. J. Prog Org Coat.. Vol. 54(2005), p.10~19

[15] J. D. Oxman, D. W. Jacobs. U.S. Patent 6,025,406.(2000)

[16] Yubai Bi , Douglas C. Neckers. Macromolecules. Vol. 27(1994), p.3683~3693

[17] L.G. Lovell, H. Lu, and J.E. Elliottn. Dental Materials. Vol. 17（2001）, p.504~511

[18] K.A. Berchtold, L.G. Lovell and J. Nie. Macromolecules. Vol. 34(2001), p.5103~5111

Advanced Materials Research Vol. 983 (2014) pp 226-230

doi:10.4028/www.scientific.net/AMR.983.226

ABAQUS based on machining simulation during metal milling

Zhu dan[1, a], Zheng yan[1]

[1] Jian yan technology co., LTD of Ji Lin Province

[a]zhudan0530@163.com

Keywords: Milling; ABAQUS; Cutting temperature; Cutting forces; Cutting stress

Abstract: Machining of metals make use of thermal-mechanical FEM model. Analysis of nonlinear elastoplastic finite element simulation of milling of 45 # steel material use software of ABAQUS that is finite element simulation technology. ABAQUS software could be carried out on prediction of the milling force. Through finite element analysis, distribution of stress field of workpiece and tool is obtained under the influence of thermal-mechanical. The prediction accuracy of the model was validated experimentally and the obtained numerical and experimental results were found in good agreement.

Introduction

Milling is one of the most widely machining method in the modern machinery industry[1-2]. Milling process used to produce physical phenomena such as cutting force, cutting heat and cutting tool wear. As a result, the numerical analysis of the milling process often involves a lot of the content of the subject such as elastic-plastic mechanics, fracture mechanics and thermodynamics.

Despite research of finite element simulation of machining is generally concentrated in 2d orthogonal cutting in this area, still there is lack of a comprehensive model which by taking into account the effects of 3D geometry of workpiece and cutter in the actual milling process[3]. In order to truly reflect the milling process, increased attention is therefore being focused on that ABAQUS of finite element software is used to establish three-dimensional model of the workpiece and cutter, and carries on the simulation, well capable to perform finite element analysis of the metal cutting process in a 3D-virtual machining environment and realistically predict the resulted part quality.

FEM-based milling model

Coupling interaction of mechanical load and thermal load uses analysis of deformation of thermal-mechanical and elastic-plastic based on the finite element method[4]. The method includes the following several key techniques: The material constitutive model; Fracture criterion; Characteristics of contact friction and Equation of heat conduction.

The material constitutive model

Johnson-Cook model is a constitutive Model with good properties, which is used to describe under the condition of the large deformation, high strain rate effect and temperature, especially the model is widely used in the transient and dynamic simulation. The governing equation of this Johnson-Cook model corresponds to:

$$\bar{\sigma}=\left[A+B\left(\bar{\varepsilon}\right)^{n}\right]\left[1+CLn\left(\frac{\dot{\bar{\varepsilon}}}{\dot{\bar{\varepsilon}}_{0}\left(s^{-1}\right)}\right)\right]\left[1-\hat{\theta}^{m}\right]$$
$$\hat{\theta}=\begin{cases}0 & \theta<\theta_{t}\\ \dfrac{T-T_{0}}{T_{melt}-T_{0}} & \theta_{t}<\theta<\theta_{m}\\ 1 & \theta>\theta_{m}\end{cases} \quad (1)$$

Where $\bar{\sigma}$ is equivalent stress, $\bar{\varepsilon}$ is equivalent plastic s-train, $\dot{\bar{\varepsilon}}$ is plastic strain rate, $\dot{\bar{\varepsilon}}_0$ is reference strain rate(1.0S-1), T_0 is room temperature， T_{melt} is melting temperature, A is yield strength of material(MPa), B is a material hardening modulus(MPa), n is a strain strengthening factor, C is strain rate coefficient of strength, and m is thermal softening coefficient.

Fracture criterion

The rupture equation using the rule of Johnson-Cook's shear failure is to make the cutting the element material taking place of failure in the process of simulation of cutting (when ω is a $\omega \geq 1$， the element material taking place of failure), which is that materials of workpiece is breaked. The damage parameters are defined as follows：

$$\omega=\sum\left(\frac{\Delta\bar{\varepsilon}^{pl}}{\bar{\varepsilon}_{f}^{pl}}\right) \quad (2)$$

$$\bar{\varepsilon}_{f}^{pl}=[d_1+d_2\exp(d_3\frac{\sigma_p}{\sigma_q})][1+d_4Ln(\frac{\dot{\bar{\varepsilon}}^{pl}}{\dot{\varepsilon}_0})](1+d_5\hat{\theta}) \quad (3)$$

where $\bar{\varepsilon}_{f}^{pl}$ is failure strain, $\dot{\bar{\varepsilon}}^{pl}/\dot{\varepsilon}_0$ is strain rate of dimensions and the plastic, p/q is dimensional compressive stress and deviatoric stress ratio, σ_p/σ_q is dimensionless bias stress ratio, $\hat{\theta}$ is dimensionless temperature, d1~d5 is failure parameters under the transformation temperature, the parameters of failure can be measured by tensile torsional test, and $\dot{\varepsilon}_0$ is a reference strain rate in equation(2)and equation(3).

Characteristics of contact friction

According to Zorev[6] proposed friction model suggests: Contact area of chip and tool rake surface has two different contact state, namely the sliding zone and the bond zone, the shear stress at every point in the bonding zone is the basic same; friction stress in the sliding area decreases with a cutting tool rake angle, and meet the coulomb law of friction. Namely：

$$\tau_f=\begin{cases}\mu\sigma_n & \mu\sigma_n<(\text{the sliding zone})\\ \tau_s & \mu\sigma_n\geq \text{ the bond zone}\end{cases} \quad (4)$$

where τ_f is a the friction stress of tool and chip interface; μ is a frictional coefficient; σ_n is a normal stress of tool and chip interface; and τ_s is a shear flow stress of cutting material.

Equation of heat conduction

The partial differential equation of two-dimensional heat conduction of orthogonal cutting corresponds to:

$$\lambda\frac{\partial^2\theta}{\partial x^2}+\lambda\frac{\partial^2\theta}{\partial y^2}-\rho C_p(\mu_x\frac{\partial\theta}{\partial x}+\mu_y\frac{\partial\theta}{\partial y})+\dot{Q}=0 \quad (5)$$

$$\dot{Q} = \frac{W_h \dot{\varepsilon} \bar{\sigma}}{J} \quad (6)$$

where λ is thermal conductivity; C is a specific heat; ρ is material density; $\dot{Q}$ is heat generation rate of per unit volume; is the ratio of plastic deformation converted into heat, here Wh=0.9, $\bar{\sigma}$ is equivalent stress; $\dot{\varepsilon}$ is the equivalent strain rate; and J is Joule equivalent coefficient in equation(5)and equation(6).

The milling model and grid technology

Grid is one of the most important steps in the process of finite element analysis, especially for the complicated geometry of the model. Grid tumble quality directly affect the precision and solve the time. Unreasonable grid can lead to solving process interruption. To simulate the milling process of finite element simulation, due to the complexity of cutter shape, the grid distortion occurs by using ABAQUS software. This paper based on the three dimensional four milling cutter, and use the hypmch software to meshing of milling cutter, then import it into ABAQUS, as shown in figure 1.

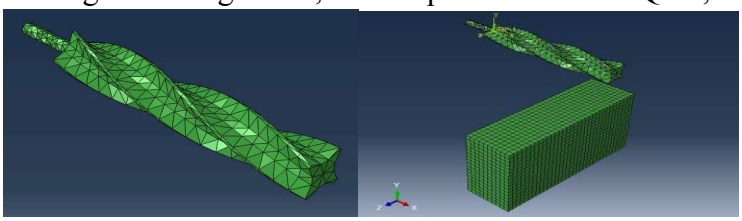

Figure 1 Mesh of workpiece and cutter

Material properties

In this article, the cutting tool is set to the rigid body. Don't consider the deformation in the process of cutting tool in cutting. Workpiece materials choose 45 # steel. Cutting tool material choose carbide cutter (WC), its material properties as shown in table 1.

Table 1 The materials properties of AISI 1045 steel and WC

material	Yang's modulus E Gpa	Poisson's ratio v	density ρ kg/m^3	heat conductivity κ w/ nk	specific heat C J/kg k	coefficient of thermal expansion α 10^{-6}/k	Heat transfer coefficient of the workpiece and tools N/s/mm/^{0}C
AISI1045	211	0.3	7800	47.68	472	α (T	30
WC	E T	0.22	15700	20	343.3	5.2	

The results of simulation and analysis

Simulation conditions are shown in table 2.

Table 2 Simulated conditions

workpiece	45 # steel	
tool	material	WC
	type	DNM234
Cutting conditions	cutting speed r/min)	600
	Feed speed (mm/s)	2
	back cutting depth(mm)	0.5

Figure 5 shows cutting three-axis force change curve. It could be seen that the change tendency of cutting three-axis force is the basic same in figure 2: Force rose from zero to maximum and then decreased gradually, the milling force presents periodic fluctuation. Because each cutter tooth cut to

cut out workpiece unceasingly in milling process, the milling force of y direction is the largest, the milling force of z direction is the minimum.

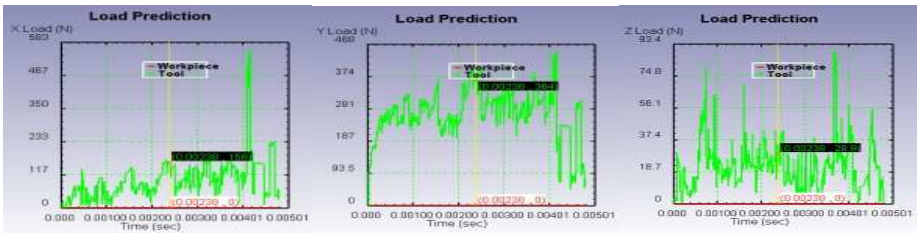

(a)F_x curve (b)F_y curve (c)F_z curve

Figure 2 Cutting three-axis force curve

The effective stress change curve is shown in figure 3. It could be seen that maximum effective cutting stress is in the shear band in figure 6, and form a shear band of certain width. The effective cutting stress replace and change with the cutter tooth cutting to cutting out the in the process of milling.

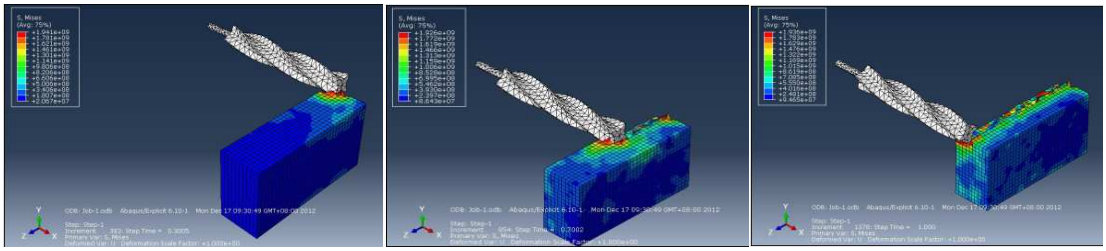

(a)Milling began (b)Milling smooth (c)End milling

Figure 3 Milling process

Experimental verification

In order to verify the simulation results, 45 # specimen was milling on XK714 type machining center. This article took the same as the simulated conditions of milling parameters (speed 600 r/min, the feed speed is 120 mm/min, the milling depth of 0.5 mm) for milling. In the process, a diameter of 12mm carbide cutting tools and dry milling methods on specimen processing were adapted. In the process of milling, 9257B dynamometer was used to measure milling force. The dynamometer connected with charge amplifier 5070 and the data read into the computer by acquisition card PC-CARD-DAS16/16, as shown in Fig.4, 5.

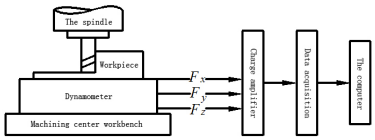

Figure 4 Principle diagram of milling force measuring

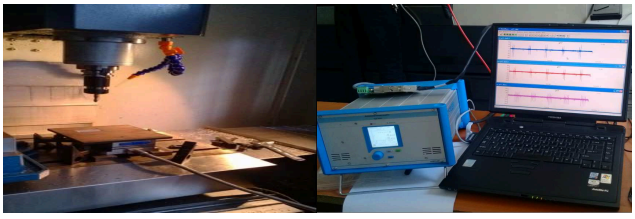

(a)Experimental workbench (b)The measured results

Figure 5 Actual measurement chart of the experimental data

In the Fig.6, it is milling three force when the spindle speed is 600r/min, the feed rate is 120 mm/min and cutting depth is 0.5mm.

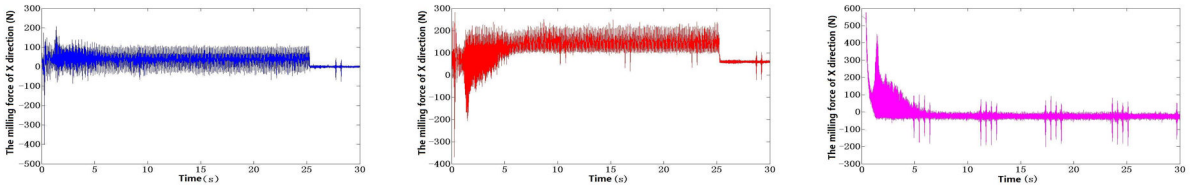

(a) F_x experimental data curve (b) F_y experimental data curve (z)F_z experimental data curve

Figure 6 Experimental data curve

The experiment of milling force compare with analog value. Comparison results as shown in table 3, Comparison results as shown in table 3, the relative error of the result is in an acceptable range. Results show that the built finite element model of the result is effective.

Table 3 Compared the experimental value and simulation value of milling force

direction	The experimental value (N)	The simulation value (N)	The relative error
X	41.72	39.61	5.06
Y	115.03	124.76	8.46
Z	-20.76	-19.47	6.21

Conclusion

Metal milling is a complex strong and dynamic physical process of thermal-mechanical, simulation of milling process is based on ABAQUS, and obtained a number of important parameters. The method can further study a variety of cutting tool and workpiece machining characteristics.It could provide reference for the design of the tool and the determination of process parameters. It could carry on the optimization of machining process and the purpose of the minimum production cost. But some of the key techniques in finite element simulation of metal cutting processing is not enough mature. Because accuracy of the material constitutive model, fracture criterion and characteristics of contact friction is not high, there is a certain error between simulated values with experiment values. The solution of these key technologies will become the focus of future research.

References

[1]Han Chengliang. Modified milling performance of nano TiN metal ceramic blade[J]. Cemented Carbide, 2004,21(4):214-217.

[2]Li Shichun, Ken peng, Liu AnMin. Dynamic analysis of high speed milling system and determination of cutting force[J]. Hydromechatronics Engineering，2011,39(23),28.

[3]Lu dong, Li jianfeng. Finite element simulation of three-dimensional milling process of Aviation aluminum alloy 7075 - T745[J]. China Mechanical Engineering,2008,19(22):2708-2710.

[4]Tang zhitao, Liu zhanqiang, Ai xing. Metal cutting processing of thermal elastic-plastic deformation finite element theory and key technology research[J]. China Mechanical Engineering,2007,18（6）,746-751.

[5]Johnson G R ，Cook W H.A constitutive model and data formetals subjected to large strains，high strain rates and hightemperatures [C].Proceedings of the Seventh International Symposium on Ballistics Netherlands，1983:541-547.

[6]Zorev N N.Inter-relationship between Shear Processes Occurring along Tool Face and on Shear plane in Metal Cutting[C]. International Research in Production Engineering. New York:ASME,1963:42-49.

CHAPTER 5:

Power Systems, Energy and Environmental Engineering

Advanced Materials Research Vol. 983 (2014) pp 233-237

doi:10.4028/www.scientific.net/AMR.983.233

Design Study of Small Gas Cooled Fast Nuclear Power Plant for Synergetic Energy System with Renewable Energy by Employing Pump Storage

Zaki Su'ud

Department of Physics, Faculty of Mathematics and Natural Sciences, Bandung Institute of Technology, Bandung, Indonesia

Email: zakisuud@gmail.com

Keywords: Gas cooled, long life, fast reactors, renewable energy, pump storage, inherent safety

Abstract. Design study of a synergetic system among small long life gas cooled fast reactors and renewable energy has been performed. A pump storage system is the center in the integration among considered energy sources. Using this system many renewable energy sources and the small nuclear power plant can be integrated to produce reliable energy sources which can be used for electricity production, desalination, etc. In this system each energy source can store energy by contributing pumping water from a low level reservoir to a high level reservoir. The nuclear power plant module must satisfy inherent safety requirement, and have flexibility in producing electricity, clean water (through desalination), etc. The reactor can be operated for 25 years without the necessity to refuel during that period. To achieve inherent safety capability it is important to minimized excess reactivity during burn-up to be below delayed neutron fraction value so that super prompt critical accident such as in Chernobyl accident case can be avoided. Here minimization of excess reactivity is carried out by adjusting core and blanket region width and plutonium enrichment in core regions.

Introduction

Indonesia has serious problem in energy security. Several provinces outside Java-Bali have severe electricity shortages. The use of oil for electric power generation is still significant especially for remote area out side Java-Bali islands. With the current consumption of oil is growing significantly while the production is tend to decrease is is important to develop new and renewable energy in Indonesia for energy security.

Nuclear energy produced by advanced 4^{th} generation nuclear power plant is a high density energy which not only reliable and competitive but also very good for environment because it does not contribute global warming gaseous production. With nuclear renaissance after chernobyl accident, current fourth generation of nuclear power plant can solve many clasical NPP problems by much higher efficiency in using natural uranium resources, inherent/passive safety capability, capability to burn radioactive wastes, and lower energy prices.

Gas cooled fast reactor is one of fourth generation NPPs which haves such advantages[1-6]. In this research very small long life gas cooled fast reactors are investigated to produce combined electricity and clean water in remote area and can be combined with renewable energy sources such as solar and wind energies through a pump storage system[7]. The NPP will be optimized to have important safety features such as near zero burnup reactivity swing, negative reactivity feedback, and small peaking factor.

The energy form each system can be stored in the form of water potential energy by pumping water from the lower reservoir to upper reservoir. The water from upper reservoir can then be flown to lower reservoir to drive the turbine to produce electricity. The system give flexibility in energy utilization. In remote area electricity sometimes dominantly used at night while the load is low at noon. In such situation some of the nuclear energy can be used to produce electricity and the other for desalination.If the energy from the nuclear is still surplus it can be stored in pump storage. On the other hand the energy from the renewable energy can be stored in the pump storage to be used at

night when the load become very high. With such system, the effect of intermitten nature of some of renewable energy resources can be minimized/solved. Fig. 1 shows illustration of a pump storage system with two water reservoirs (upper reservoir and lower reservoir) and a water channel which can be used to pump the water to the upper storage or to flow the water from the upper reservoir to the lower reservoir while driving turbines to produce

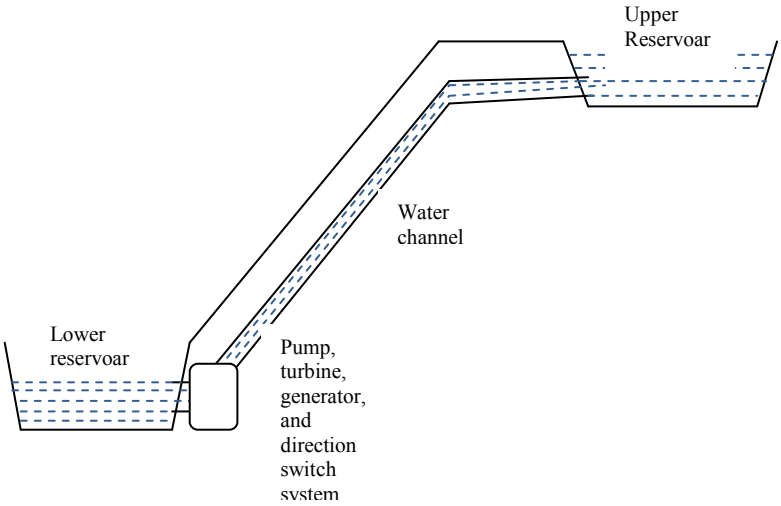

Fig. 1 Pump storage system illustration

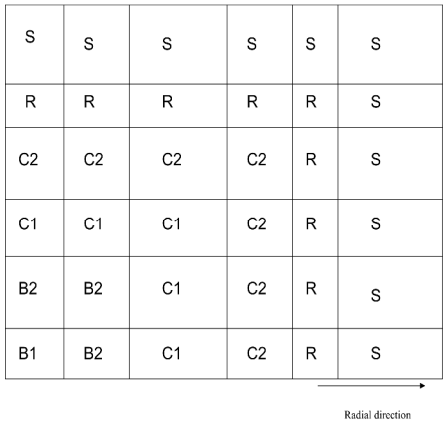

Fig. 2 Reactor Core configuration

Design Concept and Calculation Method

Detail design for the pump storage must consider the pattern of electricity and clean water consumption and available renewable energy sources. Integration of renewable energy sources with nuclear energy sources can be implemented in the electric system level or in the mechanical level. In the electric system based integration electricity produced by each energy component is integrated into single line AC power which then can be used to supply the electricity demand at that time and the rest can be used to pump the water into upper reservoir. If the integration is conducted in the mechanical level each energy component will drive independent pumps to produce higher potential energy. In this paper the detail design will be focused on the nuclear energy system.

To design an inherently safe small long life gas cooled fast reactors some important requirements must be fulfilled. First the excess reactivity during burnup should not exceed one dollar of reactivity (equal to delayed neutron fraction) in order to prevent possibility of super prompt critical accident such as in the case of Chernobyl accidents[8-9]. Second the system must be able to remove decay heat by a passive mechanism. Third the reactor must be optimized to survive the most severe hypothetical accident that is depressurized accident.

To minimize excess reactivity during burnup the core is divided into two main active cores regions and one internal blanket put in the center of the core, see Fig. 2. At the beginning the active region is core I (C1) and core II (C2). However as burnup proceeds the plutonium is accumulated in the internal blanket so that at the end of life this region give important contribution to maintain criticality of the core. By proper adjustment of the cores and blanket parameters it can be obtained configuration which give excess reactivity less than one dollar of reactivity (less then delayed neutron fraction).

Passive decay heat removal system are consisted of three independent sub systems: RVACS (Reactor vessel auxiliary cooling system, natural circulation of primary coolant, and natural circulation heat removal through dedicated closed loop. Consideration must be taken to get possibility to survive Core Depressurized Accident in which it is considered as the most severe hypothetical accident in the Gas Cooled Fast Reactors as well as in the High Temperature gas Cooled Reactors. In Such accident we must rely on the radiation to remove decay heat from the reactor core to the environment

The calculation is performed using two dimensional multi group diffusion and burn-up calculation in FI-ITBCH1 code system and SLAROM code system is used to produce necessary multigroup constants.

Calculation Results and Discussion

Table 1 General parameters of the standard core

Parameter	Value
Power (MWth)	15
Number of Radial division of the main core	4 regions
Core Geometry	2-D Cylinder
Refueling Periode(years)	25
Fuel/cladding/coolant type	UN and PuN/SS316/He gas
Active core radius/height	80 cm/100cm
Reflector width (Stainless)	50 cm
Plutonium percentage (%)	9-13
Fuel/structure/coolant volume fractions	55/12.5/32.5

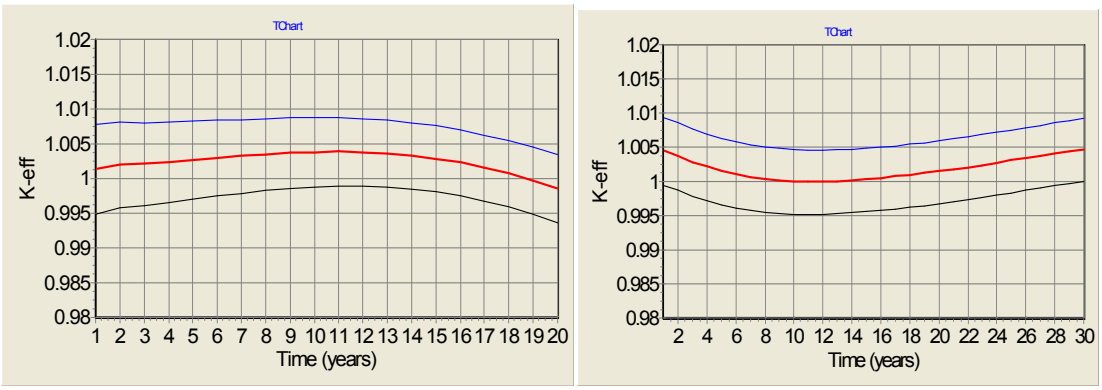

(a) (b)

Fig. 3 Effective multiplication factor change with time and the effect of outer core width(a) and inner core width (b)

Fig. 3.a shows effective multiplication factor (K-eff) change during burnup for standard case and cases with variation in the radial width of outer core. The variation is performed by increasing or decreasing the parameter by 5%. It is shown that this parameter influence the effective multiplication pattern both in the beginning of life(BOL) and in the end of life (EOL). The effiect is almost the shift up of k-eff pattern for increasing the width of the region and shift down for the reduction of the parameter.more detail observation shows that the effect is slightly higher in the beginning of life compared to that in the end of life.

Fig. 3.b shows k-eff change during burnup for standard case and cases with variation in the radial width of inner core. The variation is also performed by increasing or decreasing the parameter by 5%. It is shown that this parameter influence the effective multiplication pattern almost uniform from the beginning of life(BOL) till the end of life (EOL). It is shown that this region has almost the same importance from the beginning of life to the end of life.

Fig. 4.a shows k-eff change during burnup for standard case and cases with variation in the radial width of inner blanket. Similar to the the case of the width of the cores, he variation is also performed by increasing or decreasing the parameter by 5%. It is shown that this parameter influence the effective multiplication pattern almost uniform from the beginning of life(BOL) till the end of life (EOL) but the effect is significantly smaller compared to those of the width of the cores. It is shown that the burn-up process till the end of life make the role of this region increases but never become dominant region.

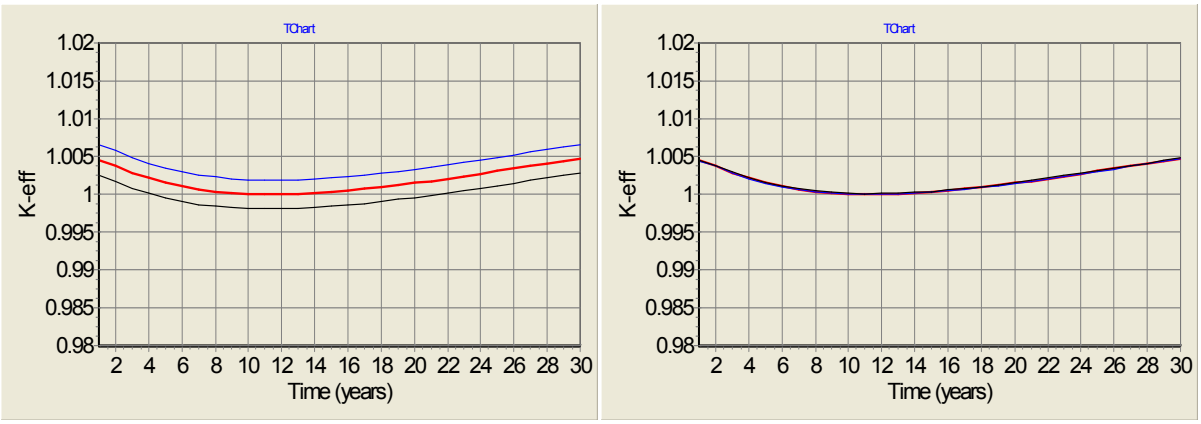

(a) (b)

Fig. 4 Effective multiplication factor change with time and the effect of inner blanket width (a) and reflector width (b)

Fig. 4.b shows k-eff change during burnup for standard case and cases with variation in the radial width of reflector. It is shown that the effect of this parameter to the k-eff change is small.

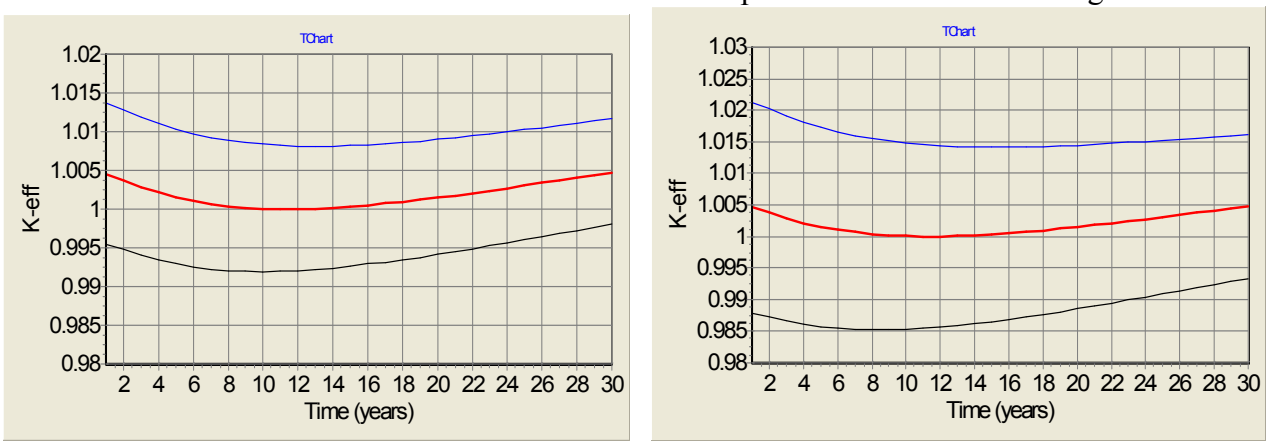

(a) (b)

Fig. 5 Effective multiplication factor change with time and the effect of outer core plutonium percentage

Fig. 5.a shows effective multiplication factor (K-eff) change during burnup for standard case and cases with variation in plutonium percentage of outer core. The variation is performed by increasing or decreasing the parameter by 5%. It is shown that this parameter strongly influences the effective multiplication pattern from the beginning of life(BOL) to the end of life (EOL). The effect is stronger than that of the region width and the effect in the BOL is slightly stronger than that in the BOL.

Fig. 5.b shows effective multiplication factor (K-eff) change during burnup for standard case and cases with variation in plutonium percentage of inner core. The variation is performed by increasing or decreasing the parameter by 5%. It is shown that this parameter has stronger influences the effective multiplication pattern compared to outer core plutonium percentatage. One of the important reason for this is that the inner core region width is much larger than outer core region width and als due to its position, it has larger importance value. The effect is also stronger than that of the region width and the effect in the BOL is also slightly stronger than that in the BOL.

Fig 6 shows power density distribution during the beginning of life. It is shown that the power distribution peak is in the inner core region due to inner blanket low contribution of power due to lack of fissile material and low contribution in the outer core due to relatively low neutron flux. As burnup proceed the contribution of inner core and internal blanket region increase and contribution of outer core decrease resulted in higher peak power density as shown in Fig. 7.

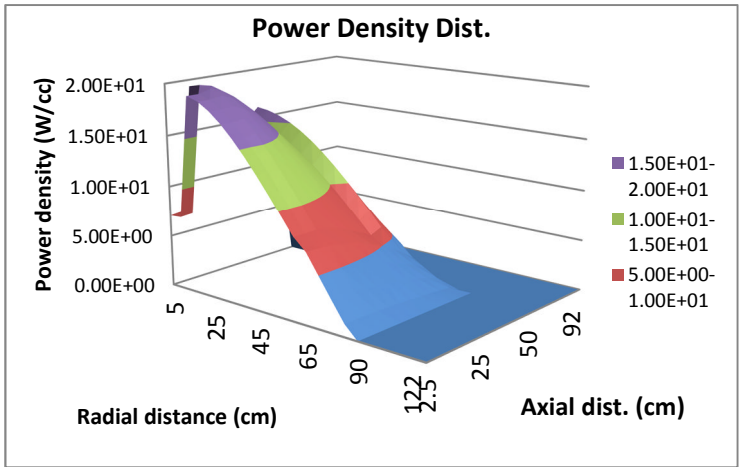

Fig. 6 Power density dist.during the BOL (half core)

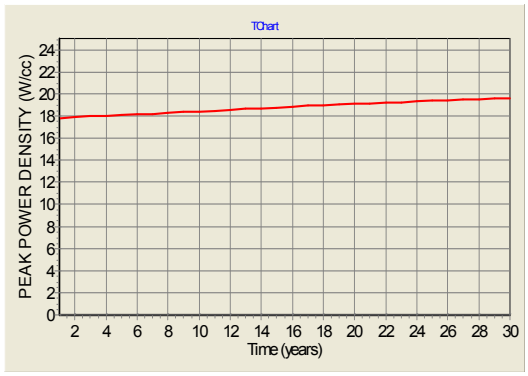

Fig. 7 Peak power density change

Summary

Design study of 15 MWt long life gas cooled fast reactor with renewable energy synergetic system employing pump storage has been performed. Each component energy system can save their energy in form of potential energy of water by pumping water from the low reservoir to the high reservoir. Using this system flexible energy utilization can be obtained by adjusting the load of electricity generation, clean water production, hydrogen production, etc. according to the pattern of the load. Nuclear reactor system inherent safety capability is achieved by minimizing excess reactivity during burn-up to be less than one dollar of reactivity, adopting decay heat removal system, and anticipating depressurized accident using passive mechanism.

Acknowledgement

This research supported by Riset Unggulan KK ITB 2013 and Riset Unggulan KK ITB 2014

References

[1] T.Y.C. Wei and K.D. Weaver: Initial Requirements for Gas-Cooled Fast Reactor (GFR) System Design, Performance, and Safety Analysis Models. (Gen IV Nuclear Energy System, INEEL/EXT-04-02242, 2004)

[2] Su'ud, Z., Sekimoto, H., Annals of Nuclear Energy Vol. 54 (2013), pp. 58-66

[3] M. Ariani, et.al., American Institute of Physics Conf. Proceeding, vol. 1454(2012), p. 69

[4] M. Ariani, Z. Su'ud, F. Monado, A.Waris, Khairurrijal, I. Arif, F. Aziz and H. Sekimoto: Applied Mechanics and Materials, Vol. 260-261(2013), p.307

[5] M. Ariani, Z. Su'ud, A.Waris, Khairurrijal, N. Asiah and M.A. Shafii: American Institute of Physics Conf. Proceeding, vol. 1325(2010), p. 249

[6] Fiber Monado, Zaki Su'ud, Abdul Waris, Khairul Basar, Menik Ariani, Hiroshi Sekimoto, Application of Modified CANDLE Burnup to Very Small Long Life Gas-cooled Fast Reactor, Advanced Material Research(AMR), Vol. 772, pp. 501-506

[7] Ruth M.F. et al., Energy Conversion and Management, Volume 78 (2014), pp 684-694.

[8] Zaki S. and H. Sekimoto : Preliminary Design Study of the Ultra Long Life Fast Reactor, Nuclear Engineering and Design, Vol. 140(1993), p.251-260.

[9] Su'ud, Z., Design study of Small Pb-Bi cooled Non-refueling Nuclear Power Reactors (SPINNORs), Applied Mechanics and Materials, Vol. 261-262 , pp. 296-301, 2013

Advanced Materials Research Vol. 983 (2014) pp 238-241

doi:10.4028/www.scientific.net/AMR.983.238

Electrochemical performance of $LiFePO_4$/C prepared from different carbon source

Ai fang Liu

School of Chemistry and Chemical Engineering
Central South University, Changsha, 410083, China

Email: liu.aifang@hotmail.com

Keywords: Lithium iron phosphate ($LiFePO_4$); Carbon source; Lithium ion battery

Abstract. Cathode material $LiFePO_4$/C was prepared via optimized solid state reaction and calcinations using different carbon source. The crystalline and morphology of the resultant powder was evaluated by X-Ray diffraction (XRD), scanning electronic microscope (SEM). The electrochemical performance was measured by galvanostatic charge-discharge test at 0.1C and 0.5C. The results demonstrated that the sample with layer-like stacking microstructure had the best capacity retention up to 96% after 50-cycle at 0.5C; the sample with good carbon coating using glucose as carbon source exhibited the lowest flat charge plateau and the highest flat discharge plateau, also the best storage performance at 60 ºC temperature. Nevertheless, the sample with spherical-like shape and homogeneous particle size had the most capacity loss, maybe due to the increased internal resistance caused by the big interstices between the particle sizes.

Introduction

Olivine structure lithium iron phosphate [1] ($LiFePO_4$) is the promising cathode material for lithium secondary battery, due to safety, low-cost raw materials, environmental friendliness and high energy power. There have been many reports about the factors influencing electrochemical performance, in sides of carbon and conductive phase coating [3], synthesis method [1] , particle size and distribution, and morphology [2]; it was reported [9] the carbon coating can cure the disorder surface and obtain plat discharge plateau; Huang B [10] reported that the sphericle particles morphology had an important role in improving the diffusion of lithium ions. However, so far today a definite conclusion which is the key point of deciding good electrochemical performance has not been put forward.

To get a conclusion, different morphology of $LiFePO_4$ material samples were prepared systematically to compare their electrochemical performance. Some relationships between physical properties and electrochemical properties were found out and discussed.

Experimental

$LiFePO_4$/C was prepared by solid state reaction using glucose, PEG (polyethylene glycol), acetylene black as reducing agent and carbon source, hereafter reported as Glu/LFP, PEG/LFP, CB/LFP, respectively. Stoichiometric amounts of $LiCO_3$, $NH_4H_2PO_4$, FeC_2O_4 and carbon precursor (16wt% in final product $LiFePO_4$) were mill-mixed for 3 h in the planetary miller with a ball-to-powder weight ratio of 5:1 at a rotation rate of 300 rpm. Then the mixed powders were dried in air for 24 h, following heated at 350 ºC for 5 h, (followed by regrouding for 3 h, reported as CB+M/LFP) and finally calcinated at 700 ºC for 12 h in the nitrogen atmosphere.

The prepared samples were characterized by X-ray diffraction (XRD, Bruker D8 ADVANCE diffractometer) using Cu Kα radiation (1.5406 Å,40 kV and10 °/min), scanning electron microscope (SEM, Japanese Electronics JSM-6390LV).

The electrochemical performance of the samples was tested via CR2032 coin-type cells. The cathodes were prepared by blending active material, acetylene black, and polyvinylidene fluoride (weight ratio 90:5:5) dissolved in N-methyl-2-pyrrolidinone. Then the slurry was coated on an aluminum foil and dried under vacuum at 120 ºC for 4 h. Electrode disks were punched from the foil and weighed. Celgard 2700 membrane was used as separator and metallic lithium as the anode, 1 M $LiPF_6$ dissolved in the mixture of ethylene carbonate (EC) and dimethyl carbonate (DMC) (1:1 in weight ratio) was used as the electrolyte. The testing coin-type cells were assembled in an argon-filled glove box, in which the oxygen and moisture is less than 1 ppm. Charge and discharge measurements of the cells were carried out on a Neware battery test system at a current density of 0.3 mA (0.1 C) with voltage cut-off of 4.2 V/2.75 V versus Li/Li^+ at 20 ºC.

Results and discussions

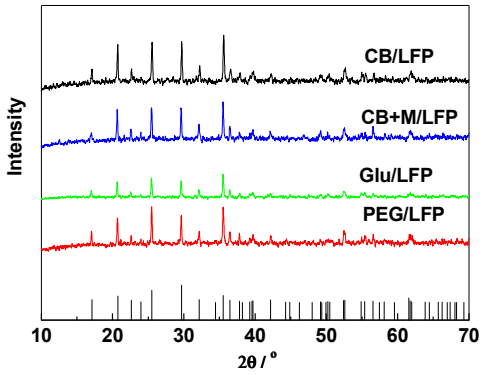

Fig.1. XRD patterns of $LiFePO_4$ samples

The X-ray diffraction (XRD) patterns of $LiFePO_4$/C samples are shown in Fig.1. The diffraction peaks are consistent with the standard $LiFePO_4$ phase pattern; there are no characteristic peaks of impurity. The peaks intensity of Glu/LFP sample is weaker than others, indicating the carbon decomposed from glucose effectively impede the growth of the particles. Thereagainst, the strongest diffraction peaks of the CB/LFP sample had well-refined crystalline. The different carbon precursor had different influence on widening the volume parameter some degree. The properly-broadening crystal parameter is beneficial for lithium ion insertion/disinsertion transfer, but over-broadening lattice will impact the stability of the material structure. Although CB/LFP and CB+M/LFP used the same carbon precursor, the lattice parameters differed each other, because the carbon layer had an influence on crystalline [9].

Fig.2 shows the SEM pictures of the sample $LiFePO_4$/C. The particles of the sample PEG/LFP is spherical-like shape, with a particle size less than 1μm and distribute evenly without agglomeration; the CB+M/LFP, layer-like stacking, the particles sizes of 1μm with some degree of agglomeration, which favors the improvement of electrochemical properties due to good connect between particles. The sample Glu/LFP and CB/LFP shows the homogeneous particles are non-regular morphology shape.

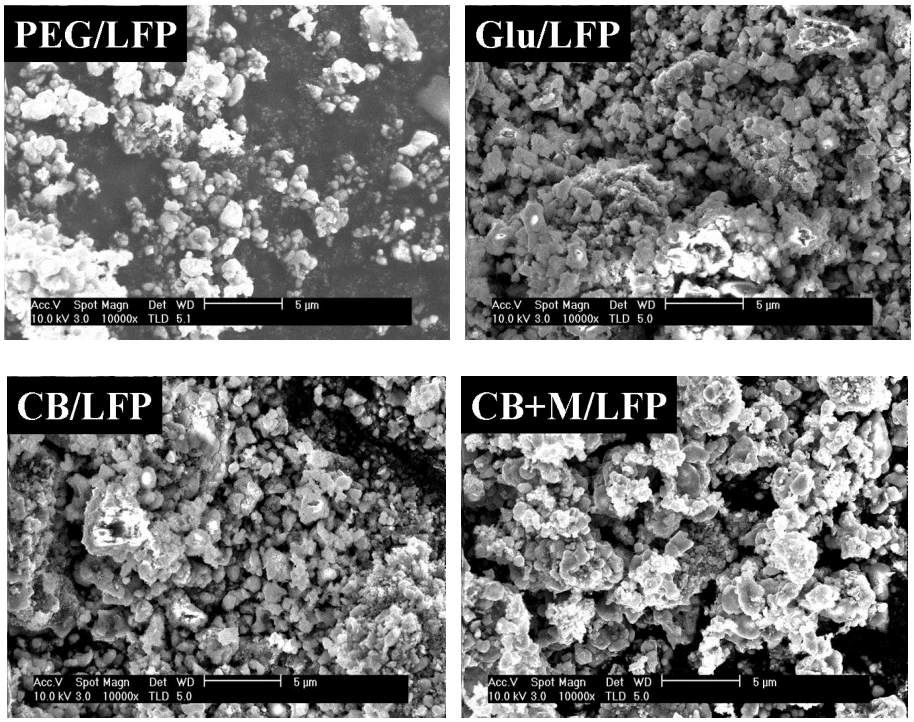

Fig. 2 SEM images of $LiFePO_4$/C sample

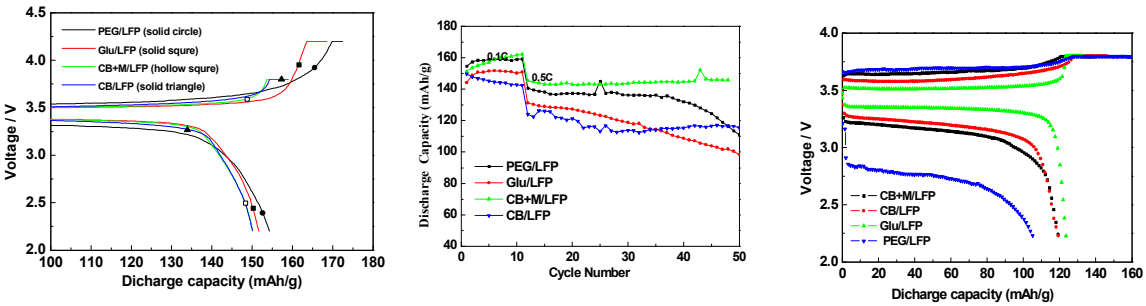

Fig.3 Initial charge-discharge curves of $LiFePO_4$/C samples at 0.1C (the most left)
Fig.4 Cyclic charge-discharge performance of $LiFePO_4$/C samples (the middle)
Fig.5 Charge-discharge curves after aging at high temperature (the most right)

Fig.3 shows the initial discharge capacity profile of different samples. Although the PEG/LFP cathode material had the highest discharge capacity about 155 mAh/g; the charge plateau is the highest and the discharge plateau is the lowest evidently. There the evidence of a polarization between the charge and discharge process which may lead to a slight reduction of the efficiency. Its initial highest discharge capacity can be attributed to good immersion with the electrolyte because of the particles interstices.

Fig.4 shows cycle charge-discharge performance of the samples. The capacity retention ratios of $LiFePO_4$/C samples were of 73.3%, 70%, 96%, and 77.9%, respectively, after a 10-cycle at 0.1 C and 40–cycle of charge-discharge at 0.5 C. The capacity retention of the sample Glu/LFP at 0.5 C rate dropped linearly, corresponding to low crystallinity even though with the homogeneous particles and good carbon coating; the sample CB+M/LFP remained hardly no capacity loss although with agglomerated particles; due to its layer-like structure, which is helpful for lithium ion transfer; the sample CB/LFP had the second better capacity retention is correlated with the

well-refined crystalline. The sample PEG/LFP dropped steeply may be caused by the big internal resistance between the particles; in general, Side reactions decrease the cell's cyclable lithium content during the charge/discharge cycles, which can be responsible for capacity fade.

Fig.5 shows the charge/discharge curves after storage at high temperature environment. The sample Glu/LFP exhibit the most flat, the lowest charge plateau and the highest discharge plateau, with hardly no change comparing with the initial charge/discharge curve, indicating excellent storage performance. It is reported that the carbon coating is responsible for the flat charge/discharge plateau [4]. the sample Glu/LFP used organic carbon source glucose to form a thin carbon film during the decomposition of the glucose. The better case of CB/LFP, showed a little slope; due to the stable structure from well-refined crystalline; but the discharge plateau of the PEG/LFP showed a significant slope and a markedly lowering the discharge potential.

Conclusions

Different crystalline and morphology $LiFePO_4$ were prepared via optimized solid state reaction. Acetylene black as carbon source is beneficial for good crystalline; high quality carbon coating on surface can be formed by using glucose, which will improve the charge/discharge plateau, and raise the stability of storage performance. The usage of PEG can reduce the particles agglomeration, but increasing the internal resistance at the same time. The usage of acetylene black combined with the ball-milling after low temperature pre-sinter, Layer structure was formed, which is beneficial to reduce the capacity loss because of easy lithium ion transfer. So the small difference between charge and discharge plateau didn't ensure the stability so improve the capacity retention. It is not truth that the smaller the particle size, the best electrochemical performance. The high-rate performance is mainly controlled by the intrinsic layer structure.

Acknowledgement

This work was supported by the Central South University Post Doctor Foundation.

Reference

[1] X.H Liu, Z.W Zhao: J. Powder Technology Vol. 197 (2010), p. 309
[2] Zhao B, Jiang Y, Zhang HJ, Tao HH and Zhong MY, Jiao Z: J. Power Source, Vol. 189 (2009), p. 462
[3] Y.Y Liu, C.B Cao, J. Li and X.Y Xu: J. Appl. Electrochem. Vol. 40 (2010), p. 419
[4] Kuwahara A, Suzuki S, Miyayama M: J. Ceramic International. Vol. 34 (2008), p. 863
[5] C.H. Mi, Y.X. Cao, X.G. Zhang, X.B. Zhao and H.L. Li: J. Powder Technology Vol. 181 (2008), p. 301
[6] Catia Arbizzani, Sabina Beninati, Marina Mastragostino: J Appl. Electrochem. Vol. 40 (2010), p. 7
[7] Konarova M, Taniguchi I: J. Power Source Vol. 195 (2010), p. 3661
[8] Oh SW, Myung ST, Oh SM, Yoon CS, Amine K, Sun YK: J. Electrochi. Acta. Vol. 55 (2010), p. 1193
[9] K. Zaghib, A. Mauger, F. Gendron, and C. M. Julien: J. Chem. Mater. Vol. 20 (2008), p. 462
[10] Huang B, Zheng XD, Jia DM, Lu M: J. Electrochi. Acta Vol. 55 (2010), p. 1227

Advanced Materials Research Vol. 983 (2014) pp 242-245

doi:10.4028/www.scientific.net/AMR.983.242

Flow Field Analysis and Response Surface Research on the Rotor in Dry Powder Inhaler

Zhi Chen Cao[a], Hao Ying Li*[b], Shi Hong Shi[c], En Long Zhou[d]

Bio-Manufacturing Research Centre, School of Mechanical and Electric Engineering, Soochow University, Suzhou 215021, China

[a]czcycit@126.com, [b]lihaoying@suda.edu.cn, [c]shishihong@suda.edu.cn,[d]lufei_1234@126.com

Keywords: Dry powder inhaler; CFD; Rotor; Numerical simulation; Response surface

Abstract. In order to find out the correspond relationship of the outlet velocity and rotor speed in dry powder inhaler, the intermediate parameter was inserted in Workbench response surface based on CFD. The simulation of the suction drive rotor rotation mechanism was based on MRF model in FLUENT. It can be easily obtained the rotor's performance curve under different aerodynamic conditions and found out the optimized flow rate is 66.127L/min. This method verifies the clinical phenomena and could guide the clinical research and machinery optimization.

Introduction

Dry powder inhalers (DPIs) are key devices for the pulmonary delivery of drug particles, as they take great responsibility for the storage, delivery and break up of drug aggregates [1]. The ideal characteristics of DPIs consisted of low internal resistance, high efficiency and good depolymerization effect. The Spinhaler®, a DPI device manufacturered by British company Fisons, is driven by the patient's inspiratory to generate the rotor rotation and vibration, thus the powder inside the capsule is fluidized and dispersed into the inhaled air. It has been proved that the optimized flow rate for Spinhaler® is 60 L/min, at which the largest amount of dry powders are emitted from the capsules. A flow rate less than that may cause the rotor less capability to revolve in high-speed, leading to a poor powder emission. In the other hand, a higher flow rate may also significantly decrease the dose emission [2].

In this paper, based on the computational fluid dynamics (CFD), the speed of rotor and velocity of outlet have been set as input parameters and the torque of rotor blade has been set as output value to simulate the internal fluid of the dry powder inhaler device. The method of response surface has been used to build the correspondence relationship between the parameters in certain range and optimize the design.

Numerical Simulation

Modelling and meshing. The Spinhaler® consists of a flow channel, inside which a rotor is contained (figure 1). The rotor is modified at one end, and a cavity is designed for the insertion of size 2 capsule. For simulation, a simplified flow channel is created following the actual size of Spinhaler®. The simplified model was imported into ANSYS Workbench Design Modeler, which were built in UGNX. The 'Fill' and 'Enclosure' tools were used to extract the flow field and build the computational zone. Since the rotor in this device is a rotation issue, the moving reference frame model (MRF) is subsequently used in FLUENT to simulate the rotor rotation. So the flow field was divided into three zones by using the 'Slice' tool in Design Modeler which are inlet zone, rotation zone and outlet zone shown in figure 2.

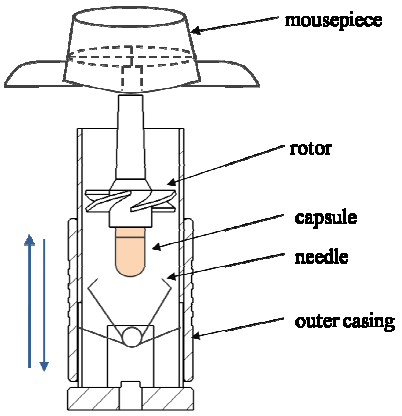

Fig.1 Structure of Spinhaler®

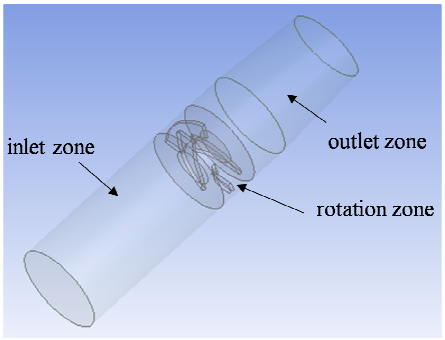

Fig.2 Fluid computational zone

The next step is meshing the model in ANSYS Meshing, and the parameters of mesh were set as follows: Relevance: 50, Advanced Size Function: curvature, Relevance: medium, Smoothing: high, Transition: slow, and Span Angle Center: medium. For all of these three zones, the Automatic method is utilized to meshing the zones as tetrahedral mesh and refine the rotation zone, and Inflation method is used to refine the near wall area. Based on the analysis, the mesh of the zones showed a total amount of 78602 nodes and 277131 elements. After meshing, it is necessary to set the boundary type by specifying the inlet, interface, outlet and wall.

Type of fluid and flow. The fluid need to be determined whether is compressible according to calculate the Mach as below

$$Ma = \frac{v}{c} \tag{1}$$

In the Eq.1, v is the air flow rate somewhere, c is the speed of sound, its value is $343m/s$, the Mach was calculated as $Ma \approx 0.01 << 1$.The corresponding density variation is

$$\frac{\rho_0}{\rho} = \left(1 + \frac{k-1}{2} Ma^2\right)^{\frac{1}{k-1}} \tag{2}$$

In the Eq.2, k is the Karman coefficient, as air the value $k = 1.4$. The density variation $\frac{\rho_0}{\rho} = 1.00005$, it could be found that the density variation can be ignored and the fluid is incompressible.

After that, the flow need to be determined whether is laminar or turbulence according to calculate the Reynolds as below

$$\mathrm{Re} = \frac{\rho v d}{\eta} \tag{3}$$

In the Eq.3, ρ is the density of fluid, v is the speed of fluid, d is the characteristic length, η is the dynamic viscosity of fluid.

For this device, fluid is the air, so the $\rho = 1.225kg/m^3$, $\eta = 1.7894 \times 10^{-5} kg/m \cdot s$. For the flow in tube, d is the inside diameter of tube, so $d = 0.02m$.The speed of fluid wad defined as $v = \frac{Q}{A}$, Q is the flow rate, A is the cross-sectional area, the value of Reynolds was calculated in the best flow rate $Q = 60L/\min$, and the result is $\mathrm{Re} \approx 4358 > 2300$. The flow type is low Reynolds turbulence.

The turbulence intensity was calculated as below

$$I = 0.16(\mathrm{Re})^{-1/8} \tag{4}$$

In the Eq.4, Re is the Reynolds calculated by Hydraulic diameter, and be substituted it into Eq.4. The value of turbulence intensity was calculated as $I = 0.05655 \approx 5.66\%$.

Equations and Turbulence model. For the simulation of this model, the Reynolds average Navier-Stokes(RANS) method was used to simulate the steady flow approximately. Since the RNG

$k-\varepsilon$ model considers the turbulent eddies, therefore RNG $k-\varepsilon$ model was used in this experiment to handle high strain rates and the streamline which has a large degree of bending.

Cell zone and Boundary conditions. The flow field was divided into three zones in Design Modeler and set as Motion zone or Stationary zone in FLUENT cell zone conditions. The rotation zone was set as Motion Zone, where the speed of rotation was set as a new input parameters 'v-rotor' whose initial value was 1000 rpm. The other two zones were set as Stationary Zone.

Some boundaries were specified names according to their types in ANSYS Meshing, there are inlet, interface, outlet and wall. In FLUENT, the inlet was set as follows: type: pressure-inlet, Gauge Total Pressure: 0, direction Normal to Boundary, Turbulent Intensity: 5.655% which was calculated in Eq.4, Hydraulic Diameter: 17.5mm.The outlet was set as follows: type: velocity-inlet, Velocity Magnitude: new input parameters 'v-outlet' which initial value is -6.366m/s, direction Normal to Boundary. The flow field type was set as interior. The faces between zones were set as interface. The wall of rotor blade was set as moving wall and relative to adjacent cell zone, the speed was set as 0 and it will has the same speed with rotation zone.

Solution. The Pressure-Based solver and time steady method was used in this experiment. The details method of solution were set as follows: Scheme type: SIMPLE, Gradient type : Green-Gauss Node Based, Pressure type: Standard and Momentum type: Second-Order Upwind. The solution was initialized from inlet. After 446 iterations the solution converged.

Design Exploration

Parameter Set. When the speed of rotation was set as an new input parameter 'v-rotor' and the velocity of outlet as new input parameter 'v-outlet', the Workbench project showed the Parameter Set that was subsequently introduced into FLUENT solver. An expression 'torque axil=torque_z()@wall-rotor' was inserted in CFD-POST and set as Workbench output parameter and response parameter, which is the torque value of rotor blade.

Response Surface Optimization. The Response Surface function was inserted into Workbench Design Exploration Toolbox. The range of 'v-rotor' parameters were set between 600 rpm and 1600 rpm, and the range of 'v-outlet' parameters were between -2.122 and -10.61m/s.

The Design of Experiment Type was modified as Optimal Space-Filling Design, Design type was set as Max-Min Distance, Maximum Number of Cycles was set as 10, Samples Type was set as User-Defined Samples and Number of Samples was set as 18. The design samples was computed automatically when updating the experiment.

Detail of Response Surface. The relevance between 'v-outlet' and 'torque-axil' can be find in Response Surface and is shown in figure 3. It is significantly shown that the blade torque decreases when the velocity of outlet decreases in the specific range. Figure 4 shows the relevance between 'v-rotor' and 'torque-axil', it can be seen that the blade torque decreases when the speed of rotor increases at the range about 700~1120rpm and reaches the valley value at the speed 1120rpm. The blade torque will increases when the speed of rotor increases over the speed 1120rpm and reaches the peak value at the speed 1422rpm. It is clearly seen the tendency of parameters by fitting the two input parameters and one output parameter as a 3D surface shown in figure 5.

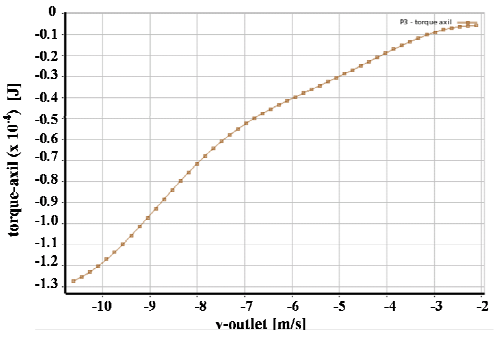

Fig.3 Curve of 'v-outlet'— 'torque-axil'

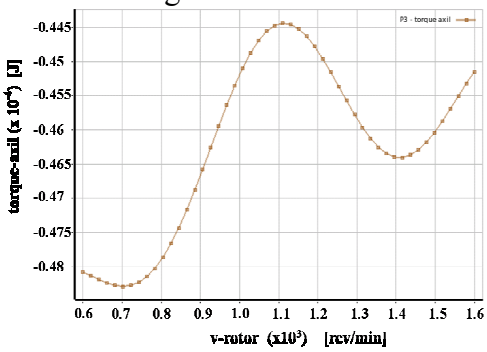

Fig.4 Curve of 'v-rotor'—'torque-axil'

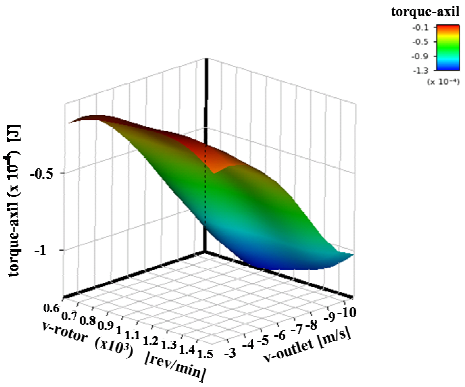

Fig.5 Surface of input and output parameters

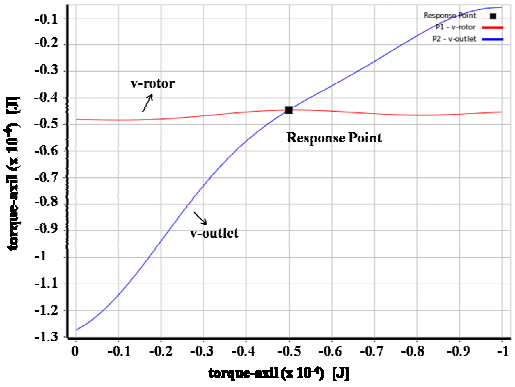

Fig.6 Local sensitivity curves of 'torque-axil'

It is also easy to find out that when the two input parameters have the same output parameter by check the curve of Local Sensitivity shown in figure 6. The Response Point in the figure represents the velocity of outlet 6.366m/s and the speed of rotor 1120rpm will generate a same blade torque 4.445e-5J at this point. The flow rate at this point according to the cross-sectional area can be computed as 66.127 L/min.

Summary

The Workbench response surface design optimization method has been used in this paper and gives a continuous output value of changes in input parameters compared to a discrete parameters set assignment method. It can be easily obtained the rotor's performance curve under different aerodynamic conditions and found the correspondence between the two input parameters in order to verify the clinical data.

This method solves the problem of difficulty to find specific theoretical values in clinical phenomenon. While this method could guide the patients how to properly use the device and provide a sufficient theoretical basis and reasonable methods for future structural optimization and device improvement.

References

[1] Islam N, Gladki E. Dry powder inhalers (DPIs)—a review of device reliability and innovation [J]. International Journal of Pharmaceutics, 2008, 360(1): 1-11.

[2] Bernstein J A, Amin H, Smith S J. Therapeutic uses of lung aerosol [J]. Lung Biology in Health and Disease, 2007, 221: 219.

[3] Chen X M. New progress of pulmonary delivery [J].Chinese Journal of Modern Drug Application, 2010, 4(001): 224-226.

[4] Zhang W, Jia Y, Zhang W M, etc. Comparative simulation of engine cooling fan of mining dump truck based on CFD [J].Coal Mine Machinery, 2012, 12: 026.

[5] Shao S Q, Lu D W, Jeon W H. Numerical analysis on the flow noise in the indoor unit and cross flow fan of air-conditioners [J].Journal of Refrigeration, 2012, 33(3): 9-13.

[6] Chen X J, Li Y, Xia L F, etc. Simulation analysis on internal flow field characteristics of engine cooling fan for construction machinery [J].Construction Machinery and Equipment, 2011, 42(11): 21-24.

Advanced Materials Research Vol. 983 (2014) pp 246-250

doi:10.4028/www.scientific.net/AMR.983.246

Gas Permeation Properties and Characterization of Polymer Based Carbon Membrane

N. Sazali[1,a], W.N.W. Salleh[2,b], Zawati Harun[1,c] and A.F. Ismail[2,d]

[1]Advanced Materials and Manufacturing Centre (AMMC Department of materials and Design Engineering, Faculty of Maechanical and Manufacturing Engineering, Universiti Tun Hussein Onn Malaysia, 86400 Parit Raja, Batu Pahat, Johor Darul Takzim, Malaysia.

[2]Advanced Membrane Technology Research Centre (AMTEC), Faculty of Petroleum and Renewable Energy Engineering (FPREE), Universiti Teknologi Malaysia, 81310 Skudai, Johor Darul Takzim, Malaysia.

[a]Melya.jandi@yahoo.com, [b]Hayati@petroleum.utm.my, [c]zawati@uthm.edu.my, [d]Afauzi@utm.my

Keywords: Polymeric precursor, heat treatment process, Permeation, carbonization, carbon membrane, gas separation.

Abstract. Membrane gas separation is a forthcoming technology that advertised a great commercial potential in diverse industrial applications. Consequently, membrane-based natural gas processing has been among the fastest growing segments of the economic growth. The turbostratic structure of carbon membranes has been affirmed to accommodate with good separation selectivity for permanent gases. With that, the most auspicious technique acquired is by controlling the carbonization temperature during the carbon membrane fabrication. In this study, polymer-based carbon tubular membranes have been fabricated and characterized in terms of its structural morphology and gas permeation properties. Polyimide (Matrimid 5218) was used as a precursor for carbon tubular membrane preparation to produce high quality of carbon membrane via carbonization process. The polymer solution was coated on TiO_2 –ZrO_2 tubular tubes (Tami) by using dip-coating method. The polymer tubular membrane was then carbonized under Nitrogen atmosphere at 600, 750, and 850 ◦C. The structural morphology of the resultant carbon membranes was analyzed by means of scanning electron microscope (SEM). Pure gas permeation tests were performed using CO_2 and N_2 gases at 8 bars and room temperature. Based on the results, the highest CO_2/ N_2 selectivity of 79.53 was obtained for carbon membrane prepared at 850 ^oC.

Introduction

In the past recent years, many efforts have been made to develop effective ways to separate the impurities in natural gases. Consequently, natural gas must designate cleansed to raise its fuel heating cost, decrease transport expenses, pipeline erosion besides atmospheric contamination [1, 2]. High permeation flux and high selectivity are essential requirements for a successful membrane [3]. Several methods assumed towards development of polyimide membranes involve tailoring molecular structure to achieve an innovative materials plus altering current polyimide materials through cross-linking method, grafting side groups on polymer backbone also heat treatment process [4].Various structures of polyimide have remained established in literatures thru changing the monomer structures [5,6].

It is well known that the membrane performance appears to be a tradeoff between selectivity and permeability, i.e. a highly selective membrane tends to have a low permeability [7]. Previous researcher stated that when the driving force (pressure ratio) was lower, the selectivity results was higher and the separation process said to be more appropriated; in fact, the operating costs for the separation system also lower [8]. Previous membrane researchers mention that membranes which have the potential to exceed such upper bound were inorganic membranes. Therefore, ultramicroporous (0.3–0.5 nm) membranes such as zeolite and carbon membranes have shown their performance [9]. The use of carbon membrane technology for the separation of CO_2 from light gases such as N_2 is still in the research stage. In fact, the carbon membranes are seemly for CO_2/N_2

separation [10]. Furthermore, former reports comprising the use of polymide precursor for carbon membrane synthesis were also stated by Tanihara et al. [11], and Tin et al. [10].

Material and Method

In this study, a commercially available Matrimid 5218 was selected as a main precursor polymer. It was dried overnight at 80 ^{o}C prior to be used. N-methyl-2-pyrrolidone (NMP) was purchased by Merck (Germany) and used as solvent polymers. Methanol was used as a solvent exchange during post treatment step for polymeric flat- sheet membranes. Matrimid 5218 was prepared by dissolving 15 wt. % of Matrimid 5218 in N-methyl-2-pyrrolidone (NMP) for 7 hours with mechanical stirring. The mixture was maintained under a controlled vacuum to remove all bubbles from the solution. Polymer supported membranes were prepared by dip-coating a uniform layer of the polymeric solution over the external surface of a tubular ceramic supported (1kD membrane of 6cm in length x 13mm outer radii; Tami). The ceramic tube consisted of TiO_2 structure that supported a ZrO_2 membrane located on the inner part of the tube. The support was dip-coating horizontally during the deposition of polymer solution. After 15 minutes coated, the membranes were then aged at 80 ^{o}C for 24 hours. The membranes next immersed with methanol for 2 hours and then placed at 100 ^{o}C for 24 hours inside oven to allow slow removal of the solvent. The same procedure was used to fabricate flat sheet membranes for characterization purposes.

The supported carbon membranes were prepared after the polymer supported membranes had been placed inside Carbolite horizontal tubular furnace, where polymeric membranes were placed in the center of the ceramic tube. The polymer carbonization was performed following a temperature program up to 600, 750 and 850 ^{o}C. Normally, the final carbonization temperature will be reached in several steps; the polymeric membranes were heated at 300 ^{o}C from room temperature at a heating rate of 3 ^{o}C/min under Nitrogen gas (200 ml/min) flow. Subsequently the temperature was raised to final carbonization temperature with the same heating rate. At 300 ^{o}C and final carbonization temperature, the membrane were held for 30 minutes before proceed to the next step. After completing each heating cycle, membranes were cooled naturally to room temperature. The detailed carbonization protocol is illustrated in Fig 1. The nomenclature of the resultant carbon tubular membranes is given in the form of CM-Carbonization Temperature.

Membranes Characterization

The cross section morphologies of the precursor membrane were observed under JEOL JSM-5610LV scanning electron microscopy (SEM). The performance of the membrane can be characterized into two important parameters which are permeance and selectivity.

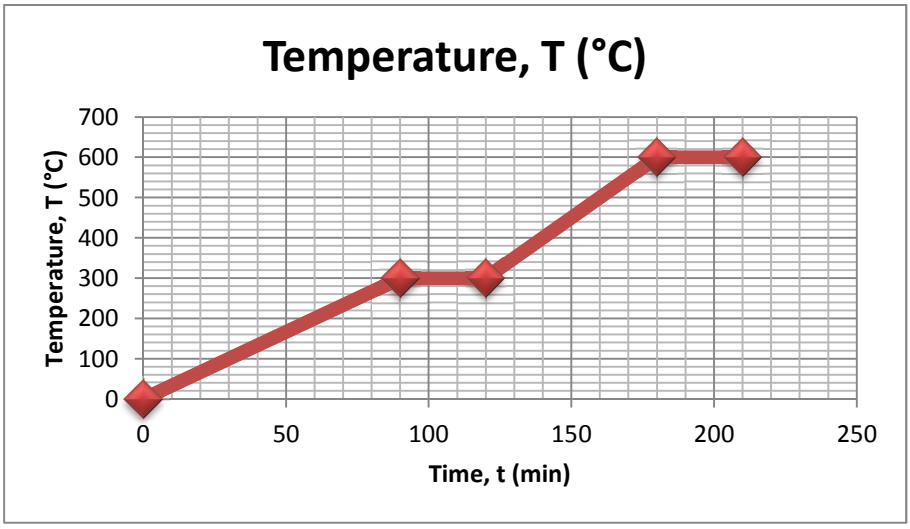

Figure 1: Carbonization protocol

The carbon tubular membranes were tested in pure gas system. The 8 cm carbon tubular was placed inside the tubular module. Pure CO_2 and N_2 were fed into the module at a trans membrane pressure of 8 bars. A tubular stainless steel module of 14 cm in length was used to contain the tubular ceramic membrane. The membrane was fitted with rubber O-rings that allowed the membrane to be housed in the module without leakages. The permeance, *P/l* (GPU) and selectivity, α of the membranes were calculated using equations below:

Permeance, *P:*

$$(P/l)_i = \frac{Q_i}{\Delta p.A} = \frac{Q}{\eta \pi D l \Delta P} \tag{1}$$

Selectivity, α:

$$\alpha_{A/B} = \frac{P_A}{P_B} = \frac{(P/l)_A}{(P/l)_B} \tag{2}$$

Where P/l is the permeance of the tubular membrane, Qi is the volumetric flow rate of gas i at standard temperature and pressure (cm^3 (STP/s), p is the pressure difference between the feed side and the permeation side of the membrane (cmHg), A is the membrane surface area (cm^2), n is the number of fibers in the module, D is an outer diameter of carbon tubular membrane (cm) and l is an effective length of carbon tubular membrane (cm).

Result and Discussion

Gas Permeation properties.

Carbonization process plays an important role in tuning the gas permeation performance of carbon membranes, while the carbonization temperature is one of the process parameters that significantly affect the gas separation performance of carbon membranes. The carbonization process was performed by heating the Matrimid-based polymeric membrane under Nitrogen flow from room temperature to final carbonization temperature of 600, 750 and 850^oC. The permeance was measured using gas permeation test apparatus at 8 bars and room temperature. The different final carbonization temperatures would result in different structure and permeation properties. The results of the permeation performance of the carbon membrane prepared from different final carbonization temperature shown in Table 1.

The permeance of CO_2 will increase while N_2 permeance significantly decreased with the increase of final carbonization temperature. This indicates that pore and carbon structure of the carbon membrane become rigid, compact and some of the pores might change into closed pores during the carbonization process. Moreover, the CO_2 permeance is consistently higher than that of N_2. With the expected of high temperature, it will induce the higher porosity. Polyimides are known to exhibit high permselectivity for various gas pairs, especially for CO_2/N_2 [13], and high chemical resistance, thermal stability and mechanical strength [12]. Many researchers reported polyimide of Matrimid 5218 as one of the best material choices for membrane based CO_2/N_2 separation, due to its attractive combination of gas permselectivity and high T_g [13, 14].

Table 1

Gas Permeation Properties of the Matrimid/NMP –Based Carbon Tubular Membrane.

Carbon Membrane	Permeability (GPU)		Selectivity
	CO_2	N_2	CO_2/ N_2
CM-600	81.29	8.06	10.09
CM-750	364.30	5.66	64.41
CM-850	400.06	5.03	79.53

According to gas permeation results, it is indicates that the transport mechanisms of the prepared carbon membrane are not dominant by Knudsen diffusion. The trend is indicative of molecular sieving, as the kinetic diameter of CO_2 is substantially smaller than N_2. A continuous increase of selectivity is observed with the rise of the carbonizations temperature from 600- 850 ^oC. The selectivity of CO_2/ N_2 increased approximately 6 times from the carbon membrane carbonized from 600 to 750^oC. The highest selectivity of 79.53 was achieved of carbon membrane carbonized at 850^oC. The result shows that Matrimid–based carbon tubular membrane with more selective behaviors' can be obtained at high carbonization temperature. Figure 3 shows comparison between CO_2 permeance readings with N_2 permeance readings. It was known that membranes that carbonized with 600 ^oC will have big pore size; therefore N_2 can go through more compared to the carbon membranes with higher temperature. Therefore, when the porosity was low, it will limit the N_2 permeance. In the nutshell, to gain the highest separation efficiency of carbon tubular membrane derived from Matrimid, the final carbonization temperature of around 750 to 850 ^oC are the best conditions for CO_2/ N_2 separation at room temperature.

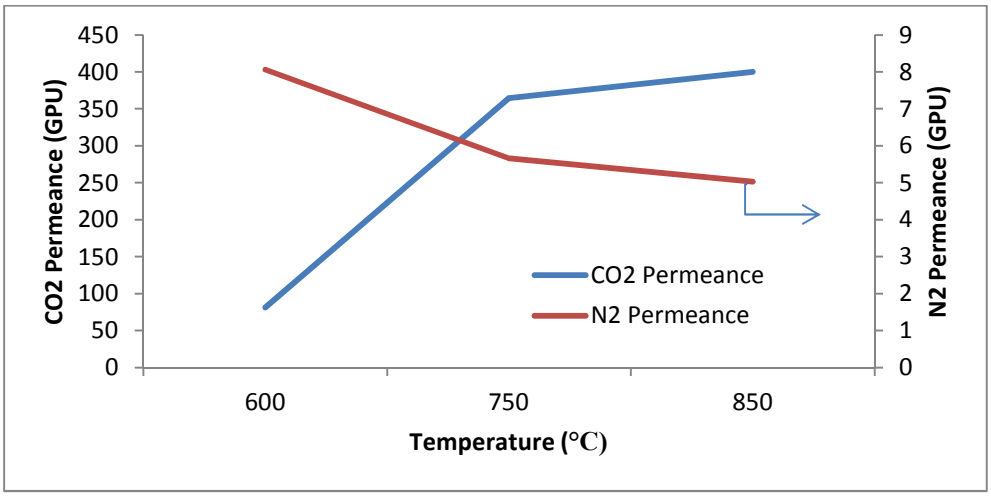

Figure 3: Comparison between CO_2 permeance readings with N_2 permeance readings

Summary

From this study, the result shows that Matrimid 5218 is a good candidate precursor for carbon membranes applied in gas separation system. The morphological structure properties together with the gas permeation of the Matrimid-based polymeric and carbon membrane are reported. It is indicated that the gas separation properties of Matrimid carbon membranes are depends on the carbonization temperature during the heat treatment process. The results reveal that an excellent CO_2/ N_2 separation of 79.53 was obtained for carbon membranes carbonized at 850^oC. It is because a high compactness of carbon membrane structure was produced at high temperature and it leads to the increase in selectivity.

Acknowledgment

The authors gratefully acknowledge the financial support of the Research University Grant Scheme (GUP) (Vot No: Q.J130000.2542.05H08) from The Ministry of Higher Education (MOHE) to University Technology Malaysia (UTM).

References

[1] R.W. Baker and K. Lokhandwala: Ind. Eng. Chem. Res. Vol.47 (2008), p. 2109-2121

[2] Y.Xiao, B.T.Low, S.S.Hosseini, T.S.Chung and D.R.Paul:A review, Prog. Polym. Sci. Vol.34 (2009), p.561-580

[3] T.S.Chung, J.J.Shieh, W.W.Y.Lau, M.P.Srinivasan and D.R. Paul:J. Membr. Sci. Vol. 152(1999), p. 211-225

[4] N.Tanihaara, H.Shimazaki, Y.Hirayama, S.Nakanishi, T.Yoshinaga, and Y.Kusuki: J.Membr.Sci. Vol. 160 (1999), p. 179-186

[5] T.C.Merkel, He Zhenjie, Ingo Pinnau and B.D. Freeman: Macromolecules. Vol, 36 (2003), p. 6844-6855

[6] C.Nistor: Envi. Eng. and Management *J.* vol. 7(2008), p. 653-659

[7] L.Robeson:J. Membr. Sci.,Vol. 62.(1991), p.165–185

[8] G.Q.Lu, Diniz da Costa, J.C.Duke, M.Giessler, S.Socolowe, R.Williams, and T.Kreutze: *J.* Coll. Interf. Sci. Vol.314. (2007), p. 589–603

[9] T.A.Centeno and A.B. Fuertes: Sep. Purif. Tech. Vol. 25 (2001), p. 284-379

[10] K.M. Steel and W.J.Koros: Carbon. Vol. 41(2003), p. 253–266

[11] P.S. Tin, Y.C.Xiao and T.S.Chung : Sep. Purif. Reviews.Vol. 35 (2006), p. 285- 318

[12] H.Strathmann: Membr. Tech. Vol. 113 (1999), p. 9-11

[13] M. Inagaki, T. Ibuki and T. Takeshi: J. Poly. Sci. Pol. Chem. Vol.30 (1992), p. 111-118.

[14] J.N.Bersema, S.D. Klijnstra, J.H.Balster, G.H.Koops and M.Wessling: J. Membr. Sci. Vol. 238 (2004), p.93-102

Advanced Materials Research Vol. 983 (2014) pp 251-256

doi:10.4028/www.scientific.net/AMR.983.251

Measurement Principle of Glass Thermal Expansion Coefficient and Technology Application of DIL402PC Dilatometer

SUN Yanhua [1, a], ZHANG Dongqing [1,b], WU Fei [1,c] SUN Kai [1,d]

[1]National special glass quality supervision and inspection center, Beng'bu 233000, china

[a]syhua1632008@163.com, [b]zhangbbzjs@126.com, [c]wufei@ctiec.net, [d]bbzjssk@126.com

Key words: Thermal expansion coefficient; Measuring principle; Dilatometer; System calibration;

Abstract: The paper introduces the measuring principle of glass thermal expansion coefficient. It expresses the features and advantages of the linear variable differential transformer measuring principle by comparing the thermal expansion coefficient measurement methods analysis. Meanwhile, the paper introduces DIL402PC dilatometer measuring devices and measurement procedures. It use standard samples to execute thermal expansion instrument system check from the accuracy and repeatability. The result shows thermal expansion coefficient of linear expansion instrument bias of DIL402PC dilatometer is within the error range of the theoretical value. The process proves it has a wide range of applications.

1 Introduction

Thermal expansion of the solid material is a very important characteristic. The average linear thermal expansion coefficient is the important parameter of engineering design, precision instrument manufacturing, materials welding and processing Accurate measurement of the average coefficient of linear expansion material for basic scientific research, technological innovation and engineering applications is very important[1].

The average coefficient of glass linear expansion is the important physical parameter. Its size directly affects the quality and thermal stability of the glass products. Between glass products and glass products, glass products and other materials or sealing, welding, the average coefficient of linear expansion is very important.

In recent years, the world build a large number of test methods and test equipments for measuring linear thermal expansion coefficient of the material, such as laser interferometer dilatometer, single pusher dilatometer, differential dilatometer putter, diffraction expansion device, silk sheets and transient microscopic method expansion device. By comparing the analytical test methods, these methods have their advantages and disadvantages. In our real life production, we propose to choose the different methods according to the different needs.

DIL402PC dilatometer has a wide range application in the material measurement of the average coefficient of linear expansion. The sample is heated to the test specified temperature by predetermined heating rate. Measured values with increasing temperature change of the sample length. In order to obtain a sample with increasing temperature coefficient of linear expansion coefficient of linear expansion and the average temperature ranges specified.

2 Measurement principle of glass thermal expansion coefficient

The conception of the average coefficient of glass linear expansion is delimited in National Standard of the People's Republic of China GB/T 16920-1997 which is the measurement of the

average coefficient of glass linear expansion[2]. The average linear thermal expansion coefficient of the glass is the one degree Celsius change rate of unit length sample from each of the temperature t1 rise to the temperature t2.

Average linear expansion coefficient is often expressed as a percentage or parts per million. In the reference temperature 20 degree Celsius, its expression formula is as follows.

$$\alpha(20-300℃)=\frac{\Delta L}{L_0\Delta t} \tag{1}$$

Using a quartz rod type instrument, the formula is expressed as follows.

$$\alpha(20-300℃)=\frac{\Delta L+\Delta L_Q-\Delta L_B}{L_0\Delta t} \tag{2}$$

In the formula, α（20-300°C） is the average coefficient of glass linear expansion between the process temperature is raised to 300 degree Celsius from 20 degree Celsius. ΔL is deformation of the sample length. L_0 is the original length of the sample. ΔL_Q is thermal expansion of quartz standard. ΔL_B is dilatometer correction term. Δt is the temperature difference between termination temperature and the initial temperature.

International Standard unit average linear thermal expansion coefficient is based on X × $10^{-6}K^{-1}$ indicates. Quartz standard average linear thermal expansion coefficient is 0.58 × $10^{-6}K^{-1}$. It is only related to the corresponding chemical composition and structure of the glass and nothing to do with the geometry of the sample.

3 Comparative analysis of the thermal expansion coefficient measurement method

An important element of the coefficient of thermal expansion of the material is to study methods of measurement studies. Currently, the determine of the thermal expansion coefficient of the material depends mainly on experiments. Pros and cons of experimental methods directly affect the accuracy of the thermal expansion coefficient of the material. Thereby, it affects the accuracy and reliability of the application process. There are a variety of materials commonly for measuring the thermal expansion coefficient. The contrasts of accuracy, range and stability are as follows[3] .

Table.1 Comparison of the thermal expansion coefficient measurement method

Measuring principle	Approximate sensitivity(μ m)	Scope	Time stability
Interferometer	2.5×10^{-2}	big	good
Optical lever	1.0×10^{-1}	big	good
Unbonded strain gauge filamentous	1.3×10^{-1}	big	good
Linear variable differential transformer	1.3×10^{-1}	big	good
Capacitance micrometer	2.5×10^{-1}	short	bad
Magnetic flowmeter	2.5×10^{-1}	short	bad
Rotating mirror analyzer	2.5×10^{-1}	big	good
Pointer meter	2.5	big	good
Mechanical lever meter	25	big	good
Wire microscope eyepiece	2.5×10^{-1}	big	good
Electric contact meter measuring microscopic	2.5×10^{-1}	big	good

In the table.1, it shows the accuracy larger difference of the various methods. The measured coefficient of thermal expansion is largely influenced by the accuracy of the selected measurement method. In addition, even using the same measuring instrument, the heated sample rate change will affect the results. The main material is the process of heating the heat transfer rate of the mixed sample so that the temperature distribution during heating is unevenness. The forming a changing temperature field will bring the inevitable impact on the value of the sample. To obtain accurate thermal expansion coefficient of the material may cause some difficulty.

4 Dilatometer DIL402PC technology applications

With the continuous development of glass, new ceramics and composite materials, the precise control of thermal expansion of the material and sintering characteristics is required. DIL402PC dilatometer collection instrument uses a horizontal design, simple operation, a wide range of applications. Even non-ideal sample size can be easily put into a tubular sample holder groove. Meanwhile, optimized design of the differential sensor makes the instrument even when no additional thermostatic device can provide ultra-high reproducibility and has excellent performance test[4].

4.1 Measuring device

DIL402PC dilatometer is manufactured by the German NETZSCH instruments company. The main parameters are as follows. Temperature range: 0-1600^{o}C.Temperature accuracy: 0.1^{o}C. Displacement sensor range: ±2.5mm. Measurement accuracy: 21nm. Heating rate: 1-30^{o}C. Increment: 0.01^{o}C. The maximum diameter of the sample: 12mm. The maximum length: 50mm. The figure 1 is a structure schematic diagram of DII402PC dilatometer.

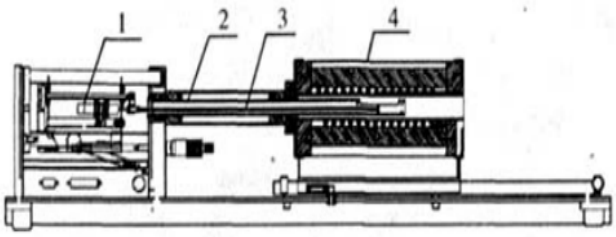

Figure.1 Dilatometer DII402PC structural representation

1. Measurement system 2. Sample holder 3. eject-rod 4. Furnace

4.2 Sample preparation requirements

DIL402PC Dilatometer uses inductive displacement sensor system. The advantages of DIL402PC have a wide measuring range, good linearity, and a high measurement resolution. The requirement of the sample size accuracy and environmental conditions are very high. Factors such as unstable voltage, air flow changes will affect the smoothness of the expansion line. To prevent contamination of the sample holder and performance changes putter occurred during the test sample, the sample should be mounted in bearings and gaskets. Put some small particle size alumina hollow ball at the bottom of the bracket if it is necessary.

4.3 Test Procedure

4.3.1 Obtain baseline file

Firstly, it makes baseline testing by standard sample before the samples is tested. The choice of test equipment is alumina bracket and putter. Standard sample choice is Al_2O_3 standard provided German NETZSCH. Put the standard sample into the sample holder. Place a thin aluminum oxide wafer between the sample and the putter to prevent samples and measurement systems adhesions. Then, turn off the furnace. Open test software and select the "fix" measurement type. Enter the standard name, number and length. Baseline measurement procedures should be consistent with the

sample to be measured program, including the initial wait, the heating rate and the sampling rate. It plays a crucial role in the entire sample testing. At the end of the baseline setting, there will be "DIL402PC Adjustment" dialog. Check whether the signal observed in the DIL value close 0um. If the deviation is too large, you need to adjust the deviation near to 0um.

After baseline file generation, Samples subsequent series of the same test conditions can be followed in the baseline document. No need to make a baseline test for each sample individually.

4.3.2 Sample test

After the baseline test is completed, the samples can be tested. Apply the appropriate baseline file. Select "sample and fix " measurement type. Enter the sample name, number and length of the sample. Check the various parameters. Generally do not modify. If the temperature program is the exactly same with temperature program, it is not necessary to modify the baseline document. If you need to make some changes in the program on the basis of the original temperature, generally only lower the temperature will be terminated. The heating rate, the sampling rate and other parameters would not be changed.

4.3.3 Data Analysis

After the sample test is completed, run the analysis program. Coefficient of linear expansion can be drawn at any point in the temperature coefficient of linear expansion and the temperature of any segment. Comparative analysis can be carried out the same type of curve. In addition, you can export the data needed to re-edit the mapping.

4.4 System Calibration

Thermal expansion instrument calibration system includes displacement sensor calibration and temperature sensor. In addition, due to the use of the jack dilatometer measurement mode, the signal is not only the length variation of the measured sample, as well as thermal expansion of the sample holder and the plunger. In order to obtain accurate measurement data, we must take into account the impact of the sample holder and the expansion mandrel to bring.

For the foregoing reasons, The calibration of the temperature sensor and displacement sensor can not characterize the overall state of thermal expansion of the instrument. In order to obtain more accurate measurement results, the system must be checked. System calibration standard samples need to be measured with a known coefficient of expansion. All measurement parameters must be consistent with measured parameters of the sample. The expansion coefficient of the selected standard sample should be known. Its use must be suitable for measuring the sample temperature range. Sample material properties would not be changed in the temperature range. Commonly the standard samples consist of quartz, alumina, graphite, platinum, cyanite, etc. The table 2 lists the standard temperature range and their characteristics[5].

Table.2 Calibration standards provided by the NETZSCH company

Material	Temperature range	Characteristic
Quartz	0-1600^{o}C	High precision, small coefficient of expansion
Cyanite	0-1680^{o}C	High precision, wide temperature range
Al_2O_3	-190-1680^{o}C	High precision, wide temperature range, low price
Platinum	-190-1400^{o}C	Wide temperature range, large expansion coefficient
Graphite	0-2400^{o}C	Slightly less accurate than sapphire, wide temperature range

This selection of standard sample calibration equipment is Al_2O_3 standard, The main test accuracy and repeatability of the test from two aspects to DIL402PC thermal expansion instrument calibration systems.

4.4.1 The accuracy of the test

Test conditions for the heating rate is 5K/min, temperature range is 100°C to 1400°C, the test carried out under static air atmosphere. First generation baseline file, Then the same test conditions. Select "sample and fix" type of measurement, Linear expansion coefficient of the samples obtained. The linear expansion coefficient measured in comparison with the standard theory of expansion , the results shown in table 3.

The table 3 lists the measured values and the deviation from the theoretical value of standard Al2O3. As can be seen , the error in the measured values are the theoretical standard deviation and the range is much smaller than the error of the theoretical value[6].

Table.3 Measured and theoretical values of standard linear expansion

Temperature /°C	theoretical value/%	measured value/%	The theoretical value error/%	The measured value error/%
100	0.04630	0.04676	0.00221	0.00047
200	0.11370	0.11428	0.00227	0.00057
300	0.18770	0.18820	0.00202	0.00050
400	0.26720	0.26766	0.00150	0.00043
500	0.34970	0.34985	0.00185	0.00016
600	0.43510	0.43543	0.00235	0.00031
700	0.52280	0.52309	0.00299	0.00028
800	0.61240	0.61293	0.00297	0.00052
900	0.70490	0.70575	0.00335	0.00083
1000	0.79950	0.80051	0.00374	0.00099
1100	0.89680	0.89780	0.00425	0.00100
1200	0.99610	0.99766	0.00488	0.00156
1300	1.09750	1.09968	0.00626	0.00216
1400	1.20230	1.20535	0.00650	0.00301

4.4.2 Repeatability test

Verify the device stability in the process of testing the same sample, it not only depends on the degree of deviation from the standard value but also depends on the repeatability. The figure 2 is the measured expansion curve of Al_2O_3 standard sample under the same conditions.

From the expansion curve in Figure 2, Al_2O_3 standard sample expansion coefficient of the first measurement can be calculated as 8.9218E-06 from 50°C to 1400°C. The standard sample expansion coefficient of the second measurement is 8.9001E-06. The two measured expansion coefficient of Al_2O_3 repeatability standard deviation is 0.0216E-06. GB/T7322 Standards set forth the linear expansion coefficient of deviation does not exceed 0.5E-06 in the same laboratory reproducibility of the test method. Description dilatometer DIL402PC accuracy is close to 25 times the standard requirements.

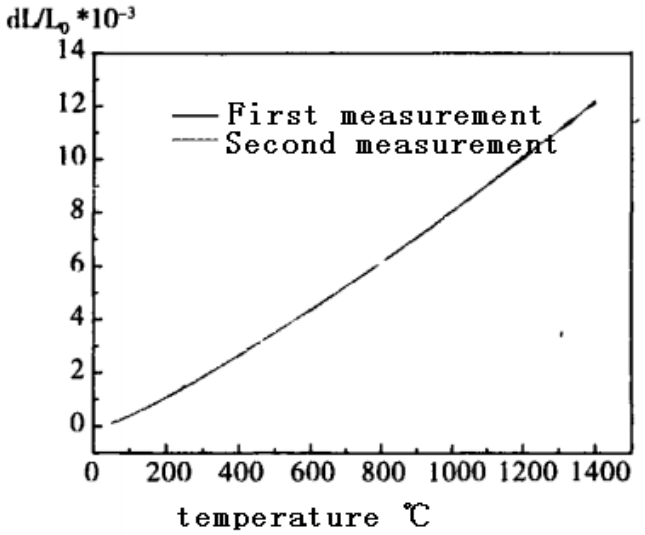

Figure.2 Al_2O_3 standard measurement repeatability expansion curve

5 Conclusions

The thermal expansion coefficient is one of the important physical properties of the glass. The combination of the glass element and the glass element, the glass element and the metal element or non-metallic element must have a suitable thermal expansion coefficient. Using a quartz rod type instrument, the paper obtains the average linear expansion coefficient formula.

The properties of materials have played an important role in the measurement process. Compare the measurement analysis methods of thermal expansion coefficient and choose the optimal measurement method according to our actual requirement. The result shows DIL402PC Dilatometer greatly improves the accuracy of the material expansion of glass, ceramics and composite materials. It also provides accurate and reliable basis for the standard revision.

References

[1] Okaji M, ymnada N. Precise, versatile interferometric dilatometer for room temperature operation: measurement on some standard reference materials. High Temp-High Press, 1997, 1(29): 89-95.

[2] Ledesma S, Goyanes S N, Duplaa C. Development of a dilatometer based on diffractometry. Review of Scientific Instruments, 2002,73(9): 3271-3274.

[3] Battaglia S, Mango F. Investigating X-ray Bragg-line displacement as a technique for determination of the thermal expansion coefficient of solid samples. Materials Science Forum, 2004, 443-444: 151-154.

[4] Heam G, Testa R B. Modal Analysis for Damage Detection in structures. Joumal of StructuralEngineering, 1991, 117(10): 3042-3063.

[5] Zhang Xiuhua, Li Dan, eta1. Control Technology of Thermal Dilatometer 402PC, ENGINEERING and TEST, 2008(48).

[6] Hideko Hayashi, Mariko Kanoh, Chang Ji Quan, eta1. Thermal expansion of Gd-doped ceria and reduced ceria. Solid State lonics. 2000(132): 227.

Advanced Materials Research Vol. 983 (2014) pp 257-260
© (2014) Trans Tech Publications, Switzerland
doi:10.4028/www.scientific.net/AMR.983.257

Methodology of Taguchi Optimization for Organic Rice Bran to Maximum Antioxidant Activity

Te-Li Su[1,*], Shuwen Wang[2], Hsu-Hsuan Chien[1], and Chia-Jung Shen[1]

[1] Department of Cosmetic Application and Management, St. Mary's Junior College of Medicine, Nursing and Management, Yilan 266, Taiwan

[2] Department of Health and Leisure Management, St. Mary's Junior College of Medicine, Nursing and Management, Yilan 266, Taiwan

*suteli66@gmail.com

Keywords: Organic rice bran, Antioxidant activity, Taguchi method, Optimization.

Abstract. The rice bran contains rich vitamin A, vitamin E, amino acid and niacin which are nutrient substances for the skin. These substances can keep moisture, prevent skin drying, postpone skin aging and prevent pigmentation effectively. This study used Taguchi method to plan experiment, and applied solvent extraction to extract organic rice bran concentrate, aiming to obtain the optimal beauty treatment quality. As the parameter setting is the key to the antioxidant activity quality of organic rice bran, it requires considerable costs of money, time and human experience. Therefore, this case study used $L_9(3^4)$ orthogonal array to plan the experimental parameters of solvent extraction which may influence the antioxidant activity of organic rice bran. The signal-to-noise ratio of experimental data was calculated to discuss the experimental results. Afterwards, the response graph was obtained by factor effects, so as to discuss the significant factors influencing the oxidation resistance quality, namely, the oxidation resistance quality characteristic of organic rice bran could be controlled effectively by controlling these factors. Finally, the confirmation experiment validated the reliability and repeatability of this experiment.

Introduction

The rice is one of the major cereal crops in the world, as well as the main food for half of the word population. Every 100 g unpolished rice contains rich Ca, P, Fe, Na, K and vitamins B1, B2, C and E and niacin. This study used solvent extraction and volatile solvent to extract essential oil, consuming less manpower and time than other methods. The treatment process can reduce the cost, and the fragrance of essential oil is closest to the plant. It is the most popular method in industry. Some slender flowers or the resin of plants is inapplicable to the extraction of essential oil by distillation, and some volatile solvent is used to extract the aromatic molecules. This method is called "solvent extraction", and the extracted aromatic molecule is called "absolute". The alcohol, ether or liquefied butane is poured onto the plant to be extracted, and then the solvent containing essential oil is separated. The solvent is removed by low-temperature distillation, so as to obtain solidified essential oil unlikely to flow [1].

However, there are numerous experimental factors influencing the extraction of essential oil from organic rice bran. The oxidation resistance quality characteristic of organic rice bran varies with the experimental parameters of solvent extraction, such as solvent type, soaking time and soaking concentration. Therefore, the optimal parameter setting for solvent extraction of essential oil uses trial and error to accumulate empirical value, and the technical heritage is unsystematic. This study used Taguchi method [2-5] to solve this difficulty in traditional trial and error, so as to obtain the optimal experimental parameters for essential oil extraction, meanwhile to keep the stability of oxidation resistance quality of organic rice bran.

Experiment

Taguchi Method. The Taguchi method [6-8] uses an orthogonal array to plan the signal-to-noise ratio (SN ratio) in order to analyze the experimental data. The employment of an orthogonal array to design the experiments and an SN ratio to analyze the experimental data enables the designer to simultaneously study the effects of multiple control factors of the average quality characteristics and variance in a fast and economical way. Thus, within the process of an experiment requiring very few experimental runs, an equally full factorial experiment can be created to obtain the optimum parameters.

The parameter design in the Taguchi method converts the quality characteristics into an SN ratio in order to evaluate the statistical values of the performance. The objective of this research was to make the antioxidant activity of australian tea tree as high as possible. The selected quality characteristic of the antioxidant activity was, therefore, the larger-the-better; the SN ratio is shown below [9]:

$$\eta = -10\log(\frac{1}{n}\sum\frac{1}{y^2}) \quad (1)$$

where y is the measured value and n is the total number of measurements.

Analysis of Oxidation Resistance of Organic Rice Bran Extract.

(1). The 5% Australian tea tree concentrated solution, 2ml antioxidant solution and 2ml 2×10^{-4}M DPPH solution are mixed uniformly, the absorbance is measured, recorded as Ai.

(2). The mixture is placed in the dark for 30 minutes, the ethanol is used as blank control group, the absorbance is measured at 517nm, recorded as Aj.

(3). In addition, 2×10^{-4}M DPPH solution is mixed with 2ml ethanol, the absorbance is measured, recorded as Ac.

(4). The free radical scavenging rate of antioxidant can be calculated by Eq. 2, higher scavenging rate represents higher antioxidant activity.

DPPH radical scavenging rate (%) = [1-(Ai-Aj)/Ac] ×100% (2)

where Ac is the absorbance of 2ml ethanol and 2ml DPPH solution; Ai is the absorbance of 2ml antioxidant solution and 2ml DPPH solution; Aj is the absorbance of 2ml antioxidant solution and 2ml ethanol.

Results and Discussion

The solvent extraction has many parameters undetermined, including the solvent adopted (ethyl acetate (EA), isopropanol (IPA), ethanol), solvent strength (30%, 60%, 90%) and soaking time (1 day, 3 days, 5 days). With numerous operating variables, in order to increase the overall experiment efficiency and to reduce the experimental cost, this case study used Taguchi experiment design method to plan the experiment. The parameters were put in the orthogonal array planning, as shown in Table 1.

First, the parameter factors influencing the oxidation resistance quality characteristic of organic rice bran and their level values were determined. In the experimental parameters of solvent extraction, the solvent type, soaking concentration and soaking time were selected according to the factors controlled in experiment, because they are the absolute keys influencing the oxidation resistance quality of organic rice bran.

The parameter factors and level values were used as experiment schedule according to L9 orthogonal array in Table 1. Nine experiments were conducted according to experimental design, and each experiment was repeated three times. There were 27 experimental data collected from the experiments. The signal-to-noise ratio of each experiment was calculated according to experimental data, as shown in Table 1.

Table 1. L_9 Experimental layout.

	Experimental parameters				Quality characteristic	SN ratio
Exp.	Solvent adopted	Antioxidant activity (%)	dB	Soaking temperature	Antioxidant activity (%)	dB
No.1	EA	30	2		95.40	39.59
No.2	EA	60	4		76.11	37.63
No.3	EA	90	6		99.80	39.98
No.4	IPA	30	4		87.62	38.85
No.5	IPA	60	6	7 °C	81.19	38.19
No.6	IPA	90	2		79.51	38.01
No.7	Ethanol	30	6		98.06	39.83
No.8	Ethanol	60	2		91.55	39.23
No.9	Ethanol	90	4		76.75	37.70

According to the response graph of factor effects, as shown in Figure 1, the experimental parameter combination for solvent extraction of organic rice bran is A1, B1, C3. The solvent type is EA, the soaking concentration is 30%, and the soaking time is 6 days.

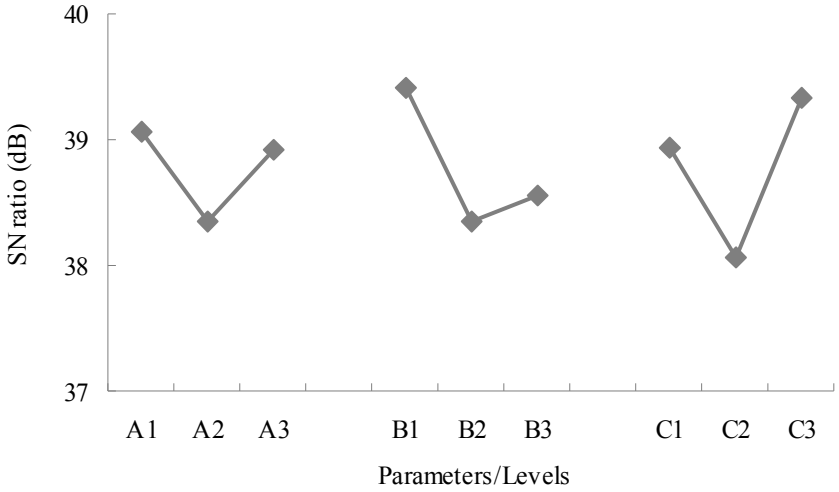

Figure 1. Response graph for SN ratios.

Finally, three confirmation experiments were conducted according to the optimal experimental parameter level combination for solvent extraction of organic rice bran. The average value of confirmation experiments was compared with the nine groups of data in Table 1, so as to confirm that the experimental factor level combination for solvent extraction of organic rice bran found in this study is the optimum combination. The bar chart is used for comparison, 1 to 9 groups in Table 1 are control group, CE is the validation group of confirmation experiment, as shown in Figure 2. It is observed that the confirmation experiment values are better than the nine groups of experimental data in L9 orthogonal array.

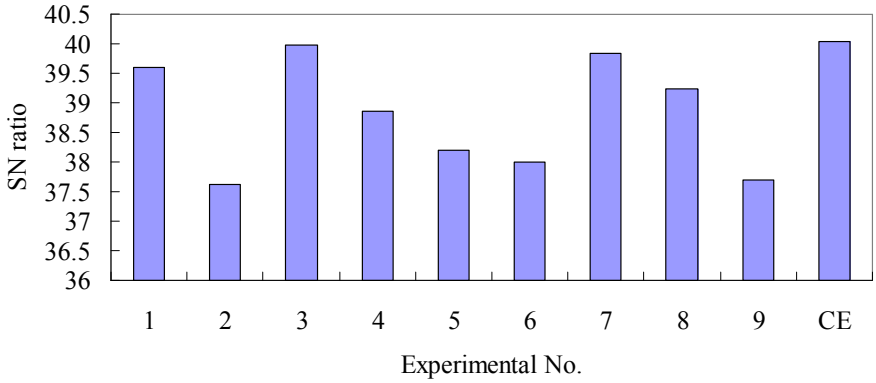

Figure 2. Comparison of confirmation experiment and L9 orthogonal array.

Conclusion

This study used Taguchi method for planning, to avoid complex complete factorial experiment, and conducted fractional factorial experiment considering the reliability of experiment, in order to save time and cost. If full factorial experiment was adopted, there should be 81 experiments, whereas the experiment was planned by using Taguchi method. The optimal minimum orthogonal array was selected, and nine experiments could represent the result of complete experiment. Therefore, the Taguchi method could reduce the number of experiments effectively. The response graph shows the order of factors influencing the oxidation resistance of organic rice bran, which is soaking time > solvent strength > solvent type. In other words, the optimal oxidation resistance can be obtained by selecting appropriate soaking time for experiment on solvent extraction of organic rice bran. Finally, the optimal solvent extraction parameters for organic rice bran obtained from response graph is solvent type of ethyl acetate, soaking concentration of 30% and soaking time of 6 days. The concentrated extract of organic rice bran with the best oxidation resistance can be obtained. Therefore, this method is also applicable to parametric optimization of other experiments, and it is significantly helpful to increasing the efficiency of experiment.

Acknowledgement

This research was partly supported by the National Science Council of the Republic of China under contract no. NSC 102-2221-E-562-002.

References

[1] C. Brunschwiler, D. Heine, S. Kappeler, B. Conde-Petit and L. Nyström: J. Cereal Sci. Vol. 58 (2013), p. 272.

[2] T.L. Su, C.F.J. Kuo and H.J. Wei: Fiber.Polym. Vol. 12 (2011), p. 657.

[3] S. Mavruz and R.T. Ogulata: Fibres Text. East. Eur. Vol. 18 (2010), p. 78.

[4] T.L. Su, H.W. Chen and C.F. Lu: Adv. Polym. Tech. Vol. 29 (2010), p. 54.

[5] G.B. Hong and T.L. Su: Iran. Polym. J. Vol. 21, p. 877.

[6] T.L. Su, C.C. Lai and P.C. Tsai: J. Surfactants Deterg. Vol. 14 (2011), p. 363.

[7] T.L. Su, C.S. Chiou and H.W. Chen: Int. J. Photoenergy Vol. 2012 (2012), Article ID 909678, p.1.

[8] G.B. Hong and T.L. Su: Fibres Text. East. Eur. Vol. 20 (2012), p. 75.

[9] T.L. Su, Y.L. Kuo, T.J. Wu and F.C. Kung: J. Chem. Technol. Biot. Vol. 87 (2012), p. 102.

Advanced Materials Research Vol. 983 (2014) pp 261-264
© (2014) Trans Tech Publications, Switzerland
doi:10.4028/www.scientific.net/AMR.983.261

RESOLVING NATIONAL ENERGY CRISIS THROUGH ENERGY EFFICIENT APPLIANCES: USE OF GROUND WATER HEAT PUMP FOR AIR CONDITIONING SYSTEMS

Dr Ahmad Aizaz*, Nauman Hafeez

National University of Sciences and Technology (NUST), Islamabad, Pakistan

*Corresponding Author: ahmadaizaz@cae.nust.edu.pk

Keywords: Energy Conservation, Air Conditioner, Ground Water Cooling, Heating.

Abstract. Energy crisis are deepening with every year passing by in a country like Pakistan. One of the major contributors of energy consumption in the domestic as well as in some commercial sector is the environment air conditioning (during summers) and heating systems (during winters). One possible solution to this national energy crisis is available in the form of tapping the available renewable natural resources of energy, specifically the Ground Water Heat Pumps (GWHP). Despite its wider applications in the advanced countries, the confidence in this technology is much feeble in less advanced countries, like Pakistan, mainly due to lack of awareness about the technology among the public and lack of subsoil temperature data for the scientific / engineering community. Thus, the aim of this study is to collect subsoil water temperature data of at least one particular location for over a year, and demonstrate the usefulness of sub soil ground water in improving the performance of conventional air-conditioning system both in cooling as well as in heating modes. This study shows significant improvement in the Coefficient of Performance (COP) of the Air Conditioner both in Cooling as well as in heating modes and thus reducing the expensive electricity consumption.

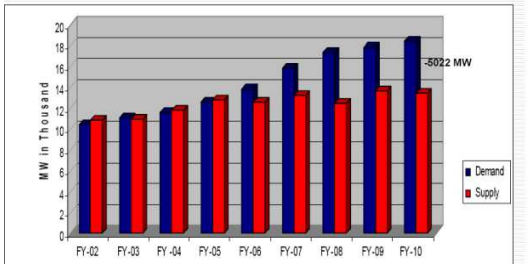

Figure 1: Yearly increase in gap between demand and the supply of electricity in Pakistan [1].

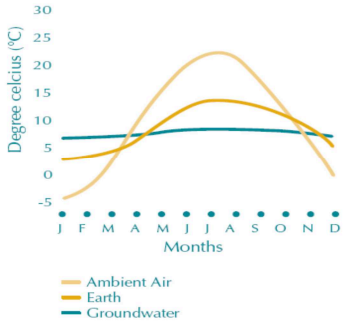

Figure 2: Typical annual variation of ground water temperature [2]

Introduction

1. Countries like Pakistan are facing worst energy crisis of their history, and the situation is getting worst with every year passing by where the gap between the energy demand and the supply is increasing on an alarming rate as shown in figure 1 [1].

2. While new power generation projects may appear lucrative for the political governments, a serious solution to resolve the energy crisis must also include the energy conservation strategy. One possible way to reduce this high energy consumption in the air conditioners is by reducing the temperature gap between the condenser unit and the medium to which energy must be thrown or rejected. Such a medium exists in the nature in the form of ground water. The water temperature , due to its availability at certain depths, is quite uniform throughout the year, independent of the outside climatic conditions, as shown in figure 2 [2].

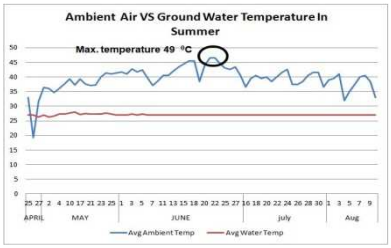

Figure 3: Ground water temperature during summer

3. M. Balat et al. [3] have found significant potential of Geothermal resources in contributing to sustainable energy use in many parts of the world. Realising the importance of the subsoil thermal energy resources, large efforts have been made by Kasumi et al. [4] to explore tropical regions of East Asia where the benefits of this technology are even lesser than the majority of non tropical areas of country like Pakistan. Similarly, Y. Biab et al., [5] have analyzed the application of

GSHP systems to different temperature zones in China. Their results show that different GSHP systems should be designed and built specifically for each zone. Later, Y. Bi et al.,[6] have carried out a comprehensive exergy analysis of complete GSHP system. Their study identified the compressor and the ground coupled heat exchanger to be the most critical equipment in the complete GSHP system. Meanwhile, B. Sanner et al. [7] have provided an extensive review of status of more than 20 years of R&D focusing on Bore Hole Heat Exchangers (BHE) in Europe. They observed that despite the fact that BHE have been in use for over 50 years now, market penetration of this technology is still in its infancy. Thus the use of this promising technology in developing countries like Pakistan is even more difficult to be adopted unless large scale research efforts are made based on the geological and atmospheric data of the selected sites in the developing countries. The present study is just the right step in this direction.

4. This study involves the use of Ground Water as the type of GSHP system for Risalpur (34°4'52N 71°58'21E) area of Pakistan. Temperature data of ground water available in the depths of about 100 m and below is made by utilizing one of the existing water pumping station for domestic use. The figures 3 and 4 show the comparison of ground water temperature data with the ambient temperature for the summer and winter periods respectively. It can readily be seen that almost isothermal temperature of ground water at 27 ^{o}C both in peak summer and extreme winter. Thus an average temperature difference of about 15 ^{o}C between ground water and the ambient air is available in Risalpur area almost throughout the year. This fact relates to huge geothermal energy potential in the form of ground water heat pump (GWHP) technology to conserve energy. In the present study, this GWHP technology is adapted to an existing air-conditioner of 2 ton capacity by adding ground water condenser which exchanges heat of the refrigerant with the ground water in addition to the air condenser. Thus the objective of this project is to demonstrate improvement in COP of a conventional household air conditioner, both in cooling as well as in heating mode, with modified condenser unit.

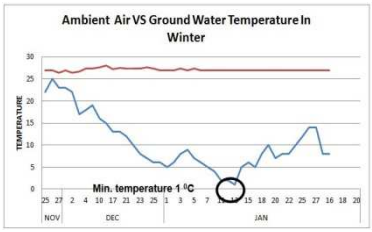

Figure 4: Ground water temperature during winter

Experimental Setup

5. Experimental setup for this research is shown in figure 5 in the form of refrigerant flow diagram with three control valves ‘a’, ‘b’, and ‘c’. After getting pressurized vapour from the compressor, the refrigerant passes through the conventional (existing) condenser giving away limited thermal energy to harsh ambient air due to small ΔT between refrigerant and the ambient air. In the conventional cycle, only control valve ‘a’ is open and the valves ‘b’ and ‘c’ are closed, which would allow the refrigerant to expand through the isenthalpic valve (shown without label) and enters the evaporator. However, in the modified circuit, the control valve ‘a’ is closed and valves ‘b’ and ‘c’ are now open. This allows the refrigerant, after passing through the conventional condenser, to pass through the ground water heat exchanger. Here, since there is a large ΔT between refrigerant and the ground water (~ 27 ^{o}C), large thermal energy transfer rates are realized. This enables the refrigerant, after expanding through the isenthalpic valve, to absorb large amounts of room heat through the evaporator and not burdening the compressor. Thus the COP of the whole system is improved. Appropriate temperature and pressure sensors are installed to measure the required pressures and temperatures at different locations on the refrigerant path for performance measurements.

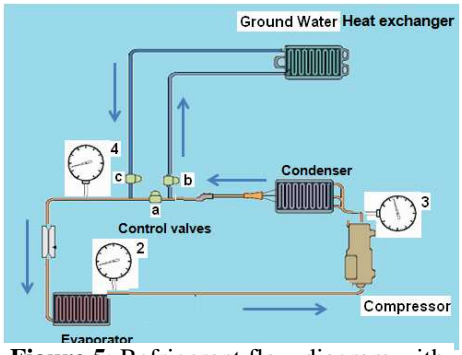

Figure 5: Refrigerant flow diagram with modified GWHP system.

Design and Manufacturing of Ground Water Heat Exchanger (Condenser)

6. The size of ground water heat exchanger can be estimated by using usual ‘Log Mean Temperature Difference’ (LMTD) approach, based on the known mass flow rates and ‘Inlet’ as well

as 'Outlet' temperatures of refrigerant and the ground water. The heat transfer rate 'q' in this heat exchanger can be related to the required area of the heat exchanger as:

$$A_i = q/(U_i F \Delta T_{LM}) \quad (1)$$

where, 'U' is the overall heat transfer coefficient of the thermal circuit between the refrigerant and the ground water and is given as:

$$U_i = \frac{1}{\frac{1}{h_{water}} + \frac{r_i)_{Cooling\ tube}}{k_{copper}} \ln\left(\frac{r_o)_{Cooling\ tube}}{r_i)_{Cooling\ tube}}\right) + \frac{r_i)_{Cooling\ tube}}{r_o)_{Cooling\ tube} \times h_{Ref}}} \quad (2)$$

here, 'r_i' and 'r_o' are the inner and outer radii of the tubes carrying refrigerant; 'h_{Ref}' and 'h_{water}' are the convection heat transfer coefficients of the refrigerant and the water, respectively. ΔT_{LM} is the Log Mean Temperature Difference whose expression is given as:

$$\Delta T_{LM} = \frac{\Delta T_1 - \Delta T_2}{\ln\left(\frac{\Delta T_1}{\Delta T_2}\right)} \quad (3)$$

where ΔT_1 and ΔT_2 are the temperature differences between the refrigerant and the water at the two ends (inlet and outlet, respectively) of a parallel flow condenser. 'F' is the fouling factor whose value varies depending upon the usage of the condenser. For a new design, its value is taken as 1. 'A_i' is the required inside area of the tubes carrying the refrigerant and for a specific diameter of the tube, the size of the condenser depends only on the length of the tube that can be fitted inside the shell of the condenser.

7. Although, for a conservative approach, a parallel flow configuration of the heat exchanger is assumed for the design of the ground water condenser. However, actually the refrigerant in half the number of tubes is in parallel configuration and in other half of the number of tubes it is in counter flow configuration with respect to the flow of ground water over the tubes.

Results and discussion

8. The COP measurements of air conditioning cycle are carried out before and after the modification are done so as to compare the performance improvement. Here COP for the cooling cycle is given by ratio of useful cooling effect to that of the work input from the compressor [9]. From figure 6, the definition of COP can be related to the ratio of difference in enthalpy values and is given as:

$$COP)_{Ref} = \frac{(h_2 - h_4)}{(h_3 - h_2)} \quad (4)$$

here, in the above equation (4), it is assumed that the enthalpy across the isenthalpic expansion valve remains constant. Now from the pressure and temperature values obtained from the gauges installed at locations 2, 3 and 4, as labelled in figure 6, and using the refrigerant property (p-h) diagram, the corresponding enthalpy values can be obtained. Table 1 provides a set of readings obtained for conventional cooling cycle as well as modified (GWHP) cycle.

Table 1: Experiment Observation Table

	T_2 (°C)	T_3 (°C)	T_4 (°C)	P_2 (kPa)	P_3 (kPa)	P_4 (kPa)
Conven Cycle	12.7	80	45	475	1792.9	1792.7
GWHP Cycle	12.5	78.5	35	470	1773.5	1773.1

9. The corresponding enthalpy values and computed COP of conventional as well as modified GWHP Cycle, in cooling mode are given in table 2. The table indicates that about 15% increase in COP is possible with the conversion of ordinary air conditioner into GWHP system.

Table 2: Enthalpy Table (Cooling Mode)

	h_2 (kJ/kg)	h_3 (kJ/kg)	h_4 (kJ/kg)	COP	% Increase
Conventional Cycle	416	470	251	3.05	15%
GWHP Cycle	415	468	229	3.51	

10. In heating mode the desired effect is the space heating and the definition of COP is now the ratio of desired heating effect to that of the energy load consumed by the compressor. For heating mode performance, now the reversible air conditioner is operated in the reverse mode by the use of flow reversing valve preinstalled in the conventional air conditioner. This reversing of flow will now switch the role of the outdoor unit as evaporator and the indoor unit as the condenser. Therefore, the definition of COP_{hP} as per refrigerant flow diagram given in figure 6 will not change, and is given as

$$\mathrm{COP})_{\mathrm{HP}} = \frac{(h_2 - h_4)}{(h_3 - h_2)} \quad (5)$$

11. Working on similar lines as of cooling mode calculations, it is revealed at about 17% increase in COP_{hp} is possible with the modified GSHP system installed in the conventional air conditioner and working in heating mode.

Conclusion

12. The research in this study has shown that ground water at the site of its use has strong energy saving potential because of its nearly isothermal behavior throughout the year independent of surface ambient temperature. Significant energy savings (15% to 17%) are possible by modifying an already available air conditioner and the ground water. However, the performance of the GSHP strongly depends upon the annual temperature profile of the ground water available at the site of its intended use. Thus, a national level project is required to map the annual temperature profiles of the ground water in all major cities of Pakistan, so that the use of this technology can be made as wide spread as possible. This will enable countries like Pakistan to conserve electricity and reduce their shortfalls in the supply and demand of electricity.

References

[1]. www.pec.org.pk/sCourse.../RENEWABLE%20INTRODUCTION.ppt,

[2]. http://archive.nrc-cnrc.gc.ca/eng/ibp/irc/cbd/building-digest-180.html,

[3]. Clean Energy Project Analysis: Retscreen® Engineering & Cases Textbook, RETScreen® International.

[4]. M. Balat, et al. J. of Energy Sources, Part B: Ec, Planning, and Policy , vol. 4, no. 3, pp. 295-309, 2009.

[5]. K Yasukawa, et al., Bulletin of the Geological Survey of Japan, vol.60 (9/10), p.459-467, 2009.

[6]. Y. Biab, et al., International Journal of Ambient Energy Volume 30, Issue 2, 2009 pages 63-72.

[7]. Y. Bi, et al., Applied Energy - APPL ENERG, vol. 86, no. 12, pp. 2560-2565, 2009.

[8]. B. Sanner, et al., Geothermics , vol. 32, no. 4, pp. 579-588, 2003.

[9]. Y. Chen, N. Hua, et al., International Journal of Refrigeration, 35 (2012) 278-289.

Advanced Materials Research Vol. 983 (2014) pp 265-269

doi:10.4028/www.scientific.net/AMR.983.265

Solar hydrogen production research status and prospect

Dezhi Wang[a], Fuzhou Zhao[b], Caili Zhu[c]

Ningbo University of Technology; Ningbo; Zhejiang; 315211; China
[a] wangdz@sina.com, [b] xjz2020@163.com, [c] 1084279037@qq.com

Keywords: Solar Hydrogen Production；Research Status； Challenge and Prospect

Abstract: The status of solar hydrogen production, solar hydrogen production from water electrolysis, solar photochemical hydrogen production, biological hydrogen production, solar thermal decomposition of water hydrogen production and other hydrogen production methods are presented in this paper. Then the key technologies of various hydrogen production are investigated in detail. Analysing the domestic and foreign research progress, the state-of-the art solar hydrogen production can be got to know in this paper. On the basis of solar hydrogen production, some prospects are put forward.

1 Introduction

Hydrogen is widely considered as a clean ,efficient and renewable energy and has become the most promising new energy sources in the 21 st century. Although there is a period of time to widely use，the research on hydrogen production has important significance for solving the problem of human in the sustainable development of energy. In addition to nuclear energy and tidal energy, other energy sources in the world come from solar energy. Rivers and lakes will become the inexhaustible hydrogen energy source. Converting solar energy into hydrogen energy can form a positive circulation of energy system. As the energy and environment problem increasingly prominent recently, the technology of photocatalytic water splitting to produce hydrogen has become research hotspot. Sevral developed countries have attached great importance to the research of photocatalytic decomposition of water hydrogen production, the key technogy is the research of the visible light catalytic decomposition of water hydrogen production ,which has made considerable progress.

2 The status of water photolysis

In the process of solar hydrogen production, current status of water photolysis experiences three processes: from the photoelectric chemical diversity to photocatalysis, then to the photocatalytic decomposition of water.

2.1 photoelectric chemical diversity(PEC)

Photoelectrochemical cell can absorb solar energy and convert solar energy to electricity through photoanode. Photoanode is usually light semiconductor material, The electronic-hole pairs can be produced after optical excitation. Photoelectrochemical cell is composed of photoanode and photocathode. In the presence of electrolytes, electrons are produced in the semiconductor when photoanode absorb light flow to the antipode through the extemal circuit, the protons in the water accept electrons from antipode to produce H_2[1].

There are two decompose types: one-step solar photoelectric chemical decomposition of water hydrogen production, that is, preparing catalytic electrode on the two electrode plates, the voltage drop generated by the solar cell decompose water into H_2 and O_2 directly. The two-step of photovoltaic

electrolysis of water is that solar photoelectric conversion and electrochemical conversion are performed in two independent process. This method can be a few solar cells in series to meet the requirements of the voltage conditions which are necessary for the electrolysis of water.The performance of semiconductor material determines the efficiency of PEC. The research of low band gap width and high corrosion resistance semiconductor materials as well as structure optimization of electrode is the key technologies to PEC method [2]. Now many scientists are studying the semiconductor materials which meet these conditions. Professor Stuartlicht is committed to research composite photoelectrode. This kind of composite photoelectrode takes AlGaAs/Si as the main material into multi-junction system.

2.2 Photo-assisted complex catalytic

Photo-assisted complex catalytic is a complex catalytic photolysis water system based on three bipyridine ruthenium for photosensitizer. Under AM1.5 simulated sunlight, the photoelectric conversion efficiency can reach 7%. The system is more complex and must add catalyst and other auxiliary materials such as electron donor, the manufacturing cost is higher, the stability of complexes is poor, the research results are hard to come out of labs.

2.3 The photocatalytic decomposition of water into hydrogen

In the 1970s, Photoelectric aquatic hydrogen phenomenon on the TiO_2 electrode has been found by Fujishima and Honda, then the photocatalytic hydrogen production research became the focus all over the world [3]. In order to use light to split water molecules and make water photolysis occurs in the light irradiation. Now we have studied mainly two kinds of system,including semiconductor and metal complexes system.

Semiconductor photocatalytic decomposition of water into hydrogen is relatively mature, through TiO_2, transition metal oxides, layered metal oxides and the composite layer material that can use the visible light these 4 processes [4]. Uv light decomposition of water hydrogen production has made great progress in technology, however uv light accounts for only about 4% of the solar spectrum. Developing catalyst with high activity, stability, low-price is the key technology to the use of solar photocatalytic hydrogen production.

Improving the conversion efficiency of solar energy mainly lies to reduce the electron -hole pairs recombination, inhibition of reverse reaction and the research and development of new type of semiconductor photocatalysts. Arkia Yohida's research shows that the tunnel structure of semiconductor catalyst values are better than ion exchange layered catalyst [5]. And add the modified semiconductor Pt can reduce the recombination of electron hole pairs to improve the catalytic efficiency. At the same time, adding the CuO catalyst can improve the utilization rate of visible light. Kyeong Hwan Chung's study showes that cesium load - potassium niobate can release hydrogen at a speed of 37.4mmpl/h. Tetsuya Kida studies a new type of nano-scale semiconductor photocatalyst $LaMnO_3$/CdS [6] Catalyst particles exist obvious quantum effects in the 1-100 nm size order. With the decrease of the particle size, the effective width of band gap increases, its corresponding absorption spectrum blue shift. So the semiconductor optical catalyst has good catalytic activity.

3 Solar hydrogen production methods

3.1 Solar hydrogen production from water electrolysis

Solar energy water electrolysis hydrogen production is a relatively mature method for hydrogen production at present, the conversion efficiency can reach 70% ~ 75%. [3] However, the solar energy water

electrolysis requires large amounts of electric energy, resulting in water electrolysis lack commercial competitiveness. But more and more energy experts believe that the cost to produce electricity reduce rapidly, the electrolysis of water has the potential to be the main ways for hydrogen production in the future.

3.2 Solar photochemical hydrogen production

Solar photochemical hydrogen, by adding the photosensitive material in the water as catalyst to help water absorbs wavelengths of light energy in the sun, is an efficient hydrogen production method. The technology has been relatively mature, but the photocatalyst efficiency for the absorption of long wave, is only 4% ~ 5%, and the technology can only be unheeded.

3.3 Biological hydrogen production

Some algae, bacteria and other organisms in rivers and lakes can release hydrogen continuously under the irradiation of sunlight. The mechanism of biological hydrogen production is that some biological exists enzymes related to the hydrogen production, which mainly includes nitrogenase enzyme and hydrogen enzyme. Biological hydrogen production has a advantage of clean, energy saving and no consume of mineral resources. As a kind of renewable resource, organisms can replicate themselves, can realize material and energy conversion through photosynthesis, and the conversion can be realized in usual condition. Now rhodospirillum rubrum, pseudomonas and other prokaryotesmore are being researched more often as photosynthetic bacteria. Nitrogenase is the main catalytic enzyme photosynthetic bacteria have photosynthetic system, when photons are captured and sent to the photosynthetic system, the charge separate, produce high energy electron, and form a protein, then generate H_2. The key technology to hydrogen production by photosynthetic organisms is having a full sun light. Therefore, it involves the reasonable design of biological hydrogen production reactor condenser system and light extractor. The prospects of biological hydrogen production is very good, so the biological and physical mechanism of the microbial hydrogen production must be clarified to cultivate microorganism to produce hydrogen efficiently.

3.4 Solar thermal water splitting hydrogen production

Solar thermal decomposition of hydrogen production is using the solar energy condenser to heat water directly to produce H_2 when the temperature reaches about 2500 ^{O}C. While the hydrogen and oxygen are produced together, the mixture is difficult to separate and easy to explode. To obtain the high temperature which is needed to realize the reaction, high magnification concentrator must be used, but this kind of condenser has very high price.

3.5 Artificial photosynthetic hydrogen production

Artificial photosynthesis is the simulation of plant photosynthesis to produce hydrogen. Firstly, metal complexes are used to make the water decompose electrons and hydrogen ions, then solar energy is used to improve the electron energy to produce hydrogen.. Artificial photosynthesis and water electrolysis is similar, just the solar energy is used instead of electricity. It is only in the laboratory can realize traces of hydrogen preparation, light energy utilization rate is only 15%--16% [7] .

4 Research status at home and abroad

4.1 Abroad research status

USA, Japan, Europe, and other countries have carried out a lot of research on semiconductor photocatalytic materials, mainly includes improving existing catalytic materials and finding out better

semiconductor photocatalytic materials. "Nature" reported the improved TiO2 semiconductor catalytic materials available with carbon doped, its light energy utilization rate reaches to 11% and does not decrease in the continuous experiment within 6 months,and the catalytic material is close to practical usage.Recently, discovering better semiconductor photocatalytic materials have also made great progress, such materials as titanium acid salt, niobium acid salts and tantalum acid salts. A new photocatalyst tantalum nitride, which can effectively absorb the wavelength of 600nm under visible light, and its light energy utilization rate reaches 10%, has been reported.Since 1990s, solar hydrogen production has attracted the attention of western developed countries, and many research progress has been made already. In 2011, Gray,who used TiO2 semiconductor catalyst photolysis of water, could not only produce hydrogen gas, but also crack carbon dioxide to carbon monoxide. So the carbon monoxide and hydrogen can be all used to energy source, the results of this study has aroused widespread concern in the world[9].In the same year, Holtz decomposes water into hydrogen through the solar radiation which can absorb 95% of the solar energy in the vacuum tube surface coated with aluminum oxide and nano particles as catalysts[10].This experiment result drew great attention of the world.

4.2 Research status in china

There are more and more chinese scientists study the solar **photochemical** water in recent years. Li Can used double catalyst to develop Pt-PdS/CdS photocatalyst. Under visible light irradiation, hydrogen quantum efficiency can reach 93% when Na_2S was used as sacrificial reagent [11]. He also found a new photocatalytic material, composed of indium and zinc sulfide. This catalyst can split water under visible light irradiation to produce hydrogen and oxygen continuously. In 2003, Zou Zhigang founded visible light response type water decomposition catalyst, developed a new kind of photocatalysis materials composed of indium tantalum oxide with a layer of nickel oxide on the surface. The catalytic material can function in the visible light wave band with better efficiency and longer life than other similar catalyst. 402nm wavelength of visible light was used to decompose water with efficency of 0.66% [12]. If the nanotechnology can be applied to the structure of catalytic surface material, the decomposition rate of water can enhance 100 times. For the first time, Zou Zhigang complete the photocatalytic decomposition experiment of water in the outdoor sunlight. This is an important research achievement of new environmental material and renewable energy in china.

5 Challenge and Prospect

The focus of solar hydrogen production research is photolysis water hydrogen production. UV light accounted for only 5% of the solar spectrum, the use of catalyst can absorb solar energy 3% of UV light, the low efficiency of photoelectric conversion is the key of research at present. However, the visible light accounts for 43% of the spectrum, the use of solar energy visible light decomposition hydrogen production from water will have broad application prospects [13]. Research shows that we can use one or more metal and nonmetal Co doped semiconductor, as well as multiple compound semiconductor surface supported by noble metal or rare earth elements to enhance the visible light photocatalytic activity.

Most of the current study utilize photoelectron ultraviolet to excite nuclear outer electronic transitions and produce photoelectron, while did not use the heat of solar energy. Therefore photochemistry can also make full use of the traditional thermochemical principle. At the same time photo electrochemical hydrogen and thermochemical cycle is other important research method. The photoelectrochemical semiconductor material selection and compound will be the focus of future research, finding more suitable

electrode materials will be the main direction of water decomposition. For catalyst with lower temperature operation is the key thermochemical cycle for preparation of hydrogen.

Reference

[1] Wang B H. Wu H J, Liu S Z. Advance on research of hydrogen production by solar water splitting [J]. Chemical Industry and Engineering Progress, 2006, 25(7): 733-738.

[2] Huang J Z, Xu Z, Li H L. Progress in study of hydrogen production by solar energy [J].Acta Energiae Solaris Sinica, 2006, 9: 947-954.

[3] Ni M, M K H Leung, K Sumathy. Hydrogen production from solar energy [J]. Renewable Energy Sources, 2004, 3(115): 29-31.

[4] Xu J S & D F Xue. Progress on hydrogen production from photocatalytic water splitting under visible light irradiation [J]. Learning Materials, 2006, 20 (10): 1-4.

[5] Wen F Y, Yang J H, Z X. Photocatalytic hydrogen production utilizing solar energy [J]. Progress in Chemistry, 2005, 20 (10): 1-4.

[6] Jingtang Li. Retrospect and prospect of solar technology development in the 20th century[J].Solar Energy Journal, 1999, 2-4.

[7] L ICHT S, GHOSH S. High efficiency solar energy water splitting to generate hydrogen fuel: Probing RuS2 enhancement of multiple band electrolysis [J]. Solar Energy Materials & Solar Cells, 2002, 70: 471 - 480.

[8] L ICHT S, WANG B. Over 18% solar energy conversion to generation of hydrogen fuel; heory and experiment for efficient solar water splitting [J]. International Journal of Hydrogen Energy, 2001, 26: 653 - 659.

[9] Huang J Z, Xu Z. Technology of photo electrochemical cells hydrogen production from decomposition water using solar energy and status of research [J]. Journal of Linyi Teachers' College, 2004, 26: 653-659.

[10] Gao W H. The development of biological hydrogen production [J]. Science and Technology Innovation Herald, 2009, 28: 114.

[11] Zuo Ran. Renewable energy Conspectus [M]. China Machine Press, BeiJing: 2007,8, 441-445.

[12] Huang J Z, Xu Z, Li H L, Kang G H, Wang W J. Progress in study of hydrogen production by solar energy [J]. Acta Energiae Solaris Sinica, 2006, 9: 947-954.

[13] Yin A G, Lin H S, Present research situation and application prospect of hydrogen production by biotechnology [J]. Anhui Agri Sci Bull, 2007, 13 (2): 51-53.

Advanced Materials Research Vol. 983 (2014) pp 270-274

doi:10.4028/www.scientific.net/AMR.983.270

Stability of a class of power system with interval parameters

Xie Di[1, a], Lu Zhanhui[2,b] and Wang Weijuan[3,c]

[1,2,3]School of Mathematics and Physics, North China Electric Power University, P.R.China,102206

[a,c]wsxiedi@ncepu.edu.cn, [bl]luzhanhui@ncepu.edu.cn

Keywords: interval parameters, power system, small signal stability, interval stability

Abstract. The main discussion in this paper is the stability of power system with interval parameters. By Lyapunov method, matrix theory and so on, the stability theorem of models with interval parameters is provided. Taking an asynchronous wind turbine model as simulation example, the interval that makes the simulation example stable is found, and the numerical simulation shows that the theorem is not only effective but also practical.

Introduction

There exist some small disturbances in the traditional power systems, such as fluctuations generated by the load, generated power grid failure, and variation of wind speed in wind power generation. These factors will affect the stability of power systems. Nowadays, there are many different ways to describe power system small signal stability, such as ordinary differential modeling[1-3], Time-domain simulation[4-5] stochastic differential modeling[6-8]. If the parameters of systems are estimated using confidence intervals, the systems are described as interval systems. In the study of power system, restricted by technology and information, the exact value of some parameters cannot be obtained. Interval model is an effective way to describe the system above. Combining interval systems and small signal stability analysis is few application in power system.

In this paper, the main aim is to study the stability of power system models with interval parameters. By Lyapunov method, matrix theory and interval theory we get the interval stability theorem. It provides a simple and effective method for judging the systems stability. Finally, applying obtained conclusion to study the stability of a asynchronous wind turbine model[1], we obtain the intervals that make the system stable, and the theoretical result was verified by numerical simulation.

Preliminaries

Vector differential system can be written as

$$dX(t) = f(X(t),t)dt + g(X(t),t) \ , \tag{1}$$

where $X(t) = (x_1(t), x_2(t), \cdots, x_n(t))^{\mathrm{T}}$ denotes a n-dimensional vector variable. f and g satisfy the conditions of existence and uniqueness theorem for the solution. If $f(0,t) = 0$ and $g(0,t) = 0$ for all $t \geq t_0$, equation (1) will have the equilibrium solution $X(t) \equiv 0$ [9].

In this paper, $|\cdot|$ denotes Euclidean norm for vector, $\|\cdot\|$ denotes spectral norm for matrix, $\lambda_{\max}(\cdot)$ and $\lambda_{\min}(\cdot)$ are used to describe the maximum and minimum eigenvalue of matrix respectively. Differential operator L is[9]

$$L = \frac{\partial}{\partial t} + \sum_{i=1}^{n} f_i(X,t)\frac{\partial}{\partial x_i} \ .$$

If $M = (m_{ij})_{u\times v}$ and $N = (n_{ij})_{u\times v}$ are two matrices with property that $m_{ij} \leq n_{ij}$ for all $1 \leq i \leq u$, $1 \leq j \leq v$, we define the $u \times v$ interval matrix $[M, N]$ by $[M, N] = \{S = (b_{ij})_{u\times v} : m_{ij} \leq s_{ij} \leq n_{ij}, \text{for all } i, j\}$.

If f in system (1) is a interval linear function $A_I X(t)$, where $A_I \in [\overline{A}, \underline{A}]$, and g is a constant vector B, we get the interval linear system

$$dX(t) = A_I X(t) + B \tag{2}$$

According to the theory of differential equations, the stability state of system (2) is consistent with

$$dX(t) = A_I X(t) \tag{3}$$

The definition of system (3) is as follows.

Definition[10] If the equilibrium solution of system (3) is asymptotically stable for any $A_I \in [\overline{A}, \underline{A}]$, then the system (3) is interval stable.

There are a few lemmas for the proof of stability theorem in section three.

Lemma 1[11] If A is a $n \times n$ real symmetric matrix, x is a n-dimensional column vector, then

$$\lambda_{\min}(A)x^{\mathrm{T}}x \le x^{\mathrm{T}}Ax \le \lambda_{\max}(A)x^{\mathrm{T}}x .$$

Lemma 2[11] If A is a $n \times n$ real symmetric positive define matrix, there must exist an invertible symmetric matrix B satisfying $A = B^2$.

Lemma 3[9] If there is a continuous positive definite function $V(X,t)$ on $I \times R^n$, such that LV is negative definite, besides there are infinitely small upper bound and infinity lower bound for $V(X,t)$, then the system $dX(t) = AX(t)$ is asymptotically stable.

Interval Stability

In this section, the sufficient condition of interval stability for system (3) is provided.

Let $A = (\overline{A} + \underline{A})/2$ and $\widetilde{A} = (\overline{A} - \underline{A})/2$. Clearly, all the elements of $\widetilde{A}$ are nonnegative. Moreover, A_I can be written as $A_I = A + \Delta A$ with $\Delta A \in [-\widetilde{A}, \widetilde{A}]$.

Then the system (3) can be described as

$$dX(t) = (A + \Delta A)X(t) \tag{4}$$

Considering the interval linear system (3), we construct the Lyapunov function $V(t,X) = X^{\mathrm{T}}QX$, and the operator LV associated with system (3) has the form $LV = 2X^{\mathrm{T}}Q(A + \Delta A)X$. Using Lemma 1, Lemma 2 and properties of norm, we obtain that LV is negative definite if the interval matrix A_I satifies the condition in the follow theorem. Then through Lemma 3, we know that the equilibrium solution of system (3) is asymptotically stable for any $A_I \in [\overline{A}, \underline{A}]$, so the interval linear system (3) is of interval stability. The interval stability theorem is as follow.

Theorem Assume there exists a real symmetric positive-definite matrix Q such that

$$c_1|X|^2 \le X^{\mathrm{T}}QX \le c_2|X|^2 \text{ and } \lambda_{\max}(Q^{1/2}AQ^{-1/2} + Q^{-1/2}A^{\mathrm{T}}Q^{1/2}) + 2\|\widetilde{A}\|\sqrt{\frac{\|Q\|}{c_1}} < 0$$

where c_1, c_2 are positive constants, then the system (3) is of interval stability.

Simulation example

The deterministic model of asynchronous wind turbine is as follow

$$dX(t) = AX(t)dt + B, \quad t \in [0,+\infty] \quad X(t_0) = (0 \quad 0)^{\mathrm{T}} \tag{5}$$

Where $X(t) = \begin{bmatrix} \Delta w_t \\ \Delta s \end{bmatrix}$, $A = \begin{bmatrix} -\dfrac{Dw_0}{T_{Jt}} & -\dfrac{Dw_0}{T_{Jt}} \\ -\dfrac{Dw_0}{T_J} & -\dfrac{Dw_0 - (dP_E/ds)_{s=s_0}}{T_J} \end{bmatrix}$, $B = \begin{bmatrix} -\dfrac{Ds_0 w_0}{T_{Jt}} \\ -\dfrac{Ds_0 w_0}{T_J} \end{bmatrix}$

and w_t, s, D, w_0, P_E, T_{Jt}, T_J denote wind turbine speed, slip, damping coefficient, synchronous sp- eed, electromagnetic power, twofold turbine inertia and twofold generator inertia respectively.

If the exact value of some parameters in the system cannot be obtained, the coefficient matrix shouuld be a interval matrix, so we replace the matrix A in the system (5) with the interval matrix A_I. What we want to obtain is the range of A_I, where $A_I = A + \Delta A$, which makes the system stable. Above all, we have the interval system as follow

$$dX(t) = A_I X(t)dt + B, \quad t \in [0,+\infty], \quad X(t_0) = (0 \quad 0)^{\mathrm{T}} . \tag{6}$$

In calculating the values of parameters refer to literature [12], and the main values are as follows $D = 700\,pu.s/rad$, $w_0 = 100\pi\,rad/s$, $T_{Jt} = 203.3kg \cdot m^2$, $T_J = 93.2kg \cdot m^2$. Therefore the coef- ficient matrix A and vector B are $A = [-0.3,-0.3;-1.2,-8.49]$, $B = [-0.024,-0.096]^{\mathrm{T}}$.

To find the interval that makes the system (6) stable, that is the range of ΔA, we need to use the Theorem.

Let $Q = E$, then $\lambda_{\max}(A + A^{\mathrm{T}}) + 2\left\|\widetilde{A}\right\| = -0.4638 + 2\left\|\widetilde{A}\right\|$. According to the the Corollary, the system $dX(t) = A_I X(t)dt$ is stable as long as $\left\|\widetilde{A}\right\| < 0.2319$, at the same time the system (6) is stable. Which means if the 2-norm of ΔA ranges in $[0, 0.2319]$, the system (6) is stable.

Then the system response with different coefficient matrix are simulated using MATLAB. The results are shown in Fig. 1 to Fig. 4.

Fig. 1 to Fig. 4 respectively signify the simulation of system with $\Delta A = [0,0;0,0]$, $\Delta A = [0.2318,0;0,0]$, $\Delta A = [0.1,0.1;0.1,0.1]$ and $\Delta A = [0.4,0;0,0]$. All the ΔA in first three cases are within the system stability range that we have already obtained, but which in the fourth is out of the range. It can be seen that all the values of Δw_t tend to zero in Fig. 1 to Fig. 3, which means the system (6) is stable. On the contrary, in the Fig. 4, the values of Δw_t tend to infinity, therefore the system (6) is unstable. All above show that the stability condition we get is valid, and the validity of the stability theorem is verified.

Conclusions

In this paper, using the theoretical knowledge of interval dynamical system and differential equation, the stability theorem of the power system with interval parameters is proved. The theorem provide a simple and effective way for the discrimination of stability. Taking an asynchronous wind turbine model as simulation example, we find the interval that makes the simulation example stable by the theorem. In addition, the numerical simulation shows that our theorem is not only effective but also practical. Further research work will be concentrated on the stability of power system based on interval models.

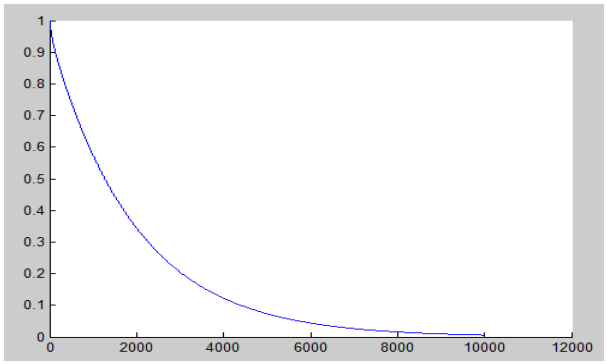

Fig. 1 Value change of w_t with $\Delta A = [0,0;0,0]$

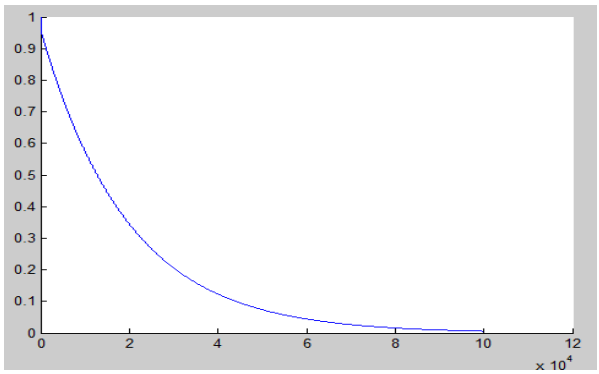

Fig. 2 Value change of w_t with $\Delta A = [0.2318,0;0,0]$

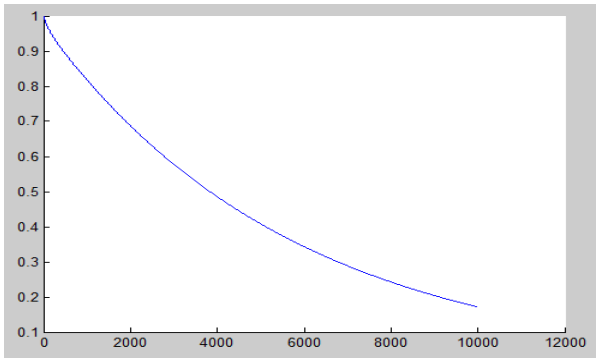

Fig. 3 Value change of w_t with $\Delta A = [0.1,0.1;0.1,0.1]$

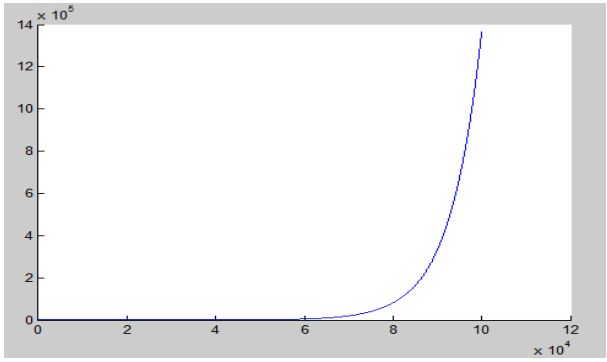

Fig. 4 Value change of w_t with $\Delta A = [0.4,0;0,0]$

Acknowledgements: This work was supported by Natural Science Foundation, P.R.China (51190103)

References

[1]H.L. Guan, Y.N.Chi and H.Z. Dai, et a1: Asynchronous wind turbines connected to the system small signal stability and control. The automation of electric power systems, Vol. 32 (2008), p. 54-57

[2]L.H. Yang, G.Y. Yang and Z. Xu, et a1: Optimal controller design of a doubly-fed induction generator wind turbine system for small signal stability enhancement. IET Generation, Transmission and Distribution, Vol. 4 (2010), p. 579-597

[3]L.B. Shi, L.Kang and Y.X. Ni, et a1: Small signal stability analysis with penetration of grid-connected wind farm of PMSG type. Automation of Electric Power Systems(in Chinese), Vol. 36 (2012), p. 171-177

[4]C. Wang, L.B. Shi and L.Z. Yao, et al: Mass type doubly-fed wind power of small disturbance stability analysis. Proceedings of the CSEE, Vol. 4 (2010), p. 63-70

[5]J.L. Jiang, Q. Chao and J.W. Chen, et al: Different frequency response characteristics of wind turbine simulation analysis[J]. Renewable energy sources, Vol. 28 (2010), p. 24-28

[6]E. Haesen, C. Bastiaensen and J.Driesen, et al: A probabilistic formulation of load margins in power systems with stochastic generation. IEEE T Power Syst, Vol. 24 (2009), p. 951-958

[7]L.C. Chen and W.Q. Zhu: First passage failure of dynamical power systems under random perturbations. Sci China Tech Sci, Vol. 53 (2010), p. 2495-2500

[8]J.Y. Zhang, P. Ju and Y.P. Yu, et al: Responses and stability of power system under small Gauss type random excitation. Science China: Technology Science, Vol. 42 (2012), p. 851-857

[9]Z. N. Ma and Y. C. Zhou: Qualitative and stability of ordinary differential equation method of (Science Publications, Peking 2001).

[10]X.X. Liao and G.L. Qian: Some new results for stability of interval matrices. Control Theory and Advanced Technology, Vol. 7 (1988) p. 265-275

[11]S.G. Wang and M.X. Wu, Z.Z. Jia: Matrix Inequality (Science Publications, Peking 2006).

Advanced Materials Research Vol. 983 (2014) pp 275-279

doi:10.4028/www.scientific.net/AMR.983.275

The Design and Implementation of Optimal Scheduling in Hydro-thermal-wind System

Tian Xuefeng[1, a *]

[1]North China Electric Power University,Peking

[a]302789507@qq.com

Keywords: electric power system, alpine region, optimal scheduling, wind power prediction, unit commitment

Abstract. This paper mainly put forwards the design and implementation of hydropower, thermal power, and wind power joint optimal scheduling system, introduces the framework and functional module of JAVA enterprise application technology, and focuses on the key technologies of the system. The system is based on provincial scheduling automation platform. It takes decision-making as the target, realizes wind power probability prediction, conventional power generation planning, hydropower, thermal power, and wind power joint scheduling, constraint checking, impact assessment and other functions, and helps the operators to make scientific and reasonable power generation plans, achieve intelligent scheduling, and enhance system operation level.

1.Introduction

With China's rapid economic development, energy needs are growing rapidly, thus resulting energy shortage, environmental pollution and climate change issues. Due to the dual pressure of energy demand and climate change, our country has spared no efforts to develop clean and renewable energy resources in order to reduce the dependence on fossil fuels and environmental pollution.

In this context, it has important theoretical and engineering application value to establish wind power prediction platform[1-2], study the joint optimal scheduling of wind power[3-5] and thermal power, hydropower and other conventional power.

It takes decision-making as the target and realizes single wind electric field output power probability as well as the total power of the province's wind electricity probability. On the basis of wind power prediction, this system enables the joint optimal scheduling of hydropower, thermal power, and wind power. It can make generation plans according to the power grid actual operation rules. It has constraint checking, impact assessment and other functions, which can provide the operators with plentiful decision-making information.

2. System structural design

The system avails Java enterprise edition (Java EE) technology. It takes multi-tier distributed framework and modular design. The overall software framework has three levels: the data acquisition layer, business logic layer and presentation layer (see Figure 1). The main function of the data acquisition layer is to exchange data with external systems, complete information receiving and provide data to support the business logic layer.

The main function of business logic layer is the realization of core algorithm: probability prediction of wind power based on component sparse Bayesian learning, wind, water and fire joint optimization.It also includes conventional planning, statistical reporting, and other functions.

The main function of the presentation layer is to display prediction and optimization results to the dispatcher, and provide a comparative assessment between the scheduling schemes, system management and other functions.

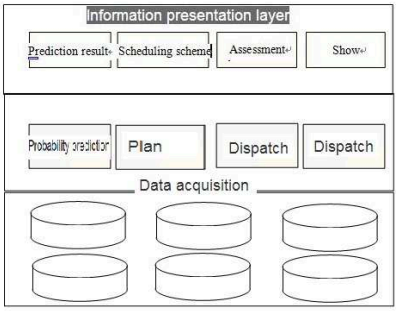

Fig. 1 Software architecture of the system

3.Main Functional Sub-module

3.1 Data interaction sub-module

This module is mainly to complete the data interactive functions with external systems. It gets data needed by the system with the Webservice means from EMS/SCADA systems, load prediction system, numerical weather forecasting system, day scheduling management system, water transfer automation systems, and heating information monitoring system. The power grid runs real-time data, which is red from EMS/SCADA system every 15min, while the other information is generally read once every 24h.

3.2 Visual display sub-module

This module displays the grid running real-time data (such as system load, wind farms, conventional units real-time output, tie-line power, reservoir water level, etc.) from multiple angles, prediction data (such as system load, wind farm output power, heat load, etc.) and trend analysis data (such as month generating capacity, electricity generation yesterday, plan completion, coal inventory of the thermal power plant, etc.) and other information. Thus the dispatcher can clearly and intuitively know the power grid operation.

3.3 Wind power probability prediction sub-module

The module uses components of sparse Bayesian learning methods to predict the output power of directly modulated wind farm in future period and that in all the province.

3.4 Conventional program sub-module

The module is compiled on actual grid operation principle. It can compile, prepare, publish and report the generation plans of various wind farms and conventional units.

3.5 Optimization program sub-module

The module is based on a mathematical optimization algorithm. It can access the largest wind power, as well as the lowest cost of water, fire, wind power joint optimal scheduling.

3.6 Effect evaluation sub-module

The module is mainly comparatively evaluate conventional plan, optimization plan in the largest wind power access and optimization plan when power purchase cost is lowest from multiple angles, such as power generation, power purchase cost, power-on way, unit output, wind power absorption level, and risk level to provide dispatchers with assist decisions.

3.7 Constraint checking sub-module

This module is mainly to achieve annual plans for electricity, power plants run unit number and operating constraint checking.

3.8 System management sub-module

It sets up and manages the basic data, system users and permissions. The basic data includes power plant ledger (plant name, plant type, company information), the unit ledger (unit name, unit type, rated capacity, failure rate, start-up costs and other information).

4.Key technologies for system realization

4.1 Wind power probability forecast

By computation and analysis Heilongjiang wind farm output power and meteorological data Pearson correlation coefficient, we found that the correlation of wind speed and wind power output is the most. First of all, the system gets the basic parameters of the probability prediction model through statistical learning of historical wind speed and wind power data, and stores them in the database. The model parameters are usually updated automatically every month, or manually updated if the dispatcher thinks it’s necessary according to the prediction error. During operation, the wind farm speed information in future period is got through interface to the numerical weather prediction system, while the wind power output information in the first three periods is got through interface to EMS/SCADA system, and then used as the input to forecast wind power probability.

4.2 Joint optimal scheduling with the largest integration of wind power

The decision target is minimizing the cost when the integration of wind power is the largest. Suppose the system contains N thermal units, M hydroelectric power plants W wind farms, so the objective function can be expressed as:

$$\min F = \sum_{t=1}^{T}\sum_{i=1}^{N}\left[F_i\left(p_i^t\right)u_i^t + S_i^t\left(\tau_{off,i}^{t-1}, u_i^t, u_i^{t-1}\right)\right] \tag{1}$$

Where, F is the total operation cost of N thermal power units in T periods. pit is the output power of thermal power unit i in period t. uit is the running or shutdown status of thermal power unit i in period t. 0 indicates shutdown, while 1 running; Fi (·) is the cost function of thermal power units i. τ toff,i is the deadline time of thermal power units i till period t; Sit (·) is the cost function of the ith thermal power unit during the startup.

The system operation must meet the following constraints:

1) Power balance constraint:

$$\sum_{i=1}^{N} u_i^t p_i^t + \sum_{j=1}^{M} p_j^t + \sum_{w=1}^{W} p_w^t = p_d^t \quad t \in T \tag{2}$$

p_j^t is the output power of hydropower plants j in period t. p^t_w is the maximum access power of wind farm w in period t. p^t_d is system load in period t.

2) Thermal power unit operation constraints:

$$u_i^t \underline{p}_i \le p_i^t \le u_i^t \overline{p}_i \qquad i \in N; t \in T \tag{3}$$

$$(\tau_{on,i}^{t-1} - M_{on,i})(u_i^{t-1} - u_i^t) \ge 0 \quad i \in N; t = \in T \tag{4}$$

$$(\tau_{off,i}^{t-1} - M_{off,i})(u_i^t - u_i^{t-1}) \ge 0 \quad i \in N; t = \in T \tag{5}$$

$$-r_{down,i}\Delta t \le p_i^t - p_i^{t-1} \le r_{up,i}\Delta t \quad i \in N; t \in T \tag{6}$$

$\overline{p}$ and $\underline{p}_i$ represent the upper and lower output power limits of thermal power unit i respectively. τ ton, i and τ toff, i represent the running and deadline time of thermal power unit i till period t respectively. Mon,I and Moff,i represent the shortest running and deadline time of thermal power unit i respectively. rdown,I and rup,I represent the maximum fall and rise speed of the output power of thermal power unit i.

3) Hydropower plant operation constraints:

$$\underline{Q}_j \le Q_j^t \le \overline{Q}_j \qquad j \in M; t \in T \tag{7}$$

$$\sum_{t=1}^{T} Q_j^t = H_j \qquad j \in M; t \in T \tag{8}$$

$\underline{Q}_j$ and $\overline{Q}_j$ represent the upper and lower current limits of hydropower plant j respectively in each period. Hj represents the water amount of the hydropower plant j in period T.

4) Maximum load loss probability constraints:

$$L(u_i^t) \le \overline{L}^t \quad i = 1,2\cdots N; t = 1,2,\cdots,T \tag{9}$$

L (·) is the load loss probability function of the system. The function is mainly subject to the impact of wind power fluctuations and unit random failures outage. $\overline{L}^t$ is the allowed upper load loss limit time period t.

4.3 Joint optimization scheduling of electricity purchase lowest

The joint optimization scheduling of electricity purchase lowest should consider each unit including wind farms bidding in a fully competitive environment. The decision-making goal is the Grid Corporation buy the electricity with the lowest cost. (Since the hydropower plants are owned by Power Grid Corporation, the model temporarily does not take into account the cost of electricity purchase). The objective function is expressed as:

$$\min F = \sum_{t=1}^{T}\sum_{i=1}^{N} f_{price,i} p_i^t u_i^t + \sum_{t=1}^{T}\sum_{w=1}^{W} f_{price,w} p_w^t \tag{10}$$

F is the total power purchase cost of N thermal power units in period T. p_i^t is the output power of thermal power unit i in period t. u_i^t is the on or off status of the thermal power unit i in period t. 0 indicates shutdown, while 1 running; $f_{price,i}$ is the price of thermal power unit I, while $f_{price,w}$ is that of wind power field w. p_w^t is the output power of wind power field w in period t.

In the target optimization process, it is necessary to meet a variety of constraints.as follows:

1) Power balance constraint:

$$\sum_{i=1}^{N} u_i^t p_i^t + \sum_{j=1}^{M} p_j^t + \sum_{w=1}^{W} p_w^t = p_d^t \quad t \in T \tag{11}$$

Different from constraint (2), the output power p_w^t of wind farm w in period t is a value to be decided, and it can not be preset.

2) Wind farm operation constraints

$$p_w^t \le p_{u,w}^t \qquad w \in W; t \in T \tag{12}$$

$p^t_{u,w}$ is the expected value of probability prediction of wind farm w in period t. if the actual output power of the wind farm is bigger than that of the optimization model p_w^t, the Grid Corporation can take wind-abandoning measures in order to reduce the cost of power purchase. If the actual output power of the wind farm is less than p_w^t, increase spear unit output to reduce the power purchase cost. The probability that the actual output power of the wind farm is in the vicinity of the expectation is larger. Therefore, in the present system, the trustable capacity which can participate in auction from each wind farm is $p^t_{u,w}$.

3) Other constraints

Other constraints include thermal power unit operation constraints, hydropower plant operation constraints, and maximum loss load probability constraints, which are that constraints (3)-(9). The solution method of the model is the same with maximum wind power access, so no more words for it here.

5.Application case

The commissioning of this system is conducted in the Power Grid Dispatch Center in Heilongjiang Province, and the result is quite satisfactory.

Figure 2 is given by this system to display wind power probability forecast results throughout Heilongjiang province. As can be seen from this figure, unlike other similar products which can only conduct a single-point prediction, this system is able to give the distribution range of the wind power in different confidence intervals, (different colors show the wind power distribution range of confidence intervals of 90% and 80% when). Therefore it can provide abundant information for scheduling decisions.

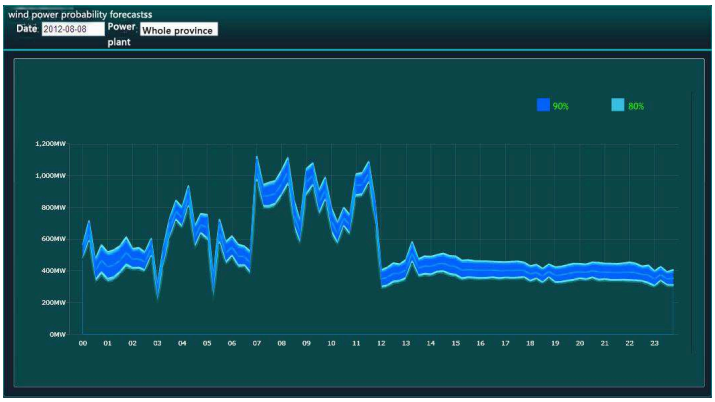

Fig. 2 Probability forecast result of wind farm generation

Figure 3 is to display the effect assessment results of conventional plan, the largest wind power access and the lowest power purchase cost. As can be seen from the figure, the system can evaluate the three scheduling results from different angles, such as generation components, water, fire, wind power generation contrast, and fire, wind power generation trends. So is can provide a vivid reference and thus play a decision support role.

Fig. 3 Impact evaluation result

6.Conclusion

The system has good prospect of promotion and application. The core algorithm has been checked in several standard tests as well as the actual grid data. It has good use and evaluation credibility. The system configuration and deployment program meet the security requirements of the Grid Cooperation. It is the upgrading of existing power generation planning platform.

References

[1] Feng Shuanglei，Wang Weisheng，Liu Chun，et al．Study on the physical approach to wind power prediction ［J］．Proceedings of the CSEE，2010，30（2）：1-6.

[2] Gu Xingkai，Fan Gaofeng，Wang Xiaorong，et al．Summarization of wind power prediction technology ［J］．Power System Technology，2007，31（S2）：335-338.

[3] BOUFFARD F，GALIANA F D．Stochastic security for operations planning with significant wind power generation［J］．IEEE Transaction on Power Systems，2008，23（2）： 306-316.

[4] Yan Yong，Wen Fushuan，Yang Shouhui，et al．Generation scheduling with fluctuating wind power［J］．Automation of Electric Power Systems，2010，34（6）：79-88.

[5] Li Zhi，Han Xueshan，Yang Ming，et al．Power system dispatch considering wind power grid integration ［J］．Automation of Electric Power Systems，2010，34（19）：15-19.

Advanced Materials Research Vol. 983 (2014) pp 280-283

doi:10.4028/www.scientific.net/AMR.983.280

The Effect of Air Cold Plasma Treatment on UHMWPE Fiber Surface Modification

Lin Xiaoxia[1,a], Huang Xin[2, b]and Wang Yimin[3, c *]

[1]College of Materials Science and Engineering, Donghua University, China

[2]College of Materials Science and Engineering, Donghua University, China

[3]State Key Laboratory for Modification of Chemical Fibers and Polymer Materials, China

[a]crystalxiaoxia@126.com , [b]1103532523@qq.com, [c]ymw@dhu.edu.cn

Keywords:UHMWPE fiber; air plasma method; surface modification; mechanical properties; adhesion performance.

Abstract: This paper adopted the air plasma treatment on ultra-high molecular weight polyethylene fiber surface modification. SEM, tensile test and fiber bundle pull out test were used to characterize the influence of processing time and voltage on the effect of fiber surface modification. The results showed that the optimum conditions of surface modification were obtained by the processing parameters of pressure 15Pa, time 5 minutes and voltage 15V. At this point, the bonding strength was increased by about 82.4%, and the breaking strengthreduced by 9.7%.

Introduction

Because of Ultra-high molecular weight polyethylene fiber smooth surface and no functional groups, the compatibility with other materials is not good enough, so surface modification should be done before it composite with adhesives[1-4]. There have been many researches about the plasma treatment of UHMWPE fiber, Jiang Sheng [5], used argon plasma to treat UHMWPE fiber before composite it with low density polyethylene (LDPE) matrix and found the adhesive properties improved significantly. The air cold plasma treatment was used to modify UHMWPE fiber surface in this article, and the influence of different processing conditions on the fiber surface modification effect was studied.

Experiment

Material. The ultra-high molecular weight polyethylene (UHMWPE) fiber （400d/120f）was purchased from Jiaxing Aegis special textile manufacturing Co., LTD.

Preparation. The initial UHMWPE fiber was modified by cold air plasma treatment, and the pressure was kept constant of 15 Pawithin the whole processing. And the influences of processing condition on UHMWPE fiber surface modification by changing the processing time and voltage were studied. After air plasma treatment, a series of modified fiber was obtained, and then performance testing and characterization were conducted.

Characterization. An air cold plasma modification treatment instrument was used to treat UHMWPE fiber. The LTD, XQ-1A Tensile Tester (Shanghai new fine instrument co.,) was used to test fibers' mechanical properties. Fiber bundle pull out test was carried out using the universal material testing machine 2TA (Changchun new test equipment company, WDW3020). And the field emission scanning electron microscopy (SU8010) was used to observe the fiber surface structure.

Results and Discussions

The Effect of Plasma Treatment Time on Fiber Microscopic Surface. Figure 1 and Figure 2 show the SEM images of both initial fiber surface and treated fiber surface. In these two pictures, we can found that the initial fiber surface is smooth, with minor grooves. These small grooves are mainly formed in the process of gel spinning and high ratio drawing. After 5 minutes processing, the grooves on fiber increased in width, depth and also in numbers. This is because air plasma etched the UHMWPE fiber surface in the process. In addition, there were granular sediments on the fiber surface. This is because fiber surface matter decomposed and formed gaseous species in the process. At the same time, gaseous species came back to the fiber surface, gathered and generated particles.

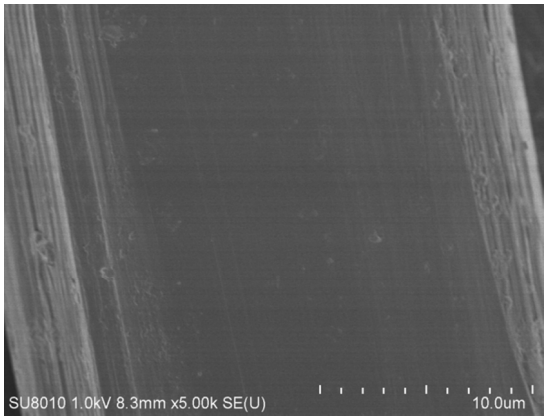

Fig.1 The initial fiber surface

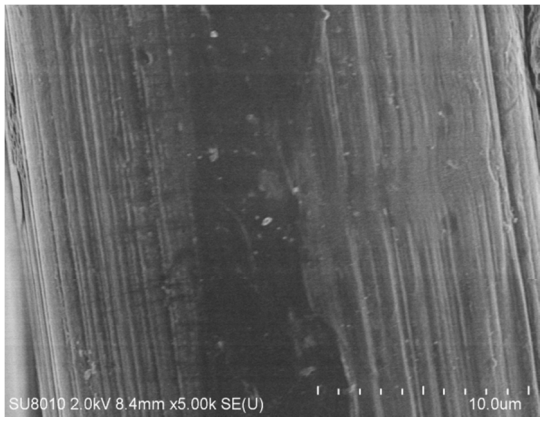

Fig.2 The fiber surface after 5 minutes treatment

The Effect of Plasma Treatment Time on Fiber Mechanical Properties. The relationship of mechanical properties and processing time under the voltage of 15V is shown in Figure 3. As processing time increases, the breaking strength of UHMWPE fiber is decreased. After 5 minutes treatment, the breaking strength downs to 12.75cN/dtex, fell by 9.7%. After 8 minutes treatment, the breaking strength declines to 10.94cN/dtex, fell as much as 22.52%. Therefore, as the treatment time exceeds five minutes, especially for eight minutes, the surface of fibers is damaged by plasma treatment and caused the mechanical property reduced greatly.

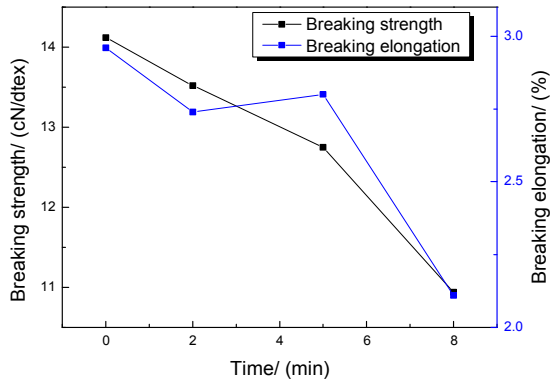

Fig.3 Mechanical properties of fiber after treatment with different processing times under the voltage of 15V

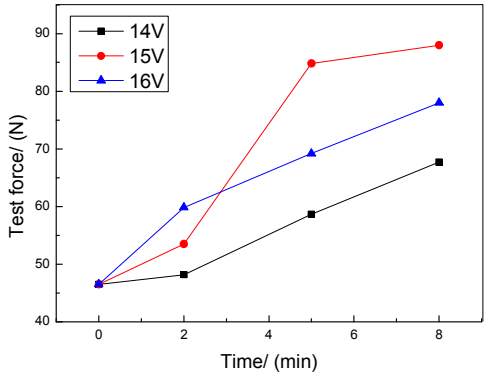

Fig.4 Adhesive properties of fiber after treatment with different processing times

The Effect of Plasma Treatment Time on Fiber Adhesive properties. The relationship of adhesive properties and processing time with different processing voltages is shown in Figure 4. As the processing time increases, the bonding strength of UHMWPE fiber under different voltage is

enhanced. At 14V, after 2 minutes processing, fibers' adhesion performance has not clearly change as compared to initial fiber, so the modification effect is not obvious. At 15V, after 5 minutes processing, fibers' adhesive properties enhanced, pull-out strength increases from original fibers' 46.5N to 84.83N, and the adhesive properties of fibers after 8 minutes treatment are close to 5 minutes treatment fibers. When the processing voltage is 16V, as the increase of the time, the adhesive properties of UHMWPE fiber also increases. Overall, combined with the fiber mechanical test, we can find that no matter the voltage is 14V, 15V or 16V, the modification effect of UHMWPE fibers is optimum when the processing time is 5 minutes. At this time, the loss of mechanical properties is in an acceptable range.

The Effect of Plasma Treatment Voltage on Fiber Microscopic Surface. Microscopic surfaces of fiber treated by 14V and 16V are shown in Figure 5 and Figure 6 separately. In Figure 5, we can find that compared with the initial fiber surface, surface of fiber modified under the voltage of 14V has not clearly change, and there is not much particulate matter deposited on the fiber surface. When processing voltage is 16V, there is no particle deposition on the surface, but there are many small holes on the surface, which diameter is about 1μm. This may be due to the strong voltage lead to the plasma beat the fiber surface. Therefore, with the increase of processing voltage, the roughness of fiber surface increases obviously, at the same time, fiber surfaces are damaged. In the other words, it can improve the pull-out strength of fiber and matrix materials, but the breaking strength of fiber will be affected.

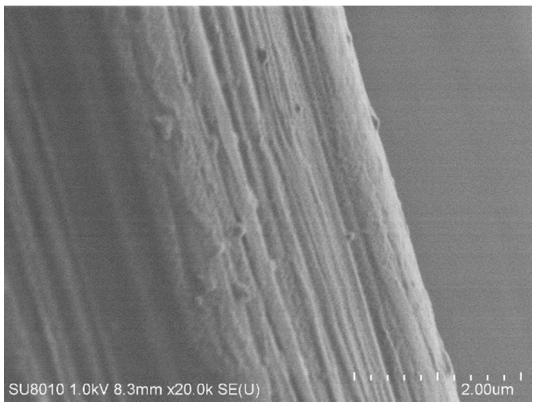

Fig.5 The fiber surface of 14V voltage treatment

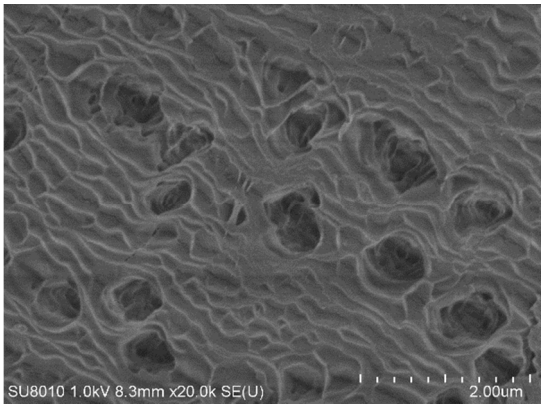

Fig.6 The fiber surface of 16V voltage treatment

The Effect of Plasma Treatment Voltage on Fiber Mechanical Properties. In Figure 7, sample NO.0 is initial fiber, sample NO.1 is fiber modified under the voltage of 14V, sample NO.2 is fiber treated under 15V and sample NO.3 is fiber modified under 16V. It shows that with the increase of voltage, the breaking strength of UHMWPE fiber is decreased, and the breaking strength declines from 14.12cN/dtex to 13.8cN/dtex, 12.75cN/dtex and 9.64cN/dtex. At 14V and 15V, fiber mechanical properties have a drop of 2.27% and 9.7% respectively, and a 31.7% decline under the voltage of 16V. Therefore, the processing voltage of 16V is not fit for the requirement.

The Effect of Plasma Treatment Voltage on Fiber Adhesive properties. The relationship of adhesive properties and processing voltage with different processing time is shown in Figure 8. As processing voltage increases, the bonding strength of UHMWPE fiber in different voltage is improved. At 2 minutes, after 14V processing, fibers' adhesion performance has not clearly change as compared to the initial fiber, so the modification effect is not obvious, and after 16V processing, the pull-out strength is 59.83N, only increases by 28.7% as compared to the original fiber. At 5 minutes and 8 minutes, the pull-out strength of fiber and adhesives decreases with the increase of the voltage after increase first. And the adhesive properties gets the peak when the processing

voltage is 15V, at this point, the pull-out strength are 84.83N and 88N respectively, increases by 82.4% and 89.2% as compared to the original UHMWPE fiber, so the modification effect is extremely obvious. However, when the voltage is 16V, the pull-out strength of fiber and adhesives declines, this may be due to the fiber was smitten by air plasma and the fiber surface was damaged. Therefore, fibers' modification effect is optimum when the processing voltage is 15V. At this time, there is a little influence on the mechanical properties of the UHMWPE fiber, and the loss of breaking strength is controlled within 10%.

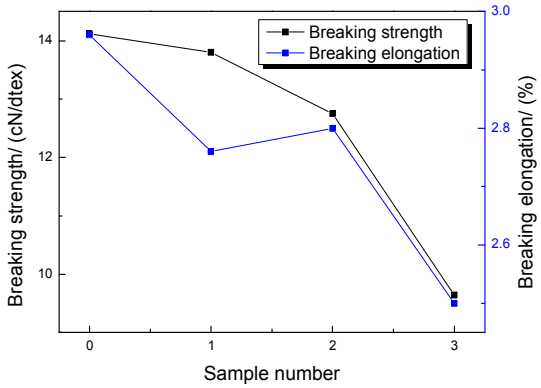

Fig.7 Mechanical properties of fiber after treatment of different voltages in 5minutes

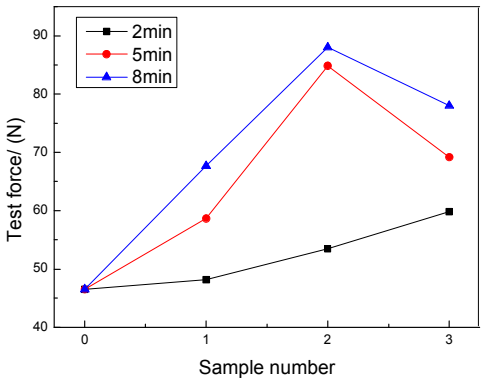

Fig.8 Adhesive properties of fiber after treatment of different processing voltages

Conclusions

The aim of this study was to investigate the effect of different surface modification techniques on the adhesion performance. As a result, we can find that particle deposited on fiber surface treated by air plasma modified. There were many small holes on fiber surface, so that surface roughness of fiber was increased. Moreover, test results show that the optimum processing parameters of surface modification were set to pressure 15Pa, time 5 minutes and voltage 15V. At this point, the adhesive properties of fiber are increased by about 82.4%, and the mechanical properties reduced by 9.7%.

Reference

[1] Andreia Leite dos Santos Alves, et al. Influence of weathering and gamma irradiation on the mechanical and ballistic behavior of UHMWPE composite armor. Polymer Testing, 2005, (24): 104-113.

[2] Hong Jianhan, Pan Zhijuan. Oxygen plasma treatment effected ultra-high molecular weight polyethylene fiber mechanical properties. The influence of industrial textiles, 2013, 31 (2): 29-32.

[3] Tang Jiuying, Chen Chengsi, Wang Shouguo. Low temperature plasma surface modified UHMWPE fibers. Journal of synthetic fiber industry, 2007, 30 (3): 39-41.

[4] Kaji K, Abe Y, et al. Radiation-grating of acrylicacid onto ultra-high molecular, high-strength polyethylene fibers. Journal of Applied Polymer Science, 1993, 47(8): 1427-1438.

[5] Jiang Sheng. The performance of the UHMWPE fiber/LDPE composite materials after the plasma treatment. Journal of textile, 2007, 28(9):57-60.

Advanced Materials Research Vol. 983 (2014) pp 284-287

doi:10.4028/www.scientific.net/AMR.983.284

The Effects of the Total Number of Regions and Average Power Density on the Overall Performance of Modified CANDLE Burn-up Scheme Based Gas Cooled Fast Reactors

Rosidah[1], I, Afifah[1], Zaki Su'ud [1,a], H. Sekimoto[2,b], and Ferhat A.[3,c]

[1]Department of Physics, Faculty of Mathematics and Natural Sciences, Bandung Institute of Technology, Bandung, Indonesia

[2]Emeritus Professor in Research Lab. For Nuclear Reactors, Tokyo Institute of Technology

[3]National Nuclear Energy Agency, Jakarta, Indonesia

[a]zakisuud@gmail.com,[b]hsekimot@gmail.com,[3]ferhat@batan.go.id

Keywords: Gas cooled, long life, fast reactors, modified CANDLE, natural uranium, fuel shuffling, total number of regions,average power density

Abstract. In this study the effects of the total number of regions and average power density in Modified CANDLE burn-up scheme are studied. In the previous studies usually 10 equal axial regions are applied in Modified CANDLE burn-up scheme, and in this study 6, 8 and 10 regions Modified CANDLE burn-up scheme performance is compared and discussed. The core power level varied from 800-1000MWt. Several comparisons are performed between 10 and 8 regions Modified CANDLE, 8 and 6 regions Modified CANDLE and some additional comparison which include some changing in power level. Some general remark which we can get from this study is that reducing region with the same cycle length and power level will resulted in significant drop of effective multiplication constant especially at the beginning of life and the reduction of discharge burn-up level. On the other hand the increase of the power level with the same region number and cycle length resulted in higher effective multiplication constant value especially at the beginning of life, while at the end of life the differences are decrease. Then when we reduce the region number and increase the power level at the same time we get the mixed effect in which the system performance is relatively go back to the original case.

Introduction

CANDLE and Modified CANDLE burn-up scheme can be used to develop nuclear power plant (NPP) which can directly utilize natural uranium as fuel cycle input can be considered will help developing countries from dependence on Uranium enrichment plant or fuel reprocessing plant which are very sensitive technology especially if they are developed in the developing countries[1-7]. Modified CANDLE burn-up scheme have been shown to have more flexible burn-up level output from about 20% up to more than 40% HM[4-8].

In this study the effect of total number of regions in Modified CANDLE burn-up scheme are studied. In previous studies usually 10 equal axial regions are applied in Modified CANDLE burn-up scheme, and in this study 6, 8 and 10 regions Modified CANDLE burn-up scheme performance is compared and discussed. The core power level varied from 800-1000MWt. Several comparisons are performed between 10 and 8 regions Modified CANDLE, 8 and 6 regions Modified CANDLE and some additional comparison which include some changing in power level. Reducing region number in this case has the consequence in reduction of total fuel residential time in the core. For example 10 regions with 10 years cycle length gives 100 years total residential time, while 6 regions with the same parameters give only 60 years residential time in the core which is more reasonable from the point of view current nuclear material technology.

Design Concept and Calculation Method

Following previous study, CANDLE burn-up strategy is slightly modified by introducing discreet regions [4-9]. In this design the reactor cores are subdivided into several parts with the same volume in the axial directions. The natural uranium is initially put in region 1, after one cycle of 10 years of burn-up it is shifted to region 2 and the region 1 is filled by fresh natural uranium fuel. This concept is basically applied to all regions, i.e. shifted the core of I'th region into I+1 region after the end of 10 years burn-up cycle (see figure 1) [4-5].

Similar to the previous study, the calculations are performed using SRAC code system [9], SLAROM code system[10], and FI-iTBCH1 code system[11]. At the beginning we assume the power density level in each region and then we perform the burn-up calculation using the assumed data. The burn-up calculation is performed using cell burn-up in SRAC code which then give eight energy group macroscopic cross section data to be used in two dimensional R-Z geometry multi groups diffusion calculation. The average power density in each region resulted from the diffusion calculation is then brought back to SRAC code for cell burn-up calculation. This iteration is repeated until the convergence is reached[4-5].

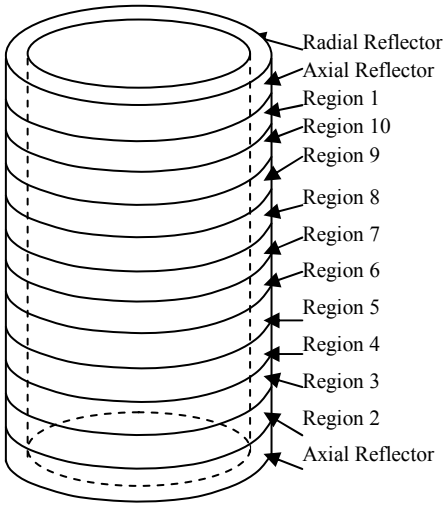

Fig. 1 Illustration of Modified CANDLE burn-up scheme for 10 axial regions

Table 1: Sample Core parameters and burnup level of the cases A and B

Parameters	Case A	Case B
Number of Regions	10	8
Active Core axial width (cm)	200	200
Active core radius (cm)	140	140
Thermal power (MWt)	800	800
Burnup level MWd/tonHM	2,63E+05	2,12E+05

Calculation Results and Discussion

In this study we discuss calculation results of 6 cases namely A, B, C, D, E and F. Case A is the standard case. Case B has 8 regions compared to the 10 regions in case A, but both has 800 MWt power level. Table 1 shows main parameters and burn-up level for the cases A and B. Both cases A and B have similar general parameters. The cladding is stainless steel. Fig 2 shows effective multiplication constant change during 10 years of burn-up for cases A and B. It is shown that reduction of the number of regions from 10 to 8 which directly reduces the discharge burn-up gives reduction of effective multiplication constant especially in the beginning of life. This reduction of the number of regions with the same other parameters resulted in reduction of burn-up level from about 26,3%HM to 21.2% HM (or 263000 MWd/tohHM to 212000 MWd/ton HM). From our previous study it is clear that these level of burn-up in Modified CANDLE cases produce fuel distribution in which the plutonium production is still less than optimal in from the point of view reactor core criticality[4,5]. Such situation resulted in continuously increase effective multiplication constant during burn-up process.

Case B and C both have 8 regions, but case C has higher power level of 1000 MWt power level compared to 800 MWt in case B. Table 2 shows main parameters and burn-up level for the cases B and C. Fig 3 shows effective multiplication constant change during 10 years of burn-up for cases B and C. It is shown that the increase of power level from 800 MWt to 1000 MWt with the same other parameters resulted in increase of burn-up level from about 21.2%HM to 26,4%HM (or

212000 MWd/tohHM to 264000 MWd/ton HM). From the Fig. 3 it is shown that the increase of the power level from 800MWt to 1000 MWt increase the discharge burn-up to almost similar to the standard case A and therefore gives increase of effective multiplication constant especially in the beginning of life. The case B is not operational because of some value of effective multiplication constant is lower than one.

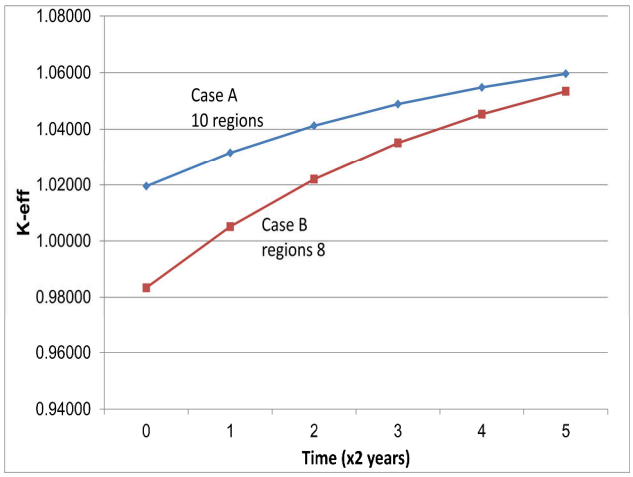

Fig. 2 K-eff change for the Cases A and B

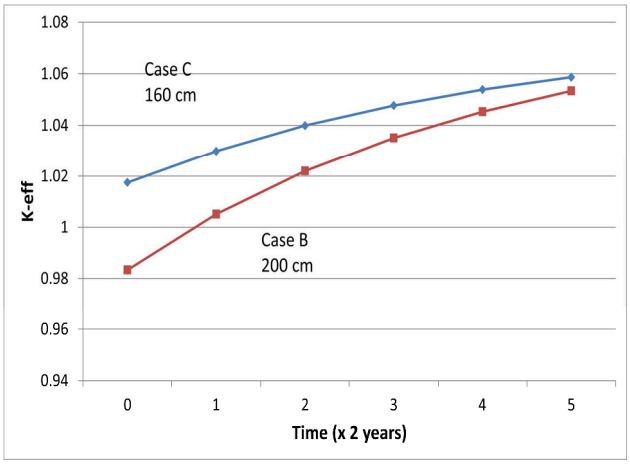

Fig. 3 K-eff change for the Cases B and C

Next we discuss the comparison between Case C and Case D. Case D is similar to the case C except that it has only 6 regions compared to the 8 regions in the case C, but both has 1000 MWt power level. Table 2 shows main parameters and burn-up level for the cases C and D.

Table 2: Sample Core parameters and burnup level of the cases B, C and D

Parameters	Case B	Case C	Case D
Number of Regions	8	8	6
Active Core axial width (cm)	200	200	200
Active core radius (cm)	140	140	140
Thermal power (MWt)	800	1000	1000
Burnup level MWd/tonHM	2,12E+05	2,64E+05	2,01E+05

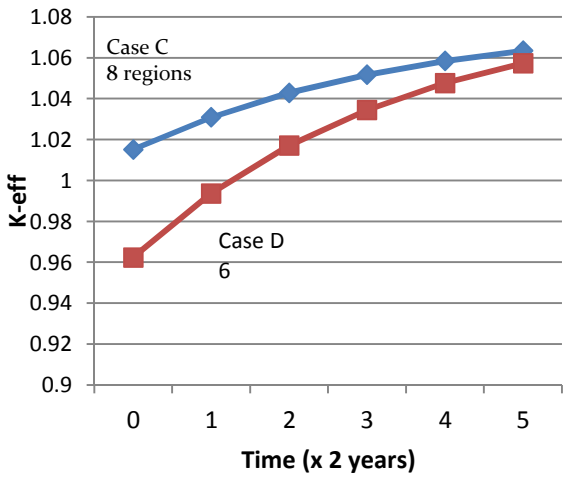

Fig. 4 K-eff change for the Cases C and D

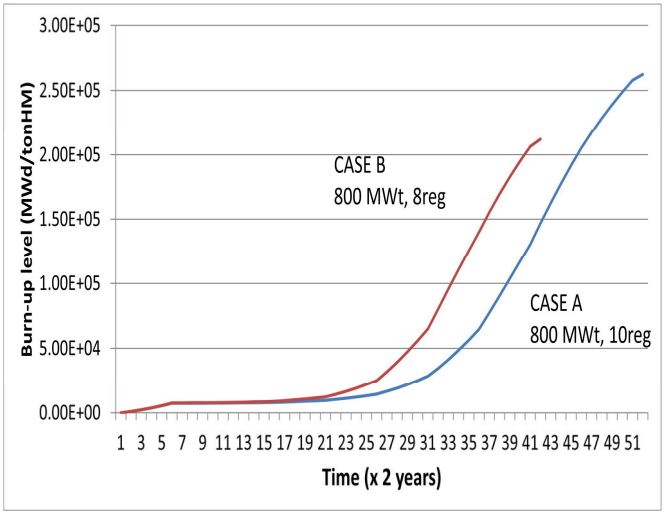

Fig. 5 Burn-up level change for the cases A and B

Fig 4 shows effective multiplication constant change during 10 years of burn-up for cases C and D. It is shown that similar to the case A and B, reduction of the number of regions which directly reduces the discharge burn-up gives reduction of effective multiplication constant especially in the beginning of life. The reduction of region from 8 to 6 with the same other parameters resulted in reduction of burn-up level from about 26,4%HM to 20.1% HM (or 264000 MWd/tohHM to 201000 MWd/ton HM).

Fig. 5 shows the burn-up level change with time (or burn-up history) for cases A and B. It is shown that in the case B the breeding processes are faster than those in the case A but maximum level of burn-up is significantly lower for case B compared to that of case A. This is mainly due to shorter overall exposure time.

Summary

In this study the effect of total number of regions in Modified CANDLE burn-up scheme are studied. In this study 6, 8 and 10 regions Modified CANDLE burn-up scheme performance is compared and discussed. From this study it is found that reducing total number of regions with the same cycle length and the same power level will resulted in significant drop of effective multiplication constant especially at the beginning of life and the reduction of discharge burn-up level. On the other hand the increase of the power level with the same region number and cycle length resulted in higher effective multiplication constant value especially at the beginning of life, while at the end of life the differences are decrease. Then when we reduce the region number and increase the power level at the same time we get the mixed effect in which the system performance is relatively go back to the original case. Adjustment such as increasing power will improve the criticallity but may have consequence such as the increase of the peak power density.

Acknowledgement

This research supported by Riset Unggulan KK ITB 2013

References

[1] H. Sekimoto, et al. : Nuclear Science and Engineering Vol 139 (2001), p. 1-12

[2] Y. Ohoka and H. Sekimoto: Nucl. Eng. Des.Vol. 229 (2004), p.15-23.

[3] Rida SNM and Zaki Su'ud: International Journal of Nuclear Energy Science and Technology Vol. 4 No. 3 (2009),p.217-222

[4] Zaki Su'ud and H. Sekimoto (2010) Int. Journal of Energy Science and Technology (IJNEST), Vol 5, No. 4 (2010), p.347-368

[5] Su'ud, Z., Sekimoto, H., Annals of Nuclear Energy Vol. 54 (2013), pp. 58-66

[6] M. Ariani, et.al., American Institute of Physics Conf. Proceeding, vol. 1454(2012), p. 69

[7] M. Ariani, et al. Applied Mechanics and Materials, Vol. 260-261(2013), p.307

[8] Fiber Monado et al. Advanced Material Research(AMR), Vol. 772, pp. 501-506

[9] OKUMURA, K., Teruhiko KUGO, Kunio KANEKO and Keichiro TSUCHIHASHI: SRAC (Ver.2002) ;The comprehensive neutronics calculation code system', JAERI Report, 2002

[10] Z. Su'ud, FI-ITB CH1 Code: Code for Fast Reactor Design Analysis, Internal Report, ITB, Indonesia (2000).

[11] Nakagawa, M. and Tsuchihashi, K. , SLAROM: A Code for Cell Homogenization Calculation of Fast Reactor, JAERI M 1294 (1984).

Advanced Materials Research Vol. 983 (2014) pp 288-291

doi:10.4028/www.scientific.net/AMR.983.288

The Research of Marine Nuclear Power two loop Simulation Software Based on the Thermal System Analysis

Zhang Guolei[1,a], Jin Xiangdong[1,b] ,Zhao Zhan[1,c] and Shi Zhijun[1,d]

[1]College of Power and Energy Engineering, Harbin Engineering University, Harbin, 150001, China

[a]zhangguolei@hrbeu.edu.cn, [b]jinxiangdong04@163.com, [c]zzcheerup@126.com, [d]1024420809@qq.com

Key words: Two Loop System; Simulation Software; GSE

Abstract. To study of Nuclear power simulation software's basic functions and mathematical model based on thermal analysis. Describes the two-phase flow model of GSE software superiority, as well as the software optimization program .Use of software tools for normal operating conditions of the simulation calculation and analysis of the results. Comparison with design data shows that,the software use in marine nuclear power two loop system simulation analysis field, the accuracy of it is higher.

Introduction

The simulation nuclear power system has become one of the essential supporting technology for nuclear technology applications in worldwide, currently[1].

There is a large coupling between nuclear-powered secondary-loop thermodynamic system and nuclear power plants primary system, when analyzing the operating characteristics of the system, the impact of the secondary-loop dynamic process of the reactor must be considered .Therefore, developing supporting dynamic simulation software for secondary-loop thermodynamic system above existing base has become an important job. Especially in terms of the marine nuclear power plant, affected by the limitations of hull dramatic and marine spatial arrangement of motor condition, relationship between security of nuclear power systems and secondary-loop thermodynamic system operating status are more close[2]. However, mainly of previous literature [3-5]are focus on the simulation research of steam generators, conventional thermal power plants, nuclear power plants, which can not well adapted to marine nuclear power two phase flow problems of secondary-loop thermodynamic system and rapid changes in load. Therefore, this paper analyzes the operation needs of marine nuclear power to study secondary-loop thermodynamic simulation of marine nuclear power systems.

Simulation object analysis

Affected by operating mode and operating environment, operating characteristics of the nuclear power plant is different from nuclear power plants and conventional power plants power system:

working conditions changes frequently and fast. Unlike secondary-loop of nuclear power plants, the marine nuclear power plant often in a load quickly transform state, which means a high degree of maneuverability. This requires a higher computing power simulation software and preciser models.

Dramatic changes in thermodynamic properties. Because of frequent conditions changing, thermodynamic properties of saturated steam is bound to dramatic changes, and soda alternating between the two phases process will more complicated. This requires to choose a more superior software, which has a better performance in two-phase flow calculation.

Diversity device. Marine secondary-loop system includes types of turbines, heat exchangers, steam separator, steam-driven pumps, electric pumps, valves, safety valves, check valves, piping and other equipment parts, different devices require different mathematical models were established, in

the simulation process, control program must be use on some equipment to achieve start, run, stop, and convert Instruction among different operating conditions.

The above issues describes the special problems of marine secondary-loop system simulation .It can be seen, the previous common software can not meet the simulation requirements of marine nuclear power secondary-loop system. In this paper, GSE simulation platform were selected for simulation study of marine secondary-loop system against the above problem.

Simulation Model

Basic equation.

Establishing the conservation equations for vapor and liquid phases on the base of the mass conservation equation, momentum conservation equation and energy conservation equation.

Mass conservation equations. For a period of closed pipe flow, it can give continuity equation:

$$A\frac{\partial(\alpha\rho)_{\mathrm{n}}}{\partial t}+\frac{\partial F_n}{\partial Z}=\sum\frac{\partial F_{bn}}{\partial Z}+\frac{\partial \Gamma_{\mathrm{n}}}{\partial Z}. \tag{1}$$

In the formula,A——a fluid flow area,m^2;α——fluid as described in the proportion of the total mass of gas and liquid;ρ——fluid density, kg/m^3;F_n——Fluid flow, kg/s;F_{bn}——source term,which represents the mass flow of the software boundary, kg/s.

Momentum conservation equation. In order to describe the relationship between pressure and branch node traffic,slip resistance characteristics is very important..Resistance characteristics described by the momentum equation:

$$p_i-p_j+p_{gr}=\frac{F_f^{\,2}}{a\rho}. \tag{2}$$

In the formula,P_i——upstream pressure, Pa;P_j——downstream pressure, Pa;P_{gr}——gravity head, Pa;F_f——fluid flow, kg/s;α——a constant related to geometry and roughness of the pipe.

Energy conservation equation. In this model,the gas and liquid energy balance is calculated separately in each node.Energy in the form of ordinary differential equations by the following formula:

$$\frac{d(M_f h_f)}{dt}=\sum h_{f,in}F_{f,in}-\sum h_{f,out}F_{f,out}+\Gamma_f h_{f,sat}+\dot{Q}_f-W_{shaft}. \tag{3}$$

In the formula,M_f——the working fluid mass node, kg;h_f——the working fluid enthalpy node, kJ/kg;$h_{f,in}$——node inlet fluid enthalpy, kJ/kg;$F_{f,in}$——node inlet fluid flow, kg/s;$h_{f,out}$——node outlet fluid enthalpy, kJ/kg;$F_{f,out}$——node exit fluid flow, kg/s;Γ_f——fluid mass change due to evaporation and condensation caused, kg/s;$h_{f,sat}$——saturation enthalpy, kJ/kg;Q_f——heat exchange with the outside node, kJ/s;W_{shaft}——turbine shaft work, which is calculatedin the turbine module, kJ/s;

Turbine Power. Turbine was made a node processing treatment,using the node instead of turbine inlet, exhaust and various extraction point. The fluid flow channel between the turbine stage and the flow line extraction node are included in the fluid network steam system.It can be calculated as the turbine shaft work,through analyzing dimensionless parameter in turbine design.

Turbine can be divided into two parts to calculate,the first part applied to calculate the power which generated by the steam impacting the steam turbine blade ,calculated as follows:

$$W_v=K_{t1}\frac{F_v}{\rho_{in}}(P_{in}-P_{out})^{K_{t2}}. \tag{4}$$

In the formula,W_v——power of superheated steam acting on the turbine blades,W;K_{t1}——turbine constant;F_v——steam mass flow rate, kg/s;ρ_{in}——entrance vapor density, kg/m^3;P_{in}——inlet steam pressure,Pa;P_{out}——outlet steam pressure, Pa;K_{t2}——turbine constant.

The second part can be considered the work have been done on the steam by turbine blades when turbine states in low load or no load.

$$W_{blade} = K_{t3}\rho_{out}N_{shaft} . \quad (5)$$

In the formula,W_{blade}——the work have been done on the steam by turbine blades when turbine states in low load or no load.W;K_{t3}——turbine constant.J.m^3/k； ρ_{out}——outlet vapor density, kg/m^3;N_{shaft}——turbine speed,r/m.

The total shaft power of the turbine:

$$W_{shaft} = W_v - W_{blade} . \quad (6)$$

$$W_{shaft} = K_{t1}\frac{F_v}{\rho_{in}}(P_{in} - P_{out})^{K_{t2}} - K_{t3}\rho_{out}N_{shaft} . \quad (7)$$

In the formula,W_{shaft}——turbine shaft work, W.

Two-phase heat transfer. Vapor-liquid heat flow at the interface of two intersecting can use the following formula:

$$Q_I = \frac{A_I h_{Ig}\frac{k_I}{X_o}}{\frac{k_I}{X_o} + h_{Ig}}(T_l - T_g) . \quad (8)$$

In the formula,A_I——interfacial heat transfer area, m^2;h_{Ig}——interfacial heat transfer coefficient,kW/(m^2.K)T_{Ig}——interface temperature, K;T_g——gas temperature, K;k_I——the thermal conductivity of the interface,kW/(m.K);X_o——Interface thickness, m;T_l——Liquid temperature, K.Where the thickness of the interface is assumed to be constant.

The simulation model and simulation results

Figure 1 is the nuclear-powered secondary-loop simulation interface which was established on GSE simulation platform for this paper.

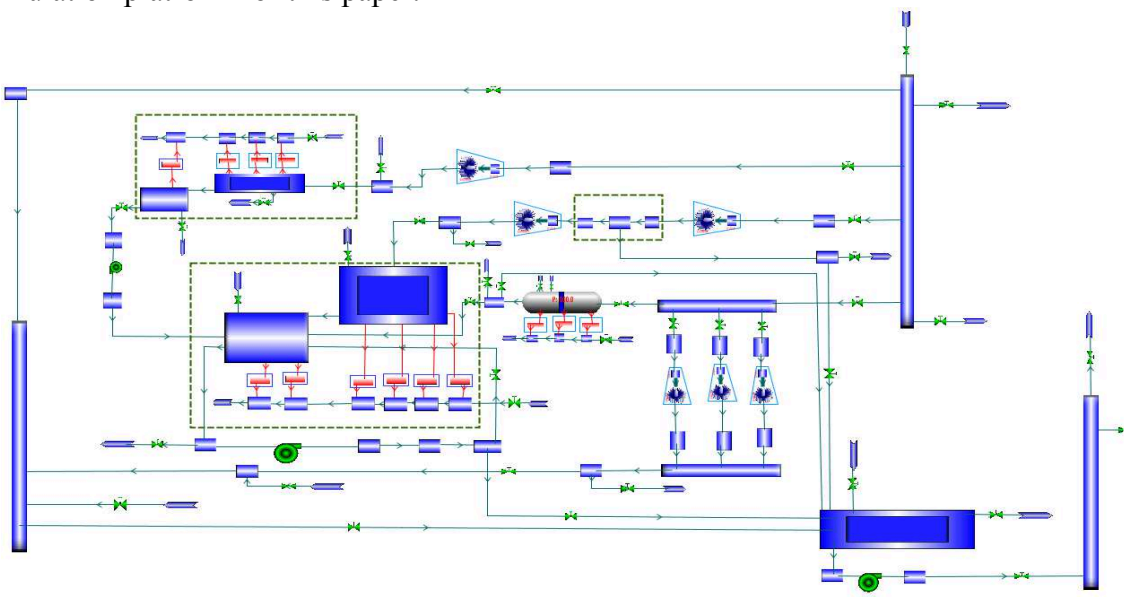

Fig 1 GSE marine nuclear power secondary-loop simulation model

According to the function of each part,The whole system is divided into three subsystems:main steam system, condensate system and feed water pipe systems.Where the main steam system is part of thermal power conversion system in the secondary-loop.The steam turbine into mechanical energy

and thermal energy in this part;The steam condensate system can cooled exhaust steam into liquid after working,which is an important guarantee for implementing system cycle; Feed-water pipe system can pump condensate water into the steam generator.

Table 1 shows the main parameters of the simulation results contrast with the design value when the model runs at full load.By contrast,it can be indicated that the model has well accuracy.

Table 1 The main parameters of the simulation errors

Main turbine							Main condenser
	High pressure turbine		Low pressure turbine				
	Inlet pressure	Inlet temperature	Inlet pressure	Inlet temperature	Outlet pressure	Outlet temperature	Pressure
Errer (%)	0.019	0.011	1.086	0.622	0.121	2.759	0.714
	Power Turbine				Deaerator	Mother pipe exhaust steam	Steam supply main pipe
	Inlet pressure	Inlet temperature	Outlet pressure	Outlet temperature	Pressure	Pressure	Pressure
Errer (%)	0.031	0.006	1	3.43	1.6	0.85	0.023

Summary

By comparing the simulation data with the design data, the models created by the software can better meet the needs of marine nuclear power secondary-loop simulation, both a high accuracy.This suggests that GSE simulation platform can meet the requirements of marine nuclear secondary-loop simulation.

Acknowledgement

This work was supported by Natural Science Foundation of Heilongjiang Province of China (E201346).

References:

[1] GUO liang,SUN baozhi,Based on C + + Builder nuclear power plant two loop thermodynamic system modeling and real-time simulation,J.Electric Power Construction.34(2013)1-4.

[2] Zhang yangwei,Cai qi,Cai zhangsheng,Marine Nuclear Power Simulation on two circuits,J.Atomic Energy Science and Technology.42(2008)177-179.

[3] Futao Zhao, Jing Ou , Wei Du,Simulation modeling of nuclear steam generator water level process—a case study,J.ISA Transactions.39(2000)143-145.

[4] Young Joon Choi,Hyun Koon Kim,Won Pil Baek,Soon Heung Chang,Hybrid accident simulation methodology using artificial neural networks for nuclear power plants,J.Information Sciences.160(2004)207–215.

[5] Chung-YuYang,L.C.Dai,ThomasK.S.Liang,B.S.Pei,C.K.Shih,L.C.Wang,S.C.Chiang,ABWR power tests simulation by using a dual RELAP5 nuclear power plant simulation platform,J.Nuclear Engineering and Design.249(2012)41-48.

Advanced Materials Research Vol. 983 (2014) pp 292-299

doi:10.4028/www.scientific.net/AMR.983.292

Transformer Impedance Determination for Power System Studies of Distribution Network integrated with Renewable Energy Resources

Jun Huat Tang[1, a], Mohammad Zamri Che Wanik[1], A.M. Busrah[1], A.K.M. Hussin[1]

[1]TNB Research Sdn. Bhd Selangor, Malaysia

[a]tangjunhuat@tnbr.com.my

Keywords: Transformer impedance, renewable energy, power system study, distribution network

Abstract. This paper presents a guideline of determining impedance of transformer when conducting system study for renewable energy interconnection. The method can be used when there is lack of information on the transformer's technical details. Simulation examples are presented to demonstrate the effect of impedance on the losses and short circuit current. The guidelines introduce in this paper will increase reliability and accuracy of the system study conducted by engineer and researchers in assessing the possible impact renewable energy integration.

I. Introduction

In Malaysia, as dictate by the Malaysian distribution code [1], before any RE plant to be connected to the distribution network, preliminary and power system study is required. Among the issues investigated in the preliminary study are network voltage profile, system adequacy, system losses and short circuit studies. In addition, the study will also determine the basic requirement for the interconnection. After preliminary study, power system study is conducted. Among the objectives are to identify additional controls and protections and operating strategies of the RE plant when it is connected to distribution network [2].

One of the challenges in performing preliminary and power system study is to get the accurate parameter and information. For example, power transformer modeling required impedance value which includes resistance, R and reactance, X. However, the values are not normally directly available on the transformer's nameplate. Eventhough for large transformer more than 500 kVA, the resistance value can be neglected because the value is very small compared to the reactance [3-4]. However, this method reduced the accuracy of power system study.

Transformer impedance is defined as the voltage drop under full load due to the winding resistance and leakage reactance. The system losses and fault levels are greatly affected by the impedance where low impedance will lead to high fault level and vice versa.

This paper provides a guideline of determining the impedance of transformer for conducting power system study when there is lack of information on the transformer's technical details. The paper is organized in the following manner. Section II describes the details of ideal and practical transformer, modeling, vector group and resistance and reactance determination. The results of the simulation studies include fault level, power losses and voltage variation are illustrated and discussed in Section III. Section IV presents the conclusion of the studies.

II. Transformer

a. Ideal transformer

For an ideal transformer, it is assumed that the windings have zero resistance, core permeability is infinite, no leakage flux and no core losses [3]. Fig. 1 shows the equivalent circuit of the ideal transformer. The voltage and current induced in the secondary winding from the primary winding are given by the equation:

$$\frac{N_s}{N_p} = \frac{V_s}{V_p} = \frac{I_p}{I_s} \tag{1}$$

where N_p and N_s are number of winding turns at primary and secondary, respectively, V_p is the primary voltage, V_s is the secondary voltage, I_p is the primary current and I_s is the secondary current.

b. Practical transformer

A practical transformer operating under the sinusoidal steady state is equivalent to an ideal transformer with additional impedance and admittance. Practically, short circuit test is carried out to find the equivalent resistance and reactance value. During the short circuit test, secondary winding is shorted out and voltage applied to the primary winding until a full load current is obtained, the voltage measured is the open circuit voltage. Open circuit voltage is normally stated on the transformer nameplate, and it is equivalent to the transformer impedance.

Fig. 2 shows the equivalent circuit of a non-ideal transformer with the impedance shifted to the primary side. The R_s and X_s referred to the primary side of the following equation:-

$$R_{s\,new} = \left(\frac{N_p}{N_s}\right)^2 \times R_{s\,old} \tag{2}$$

$$X_{s\,new} = \left(\frac{N_p}{N_s}\right)^2 \times X_{s\,old} \tag{3}$$

where $R_{s\,new}$ and $X_{s\,new}$ are the resistance and reactance refer to the primary side, respectively whilst $R_{s\,old}$ and $X_{s\,old}$ are the resistance and reactance value at the secondary side, respectively.

The total resistance and reactance refer to transformer primary side are shown in the Eq.4 and Eq.5, respectively. Eq.6 shows the combination of R and X constitutes the total transformer impedance, Z.

$$R = R_p + R_{s\,new} \tag{4}$$

$$X = X_p + X_{s\,new} \tag{5}$$

$$Z = \sqrt{R^2 + X^2} \tag{6}$$

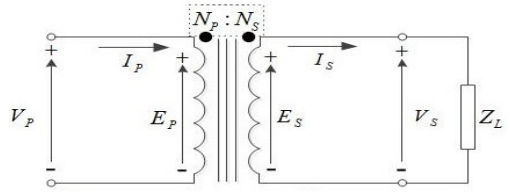

Figure 1. Equivalent circuit of an ideal transformer.

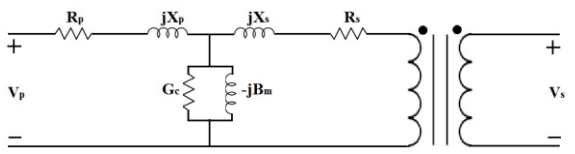

Figure 2. Equivalent circuit of the practical transformer with an impedance shifted to the primary side.

c. Transformer parameter in modeling

In performing power simulation study, accurate parameters are important to make sure the accuracy of the simulation results. Fig. 3 and Fig. 4 show the input parameters required to for transformer models in PSS/ADEPT and DIgSILENT PowerFactory, respectively. Both are well-known and commercially available power system analysis tools. The red box in the Fig. 3 and Fig. 4 show the parameter required for modeling but the information is not available on the transformer nameplate. They are R and X value or X/R ratio as well as the transformer phase angle displacement in degree.

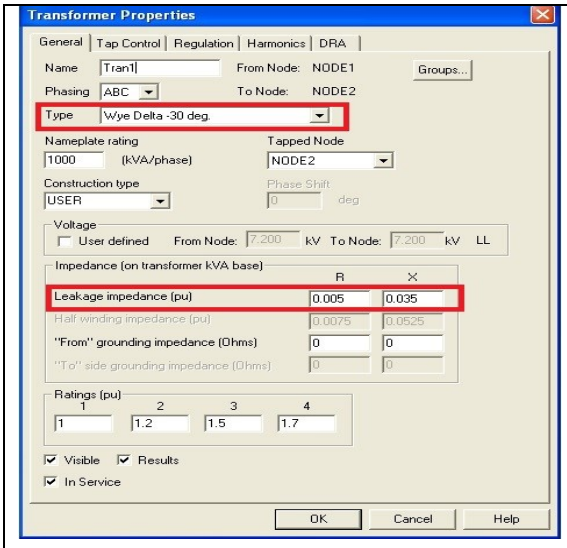

Figure 3. PSS/ADEPT transformer modeling required parameter.

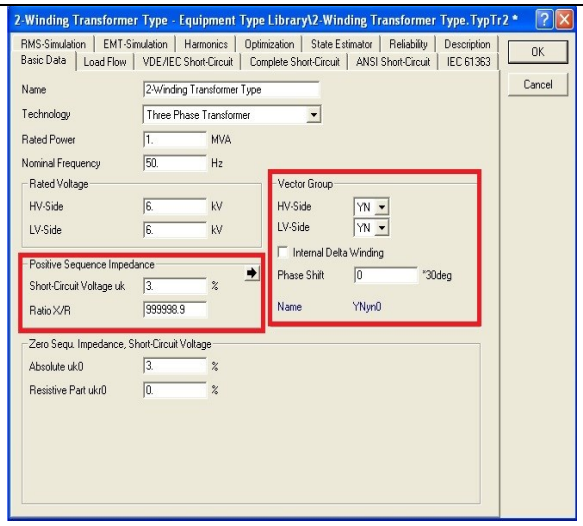

Figure 4. DIgSILENT PowerFactory transformer modeling required parameter.

d. Transformer vector group

Transformer winding can be connected in several ways. Besides than the winding connection, vector group which indicates the phase difference between the primary and secondary sides is also important in transformer modeling. The vector group is important if more than one transformer is going to be operated in parallel. If transformers operating in parallel are not belongs to the same vector group, current will circulate in between both transformer and caused overheating.

Normally, information on the winding connection and vector group are available from the transformer nameplate, e.g. Yd1. The first letter (normally in capital letter) shows the connection in primary winding, whilst the second character (in small letter) shows the winding connection on the secondary side. The number follows by the primary and secondary winding connection indicates the vector group of the transformer [5]. Table 1 shows the phase angle displacement in degree as refer to the number.

TABLE 1. PHASE ANGLE DISPLACEMENT IN DEGREE

Number	Phase angle displacement in Degree	Number	Phase angle displacement in Degree
0	0	6	Lagging 180 or -180º
1	Lagging 30 or -30º	7	Leading 150 or +150º
2	Lagging 60 or -60º	8	Leading 120 or +120º
4	Lagging 120 or -120º	10	Leading 60 or +60º
5	Lagging 150 or -150º	11	Leading 30 or +30º

e. Resistance and reactance value

In the simulation study, R and X value or ratio is required to model a transformer. But this information is not available in the transformer nameplate. This paper provide a guide for estimation method from IEEE standard C37.010-1979 as shown in Fig. 5 to obtain the X/R ratio base on the transformer rating in MVA [6].

After estimating the X/R ratio, R and X value can be calculated based on the following equation:-

$$\frac{X}{R} = \alpha \tag{7}$$

and

$$X = R\alpha \tag{8}$$

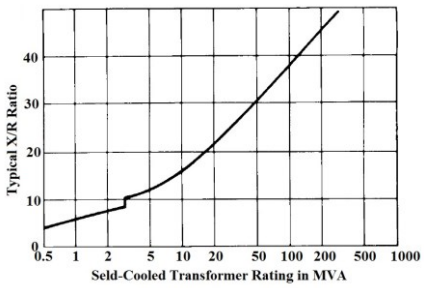

Figure 5. *X/R* ratio of a transformer based on IEEE Std C37.010-1979.

Open circuit voltage indicate in the transformer nameplate are equal to the transformer impedance, Z in Eq.6.

By substituting Eq.8 into Eq.6,

$$Z = \sqrt{R^2 + \alpha^2 R^2} \tag{9}$$

$$Z = \sqrt{(\alpha^2 + 1)R^2} \tag{10}$$

$$R = \sqrt{\frac{Z^2}{(\alpha^2 + 1)}} \tag{11}$$

Once the *R* value is calculated, *X* value can be calculated by Eq.8. In general, for the two winding transformer both the positive and zero sequence transformer impedance are equal. The exception is where there is a grounding impedance in a Wye connected winding. In this case, the zero sequence impedance is equal to the positive sequence impedance multiplied by four. If a Wye connected winding is not grounded, the zero sequence impedance is set to a very high value, e.g., 100 per unit [7].

f. Per unit system

Per unit values simplify the analysis of complex power system by converting all values to values referred to one base parameter. Thus instead of dealing with ohms, ampere, volts and watts, there is only one normalized unit available. Per unit values is usually used in transformer modeling because per unit values for transformer impedance, voltage and current are identical when referred to the primary and secondary. Per unit value are calculated as follows:-

$$Per\ unit\ value = \frac{Actual\ value}{Base\ value} \tag{12}$$

The base value for the transformer is calculated by the formula (13).

$$Z_{base} = \frac{(V_{base})^2}{S_{base}} \tag{13}$$

where Z_{base} is the transformer base value, V_{base} is transformer base voltage in kV and S_{base} is transformer rating in MVA. With *Z* base value from Eq.13 and the actual value, then per unit value can be calculated. After per unit impedance is known, per unit value of resistance and reactance can be determined by using Eq.6.

The transformer has major influence on the short-circuit contribution of the DG generation to the distribution network and therefore its parameters particular positive and zero sequence impedances must be reasonably modeled. Table 2 shows the minimum transformer impedance values based on

requirement of IEC 76 standard [8]. Table 3-5 show the typical transformer resistance, losses and magnetization. Figure 6 shows the relationship between transformer losses and size.

TABLE 2. MINIMUM TRANSFORMER IMPEDANCE

Transformer Rating (KVA)	Minimum +ve Sequence Impedance (%)
0 to 630	4
631-1,250	5
1,251-3,150	6.25
3,151-6,300	7.15
6,301-12,500	8.35
1,2501-25,000	10
25,001-200,000	12.5

TABLE 3. PERCENTAGE RESISTANCE, IDLE CURRENT[18]

Transformer	S_n/MVA	R_{ps}/%	Z_{ps}/%	I_l/%
Local network	0.1-1.6	2.3-1	3.8-6	3.2-1.3
Medium voltage network	2.5-25	1-0.5	7-8.5	1.4-0.8
110kV high voltage	16-63	0.7-0.6	12	1.25-0.9
220kV high voltage	100-250	0.5-0.3	11-14	<1.0
380 High voltage	630-1000	≈<0.2	10-16	<1.0

TABLE 4. IRON AND WINDING LOSSES OF TRANSFORMER[18]

S_n/MVA	Obersp. Wick-kV lung	P_v/S_n/%	P_R/S_n/%	P_R/P_v
0.1-1.6	6-30 Al	0.4-0.2	2.3-1	6-5
2.5-10	10-30 Al	0.25-0.14	1.0-0.6	4.0
16-25	10-30 Al	0.15-0.1	0.6-0.5	4-5
16-63	110	0.15-0.1	0.7-0.26	4.6-6
100-250	220	0.12-0.1	0.5-0.3	4-3
630-1000	380	<0.05	0.22	>4

TABLE 5. MAGNETIZATION[18]

Transformer	Q_u/S_n/%	Q_x/S_n/%	Q_x/Q_u
Local network	3.2-1.3	3.8-6	1.2-4.6
Medium voltage network	1.4-0.8	7-8.5	5-10
110kV high voltage	1.25-0.9	12	10-13
220kV high voltage	<1.0	11-14	>10
380 High voltage	<1.0	10-16	>10

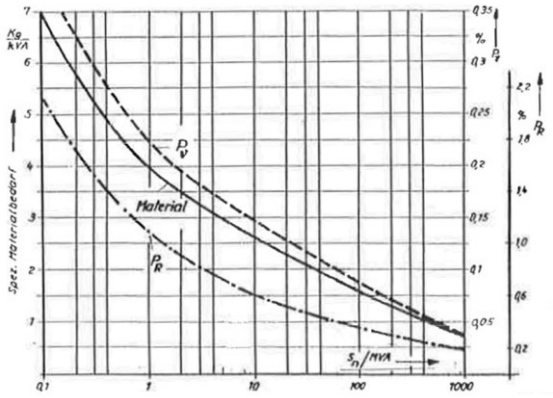

Figure 6. Relationship between losses and transformer size[18].

III. Simulations result

In order to demonstrate how transformer parameters affect the accuracy of simulation result, a few simulations are performed in PSS/ADEPT simulation software. Fig.7 show a simplified typical radial distribution network modeled in PSS/ADEPT. A transformer rated at 3 MVA 33/11kV, Yd1 is used to step down the voltage from the grid to feed the load at downstream. On load tap changer (OLTC) on the high voltage (HV) side provide voltage regulation on Wye connection. The phase displacement of the transformer is -30^{o}. For the fault level study, a three phase to ground fault at Bus_11 kV is applied. Three phases to ground fault is used because it contribute to the most severe fault current. , All the equipment such as transformer and circuit breaker must be able to sustain this fault current. The three phase load is balanced with total of 300kW.

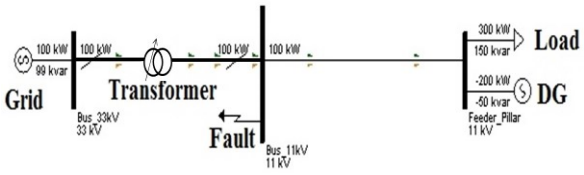

Figure 7. Radial distribution network with DG.

a. Fault Current

Fault level study in the preliminary step of planning helps engineers to determine the suitable equipment rating and also protection relays setting to ensure the reliability and security of the distribution network operation. Fig. 8 show the relationship between fault current and transformer resistance value at the primary winding. These results show that the fault current reduced gradually when the transformer resistance increase. In this case, if the transformer resistance is assumed to be zero (neglected) during the planning or power system studies, this will reduce the sensitivity of the protective relays, or malfunction of the protective devices. The malfunction of protection devices may cause severe damage, increase repairing cost and danger to the public.

In addition, neglecting the resistance value during transformer modeling may lead to the over-sizing of the equipment. Fig. 8 shows that the three phases to ground fault current is approximately 534 A when the transformer resistance is 5 mΩ, while fault current increase to 541 A if the transformer resistance is neglected. This will increase the investment cost indirectly and hence reduce the organization's profit margin.

Fig. 9 shows the fault current at the transformer secondary winding with neglected and actual winding resistance. Results show that the fault level is lower when actual resistance value is used in the transformer model. Besides, the results show that the fault current from the grid reduce when the DG capacity increase.

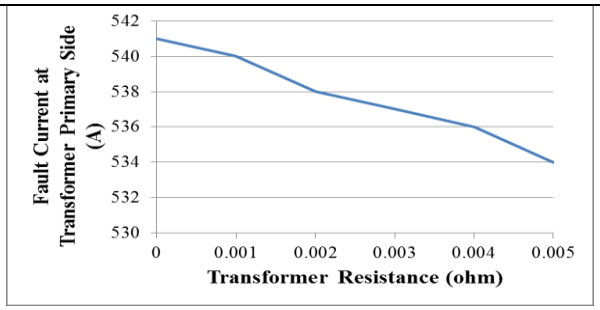

Figure 8. Relationship between fault current and transformer resistance value.

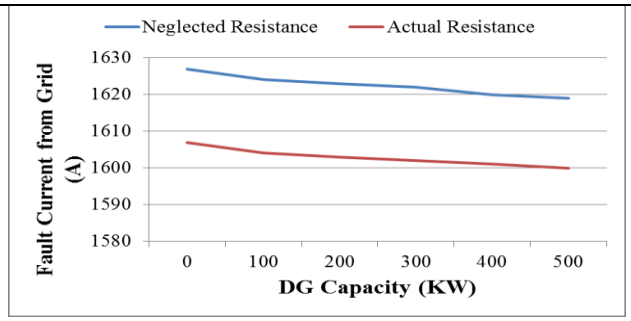

Figure 9. Relationship between fault current with neglected and actual transformer resistance.

b. Power losses

The transformer should be correctly modeled in the power system analysis tool in order to make sure the simulation studies are valid and conform to the real world situation. Fig. 10 shows the transformer losses increase proportionally with the increase of transformer resistance. The iron losses, I^2R increase when the resistance value increase. Even though the resistance value of the modern transformer is very small compared to the reactance, but the small resistance value will also cause the power losses. In the power system study that focuses on the network power losses, transformer resistance should not be neglected.

Total power losses in the radial distribution network with actual and neglected transformer winding resistance are different shown in Fig. 11. The power losses increase if the actual transformer winding resistance is included in the simulation. Furthermore, it is noticed that the DG integration have reduced the total network losses. The power losses without DG is higher than the network with DG installed.

The power loss curve has a U shape with respect to DG capacity. This is because, when the generated power of DG is less that the load demand, the network power losses have a descending trend, whereby the local load supplied by the DG instead of being supplied from utility transmission and distribution system. Power losses are at minimum when the DG generation matched the local load demand. When the DG generation power is more than the demand, network losses increase due to the reverse power flow.

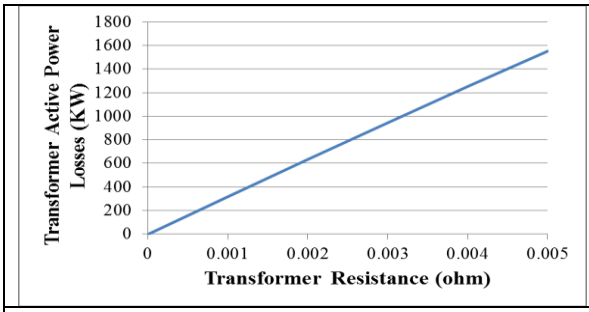

Figure 10. Transformer losses versus resistance.

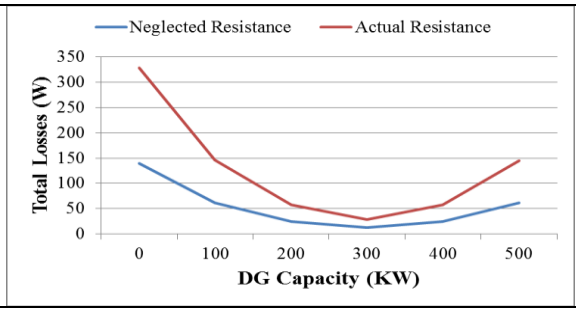

Figure 11. Total network losses with neglected and actual resistance.

c. Voltage magnitude

Power utility companies are responsible to maintain the voltage level within the statutory limit. Voltage drop along the line due to the resistance. During the planning, engineers have to make sure that the voltage magnitudes are within the allowable limit even at the end of the long feeder. Before this, the supply voltage must be maintained so that the voltage levels at the end of the feeder are

well within the limit. Fig. 12 shows the transformer secondary voltages reduce with the increase of winding resistance. But the internal voltage drop is minimal.

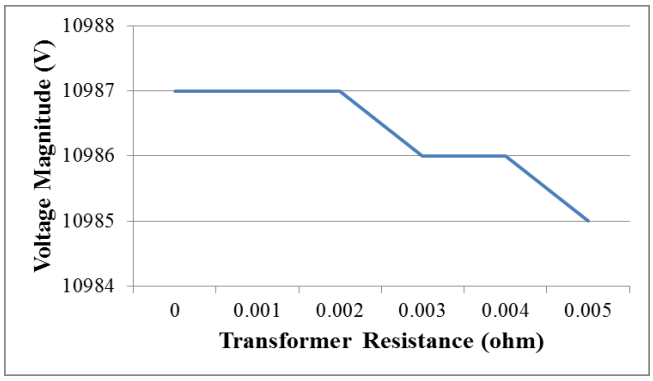

Figure 12. Secondary voltage magnitude versus transformer resistance.

IV. Conclusion

Accurate transformer technical data is important in preliminary and power system study. With the limited information on the transformer, this paper provides a guideline of determining parameter of transformer. Typical resistance, impedance, vector group and per unit system are discussed and presented. The effect of different transformer impedance on system fault level, power losses and voltage magnitude are presented. Simulations results show that, impedance of transformer have significant effect on the study results. Neglecting the resistance value during the power system study will affect the accuracy of the conducted study.

V. Reference

[1] Ahmad Johari Jaafar, “The Malaysian grid code,” Suruhanjaya Tenaga, 2010.

[2] Tenaga Nasional Berhad, 2005. *Technical Guidebook for the Connection of Generation to Distribution Network*. Tenaga Nasional Berhad.

[3] J. Duncan Glover and Mulukutla S. Sarma, *Power system analysis and design*, 3rd ed. USA: Wadsworth Group, 2002.

[4] Theodore Wildi, *Electrical machines, drives, and power systems*, 6th ed., 2005.

[5] Jignesh Parmar. (2013, July) Electrical Notes & Articles. [Online]. HYPERLINK “http://electricalnotes.wordpress.com/2012/05/23/vector-group-of-transformer/” http://electricalnotes.wordpress.com/2012/05/23/vector-group-of-transformer/

[6] IEEE Recommended Practice for Electric Power Distribution for Industrial Plants," *IEEE Std 141-1993* , vol., no., pp.1,768, April 29 1994

[7] Power Technologies, "PSS/ADEPT-4," New York, User Manual 2002.

[8] Habil.H.Pundt & P.Schegner, 1997. *Electrostatic Energy System*. Technical University of Dresden.

Advanced Materials Research Vol. 983 (2014) pp 300-306

doi:10.4028/www.scientific.net/AMR.983.300

Translational-Rotational Motion of Earth Artificial Satellite (EAS) in Hill's Gravity Field

Astemessova Kalamkas[1,a], Bekov Askar[2,b], Shinibaev Maksut[2], Ussipbekova Dinara[1]

[1]Republic of Kazakhstan, Almaty, 22 Satpaev Street, Kazakh National Technical University after K.I. Satpayev
[2]Republic of Kazakhstan, Almaty, 15 Shevchenko Street, Joint Stock Company "National Center of Space Researches and Technologies".
[a]naucha@mail.ru, [b]bekov@mail.ru
*Astemessova Kalamkas

Keywords: Hill's gravity field, proofmass, a function of time, the Moon, Moon motion theory.

Abstract. The method presented below makes it possible to obtain an approximate solution to the problem of translational-rotational motion of proofmass in Hill's gravity field, as explicit functions of time.

Introduction

The problem of studying the Moon's motion attracted and keeps attracting attention of many researchers [1-6]. In course of creating the theory of the Moon's motion, G.V. Hill suggested two methods of building the intermediate orbit of the Moon. [7] The first method was described in works published in 1878-1886 [8].

The dynamic meaning of the problem was in the following simplifications:

1) The Sun moves away to an infinite distance.

2) Simultaneously increasing its mass infinitely.

3) In the relative geocentric motion, the Sun moves along Kepler's circular orbit.

Based on this formalization, Hill replaced the power function of an exact 3 bodies problem with a simplified one.

This method of building an intermediate orbit was subsequently used in 1908-1909 by E.V. Brown in order to finalize building of a complete analytical theory of lunar motion.

The second method of building an intermediate orbit of the Moon was proposed in 1897, and was subsequently called by B.M. Schigolev [9] "the second intermediate Hill's orbit".

Here Hill considers it necessary that the intermediate orbit contains perigee and ascending node secular movement.

To this end, he proposed a simplified power function of the following form

$$U = \frac{\mu}{r} + \frac{1}{2}\nu r^2 + \frac{1}{2}(\nu' - \nu)z^2, \qquad (1)$$

here μ is the product of multiplying gravitational constant by the sum of the Earth and the Moon masses; ν and ν' are properly selected constant multipliers.

If the perturbing and the perturbed bodies are on the same side from the central body, then (1) corresponds to reality and gives a good approximation.

The defect occurs when the perturbing and the perturbed bodies are on opposite sides of the central body, but it is mitigated by the fact that the Sun at this point is far away from the Moon.

Differential equations of proofmass orbital motion in Hill's variables

In Hill's problem, the Moon is considered a passively gravitating body, and the central body is Earth, the perturbed body is the Moon and the perturbing body is the Sun, i.e., the Moon's motion is considered in the "Earth-Moon-Sun" system.

In our problem, we consider orbital motion in the "Earth - proofmass- Moon" system, and the proofmass, AES model, is considered as the passively gravitating body.

In the *Oxyz* geocentric coordinate system, differential equations of proofmass orbital motion have the form

$$\left.\frac{d^2x}{dt^2}+\frac{\mu x}{r^3}=vx,\quad \frac{d^2y}{dt^2}+\frac{\mu y}{r^3}=vy,\quad \frac{d^2z}{dt^2}+\frac{\mu z}{r^3}=v'z.\right\} \tag{2}$$

They allow the area integral

$$x\frac{dy}{dt}-y\frac{dx}{dt}=C \tag{3}$$

and the energy integral

$$\left(\frac{dx}{dt}\right)^2+\left(\frac{dy}{dt}\right)^2+\left(\frac{dz}{dt}\right)^2=2(U+h)\,, \tag{4}$$

whereas C is the area integral constant, h is the energy integral constant.

In Hill's variables, equations (2) take the form:

$$\frac{d^2w}{d\upsilon^2}+\left(1+\frac{\alpha}{w^4}\right)w-\frac{1}{(1+s^2)^{3/2}}=0\,, \tag{5}$$

$$\frac{d^2s}{d\upsilon^2}+\left(1+\frac{\beta}{w^4}\right)s=0,\quad \frac{d\upsilon}{dt}=\frac{\rho^2}{C}\,, \tag{6}$$

whereas

$$\frac{1}{\rho}=w\frac{\mu}{C^2}\,,\ \alpha=\frac{vC^6}{\mu^4}\,,\ \beta=\frac{(v-v')C^6}{\mu^4}\,, \tag{7}$$

here: ρ is the projection of radius-vector $\bar{r}$ on the Oxy plane, υ is true longitude, s - is latitude tangent, $\alpha,\beta-const$, w is Hill's variable.

If we restrict ourselves to the orbits of small inclination to the Oxy plane, $s\neq 0$, $s^2\approx 0$, then (5) allows reduction approximately

$$d\upsilon=\frac{wdw}{\sqrt{\alpha+Hw^2+2w^3-w^4}}\,, \tag{8}$$

whereas H is the constant of integration defined by the relation

$$H=\frac{2hC^2}{\mu^2}\,. \tag{9}$$

Changing constants and H, we obtain the following classification of types of motion:α

I. Rectilinear motion, H = 0. $\alpha=0$

II. Parabolic motion. $\alpha>0, H=0$

III. Elliptic motion. $\alpha>0, H<0$

IV. Hyperbolic motion. $\alpha>0, H>0$

Integrating differential equations (5) and (6) in case of elliptic motion

This case corresponds to the following parameters values $\alpha>0, H<0$.

Equation (8) takes the form

$$d\upsilon=\frac{wdw}{\sqrt{-w^4+2w^3-Hw^2+\alpha}}\,. \tag{10}$$

Subradical polynomial has three positive $\ell 1$, $\ell 2$, $\ell 3$ and one negative $\ell 4$ roots. Let's arrange them in descending order

$$\ell_1>\ell_2>\ell_3>\ell_4\,.$$

For actual movements, the subradical polynomial must be positive. Previously, in [10] it was found that it is positive within two intervals

A) $\ell_4 < w < \ell_3$, B) $\ell_2 < w < \ell_1$.

Next, let's look at the first of motion intervals. In the interval $\ell_4 < w < \ell_3$, the following transformation of expression (9) to the Legendre's normal form [11] is valid.

$$d\vartheta = \frac{w \cdot dh \cdot \mu^*}{\sqrt{1 - k^2 \sin^2 h}}, \tag{11}$$

whereas

$$w = \frac{\ell_4 \ell_{31} + \ell_1 \ell_{43} \sin^2 h}{\ell_{31} + \ell_{43} \sin^2 h}, \quad \ell_{ik} = \ell_k - \ell_i, \ (i,k = 1,2,3,4), \tag{12}$$

With $\ell_4 = w,\ h = 0,\ \ell_3 = w,\ h = \frac{\pi}{2},\ k^2 = \frac{\ell_{43}\ell_{12}}{\ell_{13}\ell_{42}},\ 0 < k < 1,\ \mu^* = \frac{2}{\sqrt{\ell_{31}\ell_{42}}}$, k is the module of elliptic integral of the 1st kind, h is an intermediate variable: $0 < h < \frac{\pi}{2}$.

Let's introduce into (10) and (11) Jacobian functions and use standard developments [12], then, keeping in developments by powers of $O(k^3)$ the module of elliptic integral of the 1st kind, we have the following expressions for ρ, υ, w, u:

$$\rho = (\rho_{00} + k\rho_{01} + k^2\rho_{02}) + (k\rho_{11} + k^2\rho_{12})\cos\frac{\pi}{K}u + k^2\rho_{22}\cos\frac{2\pi}{K}u, \tag{13}$$

$$\upsilon = \mu^*\left[(w_{00} + kw_{01} + k^2 w_{02})u + \frac{K}{\pi}(kw_{11} + k^2 w_{12})\sin\frac{\pi}{K}u + \frac{K}{2\pi}k^2 w_{22}\sin\frac{2\pi}{K}u\right], \tag{14}$$

$$w = (w_{00} + kw_{01} + k^2 w_{02}) + (kw_{11} + k^2 w_{12})\cos\frac{\pi}{K}u + k^2 w_{22}\cos\frac{2\pi}{K}u, \tag{15}$$

whereas K is the complete elliptic integral of the 1st kind,

$$u = (u_{00} + ku_{01} + k^2 u_{02})t + (ku_{11} + k^2 u_{12})\sin\frac{\pi}{K}t + k^2 u_{22}\sin\frac{2\pi}{K}t + k^2 u_{32}t\cos\frac{\pi}{K}t, \tag{16}$$

whereas t is time. Constant coefficients $\rho_{ij}, w_{ij}, u_{ij}$ are written in [13].

Expressions (12) and (13) define polar coordinates ρ, υ via (15) as explicit functions of time for the proofmass in interval $\ell_4 < w < \ell_3$. The same method can be applied in interval $\ell_2 < w < \ell_1$

Rotational motion of the proofmass relative to the center of mass in case of $A = B = mC$

Let the proofmass be fixed in the center of mass $x_C = y_C = z_C = 0$ and the main moments of inertia be related via $A = B = mC$, $m - const$, then the full set of differential equations shall have form [13]:

$$\frac{dp}{dt} + nqr_0 = \varepsilon n\gamma'\gamma'', \ \frac{dq}{dt} + npr_0 = -\varepsilon n\gamma\gamma'', \ \frac{dr}{dt} = 0, \ r_0 - const, \tag{17}$$

$$\theta = \arccos\gamma'', \ \gamma = \sin\varphi\sin\theta, \ \gamma' = \sin\theta\cos\varphi, \ \gamma'' = \cos\theta, \tag{18}$$

$$\varphi = \operatorname{arctg}\left(\frac{\gamma}{\gamma'}\right), \ \dot{\psi} = \frac{p\gamma + q\gamma'}{1 - \gamma''^2}, \ n = \frac{1-m}{m}, \ \varepsilon = \frac{3\mu}{R^3}, \tag{19}$$

$$p = \dot{\psi}\gamma + \dot{\theta}\cos\varphi, \ q = \dot{\psi}\gamma' - \dot{\theta}\sin\varphi, \ r_0 = \dot{\psi}\gamma'' + \dot{\varphi}, \tag{20}$$

$$\frac{d\gamma}{dt} = r_0\gamma' - q\gamma'', \ \frac{d\gamma'}{dt} = p\gamma'' - r_0\gamma, \ \frac{d\gamma''}{dt} = q\gamma - p\gamma'. \tag{21}$$

Differential equations (17), (20) and (21) allow the following first integrals

$$p^2 + q^2 = C_1 - \varepsilon n\gamma''^2, \quad (22) \quad \gamma^2 + \gamma'^2 + \gamma''^2 = 1, \tag{23}$$

$$\gamma p + \gamma' q = C_2 - r_0(n+1)\gamma'', \quad (24) \qquad r = r_0 = const\ . \quad (25)$$

In these equations $\overline{\omega} = (p,q,r)$ is the gravitational constant, μ is the distance to the center of mass of the Earth, R is the normalized angular velocity vector; the fixed coordinates system $Cxyz$ is associated with the moving coordinates of the system $Cx'y'z'$ according to the following table:

Table 1. Moving coordinates of the system

	x'	y'	z'
x	α	α'	α''
y	β	β'	β''
z	γ	γ'	γ''

where $\alpha,\alpha'\alpha''$, $\beta,\beta'\beta''$, $\gamma,\gamma'\gamma''$ are direction cosines; φ,θ,ψ are Euler's angles.

Excluding from the first integrals and equation

$$p^2 + q^2 = \dot{\theta}^2 + \dot{\psi}^2(1-\gamma'^2)$$

values $p^2 + q^2\ \dot{\theta},\dot{\psi}$, we obtain

$$dt = \frac{1}{\sqrt{a_0}} \cdot \frac{d\gamma''}{\sqrt{\gamma''^4 + b_1\gamma''^3 + b_2\gamma''^2 + b_3\gamma'' + b_n}}\ . \quad (26)$$

Next, let's reduce (26) to Legendre's normal form [13]. Subradical polynomial is positive in two intervals:

$$1)\ \alpha_1 < \gamma'',\ \alpha_4 > \gamma''; \qquad 2)\ \alpha_3 \le \gamma'' \le \alpha_2\ .$$

Let's consider the second interval, arranging polynomial roots in descending order

$$\alpha_1 > \alpha_2 > \alpha_3 > \alpha_4\ .$$

In accordance with [7] we have here

$$\sqrt{a_0}\,dt = \mu_0 \frac{d\lambda}{\sqrt{1-k^2\sin^2\lambda}},\ k^2 = \frac{\alpha_{42}\alpha_{32}}{\alpha_{31}\alpha_{42}},\ 0 < k < 1, \quad (27)$$

$$\mu_0 = 2(\alpha_{31}\alpha_{42})^{-1/2},\ \ell_{ik} = \ell_k - \ell_i,\ (i,k = 1,2,3,4),$$

$$\gamma'' = \frac{\alpha_3\alpha_{42} - \alpha_4\alpha_{32}\sin^2\lambda}{\alpha_4 - \alpha_{32}\sin^2\lambda} \text{ with } \gamma'' = \alpha_3,\ \lambda = 0\ , \quad (28)$$

$$\text{with } \gamma'' = \alpha_2,\ \lambda = \frac{\pi}{2}.$$

Let's introduce notations $u = n_0 t$, $n_0 = \dfrac{\sqrt{a_0}}{\mu_0}$ and move from (27) to Jacobian elliptic functions.

From (28) let's find

$$\gamma'' = \overline{\alpha}_{00} + k^2\overline{\alpha}_{02} + k^2\overline{\alpha}_{12}\cos 2q + k^2\overline{\alpha}_{22}\cos 4q + k^2\overline{\alpha}_{32}\cos 6q,\ q = K_0 n_0 t\ , \quad (29)$$

consequently, the nutation angle is:

$$\theta = \arccos[\overline{\alpha}_{00} + k^2\overline{\alpha}_{02} + k^2\overline{\alpha}_{12}\cos 2q + k^2\overline{\alpha}_{22}\cos 4q + k^2\overline{\alpha}_{32}\cos 6q]\ . \quad (30)$$

From (19) let's find the precession angle

$$\psi = (\psi_{00} + k^2\psi_{02})q + k^2\psi_{12}\sin 2q + k^2\psi_{22}\sin 4q + k^2\psi_{32}\sin 6q\ . \quad (31)$$

From (20) let's find the proper rotation angle

$$\varphi = (\varphi_{00} + k^2\varphi_{02})q + k^2\varphi_{12}\sin 2q + k^2\varphi_{22}\sin 4q + k^2\varphi_{32}\sin 6q\ . \quad (32)$$

Thus, in the interval $\alpha_3 \le \gamma'' \le \alpha_2$ let's find Euler's angles as function of time with accuracy $O(k^3)$.

Euler's kinematic equations and the Poisson's equations considering transferable angular velocity of proofmass center of gravity in orbital movement

Let's introduce the following coordinate systems O_*xyz, put the start O_* to the center of the Earth's mass, align axis O_*z with its axis of rotation, and axes *x, y* complement the system to the right and remain motionless, then let's place the center of proofmass O in the reference point of two coordinate systems $Oxyz$ and $Ox'y'z'$, with that let's point axis z to the continuation $R = O_*O$, and let's point axes *x, y* so that they complement the system to the right, and point $y \| \bar{e}_n$ normal to the orbit, $x \| \bar{e}_\tau$ along the tangent to the orbit, z - along $\bar{e}_R \| \bar{R}$, x', y', z' should be directed along the main central axes of inertia of the proofmass

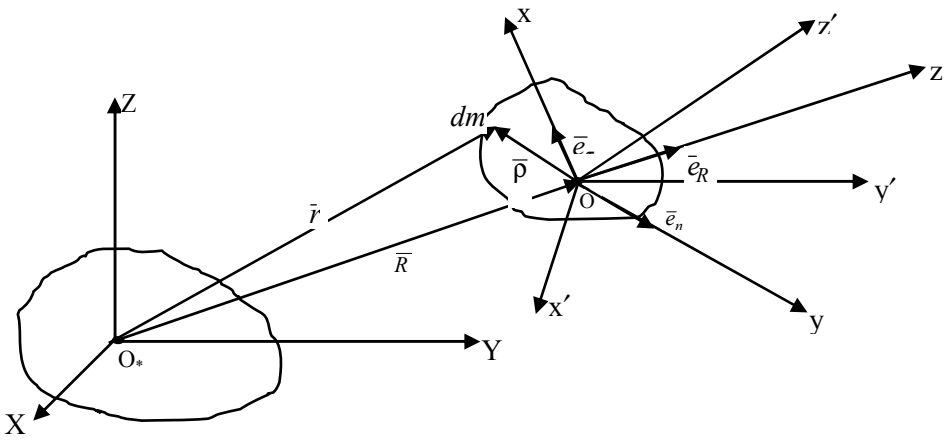

Figure 1. Coordinates of the system

Let's define position of the coordinate systems $Oxyz$ and $Ox'y'z'$ using the following table of directing cosines:

Table 2. Table of directing cosines

		x'	y'	z'
$\bar{e}_\tau$	x	α	α'	α''
$\bar{e}_n$	y	β	β'	β''
$\bar{e}_R$	z	γ	γ'	γ''

Then the strength function after discarding members of order $O(10^{-12})$ shall have the form

$$U = \frac{\mu m}{R}, \tag{33}$$

whereas t - is the proofmass.

Directing cosines are related to Euler's angles by the following equations

$$\left.\begin{aligned}
&\alpha = \cos\varphi\cos\psi - \sin\varphi\sin\psi\cos\theta,\\
&\alpha' = -\cos\psi\sin\varphi - \cos\theta\sin\psi\cos\varphi, \quad \alpha'' = \sin\theta\sin\psi,\\
&\beta = \cos\varphi\sin\psi + \sin\varphi\cos\psi\cos\theta,\\
&\beta' = -\sin\psi\sin\varphi + \cos\psi\cos\varphi\cos\theta, \quad \beta'' = -\sin\theta\cos\psi,\\
&\gamma = \sin\varphi\sin\theta, \quad \gamma' = \sin\theta\cos\varphi, \quad \gamma'' = \cos\theta.
\end{aligned}\right\} \tag{34}$$

Kinematic equations take the form:

$$\left.\begin{aligned} p &= \dot{\psi}\gamma + \dot{\theta}\cos\varphi + \omega_e\beta, \\ q &= \dot{\psi}\gamma' - \dot{\theta}\sin\varphi + \omega_e\beta', \\ r &= \dot{\psi}\gamma'' + \dot{\varphi} \quad + \omega_e\beta''. \end{aligned}\right\} \tag{35}$$

Poisson's equations, taking into account ω_e, have the form:

$$\left.\begin{aligned} &\frac{d\gamma}{dt} = \gamma' r - \gamma'' q + \omega_e\alpha, \quad \frac{d\gamma'}{dt} = \gamma'' p - \gamma r + \omega_e\alpha', \quad \frac{d\gamma''}{dt} = \gamma q - \gamma' p + \omega_e\alpha'', \\ &\frac{d\alpha}{dt} = \alpha' r - \alpha'' q - \omega_e\gamma, \quad \frac{d\alpha'}{dt} = \alpha'' p - \alpha r - \omega_e\gamma', \quad \frac{d\alpha''}{dt} = \alpha q - \alpha' p - \omega_e\gamma'', \\ &\frac{d\beta}{dt} = \beta' r - \beta'' q, \quad \frac{d\beta'}{dt} = \beta'' p - \beta r, \quad \frac{d\beta''}{dt} = \beta q - \beta' p. \end{aligned}\right\} \tag{36}$$

From (36) and (35) we shall obtain:

$$\left.\dot{\psi} = \dot{\psi}_0 - \omega_e\frac{\beta''\gamma''}{1-\gamma''^2}, \ \dot{\varphi} = \dot{\varphi}_0 - \omega_e\beta'', \ \frac{d\gamma''}{dt} = \gamma_0'' + \omega_e\alpha''\right\} \tag{37}$$

Integration of differential equations of translational-rotational motion of the proofmass in Hill's gravity field (intervals $\ell_4 < w < \ell_3$ and $\alpha_3 < \gamma'' < \alpha_2$)

Let the proofmass make translational-rotational motion in Hill's gravity field, then in accordance with [13] differential equations shall have the form:

$$\left.\begin{aligned} &\frac{d^2x}{dt^2} + \frac{\mu x}{r^3} = vx, \quad \frac{d^2y}{dt^2} + \frac{\mu y}{r^3} = vy, \quad \frac{d^2z}{dt^2} + \frac{\mu z}{r^3} = v'z, \\ &A\frac{dp}{dt} + (C-B)qr = M_{x'} \quad B\frac{dq}{dt} + (A-C)pr = M_{y'}, \quad C\frac{dr}{dt} + (B-A)pq = M_{z'}. \end{aligned}\right\} \tag{38}$$

Now, assuming that the proofmass moves along elliptic orbit type with a slight inclination to the main plane (*Oxy*), we have the solution for the first three differential equations in form (12) and (13), (15) (in the $\ell_4 < w < \ell_3$ interval):

$$\rho = (\rho_{00} + k\rho_{01} + k^2\rho_{02}) + (k\rho_{11} + k^2\rho_{12})\cos\frac{\pi}{K}u + k^2\rho_{22}\cos\frac{2\pi}{K}u, \tag{39}$$

$$\vartheta = \mu^*\left[(w_{00} + kw_{01} + k^2w_{02})u + \frac{K}{\pi}(kw_{11} + k^2w_{12})\sin\frac{\pi}{K}u + k^2w_{22}\cos\frac{2\pi}{K}u\right], \tag{40}$$

$$u = (u_{00} + ku_{01} + k^2u_{02})t + (ku_{11} + k^2u_{12})\sin\frac{\pi}{K}t + k^2u_{22}\sin\frac{2\pi}{K}t + k^2u_{32}t\cos\frac{\pi}{K}t, \tag{41}$$

Let us consider the rotational motion of the proofmass in relation to the center of masses in the interval $\alpha_3 < \gamma'' < \alpha_2$ in case $A = B = mC$. In case $\omega_e = 0$ we get Euler's angles (30), (31) and (32)

$$\theta_0 = \arccos[\overline{\alpha}_{00} + k^2\overline{\alpha}_{02} + k^2\overline{\alpha}_{12}\cos 2\upsilon_0 t + k^2\overline{\alpha}_{22}\cos 4\upsilon_0 t + k^2\overline{\alpha}_{32}\cos 6\upsilon_0 t]; \tag{42}$$

$$\psi_0 = (\psi_{00} + k^2\psi_{02})\upsilon_0 t + k^2\psi_{12}\sin 2\upsilon_0 t + k^2\psi_{22}\sin 4\upsilon_0 t + k^2\psi_{32}\sin 6\upsilon_0 t; \tag{43}$$

$$\varphi_0 = (\varphi_{00} + k^2\varphi_{02})\upsilon_0 t + k^2\varphi_{12}\sin 2\upsilon_0 t + k^2\varphi_{22}\sin 4\upsilon_0 t + k^2\varphi_{32}\sin 6\upsilon_0 t. \tag{44}$$

Now let's consider that $\omega_e = \dot{\upsilon}$, then

$$\omega_e = \mu_* n_0\left\{(w_{00} + kw_{01} + k^2w_{02}) + (kw_{11} + k^2w_{12})\cos 2\upsilon_0 t + k^2w_{22}\cos 4\upsilon_0 t\right\}, \tag{45}$$

and let's use (37), i.e.,

$$\left.\psi = \psi_0 - \int_0^t \omega_e\beta_0''\gamma_0''(1-\gamma_0''^2)^{-1}dt, \ \varphi = \varphi_0 - \int_0^t \omega_e\beta_0''dt, \ \gamma'' = \gamma_0'' + \int_0^t \omega_e\alpha_0''dt.\right\} \tag{46}$$

Having integrated (46), we have

$$\psi = \psi_0 - \left[(\bar{\xi}_{00} + k\bar{\xi}_{01} + k^2\bar{\xi}_{02})\sin\psi_{00}\upsilon_0 t + k^2\bar{\xi}_{12} + \cos\psi_{00}\upsilon_0 t + \ldots\right]; \quad (47)$$

$$\varphi = \varphi_0 - \left[(\bar{\tau}_{00} + k\bar{\tau}_{01} + k^2\bar{\tau}_{02})\sin\psi_{00}\upsilon_0 t + k^2\bar{\tau}_{12} + \cos\psi_{00}\upsilon_0 t + \ldots\right]; \quad (48)$$

$$\theta = \arccos\left\{\gamma_0'' + [(\bar{v}_{00} + k\bar{v}_{01} + k^2\bar{v}_{02}) + (\bar{v}_{10} + k\bar{v}_{11} + k^2\bar{v}_{12})\cos\psi_{00}\upsilon_0 t + \ldots]\right\}. \quad (49)$$

Constant coefficients $\bar{\xi}_{ij}, \bar{\tau}_{ij}, \bar{v}_{ij}$ are written in [13].

The solution obtained provides the possibility to define the effect of the orbital motion of proof mass center on its rotational motion:

$$\Delta\psi = (\bar{\xi}_{00} + k\bar{\xi}_{01} + k^2\bar{\xi}_{02})\sin\psi_{00}\upsilon_0 t + k^2\bar{\xi}_{12} + \cos\psi_{00}\upsilon_0 t + \ldots;$$

$$\Delta\varphi = (\bar{\tau}_{00} + k\bar{\tau}_{01} + k^2\bar{\tau}_{02})\sin\psi_{00}\upsilon_0 t + k^2\bar{\tau}_{12} + \cos\psi_{00}\upsilon_0 t + \ldots;$$

$$\Delta\theta = \arccos\left[(\bar{v}_{00} + k\bar{v}_{01} + k^2\bar{v}_{02}) + (\bar{v}_{10} + k\bar{v}_{11} + k^2\bar{v}_{12})\cos\psi_{00}\upsilon_0 t + \ldots\right],$$

here $\Delta\psi \neq 0,\ \Delta\varphi \neq 0,\ \Delta\theta \neq 0$, obviously, the value of these increments depends on initial conditions of proofmass motion.

REFERENCES

[1] Kolb, E.W. and M.S. Turner, 1994. The Early Universe. Westview Press, pp: 1-283.
[2] Guth, A., 1998. The Inflationary Universe. Basic, pp: 1-204.
[3] Turner, M.S., 2007.Quarks and the Cosmos. Science, 315: 59-61.
[4] Frieman, J., M.S. Turner and D. Huterer, 2008. Dark Energy and the Accelerating Universe. Annual Reviews of Astronomy and Astrophysics, 46: 385-432.
[5] Barcelo, C., S. Liberati, S. Sonego and M. Visser, 2008.Fate of Gravitational Collapse in Semi-classical Gravity. Physical Review, 77(4): 271-279.
[6] Susskind, L., 2008. The Black Hole War: My Battle with Stephen Hawking to Make the World Safe for Quantum Mechanics. Little Brown, pp: 1-294.
[7] Shchigolev, B.M., 1954. Intermediate orbits in a three-body problem. Bul. Sternberg Astronomical Institute Moscow University, 2: 59-92.
[8] Hill, G.W., 1878. Researchesin the Lunar theory. Journal of Mathematics, pure and applied,1: 25-33.
[9] Shchigolev, B.M., 1960. About intermediate orbit in Hill's three-body problem. Pub. Sternberg Astronomical Institute Moscow University, 28: 91-98.
[10] Shinibaev, M.D. et al, 1999. Elliptic type of body movement in second flat Hill's orbit. In the Proceedings of the 1999 Practical Conference"Auezov Readings-2", Shymkent, Vol.2, pp: 112-115.
[11] Korn, Z.G. and T. Korn, 1970.Mathematical reference book for Scientists and Engineers. Moscow: Nauka, pp: 720.
[12] Aksenov, E.P., 1986. Special functions in celestial mechanics. Moscow: Nauka, pp: 320.
[13] Shinibaev, M.D., 2010. Translational-rotational motion of a rigid body in stationary and non-stationary Earth's gravity field. Almaty: Gylym, pp: 132.

Advanced Materials Research Vol. 983 (2014) pp 307-311

doi:10.4028/www.scientific.net/AMR.983.307

A Proposed Method of Photovoltaic Solar Array Configuration under Different Partial shadow Conditions

Ali Mahmood Humada[a,1,2 *], Mojgan Hojabri [b,1], Mortaza B. Mohamed [c, 1]
Mohd Herwan Bin Sulaiman[1], Taha Hamad Dakheel[3]

[1]Faculty of Electrical & Electronics Engineering, University Malaysia Pahang, Pekan, Malaysia
[2]Electricity Production Directorate of Salahaldeen, Ministitry of Electricity, Iraq
[3]Faculty of Electronics & communications Engineering, Cankaya University, Ankara, Turkey
[*]E–mail:[a] alimhm82@yahoo.com; [b] mojganhojabri@ump.edu.my; [c]mortaza@ump.edu.my

Keywords: Photovoltaic (PV); Mismatch conditions; Partial shadow; Substring configuration; Maximum power point (MPP).

Abstract. The benefit of improving the efficiency of photovoltaic (PV) solar system has come into view because of increasing the demand for electricity, especially in the urban areas. However, these PV solar systems are vulnerable to the mismatch operating conditions. Under such conditions, the performance of solar cells has decreased rapidly since the nonuniform insolation hitting the cells and with different values. Then this leads to cause rapidly decreasing in the output power value and maximum power point, beside to hot spot points that may be occurring in the solar cell which finally leads to damage these cells. This paper proposes an optimal connection of substrings with different value of shadow conditions, based on a thorough configuration that can significantly reduce that nonuniform condition loss. The refinement over existing photovoltaic (PV) solar array interconnections is proven by extensive simulation results by using MATLAB SIMULINK.

Introduction

The role of the sources of the renewable energy systems has become a priority nowadays due to the changing in the weather conditions [1]. The progress of solar energy systems fields leads to pay research on enhancement extracted power from the PV system and increasing day by day [2]. However, in the most applications, such as building integrated photovoltaic (PV), solar power plants, or even the solar tents, solar PV systems may be illuminated non–uniformly. Thus and according to the studies done in this field, normally the photovoltaic array produces energy less than the combined capacities of the entire modules in both operating case the general and the standard condition. These losses in energy production called the mismatch losses and recently get more attention in order to identify sources of the losses power and it is causing in PV systems [3]. One of the most famous sources of mismatch spoil is the non-homogeneous illumination within the partially shadow on the photovoltaic systems [4]. In the buildings, integrating PV (BiPV) applications the PV cells and modules are subjected to shadows effect by both predictable surrounding objects, e.g., clouds, booms, nearby trees, houses neighbor to BiPV, or even unpredictable sources, e.g., dust and falling objects on the PV module, etc. In the big PV systems, where PV arrays are installed at places far from any surrounding obstacles, the shadows of adjacent rows inside the same module and passing clouds may also lead to contribute to produce partial shading conditions [3]. Fig. 1 presents a building integrated PV (BiPV) solar array that can get a partial shadow when PV module affected by some shaded cells are usually cast the other cells or from the part of the building itself [5,6].

Another example, a portable PV modules are sometimes used by soldiers to use in campers and to remote locations [7]–[9]. In any solar PV system must be made a solution for that complex problem can be cause side effect during operation conditions, i.e., relation of minimum produced power cost with maximum power output during varying the space between the strings [5]. By considering the characteristic nature of the PV cell can be concluded that the shadow doesn't proportional with maximum power losses but magnify nonlinearly [6]. The PV solar cell may be damaged due to the local hot spot in the shaded part [10].

In addition, nonuniform conditions are mostly caused partially shaded that take place in a variety of PV applications [4]. Moreover, the partial shadow conditions can be significantly affect the electrical performance of the PV array system. In more depth, meaning, beside to power output reduction of the shaded cells the unshaded cell performance also deteriorates due to their sharing connection with that shaded one [11]. In case of flows the generated current from an unshaded cell through that shaded one the shaded one will have a negative sign voltage leads to making the power will be dissipated in this cell which cause a hot spot. This can cause a breakdown resulting in permanent cell damage [12]. To avoid thermal destruction might occur in the shaded cells, a number of bypass diodes implemented from the PV manufacturers in each PV module.

Moreover, the multiple power peaks and current steps will appear in the power and current characteristics, respectively. Like this condition leads to become difficult to track the global MPP due to presence many local points on for both power and current characteristic curves [13], [14]. The wrong identification for the maximum power point (MPP) could result in considerable loss, energy within partially shaded conditions [15]. To avoid these local maxima and capturing that global one should use an effective control strategy [16]. Beside to produce a global MPP tracking strategy, the shading losses can be further reduced by introducing a suitable configurations to avoid these undesired connections of unshaded and shaded modules during the PV array [17].

It can be concluded from the preceding paragraphs, that it is very important to study, model, and understand the PV arrays within shadow conditions. This paper presents a model of PV modules within different temperature and insulation values and then in varying shades, patterns, which can be used to enhance the understanding and predict of current–voltage and power–voltage characteristics of the big photovoltaic system. The remnant parts of the research are organized as follows. Sections 2 present the Proposed PV Array Configuration in this paper. Furthermore, section 4 is dealing with the results of the proposed system within different shadow patterns. Finally, section 5 is the conclusion of the paper.

Fig. 1 The partial shadow on the PV cells in case of the BIPV

Proposed PV Array Configuration

By implementing the interconnection topology shown in Fig. 4, we can modify many temperature levels at a specific module for the sort of different shadow patterns started from 0% for the full shaded cells to 100% fully shaded, then observing the effect of that mismatch case on the whole array. In case of the basic test firstly, supposed that whole cell number will get partially shading in different levels, then assume that the cell number to be sequenced in the shaded case as 1, 2 , 3 and 4 with different sequences. The shading phenomena will lead to offer multiple power peaks are chosen such that the PV array to work under mismatch conditions for all the array configurations. This will not only affect the local operation point evaluation, but the tolerance of

specific array to the special condition in case of full shade, beside to that it can be considered in case of cell failure.

This study illustrates the influence of the partially shadowing in case different level of radiance as 60%, 80%, and 90% by 1–sun (unshaded) to show the effect of each case on the P–V and I–V characteristic curve when getting different sources of the light reaching the module. The focusing of this study is to carry out the power capturing for partially shaded system [18–20].

Each case study is related to different values of irradiance level treats it as a shadow condition with different levels and is progressively increased from string to another. To prevent the shadow pattern from affect other panels and getting the best possible maximum output power the system configuration implemented in different substrings, each string known as a powerful channel, where each substring or channel comprise the same level of insulation. These strings divided upon the radiation levels and each one regarded on the same level of arrogance connected alone. Then these powerful channels will compose multi power output and each one connected to DC–DC converter and Fig. 4 presents the proposed structure. In this paper, the system consists of four power channels, but there could be any number of channels at the expense of more hardware. Also in this system focuses on the present the bypass diodes which make the system operational continuously within presence the partial shading condition. There exist several publications on the process loading multiple PV strings with DC–DC converters such that they operate in their MPP [18], [19]. The converter type selection has an important role in terms of advantages and disadvantages, so it is up to the designer to select the most appropriate, based on the requirements of the array [20].

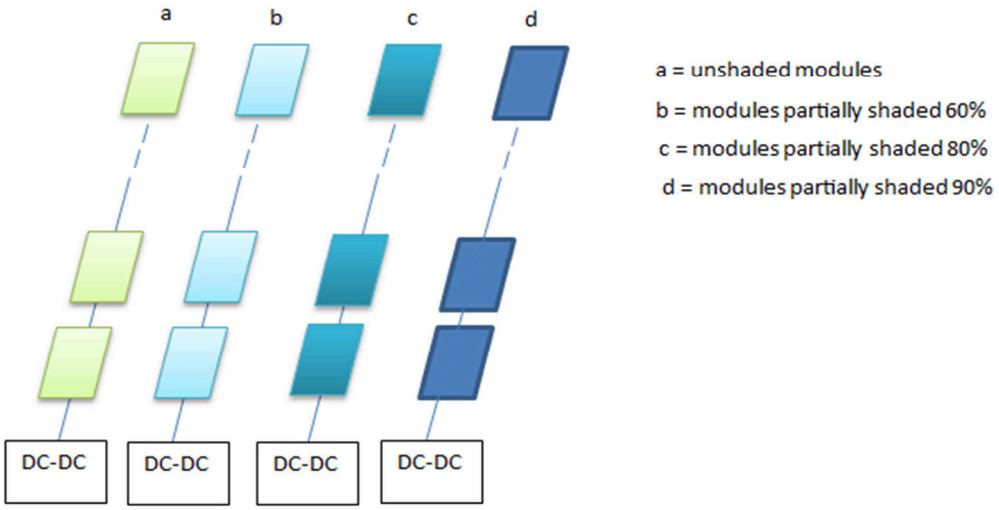

Fig. 4 The proposed configuration system with different level substring insolation.

Result of the PV Array Configuration

Referring to Figs. 5 and 6, these optimal configurations correspond to the case when each string connected to DC–DC converter then these strings are connected in parallel with the same configuration. Even with finding different shad patterns, the reference configuration is trying to be the optimal one.

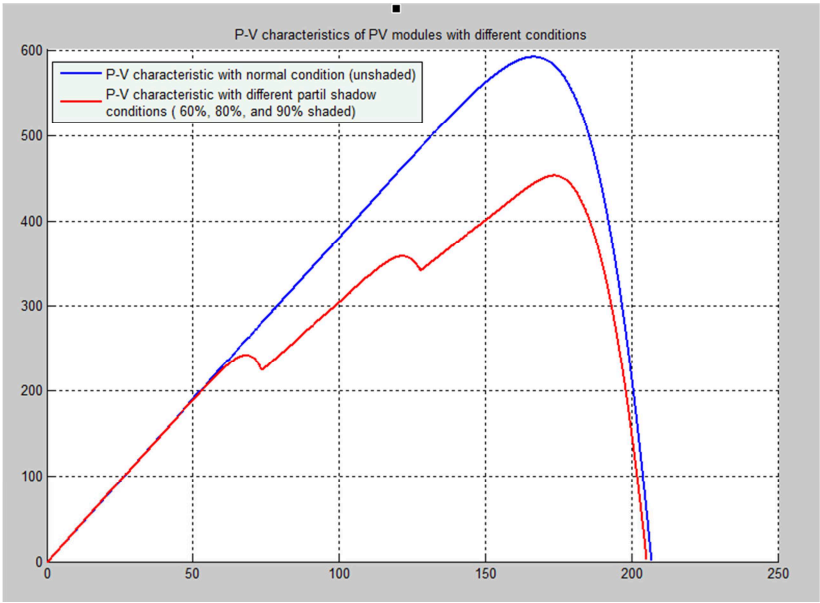

Fig. 5 Presents the effect of different insulation level (60%, 80%, and 90%) on P–V characteristic.

Different levels of partial shadow take in consideration with 60%, 80%, and 90% shaded strings. It must be underlined that the static configurations, usually employed include the use of by–pass diodes in series connected panels to avoid the mismatching effect [20]. The proposed configuration model was used to report the optimal PV module characteristics, obtaining the satisfactory results reported in Figs. 5 and 6, where the two I–V and P–V curves in the upper of these figures represent the unshaded strings.

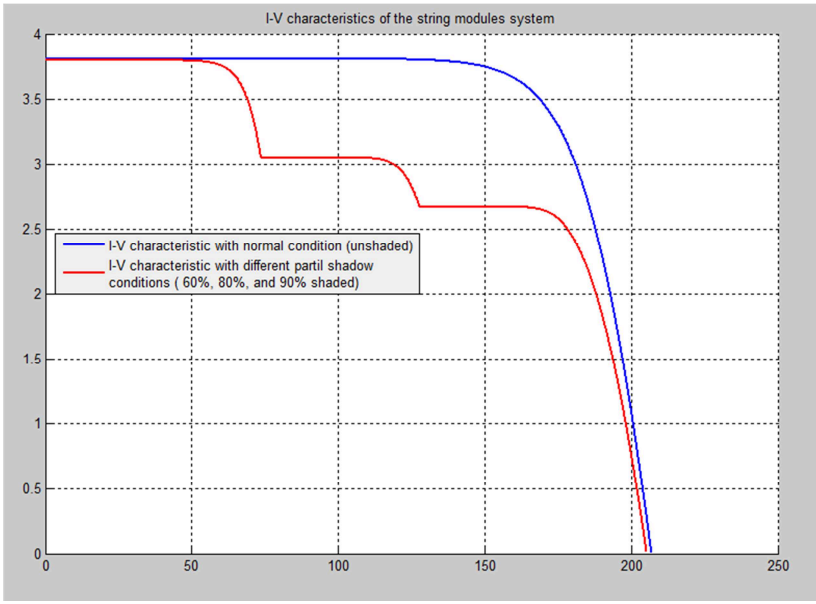

Fig. 6 Presents the effect of different insulation level (60%, 80%, and 90%) on I–V characteristic.

While the two I–V and P–V curves in the lower of these figures correspond to the second, third, and fourth strings respectively, theses strings represent the different level of shad patterns (60%, 80%, and 90% respectively). Such calculations based on prediction of the real module's electrical behavior and are characterized by a simulated model. From such results, it is demonstrated that the estimated models accurately predict the array configuration that provides the highest power production. Corresponding to the tests when the strings 2, 3 and 4 respectively increasing shading

pattern progressively will show that, several maximum local points' exhibited gradually decreased, and thereby result optimal.

Conclusions

In this paper, an optimal configuration for the photovoltaic array system was proposed to carry the mismatch conditions on the PV system. This configuration builds to recovering different level of partial shadow conditions, the cases taken in consideration for the system got (60%, 80%, and 90%) partially shaded. Moreover, it can be used for a non–equal number of modules per string. It was shown that the application of the proposed configuration concept can result in considerable reduction in partial shading losses, thus increasing the generated output power of substrings then for the whole system.

References

[1] R. Faranda, S. Leva, V. Maugeri: IEEE Power and Energy Society General Meeting conversion and Delivery of Electrical Energy Vol. 10 (2008) p.1.
[2] Information on http://www. iea.org/papers/2010/pv roadmap.pdf.
[3] N. D. Kaushika and R. Anilk: Energy Vol. 32 (2007), p. 755.
[4] D. Picault, B. Raiso, S. Bacha, J. de la Casa, and J. Aguilera: Sol. En. Vol. 84 (2010), p. 1301.
[5] D. Weinstock and J. Appelbaum: in Proc. 23rd IEEE Conv. Electr. Electron. Eng., (2004), p. 354.
[6] D.Weinstock and J. Appelbaum: in Proc. 22nd Conv. Electr. Electron. Eng., (2002), p. 163.
[7] F. Jeffrey: *Power Film Inc* (private communication, 2004).
[8] H. S. Raushenbach: IEEE Trans. Electron Devices, Vol. 18, no. 8,(1971), p. 483.
[9] V. Quas. and R. Hanitsch: in Proc. IEEE Photovolt. Spec. Conf., May 13–17, (1996), p. 1287.
[10] W. T. Jewell and T. D. Unruh: IEEE Trans. Energy Convers. Vol. 5, no. 1, Mar. (1990), p. 8.
[11] M. S. Swaleh and M. A. Green: Sol. Cells Vol.5, no. 2, , Jan. (1982), p. 183.
[12] Y. Wang and P. Hsu. : Energy Vol. 36, no. 5, May 2011, pp. 3069.
[13] E. Karatepe,M. Boztepe, andM. Colak. : Sol. Energy Vol. 81, no. 8, Aug. (2007), p. 977.
[14] R. Ramabadran and B. Mathur. : Mod. Appl. Sci. Vol.3, no.10, Oct. (2009), p.32.
[15] S. Silvestre, A. Boronat, and A. Chouder : Appl. Energy Vol. 86, (2009), p. 1632.
[16] Humad AM, M Hojabri, Mohamed MB, Sulaiman MHB, AL–Duliamy MNA. PEMC conference: Accepted at 16th Int. Pow. Elec. and Moti. Cont.l Conf. and Expos.(PEMC, www.pemc2014).
[17] Masters GM.: *Renewable and efficient electric power systems* (John Wiley & Sons, 2005).
[18] Humada AM, M Hojabri, MB Mohamed: Wulfenia Vol. 20, no.12, (2013), p. 179.
[19] AL–Duliamy MNA, M Hojabri, bin Daniyal H, Humada AM: Int. Jou. of Eng. Sci. and Res. Tech. (IJESRT) Vol. 2, no. 12, (2013), p. 3607.
[20] Humad AM, M Hojabri, Mohamed MB, AL–Duliamy MNA, Sulaiman MHB, Akorede MF: Int. Jou. of Eng. Sci. and Res. Tech. (IJESRT) Vol. 2, no. 12, (2013), p. 3634.

Advanced Materials Research Vol. 983 (2014) pp 312-318

doi:10.4028/www.scientific.net/AMR.983.312

The Development of New Steel Backing Wood Landscape Guardrail

Zhou Zhiwei[1,a], Wang Chenghu[1,b], Li Meng[1,c]

[1] Research Institute of Highway Ministry of Transport,

8 Xitucheng Rd, Beijing, China, 100088

[a]zw.zhou@rioh.cn, [b]ch.wang@rioh.cn, [c]meng.li@rioh.cn

Keywords: Steel backing wood, guardrail, simulation, impact test

Abstract: Steel-wood combination guardrail is a kind of environment-friendly and harmonious highway ancillary structure. It can provide comfortable and superior experience for highway users. At present, there is no steel-wood combination guardrail qualified for 160kj protection level of highway barriers in China. The Development of New Steel Backing Wood Landscape Guardrail takes reliability, economical efficiency, convenience of construction into account. The researchers optimize structure by computer simulation. This guardrail eventually passed the full-scale impact test with real vehicle. The test proves that it can become a model applied on the actual scenic highway.

0 Introductions

The main role of highway guardrail is to prevent the traveling vehicle from running off the highway or into the opposite lane, minimize the loss of passengers and vehicles, and make the vehicle drive back to the normal direction. During the process of guardrail design and setting, engineers often pay more attention to safety performance and cost instead of its esthetic requirement. With the rapid development of highway construction and continuous improvement of people's economic level in china, people have more meticulous and more humanized demand for highway landscape expectations. Highway engineers have also known the importance of highway landscape and embarked on the research of highway landscape. Highway landscape is composed of highway, ancillary structures, adjacent buildings, and the view along the highway. Guardrail, as the highway ancillary structure, is one of landscape factors. Good landscape guardrail can coordinate with the view along highway and create a beautiful and user-friendly environment. Otherwise, it will ruin the scenery and greatly reduce the service quality of highway.[1][2][3]

Currently, most of international solutions adopt steel backing wood guardrail to achieve aesthetic and safety on the highway with soaring requirement for landscape. However, China pays little attention on researching the steel backing wood guardrail. Several abroad landscape guardrail companies with independent intellectual property rights have not passed Chinese safety performance evaluation yet, therefore it is necessary to develop a type of landscape guardrail meeting Chinese standard specification.

1 Architectural Design

One scenic highway around Kanas Lake in Xinjiang has unique ecological and ethnic characteristics. It is required to develop a kind of steel backing wood landscape guardrail based on

the practical engineering project. Before the guardrail development and design, researchers clarify following structure design principles according to the actual situation: first, its safety performance should reach 160kj-level of Chinese JTG D81-2006 specification, the impact kinetic energy of which is 160kj, according to the roadside condition and hazard degree[4]. Secondly, it is required that the guardrail can accomplish 360°-view landscape effect, in order to achieve the harmonization with the surrounding scenic region and reflect native ecological and ethnic characteristics. Thirdly, the solution avoids waste and maximize the utilization rate of logs due to the lack of timber resources.

First of all, the steel backing wood landscape guardrail should be beam-column type structure, which consists of columns and beams. 160kj-level protection is required for both small and large vehicles according to the Chinese standard JTG D81 - 2006 specification, so 2-beam or 3-beam structure is chosen as the basic type. More types of column-beam structures can be alternatives. The first element is to use general and easy-to-processing standard components, such as square tube, I-beam, C steel, round tube, and so on. The second, the selection of structure type must be based on the consideration of steel quantity, structural strength, anti-collision and energy-absorbing effect. Through the preliminary calculation, with closed construction steel as the cross-section, two beams combined can achieve 160kj-level safety performance, while opening cross-section increases thickness of steel components or lead to a 3-beam structure to reach the same anti-collision level. So options of the cross-section are limited in square tube, torque tube, round tube, and so on. Because it is hard to process the timber connecting with the round tube and timber waste rate is quite high, square tube and torque tube are chosen as the main components of steel backing wood landscape guardrail.

The safety performance requirement of the guardrail is to avoid run-off accident. It means the guardrail can prevent vehicle from crossing, climbing and riding across barrier. Based on the relative investigation, the average heights of gravity centers in small cars and large buses respectively are 58 cm and 91 cm, and the average bumper height of small cars is 45cm. To prevent small cars and large buses from crossing the guardrails, the heights of two beams from highway surface are designed respectively as 45cm and 90cm. After the analysis above, it is initially identified that the structure type of steel backing wood landscape guardrail is beam-column structure with two beams, the heights of which from pavement are 45cm and 90cm respectively. The cross-section of beams and columns is square tube, as shown in Fig. 1.

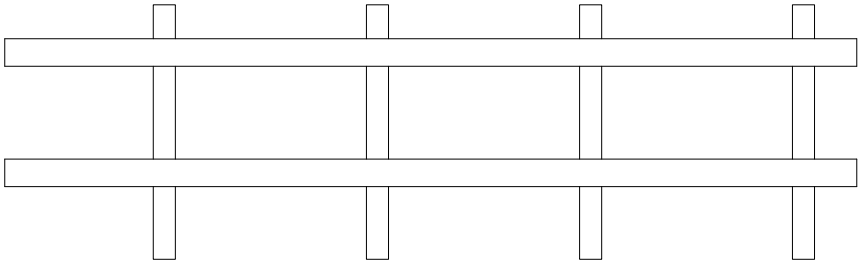

Fig. 1 The Preliminary Structural Design of Guardrail

1.1 Selection of Guardrail Column. The steel backing wood landscape guardrail requires 360°-view effect, therefore, the cross-section form of column steel components and wood components ought to be considered as whole. In order to reduce the process difficulty and the timber wasting, the following cross-section is chosen. It is a square tube steel column covered by the arc-cross-section wood panel, the advantage of which is easy to manufacture without extra wood wasting.

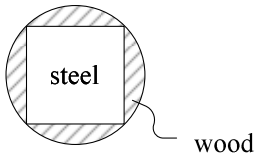

Fig. 2 The Cross-section of Column

1.2 Selection of Guardrail Beam. The guardrail of beam-column structure usually set a blockout between a column and a beam. The purpose of this system is to avoid the stumble resistance, which causes U-turn and drift of vehicles. However, since the lower beam in the 2-beam system of the steel backing wood guardrail can prevent these kinds of phenomenon, the steel backing wood guardrail does not need the blockout anymore. The beam selection should take into account the structure type of the wood components, and the type of the column should be selected at the same time. The initial design of beam cross-section adopts following 4 forms, as shown in Fig. 3.

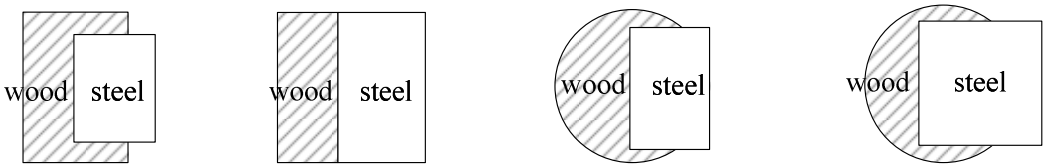

Fig. 3 The Structure Design for Guardrail Beam

The first two kinds are different combination styles between square timber and square tube; the last two kinds are different combination styles between log and square tube. Considering material saving, the log is better than the square timber because it is more compatible with the environment. The main difference between type C and D is that one is the rectangle shape tube, and the other is square shape. The rectangle tube is better than the square tube considering the aesthetic sense. Plus it shortens the length of the bolt between two components and is easy to be installed. So the type C is selected as the final design, which is a log slotted with the rectangular tube. By adjusting the diameter of the log and rectangular tube size of the steel beam, researchers get a kind of structure saving timbers most. One log can be used to manufacture wood components of both beams and columns, as shown in Fig. 4.

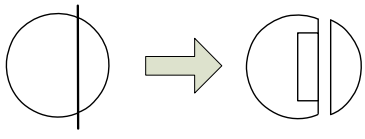

Fig. 4 The Component Manufacture for Beam and Column Wood

The initial type of guardrail has been clarified through the above design process, The structure type is as shown in Fig. 5.

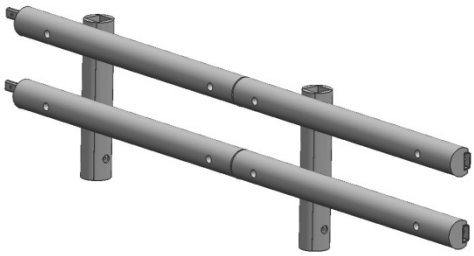

Fig. 5 Structure of Steel Backing Wood Landscape Guardrail

2 Computer Simulation

Whether the guardrail can meet the corresponding anti-collision level typically is verified by a collision test. Since the cost of full-scale collision test is quite high, experimental verification usually adopts computer simulation as the preliminary test. In the design of steel backing wood landscape guardrail, wood components are only set as decoration, and its anti-collision energy-absorbing effect is much worse than steel components. So only steel components are considered as structural members in the simulation model to test the safety performance. The impact energy reaches 160 kj; the collision condition of large vehicle should be 10t in weight, 60 km/h in speed, and impact angle of 20º.

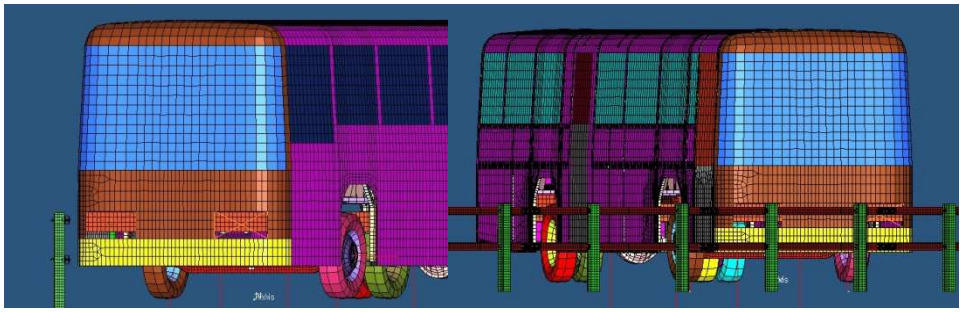

Fig. 6 Establishing Computer Simulation Model

In accordance with the structure dimension determined in the structural design, researchers first use UG software to establish the guardrail 3D model, then use Hypermesh software to design guardrail model, generate mesh, and define material parameters. Tour buses is selected for crash simulation because there are many of these vehicles on the scenic highway in Xinjiang. After adjusting the guardrail and vehicle location up to collision angle 20º, the guardrail and vehicle collision model are completed, as shown in Fig. 6.

Researchers set the vehicles stowage up to 10t, and then set vehicle collision speed at 60 km/h. The finite element calculation of the simulation is processed by LS-DYNA.

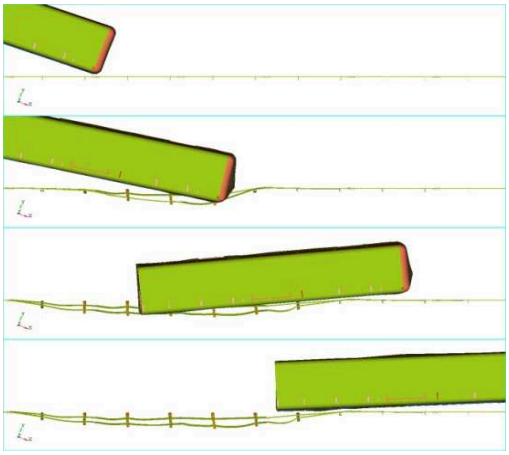

Fig. 7 Computer Simulation Collision Procedure- Top Perspectives

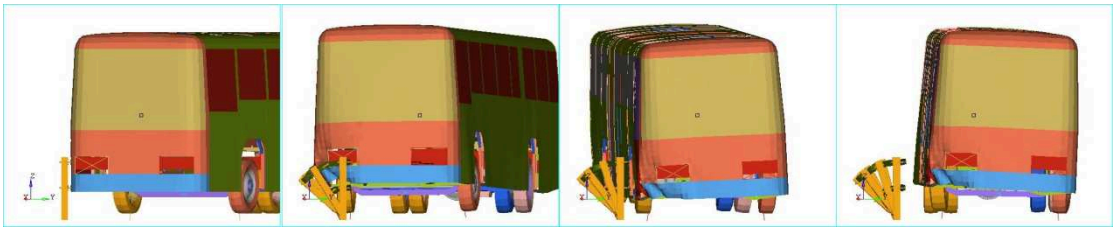

Fig. 8 Computer Simulation Collision Procedure- Front Perspectives

From the computer simulation result, it is obvious that the designed guardrail can effectively protect passenger vehicles and redirect runaway vehicles back to the correct direction of travel.

3 Structural Optimization

During the procedure of guardrail developing and designing, it is required to work with practical engineering applications. The R&D on steel backing wood guardrail will be applied to the scenic region highway in Xinjiang. There are many specific features in that highway, such as rugged terrain and lots of curves, which put forward higher requirements to the R&D on steel backing wood guardrail. Therefore, optimizing the design of steel backing wood guardrail becomes necessary. The main optimization includes 2 points: the first one is to change the length of original single beam from 4m to 2m; the second one is to change the connection between 2 beams from inner sleeve into 2 inner steel plates as cleading. The purpose of such optimization is for smooth transition at the small radius curve to avoid the phenomenon unable to turn a corner.

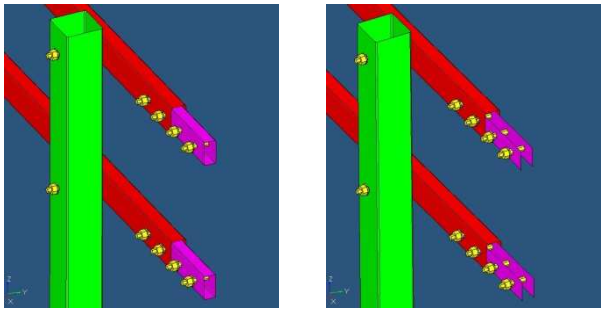

Fig. 9 Using Sleeve Connection (Left) and Using Cleading Connection (Right)

Through the re-calculation, the influence on the strength of guardrail is not great when a given thickness of cleading connection is applied instead of sleeve connection. The guardrail is still able

to bear 160kj impact energy. The gap between cleading may affect the straight-through degree of guardrail after installation, so adding a foam layer between 2 cleading can solve the problem.

4 Real vehicle crash test verification

Real vehicle crash test verification is the professional test on evaluating the safety performance of guardrail. In accordance with the requirements of JTG B05-01-2013 *Road Guardrail Security Performance Evaluation Criteria* implementing in December 2013, it is required to verify the blocking function, buffering function and redirection function of guardrail to vehicles[5]. The first step is to build and install the test section of steel backing wood landscape guardrail in accordance with the design drawings at collision test ground, as shown in Fig. 10.

Fig. 10 Test Section on Steel Backing Wood Landscape Guardrail

The second step is to prepare a large passenger bus in accordance with the test requirements. Then, workers load the vehicle and measure the position of gravity center. The full-scale impact test runs after everything is ready. Test conditions comply with 160kj protection level: the weight of vehicle is 10t; the impact speed is 60 km/h; and the impact angle is 20º.

Fig. 11 Full-scale Impact Test With Real Vehicle on Steel Backing Wood Landscape Guardrail

After the collision between the test bus and steel backing wood landscape guardrail, guardrail can redirect the bus back to the normal travel direction without crossing, climbing and riding across

guardrail. Components off the guardrail do not invade into crew cabin. The exit angle leaving guardrail is 4.9 º, and the farthest distance from the driving wheel track is less than 3.5m, without rollover phenomenon. The maximum dynamic deflection of guardrail is 91 cm. The result of the full-scale impact test indicates that new steel backing wood landscape guardrail can meet the requirement of 160kj protection level.

5 Conclusions

Based on Xinjiang scenic region highway, a new steel backing wood landscape guardrail has been developed. The guardrail from the perspective of the practical engineering application, gives full consideration on the requirements of material saving, cost saving and convenience of construction. The coordination between the steel-wood composite structure and surrounding scenery makes the scenic region highway more friendly and more humanized. The guardrail verified by the real vehicle impact test achieves the protective capacity of 160kj-level, and various performance indicators are in line with the requirements of the standard specification.

Therefore, the new developed steel backing wood landscape guardrail does not only have the environmental, friendly, safe and reliable characteristics, but also is Chinese first case of steel-wood composite guardrail which reaches 160kj-level. The guardrail has obtained the patent and will be applied in a demonstration project.

It should be added that the better horizontal and vertical highway alignment can reduce the thickness of guardrail steel components. It means the guardrail can still achieve 160kj-level safety performance with about 20% off current steel quantity. But its cost is higher than normal w- beam steel guardrail due to the usage of timber.

6.References

[1]Highway Series Editorial Board, Highway Traffic Engineering and Roadside Facilities., China Communications Press, China, 1999.
[2]American Association of State Highway and Transportation Officials Executive Committee, Manual for Assessing Safety Hardware 2009 ., AASHTO, United States, 2009 .
[3]CEN, EN 1317:1998. Road restraint systems., CEN, Belgium, 1998.
[4]The Road of Scientific Research Institute of the Ministry of Transport, JTG D81-2006 Specification for Design of Highway Safety Facilities., Ministry of Transport of the People's Republic of China, China, 2013.
[5]Beijing Shenhuada Traffic Engineering Detection Co Ltd, JTG B05-01-2013 Standard for Safety Performance Evaluation of Highway Barriers., Ministry of Transport of the People's Republic of China, China, 2013.

Advanced Materials Research Vol. 983 (2014) pp 319-323

doi:10.4028/www.scientific.net/AMR.983.319

The elimination of pollution of toxic cadmium and arsenic in lead-based alloys of lead-acid batteries in China

Xue Liu[1, 2, a], Junchao Cai[1, 2, b] and Yuehong Shu[1, 2, c*]

[1]School of Chemistry and Environment, South China Normal University, Guangzhou 510006, PR China

[2]Base of Production, Education & Research on Energy Storage and Power Battery of Guangdong Higher Education Institutes, Guangzhou 510006, PR China

[a]liuxue828128@126.com, [b]caicai.0728@163.com, [c]hongershu@163.com

Keywords: Grid materials; cadmium-free alloys; arsenic-free alloys; low-antimony arsenic alloy; rare earth alloys; lead-acid batteries

Abstract. An overview of the development of lead-based alloys in lead-acid batteries is presented. Advantages and historical achievements of toxic cadmium, arsenic alloys are affirmed. Compared to cadmium-free and arsenic-free batteries, the shortcomings and performance gapes of cadmium-containing, arsenic-containing batteries are noted. Focusing the prospect of rare earth alloy, and overall promotion of cadmium-free and arsenic-free alloys in China.

Introduction

During the past decade, lead-acid battery industry has developed rapidly in China, which has become the world's lead-acid battery production, consumption and export powerhouse. As the most important non-active element in lead-acid batteries, grid alloy has always been the focus of research and development.

Grid materials of lead-acid batteries through the evolution of pure lead → lead-high-antimony alloy → lead-low-antimony alloy and lead-calcium alloy. Lead-antimony-cadmium alloy of low-antimony alloys due to its good performances, continued to occupy the mainstream position for a long period. However, because of the dangers of cadmium metal, the production and use of this alloy has been strictly prohibited in China.

In addition, additives of low-antimony-based alloy is arsenic mainly. Adding tiny amounts of arsenic will help to improve corrosion resistance. Arsenic and its compounds are highly toxic, and will do great impact on human and environment. Limitations for heavy metal arsenic also mentioned in the regulations issued by the State. Currently, lead-calcium-tin-aluminum-rare earth alloys and other alloys are sufficient to substitute for arsenic-containing and cadmium-containing alloys as lead-acid batteries anode alloys. This paper initiative to eliminate arsenic-containing and cadmium-containing alloys, and to promote the full realization of cadmium-free and arsenic-free alloys.

Full Elimination of Cadmium-containing Alloys

Lead-antimony-cadmium (short for Pb-Sb-Cd) grid alloy of U.S. GNB company had been introduced to avoid the "antimony-free effect". Therefore, premature capacity loss and deep cycle life performance of lead-acid batteries have been significantly improved [1].

Pb-Sb-Cd alloy has excellent performance, and the main advantages are as follows:

- Contribute to the elimination of low-antimony alloy prone to cracking.
- High hydrogen over-potential of cadmium. So batteries' gassing and water loss rates with this alloy are lower than the usual lead-antimony alloy, and close to the lead-calcium alloy.
- Better deep cycle life performance compared to lead-calcium alloy.
- Low cost compared to low-calcium-high-tin of lead-calcium-tin-aluminum.

This alloy also called as "super-calcium alloy", may fit the needs in maintenance-free and deep cycle required batteries for electric vehicles and other applications [2].

Cadmium, a toxic heavy metal, which has enrichment effect and low toxicity concentration, as low as $0.001\sim0.010\times10^{-6}$. Metabolic long half-life of cadmium in human liver metabolic half-life is 6.2a, in human body metabolic half-life is 13a, in human renal metabolic half-life is up to18a. In grid manufacturing process and incinerators in the recovery of cadmium both have cadmium steam generation, also has cadmium mental in the lead slag. These do great harm. Europe, the United States and other countries and regions have explicitly restrict the use of cadmium.

In 2008, the cadmium is listed as China's first batch of high pollution, high environmental risk products in the catalogue. Countries have strictly prohibited plates containing cadmium for lead-acid battery production.

According to the guiding catalogue of eliminating backward production technology and equipment and products announced by Ministry of Industry, "higher than 0.002% cadmium lead-acid batteries", wanted to be eliminated no later than the end of 2013.

In recent years, Pb-Sb-Cd alloy has gradually been eliminated, but there are still some small plants produce this kind alloys. Fundamentally the full realization of the "cadmium-free alloy" still needs some time. Therefore, national policy must be enforced unceasingly. Cadmium-containing alloys production and use are strictly prohibited, phasing out cadmium-containing alloys.

Elimination of Arsenic-containing Alloys

Because of "antimony poisoning in negative plate" phenomenon, low-antimony alloy becomes a research hotspot. With the antimony content below 6%, alloy casting properties, mechanical strength and corrosion resistance are become poor. Other elements must be added to compensate for its mechanical damage. A series of studies indicated that arsenic is still the most important additive element of low-antimony alloy.

Studies have shown that arsenic for lead antimony alloys has two main functions. One is to increase the speed of aging, actually means reducing the storage time of grids before the next treatment after casting. The second is to increase creep resistance, thus increasing the endurance capacity of positive board, especially during the deep-cycling [3].

Adding trace amounts of arsenic in Pb-Sb-As alloy improves corrosion resistance, which has long been recognized at home and abroad. But more than 0.15% of arsenic content, the grids casting out crisp and often with hamstring. High arsenic content will affects the forming of grids during casting [4,5]. Therefore, more kinds of alloys by adding other elements on the basis Pb-Sb-As derived, such as Pb-Sb-As-Sn alloy, Pb-Sb-As-S alloy, Pb-Sb-As-Ca alloy, Pb-Sb-As-Sn-Cu alloy, etc.

In the early years about the eighties, initially using arsenic-containing alloy, many researchers measured harmful gases in battery produced process. National standard of 1962 GBJ1-62 pointed out that arsenic content in the air shall not exceed 0.3 mg/m^3. Researchers measured in the alloy casting, welding and charging. Air trioxide is 0.063 mg/m3 to 0.26 mg/m^3 range, which is simply concluded that only if we do some ventilation measures, production of arsenic-containing alloy is feasible [6]. Then in 1997, GB/T 16034 provides that arsenic and its inorganic compounds maximum allowable concentration is 0.015 mg/m^3 in the air of workshop. According to this, the above arsenic content has been seriously overweight. On December 15, 2004, World Health Organization officials announced that more than 50 million people in the world are facing the endemic arsenic threat. Among those countries, the majority are Asian countries, and China is one of the most serious arsenic poisoning hazard countries affected.

Earlier years abroad, there were a lot of studies on arsenic. Arsenic toxicity impacts on environment pollutions and humans are analyzed very thoroughly, such as Alfred a. Duker, Prosun Bhattacharya, Thomas S.Y. Choong [7-9]. Numerous people pointed out all applications and effects of arsenic in different areas, especially the great harm to the human body, wanted to be used restrictedly.

In 2012, issued by the Ministry of Environmental Protection, "lead-acid battery production and regeneration of pollution control technology policies": industry consolidation of lead-acid battery will be sounded overture based on green production. Repeatedly highlighted the prevention, treatment, and recycling of lead, cadmium, arsenic and other heavy metals, to achieve full control of heavy metal pollution. Lead acid battery production should be used with alloys without cadmium and arsenic. Elimination of hazardous lead-cadmium alloy, and promote the use of environmentally alloys such as lead-calcium alloy.

On April 23, 2013, Peking University School of Public Health and the environmental organization Greenpeace jointly issued the study of "PM 2.5 concentrations measurement of heavy metals in Beijing". Through the Beijing atmosphere and individual samples for concentrations of heavy metals testing and analysis, the study found that Beijing PM 2.5 concentrations of arsenic nearly three times higher than the national standard.

Arsenic is highly poisonous, especially trivalent arsenic compounds. Arsenic and arsenic compounds can be ingested, including through water, air and food. Arsenic poisoning (acute arsenic poisoning) or pollution-caused diseases (chronic arsenic poisoning) is not uncommon. Arsenic and arsenic-containing metal mining, smelting, or arsenic and arsenic compounds as raw materials used to make glass, pigments, the original drug, paper production, and coal combustion processes, can produce arsenic-containing wastewater, waste gas and waste residue, causing environmental pollution. Accumulation of arsenic in the soil entered crops organization and cause disease.

Therefore, combating arsenic contamination should pay close attention to the source, grabbed from pollution sources. Limiting the production and use of arsenic-containing alloys, and advocate the popularization of arsenic-free alloys to achieve green lead-acid batteries.

Prospect of Lead-calcium Alloy with Rare Earth

As a maintenance-free lead-acid battery grid material, lead-calcium alloy biggest advantages are: high over-potential of hydrogen evolution, less hydrogen evolution and water loss, with excellent maintenance-free performance. However, lead-calcium alloy also has poor casting properties, deep cycle life performance and premature capacity loss. Additives are, therefore, often used to improve the properties of Pb-Ca alloys. Aluminum and tin are widely used as additives. There succession tellurium, bismuth, silver, copper, sodium and rare earth elements as additives appear. At present, many good performance at home and abroad of cadmium-free arsenic-free alloys developed. Pb-Ca-Sn-Al-Re (rare earth alloy) is a typical category, which has become a research focus, and its excellent performance has been better than the cadmium-containing, arsenic-containing alloy.

Rare earth elements is added be a monosodium glutamate way. Li Dangguo [10,11] considered refractory metal compounds can be formed with rare earth elements and lead, which can neutralize intergranular tearing of some lead alloys to improve the thermal processing of alloys, and increase toughness and creep resistance of alloys. At present, rare earth elements added in the Pb-Ca-Sn-Al alloy mainly including La, Ce, Sm, Yb, etc.

Lanthanum (La) [12], adding lanthanum additive has the following advantages: refine grain effectively; enhance viscosity between corrosion layer and active substances; improve the corrosion resistance of Pb-Ca-Sn-Al alloy; increase conductivity of anode layer; reduce Pb (Ⅱ) generation, thereby, reducing the premature capacity loss and extending the life of lead-acid batteries.

Cerium (Ce), has similar negative electrode potential with the metal calcium (Ca), and higher hardness and better mechanical properties than lead, calcium, tin. Adding cerium can improve the deep cycle performance of batteries [13,14]. Liu Houtian’s tests showed that cerium is added to improve the impedance characteristics of lead anode film, and deep charge cycle performance of the maintenance-free batteries [15] .

Samarium (Sm), with lower impedance of lead anode film role. Adding samarium has non-effect on forming the surface of α-PbO_2, while benefits generating β-PbO_2 which has good conductivity, and also improving the deep charge and discharge performance of lead-acid batteries. Sm can be added to improve the hardness of lead-based alloys day, enhance the mechanical strength of the grid

alloy, improve oxygen evolution over-potential of Pb-Ca alloy. Compared with Pb-Ca-Sn-Al alloy, batteries with Pb-Ca-Sn-Al-Sm alloy have much longer deep cycle life, approaching Pb-Sb-Cd alloy batteries[16].

In recent years, a lot of high performance rare earth alloys have been covered, such as Zhao Jinzhu's studies have shown that rare earth elements added to improve the corrosion resistance of the alloy, especially to improve the performance deep cycle batteries [17]. S. Zhong, H. Li et al. have reported the performance of Pb-Ca-Sn-Al alloy, mainly in the more refined and uniform grain, can inhibit the growth of the passivation layer and so on [18,19] . Wenqing Zhang reported that Pb-Ca-Sn-Al-Re has high performance, reflected in the grain refinement, reduction of Pb (Ⅱ) growth, increasing the conductivity of passivation layer, reducing the premature capacity loss and extending the life of lead-acid batteries and even had determine the appropriate amount [12]. Dou Chuanlong's research has shown that the addition of rare earth can inhibit the growth of the high impedance anodic film of Pb (Ⅱ) compounds, reduce the resistance of corrosion film, and increase the porosity of the films. Also increasing the hydrogen and oxygen evolution over-potential, thereby inhibiting the release of hydrogen and oxygen, helping to improve the performance of maintenance-free batteries [20].

Until today, there have been a variety of rare-earth elements as additives into the lead-calcium or other alloys. Results show that, after adding the rare earth alloys with excellent performance, a large number of experiments proved the feasibility of rare-earth joined. Enough to prove that lead-calcium- rare earth alloys has a fully qualified replacement for cadmium-containing and arsenic-containing alloy as a cathode alloy for lead-acid batteries.

Conclusion

Lead-based alloy for lead-acid battery has undergone many stages of development, currently on the market used alloys is Pb-Ca-Sn-Al, and other alloys, which derived. Pb-Sb-Cd alloy was all the rage, but it has been discontinued due to environmental pollutions and threats to humans by cadmium. Similarly, arsenic contamination is very serious now. With the advance of grid alloy, numerous experimental results showed that there are enough other alloys can substitute arsenic alloys as lead-acid battery grid materials. Thinking of arsenic poses a serious threat, restrictions on the use of arsenic-containing alloy can not delay. Therefore, advocating the full realization "cadmium-free alloys", "arsenic-free alloys" imperative, to achieve green lead-acid batteries.

In fact, lead-antimony alloy still has space. Future trends of the grid materials should be to the basement of Pb-Ca-Sn-Al alloys, and adding rare-earth metals has much space to dig.

Acknowledgments

This work was funded by the Production, Education & Research Combining Project of Guangdong Province and Ministry of Education (No. 2011B090400560), Science and Technology Project of Guangzhou (No. 11A92091438), Science and Technology Project of Panyu District (No. 2010-zhuan-12-2).

References

[1] Guo Ziqiang, *"green electric bike use "green" battery - from cadmium-containing battery to cadmium-free battery*, J. Chinese Bicycles (2009), p. 40-44.

[2] Guo Ziqiang, *Lead-acid batteries with cadmium-free alloy will replace cadmium-containing batteries imperatively,* J. Battery Industry, vol. 13 (2008), p. 401-404.

[3] Shenyang Institute of Mining and Metallurgy, Liu Yumin, and Sun Zhen, *Status and development direction of lead-acid battery grid allo*y, J. Nonferrous Metallurgy, Section 5 (1997), p. 46-48.

[4] Harbin Institute of Technology Department of Electrochemical, Dong Baoguang, and Liu Xiurong, *Lead-antimony-arsenic-selenium (sulfur) study on quaternary alloys,* J. Batteries, vol. 1 (1983), p. 10-13.

[5] Tangming Cheng, Zhou Huawen, *Study of lead-acid batteries with lead alloy,* J. Hunan Nonferrous Metals, vol. 21 (2005), pp. 27-29.

[6] Shanghai Battery Plant, *Testing and use of lead-antimony-arsenic alloy,* J. Batteries, vol. 4 (1983), p. 1-6.

[7] Alfred A. Duker, E.J.M. Carranza, *Arsenic geochemistry and health,* [J]. Environment International, vol. 31 (2005), p. 631-641.

[8] Prosun Bhattacharya, Alan H. Welch, Kenneth G, *Arsenic in the environment: Biology and Chemistry,* J. Science of The Total Environment, vol. 379 (2007), p. 109-120.

[9] Thomas S.Y. Choong, T.G. Chuah, Y, *Arsenic toxicity, health hazards and removal techniques from water: an overview,* J. Desalination, vol. 217 (2007), p. 139-166.

[10] Li Dangguo, Zhou Genshu, Yao Liang, *Study on the anodic behavior of rare-earth lead alloy in sulfuric acid solution,* J. Chinese Journal of Rare Earth, vol. 23 (2005), p. 224-227.

[11] Li Dangguo, Zhou Genshu, Zheng Maosheng, *Orthogonal experimental design of new lead-acid battery grid materials,* J. Non-ferrous Metals, vol. 56 (2004), p. 48-51.

[12] Wenqing Zhang, Aiju Li, Hongyu Chen, *The effect of rare earth metals on the microstructure and electrochemical corrosion behavior of lead calcium grid alloys in sulfuric acid solution,* J. Journal of Power Sources, vol. 189 (2009), p. 1204-1211.

[13] Li Dangguo, Zhou Genshu, Zheng Maosheng, *Research progress of grid materials of lead-acid batteries,* J. Battery, vol. 34 (2010), pp. 132-135.

[14] Tong Ming Xin, Lin Guanfa, *Study on properties of lead-based grid materials of rare earth,* J. Physical and Chemical Testing, vol. 42 (2006), p. 60-62.

[15] Liu Hou-Tian, Yang jiong, Liang Haihe, *Cerium content effects on anodic behavior of Pb-Ce alloy in sulfuric acid solution,* J. Fudan Journal, vol. 40 (2001), p. 401-407.

[16] H.Y. Chen, S. Li, A. J. Li, D. Shu, *Lead–samarium alloys for positive grids of valve-regulated lead–acid batteries,* J. Journal of Power Sources, vol.168 (2007), p. 79-89.

[17] Zhao Jinzhu, Dai Changsong, Wang Jinyu, *Overview of lead-acid batteries grid alloy,* J. Power Technology, vol. 26 (2002), p. 16-18.

[18] S. Zhong, H.K. Liu, S.X. Dou, *Evaluation of lead-calcium-tin-aluminium grid alloys for valve-regulated lead/acid batteries,* J. Journal of Power Sources, vol. 59 (1996), p. 123-129.

[19] H. Li, W.X. Guo, H.Y. Chen, *Study on the microstructure and electrochemical properties of lead-calcium-tin-aluminum alloys,* J. Journal of Power Sources, vol. 191 (2009), p. 111-118.

[20] Dou Chuanlong, Li Ruizhen, Chen Hongyu, *Study of lead-acid batteries of lead-based alloy for positive grid,* J. Power Technology, vol. 34 (2010), p. 276-279.

Advanced Materials Research Vol. 983 (2014) pp 324-327

doi:10.4028/www.scientific.net/AMR.983.324

Thermal stability and smoke suspension of cotton cellulose modified with magnesium complexes*

Fachao Wu[1, a] ,Chunyan Chao[1, b],Shuang Tian[1, c]

[1] School of Environmental Engineering, North China University of Science and Technology, Box 206,Yanjiao Beijing 101601, China

[a]ahxmsw@ncist.edu.cn, [b]chaochunyan@ncist.edu.cn, [c]wfchljhnyj@163.com

Key words: cotton cellulose, thermal stability, flame retardant, smoke suspension

Abstract Complexes of cell-THPC-thiourea-ADP with Mg^{2+} have been prepared. The thermal stability and smoke suspension of the samples are determined by TG, DTA and cone calorimetry. Experimental data show that for the complexes of cell-THPC-thiourea-ADP with Mg^{2+}, thermal decomposition temperatures are higher than those of cell-THPC-thiourea-ADP, which shows these metal ions can increase the thermal stability of cell-THPC-thiourea-ADP. The cone calorimetry data indicate that the metal ions greatly decrease the smoke, CO and CO_2 generation of cell-THPC-thiourea-ADP, which can be used as smoke suppressants. However, there are no obvious effects for these metal ions on heat release of samples.

Introduction

With environmental sustainability required, the effects of flame-retardants on both smoke generation and the toxicity of combustion products have become special important, as flame retardant cellulose has been reported to produce denser smoke than pure cellulose [1]. In previous papers [2-4], compounds of transition metals have been found to be effective smoke retarders. However, there is no information about the effects of Mg^{2+} on smoke suspension and thermal degradation of cotton cellulose treated with flame retardants. So the main objective of the work reported here is to investigate the effects of Mg^{2+} on the thermal degradation and smoke suspension of cotton cellulose modified with flame retardant.

In this paper, complexes of cell-THPC-thiourea-ADP with Mg^{2+} were prepared. The thermal degradation of samples was studied from ambient temperature to 800°C by TG, DTA. The smoke suspension of samples was determined by cone calorimetry.

Experimental

Materials

Cotton cellulose of commercial grade (Hebei province, China) was selected for flame-retardant treatment. The cotton cellulose was immersed in 24% NaOH solution at room temperature for 24 h (mercerization process). The alkali was then filtered off and the sample was washed repeatedly with distilled water. The sample was dried in an oven at 60 °C and then stored in a desiccator.

Instrumentation

The elemental analysis was carried out using a Carlo Eroa 1102 Elemental Analyzer. LOI values were determined in accordance with ASTM D2863-70 by means of a General Model HC-1 LOI apparatus. Thermogravimetry (TG) was carried out on a DTA-2950 thermal analyzer (Dupont Co. USA) under a dynamic nitrogen (dried) atmosphere at a heating rate of 10°C min^{-1}. The test method using the cone calorimeter was ASTM M 1354 with the external heat fluxes of 35 kW/m^2.

Cotton cellulose treatment

The preparation of the samples is corresponded to references [2-4]. THPC (Shanghai, China) was neutralized with NaOH to give a pH value equal to 6.5 and its 45% solution was mixed with 22.5% thiourea solution. The pH value was adjusted to 6.5 and a small amount of ADP was added. The resulting mixture was used as the treating solution. The mercerized cotton cellulose was immersed in the treating solution for 30 min at room temperature. The treated cotton cellulose was dried at 60 °C in an oven for 60 min. Curing of these treated cellulose was carried out by heating at 160 °C for 5 min in the oven. After cooling, the sample was thoroughly washed with distilled water for an hour and dried in an oven at 60 °C. Mg^{2+}complexes of cell-THPC-thiourea-ADP were prepared by treating 6g of cell-THPC-thiourea-ADP in each instance with 5% aqueous solutions of $MgSO_4$ at room temperature for 72 h under constant stirring. Each product was washed repeatedly with water until the filtrate was free from metal salt and dried overnight in an oven at 60 °C then stored in a desiccator.

RESULTS AND DISCUSSION

The DTA, TG curves of (1) cotton cellulose, (2) cell-THPC-thiourea-ADP, (3) Mg^{2+} complexes of cell-THPC-thiourea-ADP were obtained in a dynamic air atmosphere from ambient temperature to 800 °C and are shown in Figure 1.

Differential thermal analysis

From the DTA curves of samples 1-3, the initiation temperatures (T_i), peak temperatures (T_p) and termination temperatures (T_t) of the various endotherms and exotherms were investigated and are given in Table1. The DTA curve of cotton cellulose shows two large exotherms with their respective peak maxima at 363 and 459°C. Before 350°C, decomposition and dehydration occur to form some flammable volatile products, and the first exotherm peaking at 363°C is due to the oxidation of these volatile products. Another exotherm, peaking at 459°C, represents oxidation of the charred residues. The DTA curve of cell-THPC-thiourea-ADP is quite distinct from that of pure cotton cellulose. Two large exotherms with peak maxima at 326 and 485°C are shown in Fig.1, respectively. In the DTA curves of the metal complexes of cell-THPC-thiourea-ADP (sample 3), the first peak, a new endotherm with peak maxima in the range 230-280°C, represents depolymerization, a catalyzed dehydration of the cellulose and some bond formation. For the metal complexes (sample 3), there are also two large exotherms in each case. The decomposition stage, which is represented by the first exotherm, is very different in the decomposition temperature in the complexes. The peak temperature of the complexe is 326°C. The last exotherm, which is due to oxidative decomposition of the residual products, also shows considerable variation in the complexes.

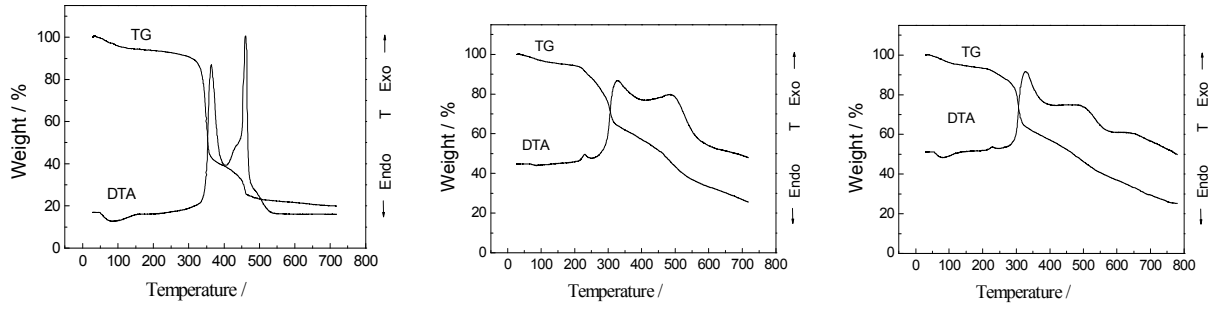

Fig. 1 Thermal analysis curves of samples1-3(1-left, 2-middle, 3-right)

For cotton cellulose, the two exotherms are sharp and narrow, which shows a large rate of heat release. For the samples 2-3, the two exotherms become small and broad. Heat release is distributed

between two broad peaks covering a wide area, resulting in a major reduction in rate of heat release and flammable products which fuel the flaming combustion reaction. In the other hand, the second exotherms become much smaller for the samples 2-3, which indicates that oxidation of the charred residues becomes more difficult due to the existence of flame retardants.

Table 1 Peak temperatures in DTA curves of samples 1-3

No.	Compound	DTA curve			Nature of peak
		T_i	T_p	T_t	
1	Cellulose	230	363	403	Exo(large)
		403	459	539	Exo(large)
2	Cell-THPC-thiourea-ADP	255	326	414	Exo(large)
		414	485	614	Exo(large)
3	Mg^{2+} complex of cell-THPC-thiourea-ADP	230	260	280	Endo(small)
		280	328	413	Exo(large)
		413	500	567	Exo(large)

Thermogravimetry

From Figure 1, it can be seen that the second stages in thermal decomposition of the samples, decompose mainly and quickly, play a key role attributed to the combustibility. So we mainly discuss this stage. Temperature Range (TR), Mass Loss (ML) at the second stage (quick mass loss rate) in TG, are listed in Table 2.

Table 2 Thermal degradation and analytical data of samples 1-3

No.	TR (°C)	ML (%)	Ea (kJ/mol)	CY (%)	LOI (%)	P (%)	N (%)	M (%)
1	326-365	46	198.3	20.2	18.0	-	-	-
2	214-318	28	78.1	26.5	29.6	1.69	3.78	-
3	227-321	26	87.6	27.6	27.9	1.39	2.98	0.70

From Figure 1 and Table 2, it can be seen that for the cotton cellulose (sample-1), initial decomposition temperature is 326°C, the second stage is in a range 326-365°C, and the mass loss is 46%. For cell-THPC-thiourea-ADP, initial decomposition temperature is 214°C, the second stage is in a range 224-318°C, all these much decreased compared with those of cotton cellulose, which shows that the thermal stability of the cell-THPC-thiourea-ADP is much decreased because of the catalyzing dehydration and decomposition reaction. For sample 3, the decomposition temperature range is 227-321°C, higher than that of cell-THPC-thiourea-ADP, which shows that the thermal stability of samples is increased.

In order to understand the flame retardant properties of these samples, LOI of samples is measured, given in Table 2. From Table 2, we can see that samples 2-3 show high values of LOI. This suggests that the combustibility of cotton cellulose treated with flame retardants decreases. Moreover, the sample-2 containing highest content of phosphorus and nitrogen shows highest value of LOI. The second stage of decomposition for sample-2 occurs at lower temperatures (214-318°C) and produces less flammable volatile products, resulting in higher flame retardancy.

Cone Calorimetry

Generally, the smoke production and toxic gas formation play a critical role in fire conditions. Carbon monoxide yield, carbon dioxide yield and specific extinction area of smoke (SEA) for the samples are measured by cone calorimeter, listed in Table 3. Cotton cellulose burns out in a few seconds, so there are no cone data for sample-1. The smoke production is measured by SEA. The higher the SEA value is, the more the smoke releases. From Table 3, we can see that for

cell-THPC-thiourea-ADP, the peak and average values of SEA are 2912 and 197 m^2/kg while for the Mg^{2+} complexes of cell-THPC-thiourea-ADP (sample-3) the peak and average values of SEA are 1685 and 158 m^2/kg, much decreased, which shows these lanthanide metal ions, similar to transition metal, act as smoke suppressants. It is suggested that the metals act as flame inhibitors in the vapor phase under normal flame conditions, resulting in the formation of condensed char [5-7]. This means that the complexes of cell-THPC-thiourea-ADP with metal ions eliminated the negative effect of cell-THPC-thiourea-ADP on smoke formation in some degree, which is favorable.

Table 3 SEA, EHC, CO and CO_2 yield values of samples 1-3

No.	SEA (m^2/kg)		EHC(MJ/kg)		CO yield (kg/kg)		CO_2 yield (kg/kg)	
	Peak	Average	Peak	Average	Peak	Average	Peak	Average
1	-	-	38.5	16.3	-	-	-	-
2	2912	197	25.6	6.8	1.83	0.0088	34.46	1.44
4	1685	158	26.7	8.2	0.68	0.0062	28.98	1.13

Carbon monoxide yield is defined as the mass of CO formed from the unit mass of burned material. Generally, for the flame retardant modified cotton cellulose, the CO yield is higher than that of untreated one which is due to an incomplete combustion. For cell-THPC-thiourea-ADP, the peak and average values of CO yield are 1.83 and 0.0088 kg/kg. In the case of sample 3, the peak and average values of CO yield are 0.68 and 0.0062 kg/kg, respectively, all much decreased. Moreover, the values of CO_2 yield for the sample 3 are also much lower than those for sample-2. Thus, the Mg^{2+} decrease the associated CO, CO_2 generation and reduce the formation of volatiles, thereby enhancing char formation.

Conclusions

For complexes of cell-THPC-thiourea-ADP with metal ions, thermal decomposition temperatures are higher than those of cell-THPC-thiourea-ADP. The metal ions Mg2+ can increase the thermal stability of cell-THPC-thiourea-ADP. Moreover, Mg2+ can greatly decrease the smoke, CO and CO2 generation of cell-THPC-thiourea-ADP, which can be used as smoke suppressants.

*Contract grant sponsor: 1Fundamental research funds for the Central Universities: B09013; 2Hebei Province Natural Science of China; contract grant numbers: E2011508001

References

[1] O. Grexa, H. Lubke, Flammability parameters of wood tested on a cone calorimeter[J].Polymer Degradation and Stability, 74 (2001) 427-432.

[2] B. Kaur, R. K. Jain and I. S. Gur, Thermal stability of phosphorylated cellulose modified with various transition metals [J]. J. Anal. Appl. Pyrol., 9 (1986)173-206.

[3] S. L. Bagga, R. K. Jain and I. S. Gur, et al., Thermaland Spectroscopic Studies on Flame Retardant Cotton Cellulose Modified with THPC-urea-ADP and Its Transition Metal Complexes [J]. British Polymer Journal. 22(2) (1990) 107.

[4] B. Jai and L. Krishan, Cellulose Ammonium Dithiophosphate and its Metal Complexes in Air [J]. Indian J. Fibre Text. Res., 17 (1992) 32-38.

[5] M. Gao, C. Y. Sun and K. Zhu, Thermal Degradation of Wood Treated with Guanidine Compounds in Air [J]. J. Therm. Anal. Cal, 75 (2004) 221-232.

[6] M. Gao, B. Ling, S. S. Yang., Flame retardance of wood treated with guanidine compounds characterized by thermal degradation behavior [J]. J. Anal. Appl. Pyrolysis, 73(1) (2005) 151-156.

[7] M. Gao, W. Wu and Y. Yan, Thermal Degradation and Flame Retardancy of Epoxy Resins Containing Intumescent Flame Retardant [J]. J. Therm. Anal. Cal. 95(2009) 605-608

Advanced Materials Research Vol. 983 (2014) pp 328-337

doi:10.4028/www.scientific.net/AMR.983.328

Phonon Interaction of Ultrasound Waves in Condensed Media

Serik Omarov[1,a], Turarbek Begimov[1,b], Makhabbat Tukibayeva[1,c], Khamaria Maylina[1,d], Gulnara Bedelbaeva[1,e].

[1]Republic of Kazakhstan, Almaty, Satpayev street, 22, Kazakh National Technical University named after K.I. Satpayev

[a]serik.om@yandex.ru, [c]kulager-18@mail.ru, [d]mailxp@mail.ru, [e]bd.gulnar@gmail.com

Keywords: phonons, ultrasound, crystal lattice, sound absorption, coefficient of sound absorption, Debye temperature.

Abstract. Based on phonon theory the interaction of high frequency sound (ultrasound and hypersonic) with crystal lattices in solids was estimated. The coefficients of absorption in dielectrics and metals, with respect to temperature and sound frequency, were calculated. Analysis of the calculated dependences allows obtaining of nanomaterials with the set sound conductivity and sound absorption in high frequency range.

Introduction

Dissipation mechanism of hypersound and ultrasound energy in solids has a complex pattern. Absorption of sound energy with the frequency Ω in solids can happen both due to electron-phonon interactions, when energy of a sound wave is taken away by free electrons of lattice, and due to interaction of the lattice with sound wave. Analysis of the theoretical research of the interaction of high frequency sound oscillations with crystal condensed mediums (including hard crystal solids) shows the need of integrated approach [1,2] at calculation of sound absorption coefficient (ratio of absorbed from the falling sound energy) i.e. it is necessary to consider phonon interactions (also between thermal phonon of crystal lattice and acoustic phonons); existence of impurity in crystals; dislocation phenomenon on impurities; electron-phonon interactions; temperature phenomenon in solids (interaction between thermal phonons).
The cumulative absorption coefficient of ultrasound wave in crystals of solids $\alpha_\sum$ is estimated as follows:

$$\alpha_\sum = f(\alpha_f, \alpha_n, \alpha_{ef}, \alpha_d, \alpha_T, \alpha_\Omega) \quad (1)$$

where:
α_f - coefficient of ultrasound absorption, based on the interaction of phonons;
α_n - coefficient of ultrasound absorption, based on the existence of impurity in crystals;
α_{ef} - coefficient of ultrasound absorption, based on the electron-phonon interaction;
α_d - coefficient of ultrasound absorption, based on the existence of dislocation phenomenon;
α_T - coefficient of ultrasound absorption, based on the temperature phenomena in crystals of solids;
α_Ω - coefficient of ultrasound absorption, based on the acoustic frequencies.
$\alpha_f, \alpha_n, \alpha_{ef}, \alpha_d, \alpha_T, \alpha_\Omega$ - coefficient of ultrasound absorption based on the interaction of phonons.

Depending on the type of a crystal solid the components value of full sound absorption coefficient can significantly change. If, for example, in dielectrics phonon interactions α_f play a big role then for metals electron-phonon interactions make main contribution.

The goal of this research is to estimate the contribution of phonon interactions α_f for calculating of coefficient of ultrasound and hyper sound absorption in crystal lattice of dielectrics and metals. Comparing of the dependency of sound absorption coefficient from temperature and frequency for dielectrics and metals is of a scientific interest.

Thermal movement in crystal lattice of a solid can be presented in the form of quasi-particle-phonons gas or the so called phonon gas. Thermal phonons are sometimes called as the Debye quanta of elastic energy. Each thermal phonon is a plane elastic harmonic wave with energy $\hbar\omega$ ($\hbar$ -

Planck's constant, ω - thermal phonon frequency) and quasi-momentum ħk (k - wave vector). Thermal phonons have a wide phonon spectrum. Low phonon frequency are determined by the size of a sample (by length of elastic waves), highest frequencies are determined by lattice parameter **a**.

In equilibrium thermodynamic state crystal lattice makes thermal oscillations (phonon gas) that are interconnected with its structure and temperature. Sound wave influences on the equilibrium thermodynamic system. As a result of variable deformation the system of thermal phonons is brought out of equilibrium state and strives for this state by means of collision between thermal and acoustic phonons or between thermal phonons i.e. there is a mechanism of relaxation. Frequency of an incident sound is taken as Ω, and τ as a life expectancy of thermal phonons (or mean length free path l_f). Life expectancy of thermal phonons is determined [2] by the thermal conductivity formula:

$$\chi=Cc^2\tau/3, \quad (2)$$

where c - phonon middle speed, C - lattice heat capacity.

Fig.1 shows [3] comparative temperature dependencies of heat conductivity χ for dielectrics and metals. Qualitative picture of dependency of the thermal conductivity coefficients between crystals of pure metals and dielectrics resulted from the fact that lattice interactions greatly contribute to sound absorption in dielectrics and as for metals it is necessary to take into account electron-phonon interactions.

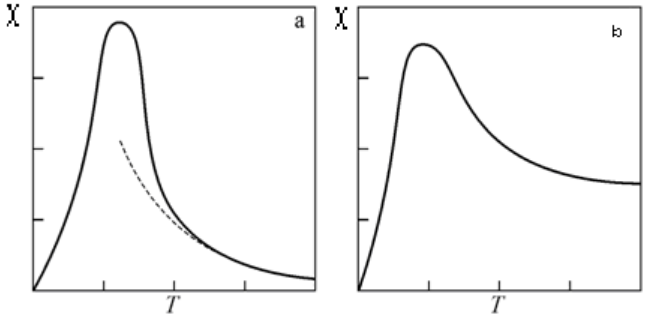

Figure 1. Comparative temperature dependences of the thermal conductivity coefficient χ: a - for dielectrics; b- for metals.

In dielectrics contribution of sound absorption is made by lattice oscillations caused by lattice anharmonicity and which is explained at Ωτ>>1 by three-phonon interaction (Landau-Rumer mechanism), and at Ωτ<<1 it is explained by the Akhiezer mechanism.

Calculations, Results and Discussion

According to the Landau-Rumer theory the coefficient of sound absorption depends on phonons speed decrease of sound modes at collisions of sound and thermal phonons. At such interactions a sound phonon disappears forming a third phonon is created. If to take the number of sound phonons with frequency Ω as m, and the initial number of thermal phonons before interaction with frequency ω_1, as n_1, then the number of thermal phonons after fluctuating interaction with frequency ω_2 will be n_2. Then the scheme of such three-phonon interaction will be as follows:

$$m + n_1 = n_2. \quad (3)$$

Thermal phonons in an equilibrium state of a solid obey the Bose-Einstein statistics. The function of phonon distribution n_1 with wave vectors k_1 and polarization J_1 [3] is given by

$$n_1(k_1, J_1) = \left[\exp \frac{h\omega(k_1 J_1)}{2\pi k_b T} - 1 \right]^{-1} \quad (4)$$

where, h - Planck's constant; ω - oscillations frequency of crystal lattice; k_b - stiffness coefficient of crystal lattice.

Calculated data of thermal $n_1(\omega_1)$ phonons distribution at absence of acoustic impact on crystal lattice and of thermal $n_2(\omega_2)$ phonons after acoustic interaction (See Fig. 2, 3).

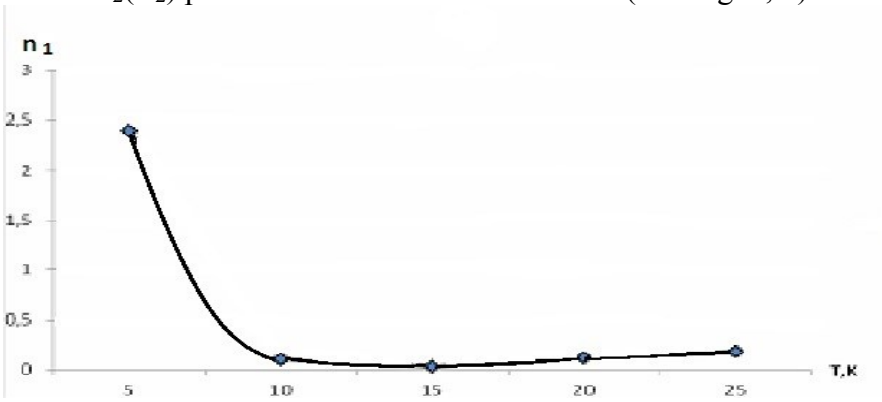

Figure 2. Calculation of dependency of the thermal phonons number n_1 on T, K.

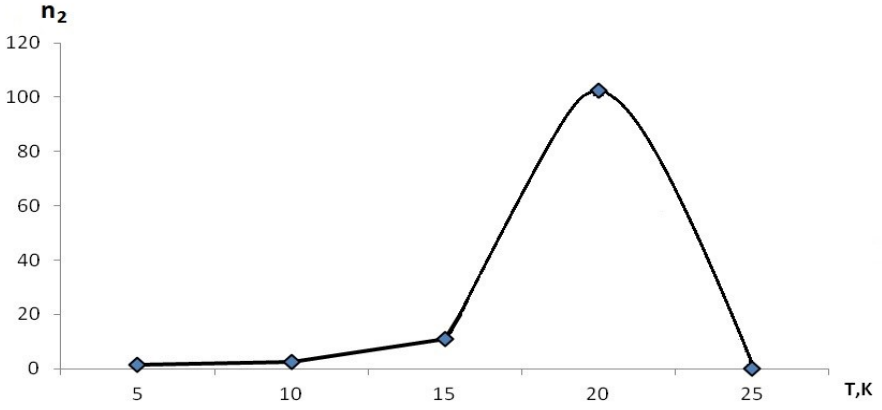

Figure 3. Calculation of dependency of the thermal phonons number n_2 on T, K.

Processes in which energy and quasimomentum are preserved are called "normal" or N-processes:

$$\hbar\Omega \pm \hbar\omega_1 = \hbar\omega_2; \qquad \hbar k \pm \hbar k_1 = \hbar k_2 \quad (5)$$

According to the thermal conductivity theory at alone presence of N-processes heat could be spread over the dielectric model with speed of a sound. Due to periodic structure of crystal flipping processes (U-processes) also happen, at which energy is conserved, but a quasi-momentum law modifies with the accuracy of reciprocal lattice vector:

$$\hbar\Omega \pm \hbar\omega_1 = \hbar\omega_2; \qquad \hbar k \pm \hbar k_1 = \hbar k_2 + \hbar g. \quad (6)$$

Statements (5) and (6) indicate that thermal and sound phonons can be longitudinal (L) and transverse (T) i.e. merger (sign+) and decay (sign -) processes are quite possible. Two types of interaction are possible by the rules of selection:

$$L + L \rightarrow L \quad (7)$$
$$T + L \rightarrow L. \quad (8)$$

Thus, at interaction type (7) - longitudinal plus longitudinal phonons move in one direction (L); at interaction type (8) - a longitudinal plus and transverse phonons also move longitudinally.

Then at calculation of absorption coefficient α, that happens due to interaction (7), the largest contribution happens when all three longitudinal phonons move in one direction. Absorption coefficient for this case will be given by $\alpha_{LL,L}$.

Coefficient of sound absorption $\alpha_{LL,L}$ for the case number two when a longitudinal direction of sound wave LL,L is considered and will be given by:

$$\alpha_{LL,L} = \frac{\pi^2 h\Omega}{480\rho v^6}\left(\frac{2\pi k_b T}{h}\right)^4 \gamma^2, \quad (9)$$

where h - Planck's constant; Ω - sound frequency; ρ – mass density; ν - frequency of longitudinal sound; k_b - stiffness in the lattice or sound conductivity of a lattice, T - temperature of the lattice; γ - Gruneisen acoustic coefficient.

Firstly is made the calculation (9) of the k_b stiffness and Gruneisen coefficient γ (in this case it is a Gruneisen acoustic coefficient γ_a) [4].

Degree of stiffness or sound conductivity of the crystal k_b can be given by the formula:

$$k_b = \hbar\omega_D/\theta_D, \quad (10)$$

where θ_D - Debye characteristic temperature; ω_D - maximal oscillation frequency of the crystal lattice that is equal to a total number of vibrational degrees of freedom of the lattice.

Debye temperature θ_D is defined by the formula [5]

$$\theta_D = \frac{hc}{2\pi r}\left(\frac{6\pi^2 N\nu}{V}\right)^{1/3}, \quad (11)$$

where N - number of unit cells, V - solid volume, ν - number of particles in the unit cell.

Debye frequency (maximum oscillation frequency of the crystal lattice, which is equal to a total number of vibrational degree of freedom of lattice):

$$\omega_D = \left(\frac{6\pi^2 N v_0^3}{V}\right)^{1/3}. \quad (12)$$

Sound conductivity or hardness degree shows that the higher is the Debye temperature the less is sound conductivity and the higher is sound absorption.

Calculation results of stiffness coefficient in a crystal for some metals and dielectrics are shown in Tables 1 and 2.

Table 1. Calculation of k_b for metals.

Element	θ_D, K	ω_D, $\cdot 10^{11}$ GHz	k_b, $\cdot 10^{-26}$
$_{13}Al^{27}$	394	1,78	4,76
$_{29}Cu^{64}$	315	1,95	4,39
$_{26}Fe^{56}$	420	1,96	4,92
$_{28}Ni^{59}$	875	2,03	5,69

Table 2. Calculation of k_b for dielectrics.

Element	θ_D, K	ω_D, $\cdot 10^{11}$ GHz	k_b, $\cdot 10^{-26}$
$_{33}As^{75}$	394	2,12	7,85
$_{14}Si^{28}$	285	1,65	2,79
$_{6}C^{12}$	1860	2,19	1,20

Comparison of the calculated values shows that sound conductivity of dielectrics (eg, $_{6}C^{12}$ and $_{14}Si^{28}$) is lower than that of the metals, but sound absorption is higher. Consequently, solids with carbon and silicon in its structure will have a higher sound absorption coefficient.

Acoustic Gruneisen coefficient γ_a [5] that characterizes an "average" lattice anharmonicity will be given by:

$$\gamma_a = \left(\frac{9(\upsilon_L^2 - 4\upsilon_t^2/3)}{2(\upsilon_L^2 - 2\upsilon_t^2)} \right), \tag{13}$$

where υ_L - sound speed in longitudinal direction; υ_t - sound speed in transverse direction.
With the formulas (9) and (13) the absorption coefficient of ultrasound waves in longitudinal direction in solids is given by

$$\alpha_{LL,L} = \frac{\pi^2 h\Omega}{480\rho v_L^6} \left(\frac{2\pi k_b T}{h} \right)^4 \cdot \left(\frac{9(\upsilon_L^2 - 4\upsilon_t^2/3)}{2(\upsilon_L^2 - 2\upsilon_t^2)} \right)^2 . \tag{14}$$

Table 3 presents the Gruneisen Coefficient calculated by formula (13) for certain metals.

Table 3. Gruneisen coefficient for metals [6].

Element	Sound speed, m/s		Gruneisen coefficient γ_a
	υ_L	υ_t	
Aluminium	6422	3235	1,98
Cuprum	4726	2298	2,09
Ferrum	6064	3325	1,68
Nickel	5894	3219	1,70

Fig. 4-8 present calculations of coefficient dependencies of absorption of longitudinal ultrasound waves $\alpha_{LL,L}$ from the temperature for different sound frequencies in crystal lattice.

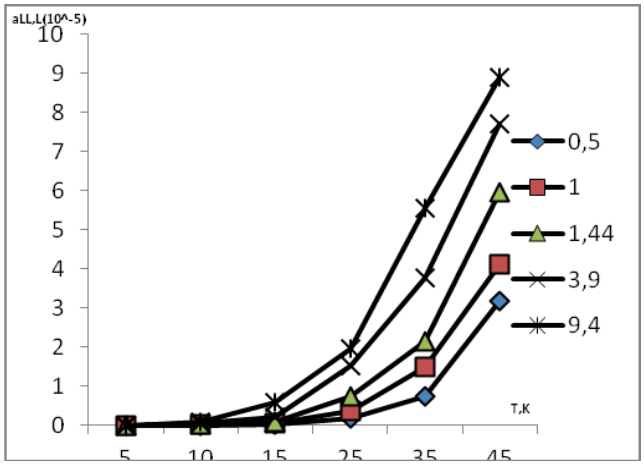

Figure 4. Calculation of dependence of the absorption coefficient of longitudinal ultrasound waves α_{LL} in crystals $_{13}Al^{27}$ on the temperature at values of sound frequencies Ω = (0,5; 1, 1.44, 3.9, 9.4) GHz

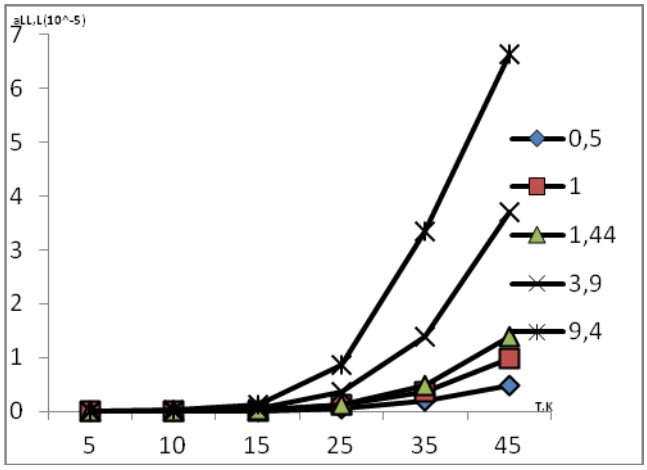

Figure 5. Calculation of dependence of the absorption coefficient of longitudinal ultrasound waves in crystals $\alpha_{LL\ 29}Cu^{64}$ on the temperature at different values of frequency Ω = (0,5; 1, 1.44, 3.9, 9.4) GHz

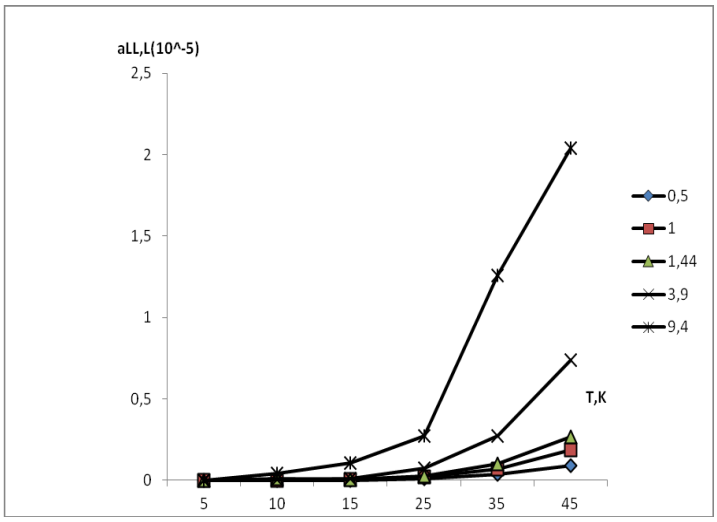

Figure 6. Calculation of dependence of the absorption coefficient of longitudinal ultrasound waves in crystals $\alpha_{LL\ 26}Fe^{56}$ on temperature at different values of frequency Ω = (0,5; 1, 1.44, 3.9, 9.4) GHz

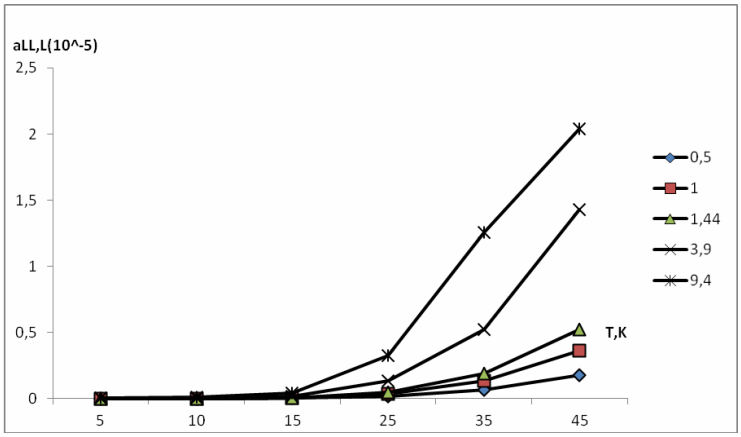

Figure 7. Calculation of dependence of the absorption coefficient of longitudinal ultrasound waves in crystals $\alpha_{LL\ 28}Ni^{59}$ on the temperature at different values of frequency Ω = (0,5; 1, 1.44, 3.9, 9.4) GHz

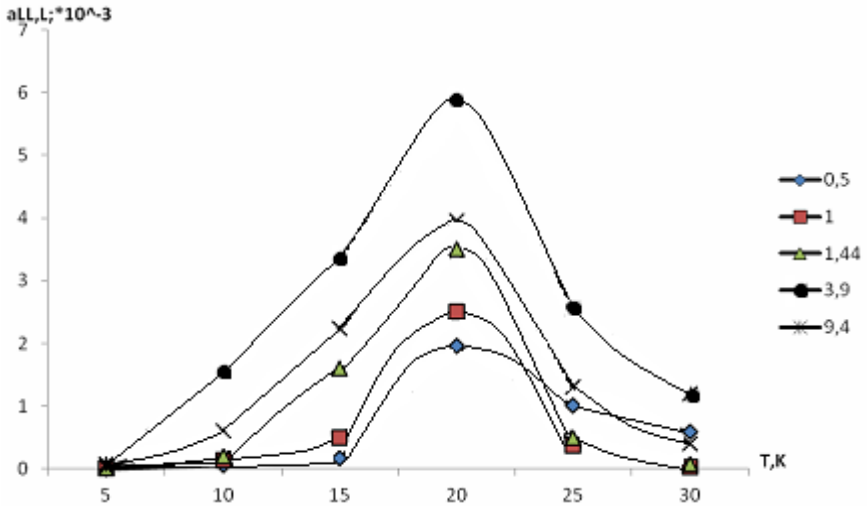

Figure 8. Calculated values of dependency for absorption coefficient of longitudinal ultrasound waves in silicon α_{LL} on temperature for different sound frequencies Ω = (0,5; 1, 1.44, 3.9, 9.4) GHz.

The analysis of calculated data presented in Fig. 2-6 shows that:
1) The largest value of the coefficient of absorption for longitudinal ultrasound wave is observed in crystal lattice of silicon;
2) Dependence of sound absorption coefficient in a crystal lattice of silicon from the temperature has a maximum at a temperature $T = 25^0K$;
3) For crystal lattice of metals Al, Cu, Ni and Fe absorption coefficient of longitudinal ultrasound waves have significantly smaller values;
4) Sound absorption coefficient in crystal lattice of Al, Cu, Ni and Fe increases with the temperature raise.

Calculation of the dependence of ultrasound absorption coefficient from the temperature for graphite also showed the same dependence for silicon.

Smaller values of sound absorption coefficient for metals are explained by the role of phonon interactions - phonon is significantly ranked below to interactions: electron - phonon wherein free metal electrons absorb the main ratio of sound energy. On the contrary in dielectrics the role of "lattice" absorbs increases greatly as it can be seen in above mentioned calculations.

The difference is explained by microstructural composition of metals and dielectrics shown in Figures 9-12. Graphite is mostly composed from such elements as carbon, its stiffness coefficient is higher than of aluminum. This leads to different values of sound absorption coefficient for dielectrics and metals.

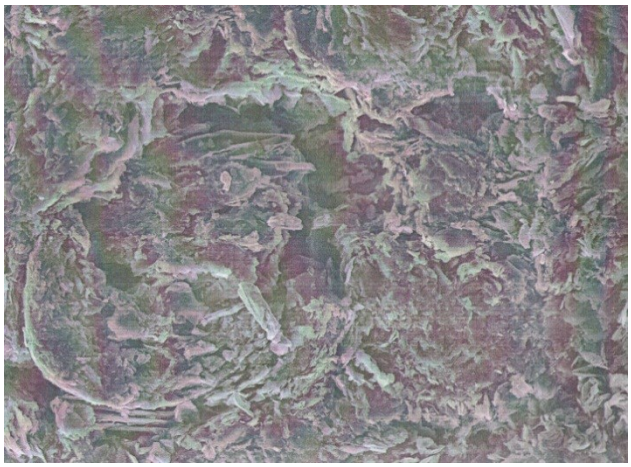

Figure 9. Microphotography of graphite under 500-fold magnification.

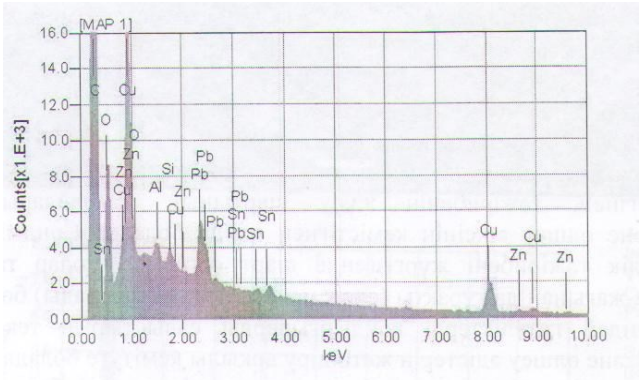

Elements	ms%	mol%	Sigma	Net	K ratio	Line
C	90.53	95.97	0.48	847742280	0.0000000	K
O*	3.94	3.14	5.24	1214872	0.0000000	K
Al*	0.07	0.03	1.32	193177	0.0000000	K
Si*	0.06	0.03	1.48	173822	0.0000000	K
Cu*	3.12	0.63	27.27	757994	0.0000000	K
Zn*	0.40	0.08	39.19	71897	0.0000000	K
Sn*	0.22	0.02	7.66	216321	0.0000000	L
Pb*	1.65	0.10	7.76	1831549	0.0000000	M
Total	100.00	100.00				

Figure 10. Structural composition of graphite.

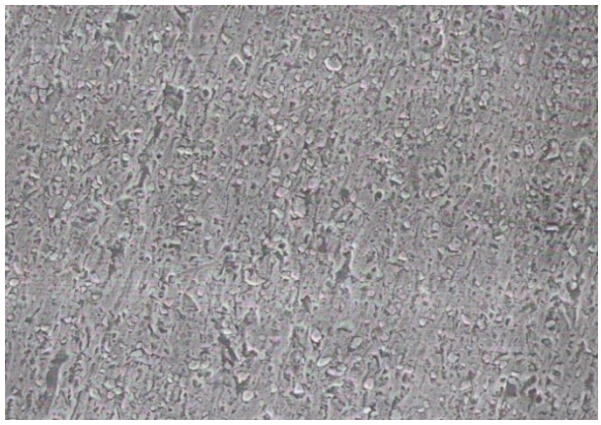

Figure 11. Microphotography of aluminum sample without etching. Under 500-fold magnification.

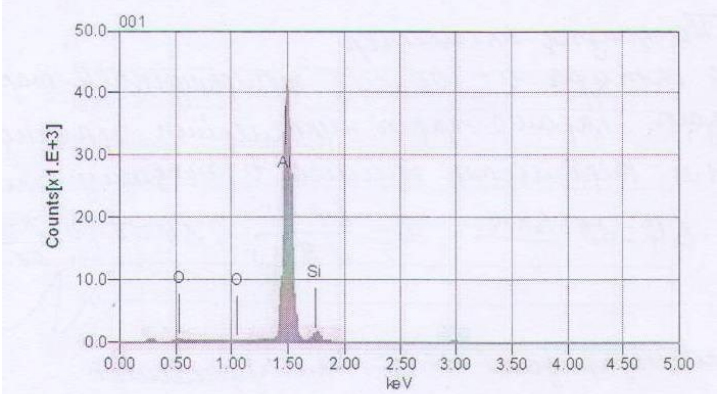

Elements	ms%	mol%	Sigma	Net	K ratio	Line
O	4.15	6.82	2.71	91634	0.0145574	K
Al	87.49	85.34	1.27	9918769	0.6981505	K
Si	8.36	7.84	2.88	465168	0.0368673	K
Total	100.00	100.00				

Figure 12. Structural composition of aluminum.

While values of sound absorption coefficient α_{LL} for crystal lattices of metal raise, at the same time the temperature increases. This fact is explained by temperature rising which leads to a sharp increase of thermal phonons and to increase of α_{LL}. For dielectrics such dependence has a resonant character.

Fig.4-8 shows the progress of diagrams of curves up to the temperature of 45 K coincides in quality with curves of Fig.13 in which experimentally obtained results [3] of Jacobsen are presented. In the experiment was measured the L- wave absorption in quartz (along X-axis) depending on the temperature at various frequencies.

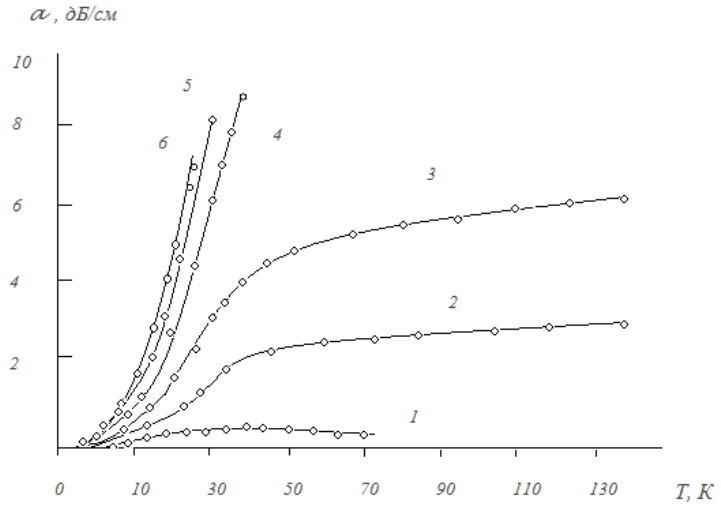

Figure 13. Absorption of L- waves in quartz (along axis X) depending on temperature at different frequencies, [8] , curve 1 - 0.5 GHz, 2 - 1 GHz, 3 - 1.44 GHz, 4 - 3.9 GHz, 5 - 9.4 GHz and 6- 24 GHz.

Theoretical and experimental results show that at $T \leq 50K$ the absorption falls sharply, at frequency increasing the decline steepness rises.

In order to compare experimental data, shown in Fig. 13, for diagrams of Fig. 4-8 were used frequencies and temperatures up to 45^0C.

Differences between experimental and numerical values of the diagram 13 and in the calculations of Fig. 4-8 are explained by the fact that the diagram shows modification of sound absorption resulted from sound frequency and temperature, as for the Fig. 2-5, there is shown the dependency of sound absorption for the same frequencies and temperatures up to 45 K. Theoretical curves follow that experimental qualitatively within the temperature up to 45 K.

Data of Fig. 4-8 demonstrate methods of increasing or decreasing of the sound conductivity and as a result the possibility to increase the sound-absorbing properties of materials, e.g. such as alloys.

This experimental data allow predicting the acoustic properties of solids. We can determine the material which can have the greatest sound-absorbing properties based on the example of automatic alloys [6]. Table 4 presents the structural composition of different types of automatic steels.

Table 4. Structural composition of automatic steels.

Type	Substance of the elements, %										
	C	Si	Mn	Pb	Ni	Cr	Se	Cu	S	P	Fe
A12	0,16	0,35	1						0,2	0,15	98,14
A20	0,24	0,35	1						0,15	0,06	98,2
A30	0,35	0,35	1						0,15	0,06	98,09
A35	0,4	0,35	1						0,15	0,06	98,4
A40G	0,45	0,35	1,55						0,3	0,05	97,3
A11	0,15	0,1	1,2	0,3					0,25	0,1	97,9
AS 40	0,17	0,12	1,3	0,3					0,2	0,1	97,81
AS 14	0,48	0,1	1,65	0,35					0,35	0,04	97,3
AS35G2	0,45	0,37	0,8	0,3	0,25	0,25			0,04	0,04	97,5
AS45G2	0,39	0,37	1,65	0,3	0,25	0,25			0,13	0,04	96,62

A35E	0,4		0,8		0,12	0,25	0,1	0,3	0,12	0,04	97,87
A45E	0,4		0,8		0,12	0,25	0,1	0,3	0,12	0,04	97,87
A40XE	0,44		0,8		0,3	1,1	0,1	0,3	0,12	0,35	96,49

Table 5. Temperature, the Debye frequency and stiffness coefficient for automatic steel

Steel type	Debye temperature θ_D, K	Debye frequency ω_D, $\cdot 10^{13}$ c^{-1}	Stiffness coefficient k_b, $\cdot 10^{-23}$ J/K
A12	621,2471	8,6006	1,45917
A20	621,2497	8,6006	1,45917
A30	621,4296	8,60313	1,45917
A35	621,5115	8,60426	1,45917
A40G	621,7387	8,60741	1,45917
A11	619,3054	8,57372	1,45917
AS 40	619,3179	8,57389	1,45917
AS 14	619,6110	8,57795	1,45917
AS35G2	619,8225	8,58088	1,45917
AS45G2	619,8361	8,58107	1,45917
A35E	620,9494	8,59648	1,45917
A45E	620,9494	8,59648	1,45917
A40XE	621,4088	8,60284	1,45917

The calculation results of coefficient k_b for dielectrics $_{33}As^{75}$, $_{14}Si^{28}$, $_{6}C^{12}$ are shown in Table 2.

Analysis of the calculated data of Tables 2 and 5, shows that the stiffness of crystal lattices is higher in dielectrics $_{6}C^{12}$ and $_{4}Si^{28}$. Consequently, the presence of silicon and carbon, according to the theory of phonon, increases the sound absorption capability of solids. Analysis of Table 4 shows that the highest percentage of carbon and silicon is in A40G, AS35G2 and AS45G2 types of automatic steel. The increase of the $_{6}C^{12}$ and $_{4}Si^{28}$ components in alloys of the studied steels increases the dissipation of the ultrasound energy in whole acoustic range. Constructions having an increased amount of carbon will have greater sound absorption. In the calculations of absorption coefficient of ultrasound oscillations for metals were taken only lattice oscillations. There wasn't considered the electron-phonon interactions, dislocation processes at interaction of sound oscillations with crystal lattice, and also the dependence of ultrasound absorption in crystal lattices of metal during its interaction with defects.

References:

[1] Omarov S.S., Insepov Z.A., Tukibayeva M.A., Dislocation dissipation of sound energy in single crystals and alloys. Proceedings of business conference "20 years of informatization in Kazakhstan: status, innovations, development management " Almaty. (2011), pp. 500-503.

[2] Omarov S.S., Begimov T.B., Tukibayeva R.M., Rakhmatullaev R.M., Estimation of absorption coefficient at interaction of ultrasound oscillations with crystal solid. J. "Vestnik KazNTU named after K.I. Satpayev» № 1 (95), (2013), pp.172 -175.

[3] Krasil'nikov V.A., Krylov V.V., Introduction to physical acoustics. 1984 - M. "Science." p.236.

[4] Musatai S.S., Tukibayeva M.A., Omarov S.S., Bakhitzhanova A.A. Amanzholova A.A., Study of acoustic parameters of crystal lattices of solids based on phonon theory. J. "Vestnik of KazNTU named after K.I. Satpayev", № 1 (101), (2014), pp.79-83.

[5] Belomestnykh V.N., Acoustic Gruneisen parameter. Journal of Theoretical Physics, t.30. Vol. 3. (2004), pp.14 -18.

[6] Nurgaliyev A.K., Omarov S.S., Tukibayeva M.A., Abzalieva A.M., Study of dissipation of ultrasound energy in alloys of automatic steels. J. "Vestnik of KazNTU named after K.I. Satpayev", № 1 (101), (2014), pp.89-92.

Advanced Materials Research Vol. 983 (2014) pp 338-341
© (2014) Trans Tech Publications, Switzerland
doi:10.4028/www.scientific.net/AMR.983.338

Research on Internal Flow Field of Control Valve Outlet Blockage Fault

Yantao An [a*], Rujian Ma[b] and Dong Zhao[c]

School of Mechanical Engineering,University of Jinan, Jinan 250022, China

[a] me_anyt@ujn.edu.cn, [b] rjma@ujn.edu.cn, [c] me_zhaod@ujn.edu.cn

Keywords: Control valve, Blockage, Flow field, Noise

Abstract. Internal flow field and noise of outlet blockage fault and trouble-free for control valve are studied by CFD. The study shows that the pressure of front-end and back-end for blockage is respectively increased, but the upper pressure is reduced. Two strong vortexes are formed at front-end and back-end of blockage, which reduce noise of pipe after valve.

Introduction

Control valve is the key equipment for chemical industry, nuclear power, etc, its working status directly related with operation of whole system[1-2]. However, for a long period of time to run, the impurities of fluid are easy to form blockage in control valve. The blockage fault not only increases the energy consumption of system, but also will cause the pressure pulsation of system, which destroys control valve and equipment of whole pipeline system[3-5]. Therefore, the study on blockage fault of control valve becomes extremely important. In this paper, based on the analysis of easily blocked parts, the outlet blockage fault is focused to research.3D flow model of outlet blockage fault and trouble-free for control valve are established, the internal flow field and noise distribution are simulated by CFD, the results provides the theoretical foundation for further study on the blockage fault of control valve.

Blocked Parts Analysis

At the beginning of running and after overhaul, the welding slag, rust, pulp of pipe and valve, as well as some medium which are easy to precipitate and contain solid particles, are easy to produce blockage fault in the valve body, inlet and outlet, as shown in Fig. 1. The blockage can produce strain, scratch and indentation at he valve core, valve body and pipe, and it affects the normal operation of valve.

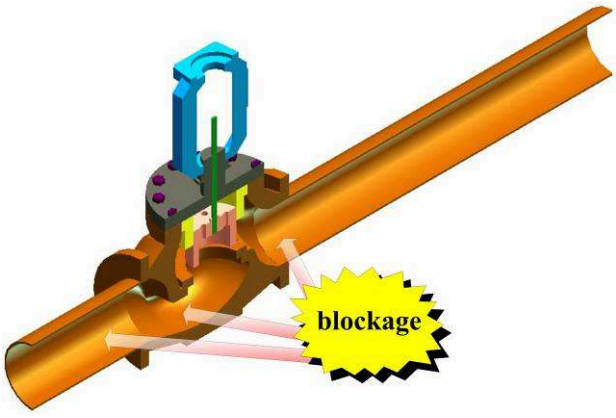

Fig. 1 Blockage of valve

Flow Channel Model

When setting up flow channel model of valve, in order to make the fluid flow fully, increase 2 times pipe diameters at inlet of valve, and increase 6 times pipe diameters at outlet of valve. The reason why pipe length of outlet is large, that is to consider the flow is smooth at the front of valve, and after the valve, fluid flow at high-speed by orifice, it a distance to flow smoothly.

When simulating the outlet blockage fault, a block is designed the interface section of valve and pipeline, as shown in Fig. 2. On the basis of it, the flow channel model of outlet blockage is set up, as shown in Fig. 3.

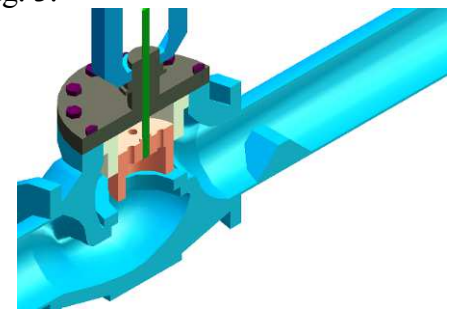

Fig. 2 3 d model of outlet blockage

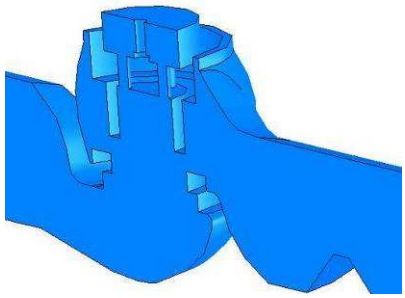

Fig. 3 Flow channel model of outlet blockage

Simulation Pretreatment

Before the analysis of internal flow field, flow channel model is need to meshing, and the simulation parameters should be set.

Meshing

When meshing the flow channel, according to the complexity of structure and the flow of fluid, the grid need refinement or sparse processing, and select the unstructured tetrahedral grid or hexahedral grid cell. Specific to structure, fluid state, grid process and unit selection for the outlet blockage of valve are shown in Table 1.

Table 1 Meshing

divided area	structure	fluid state	mesh processing	element type
valve inlet	simple	stable	sparsity	hexahedral
valve body	complex	unstable	refinement	unstructured tetrahedral
valve outlet	simple	unstable	refinement	unstructured tetrahedral

Mesh model of fully opening for outlet blockage is shown in Fig. 4.

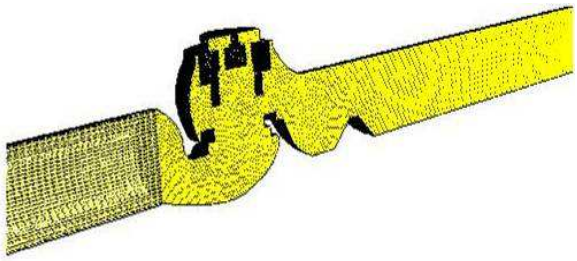

Fig. 4 Outlet blockage mesh model

Solution Setting

Solver type, turbulence model, the fluid medium and boundary conditions are needed to set, it is as shown in Table 2. In addition, it selects stationary flow, sets the inlet pressure is 1 MPa, and outlet pressure is 0.6 MPa. Speed and pressure field uses the implicit full iterative method. The coupling of pressure and velocity uses SIMPLE algorithm, all the discrete format use the second order wind format.

Table 2 Simulation Settings

settings	solver	turbulence model	media	boundary conditions
parameters	separating	Standard k-ε equation	mixed gas	pressure inlet / outlet

Internal Flow Field Analysis

Choosing relative opening is 100%, the inlet pressure is 1 MPa, outlet pressure is 0.6 MPa, to analyze the internal flow field of outlet blockage, and contrast analysis the trouble-free.

(1) Fig. 5 and Fig. 6 are pressure contours of internal flow field for trouble-free and outlet blockage. They show that compared with the trouble-free, it makes the minimum and maximum pressure increase, and makes the pressure of front-end and back-end are also increase, but the upper pressure is reduced.

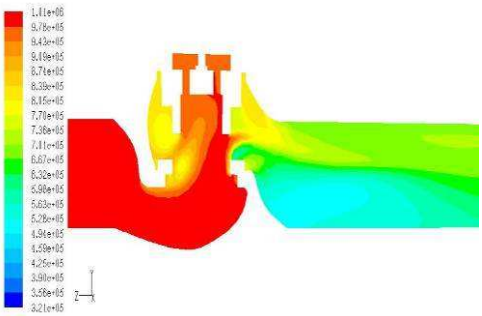

Fig. 5 Trouble-free pressure contours

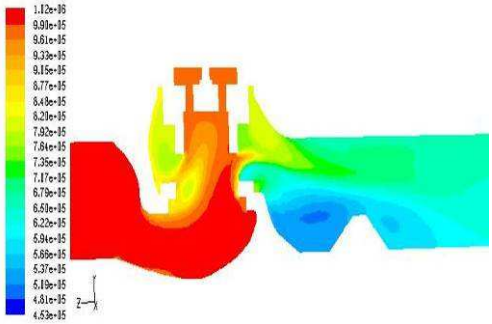

Fig. 6 Outlet blockage pressure contours

(2) Fig. 7 and Fig. 8 are velocity contours of internal flow field for trouble-free and outlet blockage. They show that compared with the trouble-free, it reduces the maximum speed, at the front upper and the upper, the velocity value almost no change, this is due to the fluid through the orifice is high-speed, high-speed fluid is mainly at the upper pipe, and therefore, it is little influence on its velocity. But at the after upper of blockage, the speed value is significantly reduced. This is because of the existence of block, it make a similar secondary orifice at the back-end of valve. Sectional area of back-end is suddenly increased. It makes the loss of pressure increase, which resulting the velocity decrease sharply.

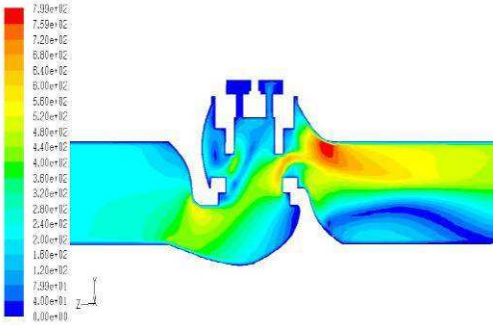

Fig. 7 Trouble-free velocity contours

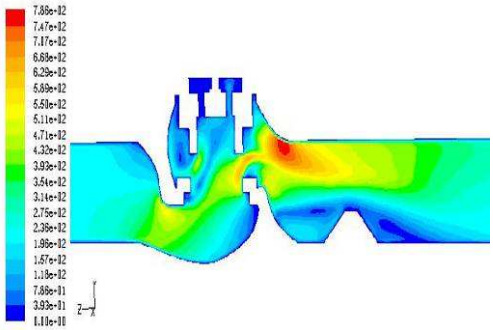

Fig. 8 Outlet blockage velocity contours

(3) Fig. 9 and Fig. 10 are velocity vector of internal flow field for trouble-free and outlet blockage. They show that compared with the trouble-free, it makes the Weak vortex of outlet become two strong vortex. The front-end vortex is due to fluid is blocked and flow direction is changed. The backend vortex is due to speed difference, which is the velocity of top is high, and the velocity of lower is low.

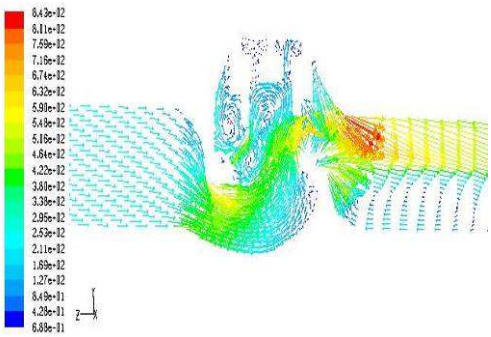

Fig. 9 Trouble-free local velocity vector

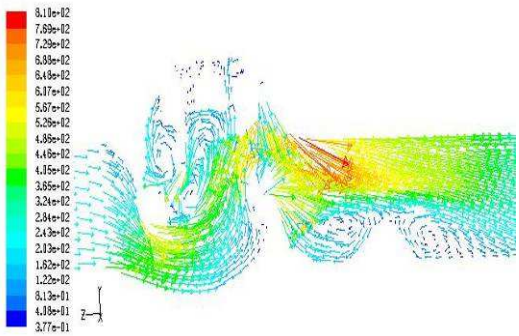

Fig. 10 Outlet blockage local velocity vector

Noise Analysis

Fig. 11 and Fig. 12 are acoustic power distribution of internal flow field for trouble-free and outlet blockage. They show that compared with the trouble-free, it increases the maximum noise value. The two small vortexes consume energy and reduce the flow rate, which reduce noise of pipe after valve.

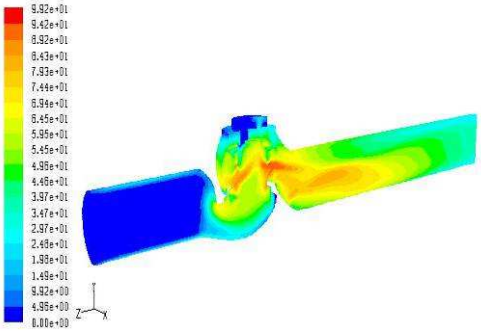

Fig. 11 Trouble-free local acoustic power

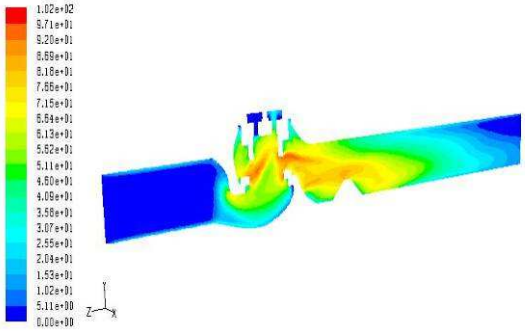

Fig. 12 Outlet blockage acoustic power

Conclusion

Establishing the valve trouble-free and outlet blockage flow model, and applying the CFD numerical simulation of internal flow field and noise, obtained the following conclusions.

(1) Outlet blockage makes the minimum and maximum pressure increase, and it also makes the pressure of front-end and back-end increase, but the upper pressure is reduced.

(2) Outlet blockage reduces the maximum speed, at the front upper and the upper, the velocity value almost no change, but at the after upper of blockage, the speed value is significantly reduced.

(3) Outlet blockage makes the weak vortex of outlet become two strong vortex at front-end and back-end of blockage.

(4) Outlet blockage increases the maximum noise value. The two small vortexes consume energy and reduce the flow rate, which reduce noise of pipe after valve.

Acknowledgements

This project is supported by Doctoral Fundation of University of Jinan (XBS1303) and Scientific Research Foundation of University of Jinan (XKY1312).

References

[1] Yantao An, Rujian Ma, Yong Wang, Simulation and Analysis the Internal Flow Field of Control Valve Bonnet Leakage, Applied Mechanics and Materials [J], 2013, 425, 2078-2081.

[2] Yantao An, Rujian Ma , Yong Wang, Research the Internal Flow Field of Valve Stem Leakage, Applied Mechanics and Materials[J], 2013,397, 257-260.

[3] D. Huang, Z.L. He, X.L. Yuan. Dynamic characteristics of an air-to-water heat pump under frosting/defrosting conditions [J].Applied Thermal Engineering,2007, 27(11-12):1996-2002.

[4] Zhang Deshegn，Zhao Juyun，Liulibao, etc. Analysis on electric and hydraulic valve jam problem of valve controlled hydraulic filling type hydraulic coupling [J]. COAL ENGINEERING, 2010(8: 81-82.

[5] Tang Yanchun. Study on Blocking Problem of Control Valve[J]. Process Equipment&piping, 2009, 46(2): 47-51.

Advanced Materials Research Vol. 983 (2014) pp 342-346

doi:10.4028/www.scientific.net/AMR.983.342

Migration Study of Biodegradable Blends of Polylactic Acid and Epoxidized Natural Rubber

Tarinee Nampitch

Department of Packaging Technology, Faculty of Agro-Industry, Kasetsart University, Bangkok 10900, Thailand

Corresponding author: fagitnn@ku.ac.th

Keywords: epoxidized natural rubber; migration; biodegradable film; polylactic acid

Abstract. Nowadays the use of biodegradable plastic in the food industry has increased dramatically. Because of its outstanding characteristics, i.e. environmental friendliness and non-toxicity, researchers are interested in studying how to improve the properties of plastic, especially polylactic acid or PLA, which is very fragile and intolerant to high impact force. Attempts have been made to improve the weak points of PLA by mixing PLA with epoxidized natural rubber. The natural rubber goes through an epoxidation process, resulting in epoxidized natural rubber (ENR) as the finished product. ENR contains epoxy groups which can efficiently react with PLA. Ratios of PLA and ENR employed in this study were 50:50, 60:40, 70:30, 80:20 and 90:10. In addition to finding a suitable ratio between PLA and ENR, the mixtures were subjected to migration tests according to the guidelines specified in European Commission Regulation (EU) No 10/2011 in order to prove whether the mixed materials are safe and suitable for consumer use. Migration testing was conducted by soaking samples in four different food simulants – 10% (v/v) ethanol in aqueous solution, 3% (w/v) acetic acid in aqueous solution, 20% (v/v) ethanol in aqueous solution and vegetable oil – for 24 h at 40 °C. The results showed that the PLA/ENR blends at every ratio had an overall migration amount of less than 10 mg/dm^2 in three of the sample simulants, while the overall migration from materials soaked in vegetable oil exceeded this standard. Migration tests of one of the sample blends conducted at 100 °C for 2 h showed similar results. In conclusion, polymer blends of PLA and ENR are appropriate for food packaging applications, but are not appropriate for foods containing vegetable oil.

Introduction

As environmental issues are a matter of increasing concern, biodegradable materials have attracted considerable attention for their potential use as sustainable plastics. In this research, blends of epoxidized natural rubber (ENR) and poly(lactic acid) (PLA) were prepared using a twin-screw extruder followed by injection molding to produce study samples. To obtain a lower cost, attain biodegradation and improve some of the properties of the blends, ENR derived from the partial epoxidation of natural rubber molecules was selected to be introduced into the biodegradable blends.

Polymer blending is an important method to obtain new materials that can meet different requirements. The blending of ENR with other polymers represents an important route to overcome the limitations of biodegradable materials. PLA is a biodegradable thermoplastic derived from renewable resources. Its good physical properties and commercial availability make it very attractive, not only as a substitute for non-biodegradable polymers for commercial applications, but also for specific applications in medicine and agriculture. The main limitations of PLA are its high price and brittleness, which restricts its use. Blending PLA with ENR has been shown to improve its toughness [1] and is a good way to address the issue of cost-effectiveness.

Consumer exposure to these blends is likely since they are present in food packaging. European Commission Regulation (EU) No 10/2011 and Council Directive 82/711/EEC address issues related to plastic materials and articles intended to come in contact with food and foodstuffs, as well as the simulants used in the migration assays. Their guidelines state that risk assessment should cover the potential migration under the worst foreseeable conditions of use and toxicity. Moreover, the European Commission Regulation (EU) No 10/2011 also establishes an overall migration limit of 10 mg/dm^2, specifying that plastic materials and articles should not transfer their constituents to food simulants in quantities exceeding 10 mg of total constituents released per dm^2 of food contact surface. The control of potentially migrant compounds are a key issue for the design of biodegradable systems for food packaging. PLA is among the most promising biopolymers for manufacturing these materials, and consequently it should be prepared to allow safe contact with different types of food simulants. Lactic acid is the lone monomer in the PLA structure, but migrants in PLA-based systems could include lactic acid itself, joined to dimers and other oligomers, produced by PLA hydrolysis [2–5]. However, different results could be found for PLA blends and copolymers with more complex migration processes. In general, food packaging materials should be designed to minimize the migration of additives and other compounds during storage or processing.

The aim of this research work was to study the migration properties of biodegradable blends of polylactic acid (PLA) and epoxidized natural rubber (ENR). Migration tests were performed according to the guidelines of the European Commission Regulation (EU) No 10/2011. All sample blends of PLA and ENR at various ratios had an overall migration amount of less than 10 mg/dm^2 when in contact with three different food simulants – 10% (v/v) ethanol in aqueous solution, 3% (w/v) acetic acid in aqueous solution, 20% (v/v) ethanol in aqueous solution – for 24 h at 40 °C. However, sample materials soaked in vegetable oil had an amount of overall migration exceeding the EU standard (10 mg/dm^2). Migration tests of the P60E40 blend conducted at 100 °C for 2 h showed similar results.

Materials and methods

Materials

Polylactic acid (PLA), type 2003D with a specific gravity of 1.24, was obtained from NatureWorks, USA. The PLA was dried in a hot-air oven at 60 °C for 24 h. Epoxidized natural rubber (ENR) was purchased from Muang Mai Guthrie Public Co. Ltd., Thailand. The ENR had an average molecular weight of 6.4×10^5.

Sample preparation. PLA and ENR were mixed in different proportions. The sample mixtures were placed into the hopper of a twin-screw extruder. The processing conditions were 180–190 °C with a screw speed of 60 rpm. The extrudates were pelletized at 700 cycles per min, followed by injection molding to produce samples. The formulation ratios are shown in Table 1.

Table 1. Formulation ratios of PLA and ENR blends

No.	PLA:ENR ratio	Sample name
1	50:50	P50E50
2	60:40	P60E40
3	70:30	P70E30
4	80:20	P80E20
5	90:10	P90E10

Overall Migration Tests

Overall migration tests were performed in four different food simulants – 10% (v/v) ethanol in aqueous solution, 3% (w/v) acetic acid in aqueous solution, 20% (v/v) ethanol in aqueous solution, and vegetable oil – for 24 h at 40 ^{o}C, for 24 h at 100 ^{o}C, and for 2 h at 100 ^{o}C, according to the guidelines of European Commission Regulation (EU) No 10/2011 Annex I and Regulation (EC) No 1935/2004 on overall migration from plastic.

Mechanical testing of blends

Tensile testing was done according to ASTM D638, using an Instron testing machine. The crosshead speed was set at 50 mm/min. Impact testing was done according to ASTM D256 by using a pendulum impact tester.

Results and Discussion

Migration is the quantity of material, mainly additives, which can be transferred to foodstuff when they are in contact. Recent time migration has been considered a negative issue since substances are likely to constitute a danger to human health and/or alter the composition of foodstuff in an unacceptable manner. However, a new trend to packaging is based on the migration as a positive issue in condition of the beneficial effect of some material additive [2–6] in foodstuffs.

Table 2. Migration tests over 24 h at 40 ^{o}C

Sample	Acetic acid 3% (w/v) (mg/dm^2)	Ethanol 10% (v/v) (mg/dm^2)	Ethanol 20% (v/v) (mg/dm^2)	Vegetable oil
P50E50	2	<1	2	18*
P60E40	<1	1	<1	16*
P70E30	<1	<1	<1	14*
P80E20	1	2	2	24*
P90E10	<1	<1	<1	17*

mg/dm^2 = mg per square decimeter
* = failed item

In this part of the study, the overall migration from biodegradable blends of polylactic acid and epoxidized natural rubber was evaluated. Tables 2, 3 and 4 show the results of the overall migration in four different food simulants: 10% (v/v) ethanol in aqueous solution, 3% (w/v) acetic acid in aqueous solution, 20% (v/v) ethanol in aqueous solution, and vegetable oil. Table 2 shows the overall migration results for five sample blends in four food simulants. Except in the case of vegetable oil, none of the samples exceeded the overall migration limit of 10 mg/dm^2. However, as shown in Table 3, migration tests of three sample blends for 24 h at 100 ^{o}C show that the values exceeded the overall migration limit (10 mg/dm^2) in all simulants. In migration testing for 2 h at 100 ^{o}C, the P60E40 blend had a value below the overall migration limit in all kinds of simulants except vegetable oil. In conclusion, biodegradable blends of PLA and ENR are appropriate for food packaging applications, but are not appropriate for foods containing vegetable oil.

Table 3. Migration tests over 24 h at 100 ^{o}C

Sample	Acetic acid 3% (w/v) (mg/dm^2)	Ethanol 10% (v/v) (mg/dm^2)	Ethanol 20% (v/v) (mg/dm^2)	Vegetable oil
P50E50	20*	30*	24*	<1
P80E20	63*	92*	77*	90*
P90E10	247*	58*	51*	75*

mg/dm^2 = mg per square decimeter
* = failed item

Table 4. Migration tests over 2 h at 100 ^{o}C

Sample	Acetic acid 3% (w/v) (mg/dm^2)	Ethanol 10% (v/v) (mg/dm^2)	Ethanol 20% (v/v) (mg/dm^2)	Vegetable oil
P60E40	2	5	4	41*

mg/dm^2 = mg per square decimeter
* = failed item

Table 5. Mechanical properties of PLA/ENR binary blends

Samples	Modulus (MPa) ± SD	Elongation at break (%) ± SD	Tensile strength (MPa) ± SD	Impact strength (KJ/m^2) ± SD
PLA	1874.34 ± 1.62	2.26 ± 1.84	44.67 ± 1.62	3.33 ± 0.98
P90/E10	885.67 ± 1.08	2.86 ± 0.92	18.34 ± 1.62	5.56 ± 1.56
P80/E20	815.67 ± 1.15	0.93± 0.98	8.00 ± 0.56	4.40 ± 0.65
P70/E30	175.00 ± 0.98	0.70± 1.35	0.70 ± 0.26	4.50 ± 1.47
P60/E40	138.34 ± 1.82	0.75± 1.88	1.17 ± 0.73	10.80 ± 0.87
P50/E50	29.00 ± 1.41	0.70± 1.64	0.86 ± 0.11	10.30 ± 1.18

The effect of PLA and ENR blending on the modulus, elongation at break, tensile strength, impact strength and hardness are shown in Table 5. As expected, compared with neat PLA, the addition of ENR reduced the modulus and strength significantly, while the elongation at break was improved. However, for compositions containing more than 10% ENR, the elongation at break dropped dramatically, as did the modulus and the tensile strength. Impact strength increased with increasing amounts of ENR. However, the tensile properties of PLA/ENR composites decreased with increased loading of ENR. This may be attributed to the elastomeric behavior and compatibilization effects of ENR. At 10% ENR or less, chemical interactions probably occurred between the oxirane groups of ENR and the hydroxyl groups in PLA. The chemical interactions between PLA and ENR were proposed in Fig. 1. It was believed that the hydrogen bonding could form between the OH group of PLA and the expoxide group of ENR [7]. The results from the mechanical properties indicated that the 90/10 composition of the PLA/ENR blend had the highest modulus, elongation at break and tensile strength compared to other compositions. In order to improve toughness and strength to PLA, the ENR must be distributed as small domains (usually 0.1–1.0 μm) in the matrix PLA, and the ENR must have good interfacial adhesion to PLA [8].

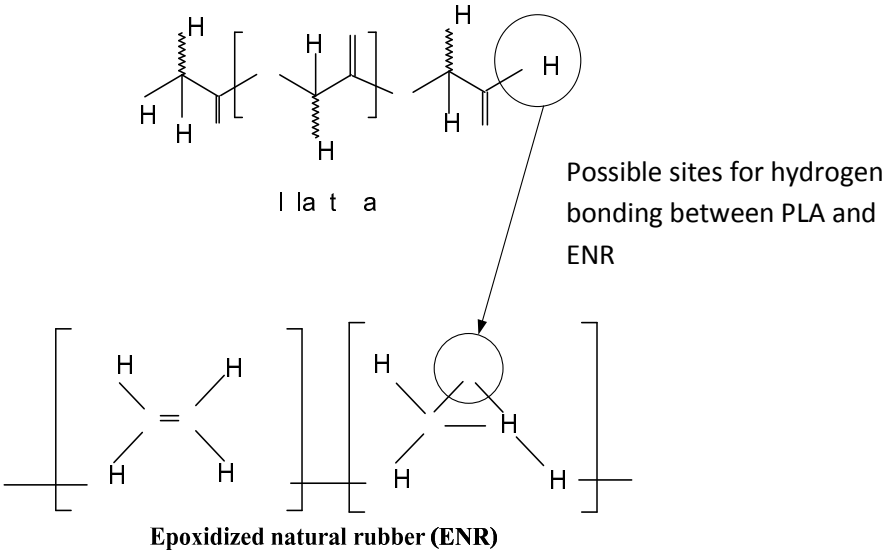

Fig. 1 Proposed chemical interactions between PLA and ENR

Summary

The production and migration properties of biodegradable blends of polylactic acid and epoxidized natural rubber for food packaging applications were investigated. Brittle PLA was blended with epoxidized natural rubber (ENR) with an aim to increase the ductility of PLA.

However, the blends greatly sacrificed the modulus and tensile strength. The 90/10 composition of the PLA/ENR blend gave the highest elongation at break, modulus, tensile strength and impact strength when compared with other blends. The migration levels of the studied biodegradable blends were below the overall migration limits under some conditions and simulants, suggesting the possibility of using these systems in food packaging applications. Therefore, the final conclusion of this work would be that the proposed biodegradable blends of polylactic acid and epoxidized natural rubber would be adequate alternatives to current formulations for food companies.

Acknowledgements

The authors gratefully acknowledge financial support from Kasetsart University Research and Development Institute (KURDI).

References

[1] T. Nampitch, M. Rattanawan, Preparation, characterization and properties of ternary blends with epoxidized natural rubber, poly(lactic acid) and poly(butylene adipate-co-terephthalate), Adv. Mater. Res. 335–336 (2011) 762–768.

[2] S. Maisanaba, S. Pichardo, M. Jordá-Beneyto, S. Aucejo, A.M. Cameán, A. Jos, Cytotoxicity and mutagenicity studies on migration extracts from nanocomposites with potential use in food packaging, Food Chem. Toxicol. 66 (2014) 366–372.

[3] R.E. Conn, J.J. Kolstad, J.F. Borzelleca, D.S. Dixler, L.J. Filer Jr., B.N. LaDu Jr., M.W. Pariza, Safety assessment of polylactide (PLA) for use as a food-contact polymer, Food Chem. Toxicol. 33 (1995) 273–283.

[4] E. Fortunati, M. Peltzer, I. Armentano, A. Jiménez, J.M. Kenny, Combined effects of cellulose nanocrystals and silver nanoparticles on the barrier and migration properties of PLA nano-biocomposites, J. Food Eng. 118 (2013) 117–124.

[5] E. Fortunati, M. Peltzer, I. Armentano, L. Torre, A. Jiménez, J.M. Kenny, Effects of modified cellulose nanocrystals on the barrier and migration properties of PLA nano-biocomposites, Carbohydr. Polym. 90 (2012) 948–956.

[6] N. Poovarodom, P. Suppakul, R. Ta-ieng, W. Visitsart, Migration potential from plastic food contact materials – Case study: stretch films, Kasetsart J. (Nat. Sci.) 33 (1999) 397–406.

[7] G.H. Yew, A.M. Mohd Yusof, Z.A. Mohd Ishak, U.S. Ishiaku, Water absorption and enzymatic degradation of poly(lactic acid)/rice starch composites, Polym. Degrad. Stab. 90 (2005) 488.

[8] S. Wu, Chain structure, phase morphology, and toughness relationships in polymers and blends, Polym. Eng. Sci. 30 (1990) 753.

Advanced Materials Research Vol. 983 (2014) pp 347-352

doi:10.4028/www.scientific.net/AMR.983.347

Numerical Simulation of NOx Emission in Supercharged Boiler

Zhang Hongyan[1, 2], Zhao Jing[1, a *], Yang Longbin[1], Li Yanjun[1]

[1]College of Power and Energy Engineering, Harbin Engineering University, Harbin, 150001, China

[2]Department of naval equipment, Beijing, 100071, China

[a]zhaojingcopaee@163.com

Keywords: Supercharged boiler, Numerical simulation, NOx emission

Abstract. The actual supercharged boiler is reasonably simplified and the geometric model of the furnace and the mathematical model of steady-state three-dimensional turbulent reaction are built in this paper. Numerical simulation of the thermal NOx emission under three different loads in the furnace of a supercharged boiler is conducted with FLUENT software. The thermal NOx emission increases in the furnace when the load increases and the largest mole fraction of the thermal NOx mainly exists at the back edge of high temperature.

Introduction

Supercharged boiler plays a significant role in the steam power plant [1] due to its small volume, light weight and high output power and it can also be applied in stationary power plants on land [2].At present the number and the application range of the supercharged boiler are far less than that of coal-fired boiler, but NOx emission can not be ignored. Some domestic researchers have investigated NOx emission in the supercharged boiler by using numerical simulation method [3,4] and approximate calculation method [5]. However, the research on NOx emission in the supercharged boiler is still less.

The supercharged boiler is studied in this paper by CFD methods. FLUENT is used to simulate the thermal NOx emission under three different loads in the furnace. Influence of the three different loads on the thermal NOx emission is discussed to provide some reference for reduction of NOx in the supercharged boiler.

Formation Model of the Thermal NOx

The formation of nitrogen oxides in the combustion process is mainly NO and NO_2. NO and NO_2 are usually known as nitrogen oxides NOx. Test shows that NO content is more than NO_2 content among the nitrogen oxides emitted from combustion device. Moreover NO_2 is generated by NO. So it is mainly considered the generation of NO in the mathematical model of nitrogen oxides [6].At present the formation mechanism of nitrogen oxides mainly includes the thermal NOx, the prompt NOx and the fuel NOx. Due to the less of the nitrogen content, so the fuel NOx is ignored. Due to the prompt NOx generated is less, so the prompt NOx is also ignored. The thermal NOx emission in the furnace is numerically simulated in this paper.

According to expanding Zeldovich mechanics, the process of the thermal NOx generation is expressed as follows:

$$N_2 + O \underset{k_{-1}}{\overset{k_1}{\rightleftharpoons}} N + NO \,. \tag{1}$$

$$O_2 + N \underset{k_{-2}}{\overset{k_2}{\rightleftharpoons}} NO + O \,. \tag{2}$$

$$N + OH \underset{k_{-3}}{\overset{k_3}{\rightleftharpoons}} NO + H \,. \tag{3}$$

According to the partial temperature T, the concentration of O_2, N_2, O and OH in the equilibrium state, the reaction rate of NO is calculated as follows:

$$\frac{dc_{NO}}{dt} = 2k_1 c_O c_{N_2} \frac{(1 - \frac{k_{-1}k_{-2}c_{NO}^2}{k_1 c_{N_2} c_{O_2}})}{(1 + \frac{k_{-1}c_{NO}}{k_2 c_{O_2} + k_3 c_{OH}})} \,. \tag{4}$$

Where c stands for mole fraction, and the unit is gmol/m^3; k_1, k_2 and k_3 represent positive reaction rate; k_{-1} and k_{-2} stand for the reverse reaction rate, and the unit of them are both m^3/(gmol·s).

O_2 decomposition is:

$$O_2 + M \rightleftharpoons O + O + M \,. \tag{5}$$

Using patial equilibrium method:

$$c_O = 36.63 T^{0.5} c_{O_2} e^{-27123/T} \ \text{gmol/m}^3. \tag{6}$$

The OH concentration in Eq. 3 is :

$$c_{OH} = 2.129 \times 10^2 T^{-0.57} e^{-4595/T} c_{O_2}{}^{0.5} c_{H_2O}{}^{0.5} \ \text{gmol/m}^3. \tag{7}$$

Geometric Model, Mesh Generation and Boundary Conditions

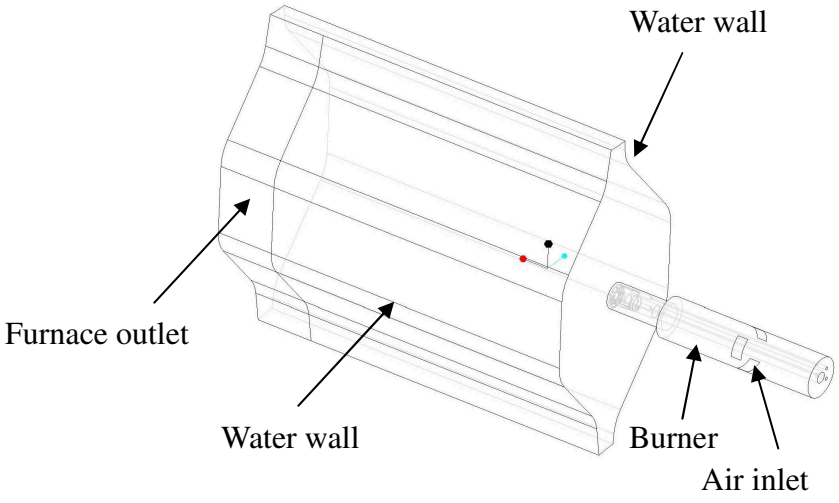

Fig.1. Geometric model of numerical simulation

The geometric model of numerical simulation is shown in Fig.1. The burner consist of two nozzles and flame holder et al. The furnace mainly include upper drum, lower drum, water wall, convection tube bank and furnace wall. The structure of the boiler's furnace and combustion equipment are complex, so it is necessary to simplify the geometric model for numerical simulation. The water wall is simplified to an isothermal surface and the convection tube bank is simplified to a surface as the outlet. The final three dimensional computational domains include the water wall, the convection tube bank, the front and back wall and a burner.

As the geometric model of numerical simulation is complex, we split the volume into several ones and then mesh one by one.

To improve the accuracy, tetrahedral elements are used for the burner. And hexahedral or hexahedral/wedge elements are used for the boiler's furnace to improve calculation speed.

The main boundary conditions for three different loads are shown in Table1.Thermal conductivity and viscosity are both set with a linear function. Constant pressure specific heat is set with polynomial function.

Table1 Boundary conditions

load		30%	50%	80%
Pressure(Pa)		171950	208150	208150
Inlet of fuel oil (Discrete phase particle source)	Oil temperature (K)	20	20	20
	Mass flow rate of fuel oil for a nozzle (kg/s)	0.0093	0.01125	0.01667
Inlet of air (Mass flow inlet)	Air temperature (K)	336.05	365.25	365.25
	Mass flow rate of air (kg/s)	0.48	0.59	0.59
The convection tube bank (Pressure outlet)	Backflow total temperature (K)	1100	1100	1100
	External black body temperature (K)	600	600	600
	Internal emissivity	0.8	0.8	0.8
Water wall (Isothermal wall)	Wall temperature (K)	471	471	471

Numerical Simulation Results and Analysis

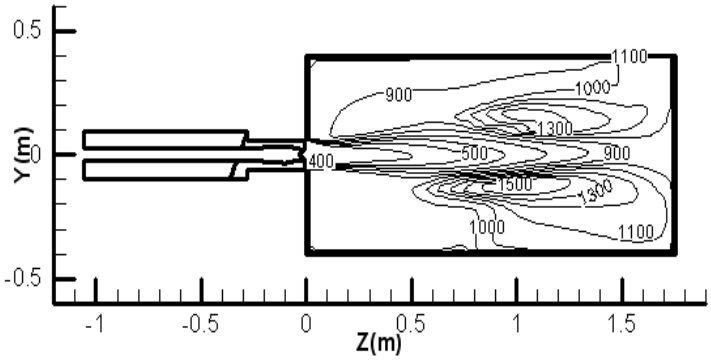

Fig.2 Contour map of temperature for 30% load

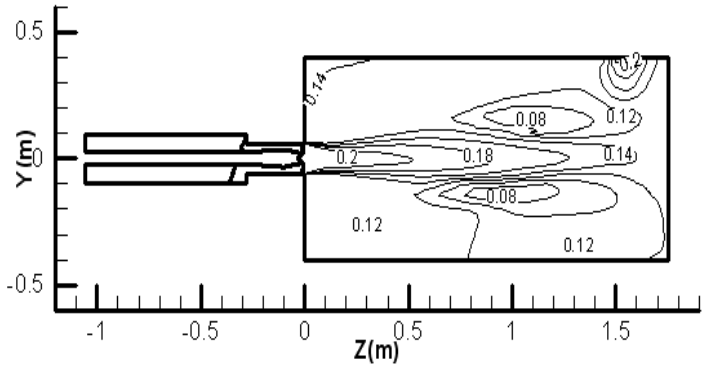

Fig.3 Contour map of mole fraction of O_2 for 30% load

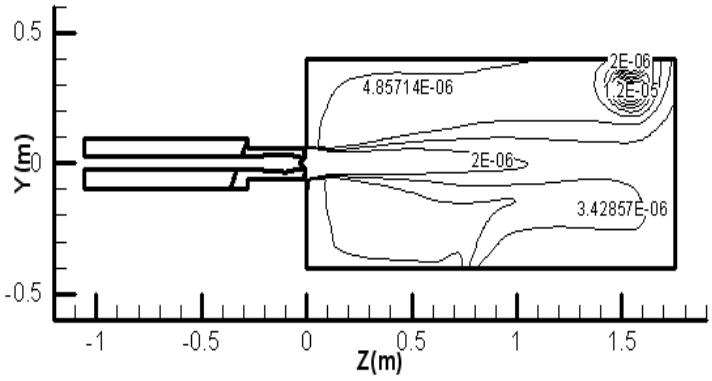

(c) 80% load

Fig.4 Contour map of mole fraction of NO for 30% load

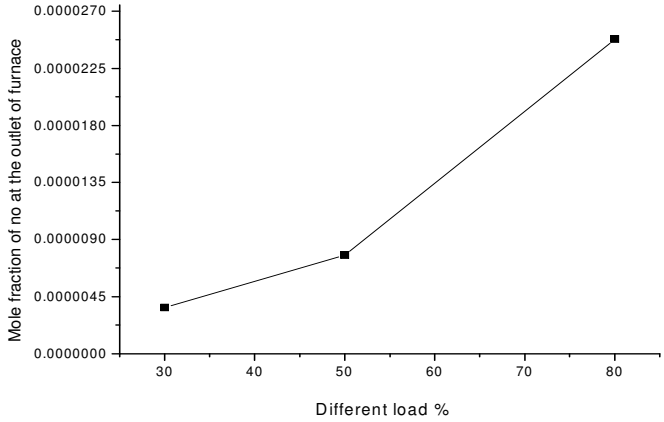

Fig.5 Mole fraction of NO at the outlet of furnace under different loads

The distribution of temperature for 30% load is shown in Fig.2. Fig.3 shows the distribution of O_2 mole fraction for 30% load. The figure shows that the largest mole fraction of O_2 mainly exists at the back edge of high temperature. Fig.4 shows that the largest mole fraction of the thermal NOx mainly exists at the back edge of high temperature for 30% load. Because the thermal NOx generated not only needs higher temperature, but also the sufficient O_2. Temperature and the mole fraction of O_2 at the back edge of high temperature can satisfy conditions of N_2 and O_2 reaction. So the thermal NOx generated in the area is much more. The largest mole fraction of O_2 mainly exists at the back edge of high temperature. The results of the distribution of the thermal NOx are also obtained for 50% load and 80% load. The largest mole fraction of the thermal NOx also mainly exists at the back edge of high temperature respectively for 50% load and 80% load. Fig.5 shows that the mole fraction of NOx increases at the outlet of furnace when the load increases. Because the fuel supplied to the furnace increases and burning more fully when the load increases. So the quantity of released heat and the maximum temperature of the furnace increase.

Conclusions

1.The thermal NOx emission increases in the furnace when the load increases.
2.The thermal NOx generated in the furnace is close to the distribution of temperature and the mole fraction of O_2.Moreover the largest mole fraction of the thermal NOx mainly exists at the back edge of high temperature.

Acknowledgement

The financial support of the Fundamental Research Funds for the Central Universities (HEUCF110303) is gratefully acknowledged.

References

[1] LIU Chang he, New Developments in Marine Supercharged Boilers, Journal of Engineering for Thermal Energy and Power. 14 (1999) 241-245.

[2] JI Gui ming, LI Hui wen, Pressurized Main Boiler Being Used in Naval Ships and Marine, Boiler Manufacturing. (1999) 23-30.

[3] MU Yong, ZHENG Hong tao, Numerical Analysis of Flow Field and Pollutant Emission in Flue Gas Generator of Supercharged Boiler, Machinery Design & Manufacture. (2010) 190-192.

[4] HAN Qing, ZHENG Hong tao, LIU Ming ming, Numerical Simulation of NOx in Flue Gas Generator of Supercharged Boiler, Applied Science and Technology. 35 (2008) 69-72.

[5] QIN Xiao yong, LI Jun, ZHANG Xiao dong, The approximate calculation methods of NOx Generation and Emission in Marin Supercharged Boiler, Journal of Engineering for Thermal Energy and Power. 28 (2013) 82-85.

[6] ZHAO Jian xing, Numerical Simulation of Combustion, Science Press, Beijing, 2002.

Advanced Materials Research Vol. 983 (2014) pp 353-356

doi:10.4028/www.scientific.net/AMR.983.353

Conceptual Design Study of Small 400 MWt Pb-Bi Cooled Modified Candle Burn-up Based Long Life Fast Reactors

Zaki Su'ud [1,a] and H. Sekimoto[2,b]

[1]Department of Physics, Faculty of Mathematics and Natural Sciences, Bandung Institute of Technology, Bandung, Indonesia

[2]Emeritus Professor in Research Lab. For Nuclear Reactors, Tokyo Institute of Technology

[a]zakisuud@gmail.com,[b]hsekimot@gmail.com

Keywords: Pb-Bi cooled, long life, fast reactors, modified CANDLE, natural uranium, fuel shuffling

Abstract. In this paper conceptual design study of modified CANDLE burn-up scheme based 400 MWt small long life Pb-Bi Cooled Fast Reactors with natural Uranium as Fuel Cycle Input has been performed. In this study the reactor cores are subdivided into 10 parts with equal volume in the axial directions. The natural uranium is initially put in region 1, after one cycle of 10 years of burn-up it is shifted to region 2 and the region 1 is filled by fresh natural uranium fuel. This concept is basically applied to all regions, i.e. shifted the core of I'th region into I+1 region after the end of 10 years burn-up cycle. For small reactor core, it is important to apply high breeding material, so that high volume fraction of 60% fuel volume fraction nitride fuel is applied. The effective multiplication factor initially at 1.005 but then continuously increases during 10 years of burn-up. The peak power density initially about 307 W/cc but then continuously decreases to 268 at the end of 10 years burn-up cycle. Infinite multiplication factor pattern change, conversion ratio pattern change, and Pu-239 accumulation pattern change shows strong acceleration of plutonium production in the first region which is located near the 10^{th} region. Maximum discharged burn-up is 31.2% HM.

Introduction

Small long-life modular Pb-Bi cooled fast reactors are very prospective for remote area with small-medium power consumption level. They also very good to be combined so that large turbine can be used and produces very competitive nuclear energy[1-3] .

Modified CANDLE burn-up scheme is an alternative burn-up strategy to optimally utilize natural uranium resources without the necessity of nuclear fuel enrichment and nuclear fuel reprocessing plants which are two very sensitive issues related to the nuclear non-proliferation in the world especially when it is carried out in the developing countries [3-7].

In this study, conceptual design study of small long life Pb-Bi cooled fast reactors which can be continuously operated by only supplying natural uranium without fuel enrichment plant or fuel reprocessing plant has been performed[6-7]. The optimization processes include adjustment of fuel region movement scheme, volume fraction adjustment, core dimension, etc.

Design Concept and Calculation Method

In this study CANDLE burn-up strategy is slightly modified by introducing discreet regions [4-7]. In this design the reactor cores are subdivided into several parts with the same volume in the axial directions. The natural uranium is initially put in region 1, after one cycle of 10 years of burn-up it is shifted to region 2 and the region 1 is filled by fresh natural uranium fuel. This concept is basically applied to all regions, i.e. shifted the core of I'th region into I+1 region after the end of 10 years burn-up cycle (see figure 1) [7].This type of NPP need high conversion/breeding fuel, so a high fuel volume fraction based on nitride fuel is proposed (fuel volume fraction is 60%). The core

is then optimized to fulfill the criteria that the core can maintain criticality during 10 years of burn-up using the proposed refueling scheme.

The calculation is performed using SRAC code system [8], SLAROM code system[9], and FI-iTBCH1 code system[10]. At the beginning we assume the power density level in each region and then we perform the burn-up calculation using the assumed data. The burn-up calculation is performed using cell burn-up in SRAC code which then give eight energy group macroscopic cross section data to be used in two dimensional R-Z geometry multi groups diffusion calculation. The average power density in each region resulted from the diffusion calculation is then brought back to SRAC code for cell burn-up calculation. This iteration is repeated until the convergence is reached[7].

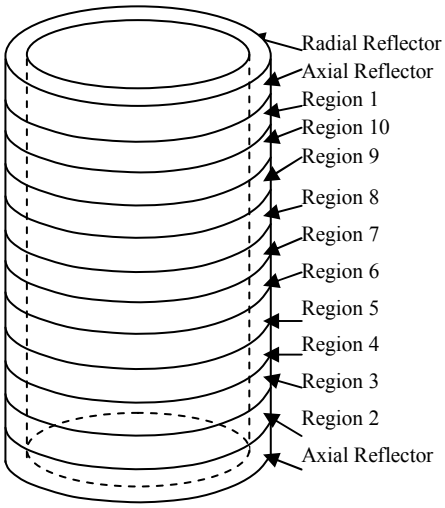

Fig. 1 Illustration of Modified CANDLE burn-up scheme for 10 axial regions

Table 1: Sample Core parameters

Parameter	Value/description
Power (MWth)	400
Number of equal volume region in core	10
Sub cycle length (years)	10
Fuel type	Nitride (UN-PuN)
Fuel/cladding/coolant vol.frac.	60 /12.5/27.5 %
Fuel diameter	1.2 cm
Coolant type	Pb-Bi
Axial width of each region	17.5 cm
Active core radial width	90-105 cm
Radial/axial Reflector width	70 /70 cm

Calculation Results and Discussion

Table 1 shows main parameters of 400 MWt Modified CANDLe burnup core.
The cladding is stainless stell, which need replacement (recladding process) after about 10% of burn-up level. For the standard case the change of effective multiplication factor during 10 years of operation is shown in Fig. 2. It is shown that the k-eff value increases monotonously. It means that the accumulation of plutonium due to the burn-up process in the regions 1-7 is still dominant compared to the plutonium and other minor actinide burning process in the regions 8-10. On the other hands, the peak power density tends to decrease during 10 years of continuous operation. This phenomenon occurs due to the shifting of the burning region toward regions 2-6 due to accumulation of fissile materials during 10 years of operation. This phenomenon has been explained for the large size modified CANDLE designs [7].

Fig. 4 shows burn-up level change during fuel history. It is shown that for about 50 years of life the accumulation of fissile material is more dominant than burning process. After the fuel moved to the region 6-10 then the burning process becomes more dominant, especially in the regions 7-10. In the region 10 (burn-up history of 90-100 years) there is a little decrease in the burn-up rate of change. This is occur due to the significant decrease of U-238 atmic density so that the production level of Pu-239 decreases significantly. On the other hands the accumulation of the fission products causes higher absorbtion cross section. Therefore the neutron flux level and power level in the regions10 tend to decrease

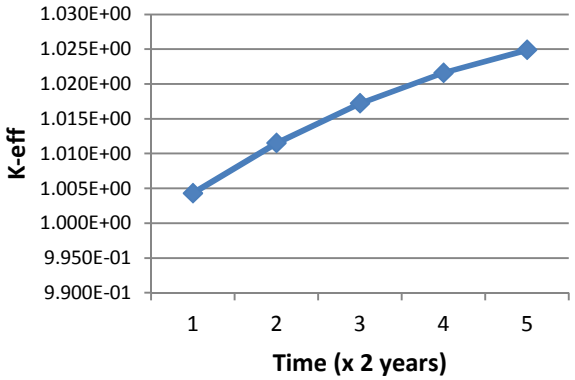

Fig. 2 k-eff change during 10 years operation

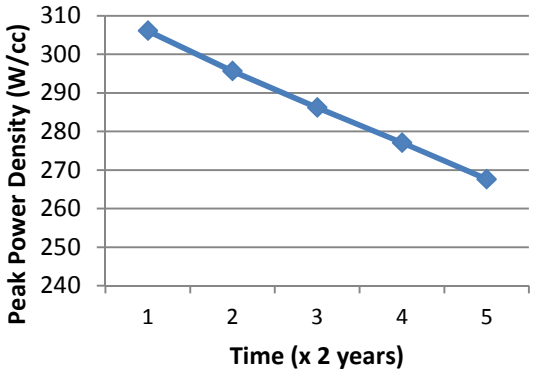

Fig. 3 Peak power density change during burnup

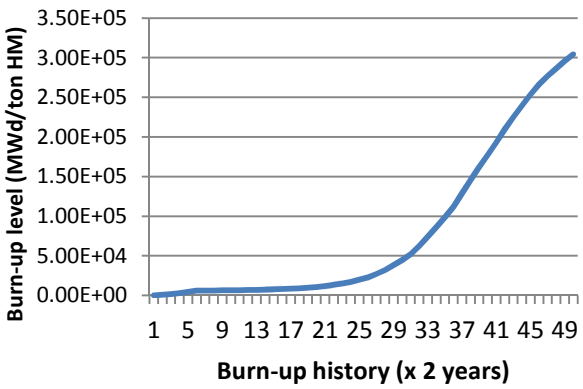

Fig. 4 Burn-up level change in 100 years history

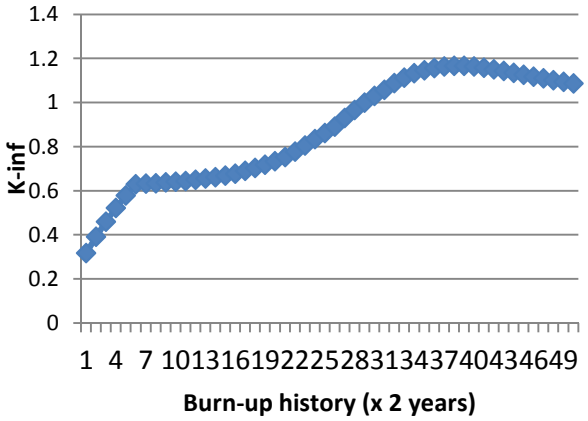

Fig. 5 K-inf change during 100 years history

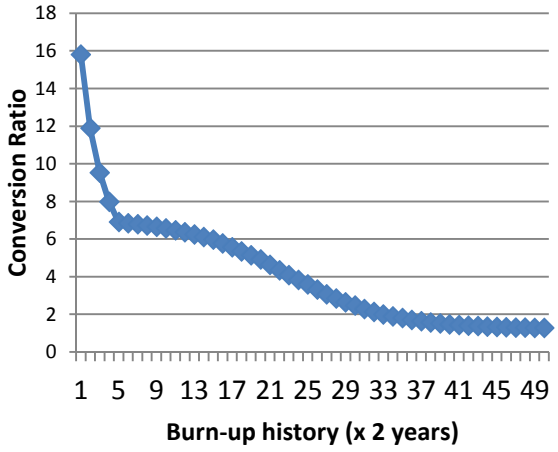

Fig. 6 Conversion ratio change during burnup

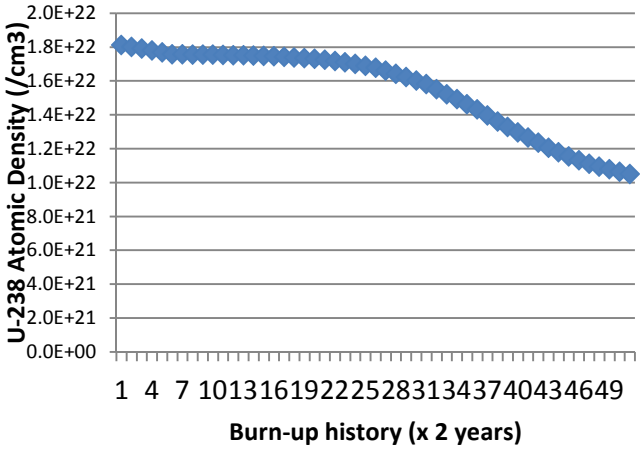

Fig. 7 U-238 atomic density change during burnup

Fig. 5 shows infinite multiplication constant change during burn-up. It is shown that after sharp increase of its value during in the first region, the value increases slowly till about 40 years of burn-up history. After that the k-inf value increases significantly till reach the peak in about78 years in burn-up history and after that decreases due to the accumulation of fission product and the significant decrease of U-238 atomic density.

Fig. 6 shows conversion ratio change during burn-up history. It is shown that there is a sharp decrease of conversion ratio during in the the first region. This is due to significant plutonium accumulation during in this region due to its position near the 10th region

Figs. 7 and 8 shows U-238 and Pu-239 atomic density during burn-up history.. U-238 atomic density decreases slowly till about 50 years of burn-up history, but then significantly decreases after

entering the most active regions. It is shown that Pu-239 accumulated very fast in the first 10 years, but then slowly accumulated till about 40 years of burn-up history. Then the fuel enter the more active region in which Pu-239 accumulation become significant and reach the peak in about 76 years and after that decreases. The reduction of U-238 stock at the last period of burn-up becomes the main cause of the Pu-239 atomic density decrease since 66th year.

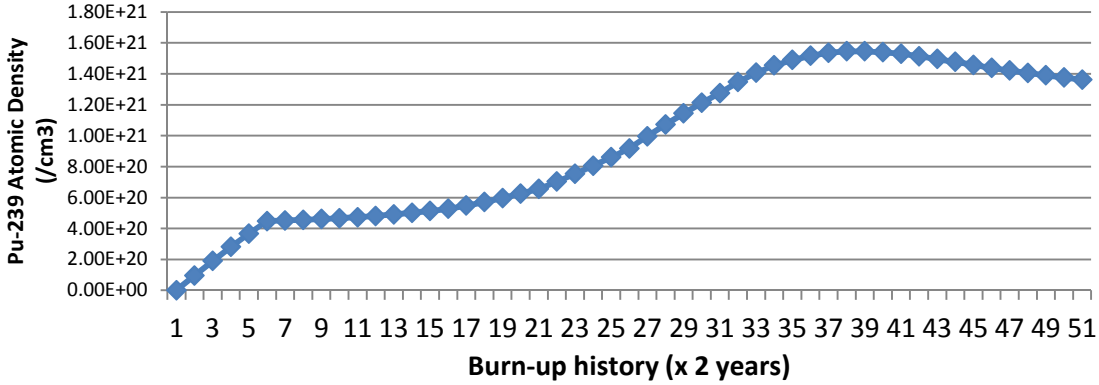

Fig. 8 Pu-239 atomic density change during 100 years fuel history

Summary

Pb-Bi cooled Small long life fast reactors with natural uranium as fuel cycle input can be implemented using nitride fuel with about 60% fuel volume fraction or more employing Modified CANDLE burn-up scheme. The effective multiplication factor initially at 1.005 but then continuously increases during 10 years of burn-up. The peak power density initially about 307 W/cc but then continuously decreases to 268 at the end of 10 years burn-up cycle. Infinite multiplication factor pattern change, conversion ratio pattern change, and Pu-239 accumulation pattern change shows strong acceleration of plutonium production in the first region which is located near the 10^{th} region. Maximum discharged burn-up is 31.2% HM.

Acknowledgement:

This research supported by Hibah Kompetensi 2014 and Riset Unggulan KK ITB 2013

References

[1] Zaki Su'ud: Progress in Nuclear Energy Vol. 50 (2008), p.276-278.
[2] Zaki Su'ud: Progress in Nuclear Energy, Vol. 50 (2008), p.157-162.
[3] Epung S.B. et.al.: Progress of Nuclear Energy Vol. 50 (2008), p. 434-437.
[4] H. Sekimoto, et al. : Nuclear Science and Engineering Vol 139 (2001), p. 1-12
[5] Y. Ohoka and H. Sekimoto: Nucl. Eng. Des.Vol. 229 (2004), p.15-23.
[6] Rida SNM and Zaki Su'ud: International Journal of Nuclear Energy Science and Technology Vol. 4 No. 3 (2009),p.217-222
[7] Zaki Su'ud and H. Sekimoto (2010) Int. Journal of Energy Science and Technology (IJNEST), Vol 5, No. 4 (2010), p.347-368
[8] OKUMURA, K., Teruhiko KUGO, Kunio KANEKO and Keichiro TSUCHIHASHI: SRAC (Ver.2002) ;The comprehensive neutronics calculation code system', JAERI Report, 2002
[9] Z. Su'ud, FI-ITB CH1 Code: Code for Fast Reactor Design Analysis, Internal Report, ITB, Indonesia (2000).
[10] Nakagawa, M. and Tsuchihashi, K. , SLAROM: A Code for Cell Homogenization Calculation of Fast Reactor, JAERI M 1294 (1984).

CHAPTER 6:

Applied Mechanics and Engineering

Advanced Materials Research Vol. 983 (2014) pp 359-362

doi:10.4028/www.scientific.net/AMR.983.359

Based on RFID prefabricated building component design and monitoring system research

Jing Wang [1,2,3]

[1]China Construction Eighth Engineering Bureau workstation of postdoctoral scientific research, Shanghai 200135

[2]Management science and Engineering in Shanghai Jiao Tong University post-doctoral research station, Shanghai 200240

[3]Northwest University of Politics and School of Economics and Management , Xi'an 710063

wjing818@126.com, 719428937@qq.com

Key words: RFID; Prefabricated buildings; Component design; Monitoring system

Abstract: Long-term since, our country concrete building mainly adopts the construction of the traditional mode of production, design and build extensive, poor operation condition, high labor intensity, large building materials loss and building garbage, construction quality is not stable, the whole life cycle of building energy consumption is high, the low degree of industrialization, and the energy conservation, emission reduction and environmental protection policies carried out by the state. Prefabricated buildings are the main characteristics of the sustainable development of construction industry, the integration of the supply chain of the project life cycle, emphasizes the decisive automation and intelligent technology. The emergence of the RFID theory for the research of prefabricated construction provides a new perspective.

1. An overview of the

Prefabricated construction refers to the PC Prefabricated structure (Prefabricated concrete), Prefabricated components or parts as the main component, the assembly and connection of reinforced concrete structure, in construction field assembly of residential buildings and commercial, office and other public buildings. Construction speed, short construction period, not only greatly save labor, and make full use of industrial waste, the structure system in overseas mature and a large number of applications, while in the country has just started in[1]. RFID Radio Frequency Identification technology (Radio Frequency Identification) is in the 1990 s began to rise and cause wide attention and industry at the forefront of international economics theory, is a use of rf signal through space coupling (alternating magnetic field or electromagnetic field) and transmit information through non-contacting technology's message to identify the purpose of [2]. The theory is put forward, then get the positive response of academia. On the one hand, the modern economic system in the construction industry is important industry of national economy and people's livelihood, with deepening the concept of sustainable development, industrialization and prefabricated buildings to become the hot spot of the construction industry, show some new characteristics, prefabricated building advocates the project life cycle of the supply chain integration, however, due to a lack of decisive automation and intelligent technology, in the still makes it hard for each member of supply chain data integration, increase the difficulty of integration. Using the theory of traditional engineering construction management is difficult to solve in a timely manner under the high speed operation of supply chain information acquisition

and processing, unable to improve the degree of information sharing and the relationship between each node enterprise and cooperation; , on the other hand, in practice, due to the harsh environment construction site, RFID mostly used in construction product identification and tracking, and few application in prefabricated construction engineering, management in planning and design phase, component manufacturing stage management, prefabricated field assembly stage management in construction, building construction phase of the management, operation and maintenance phase of the management, and government regulation policies are difficult to use traditional engineering construction management theory to research, and the emergence of the theory of RFID technology just provides a new research perspective.

2. The prefabricated building components and the node stress analysis of the performance, design technology and construction requirements

Prefabricated buildings in the early 20th century began to arouse people's interest, to the second world war, European countries and Japan and other countries a severe housing shortage, pressing for solve the problem of housing, promote the development of prefabricated buildings. In the 60 s, prefabricated building got a promotion. Because of prefabricated construction speed, low production cost, quickly spread all over the world. Research and application of precast concrete structure in China began in the 1950 s, the main learning technology system from the former Soviet union and other countries; Until the 1980 s, in industrial and civil construction has been more widely used. After the 1990 s, due to various reasons, the application of precast concrete structure especially in the civil construction, the application of gradually reduce, experienced a relatively low stage. With the sustained and rapid development of national economy, improvement of energy conservation and environmental protection, Labour costs rising, in the past decade, research in the prefabricated concrete building in China gradually heating up, some technical researches on several units, and in China vanke co., LTD., shui co., LTD., jiangsu zhongnan construction group co., LTD., heilongjiang youwe construction group for development projects such as the demonstration and application of a certain size [3]. Prefabricated concrete structure is proposed, which can effectively save resources and energy, improve the material in the realization of efficiency of building energy efficiency and the structure performance, reduce the construction claim to the fields such as environmental conditions, reduce construction waste and adverse impact on the environment and improve the building function and the structure performance, effective implementation "four - environmental" green development requirements, realize the construction process of low energy consumption, low emissions, promote the overall development of China's construction industry, achieve energy saving, emission reduction targets. At present, the development of prefabricated concrete structure in our country, in the architectural design, production, installation of components and structure model, component connection structure is better than that of our country s and eighty s of the 20th century the development of the traditional prefabricated building structure, the building exterior quality, energy saving and comprehensive economic benefits and other aspects have close to, is equivalent to the performance of the cast-in-site concrete structure.

In recent years, the China construction science research institute of southeast university, tongji university, Harbin institute of technology to study, and other units are made of prefabricated frame structure research.

Gui China architectural scientific research courtyard cooperation with China vanke co., LTD., the pulp sleeve anchor connection technique of precast frame structure, the beam end of prespliced joint friction shear mechanism, stack assembled column, beam, roof system prefabrication beam-column joints, the systematic experimental study on the composite plate. The component and the node

design technology used for the test mainly based on the former field construction company adopted by the Japanese prefabricated frame structure technology; All test adopt full scale specimen, specimen in the section size of column is 600 mm×600 mm to 800 mm× 800 mm, and beam section size is 350 mm ×600 mm, 70 mm thickness for prefabricated layer + cast-in-place layer of 70 mm. Through test research, preliminary summarized the prefabricated frame structure and node stress performance, design and construction requirements. The test results show that the beam-column joints can achieve equivalent basic structure of cast-in-situ request [4].

Tongji university, Harbin industrial university, southeast university, guangzhou university has made important research results, to technology development and application of prefabricated frame structure provides technical basis [5].

3. based on RFID prefabricated building steel construction progress monitoring system research

The study of the theory of the progress monitoring and adjustment. Develop a scientific and reasonable construction project schedule is the premise to realize schedule control. However, in the process of project implementation, because of the influence of the external environment and internal management factor, is often biased actual schedule and schedule. Therefore, in the execution of the project progress plan system of progress control measures must be taken in the process, namely the constantly found the problem, by using accurate monitoring means and effective progress adjustment method is applied to solve the problem in a timely manner. First of all, according to the schedule of construction, data collected progress in the process, and the data collection and analysis. Then, the actual schedule data analysis results compared with the original schedule, progress deviation value are obtained. Finally, entering the schedule adjustment system, adjust measures to speed up the actual schedule, make sure the total time limit for a project are not affected. Schedule control method of the existing general progress of the software. Now in general use in the market for the progress of the control software adopts the progress of the tracking and monitoring methods are crossing and progress method of front line, Microsoft Project 2000 main monitoring network in progress monitoring progress line in the figure, the content of the two aspects of resources.

The RFID in the experimental study of building products. RFID technology is mature and widely used in other field, laid the groundwork for the research in the field of architecture. The research in the field of construction are mainly concentrated in the following aspects: (1) building products (2) (3) quality control operation control (4) (5) in and out management facility management and maintenance (6) positioning system (7) security control (8) asset management.

RFID technology application in the field of architecture is a difficulty faced by the bad site environment. Caused by the field of materials and mechanical equipment, effective identification RFID reader distance than in without interference. Aiming at this problem, Esin Ergen a, Bureu Akinci b, Rafael Saeks c did three tests used to verify RFID data collection effect in different environment, a test: test object is prefabricated. B: test object for the bobbin. C: test object for the fire hydrant. The three experiments with different environmental characteristics, different demands on RFID technology. The test results show that the UHF RFID technology meet the needs of the identifying artifacts and access to information. In A test, the electronic label actually read range reduced to 1/4 ~ 1/5 of the normal state, reduced from 30 m to 6 ~ 8 m. But the scope of reading and writing are still meet the needs of the distance to identify artifacts. Within the component yard mobile tower crane with reader, succeeded in identifying all of the prefabricated steel components, data exchange 100% accuracy. In experiment B, there are 9 trucks carrying bobbin, the car all the

components are correctly identify. Tested under different speed identification test conditions (speed range from 2 MPH to 10 MPH) [6].

Test data show that when using the four antennas and speed in 1 to 2 MPH, all the components on the truck can be identified correctly. In experimental C, tag reading range between 3.2 m and 3.2 m fully meet the range of normal maintenance activities need (lm), the average accuracy of read and write operations on label is as high as 97%. The above test results show that the RFID technology in the construction site of steel members has the feasibility of automatic identification.

Acknowledgements

1.54 batch on China postdoctoral science foundation projects "ecological assessment and comprehensive management paradigm of manufacturing supply chain research", number: 2013 m541552. 2.2013 annual shaanxi province social science fund research project "manufacturing and logistics industry linkage development mode study", number: 13 d085. 3.2014 postdoctoral funding annual Shanghai pudong new area of science and technology development fund project "China building industry chain and ecosystem coupling: factor and the model and mechanism study. 4. China construction eighth engineering co., LTD. Science and technology research and development project "construction production line based on the theory of lean construction theory research and practice", number: 2012-28.

Corresponding Author

Wang jing (1970-), female, xi 'an, engineering, Ph.D., shaanxi normal university station postdoctoral marxist theory, China construction eighth engineering and management science and engineering of Shanghai jiao tong university station postdoctoral, associate professor of northwest university of politics and law. The research direction for the socialism with Chinese characteristics, theory and practice of logistics engineering and management.

References

[1] lv Westwood, Fan Li Zhao Bin, precast concrete frame structure scale model pseudo dynamic test research, journal of building structures, 2008, 29 (4) : 58-65

[2] Xue Weichen Yang Xinlei, aggregates, wang DouZuRong, six layer framework cast-in-site column precast beam, experimental study on seismic performance of journal of building structures, 2008, 29 (6), 29-32

[3] Zhu Hongjin, precast concrete prefabricated assembly stress integral frame structure (structure) node test research [D], master thesis of southeast university, 2006

[4] Pan Jijian, prefabricated stress test of concrete frame structure seismic capability research [D], master thesis of southeast university, 2006

[5] Li Nan Zhang Jichao, chu pioneer, liu, cast integral precast concrete structure beam-column joints aseismic capacity test and research, engineering mechanics, 2009 (SI), 41-44

[6] Klaus Finkenzeller Chen Dacai, Wang Zhuo. Radio frequency identification (RFID) technology [M]. Beijing: electronic industry press, 2001.

Advanced Materials Research Vol. 983 (2014) pp 363-367

doi:10.4028/www.scientific.net/AMR.983.363

Design Optimization and Control Analysis of Mechanical Arm Equipped on Wheelchair

Guibin Luo[1,a], Cancan Zeng[2,b], Lida Zhu*[3,c]

[1,2,3]School of Mechanical Engineering and Automation, Northeastern University, Shenyang, China
[a]978023265@qq.com, [b]zcc.neu@gmail.com, [c]zld1999@gmail.com

Keywords: Wheelchair; Four DOF Mechanical Arm; Structural Optimization; Motion Control

Abstract. Aiming at the phenomenon that our country has a large number of disabled due to illness or accident but the corresponding assistive devices is extremely deficient, we have designed a kind of mechanical arm which is intended to be equipped on wheelchair. We adopted articulated mechanical arm with multi-DOF as its mechanical structure, and chose MCU as the main controller; therefore it could make all kinds of flexible action to achieve a variety of functions. In order to improve the accuracy of manipulator, based on experimental results, we optimized the mechanical arm's structure, improving its strength and stiffness; in order to realize the motion control of the manipulator, the kinematics analysis was conducted, and when solving the mechanical arm's anthropomorphic action problem, we set key points and then optimized the trajectory with linear interpolation, at last achieved anthropomorphic movement.

Introduction

According to the Second China National Sample Survey on Disability in 2006，there were more than 80 million people with disabilities in China, and the number of physically disabled persons reached 24.12 million[1]. Apparently, the disabled and sick old people in our society form a considerable group. However, robots used in medical or helping the disabled are rare both at home and abroad, they mostly exists only in the laboratory, and are rarely used in practice. Foreigners have developed some advanced caring and service robots in the laboratory, taking American Handy1 rehabilitation robot as an example, it allows an 11-year-old boy with cerebral palsy to eat independently. But it is too expensive to extend. Although we started relatively late in developing service robots, supported by 863 Program and the National Natural Science Foundation project, the academia and the business community have achieved a large number of results. Nevertheless, most of them remain in the theoretical level. In this paper, we mainly focus on the design optimization and motion control of a practical mechanical arm that is equipped on wheelchair.

Design and optimization of the structure of the mechanical arm

Because it is intended to be installed on a wheelchair, the mechanical arm ought to have the advantages of light weight, stable and accurate movement, less power consumption etc. And considering the cost, weight and space requirements of the mechanical arm, we select 4DOF mechanical arm as the research object [2]. Preliminary Design is shown in Fig.1

Preliminary design of the mechanical arm is composed of a base, an arm, a forearm and a hand. It has five motors: four steering engines (from bottom to top are numbered 1,2,3 and 4) control the attitude and position of the gripper, one DC servo motor controls the gripper sheets together. The rotation of steering engine1 causes the rotation of the arm as a whole, then the rotations of steering engine2, 3 and 4 control the pitching of the gripper cooperatively. Gripper part introduces the underactuated structure: using two springs and two CAM to constraint and release the gripper's DOF.

Test of the preliminarily designed arm shows that it is already able to meet the design requirements, and has good control characteristic; its work space also satisfies the requirement of experiment. But further precision experiment found that positioning accuracy of the hand is relatively low, besides, steering engine2 is prone to overheating. So we put forward the assumption that the steering engine's output power is insufficient and the mechanical arm's rigidity is inadequate. Accordingly, we optimized the structure of mechanical arm, as is shown in Fig.2.

Fig.1 The original structure of the arm

Fig.2 The optimized structure of the arm

The main improvement lies in the selection of the type of steering engine2, structure and size of the arm and forearm. And we choose 7075-T651 aluminum alloy with light weight and high strength to build the robot.

We have made a prototype for the optimized arm, and now it is under test in our laboratory.

Fig.3 The optimized mechanical arm

Fig.4 The wheelchair and mechanical arm

What this paper studies is robotic arm with four DOF, which can be seen as an open kinematic chain consisting of four rotary joints, and the relative rotation drive the rotation of the connecting rod joints. Establish the reference coordinate system which is shown in Fig. 5.

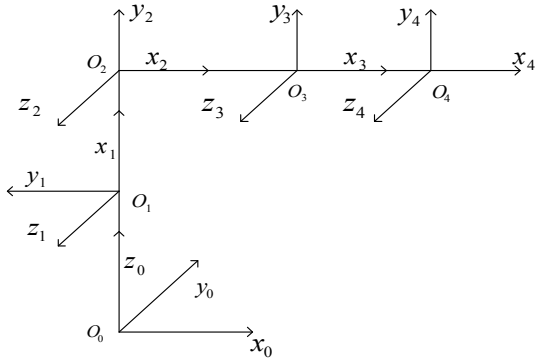

Fig5. Mechanical arm reference coordinate system

Design and analysis of control system

Hardware system. The hardware design of the control system needs to satisfy functional requirement of mechanical arm, and be able to run for long time stably with lower power. In order to install on the wheel, we use battery as the power source of the mechanical arm. Battery's voltage is stable and has small fluctuation, also, its small size is convenient to install on the wheelchair. We adopt high-performance micro-controller as the main controller, because of its high processing speed, low power consumption and high ability of calculation [4]. For users in different situations, we designed various kinds of input mode, including keyboard, rocker, and voice. In this way, users can control the mechanical arm via different ways.

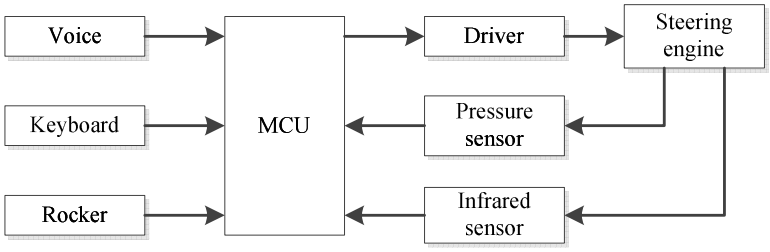

Fig6. Structure of hardware system

As the figure3 shows, control system's hardware consists of input section, main controller and sensors. The input section is in charge of helping users input theirs commands; keyboard, rocker, and voice are available for them. Main controller is the core of the whole control system, which is responsible for receiving input signals, and output control signals, driving steering engine to go to the corresponding angle. Another responsibility is detecting the feedback signals from sensors, and analyzing these signals to get the state of mechanical arm. According to the analyzing result, main controller will output controlling signals with closed-loop control [5].

Software system. It needs to be taken into account when design the software how to deal with input signals and feedback signals, specific program flow is shown below.

After powering on, the MCU will initialize internal register and configure the function module firstly. Then it will detect whether there are input signals or sensor signals input. If there are, the corresponding handler program will be executed. Part of the handler programs are in the form of interrupt service routine, and others are in the form of query routine.

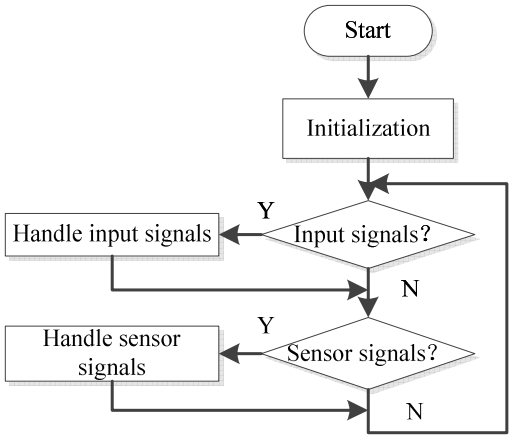

Fig.7. Software flow chart

Before the design of software, we should design the communication protocol and form of command word. We use 13 characters in length string as the command word, which includes lots of information of prefix, steering engine number, angle position, speed and the sign of end.

Trajectory control. The primary purpose of control is to make the mechanical arm imitate the human arm to capture objects. We determine the trajectory by setting a number of key points in the work space, but the actual trajectory of mechanical arm is broken line with a pause at the key points. To solve this problem, we use linear interpolation to optimize the trajectory [6], which makes the movement of mechanical arm soft, smooth and more anthropomorphic.

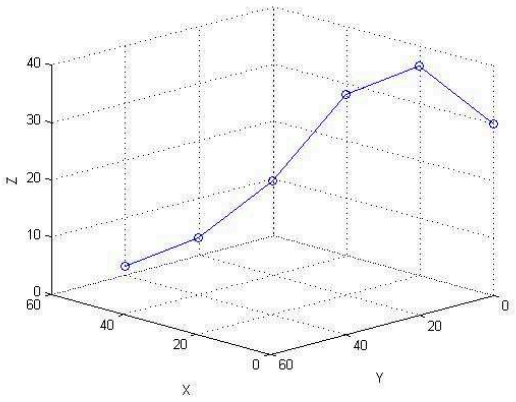

Fig8. Key point determining the trajectory

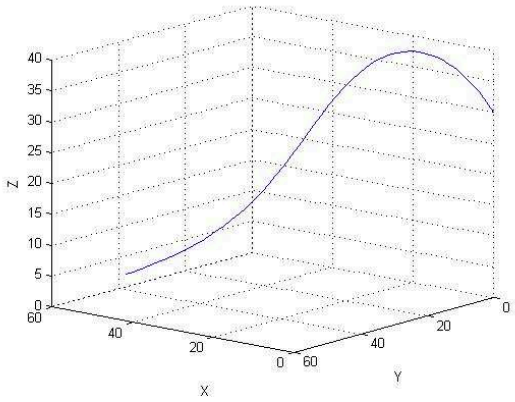

Fig9. The trajectory after linear interpolation

As the figure8 shows, if we use this point to control mechanical arm, the trajectory will be broken line and the mechanical arm will pause at the key point. But after linear interpolation, as the figure9, the trajectory will be soft and smooth.

Analysis of stability and precision. Stability problem mainly exists in the detection to mechanical arm's state of sensor, if the sensor due to external environmental factor leads measurement errors, main controller will also make an incorrect decision. Precision error is mainly from the back play between the mechanical joints and elastic deformation of arm. But for the same type of steering engine, mechanical error is fixed, so we can translate the fixed error by kinematic equations, and then compensate them in control.

Summary

1) After optimizing the structure of mechanical arm, intensity and stiffness are enhanced; this improves the accuracy of movement and expands the load range.
2) We optimized the trajectory control algorithm by interpolation fitting algorithm, and achieved anthropomorphic action.
3) Study of the mechanical arm that is equipped on wheelchair contributes to the development of medical domain. It will provide more practical and convenient assistive medical devices to the elderly and people with disabilities.

Acknowledgements

This work was supported by (National Natural Science Foundation of China) NSFC (51105072) and (51105258), supported by Doctoral Fund of Ministry of Education (20110042120019), Shenyang Science Foundation (F12-277-1-43) and the Fundamental Research Funds for the Central Universities (N130403010).

References

[1] Zheng Zhidong, Zhen Bocheng. Research and technology development status on assisting elder and disabled robotics industry [J]. Robot Technique and Application, 2009 (2)

[2] Wang Zhan. Research on wheel chair mounted robotic arm for assisting elder and disabled [D].Harbin: Harbin Institute of Technology .2008

[3] Chu Zhongyi, Qu Dongsheng, Sun Lining, Cui Jing etc. The method of Robot dynamics analysis of finite element modeling [J].Chinese Journal of Mechanical Engineer .2005.41 (6) :15-18

[4] Zheng Xiaohong, Wu Daowu etc. Industrial robot technology and its application [M]. Beijing: Coal Industry Press .2004.

[5] Zhang Peiyan. Industrial Robots Operation and Application Practice Guide [M]. Shanghai: Shanghai Jiao Tong University Press .2009

[6] Wu zhenbiao, Wang zhengjia etc. Industrial Robots [M]. Wuhan: Huazhong University of Science and Technology Press .2006.

Advanced Materials Research Vol. 983 (2014) pp 368-373

doi:10.4028/www.scientific.net/AMR.983.368

In 16V265H Locomotive Diesel Engine Nozzle Flow Field Simulation Analysis

Shihe Li[1,a], Minghai Li[1,b], Xiao Du[2]

[1]School of Traffic and Transportation,Dalian Jiaotong University,Dalian 116028,China
[2]CNR Dalian Locomotive Research Institute Co.,Ltd,Dalian 116028,China
[a]43665222@qq.com,[b]dlminghai@vip.sina.com

Keywords: FLUENT; boundary conditions; computerized simulation; diesel engine; injector nozzle

Abstract. The investigation of the flow characteristics inside the nozzle becomes more and more important because the flow status in the nozzle and fuel injection significantly influence the emission and economy of diesel engines. Due to limited experimental conditions, we can make use of computer simulation, UG models can be used to predict the flow pattern inside the injectors and promote the level of selection and design of injectors. In this investigation, the UG model is calculated by FLUENT software after considering the compressibility and the viscosity of the fuel. By studying, we can predict the distribution of flow field inside the nozzle, analysis the rationality of the design of nozzle, determine the appropriate boundary conditions, mainly includes the nozzle pressure chamber and the needle tip structure, points out that the improvement direction.

Introduction

With the rapid development of modern railway construction in our country, the pros and cons of locomotive diesel engine performance, people's environmental awareness, the requirement of energy conservation and emissions reduction, the challenge of comprehensive performance of locomotive diesel engine is becoming more and more big. Mixture formation and the atomization of fuel oil are the primary factors that affect the performance of diesel engine, and that, the structure of the nozzle directly affect the degree of atomization of fuel oil, the degree of mixing of the mixed gas, the velocity distribution of gas mixture injected into the cylinder, etc[1]. In this article, taking 16V265H diesel engine as the research object, after using UG software to build entity model, put the entity model of the nozzle imported into GAMBIT, meshing and set the import and export of the fluid, then, using FLUENT, considering the characteristics of nozzle and the test data to determine the reasonable boundary conditions, doing a data simulation of porous nozzle fuel three-dimensional flow field and proving the validity of the results.

The entity model

According to the entity drawing of 16V265H locomotive diesel engine nozzle and related data, using UG to build the entity model of nozzle. First, as shown in Fig.1 is the establishment of three-dimensional solid model of the needle valve. Then creating the needle valve body entity model which have two positioning pin holes, one oil inlet hole, nine orifices evenly distributed whose diameter is 0.455mm, as shown in Fig.2. The following is generating the assembly drawing of nozzle and the distance between the top of the needle valve and the top of the needle valve body is 6 mm, then according to the related data of nozzle, establishing the physical model of nozzle flow channel, as shown in Fig.3. Since the nine orifices are uniformly distributed over the needle valve body, The angle between the adjacent two orifice is 40^{o}, simply for ease of accounting, we just need to research one-ninth of the fluid in the nozzle flow channel, as shown in Fig.4[2,3].

Fig.1 Three-dimensional entity model of the needle valve

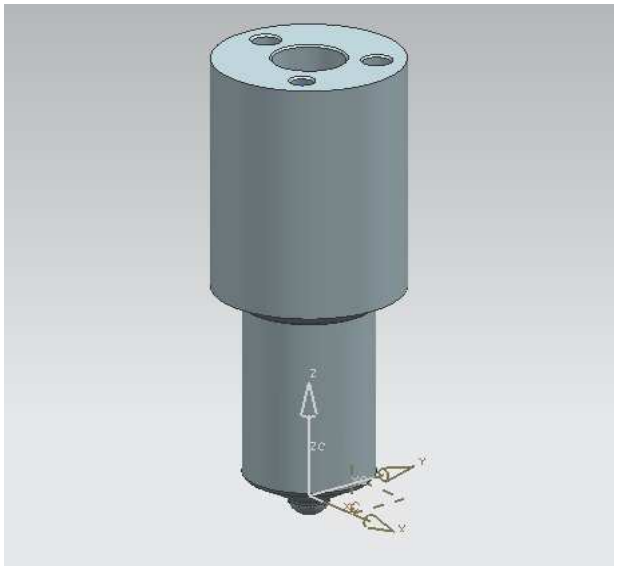

Fig.2 Three-dimensional entity model of the needle valve body

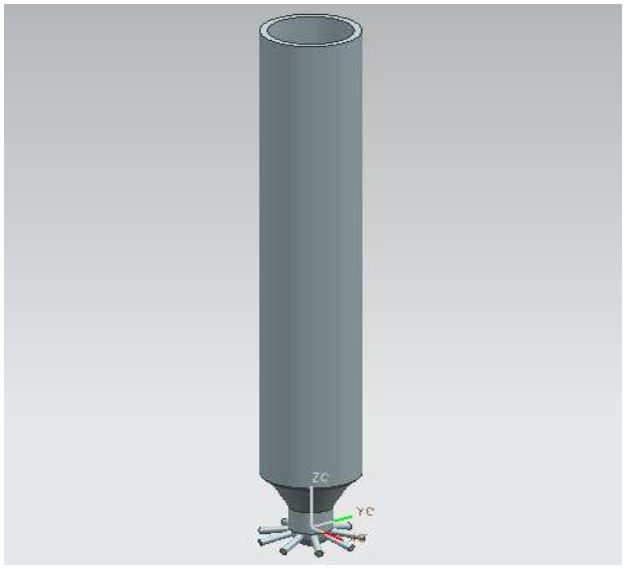

Fig.3 The physical model of nozzle flow channel

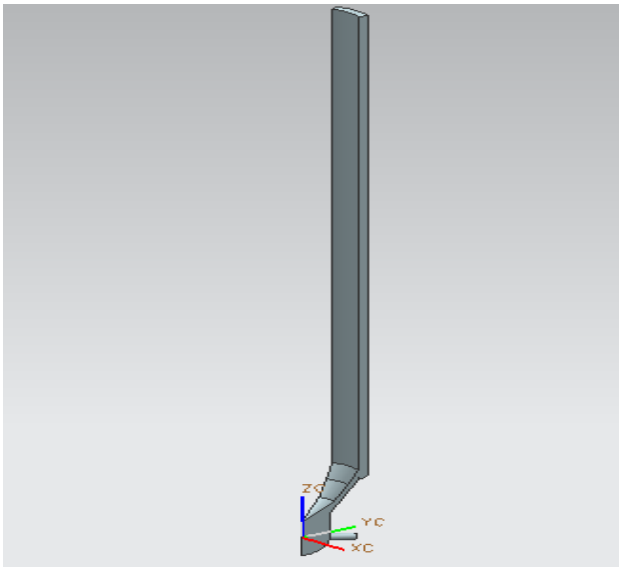

Fig.4 Shear diagram of nozzle flow channel

Meshing for the entity model

Meshing for the entity model of nozzle flow channel, as shown in Fig.5, there are about forty thousand mesh generated which are made up of tetrahedron and hexahedron. In order to ensure the accuracy of the numerical simulation, especially the sharp drop in pressure, it must be sure that the mesh size of the orifice is small enough[4].

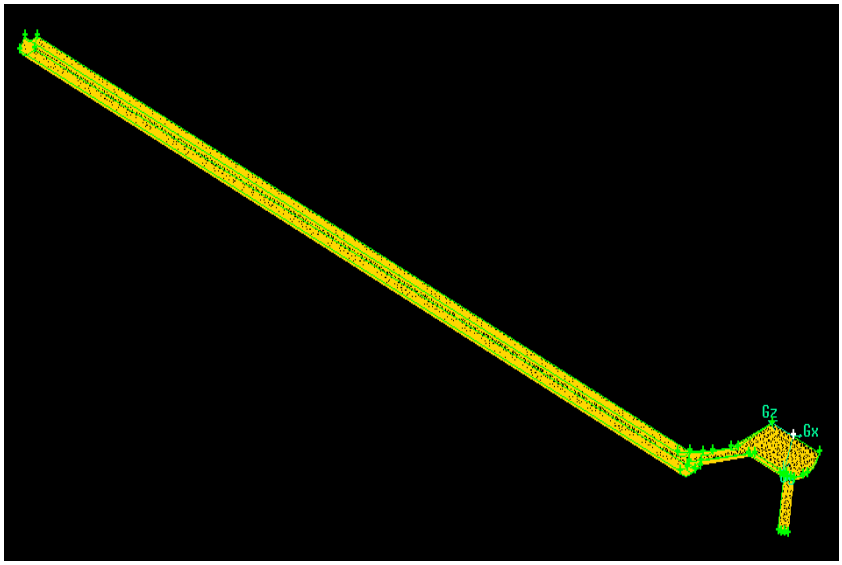

Fig.5 The mesh model of nozzle tip

The simulation program and results analysis

Define fuel injection quantity per cycle $g = (t_\theta \cdot g_e \cdot 1000^{-3})/(60n \cdot z \cdot i)$, Among them, for two-stroke diesel engine $z = 1$, for four-stroke diesel engine $z = 1/2$, the average mass flow of nozzle $Q = g/t_\theta$, t_θ is cycle fuel injection duration, $t_\theta = \theta \cdot 60/(360^o \cdot n)$, θ is the crank angle of injection continued. If we have the actual test data, we could directly calculate the average mass flow of fuel. For 0 # diesel oil, take v(kinematic viscosity) =5.882mm^2/s, so μ(dynamic viscosity)=$\rho \cdot v$= 0.005kg/(m·s), under atmospheric pressure, take ρ(diesel density)=850kg/m^3. Enter the Fluent software, read the mesh file, set the entrance pressure of 150MPa, after calculating, finally we can get the pressure contour line and the velocity contour line of the nozzle tip, as shown in Fig.6 andt Fig.7[5].

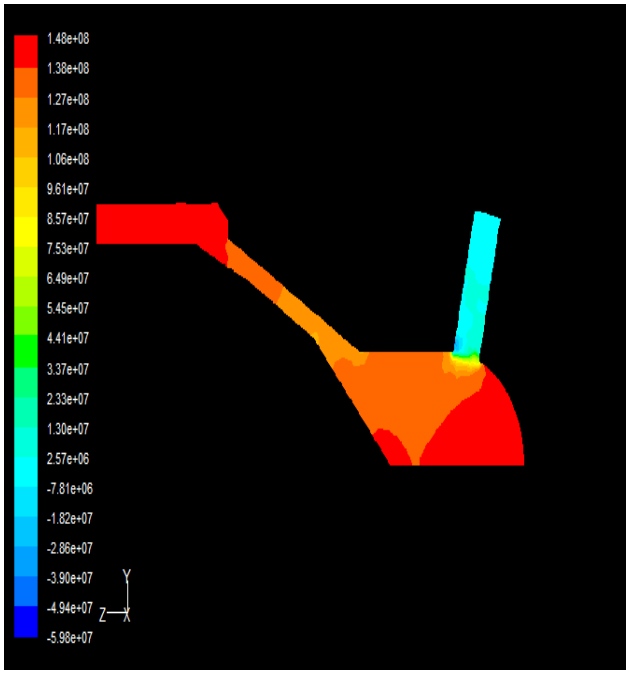

Fig.6 The pressure contour line of the nozzle tip

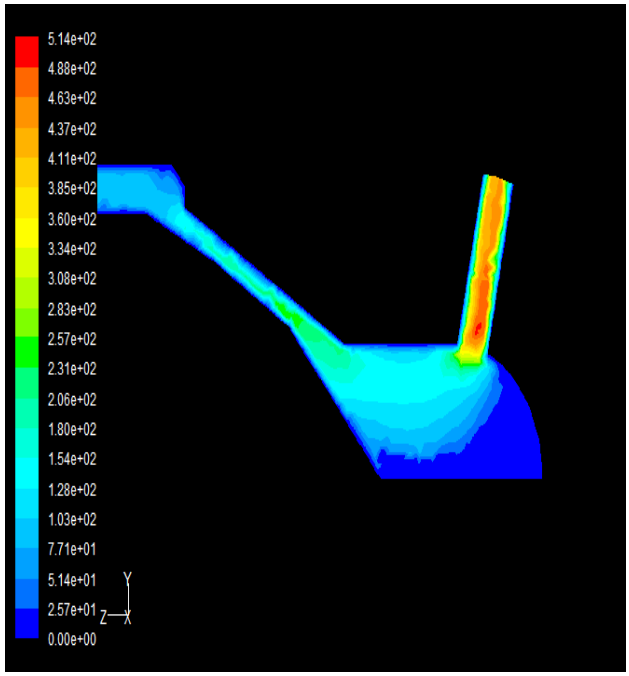

Fig.7 The velocity contour line of the nozzle tip

Fig.6 is the pressure contour line of the flow field in the nozzle, it also represents the liquid pressure contour line of the flow field of the nozzle head, when the fluid from the pressure chamber inflow orifices with a high-speed, since the flow direction of the fluid change is too big, under the guiding role of pressure chamber inner wall, the fluid flow the lower edge of orifices at high speed, it can be seen on the entrance corner of the orifice, a negative pressure zone formed, reduce the orifice flow coefficient, and prone to cavitation, causing cave corroding.

Fig.7 is the velocity contour line of the nozzle, from that we can see pressure first decreased and then rebounded slightly, then decreased again, and finally increase sharply.

Chamfering the the entrance corner of the orifice, make the radius r is 0.1 mm, it means dimensionless quantity R is 0.220(Studies have shown that r is not the bigger the better, $R = r/D$, r represents chamfering radius, D represents orifice diameter, when $R \geqq 0.3$, flow factor α_k tends to be stable, as shown in Fig.8), calculating again, we get the better pressure contour line and the better velocity contour line of the nozzle tip, as shown in Fig.9 andt Fig.10[5,6].

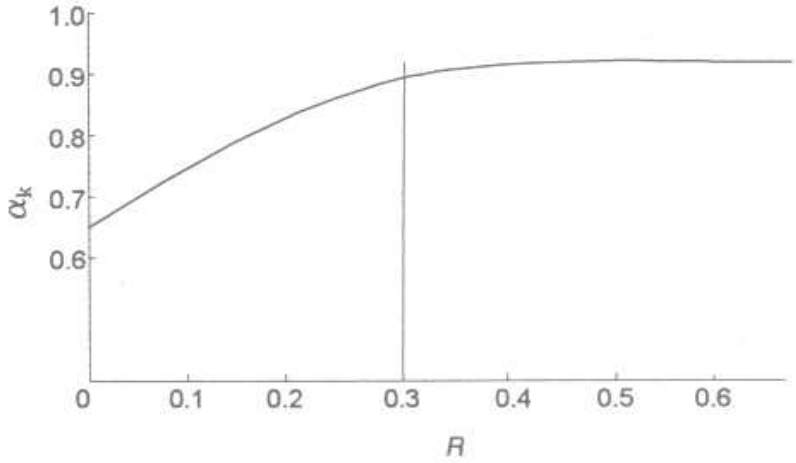

Fig.8 Relationship between dimensionless quantity R and flow factor α_k

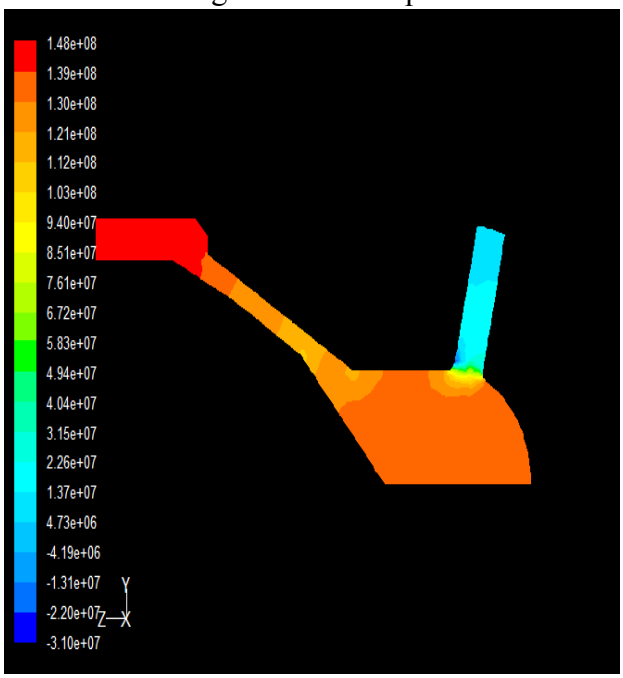

Fig.9 The pressure contour line of the nozzle tip after chamfering

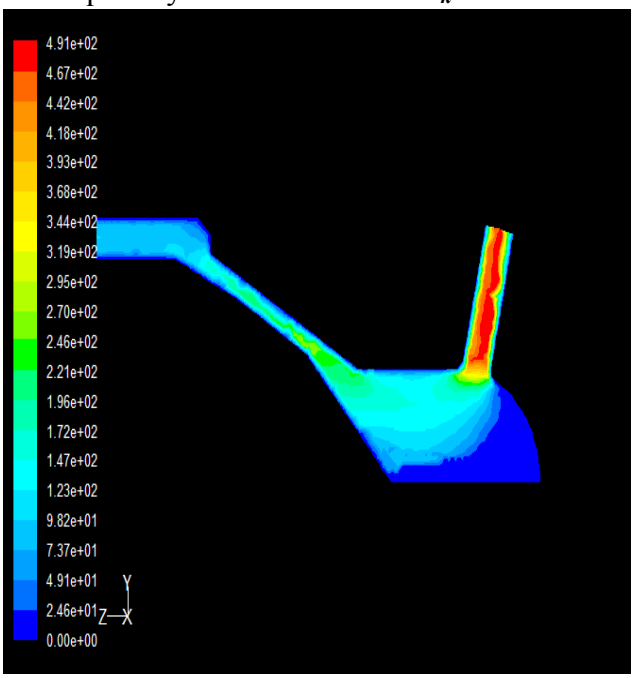

Fig.10 The velocity contour line of the nozzle tip after chamfering

In the case of both the mass flow and the entrance pressure are not change, Fig.9 is the pressure contour line of the flow field in the nozzle after chamfering, from the figure, we can see that the

range of the negative pressure zone is greatly reduced, the absolute value of negative pressure is decreased obviously. In addition, the pressure loss of orifices is reduced, effective injection pressure increased significantly, it is great benefit for improve combustion conditions.

From Fig.10, the velocity distribution of the flow field in orifices is more uniform after chamfering, the absolute value also become more big. This is because it weakened the intercepting effect of the side in original structure ,and there is little influence on the downstream flow field. But the chamfering radius should not be too big, otherwise it will cause orifices connect to each other, reduce the rate between length and diameter, affect spray penetration distance.

The results analysis

In this paper, the flow field of the nozzle is studied by numerical simulation, in terms of two-phase flow within the nozzle, it belongs to a problem about two-phase flow of gas-liquid, according to the results of numerical simulation, below for further discussion and analysis:

(1) In Fig.6, from the needleseat to the orifice, fuel pressure decreases gradually, orifice exit pressure is much smarller than orifice entrance pressure, this is due to that the moment the needle valve is opened, nozzle pressure chamber and high pressure tubing are connected, volume increases in an instant. Diesel from large pressure chamber, suddenly into the small cross-sectional area of orifice, causing greater throttling losses, resulting in oil pressure of orifice exit decreases, the simulation result is consistent with the experimental results.

(2) In Fig.7, from the needleseat to the orifice exit, fuel flow velocity increased rapidly. With the increase of entrance pressure, fuel flow velocity will also be more and more big, reynolds number is far greater than turbulent critical value, the fuel flow of orifice exit is turbulent.

(3) By the comparison of Fig.6 and Fig.9, the range of the negative pressure zone is greatly reduced, the absolute value of negative pressure is decreased obviously, the pressure loss of orifices is reduced, effective injection pressure increased significantly, to improve the atomization of fuel. By the comparison of Fig.7 and Fig.10, the velocity distribution of the flow field in orifices is more uniform after chamfering, the absolute value also become more big. This is due to that it weakened the intercepting effect of the side in original structure ,and there is little influence on the downstream flow field. So chamfering in the nozzle can improve the fuel injection quantity and flow coefficient at the same time.

Conclusions

(1) For injector, using UG software to build entity model, and then using the FLUENT software to simulate analysis, research the three-dimensional flow of fuel inside the nozzle, the simulation result is consistent with actual, it can provide reliable basis for the structure of the nozzle design and improvement provide reliable basis, improve the design quality and efficiency of nozzle effectively, reduce development costs.

(2) In this case, chamfering the the entrance corner of the orifice and make chamfering radius is 0.1 mm, the quality flow of the single-hole Increased from the original 0.055 kg/s to 0.059 kg/s, an increase of 7.27%, effectively improve the speed in the nozzle under the same injection pressure.

(3) Chamfering the the entrance corner of the orifice and make chamfering radius is appropriate, that can improve the injection pressure, resistance to flow resistance, shorten the duration of injection, improve the flow characteristics of nozzle, increase injection rate, it is advantageous to the comprehensive performance improvement for diesel engine.

Literature References

[1] Zongying Gao, Jianming Zhu. Fuel Injection and Control for Diesel Engines[J], (2010). In Chinese.

[2] Minghai Li, Xiaokun Zhang, Hongjiang Cui, Ying Guan. Research on Locomotive Diesel Engine Nozzle three-dimensional Flow Field Numerical Simulation and Improvement[J]. Chinese Internal Combustion Engine Engineering, (2007). In Chinese.

[3] Bo Xu, Zongjie Zhang. Analysis of the Flow in the Nozzle of a Multi-Hole Diesel Engine Injector [J]. MODERN VEH ICLE POWER, (2005). In Chinese.

[4] Zhixia He, Jianping Yuan, Detao Li. Numerical Simulation on Optimization of Diesel Nozzle[J]. Transactions of CSICE, (2006). In Chinese.

[5] Dongjian Zeng, Haibo Huang, Youchang Jia. Research on Numerical Simulation Analysis of Flow Field in the Diesel Engine Nozzle[J]. Journal of Xihua University·Natural Science, (2008). In Chinese.

[6] Jiangtao Yuan, Guangyao Ouyang, Zhen Liu. Research on CFD analysis of the Flow in Diesel Nozzle[J]. Diesel Engine, (2005). In Chinese.

Advanced Materials Research Vol. 983 (2014) pp 374-378
© (2014) Trans Tech Publications, Switzerland
doi:10.4028/www.scientific.net/AMR.983.374

Mechanical Design to Adapt Changes to Existing Universal Test Bed Facility of Turbojet Engine for the Turbofan Engine

Fawwad Ahmed, Ahmad Aizaz[1], and Zahid Mahmood

CAE, National University of Sciences & Technology, Islamabad, Pakistan

[1]ahmadaizaz@cae.nust.edu.pk

Keywords: Universal Test Bed, Engine Mount, CAD Model, Structural Analysis, Turbojet, Turbofan.

Abstract: The existing Universal Test Bed (UTB) is a facility to ground test Turbojet Engines before installation on the aircraft. This work provides a feasibility study to adapt changes to this UTB for the Turbofan Engine. Necessary design modification of existing UTB is performed by applying propulsive and structural analysis for the adaptation of Turbofan engine. Physical measurements of the UTB and the mounts of Turbofan Engine reveal their mutual compatibility. Based on these measurements, six different CAD models are generated in Solid Works® and analyzed in ANSYS® Workbench. After grid independence check, validation of the model with applied loads and the boundary conditions was done through comparison of analytical calculations with those of a simplified CAD model. Based on minimum stress vis-à-vis maximum Factor of Safety (FOS), the best design is finally selected through this research.

1. Introduction

In present research, a feasibility and structural design modification study has been carried out to ascertain the use of this UTB such that it has the enhanced capability of testing the Turbofan engines also. The adaptability of UTB requires its physical measurements and compatibility with Turbofan engine mounts.

2. Measurements

2.1 Universal Test Bed

Physical measurements of distances between the two rails of the UTB as well as the three attachment points of Turbojet engine are shown in figure 1 with measuring accuracy of 0.1 cm. Dimensions in all figures are in cm.

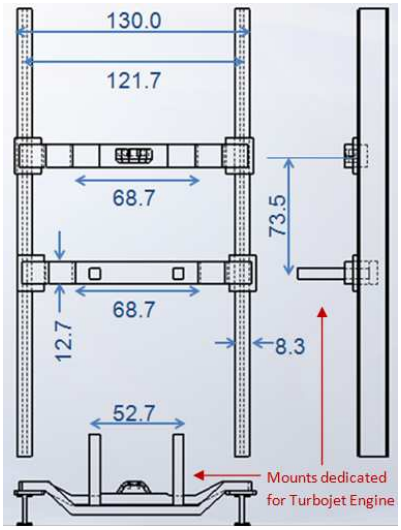

Figure 1: Drawing of UTB Rail Assembly.

2.2 Turbofan Engine

The Turbofan engine has a total of seven dedicated attachment points. Four are at the front as shown in figure 2(a) and the remaining three are at the rear side of the engine as shown in figure 2(b).

The maximum diameter of 100 cm exists at about middle of the Turbofan Engine (not shown in the diagrams), which is well within the limits of UTB's rail assembly of 130 cm. These measurements revealed the mutual dimensional compatibility of the Turbofan engine with the UTB.

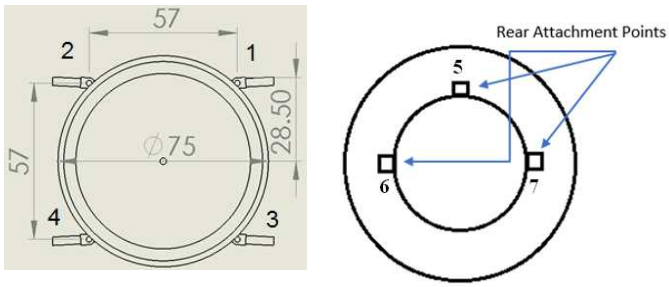

Figure 2(a): Front view of Turbofan engine showing four attachment points; (b): Rear view of the Turbofan engine showing three rear attachment points

3. Analytical Calculations

To ensure the correct boundary conditions, validation of the results obtained from ANSYS® Workbench, along with analytical calculations is carried out.

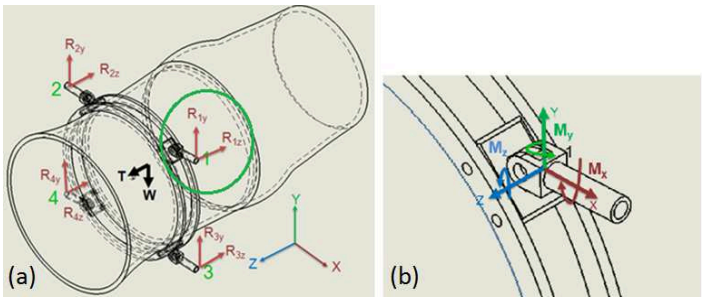

Figure 3(a): FBD of the Turbofan engine; 3(b): Directions of reactive moments on attachment point 1

3.1 Assumptions

A statically indeterminate problem is converted into a determinate problem by application of following few assumptions:

a) Only the front four attachment points are considered for analytical calculations
b) The reactive forces along x direction are zero because the applied forces are planar in y-z plane. (See figure 3)
c) The reactive forces along y and z directions are divided equally as these forces are acting exactly at equal distances 'R' from all the attachment points as shown in figure 4.

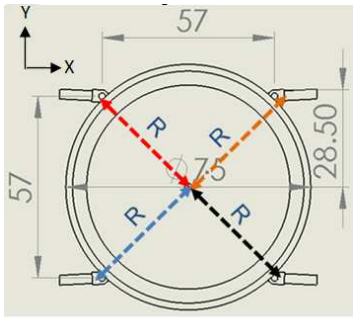

Figure 4: Turbofan engine 2D front view

3.2 Mathematical Model

Equations regarding summation of forces (∑F=0) and summation of moments (∑M=0) are used to determine the reactive forces and reactive moments which results in calculating the Von Mises (equivalent) stress. It is then compared with the value obtained from analysis in ANSYS® Workbench.

3.3 Results of Simplified Analytical Calculations

The computed results are presented in table 1:

Table 1: Results of simplified analytical calculations

$\mathbf{R_{1x}}$	0
$\mathbf{R_{1y}}$	952.5 N
$\mathbf{R_{1z}}$	3900 N
$\mathbf{M_{1x}= M_{2x}}$	1231.52 Nm
$\mathbf{M_{3x}= M_{4x}}$	991.49 Nm
$\mathbf{M_{1y}= M_{2y} = M_{3y} = M_{4y}}$	1111.5 Nm
$\mathbf{M_{1z} = M_{2z} = M_{3z} = M_{4z}}$	271.46 Nm

The moments and forces calculated at attachment point 1 are finally transferred from point 2 to point as shown in figure 5. After the solution of a combined loading problem, the stress at the base plate is calculated. During the analysis, I-beam is considered as a cantilever beam as shown in figure 6.

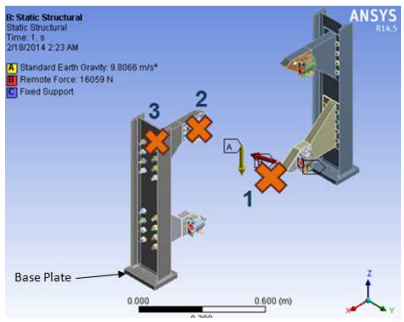

Figure 5: Test frame depicting transfer of loads

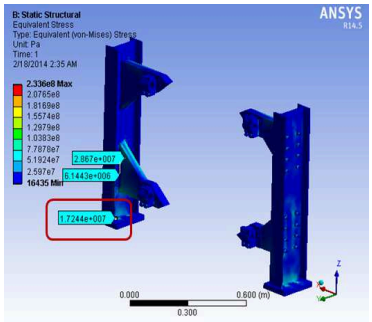

Figure 6: Von Mises Stress on simplified model

The same problem is analyzed in ANSYS Workbench®, and the value at the base plate of I-beam comes out with a difference percentage of 2.4% to the value analytically solved. This small difference indicates the correct loading and applied boundary conditions.

Table 2: Validation of Model Analysis

	Von Mises Stress	Percentage Error
Analytical Calculation	1.68 e07	2.4 %
ANSYS Workbench® Analysis	1.72 e07	

4. CAD Modeling

A detailed CAD model is generated using Solid Works®. Different part files are made after which a final assembly is constructed. A list of different parts modeled is as follows:

a) UTB rail structure
b) Double roller adapters
c) Extension
d) Attachment points
e) Rear frame and mount
f) Various sizes of nuts and bolts

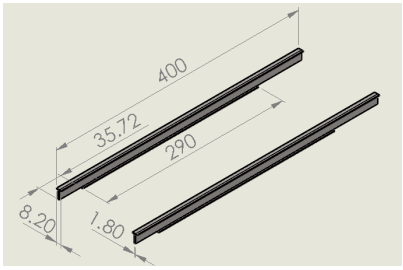

Figure 7: UTB rail assembly

The model shown in figure 7 is the rail assembly of the UTB. This main chassis is connected to the main body of the UTB.

A double roller adapter shown in figure 8 is used on the test beds along with a flat plate attached on top of it to provide a platform for the installation of thrust frames/mounts. Fasteners are used on the existing holes of double roller adapter for the attachment of the beam structure.

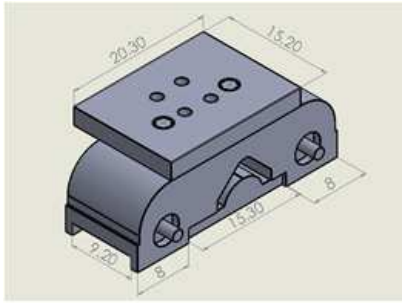

Figure 8: Double roller adapter assembly

The part shown in figure 9 is an extension modeled on which the (front side) attachment points will connect. This is because the engine diameter is less as compared to the distance between the thrust stand rail assembly.

The attachment points of Turbofan engine's mounts, required to be designed for test bed are shown in figure 10. They are modeled keeping in view their compatibility with the attachment points of the Turbofan Engine.

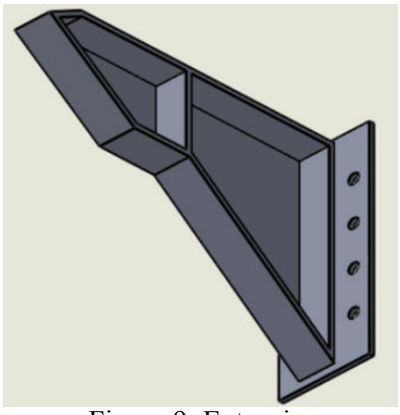
Figure 9: Extension adapter assembly

An ISO SB Beam (140x15 I-beam) is modeled for the formation of both front and rear frames. The extension modeled will be bolted to the I-beam further on which the attachment points will be bolted. Figure 11 shows the proposed design of the test frame.

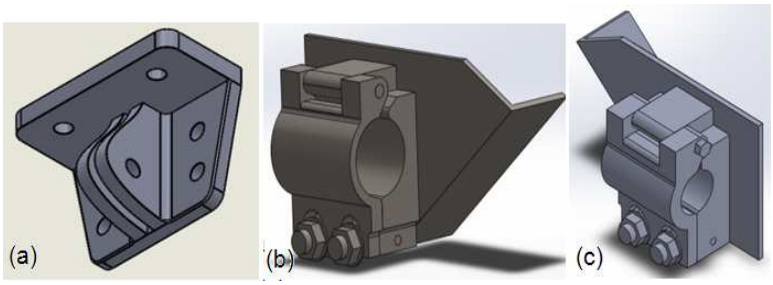

Figure 10(a): Rear attachment point of Turbofan Engine; (b): Top left attachment point; (c): Top right attachment point adapter assembly

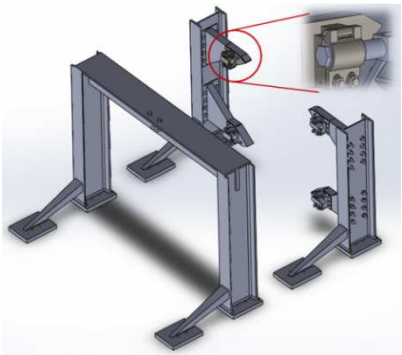
Figure 11: CAD model assembly of testing frame with a zoom in view of the front attachment point

4.1 Various CAD Design Options

Six different design options are considered to select the best design based on minimum stresses or maximum factor of safety. These configurations are given in table 3 below.

Table 3: Different CAD Model Configurations

Conf. No.	Description
1	Unsupported Frames with top two attachment points only
2	Unsupported frames with four attachment points
3	Low supported frames
4	Mid supported frames
5	High supported frames
6	High supported frames with two attachment points only

5. Structural Analysis

The CAD Models are imported to ANSYS Workbench® for static structural analysis. Structural Steel AISI 4130 is selected with a tensile strength of 560 MPa [1] for the analysis. However for nut and bolts, material specified is low carbon steel.

5.1 Loading and Boundary Conditions

Figure 12(a) below shows constrained holes as fixed supports. In figure 12 (b) the contact type between the nuts, solid-bolts [2], and I beams are treated as bonded. In the analysis, all the connections related to nuts, bolts, and pin type contacts are modeled as joints.

Table 4: Applied forces on mounts

Force Direction	Force Magnitude (N)
X	0
Y	-3810
Z	15600

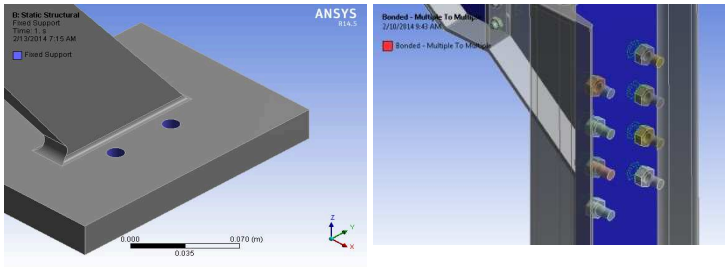

Figure 12(a): Constrained holes as fixed supports; (b): Close up view of front side test frame showing nuts and bolts

The forces applied on the model are shown in figure 13. Table 4 depicts component wise force magnitudes.

The directions of mentioned forces are with respect to the user defined co-ordinate axis. The forces are applied such that the attachment points first experience the applied force after which the load is distributed throughout the frame. The standard earth gravity is also applied to cater the weight of the frames modeled.

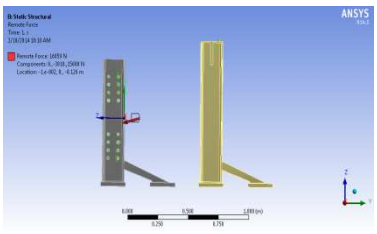

Figure 13: Applied forces on mounts of Turbofan engine

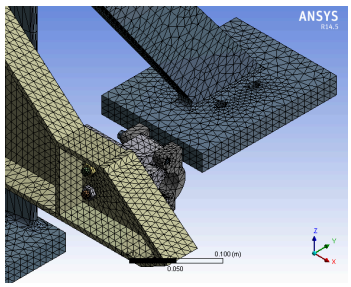

Figure 14: Final Mesh of one of the proposed models

5.2 Mesh Generation

'Free tetrahedral' mesh element is selected for meshing with 'extra fine' element size for greater accuracy. The variation of results decreases considerably, as shown in table 5, with the refinement of mesh. This ensures grid independence of the solution.

Table 5: Grid independence

No. of elements	Von Mises stress (MPa)	Percentage difference (%)
441896	197.8	-
480578	177.5	10.26
492789	165.1	6.98
503717	157.6	4.54
506894	153.4	2.66
508796	153.3	0.065

Figure 14 shows the surface mesh in which 10 node solid elements 186 and 187 are used. They possess a quadratic displacement behavior and are well suited to model irregular mesh.

6. Results and Discussion

Out of the six different configurations, configuration number 4 is finally selected as the best design due to low deformations and Von Mises stresses and high factor of safety (FOS).

Table 6: Final Results

Configurations		Von Mises Stress (Pa)	Total Deformation (mm)	F.O.S
1	Unsupported with top two attachment points only	1.5040 e9	8.82	0.37
2	Unsupported with four attachment points	2.2122 e8	3.36	2.21
3	Low supported	1.6126 e8	2.56	3.47
4	Mid supported	1.5326 e8	1.77	3.66
5	High supported	1.5431 e8	1.62	3.63
6	High supported with two attachment points	7.0217 e8	3.74	0.79

Even though option 5 with high supports has slightly less deformation, but it is not a feasible solution as the large sized back support only adds more weight and cost during manufacturing. It is deduced from the results that with supports installed, the Von Mises stresses reduce considerably and the factor of safety increases. The Von Mises stress and the total deformation of the selected configuration is shown in the figure 15 and 16 respectively, whereas the complete CAD model of the final assembly is shown in figure 17.

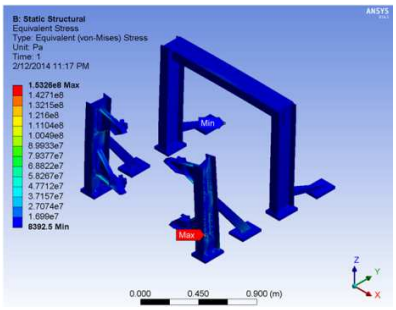

Figure 15: Von Mises stress on mid supported frames

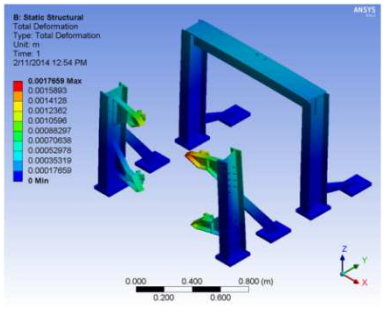

Figure 16: Total deformation on mid supported frames

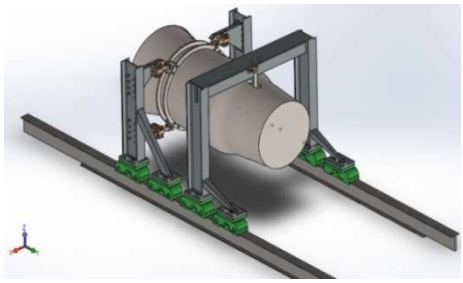

Figure 17: Final selected model with mid supported frame

7. Conclusion

In this study a total of six different CAD models are structurally analyzed out of which 'mid supported frame' (configuration number 4) is selected as the final design. The analysis of initial design and its further improved versions in this study serves as a guide to select the best design such that it meets the strength criteria. Hence to conclude, the testing of Turbofan engine is feasible on the existing UTB by using the designed frame selected through this study.

8. References

[1] Budynas, R.; Nisbett, J.: Shigley's Mechanical Engineering Design, Tata McGraw-Hill, ISBN-10: 0-07-107783-9, New Delhi, (1977).

[2] Jeong K., Yoon J., & Kang B.: Finite element analysis and modeling of structure with bolted joints, Applied Mathematical Modelling 31 (2007) 895–911, Korea, (2007).

[3] Kolte S., Neihguk D., & Prasad A.: Structural Durability Analysis of Power-train Mounting Bracket, Proceedings of 2013 COMSOL Conference, Bangalore, (2013).

[4] Ishaq I: Optimization of engine mounting bracket location, Iraq, (2008).

Advanced Materials Research Vol. 983 (2014) pp 379-382

doi:10.4028/www.scientific.net/AMR.983.379

Simulation Analysis of Kinematics and Dynamics of 3-TPS Hybrid Robot

Shi Jiashun[1], Wang shuang[1], Zhu Lida[1]*, Wang wanshan[1] and Yu Tianbiao[1]

[1.] School of Mechanical Engineering and Automation, Northeastern University, Shenyang I10819, China

Keywords: Wheelchair; Four DOF Mechanical Arm; Structural Optimization; Motion Control

Abstract: The paper aims at the questions of electromotor selection and mechanism design, which is effectively solved by the virtual prototype technology. Firstly, the three-dimensional model of hybrid machine tool is built by using SolidWorks software. Secondly, the assembled model is channeled into ADAMS/View, and then formed the virtual prototype simulation model with mute-body dynamics. Velocity and driving force curve of each driving shaft is got by analyzing the kinematics and dynamics of the hybrid machine tool. Maximum velocity and maximum driving force each driving shaft can find out by the method of space search. Therefore, the kinematics and dynamics properties of 3-TPS hybrid machine tool is obtained, which provide proof for machine electromotor selection, framework design and control system design.

Introduction

The 3-TPS hybrid machine tool is designed by the Institute of Advanced Manufacturing Technology of Northeastern University lately. The machine tool is a new type of parallel machine tool which bases on the parallel mechanism under the constraints of series connection. Link speed and the driving force are of important indicators which must be considered under the circumstances of design. Both two indicators are directly related to the drive motor parameter selection and part design; however, it's difficult to analyze the changes of each link speed and driving force accurately via the ordinary method which generally aims the 5 degree of freedom machine tool. By means ofADAMS, the complex problem can be solved. Under that certain circumstance, based on the model of mechanical system it would create a system of kinematic and dynamic equations automatically and solving the formula by itself. Therefore, it's of important significance using the simulation methods to analyze the force and speed when the hybrid mechanisms under movement.

The mechanical feature of the 3-TPS hybrid machine tool

As shown in the illustration 1, the drive rod of the 3-TPS hybrid robot is made up with 3 telescopic rods, which couple the fixed platform(B_1, B_2, B_3)through the Hooke Hinge, the moving platform on a RRC(b_1, b_2, b_3)basis either. In order to constrain the posture of the moving platform, attach a parallel constraint mechanism 4in between the moving platform and the back. The parallel linkage 4, which consists of 2 parallelogram linkages, belongs to the series structure in that the length of each rod is equal to the one that is parallel to it, what's more, the rod couple to the one next to it through the turning pair and the axial cord of each turning pair is parallel to others. As a result of that, the revolving shaft A_3A_6 of the moving platform will be forced to move parallel to the revolving shaftC_1C_2 of the double spider all the time, so the moving platform will revolve around the axisC_1C_2,A_1, and A_2 respectively, which is θ_1, θ_2, θ_3.When the 3 rods extend or shorten according to the processing requirement, due to the combined effect of the parallel linkage,$\theta_1$and θ_4.

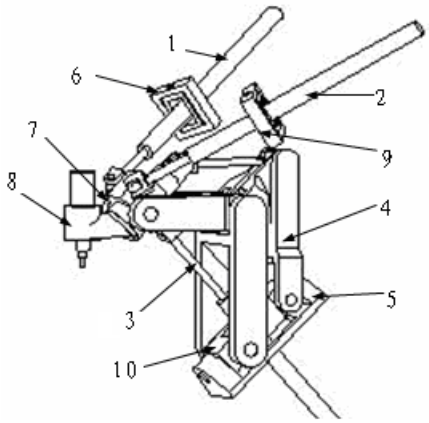

1,2,3-flexable actuating arm; 4-parallel linkage; 5-fixed bearing; 6,9-fixed frame; 7-moving platform; 8-cutter head;10-double spider

Fig.1 Sketch of the 3-TPS hybrid machine tool

The establishment of 3D model of hybrid machine tool and its parameterization

According to the machine design specifications and the drawings, take a series of processes just like three-dimensional modeling and assembly under the environment of 3D software$SolidWorks$, and thenchannel the geometrical relationship, restraint, mass of the three-dimensional model into the $ADAMS$ as a $Parasolid$ geometry format. It's of significant importance for correctness and validity of the simulation results to take the format of $Parasolid$during the process of graphics interchange preventing the loss of the important data. Being added and amended, the simulation model of the machine tool is shown in Fig. 2.

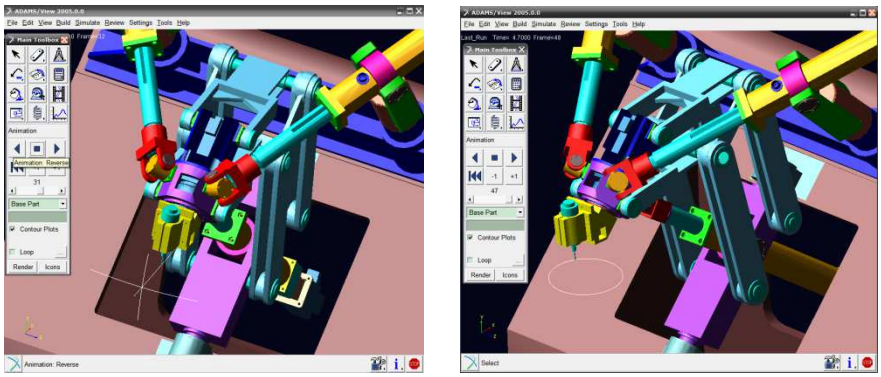

(a)Track when tool moving along a line (b) Track when tool moving around circle

Fig. 2 Simulation model after adding in ADAMS

After the process of parametric modeling, it's acceptable to set the parameter to be changed flexible. During the process of analysis, it's simple to update the entire prototype model automatically by changing the related parameter of the prototype. If there's any fault, some changes can be made to the simulation model and adjust the structure, assembly location, and the constraints between parts.

The kinematics and dynamics simulation of the hybrid machine tool

According to the demand at the very first beginning of designing the 3-TPS hybrid robot, the maximum velocity of the machine tool cutter is $0.3\mathrm{m/s}$. The specific process is as follows: makes the cutter motion in the XOY plane by uniform circular motion, the linear velocity of $0.3\mathrm{m/s}$, a radius of $100\mathrm{mm}$. By kinematics simulation, the velocity curve of 3 actuating arm could be shown in Fig, 3, and the acceleration curve could be shown in Figure 4.

The simulation results: when the linear velocity of cutter reaches to 0.3m/s by the uniform circular motion, the driving velocity of every rods are below0.3m/s, and the speed and acceleration of the rods were at a periodic change. The maximum velocity of rod 1is same as that ofrod2, which is282.99mm/s. when the cutter motion at a uniform velocity along the x-axis, the force of each rod was small and steady, the maximum less than5N. In the cutter motion at a uniform velocity along the y-axis, the force of each rod act a monotonic increasing change. Moreover, the force curve of rod 1 overlap that of rod 2 and the force of rod 3 is a little bigger than those of rod 1 and rod 2. When the cutter motion at a uniform velocity along the z-axis, the force curve of each rod was steady, and the force curve of rod 1 overlapped that of rod 2. Moreover, the curve acted a monotonic decreasing, the force of rod 3 acting a monotonic increasing. When the cutter produces a circular motion, the force of each rod acts periodical change. Moreover, the force is a little larger, the maximum being rod 3, which is315.27N.

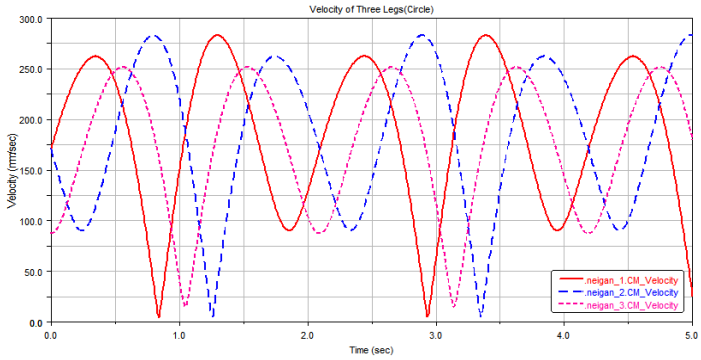

Fig. 3 Velocity curve of 3 legs when tool moving around circle

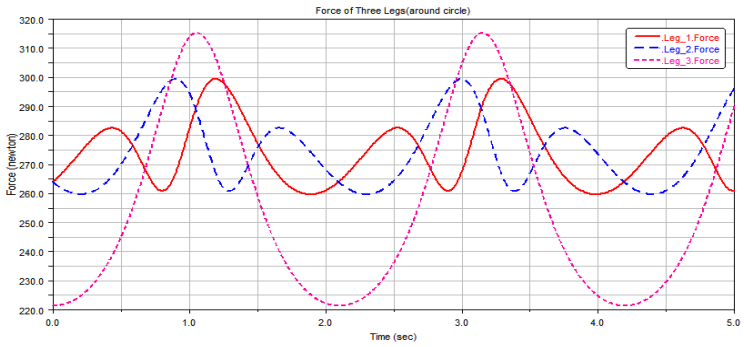

Fig.4. Force curve of 3 legs when tool moving around circle

The rotational speed and power of the actuating arm motor

According to the simulation results of the velocity, acceleration and the driving force of these 3 rods, you could calculate the maximum rotational speed and the maximum power of the motor and make requests towards the driving motor.

Table 1 Max velocity and Max driving force

	l-Maxi velocity（*mm/s*）	l-Max force（*N*）	c-Maxi velocity（*mm/s*）	c-Max force（*N*）
Driving rod 1	257.53	444.35	282.99	299.40
Driving rod 2	257.53	444.35	282.99	299.40
Driving rod 3	269.73	509.57	215.53	315.27

Because of the direct coupling between the motor and the ball screw during the designing, the transmission ratio equals 1, that is$i = 1$. The lead of ball screw equals 5, that is $p = 5mm$. The maximum velocity and the maximum driving force of each rod are displayed in the table 1. According to the calculation, the maximum rotational speed and the maximum power of the driving motor of the rod are displayed in the table 2.

Table 2 Max rotate speed and Max power

	Max speed（r/min）	Max speed（r/min）	Max driving power（kw）
Motor1 of driving rod	3090.36	3395.88	0.114
Motor2 of driving rod	3090.36	3395.88	0.114
Motor3 of driving rod	3236.76	2586.36	0.137

According to the calculation, the motor, the rated power and the rated speed of which are $1kw$ and $3000r/min$ respectively, meets the requirements of driving.

Summary

(1) According to the analysis simulation of the 3-TPS hybrid robot under the environment of ADAMS, when feed at the maximum velocity $0.5\mathrm{m/s}$ and the maximum acceleration$1\mathrm{g}$, the velocity range and the driving force range of these 3 driving rods can be obtained. According to the results of the analysis and simulation, it proves that the velocity of these 3 driving rods is steady, same as the driving force.

(2) It's convenient for simulation and analysis under the environment of ADAMS on the basis of systematic kinematics and dynamics on the 3-TPS hybrid robot. The results of the simulation are important reference for the speed programming of the 5-axis hybrid robot CNC system and the choice of the driving motor.

Acknowledgements

This work was financially supported by the National Natural Science Foundation (51105258) and Liaoning Natural Science Foundation (201202055) and Shenyang Science Foundation (F12-277-1-43). The Fundamental Research Funds for the Central Universities (N130403010)

Reference:

[1] Lee M K, Park K W. Kinematic and dynamic analysis of a double parallel manipulator for enlarging workspace and avoiding singularities [J].I EEE Transactions on Robotics and Automation, 1999, 15:1025 - 1033.

[2] Huang T, Whitehouse D J, Wang J S. The local dexterity optimal architecture and design criteria of parallel machine tools[J]. Annals of the CIRP, 1998, 47 (1):347 - 351.

[3] L. Romadhane. Design and analysis of a hybrid serial-parallel manipulator[J] , Mechanism and Machine Theory, 34(1999)：1037-1055

[4] Cai G Q , Wang Q M , Hu M , et al. Study on the kinematics and dynamics of a 3-DOF parallel machine tool [J]. Journal of Materials Processing Technology, 2001, 111(1-3):269 - 272.

[5]. Rasim S, Alizade I. Forward and reverse displacement analysis of a 62DOF in2parallel manipulators [J].International Journal of Tools & Manufacture, 1997, 39(2):321 - 342.

[6]Kong X W, Gosselin C M. Uncertainty Singularity Analysis of Parallel Manipulators Based on the Instability Analysis of Structures[J], The International Journal of Robotics Research, 2001, 20(11): 847-856.

[7]Huang Z, Chen L H, Li Y W. The Singularity Principle and Property of Stewart Parallel Manipulator [J], Journal of Robotic Systems, 2003, 20(4): 163-176.

Advanced Materials Research Vol. 983 (2014) pp 383-387

doi:10.4028/www.scientific.net/AMR.983.383

The Experiment Research on Storage Characteristic of PCM Storage Device by Spheres Piled Encapsulated For Vehicle Waste Heat

Tianshi Zhang[1,2,a] ,Qiyi Wang[1,2], Guohua Wang[1,2], Chun Gao[1,2],Qing Gao[1,2, *,b]

[1]State Key Laboratory of Automotive Simulation and Control, Jilin University, Changchun 130025,China

[2]College of Automotive Engineering, Jilin University, Changchun 130025,China

[a]email:zhangtianshi@jlu.edu.cn, [b]email: gqing@jlu.edu.cn

Keywords: phase change energy storage; waste heat recovery; spheres encapsulated; multi-melting point delamination

Abstract: For the thermal environment and the warming requirement of Vehicle, carry out experiment study on heat storage characteristic of phase change materials（PCM）encapsulated by Spherical stack. heat storage and release experiment process , changing factors such as medium flow rate and melting point which impact on PCM heat transfer characteristics , melting rate and response time have been analyzed. The results show that within the scope of experiment high medium flow rate is conducive to promote PCM melting rate and heat storage. In the experiments process, high melting point of PCM storage heat grade is high, but the low melting point of PCM is more suitable for vehicle motor, batteries in low temperature waste heat recovery. At the same time, multi-melting point PCM storage device with spheres piled encapsulated delamination mixed stowage was better satisfy the different condition of waste heat recovery and utilization than single melting point of PCM.

1Introduction

As one of the important areas of energy consumption and environmental protection, new energy vehicles and energy-saving is an important development direction, effective automobile waste heat can be used to promote the development of low energy consumption. Cars are based on waste heat from engine cooling water and the exhaust waste heat, the former is to as for the cooling medium in the low temperature energy, which is to as for exhaust flue gas of high temperature energy. The car in low temperature energy using Phase Change Materials (PCM, Phase Change Materials) waste heat storage is the best scheme selection, the high energy rate for vehicle energy efficiency play a key role, in recent years gradually get technology application [1, 2].

Phase change energy storage to endothermic melting and condensing heat release to large heat capacity, and will be discontinuous and unstable heat storage, real-time across the time needed to release using [3]. 1991, Oskar Schatz proposed thermal pool (Heat) 'concept, use of waste Heat and phase change materials for energy storage, the car engine cooling water Heat storage, used for preheating of indoor air, when the winter start defrost glass, improve comfort and safety, and improve the cold start performance [4]. E.K orin and others on the catalysts using phase change energy storage, when starting out storage heat warms catalysts as soon as possible to achieve [5]. In addition, Adamczyk, puts forward the Vacuum adiabatic VICC (Vacuum Insulated Catalytic Converter) [6], reduce heat conduction and radiation loss, in order to improve the heat capacity, realize the long span of time energy storage and temperature cooling from 600 to 250 ℃, thermal insulation properties from 20 ~ 30 min up to 18 ~ 24 h. Shen Weidong researchers such as PCM encapsulation and fill in the balloon in porous adiabatic vacuum thermal storage device, charger, exothermic experiments, carried out using vehicle flow and heat transfer of the latent heat storage heat exchanger experimental study [7].

For electric vehicles, power system can be heat storage, on the one hand, help the battery temperature, on the other hand help the winter preheating. Waste heat energy storage is one of the automobile energy saving and low carbon economy utilization way, it not only involves the

advantageous alleviate cold start emissions, there is conducive to improve vehicle dynamic performance. Phase change heat storage in the field of internal combustion engine and thermal engineering research, also has carried out many experiments, but more is to carry out the numerical simulation analysis of jilin university step such as [8, 9] according to engine operating conditions, the design module of composite phase change thermal storage in PCM three-dimensional numerical simulation analysis of thermal fluid heat storage performance.

However, past research often focused on a single melting point PCM, to improve the car more temperature waste heat recovery in PCM temperature adaptability, this paper presents the spherical stack encapsulated melting point of the PCM composite structures, and to carry out the experimental study on the heat storage and release characteristics, the results of the study for the future car has reference value and phase change heat storage and utilization of waste heat.

2 Experiment System and Equipment

2.1 Experimental Materials

This paper mainly study the melting point of 25, 36, 58 three spherical PCM encapsulation body, ball diameter of 40 mm, shell is made of polyethylene plastic, spherical shell thickness of 0.5 mm, spherical shell coefficient of thermal conductivity and other physical parameters PCM as shown in table 1:

Table 1 Spherical shell and PCM parameters

Melting point /℃	Latent Heat /kJ·kg^{-1}	Density /kg·L^{-1}	Spec. Heat /kJ·kg^{-1}·K^{-1}	Thermal Conductiviy Solid /W·m^{-1}·K^{-1}	Thermal Conductiviy Liquid /W·m^{-1}·K^{-1}
25	200	1.6	2.1	1.1	0.6
36	232	1.5	2.0	0.6	0.5
58	235	1.4	2.5	1.9	1.0

2.2 experimental system

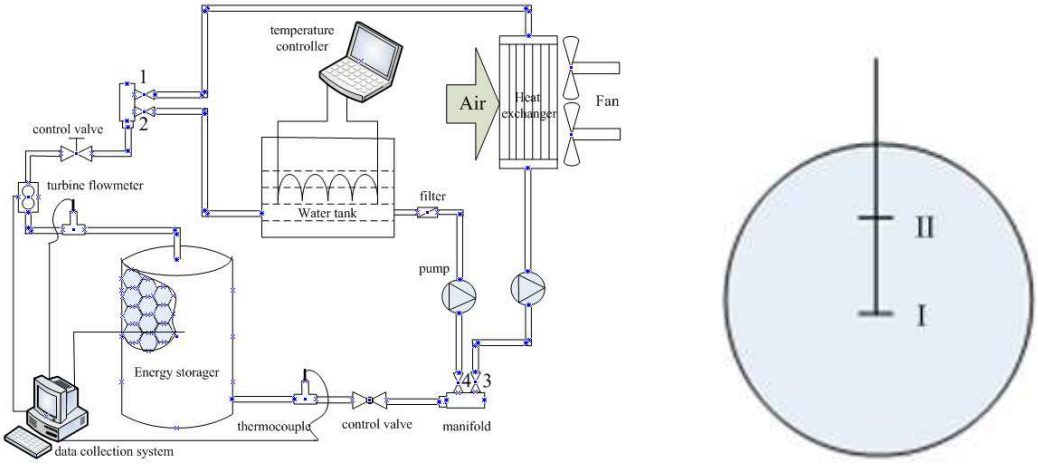

(a) System diagram (b) Temperature measuring points arrangement

Figure 1 The experimental system diagram and temperature measuring point layout

As shown in figure 1 (a), the experiment system by the energy storager, data collection system, water tank, fan, pump, turbine flowmeter, thermocouple, manifold, control valve, etc. Among them, the PCM spherical deposit placed in cylindrical heat preservation box, thermocouple temperature sensor respectively in the energy storager import and export, the ball in pile up and down. Internal spherical monomer as shown in figure 1 (b), decorate two temperature measuring point I and II, respectively, is located in the center of sphere diameter and length of 1/4.

3 Experimental Data Collection and Analysis

This section mainly studied the melting point of the ball, the medium flow's influence on the heat storage properties, melting point, traffic different ball performance difference is bigger.

3.1 Medium flow rate

As shown in figure 2, 3, in view of the three kinds of PCM in different flow rate of 5 L/min and 1.333 L/min contrast, heat storage process can be seen, within the scope of experiment with the increase of traffic to the main storage, process release rate has been increased significantly.

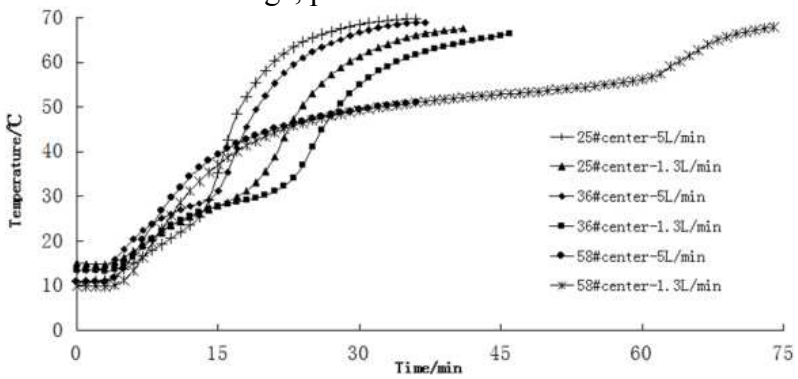

Figure 2 Medium flow impact on heat storage performance

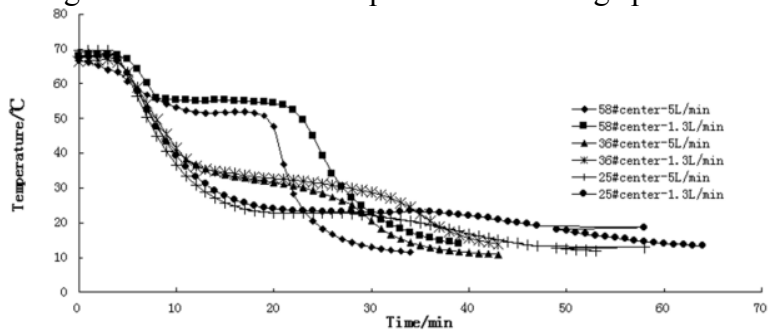

Figure 3 Medium flow impact on heat release performance

3.2 Multi-Melting Point

As shown in figure 4, the working condition of two kinds of different melting point PCM ball the same regenerative comparison shows that the lower initial temperature compared with figure 3 and the energy ball formed between the melting point of temperature difference is big, 36 # have bigger difference, the ball curve in figure 4 has obvious prophase, difference in temperature big curve slope compared with figure 3 has a lot to ascend. 58 # ball curve transformation period of long duration, amount of latent heat due to three ball close, 58 # heat storage capacity of a small ball.

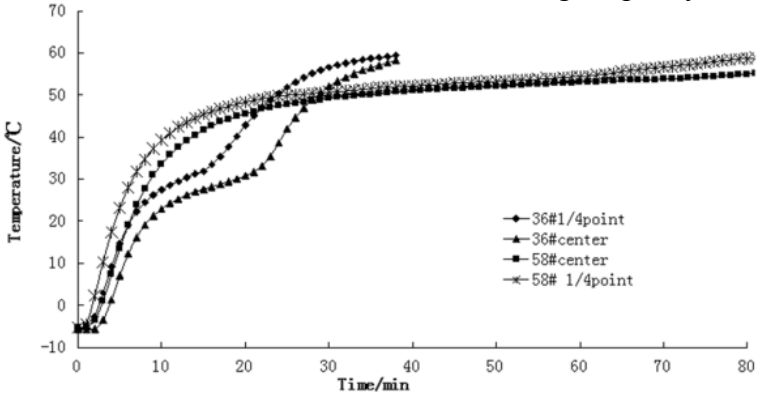

Figure 4 Multi-melting point PCM heat storage contrast

As shown in figure 5, PCM heat release process can be divided into preliminary downhill section, latent period and slow down the period of late. Compared with 25 #, 36 #, 58 # three heat release curve can be seen that the experimental range high melting point PCM58 # cooling rate of the slowest, along with the melting point in descending order. At the same time, in the cooling process of the high melting point temperature PCM keep ability stronger than the low melting point of PCM.

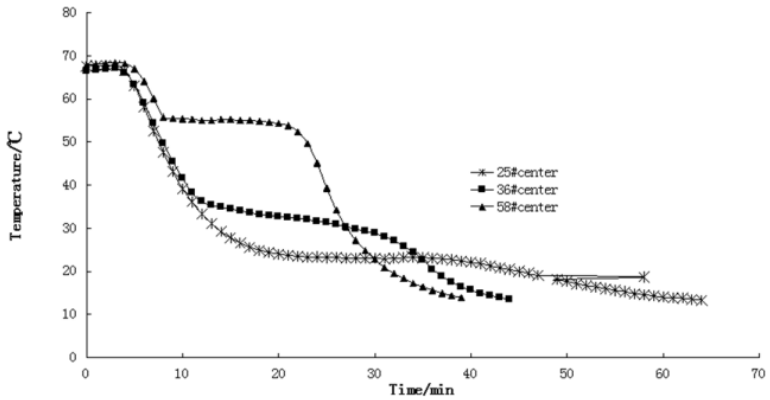

Figure 5 Multi- melting point PCM heat release contrast

4 Conclusion

1. 1:Under the experimental conditions, the 58 # ball has a big heat large latent heat, heat storage density is big, other than the two ball to heat storage performance is poor.
2. High medium flow rate is conducive to promote the storager heat release rate and heat power, storage and packaging 58 # ball accumulator in thermal power had better.
3. High melting penalty, regenerative heat release potential temperature keep at a higher position, to achieve recycling of waste heat; For better research on the accumulator performance, accumulator can put layered internal different melting point of the ball, which can realize hierarchical heat storage and heat release, meet the demand of different working conditions.

Acknowledgement：

The authors gratefully acknowledge the financial support from:

1. the NSFC (National Natural Science Foundation of China) under the grant No. 51376079.
2. Jilin province science and technology development plan item (No.20130204018GX).
3. High-Tech Industry Development Special Project by the National Development and Reform Commission of Jilin province.
4. Jilin province Association of Science and Technology Project Item.
5. National Undergraduate Training Programs for Innovation and Entrepreneurship (No.2013A42112)

Reference

[1] Robert Hupfer and Georg Habbel. Development of a Method for the Long-Term Efficiencyand Cost Evaluation of Mobile Idle-Reduction Technologies (MIRT). SAE Paper 2010-01-2031, 2010

[2] Gi-Heon Kim, Jeff Gonder, Jason Lustbader, Ahmad Pesaran. Thermal Management of Batteries in Advanced Vehicles Using Phase-Change Materials. NREL/PR-540-42544, The Future of Transportation, 2007.12

[3] Belen Zalba Jose M Marın, Luisa F. Cabeza and Harald Mehling. Review on thermal energy storage with phasechange: materials, heat transfer analysis and applications. Applied Thermal Engineering, 23(3), 2003, 251–283

[4] Oskar Schatz. Cold Started Improvement with a Heat Store. SAE Paper 910305, 1991

[5] E.Korin, R.Reshef, D.Tshernichovesky and E.Sher. Improving Cold-Start Functioning of Catalytic Converters by Using Phase-Change Materials, SAE Paper 980671, 1998

[6] A. A. Adamczyk, C. P. Hubbard, F. Ament, S. H. Oh, M. J. Brady and M. C. Yee. Experimental and Modeling Evaluations of a Vacuum-Insulated Catalytic Converter. SAE Paper 1999-01-3678, 1999

[7] SHEN Weidong, Zheng Danling. Experimental Study on the Character of Flow and Heat Transfer of Thermal Energy Storage System for Vihicles. Journal of Engineering Thermophysics, 23(1), 2002:9-13(in Chinese)

[8] GAO Qing, Wang Yongzhen, etc. Characteristics of thermal energy storage on automobile waste heat for vehicle heating. Journal of Thermal Science and Technology, 7(4), 2008: 314-319(in Chinese)

[9] WAN G Diao. Analysis of thermal storage containerwith phase change materials on automobile waste heat[D] . Changchun : Jilin University, 2007 (in Chinese)

Advanced Materials Research Vol. 983 (2014) pp 388-391

doi:10.4028/www.scientific.net/AMR.983.388

The phase shift of reflection and refraction of SH-wave at an interface of two media

An-ling Wang [a],Fu-ping Liu[b]

Beijing Institute of Graphic Communication, Beijing 102600 China
[a]wanganling@bigc.edu.cn, [b]fupingliu60@sina.com

Keywords: SH-wave, Phase shift , reflection and refraction.

Abstract: Using the reflection and refraction coefficient of SH wave at the interface of strata, we derived the phase shift of total reflection and refraction SH-wave, The results show that, the phase shift reflection than the phase shift refraction, phase shift of reflection 2 times the phase shift of refraction.

Introduction

The totally linearly reflection and relraction polarized beam of light is displaced in the plane of incidence and parallel to a ray which would be refraction geometrically at the interface between the two optically transparent, homogenous and isotropic media[1-3]., pointed out the phase shift phenomenon is that waves possess of a common characteristic. At present it is extended to research the phase shift problem of refraction electromagnetic wave and particle beam[2-6]. In recent research results also shown that the refraction wave exists negative shift In fact the lateral shift has the same order of magnitude as the wavelength. In certain special angle of incidence, the lateral shift is very large [7,9] We apply the phase shift of reflection and refraction coefficient of SH-wave to study the phase shift of SH-wave, to give the formulae of phase shift.

The phase shift 0f reflection and refraction of sh-wave at an interface of two media

When SH-wave is incident on the interface of strata, its reflection and refraction coefficients can be expressed as (see Figure2) [12,13]

$$\frac{B_2}{B_1}=\frac{\mu_1\cos\beta_1-\mu_2\left(V_{s1}/V_{s2}\right)\cos\beta_t}{\mu_1\cos\beta_1+\mu_2\left(V_{s1}/V_{s2}\right)\cos\beta_t}, \tag{1}$$

$$\frac{B_3}{B_1}=\frac{2\mu_2\cos\beta_1}{\mu_1\cos\beta_1+\mu_2\left(V_{s1}/V_{s2}\right)\cos\beta_t}\cdot\frac{\rho_1}{\rho_2}, \tag{2}$$

where, B_1, B_2 and B_3 are the amplitudes of incident, reflected and refracted waves, respectively, β_1 and β_t are the incidence and refraction angles of SH-wave, V_{s1} and V_{s2} are the velocities of SH-wave in media 1and 2, μ_1 and μ_2 are the Lame constants of media 1and 2, ρ_1 and ρ_2 are the densities of media 1and 2. With the relations $\mu_1=V_{s1}^2\rho_1$ and $\mu_2=V_{s2}^2\rho_2$, the Eq.(1), （2） can also be written as

$$\frac{B_2}{B_1}=\frac{V_{s1}^2\rho_1\cos\beta_1-V_{s2}^2\rho_2(V_{s1}/V_{s2})\cos\beta_t}{V_{s1}^2\rho_1\cos\beta_1+V_{s2}^2\rho_2(V_{s1}/V_{s2})\cos\beta_t}$$
$$=\frac{V_{s1}\cos\beta_1-V_{s2}(\rho_2/\rho_1)\cos\beta_t}{V_{s1}\cos\beta_1+V_{s2}(\rho_2/\rho_1)\cos\beta_t} \tag{3}$$

$$\frac{B_3}{B_1}=\frac{2V_{s2}^2\rho_2\cos\beta_1}{V_{s1}^2\rho_1\cos\beta_1+V_{s2}^2\rho_2(V_{s1}/V_{s2})\cos\beta_t}\frac{\rho_1}{\rho_2}$$
$$=\frac{2V_{s2}^2\rho_1\cos\beta_1}{V_{s1}^2\rho_1\cos\beta_1+V_{s2}^2\rho_2(V_{s1}/V_{s2})\cos\beta_t} \tag{4}$$

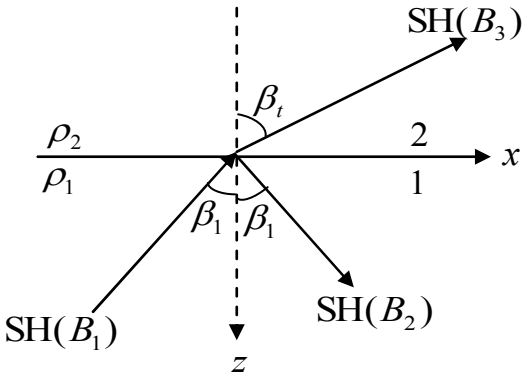

Fig.2 Reflection and refraction of SH-wave on an interface of strata

By the Snell's formulae $\frac{V_{s1}}{\sin\beta_1}=\frac{V_{s2}}{\sin\beta_t}$,we have $\beta_t>\beta_1$ when $V_{s2}>V_{s1}$ .If $\beta_t=90^\circ$, $\sin\beta_c=\frac{V_{s1}}{V_{s2}}$,i.e. $\beta_c=\sin^{-1}\frac{V_{s1}}{V_{s2}}$, β_c is the critical angle. When $\beta_1>\beta_c$, β_t becomes a complex angle, $\frac{B_2}{B_1}$ becomes a complex number. Thus we have $\sin\beta_t=\frac{V_{s2}}{V_{s1}}\sin\beta_1$,

$$\cos\beta_t=j\sqrt{\left(\frac{V_{s2}}{V_{s1}}\sin\beta_1\right)^2-1}\ ,$$

$$R_{s1}=\frac{B_2}{B_1}=\frac{V_{s1}\cos\beta_1-V_{s2}(\rho_2/\rho_1)j\sqrt{\left(\frac{V_{s2}}{V_{s1}}\sin\beta_1\right)^2-1}}{V_{s1}\cos\beta_1+V_{s2}(\rho_2/\rho_1)j\sqrt{\left(\frac{V_{s2}}{V_{s1}}\sin\beta_1\right)^2-1}}$$

$$=\frac{\cos\beta_1-n(\rho_2/\rho_1)j\sqrt{(n\sin\beta_1)^2-1}}{\cos\beta_1+n(\rho_2/\rho_1)j\sqrt{(n\sin\beta_1)^2-1}}=e^{-j\delta_{s1}}\ , \tag{5}$$

$$R_{s2}=\frac{B_3}{B_1}=\frac{2V_{s2}^2\rho_1\cos\beta_1}{V_{s1}^2\rho_1\cos\beta_1+V_{s2}^2\rho_2(V_{s1}/V_{s2})j\sqrt{\left(\frac{V_{s2}}{V_{s1}}\sin\beta_1\right)^2-1}}$$

$$=\frac{2n^2\cos\beta_1}{\cos\beta_1+n(\rho_2/\rho_1)j\sqrt{(n\sin\beta_1)^2-1}}=2n^2\cos\beta_1 e^{-j\delta_{s2s}}, \tag{6}$$

where j is the imaginary unit,

$$\delta_{s1}=\tan^{-1}\frac{2n(\rho_2/\rho_1)\sqrt{(n\sin\beta_1)^2-1}}{\cos\beta_1},$$

$$\delta_{s2}=\tan^{-1}\frac{n(\rho_2/\rho_1)\sqrt{(n\sin\beta_1)^2-1}}{\cos\beta_1},$$

$$n=\frac{V_{s2}}{V_{s1}}$$

In order to make the computational example,we choose $V_1=$ 2500 m/s, $V_2/V_1=1.3$, $\rho_2/\rho_1=1.1$. The computing results phase shift δ_{s1},δ_{s2} changes with β_1

Table 1 The computing results phase shift δ_{s1},δ_{s2} changes with β_1

β_1	60	62	64	66	68
δ_{s1}	55.94	59.77	63.10	66.06	68.73
δ_{s2}	27.97	29.89	31.55	33.03	34.36
β_1	70	72	74	76	78
δ_{s1}	71.18	73.45	75.58	77.59	79.51
δ_{s2}	35.59	36.72	37.79	38.80	39.97
β_1	80	82	84	86	88
δ_{s1}	81.36	81.15	84.90	86.62	88.31
δ_{s2}	40.68	41.58	42.45	43.31	44.16

Conclusions

The phase shift of SH wave at the refraction interface have been deduced from the phase shift of refraction coefficient of SH-wave, The results show that, Larger β_1, δ_{s1}, δ_{s2} becomes large,the phase shift reflection than the phase shift relraction, phase shift of reflections 2 times the phase shift of relraction.

Acknowledgements

This work was Supported by BIGC Project（E-b-2014-18）.Supported by Beijing Natural Science Foundation(4142016).Supported by BIGC Key Project(E-a-2013-19). Supported by the Funding Project for Academic Human Resources Development in Institutions of Higher Learning (PHR201107145). Supported by the Beijing City Board of Education Science and technology key project (KZ20110015017).National Natural Science Foundation (61272030).

References

[1] Lotsch H K V. Beam Displacement at Total Reflection: The Goos-Hänchen Effect (I, II, III, IV). Optik, Vol. 32, 1970: 116~137, 189~204, 299~319, 553~569

[2] Ignatovich V K. Neutron from condensed matter, the Goos-Hänchen effect and coherence. Physical Letters A, 2004, **322**(1):36~46

[3] Liu F P, Zhang H M, Yang C C, et al. The lateral shift of quasi total reflection of inhomogeneous electromagnetic wave when the electric field is perpendicular to the incident plane. Chinese J. Geophys. (in Chinese), 2005,**48**(4) :924~931

[4] Liu F P, Zhang H M, Yang C C, et al. The lateral shift of quasi total reflection of inhomogeneous P-electromagnetic wave on the interface of conductive media(in Chinese). Chinese J. Geophys,2007,**50**(2) : 556~566

[5] Ziolkowski R W. Pulsed and CW Gaussian beam interactions with double negative metamaterial. The International Electronic Journal of Optics, 2003,**11**:662~681

[6] Lai H M, Chan S W. Large and negative Goos-Hänchen shift near the Brewster dip on reflection from weakly absorbing media. Optics Letters, 2002,**27**: 680~682

[7] Lakhtakia A. On plane wave remittances and Goos-Hänchen shifts of planar slabs with negative real permittivity and permeability. Electromagnetics, 2003,**23**(1): 71~75

[8] Resch K J, Lundeen J S, Steinberg A M. Total reflection cannot occur with a negative delay time. IEEE journal of quantum electronics, 2001,**37**(6): 794~799.

Advanced Materials Research Vol. 983 (2014) pp 392-395

doi:10.4028/www.scientific.net/AMR.983.392

The Research on Fault Diagnosis of Civil Aircraft Information Fusion based on the Evidence Theory

Xue Peng

Engineering Technology Training Center,

Civil Aviation University of China, Tianjin 300300, China;

pxue@cauc.edu.cn

Keywords: Evidence Theory, Information Fusion, Fault Diagnosis, Similarity Coefficient, Full Factor

Abstract: In this paper, information fusion theory based on the evidence theory is used in the fault diagnosis field of civil aircraft. Considering the conflict resulted from information fusion in some certain conditions, two improved methods, including Similarity Coefficient and Full Factor are put forward to solve the conflict problems. In a nutshell, the methods are pretty effective and reliable, and the maintenance cost of airlines can be reduced obviously.

Introduction

Information fusion technology was born in the 1980s, a number of thematic research on data fusion technology program are done in the military. With the development of computer technology and information fusion technology, information fusion technology has been applied in the industrial and civilian use, such as industrial process monitoring, industrial robots, air traffic control, financial systems, weather forecasting, etc.

In the field of civil aircraft fault diagnosis, due to the complexity of aircraft equipments and the harsh operating environment, the fault information is often uncertain, incomplete, unreliable, and more uncertain faults are caused by human disturbance. These are the objective factors of uncertainty fault diagnosis results. Therefore, how to deal with the uncertainty information is an important problem for troubleshooting. In order to deal with the subjective uncertainty multi-source diagnosis problem, Bayesian methods and evidence theory provides an effective solution [1]. Sometimes, the Bayesian method is difficult to obtain a priori information, so the evidence theory is very useful to deal with uncertain information [2].

Synthesis rule of evidence theory

The description of an uncertain proposition is based on the probability distribution function. Sometimes, there are different probability distribution functions with the same evidence because of different sources of data. In order to measure the probability of evidences from multiple sources distribution functions, Dempster proposed a combination of methods to reflect the combined effect of the evidence, the Dempster combination rule [3]. For example, there are several trust functions with different sources of evidences in an identify frame. A new trust function can be calculated according to the Dempster combination rule, and this function can be used as the trust function under the combined effect of the evidences [4].

$$m(C) = m_i(X) \oplus m_j(Y) = \sum_{X \cap Y = C} m_i(X) \times m_j(Y) \Big/ (1 - \sum_{X \cap Y = \Phi} m_i(X) \times m_j(Y)) \quad (1)$$

In the Eq.1, i or j means the evidence No. i or No. j, and $m_{i(j)}(X)$ means the trust distribution function of the evidence of No. i or No. j. And $K_{ij} = \sum_{X \cap Y = \Phi} m_i(X) \times m_j(Y)$ is called the conflicting evidence factor, which means the degree of the conflict between the two evidences.

Conflict between the evidences and the improvement methods

Some of evidences may conflict when they are making multi-source information fusion because of the complexity of application objects. The conflict refers that two trust functions of elements with empty intersection are mishandled, resulting in the counterintuitive phenomenon. The key to solving the problem is how to handle the conflict in accordance with the synthesis rules [5].

Generally, DS evidence theory is more suitable for high-trust and low-conflict case, and there will be some illogicality results for the high-conflict situations. In order to maintain basic trust normalization of the distribution function, the main reason is that the DS combination rules make the basic trust function of two common elements into $(1-K)^{-1}$ times of the original, but conflicts do not cause by all elements. Actually, conflict is also the information. The conflict between the instructions can be very similar in some respects. In addition, conflicting information of the evidence can not be ignored completely, and some very important information will lose if conflicts are all abandoned. And synthesis results will be more effective and reasonable if the conflict information exists.

Murphy Method

In order to solve the conflict of evidences, Murphy proposed a modified mode with original DS synthesis rules [6, 7]. This method can deal with the conflict of evidences, and the convergence speed is fast. The step of the method is: the average value of the basic trust value of N set of evidences is synthesized N-1 times in accordance with DS rules. Compared with other methods, this method can deal with the conflict rules of evidences, and the convergence is faster. But this modified model is just a simple multiple average of evidences, the correlation between the various evidences has not been taken into account. if there is an error or wrong data, there would be a very serious impact on results.

Correction method of evidence conflict based on similarity coefficient

The weights of all evidences are same in the DS evidential reasoning procedures. In order to improve this insufficient, a kind of method is to determine whether the evidence has a similar with other evidences, which means that the degree of evidences supported by other evidences is taken into account. If the evidence is supported by a lot of evidences, the evidence should be relatively credible, of course the weight of the evidence is higher, and the effect to the final integration result will be greater. In order to describe the similarity and the support quantitatively [8, 9], a method which is based on the similarity coefficient is proposed to deal with the conflict of evidences.

Evidence similarity coefficient: There are two evidences, E_1 and E_2, in the identify framework Θ. m_1 is the basic trust function of element A_i ,and m_2 is the basic trust function of element B_j .The similarity coefficient between evidences E_1 and E_2 is as follows :

$$d_{12} = \sum_{A_i \cap B_j = A_k \neq \Phi} m_1(A_i) m_2(B_j) \Big/ \sqrt{(\sum m_1^2(A_i))(\sum m_2^2(B_j))} \tag{2}$$

The number of collected evidences is set to N. So similarity coefficients between elements E_i and E_j can be calculated according to eq.2, and it can be expressed as a similarity matrix form such as follows:

$$S = \begin{bmatrix} 1 & d_{1,2} & \cdots & d_{1,N-1} & d_{1,N} \\ d_{2,1} & 1 & \cdots & d_{2,N-1} & d_{2,N} \\ \vdots & \vdots & \ddots & \vdots & \vdots \\ d_{N-1,1} & d_{N-1,2} & \cdots & 1 & d_{N-1,N} \\ d_{N,1} & d_{N,2} & \cdots & d_{N,N-1} & 1 \end{bmatrix} \tag{3}$$

The support degree to E_i of the evidence in the similar matrix eq.3:

$$S(m_i) = \sum_{j=1}^{n} d_{ij} \tag{4}$$

The credibility of evidences is the normalization result of the evidence support degree, and it is described as follows:

$$C(m_i) = S(m_i) \Big/ \sum_{i=1}^{n} S(m_i) \qquad (i, j = 1,2,\ldots,n) \tag{5}$$

It can be seen from eq.5 that $\sum_{i=1}^{n} C(m_i) = 1$. That means that the credibility $C(m_i)$ can be seen as the weight of evidence E_i. After all weights of the evidence are obtained, synthesis procedure can be done in the user of Murphy method mentioned above.

A simple example is listed to explain the performance of similarity coefficient method in the case of certain high conflict or even completely conflict.

There are two fault data sources E_1 and E_2 .whose fault reasons are A, B, C, and basic trust distribution functions are m_1 and m_2 : $m_1(A) = 0.9$, $m_1(B) = 0.1$, $m_1(C) = 0$; $m_2(A) = 0$, $m_2(B) = 0.1$, $m_2(C) = 0.9$. So the result of the calculation by DS method with general synthesized rules is as follows: $m(A) = m(C) = 0$, $m(B) = 1$.

Although the support degree for B by m_1 and m_2 are very low, the result is that fault reason B is the most possible causes, which is obviously unreasonable. If another two new fault data sources E_3 and E_4 are added whose basic trust distribution functions m_3 and m_4 : $m_3(A) = 0.7$, $m_3(B) = 0.1$, $m_3(C) = 0.2$; $m_4(A) = 0.8$, $m_4(B) = 0.1$, $m_4(C) = 0.1$. Then the result of the calculation by DS method with general synthesized remains: $m(A) = m(C) = 0$, $m(B) = 1$.

This shows that although the majority of evidences prove that A is correct, but because certain evidence contradicts A, synthesis results will be negative. So for some multi-source information systems, if there are some different data in one or more data source, entire systems would not work properly.

The example mentioned above is recalculated based on the evidence conflict based on similarity coefficient, and the result is listed as follows:

Support: $S(m_1) = 2.962$, $S(m_2) = 1.442$, $S(m_3) = 3.24$, $S(m_4) = 3.12$

Credibility: $C(m_1) = 0.28$, $C(m_2) = 0.13$, $C(m_3) = 0.3$, $C(m_4) = 0.29$

The weighted average of evidences: $m_c(A) = 0.694$, $m_c(B) = 0.1$, $m_c(C) = 0.206$

The final result of the weighted average method according to Murphy method is as follows:
$m(A) = 0.99$, $m(B) = 0.002$, $m(C) = 0.008$

It is clearly shown that there are three groups of four groups of evidence support A, and all the support of evidences are very low, but the result of original synthesis DS rules is the support to B is 100%, which is obviously unreasonable; while after the calculation is done by the method of evidence conflict based on similarity coefficient, the result is A, which is very logical.

Case Study

An actual example is shown as follows: there is a warning says AIR PACK1 OVHT on the post flight report some day, and there are three fault data sources DS1, DS2, DS3.Three methods, including the Murphy method, the original DS method and the evidence conflict based on similarity coefficient method mentioned above, are used to calculate information fusion of the three different data sources to find the most possible cause or causes of the fault. The result is listed on table 1 as follows

Table 1 Information fusion results

Reason	DS1	DS2	DS3	Murphy method	Original DS method	Similarity coefficient
VALVE FLOW CTL	1	0	0.5	0.52530	0.71398	0.91045
FLOW CTL SYSTEM-PACK 1	0	1	0.2	0.37035	0.28559	0.08953
SENSOR-COMPRESSOR OVHT	0	0	0.3	0.10565	0.00043	0.00002

The result in table 1 shows that the fault most possible cause is VALVE FLOW CTL. Based on the actual troubleshooting record the cause of the fault is this component, which is consistent with the result of the proposed algorithm in this paper.

Summary and Outlook

According to this paper, many multi-source data fusion problems with few conflicts can be solved with the help of the original DS evidence theory, but there will be some problems when there are some data conflicts between data sources. While, the familiar degree of data sources is take into consideration by the similarity coefficient. So, it can deal with the data fusion problems with highly conflicts. If maintenance person use the conclusion made by the theory mentioned in this paper, it will greatly improve the efficiency of maintenance work and it will generate lots of cost savings.

References

[1] Liu Tong-ming, Xiazu Xun, Xie Hong compiled into a data fusion technology and its application [M] Beijing: National Defense Industry Press .1998, 1st Edition :20-160.

[2] Xiaofei. Based on Bayesian networks and network fault diagnosis model D_S evidence theory research [D]. [Master's thesis]. Southwest Jiao tong University, 2010.5

[3] Dempster A P. Upper and Lower Probabilities Induced by a Multi-valued Mapping [J]. Annual Mach Statistic, 1967, 38 (4) :325-339.

[4] Shafer G. A Mathematical Theory of Evidence [M]. Princeton University. Press, Princeton, 1976:121-138.

[5] Zhang Eagle Pan Quan Zhang was studied. Evidence conflicts. Aeronautics [J]. 2001,22 (7) :369-372.

[6] Murphy CK Combining belief functions when evidence conflicts [J]. Decision Support System. 2000, 29 (1) :1-9.

[7] Josang A, Daniel M, Vannorenberhghe P. Strategies for combining conflicting dogmatic beliefs [J]. Proceedings of the Sixth International Conference on Information Fusion. Queensland, Australia. July :2003:1133-1140.

[8] Chen Lei, Wang Junjie improved method of DS evidential reasoning [J] Journal of System Simulation 2004,1 (16): 28-30

[9] Chen Tianlu ACTUATORS information fusion method and its application to determine the credibility of multi-sensor [J] Test and Measurement Technology 2005, 1 (19): 61-64.

Advanced Materials Research Vol. 983 (2014) pp 396-399

doi:10.4028/www.scientific.net/AMR.983.396

A characteristic seismic study and development of Earthquake resistant techniques in existing structures

Yasuhide Mochida [1, a], Yashwanth Hanumantharayappa [1, b *]

[1]1-1-1 Noji-Higashi, Kusatsu, Shiga, 525-8577, Japan

[2] NMAMIT, Nitte, Karkala Taluk, Udupi District, Karnataka 574110, India

[a]mochida@fc.ritsumei.ac.jp, [b]hyashwanth90@gmail.com.

Keywords: geotechnical risk, preservation, earthquake, construction management, isolation, structure analysis.

Abstract. The characteristic methods involved in underpinning construction are studied in this research. The analysis of the structure is performed with respect to the geotechnical risk and possible retrofitting techniques. In the past several decades, a number of studies mainly focused on base isolation techniques to preserve the structure, but the merits of underpinning technique, geotechnical risk involved, temporary support for safety measures and cost ratio induced were unexpressed. The second generation of research evaluates the measure to reduce ground risk with characterization methods and detailed quality check through construction management system. Current research has pointed out the crucial features of underpinning construction process and its scope in restricted locations and geotechnical perils.

Introduction

The construction stages are subjected to various risks in a structure. Some of them are ground risk (geotechnical risk) in conjunction with the foundation work of design. Many sectors are involved in order to optimize these risks. Nevertheless, the process is confirmed by analyzing the structure, rework in foundation and ensure structural performance and accuracy in design stage and fall of production in the building construction.

Japan has a long history of earthquakes, ground risks and seismic activity. It is an area of high seismicity has it is located near tectonic plate boundaries. The leading geotechnical engineering firms and construction corporations are engaged in control and protecting the structures from the downfall.

Base isolation is an effective way to improve structural seismic response and reduce damages that may be caused by earthquakes. A reinforcement plan of isolation retrofitting in the existing building is practiced, on the assumptions of functional requirement of the building, safety and need for improvement of seismic performance have been made. In the study the actual isolation of the range variety is diversified and focused on preservation and safety of the building. Especially the underpinning construction in particular with its effects and impact of geotechnical risk is high, due to its uncertainty, the plan is greatly affected.

In this study we have focused on the structure located at Ishikawa prefecture, Chubu region, Japan. The research emphases on the seismic isolation retrofit with a basement, the dissimilar underpinning works, characterization methods of construction, differences in construction management and the differences of each layer of seismic base isolation are shown.

This paper indicates the geotechnical risk reduction and study carried out in the building site and reduction in the loss of construction (temporary) in the existing building and safety measures. Earlier studies mainly dealt with the efficiency of seismic isolation in foundations but the risk and seismic responses with respect to structure are greatly attenuated. In the second generation of study the different isolation materials & layers and review in underpinning techniques from previous studies are shown. No research is complete in itself, as each question leads to other research questions and this process and developing needs to update incrementally.

Experiment

The experiment were conducted according to Japanese Industrial Standards (JIS) and Japanese Concrete Institute

Construction Overview

This building is a seismic isolation building construction, due to regular earthquake situation, safety of human life & functional purpose and prevent disaster as a base; it is subjected to seismic isolation retrofit construction. The construction process and the seismic isolation renovation in the existing structure and to understand the loss in construction are studied in this paper.

Building overview

It is an Eight-story structure of Steel Reinforced Concrete (SRC) structure located at Ishikawa prefecture, Japan. The site area is exposed to high seismicity and regular earthquakes. It is a tall building of 31.58m height and the building measured about 90m from long side and 21.5m short side. Summary of the building is illustrated in Table 1.

In accordance with the provisions of article 4 of the Act for promotion of renovation for earth resistant structures of buildings in 2009, the seismic performance of reinforcement by interlayer seismic verification was performed. And the central portion of 18m x 21.5m base isolation was confirmed in the structure.

Table 1, Building summary

Structure type	SRC
Construction area	2219.01m2
No of basement-floors	1-8-0
Eave height	31.38m
Total floor area	14948m2
Seismic retrofitting contractors	Shimizu corporation

Method of Underpinning

The process of underpinning is to strengthen the existing building and is practiced for variety of reasons; like to increase the load capacity of existing foundations, stabilization of foundation soils, reduce geotechnical risks, mainly when the original foundation is simply not strong and move the existing structure.

The seismic isolation retrofit are classified into various isolation techniques(layers) and illustrated in fig.1, Schematic representation of Seismic Isolation Retrofit layers.Previous studies of research explained the classification in detail, In this study, the construction process, ground risk, cost control measure and safety are studied.

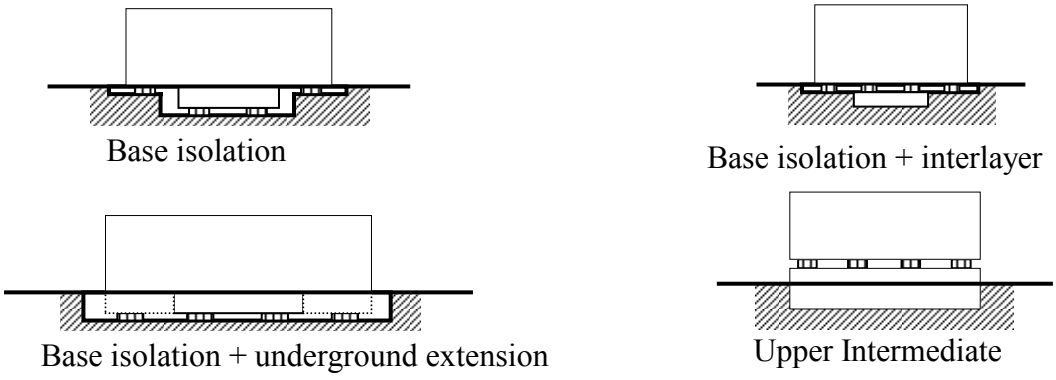

Fig.1, Schematic representation of Seismic Isolation Retrofit layer

Seismic Isolation System Overview

The process includes different kind of bearings supporting the existing structure. Fig.2, shows the seismic isolation system overview. The variety of isolation layers include Lead (plug) rubber bearings, Rubber bearings, Sliding Bearings and an oil damper.

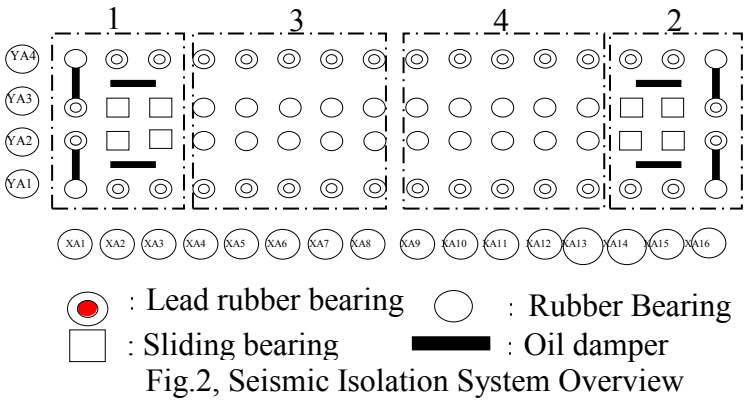

Fig.2, Seismic Isolation System Overview

Basically, the lead plug bearings are in outside pillar bottom, plug into sliding bearings and base isolation underpillars with rubber bearings as an interlayer isolations in columns and finally isolating with oil dampers on seismic foundations.This process provides a grip and support to the existing foundation and offers great flexibility and potential to engineers faced with underpinning problems.

Construction process

The process is divided into different wards of base isolation work. Fig.3, shows the seismic isolation in existing structure. The construction process is performed for safety purpose(temporary) and resist the existing structure from vertical loads and disaster .Temporary structure are loaded YA2 ways between YA1 ways and the reinforcement of footing beams are removed by drilling and installing a short strut between the existing building and peripheral portion at the same time.

Fig.3, Represents the seismic isolation in existing structure

Concrete casting and foundation reinforcement are performed as temporary ground support within the permisssible range . From the bottom panel based on the preload is set up to insert position seismic isolation materials etc., the temporary short strut of outer periphery is removed.

Results and discussions

For bearing capacity of the ground(isolation unit+ support) and temporary recieving member, the medium term allowable bearing capacty or less with respect to the vertical stress was confirmed. For earthquake axial force against short term allowable bearing capacity was inveterate.This is practised inorder to tolerate ground risk in the existing structure. The draft received over proposed method is 3 times each basic support weight (temporary) in bid proposal of comprehensive evaluation. The substitute for temporary support with general evaluation was proposed in a draft twice the number of times.Fig.4, illustrates the results of Flat plate test results.

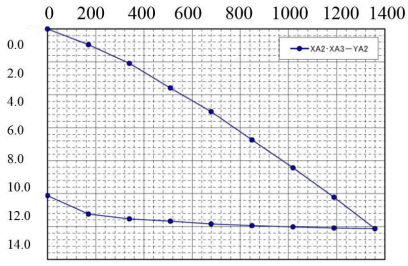

Fig.4, Flat plate test results

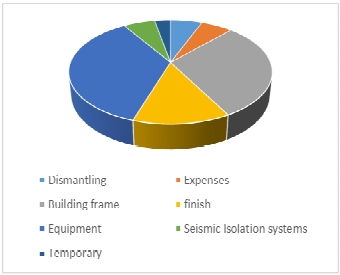

Fig .5, Cost ratio in temporary construction

Cost induced in temporary supporting for ground risk reduction

Fig.5, Illustrates the cost ratio in construction of temporary structure at site to support the existing structure and geotechnical risk. From this it shows that it has affected a lot of construction costs related to temporary supporting and earthwork. In particular, the construction quality was intensively managed by detailed check through management system and the process are well explained using 3D CAD system as shown below, to extract the problems in each step in detail.

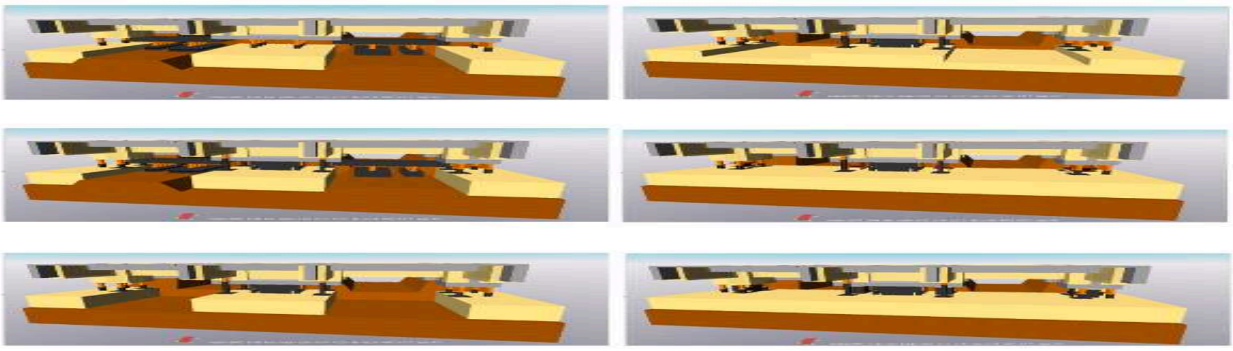

Conclusion

(1) In this paper development of underpinning construction as shown that the impact on ground risk is significabtly different and achieves reduction in ground risk.

(2) This process shows the ability to be installed from very restricted and high seismic location with fewer disturbances to the existing structure.

(3) This process underlines the crucial features of underpinning technique performed in the study and flexibility for designers to solve ground risks and ensure safety to structure & human life.

References

[1] JSCE, 1988. Earthquake Resistant Design for Civil Engineering, Structures in Japan. Japanese Society of Civil Engineers, Tokyo

[2] Kiyomiya.O, Earthquake-resistant design features of immersed tunnels in Japan. Tunneling Underground Space Technol. 10 (4), 463-475, 1995.

[3] Kramer.S, Geotechnical Earthquake Engg. Prentice-Hall, Upper Saddle River, NJ, USA. (1996)

[4] Jangid RS, Seismic response of an asymmetric base isolated structure.Comput Struct; 60(2):261–7.

[5]Jia G.F,ShiZF,A new seismic isolation method and its feasibility study,EarthqEngVib,75–82, 2010.

[6] F.Menter and L.Greev, ‘‘EMTP-Based Model for Grounding System Analysis‘‘, IEEE Transachons on Power Delivery, Vol.9, October 1994.

[7] Baecher G, Christian J. Reliability and statistics in geotechnical engineering.Wiley; 2008.

[8] TsaiHC, Kelly J.M. Buckling load of seismic isolators affected by flexibility of reinforcement. Int J Solids Struct; 42: 255–69(2005).

Advanced Materials Research Vol. 983 (2014) pp 400-403

doi:10.4028/www.scientific.net/AMR.983.400

Shock Response Analysis of Marine Gearbox

Wen Liu[1, a], Tengjiao Lin[1, b] and Zeyin He[1, c]

[1]State Key Laboratory of Mechanical Transmission, Chongqing University, P. R. China

[a]liuwen@cqu.edu.cn, [b]tjlin@cqu.edu.cn, [c]hezeyin_sklmt@126.com

Keywords: Finite element method; Shock response; Shock spectrum; Gearbox.

Abstract. The shock spectrum of gearbox was gotten according to German specification. And the equivalent time-domain acceleration curve was converted from shock spectrum. After the dynamic finite element model of entire gearbox was established by using the truss element, spring element and tetrahedral element, the shock response including the vibration velocity, acceleration and dynamic stress of gearbox subjected to the acceleration shock excitation were simulated. At last, the anti-shock performance of gearbox was analyzed combining with the strength criterion.

Introduction

During voyage, the ship may encounter unpredictable impact load. With its dynamic response such as the vibration velocity, acceleration and the dynamic stress arising, damage may occur on marine equipment. So it is necessary to analyze the shock response and the anti-shock performance of marine equipment.

In recent years, domestic and foreign scholars have done a lot of research work on shock response analysis of marine equipment. Rajendran has calculated the response of ship under impact load [1]. Lam has studied the dynamic response of hull piping after the underwater explosion shock wave function, also, the impact resistant performance of vibration isolation device is analyzed [2]. Carcaterra has analyzed the response of hydraulic shock absorber under impact load condition [3]. Jiang has calculate the shock response of floating raft isolation system with a limiter by Pseudo force method [4]. Wu has calculated the shock resistance on diesel engine base with reference to the German army specification BV043/85[5]. Zhu has done the numerical simulation of shock response on the main propulsion shaft by considering the influence of rotation rate under exterior impact[6]. Liu has calculated the shock response of the parts after studied the calculation method of the shock response of the diesel engine spare parts under the normal operation [7]. Lin has done the numerical simulation of shock resistance on marine gearbox by considering the influence of internal dynamic excitation and external acceleration excitation[8].

The spring element, the truss element and the tetrahedron element was used to establish the gear-shaft-bearing-housing coupled finite element model in the paper. The shock spectrum is determined according to the German specification, and then converted it into equivalent double half sine acceleration impact load. By calculating the inherent characteristics of gearbox and the dynamic response under acceleration impact load, the shock resistance of gearbox can be determined.

Finite element model

The finite element model of gearbox is shown in Fig. 1, there are total of 86724 nodes and 293148 elements, including 662 truss elements, 68 spring elements and 292418 tetrahedral elements.

The element of model involved the following types: truss element, spring element and tetrahedron element. Truss element is used to simulate the bolted connection and the axial support between bearing and shaft, spring element is used to simulate the meshing of the gears and the radial support between bearing and shaft.

The boundary conditions in finite element dynamic model of marine gearbox include the gear pair meshing relationship, the bolted connection, the bearing support and fixed constraint.

Shock excitation

Shock excitation of gearbox can be treated as shock pulse or shock spectrum. The shock pulse usually takes as a half sine wave or a post-peak sawtooth wave. The shock spectrum is the relationship curve between the response's maximum amplitude of a series of none quality linear oscillators with different natural frequency and its natural frequency, when the oscillators are installed on the same foundation bed and applied the same impact acceleration and velocity. According to the German specification BV043/85, the curve of the typical shock spectrum is shown in Fig. 2.

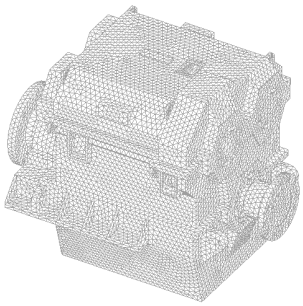

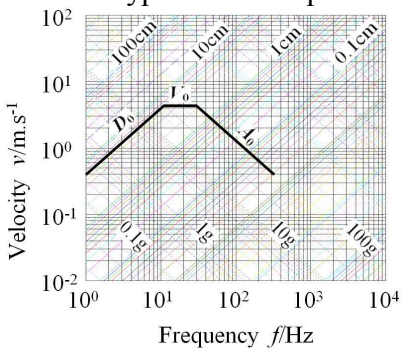

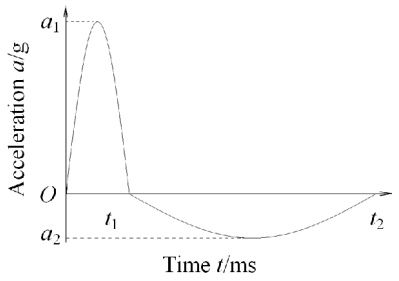

Fig. 1 Finite element model Fig. 2 Typical shock spectrum Fig. 3 Time-domain acceleration curve

The shock spectrum include the relative displacement, relative velocity and absolute acceleration. In the impact dynamic response analysis of marine equipment, the shock spectrum is commonly described as four dimensional coordinates, velocity spectrum as the ordinate, frequency as the abscissa, and the relative displacement spectrum and acceleration spectrum, respectively as the coordinate system which are + 45° and -45° with abscissa. Displacement spectrum is D_0, velocity spectrum is V_0, acceleration spectrum is A_0, the frequency of velocity spectrum is from f_1 to f_2, $f_1=V_0/(2\pi D_0)$, $f_2=A_0/(2\pi V_0)$. The parameters of shock spectrum are shown in Table 1.

Table 1 The parameters of shock spectrum

shock spectrum	A_0/g	V_0/m·s^{-1}	D_0/mm	f_1/Hz	f_2/Hz
1	30	1.575	22.5	11.1	30.3
2	40	2.1	30	11.1	30.3
3	50	2.625	37.5	11.1	30.3
4	60	3.15	45	11.1	30.3

The shock spectrum can be converted into an equivalent time-domain acceleration curve of double triangle or double half sine. The time history curve of double half sine adopted in this paper is shown in Fig. 3, the parameters of equivalent double half sine acceleration excitation are given in Table 2.

Table 2 The equivalent double half sine acceleration excitation

shock spectrum	a_1 /g	t_1/ms	a_2/g	t_2/ms
1	15	11	3.9	53.9
2	20	11	5.2	53.9
3	25	11	6.5	53.9
4	30	11	7.8	53.9

The equivalent double half sine acceleration time history curve is composed of one positive pulse and one negative pulse, with different peak and duration but equal area. So the final speed of foundation bed is zero. In Fig. 2, a_1 and t_1 are respectively positive pulse peak and pulse width of acceleration. a_2 and t_2-t_1 are respectively negative pulse peak and pulse width. The relationship between these parameters and the shock spectrum are shown in follow:

$$a_1 = 0.5A_0, \quad t_1 = 2\pi V_0 / (3A_0), \quad t_2 - t_1 = 3D_0 / V_0, \quad a_2 = \pi V_0 / 3(t_2 - t_1) \tag{1}$$

Impact dynamic finite element analysis method

Modal displacement method is used for impact dynamic response analysis. If a forced movement excitation is applied in structure, the modal model will contain not only the normal modal, but also the

constraint modal and the effective mass. The normal modal indicates the dynamic characteristic of finite element model. The constraint modal is used to define the static correction of forced movement excitation. Effective mass is used to convert movement excitation into modal force.

The dynamic motion equations of structure with degrees of motion freedom

$$\begin{bmatrix} \boldsymbol{M}_{ii} \boldsymbol{M}_{is} \\ \boldsymbol{M}_{si} \boldsymbol{M}_{ss} \end{bmatrix} \begin{Bmatrix} \ddot{\boldsymbol{x}}_i \\ \ddot{\boldsymbol{x}}_s \end{Bmatrix} + \begin{bmatrix} \boldsymbol{C}_{ii} \boldsymbol{C}_{is} \\ \boldsymbol{C}_{si} \boldsymbol{C}_{ss} \end{bmatrix} \begin{Bmatrix} \dot{\boldsymbol{x}}_i \\ \dot{\boldsymbol{x}}_s \end{Bmatrix} + \begin{bmatrix} \boldsymbol{K}_{ii} \boldsymbol{K}_{is} \\ \boldsymbol{K}_{si} \boldsymbol{K}_{ss} \end{bmatrix} \begin{Bmatrix} \boldsymbol{x}_i \\ \boldsymbol{x}_s \end{Bmatrix} = \begin{Bmatrix} \boldsymbol{F}_i \\ \boldsymbol{R}_s \end{Bmatrix} \tag{2}$$

Where $\boldsymbol{M}$, $\boldsymbol{C}$, $\boldsymbol{K}$ are the mass matrix, damping matrix and stiffness matrix respectively. The subscript i, s are the degrees of freedom with constraint and without constraint respectively. $\boldsymbol{x}$, $\dot{\boldsymbol{x}}$, $\ddot{\boldsymbol{x}}$ are the displacement vector, velocity vector and acceleration vector respectively. $\boldsymbol{F}_i$ are the applied force vector, R_s are the reaction force vector.

If the structure is applied with forced movement, x_s is defined as movement forms, the physical degrees of freedom can be expressed as

$$\boldsymbol{x}_i = \boldsymbol{\Phi}_n \boldsymbol{\gamma} + \boldsymbol{\Phi}_s \boldsymbol{x}_s \tag{3}$$

Where $\boldsymbol{\Phi}_n$ is the normal modal matrix. $\boldsymbol{\gamma}$ is the modal coordinates vector. $\boldsymbol{\Phi}_s$ is the constraint modal matrix for degrees of freedom in forced movement, $\boldsymbol{\Phi}_s = -\boldsymbol{K}_{ii}^{-1} \boldsymbol{K}_{is}$.

The condensation modal dynamic equation (2) can be expressed as

$$\boldsymbol{M}_{ii} \boldsymbol{\Phi}_n \ddot{\boldsymbol{\gamma}} + \boldsymbol{C}_{ii} \boldsymbol{\Phi}_n \dot{\boldsymbol{\gamma}} + \boldsymbol{K}_{ii} \boldsymbol{\Phi}_n \boldsymbol{\gamma} = \boldsymbol{F}^* \tag{4}$$

Where $\boldsymbol{F}^* = \boldsymbol{F} - \boldsymbol{\Phi}_m \ddot{\boldsymbol{x}}_s - \boldsymbol{\Phi}_c \dot{\boldsymbol{x}}_s$ is the effective external load, $\boldsymbol{\Phi}_m = \boldsymbol{M}_{ii} \boldsymbol{\Phi}_s + \boldsymbol{M}_{is}$ and $\boldsymbol{\Phi}_c = \boldsymbol{C}_{ii} \boldsymbol{\Phi}_s + \boldsymbol{C}_{is}$ are the effective mass matrix and damping matrix of forced movement respectively.

Solving equation (4) using duham integral formula

$$\gamma_i = \frac{1}{\omega_{di}} \int_0^t f_i e^{-\xi_i \omega_i (t-\tau)} \sin \omega_{di} (t-\tau) \mathrm{d}\tau + e^{-\xi_i \omega_i t} (A_i \sin \omega_{di} t + B_i \cos \omega_{di} t) \tag{5}$$

Where $f_i = \boldsymbol{\varphi}_i^{\mathrm{T}} \boldsymbol{F}^*$ is the modal force, ξ_i is the modal damping factor, ω_i, ω_{di} are undamped natural frequency and damped natural frequency respectively; $\boldsymbol{\varphi}_i$ is the modal vibration mode vector of i order, A_i, B_i are constants depended on the initial conditions.

Using modal displacement method, the response and the dynamic stress can be expressed as

$$\left.\begin{aligned} \boldsymbol{x} &= \boldsymbol{\Phi}_n \boldsymbol{\gamma} + \boldsymbol{\Phi}_s \boldsymbol{x}_s \\ \dot{\boldsymbol{x}} &= \boldsymbol{\Phi}_n \dot{\boldsymbol{\gamma}} + \boldsymbol{\Phi}_s \dot{\boldsymbol{x}}_s \\ \ddot{\boldsymbol{x}} &= \boldsymbol{\Phi}_n \ddot{\boldsymbol{\gamma}} + \boldsymbol{\Phi}_s \ddot{\boldsymbol{x}}_s \end{aligned}\right\} \tag{6}$$

$$\boldsymbol{\sigma} = \boldsymbol{\Phi}_n^{\sigma} \boldsymbol{\gamma} + \boldsymbol{\Phi}_s^{\sigma} \boldsymbol{x}_s \tag{7}$$

Where $\boldsymbol{\Phi}_n^{\sigma}$ is the natural modal stress matrix, $\boldsymbol{\Phi}_s^{\sigma}$ is the constraint modal stress matrix.

Shock resistance analysis of gearbox

When the equivalent double half sine acceleration shock excitation as shown in Table 2 is applied on the base of housing in X, Y and Z direction respectively, the vibration velocity, acceleration and the dynamic stress of gearbox can be calculated by modal displacement method. The maximum dynamic equivalent stress of gearbox subjected to various acceleration excitation are shown in Table 3.

Table 3 The maximum dynamic equivalent stress of gearbox under acceleration excitation

shock spectrum	The dynamic equivalent stress /MPa		
	X	Y	Z
1	232	118	167
2	309	157	227
3	387	197	278
4	464	235	334

The dynamic response curves of node 13421 are shown in Fig. 4, and the dynamic equivalent stress contour of gearbox is shown in Fig. 5 when the equivalent double half sine acceleration excitation which converted from the shock spectrum with the value of A_0=30g, V_0=1.575m/s, D_0=22.5mm in X direction is applied on gearbox.

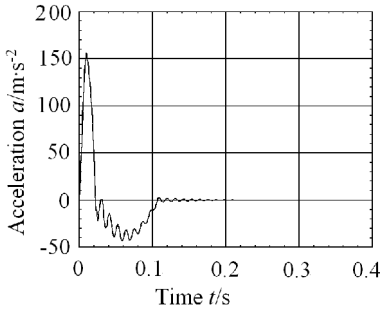

(a) Vibration acceleration

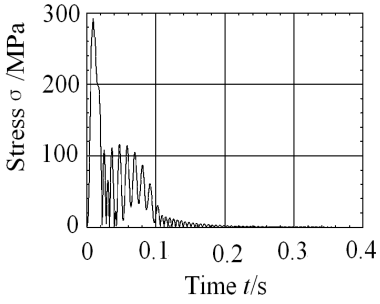

(b) Dynamic stress

Fig. 4 The dynamic response of node 13421

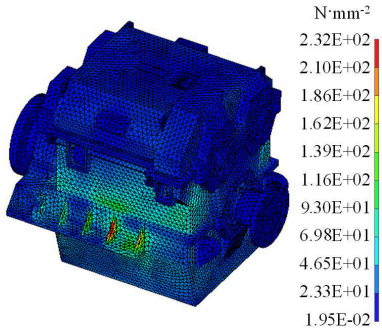

Fig. 5 The dynamic equivalent stress

In this paper, we use the strength criterion to judge the marine gearbox's impact resistant ability. Due to the yield strength of material is 235 MPa, when the equivalent double half sine acceleration excitation which converted from the shock spectrum with the value of A_0 =30g, V_0=1.575m/s, D_0=22.5mm in X direction, A_0=60g, V_0=3.15m/s, D_0=45mm in Y direction and A_0=40g, V_0=2.1m/s, D_0=30mm in Z direction is applied on gearbox respectively, the dynamic stress as shown in Table 3 is not beyond the yield limit of material, and the plastic deformation, the crack or other mechanical damage will not be occurred in the gearbox.

Conclusion

1) After the meshing of the gears and the bearing support are treated as spring element, the bolted connection is treated as truss element, the finite element model of gearbox is established.

2) The vibration velocity, the acceleration and the dynamic stress of gearbox is numerical simulated. According to the calculation result, the marine gearbox can withstand the acceleration impact load with spectrum value of A_0=30g, V_0=1.575m/s, D_0=22.5mm.

Acknowledgements

This work was financially supported by the Natural Science Foundation Project of Chongqing (cstcjjA70002), the National Natural Science Foundation of China (51175524) and the National Science and Technology Support Project (2013BAF01B04).

References

[1] R. Rajendran, K. Narasimhan: International Journal of Impact Engineering, Vol. 25 (2001): p 493-506
[2] K. Y. Lam, Z. Zong, Q. X. Wang: Composites Part B, Vol. 34 (2003): p. 59-66
[3] A. Carcaterra, E. Ciappi: Journal of Sound and Vibration, Vol. 271 (2004): p. 411-439
[4] G. H. Jiang, R. Y. Shen, L. G. Yin: Journal of Ship Mechanics, Vol. 10(2006): p. 138-150
[5] G. M. Wu, Y. J. Mei, X. J. Zhu: Chinese Journal of Ship Research, Vol. 1(2006): p. 41-43
[6] X. P. Zhu, Q. Feng: Journal of Ship Mechanics, Vol. 11 (2007): p. 143-151
[7] S. J. Liu, G. Z. Bao, H. Q. Chen: Chinese Internal Combustion Engine Engineering, Vol. 28(2007): p. 39-42
[8] T. J. Lin, R. K. Jiang, R. F. Li and W. Liu: Chinese Journal of Vibration and Shock, Vol.26 (2007): p. 14-17,22

Advanced Materials Research Vol. 983 (2014) pp 404-407

doi:10.4028/www.scientific.net/AMR.983.404

Design on the detection system of stud welding dynamic parameters

Bin Wang[1, a], Xiaoxu Li [1, b *], Wenming Zhang[1, c]

[1]College of Mechanical Engineering, Shengyang University, Shenyang 110044, China

[b] 513703053@qq.com

Keywords: Stud welding; Dynamic parameters; Detection system.

Abstract: Stud welding plays an important role in fixing stud on car bodies. The quality of stud welding is seriously affect automotive security. During the stud welding process,stud welding machine by monitor welding current,welding voltage and welding time to determine the welding quality is good or bad,and uses the average parameter monitoring system,but there are many defects of welding quality relate to these instantaneous value of the parameter.Based on the above issues, designed a dynamic parameter detection system.through the real-time monitoring of dynamic parameter,it can more accurately detect the defects of welding quality.

Introduction

With the development of modern industry, especially in the automotive industry, the stud demand more and more. Stud welding as one of the main fixed form of stud, has been widely used. In the actual production, the stud welding shows its advantages. Its performance is reliable and easily to master. The development trend of stud welding is intelligent, high efficiency, stability, special and etc.With the progress of automation technology and the development of modern monitoring technology, when the stud welding going on the welding parameters can be observed directly. The parameters can be adjusted at any time to reduce the failure rate of the welding. Therefore, the information collection and analysis of welding parameters is very important.

In order to improve the precision of welding, stud welding machine is special development, the data shows that more than 80% of stud welding has the specialty welding machine for welding in the abroad. Through the use of stud welding, it can ensure the quality of the stud fixed and improve production efficiency at the same time.

Stud welding and the problems in the process of welding

Stud welding is a special method for stud welding.In the process of welding, first of all, through the low current to ignition the arc.And then through a large current, the nugget is big enough which contacted by the plate and the stud. At last, Exert enough pressure to the stud, which will fixed on the board[1].

In production, there is many factors influence the quality of welding. According to the characteristics of stud welding, the problem in the process of welding have proposed as the following.

Firstly, the output data of the machine is instability.

Secondly, the stub and the workpiece are not cleaning enough.

Finally, stud welding nucleation time is short and in a closed state so that it brings difficulty for the quality detection of the stud welding.

Through the real-time monitoring for the welding parameters in the process of transformation, to establish the curve of dynamic parameters and welding quality. It will more accurately judge for the welding quality

The Composition and the function of each part for the detection system

The detection system is mainly composed of hardware system and software system. The hardware system includes a current sensor, voltage detection system, data acquisition card, etc. The LHB - 800 Hoizer sensor is the current sensor which we used. The data acquisition card includes a control unit, ADC converter, transmission unit and storage unit. The data transfer and conversion is the main work for hardware system. The software system uses virtual instrument. It includes two parts, namely the hardware and the software. The main function of the hardware parts of the virtual instrument is to conversion, acquisition and transmission of signal. While function of the computer system is to analysis storage, display, processing of the data. The design of the software is the key part of the whole system. Methods is introduced by the LabVIEW software which is launched by the NI company. It uses the special G language programming.

The Design of the current sensor system. Fig.1 shows the principle of the Hall-effect. In the process of stud welding, in order to obtain enough nuclear heart to formation the nugget in a short period of time. Usually, uses the large electric current as high as 1500A and Low voltage as 5V. According to the Characteristics, uses the LHB Hoizer Current sensor and the JMD types of ac/dc to supply the power. Using the principle of Holzer effect[2].

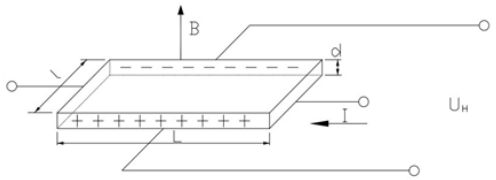

Fig.1 Hall-effect Diagram

Passing a current in the ends of the Hall-element. When the current passing, The induced magnetic field is produced. Use the B express the Magnetic field intensity. With the function of the Magnetic field, the Induction electromotive force will produce on the Holzer components. The output Electromotive force is showed as the following[3].

$$U_H = \frac{R_H IB}{d}$$

U_H—Induction electromotive force;R_H-hall constan（$m^3.C^{-1}$）;I-electric current（A);
B-magnetic field intensity（T）;d-Holzer element thickness（m).

The Design of the data acquisition card. The data acquisition is an essential part of the digital signal processing. It plays an important role for the whole system. The rapid development of the Computer technology. The connection of computer is used more standardization. While, the data acquisition card connected with the computer is more conform to the corresponding standard. Currently widely used bus standard is the PCI, SIA,USB and so on. It should be guarantee the stability of high-speed data acquisition and transmission in the process of stud welding dynamic data collection. So it choices the USB as the bus. Its characteristic is high acquisition speed, high transmission rate, feature-rich, Stable performance, low price,etc. Fig.3 shows the data acquisition card structure.

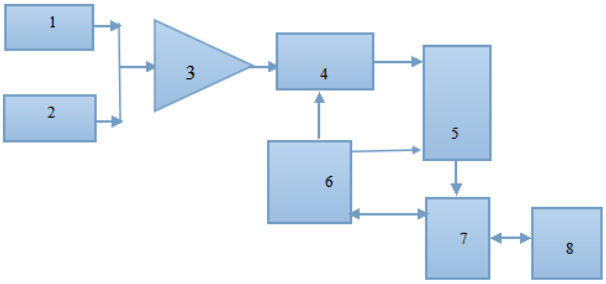

Fig.3 Date Acquisition Card Structure

1-sensor；2-voltage signal；3-amplifier；4-A/D conversion circuit；
5-memorizer；6-controller；7-USB interface；8-industrial computer.

The process of it works shown as the following. At first, the analog signal will be changed into a voltage range of ADC to accept through the probe and the amplifier. According to the fixed sampling and holding circuit sampling rate, the signal will be decomposed into independent level signal. And then, the A/D conversion circuit will changes the level signal into digital sampling point. The data is stored in the high speedcache. At last, through the USB interface, the data in the PC will be processing and analysis.

The design of the software. Fig.4 shows the data acquisition interface.

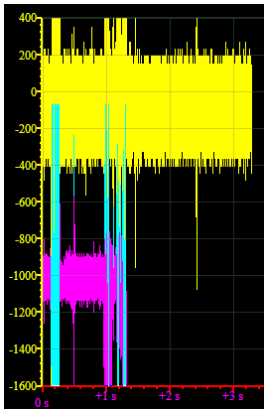

Fig.4 Date Acquisition Interface

Through the LabVIEW software the multi-channel parallel data acquisition system of information interaction can realize simple and quickly. It doesn't use the special data acquisition card by NI company, so the USB port should be modulated by the VISO bus I/O software[4]. The configuration of VISO bus step shows as the following.

Firstly, Drive Development Wizard to create INF file.

Secondly, Installation INF file, and Installation the USB equipment of the INF file.

Lastly, debugging the equipment by the NI-VISO, Monitoring of USB devices are installed correctly and abtain all kinds of attribute values of the USB.

The detection system is mainly monitoring the changing of current and voltage. In the program development, the detection system should call the AI config VI modular, AI start VI modular, AI read VI modular, AI clear VI modular in the function module to collect the data.The preparation steps are as the followsing[5].

Firstly,calling the AI config VI modular, configuration data acquisition card so that thethe cache configuration is twice of the sampling rate. Channel configuration set for both collection.

Secondly, calling the AI start VI modular to realize analog input operation. The main work is to realize the set of channel samples and data sampling rate.

Thirdly, calling the AI read V modular in the cycle of while. Using the cycle of while and the AI read VI modular reads the data from the cache cycle continuously. By setting the number of scanning to detect the number of readout. Set the trigger level(0.1V) by the Triggering setting in the modular. In order to accurately to the collected signals, after the signal to filter was calibrated and the waveform display and calculation of effectivevalue.

Lastly, calling the AI clear VImodular after the data acquisition. Stop collecting device for data and eliminate the simulation operation and buffer data configuration.

Conclusion

The detection system applied to the actual work. The Sampling rate and the depth of the storage can meet the needs of the monitoring. At the sanme time, it can be detected that there is a correspondence between the welding defects and parameters. It is suggests that the parameters could be monitor with the change of the current and voltage. Compared with the average parameters, it is easy to test out the stud which have the welding quality problems. It Improves the ability of remote monitoring of stud welding.

References

[1] Yuanliang Wang. Development and Application of Stud Welding. Electic Welding Machine. Vol. 36 No.1 (2006), p.15-18.

[2] Yuquan Chen. Wenxun Ge. The principle and application of modern sensors. Scientific Publications, Beijing (2007).

[3] Lifan Meng, Jinhui Lan. Electronic industry press Publications: The principle and application of sensor（2007）.

[4] Tao Li, Wangzhong Lei. Research of Data Acquisition System Based on LabVIEW. Industry and Mine Automation. Vol.11 No.11(2010), p122-123.

[5] Guimei Liu. Design and Development on Messuring System of Dynamic Parameters in Resistant Spot Welding, Inner Mongolia agricultural university (2006).

Advanced Materials Research Vol. 983 (2014) pp 408-411

doi:10.4028/www.scientific.net/AMR.983.408

INFLUENCE OF LATERAL SHIFT ON NORMAL MOVEOUT OF SH-WAVE

An-ling Wang [a], Fu-ping Liu[b]

Beijing Institute of Graphic Communication, Beijing 102600 China
[a]wanganling@bigc.edu.cn, [b]fupingliu60@sina.com

Keywords: SH-wave, Lateral shift, Normal move out

Abstract : Using the lateral ,shift and shift time of REFRACTION coefficient of SH seismic wave at the interface of strata, we derived and given formulae of normal move out of lateral shift, discussed the influence of lateral shift on normal move out of SH-wave, and drawn the curves of normal move out of lateral shift and the error of normal move out caused by lateral shift with respect to the angle of incidence. The results show that for glancing wave or angle of incidence being near the critical angle, A large error can be caused by lateral shift; The error correction of lateral shift should be done before seismic data processing.

Introduction

The totally linearly refraction polarized beam of light is displaced in the plane of incidence and parallel to a ray which would be refraction geometrically at the interface between the two optically transparent, homogenous and isotropic media[1] Thereafter lateral shift ever became a research hotspot of optics, and the conception of later shift was rapidly introduced in other branches of physics such as, for example, acoustics, plasma, quantum mechanics, and so on[1-3].We apply the lateral shift and shift time of SH-wave, to give the formulae of normal move out of lateral shift, to draw the curves of the normal move out curves of lateral shift and the error curves of normal move out caused by lateral shift. The results show that a large error can be caused by lateral shift. For glancing wave or angle of incidence being near to the critical angle, so lateral shift. Can bring about large influence on the travel time of SH-wave [2-4]. The error correction of lateral shift. Should be done before seismic data processing.

Influence of lateral shift on normal move out of SH-wave

It is needed to do normal-move out correction in seismic data processing, which demands to know the normal-move out of reflection wave. In following, based on the model of computing normal move out as shown in Figure1, we consider the influence of lateral shift on the normal move out, analyze and discuss the measure error caused by lateral shift in seismic exploration, where, the source point of wave is at O, the receiving point at S, the distance between O and S is *x*. The seismic wave is emitted at O, reflected at R, received at S by seismometer, its time-distance equation [12] $t_1 = \frac{1}{V_1}\sqrt{4h^2 + x^2}$. Taking into account the lateral shift effect, the seismic wave emitted at O, will travel along O—C—D—S then arrive at S. The time-distance equation is $t_2 = \frac{2h}{V_1 \cos\beta} + t_s$. Expression t_2 is the result which is taken into account the lateral shift effect, is much more accordant with the practice than expression t_1 , should be more accurate.

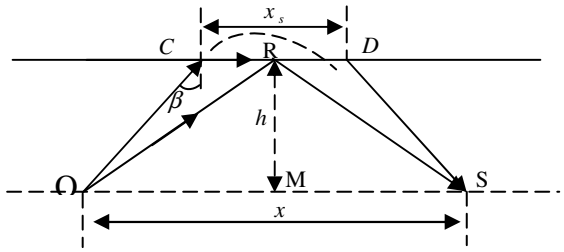

Fig1. Propagation path of SH seismic wave

The normal move out of reflected wave is (travel time of reflected wave caused due to the difference of geophone offset when the reflected interface of stratum is horizontal

$$\Delta t_s = \frac{1}{V_1}\sqrt{4h^2 + x^2} - t_0 \quad . \tag{1}$$

where $t_0 = (2h)/V_1$, is travel time of zero offset reflection. After taking account into the influence of lateral shift the normal move out of reflected wave can be modified as

$$\Delta t_{sg} = \frac{2h}{V_1 \cos\beta} + t_s - t_0 \, . \tag{2}$$

The difference of the two expressions above is

$$\Delta\tau_s = \Delta t_1 - \Delta t_2 = \frac{1}{V_1}\sqrt{4h^2 + x^2} - \frac{2h}{V_1 \cos\beta} - t_s \, . \tag{3}$$

Eq.(10) is the time difference which is caused by the lateral shift effect, is the normal move out of lateral shift, which can be used to do the error analysis and error correction of lateral shift in measurement of seismic wave. The following constraint condition should be taken into account when using that equation

$$x = 2h\tan\beta + x_s \, . \tag{4}$$

Only the reflected wave that satisfy the constraint condition (4) can be received by the seismometer(the energy center of the beam go through receiving point S), then the angle of incidence β is not arbitrary, can but take some special angles. Because the expression of x_s is very complex, constraint condition equation is non-linear equation about angle of incidence β, and has no analytic solution, can but be resolved by numerical method or graphic method.

With above relations we can obtain

$$x_s = \frac{\partial\delta_s}{\partial k_x} = \frac{n\rho_2 V_{s1}}{\omega\rho_1 \cos^2\beta_1} \frac{n^2 \sin\beta_1 \cos\beta_1 + \left(n^2 \sin^2\beta_1 - 1\right)\tan\beta_1}{\left[1 + \left(nm\rho_2/\rho_1\right)^2\right]\sqrt{\left(n\sin\beta_1\right)^2 - 1}} \, . \tag{5}$$

$$t_s = -\frac{\partial\delta_s}{\partial\omega} = \frac{\sin\beta_1}{1 + \left(nm\rho_2/\rho_1\right)^2} \frac{n\rho_2}{\omega\rho_1 \cos^2\beta_1} \left[\frac{n^2 \sin\beta_1 \cos\beta_1}{\sqrt{\left(n\sin\beta_1\right)^2 - 1}} + \tan\beta_1 \sqrt{n^2 \sin^2\beta_1 - 1}\right] . \tag{6}$$

Where $\delta_s = \tan^{-1}\dfrac{n(\rho_2/\rho_1)\sqrt{(n\sin\beta_1)^2-1}}{\cos\beta_1}$ [5], and $n = \dfrac{V_{s2}}{V_{s1}}$

$\boldsymbol{k} = k_x\boldsymbol{\xi} + k_z\boldsymbol{\eta}$ and $\boldsymbol{k}' = k_x'\boldsymbol{\xi} + k_z'\boldsymbol{\eta}$ $\boldsymbol{k}' = k_x'\boldsymbol{\xi} + k_z'\boldsymbol{\eta}$ are the wave vectors of incident and reflected SH-wave respectively, $\boldsymbol{\xi}$ and $\boldsymbol{\eta}$ are the unit vectors in x and z directions .

Where, β_1 are the incidence angles of SH-wave, V_{s1} and V_{s2} are the velocities of SH-wave in media 1and, ρ_1 and ρ_2 are the densities of media 1and 2. ω is the circular frequency of SH-wave With the relations $\mu_1 = V_{s1}^2\rho_1$ and $\mu_2 = V_{s2}^2\rho_2$, the Eq.(1) can also be written as .

Numerical simulation example

we choose the computational characters are as follows: For the reflection IBS-CS, $V_{s1} = 2500$ m/s, $V_{s2}/V_{s1} = 1.3$, $\rho_2/\rho_1 = 1.1$, the frequency of seismic wave $f = 50$ Hz, $h = 800$ m; where the frequency $f = [50,60,70,80]$,

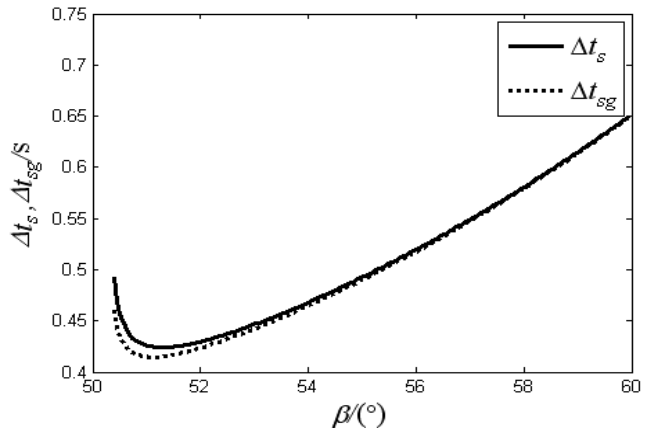

Fig.2 Normal move out and Goos-Hänchen normal move out of SH- wave

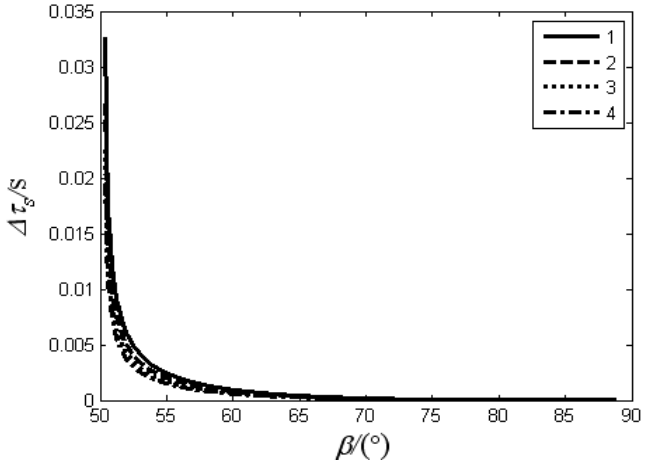

Fig.3 Normal move out of Goos-Hänchen effect of SH-wave

Figure 2 gives the curves of normal move out of lateral shift and SH-wave when the reflection interfaces is the IBS-CS, in the figure , curve Δt_{sg} are the normal move out curve of lateral shift of SH reflection wave, but curve Δt_s is not considering the influence of lateral shift. The two kinds of curves have large difference near the critical angle. In order to give an intuitionistic cognition for the two normal move outs,

Figure3. For the angle of incidence being near the critical angle, a large error can be caused lateral shift. It is indicated that the errors caused by lateral shift can not be ignored for the normal move out curve of reflection SH-wave.

Conclution

This studying result can be used to do the error analysis of lateral shift effect and the normal move out of lateral shift effect for SH-wave, which is an important direction of research. In acoustic log the basic theory is the slide wave theoretics, so the analysis and explanation of transverse wave logging would also have an important applied foreground. At present based on the problem of lateral shift of wave has not been taken into account in seismic exploration theory, seismic data processing and in acoustic log, and the soft has no the function to deal with the error correction of lateral shift effect. This paper has studied the lateral shift effect of SH-wave, but not related to the Goos-Hänchen effect of conversion wave, not been used to do the error correction and computation of lateral shift effect for conversion wave. This is a problem to await study for the future.

Acknowledgements

This work was Supported by BIGC Project（E-b-2014-18）.Supported by Beijing Natural Science Foundation(4142016）.Supported by BIGC Key Project(E-a-2013-19). Supported by the Funding Project for Academic Human Resources Development in Institutions of Higher Learning (PHR201107145). Supported by the Beijing City Board of Education Science and technology key project (KZ20110015017).National Natural Science Foundation (61272030).

References

[1] Lotsch H K V. Beam Displacement at Total Reflection: The Goos-Hänchen Effect (I, II, III, IV). Optik, Vol. 32, 1970: 116~137, 189~204, 299~319, 553~569

[2] Lai H M, Chan S W. Large and negative Goos-Hänchen shift near the Brewster dip on reflection from weakly absorbing media. Optics Letters, 2002,27: 680~682

[3] Lakhtakia A. On plane wave remittances and Goos-Hänchen shifts of planar slabs with negative real permittivity and permeability. Electromagnetics, 2003,23(1): 71~75

[4] Resch K J, Lundeen J S, Steinberg A M. Total reflection cannot occur with a negative delay time. IEEE journal of quantum electronics, 2001,37(6): 794~799

[5] Liu Fu-Ping, Wang An-Ling, Li Rui-Zhong, Chen Hui-Guo, Yang Chang-Chun.THE INFLUENCE ON NORMAL MOVEOUT OF TOTAL REFLECTED SH-WAVE AT AN INTERFACE OF STRATA BY GOOS-H Ä NCHEN EFFECT.CHINESE JOURNAL OF GEOPHYSICS,2009,52(8) 2128～2134.

Advanced Materials Research Vol. 983 (2014) pp 412-419

doi:10.4028/www.scientific.net/AMR.983.412

Mixed Interface stress Element-Finite Element Model with Its Application

SUN Yanhua [1, a], WU Fei [1,b], SUN Kai [1,c], LI Dongdong[1,d]

[1]National special glass quality supervision and inspection center, Beng'bu 233000, china

[a]syhua1632008@163.com, [b]wufei@ctiec.net, [c]bbzjssk@126.com, [d]dongstone@163.com

Key words: Finite element method; interface stress element model; transitional interface element; Mixed interface stress element-finite element model

Abstract: Based on the model of rigid-spring element suitable for homogeneous elastic problem, which was developed by Japanese professor Kawai, the interface stress element model (ISEM) for solving the problem of discontinuous media mechanics has been established. Compared with the traditional finite element method (FEM), the ISEM is more accurate and applicable. But on the other hand, the total number of freedom degree of ISEM in dealing with three-dimensional problems is higher than that of FEM, which often brings about the negative effects on efficiency of calculation. Therefore, it is necessary to establish a mixed model by gathering the advantages of ISEM and FEM together. By making use of the good compatibility of ISEM and introducing the concept of transitional interface element, this paper combines the counting methods of ISEM and FEM, and proposes a mixed model of ISEM-FEM, which can solve, to a large extent, the contradictions between accuracy and efficiency of calculation. The examples prove the applicability and adaptability of this model to engineering.

1 Introduction

Viewed from the theory and methods of engineering structures, numerical analysis has a wide range of applications. The determining of the merits of a numerical method is often based on its comprehensive aspects such as accuracy, efficiency and applicability. Finite element method has been able to develop rapidly and to be the most powerful tool in engineering structural analysis because of its good accuracy, efficiency and adaptability advantages in the most common macro-structural analysis of continuity. However, with the development of engineering construction and the improvement of science and technology, the finite element method has flaws in some engineering problems. It has failed to solve a continuous shift problem in the media section, the gap surface and the contact surface. This challenge is bound to inspire for generating a new numerical method for solving problems in discontinuous media. Early medium modulus of analyzing discontinuous issues mostly are fragmented rigid discrete model. In recent years, the block distortion has been considerate, but it is still not ideal and complete and it has not been able to reach the perfect mature stage of continuum deformation finite element model. Therefore, the possibility of establishing a finite element analysis of similar processes reflecting the unit deformation new models and methods and describing the displacement discontinuity interface has become many Computational Mechanics practitioners' hotspot[1].

2 Interface stress element method

Interface element is also known as rigid spring element, rigid element, and the interface stress element. It is a small deformation of numerical methods for solving the discontinuous problem, because it is decided by the presumption that the element accumulates by means of the interface layer. It is based on a rigid-spring element mode which proposed by professor Kaiwai coming from Tokyo University[2]. This method is based on the displacement of six overall centroid displacement components of each unit consisting of arrays of basic unknown quantity. Thus, it is unrelated to the unit's shape. Compared with other numerical methods, the interface element has the following advantages.

Firstly, because of applying fragmentation rigid displacement mode, the displacement between the interface block elements can be discontinuous. It can reflect the characteristics of slippage and crack.

Secondly, interfacial stress is dependent on the adjacent cell differentiation between the relative deformations. So the stress precision is not less than the displacement precision which improves the reliability criterion stress state so that the nonlinear solution will not appear drift.

Thirdly, the overall effect of discrete interface element model focuses on each interface, therefore, the main computing has nothing to do with unit block form. Then, it is convenient for realizing digital imitation and meshing for these complex distribution structure objects.

3 Fundamental equations of interface stress element method

The theory of interface element method is similar to the finite element method. The basic equations of interface element in the derivation can be calculated by the derivation of the finite element idea[3]. The similar formula is formed.

3.1 Displacement mode of interface stress element

Since the deformation of the interface element method accumulates in the interface layer, the unit displacement just considers rigid displacement, including three translational components (u, v, w) and three rotational components (θ_x, θ_y, θ_z). The rigid displacement which mode similar in shape functions of finite element method can be established[4].

$$\underset{\sim}{u} = N \underset{\sim g}{u} \quad \underset{\sim}{u} = N \underset{\sim g}{u} \tag{1}$$

In the formula, $\underline{u}=[u,v,w]$ is the displacement vector at any unit point. $\underline{u}_g=[u_g,v_g,w_g,\theta_x,\theta_y,\theta_z]$ is the displacement of unit centroid. N is the shape function of unit centroid. The details are as follows.

$$N=\begin{bmatrix} 1 & 0 & 0 & 0 & z-z_g & y_g-y \\ 0 & 1 & 0 & z_g-z & 0 & x-x_g \\ 0 & 0 & 1 & y-y_g & x_g-x & 0 \end{bmatrix} \tag{2}$$

In the local coordinate of Figure 1, the displacement vector at any interface point A can be expressed by $\underline{\delta_l}$. $\underline{\delta_l}=[\delta_n,\delta_{s1},\delta_{s2}]$. The normal displacement component and two tangential displacement components can be expressed by δ_n, δ_{s1} and δ_{s2}. The relative displacement of A after two elements' movement can be expressed by $(\underline{\delta}_l^{(1)}+\underline{\delta}_l^{(2)})$.

$$\begin{aligned} (\underset{\sim}{\delta}_l^{(1)} + \underset{\sim}{\delta}_l^{(2)}) &= (L^{(1)}\underset{\sim}{u}^{(1)} + L^{(2)}\underset{\sim}{u}^{(2)}) \\ &= (L^{(1)}N^{(1)}\underset{\sim}{u}_g^{(1)} + L^{(2)}N^{(2)}\underset{\sim}{u}_g^{(2)}) \\ &= L^{(1)}(N^{(1)}\underset{\sim}{u}_g^{(1)} - N^{(2)}\underset{\sim}{u}_g^{(2)}) \end{aligned} \tag{3}$$

The local coordinate direction between two adjacent cells in the interface is opposite (Figure 1). Therefore, $L^{(2)}$=-$L^{(1)}$. In the formula, i=1,2 represents unit between the interface, $L^{(i)}$ represents transformation matrix between local coordinator and whole coordinator. The details are as follows.

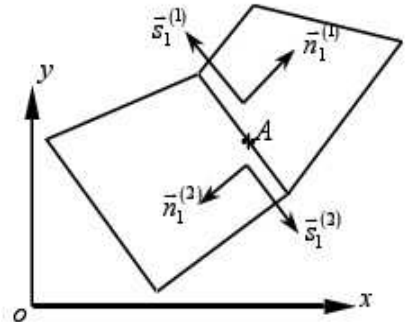

Figure.1 Neighboring unit overall coordinate and local coordinates relations

$$L=\begin{bmatrix} \cos(\tilde{n},\tilde{x}) & \cos(\tilde{n},\tilde{y}) & \cos(\tilde{n},\tilde{z}) \\ \cos(\tilde{s}_1,\tilde{x}) & \cos(\tilde{s}_1,\tilde{y}) & \cos(\tilde{s}_1,\tilde{z}) \\ \cos(\tilde{s}_2,\tilde{x}) & \cos(\tilde{s}_2,\tilde{y}) & \cos(\tilde{s}_2,\tilde{z}) \end{bmatrix} \tag{4}$$

3.2 The processing of interface constitutive relation

Since the unit is rigid, the deformation can only be expressed through the relative displacement between the units. Then, the deformation can be completely stored in the unit at the interface. Therefore, we must establish a relationship between the stress and the unit relative deformation at any point on the interface. Three-dimensional interface stress formula usually has the following form.

$$\underset{\sim}{\sigma} = D(\underset{\sim}{\delta}_l^{(1)} + \underset{\sim}{\delta}_l^{(2)}) \tag{5}$$

In the formula, $\underline{\sigma}$=[σ_n,τ_{s1},τ_{s2}]. D is elasticity matrix of interface stress element. D contains the hypothesis of interfacial strain. Therefore, we obtain different calculation methods. For isotropic material interface, the literature [6] has the following form.

$$D=\frac{1}{C}\frac{E(1-\mu)}{(1+\mu)(1-2\mu)}\begin{bmatrix} 1 & 0 & 0 \\ 0 & \frac{1-2\mu}{2(1-\mu)} & 0 \\ 0 & 0 & \frac{1-2\mu}{2(1-\mu)} \end{bmatrix} \tag{6}$$

In the formula, E is elasticity matrix of interface stress element. μ is Poisson's ratio of interface stress element. C is the characteristic length of the cumulative deformation on both sides of the interface unit. The formula usually has the following form.

$$C = h_1 + h_2 \tag{7}$$

In the formula, h_1 and h_2 express the vertical distance between unit centroid and interface.

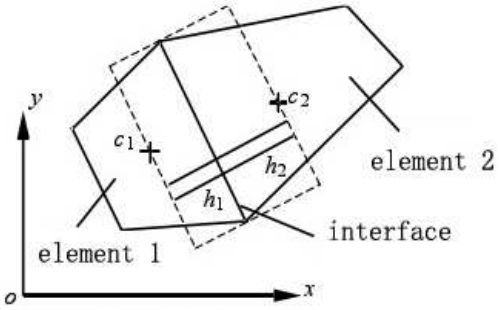

Figure.2 Contact surface both sides distortion accumulation schematic drawing

The literature [1] has the following form.

$$D=\begin{bmatrix} d_n & 0 & 0 \\ 0 & d_s & 0 \\ 0 & 0 & d_s \end{bmatrix} \tag{8}$$

In the formula

$$d_n=\left(\frac{h_1}{a_1}+\frac{h_2}{a_2}\right)^{-1}, d_s=\left(\frac{h_1}{b_1}+\frac{h_2}{b_2}\right)^{-1}$$
$$a_i=\frac{E_i(1-\mu_i)}{1-\mu_i-2\mu_i^2}, b_i=\frac{E_i}{2(1+\mu_i)}, (i=1,2) \tag{9}$$

In the formula, E is elasticity matrix of interface stress element. μ is Poisson's ratio of interface stress element.

As can be seen, the formula (6) is different from the formula (8). The formula (6) expresses material properties of the interface. The formula (8) expresses materials of the element. If the material is uniform, the elasticity matrixes of (6) and is same as the elasticity matrixes of (8). All parameters in the D not only reflects the isotropic nature of the interface but also reflects the stiffness nature of the interface.

By the formula (5) and (3), we can see that the interface element method in the interface stress is linearly dependent on the relative displacement of the interface.

In addition, the displacement pattern of the block (in the formula (1)) is a incomplete polynomial. The distribution of interface relative displacement in the interface is linear, so the distribution interface stress in the interface is also linearly.

3.3 The discussion of governing equations

The interface displacement and interfacial stress insert (1) and (5) to the interface element discrete model principle of virtual work expression[5].

$$-\sum_e \iint_{S_o^e} \sigma \delta u_i ds = \sum_e \left[\iiint_{\Omega^e} f_i \delta u_i d\Omega + \iint_{S_\sigma^e} p \delta u_i ds \right]$$

The governing equations can be deduced with a similar interface element in the form of FEM

$$K\underset{\sim}{U}=\underset{\sim}{R} \tag{10}$$

In the formula, U=[u_{g1},u_{g2},…,u_{gn}]. U is displacement vector of the whole centroid. R is load matrix. K is the whole stiffness matrix.

$$K=\sum_n C_e^{*T} k_n C_e^* \tag{11}$$

In the formula, $C_e^* = \begin{bmatrix} \cdots & 0 & C_e^{(i)} & 0 & 0 & \cdots \\ \cdots & 0 & 0 & -C_e^{(j)} & 0 & \cdots \end{bmatrix}$

C_e satisfy $\underline{u_g}=C_e\underline{U}$. It can be called selection matrix. (i) and (j) express two elements of the interface n. K_n is the stiffness matrix of the interface n. The details are as follows.

$$\begin{aligned} K_n &= \int_{S_n} N^{*T} L^{(i)T} D L^{(i)} N^* ds \\ &= \int_{S_n} \begin{bmatrix} N^{(i)T} L^{(i)T} D L^{(i)} N^{(i)} & N^{(i)T} L^{(i)T} D L^{(i)} N^{(j)} \\ N^{(j)T} L^{(i)T} D L^{(i)} N^{(i)} & N^{(j)T} L^{(i)T} D L^{(i)} N^{(i)} \end{bmatrix} ds \\ &= \begin{bmatrix} (K_n)_{6\times6}^{(i)(i)} & (K_n)_{6\times6}^{(i)(j)} \\ (K_n)_{6\times6}^{(j)(i)} & (K_n)_{6\times6}^{(j)(j)} \end{bmatrix} \end{aligned} \tag{12}$$

In the formula, S is the area of the n-th interface. $N^*=[N(i),N(j)]$.

As we know, K_n is the 12×12 matrix. K_n reflects both sides of the interface i, j unit generalized displacement cause a degree of freedom of the generalized force 12 degrees of freedom. Therefore, the formula (10) reflects the equilibrium condition of the element centroid point.

In summary, the interface element governing equations and finite element governing equations of the form are very similar. The essence is the equilibrium conditions on discrete points. Finite element dominated equation reflects the balance of unit node. Interface element dominated equation represents the balance of block element centroid[6]. Two methods of problem-solving ideas, formulas and calculation steps are very similar. Both methods perform element analysis firstly, and then determine the overall to set the basic unknown quantities. Ultimately, all of the displacements and stresses can be solved. In the element analysis, the displacement pattern of fragmentation element is constructed firstly. Secondly, the element strain vector can be obtained after the derivation. Then the stress vector can be derived from the constitutive relationship. In the interface element analysis, rigid body displacement pattern is constructed firstly. The unit deformation accumulated in the interface, according to the strain calculated relative displacement vector interface, then constitutive relation derived by the stress vector interface. In the overall analysis, FEM is based on the principle of minimum potential energy. Governing equations are established on the unknown nodal displacements as the basic unknown quantities. It reflects the equilibrium condition of element node. However, interface element is based on the principle of virtual work units exported to block centroid point generalized displacement as the basic unknown interface element governing equations discrete model, reflecting the equilibrium condition unit centroid point. Two basic methods and algorithms matrix set is similar. Shape function matrix , load vector, displacement vector, strain vector , stress vector and matrix stiffness matrix and other basic settings are the same. Just Specific formulas differ. For example, finite element stiffness matrix is obtained by integrating unit. Interface element in the interface stiffness matrix is obtained by integrating.

4 Transition interface element

Using the good compatibility of interface element, we can introduce the concept of transition interface elements to achieve a combination of interface element and FEM numerical methods. Figure 3 shows the connection diagram between ISE network interface element and finite element (FE) network. S_j^0 is the interface in two types of network. The relative displacement of the interface in the local coordinate direction is the displacement accumulation of the left block S_j^0 interface and the right amount of deformation caused by the finite element in the S_j^0 interface[7]. For example, M is a point on the interface S_j^0. The relative displacement is $\underline{\delta_1}=[\delta_n,\delta_{s1},\delta_{s2}]^T$. Then

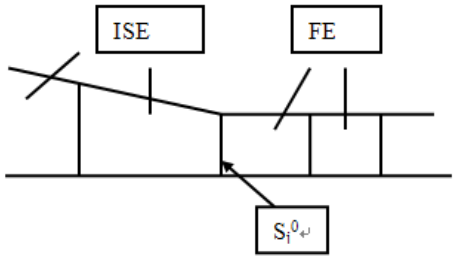

Figure.3 Transition interface element

$$\begin{aligned}\underset{\sim}{\delta}_l &= \underset{\sim}{\delta}_l^{(1)} + \underset{\sim}{\delta}_l^{(2)} \\ &= -\underset{\sim}{L}^{(1)}\underset{\sim}{N}_{ISE}\underset{\sim}{u}_{ISE} - \underset{\sim}{L}^{(2)}\underset{\sim}{N}_{FE}\underset{\sim}{u}_{FE} \\ &= \underset{\sim}{L}^{(1)}(\underset{\sim}{N}_{ISE}\underset{\sim}{u}_{ISE} - \underset{\sim}{N}_{FE}\underset{\sim}{u}_{FE})\end{aligned}$$

In the formula, $\underline{L}^{(2)}$=-$\underline{L}^{(1)}$ is the S_j^0 interface's direction cosine matrix of the local coordinate in the global coordinate. $\underline{N}_{ISE}$ is the block element shape functions of interface element model. $\underline{u}_{ISE}$ is the block element Centroid displacement of interface element model. $\underline{N}_{FE}$ is the block element shape functions of finite element model. $\underline{u}_{FE}$ is the block element node displacement of finite element model[8]. Then

$$\underset{\sim}{N}^{**} = [\underset{\sim}{N}_{FE}, -\underset{\sim}{N}_{ISE}], \quad \underset{\sim}{U}^{**} = [\underset{\sim}{u}_{FE}, \underset{\sim}{u}_{ISE}]^T$$

Therefore

$$\underset{\sim}{\delta}_l = \underset{\sim}{L}^{(1)}N^{**}U^{**} \tag{13}$$

The interface stress of S_j^0

$$\underset{\sim}{T}_l = \underset{\sim}{D}\underset{\sim}{\delta}_l = \underset{\sim}{D}\underset{\sim}{L}^{(1)}\underset{\sim}{N}^{**}U^{**} \tag{14}$$

Then, the saving potential energy on interface S_j^0 of the resistance force and the relative displacement acting on the interface can be expressed as follows.

$$W_0 = \iint_{S_j^0} \frac{1}{2}\underset{\sim}{\delta}_l^T \underset{\sim}{D}\underset{\sim}{\delta}_l ds \tag{15}$$

Stiffness matrix k_j^0 can be expressed as follows.

$$\underset{\sim}{k}_j^0 = \iint_{S_j^0} (\underset{\sim}{N}^{**})^T (\underset{\sim}{L}^{(1)})^T \underset{\sim}{D}\underset{\sim}{L}^{(1)}\underset{\sim}{N}^{**} ds \tag{16}$$

The whole stiffness matrix K of Hybrid model can be expressed as follows.

$$\underset{\sim}{K} = \sum_j (\underset{\sim}{C}_e^*)^T \underset{\sim}{k}_j \underset{\sim}{C}_e^* + \sum_{j^0} (\underset{\sim}{C}_e^{**})^T \underset{\sim}{k}_{j^0} \underset{\sim}{C}_e^{**} + \sum_{ne} \underset{\sim}{C}_e^T \underset{\sim}{k} \underset{\sim}{C}_e^* \tag{17}$$

In the formula, C_e^* is the Selection Matrix of interface element. C_e^{**} is the Selection Matrix of transition interface element. C_e is the Selection Matrix of finite element. It expands positioning transformation matrix from cell array to a whole array.

$$\underset{\sim}{R} = \sum_{ISE} \underset{\sim}{C}_e^T \underset{\sim}{R}_{ISE}^e + \sum_{ne} \underset{\sim}{C}_e^T \underset{\sim}{R}_{FE}^e \tag{18}$$

In the formula, $\underline{R}^e_{ISE}$ is the equivalent load of the block element centroid in the interface element model. $\underline{R}^e_{FE}$ is the equivalent load of element nodes in the finite element model. In the formula $KU=R$, we can obtain U. The selection matrixes Convert Centroid displacement of interface element and node displacement of finite element. Finally, the stress of interface element, transition interface element and finite element calculated can be concluded by using the formula.

5 Test and count model

The Figure 5 is a simply supported beam. Its long is 12.0m. Its high is 2.0m. Elasticity matrix E=2.0×10^{4}Mpa. Poisson's ratio μ=0.20. On left beam the force Q=2kN/m, the concentrated force on the center P=8kN. We can use separately 8-node hexahedral finite element (coordination element), the interface element and finite element - interface element hybrid model to discrete. C -section is the transition interface element. Finite element is as the right and interface element is as left. We can draw up the whole analysis procedures of the cantilever beam (Figure.4). In Table 1 and figure 5, We can obtain the horizontal normal stress of node A, B and count the vertical displacement of C. Then, the counting results compared with the theoretical solution is as follows.

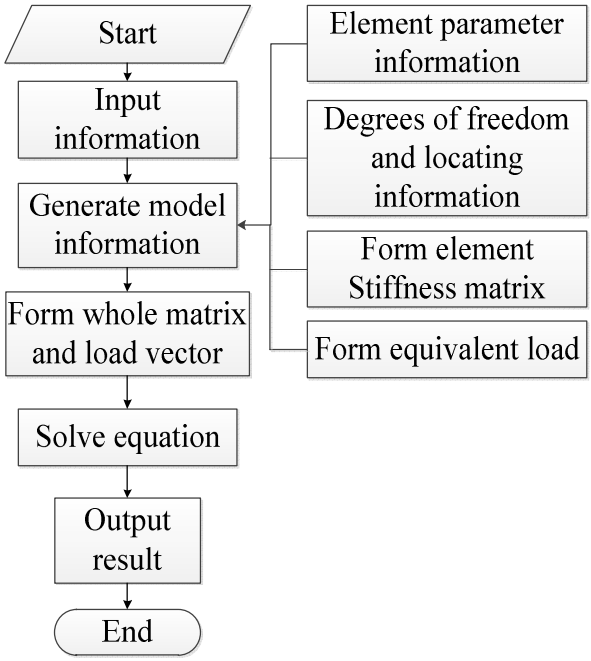

Figure.4 The schematic diagram of program

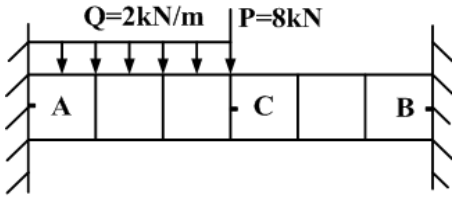

Figure.5 Simply supported beam and its mesh

Table.1 The calculation results of simply supported beam

	Node A' stress (0.001 Mpa)	Node B' stress (0.001 Mpa)	Node C' displacement (0.001 Mpa)
FEM' result	28.72	14.33	3.55
ISEM' result	29.48	15.02	3.82
FEM and ISEM' result	29.31	15.56	3.75
Theoretical value	30.00	15.00	4.00

As can be seen from the results, the accuracy of interface element is higher than that of the finite element. The accuracy of the transition element interface element's stress is slightly lower than that of finite element.

6 Conclusions

Using good compatibility of interface element, this paper introduces the concept of transition interface elements to achieve a combination of the interface element method and FEM numerical method. By proposing a interface element - FEM hybrid model, we can solute the conflict between computational accuracy and efficiency. Numerical examples show that the efficiency of the establishment of hybrid model. It reveals that the hybrid model has broad prospects for engineering applications.

References

[1] ZHUO Jia-shou, ZHANG Qng. *Interface Stress Element Method of Discontinuous Mechanical*. Beijing: Science Press, 2000.

[2] ZHANG Qing, ZHOU Zi-bin, ZHOU Jia-shou. Mixed Mod- el for Partitioned Interface Stress Element Method-Finite Element Method-Infinite Element Method. Chinese Journal of Computational Mechanics, 2005, 22(1):8-12.

[3] GAO Pei-zheng. Dynamic Elasto plastic Rigd-Body Surface Element Method.Engineering Mechnics, 1996, 13(4):135-144.

[4] PHOONK, CHANS, TOHK, etal. Fast Iterative Solution of Large Undrained Soil-Structure Interaction Problems.Int J Numer Anal Meth Geomech, 2003, 27(3):159-181.

[5] KawaiT.A new discrete model for analysis of solid mechanics problem. Seisan Kenkyn, 1977, 29(4):204-207.

[6] Zhang Jianhai, Fan Jingwei, Hu Ding. Theory and Application of rigid body spring. Chengdu: Chengdu University of Science Press. 1997.11.

[7] A M Sharan. Dynamic Behavior of Lathe Spindles with Elastic Supporters including Damping by Finite Element Analysis. Shock and Vibration Bulletin. 2001,(51): 83-97.

[8] Moaveni S .*Finite Element Analysis-Theory and Application by ANSYS*. Beijing: Publishing House of Electronics Industy, 2003: 4-34.

Advanced Materials Research Vol. 983 (2014) pp 420-423

doi:10.4028/www.scientific.net/AMR.983.420

Modeling of Mass-Spring-Damper System by Complex Stiffness Method

Shengguo Zhang[1, a *], Xiaoping Dang[2, b]

[1]School of Electrical Engineering, Northwest University for Nationalities, Lanzhou, 730030, China

[2]School of Continuing Education, Northwest University for Nationalities, Lanzhou, 730030, China

[a]zhangshengguo@tsinghua.org.cn, [b]gs_dxp@126.com

Keywords: Complex stiffness, Laplace transformation, Mass-spring-damper system.

Abstract: This paper aims at directly modeling the transfer functions of mass-spring-damper systems. Using complex stiffness of mass, spring, and damper elements and equivalent complex stiffness of these elements in series and/or in parallel, the transfer functions of the mass-spring-damper systems are modeled quickly. This is very convenient to the modeling of the complicated mechanical systems.

Introduction

The complicated mechanical system is used to be looked upon as a mass-spring-damper system to model system's dynamics [1]. This equivalent mass-spring-damper system usually includes a few mass elements, a few spring elements, and a few damper elements. And some of these elements are connected in series and some of these elements connected in parallel. In addition, this dynamics has to be transformed into transfer function model by Laplace transformation so as to analyze the system in frequency domain and to design the motion controller [2]. Thus, the modeling and analyzing of the system is quite complicated and tedious.

In this paper, complex stiffness concepts of mass, spring, and damper elements are defined first and the equivalent complex stiffness of these elements connected in series and in parallel are educed and derived. Then, the complex stiffness and the equivalent complex stiffness are applied to model the transfer functions of complicated mechanical systems, directly.

Complex Stiffness and Equivalent Complex Stiffness

Definition of Complex Stiffness. There are three kinds of elements in a mass-spring-damper system: mass, spring, and damper elements. They are named complex stiffness elements in this paper. Referred to the theory of elastic mechanics, the stiffness of elastic body is defined as the ability of which an elastic body can resist the deformation. It is usually characterized by elasticity modulus and the elasticity modulus equals to the ratio of the stress which is given to the elastic body and the strain which the elastic body deduces [3]. In the light of above mentioned, the complex stiffness of a complex stiffness element in a mass-spring-damper system, $K(s)$ can be defined uniformly as the ratio of the Laplace transformation force $F(s)$ and the Laplace transformation deformation or displacement $X(s)$ of the mass/spring/damper elements:

$$K(s)=\frac{\measuredangle[f(t)]}{\measuredangle[x(t)]}=\frac{F(s)}{X(s)}, \tag{1}$$

this is under the zero initial conditions of the force and the deformation/displacement of the elastic/viscous/rigid body which is given force:

$$f(0)=\dot{f}(0)=\ddot{f}(0)=\dddot{f}(0)=\cdots=0,\ x(0)=\dot{x}(0)=\ddot{x}(0)=\dddot{x}(0)=\cdots=0, \tag{2}$$

where $\measuredangle$ means Laplace transformation, and $f(t)$ and $x(t)$ indicate the stress and the strain of the elastic body in time domain. Complex variable factor $s=j\omega$, j is imaginary unit and ω is angular frequency variable.

Complex Stiffness of Spring Element. In accordance with the Hooker's law, there gets:

$$f(t) = k\,x(t), \tag{3}$$

where $f(t)$ and $x(t)$ are the given force and the deformation of the spring in time domain, respectively. And k is the elasticity coefficient of the spring.

According to Eq. 1, under the zero initial conditions, using Laplace transformation to Eq. 3, the complex stiffness of a spring element can be got as:

$$K(s) = \frac{\mathcal{L}[f(t)]}{\mathcal{L}[x(t)]} = \frac{F(s)}{X(s)} = k. \tag{4}$$

So the complex stiffness of a spring element is a constant and it is equivalent to its elasticity coefficient.

Complex Stiffness of Damper Element. In accordance with the theory of viscosity-elasticity, the damping force of a damper is proportional to its moving speed:

$$f(t) = \mu \frac{dx(t)}{dt}, \tag{5}$$

where μ is the viscosity coefficient of the damper. Then using Laplace transformation to Eq. 5 under the zero initial conditions, there gets the complex stiffness of a damper element to be:

$$K(s) = \frac{\mathcal{L}[f(t)]}{\mathcal{L}[x(t)]} = \frac{F(s)}{X(s)} = \mu s. \tag{6}$$

So the complex stiffness of a damper element equals to the product of its viscosity coefficient and the complex variable factor s.

Complex Stiffness of Mass Element. In accordance with Newton's second law, the inertia force of a moving body is proportional to its moving acceleration:

$$f(t) = m \frac{d^2x(t)}{dt^2}, \tag{7}$$

where m is the mass of the moving body. Then using Laplace transformation to Eq. 7 under the zero initial conditions, the equivalent complex stiffness of a moving body can be got as:

$$K(s) = \frac{\mathcal{L}[f(t)]}{\mathcal{L}[x(t)]} = \frac{F(s)}{X(s)} = ms^2. \tag{8}$$

So the equivalent complex stiffness of a mass element equals to the product of its mass and the square of complex variable factor s.

Equivalent Complex Stiffness of Elements Connected in Series. As Fig. 1 (a) shown, two complex stiffness elements are connected in series and their complex stiffnesses are denoted with $K_1(s)$ and $K_2(s)$ respectively.

According to the definition of complex stiffness and using Rayleigh method [4], Eq. 9 is workable:

$$X_1(s) = \frac{F_1(s)}{K_1(s)} = \frac{F_i(s)}{K_1(s)}, \quad X_2(s) = \frac{F_2(s)}{K_2(s)} = \frac{F_i(s)}{K_2(s)}, \tag{9}$$

so there gets:

$$X_o(s) = X_1(s) + X_2(s) = F_i(s)\left[\frac{1}{K_1(s)} + \frac{1}{K_2(s)}\right], \tag{10}$$

then the equivalent complex stiffness $K_{se}(s)$ of two complex stiffness elements in series, according to Eq. 1, can be derived as:

$$K_{se}(s)=\frac{\mathcal{L}[f_i(t)]}{\mathcal{L}[x_o(t)]}=\frac{F_i(s)}{X_o(s)}=\frac{K_1(s)K_2(s)}{K_1(s)+K_2(s)}. \tag{11}$$

In other words, Eq. 12 is workable:

$$\frac{1}{K_{se}(s)}=\frac{1}{K_1(s)}+\frac{1}{K_2(s)}. \tag{12}$$

Analogously, if complex stiffness elements of n number, whose complex stiffness are denoted with $K_1(s)$, $K_2(s)$, … , and $K_n(s)$ respectively, are connected in series, their equivalent complex stiffness $K_{se}(s)$ satisfies:

$$\frac{1}{K_{se}(s)}=\frac{1}{K_1(s)}+\frac{1}{K_2(s)}+\cdots+\frac{1}{K_n(s)}. \tag{13}$$

Equivalent Complex Stiffness of Elements Connected in Parallel. As Fig. 1 (b) shown, two complex stiffness elements are connected in parallel and their complex stiffnesses are denoted with $K_1(s)$ and $K_2(s)$ respectively. According to the definition of complex stiffness, there gets:

$$F_i(s)=F_1(s)+F_2(s)=K_1(s)X_o(s)+K_2(s)X_o(s)=[K_1(s)+K_2(s)]X_o(s), \tag{14}$$

so the equivalent complex stiffness $K_{pe}(s)$ of two complex stiffness elements in parallel, according to Eq. 1, can be got as:,

$$K_{pe}(s)=\frac{\mathcal{L}[f_i(t)]}{\mathcal{L}[x_o(t)]}=\frac{F_i(s)}{X_o(s)}=K_1(s)+K_2(s). \tag{15}$$

Likewise, if complex stiffness elements of n number, whose complex stiffness are denoted with $K_1(s)$, $K_2(s)$,…, and $K_n(s)$ respectively, are connected in parallel, their equivalent complex stiffness $K_{pe}(s)$ satisfies:

$$K_{pe}(s)=K_1(s)+K_2(s)+\cdots+K_n(s). \tag{16}$$

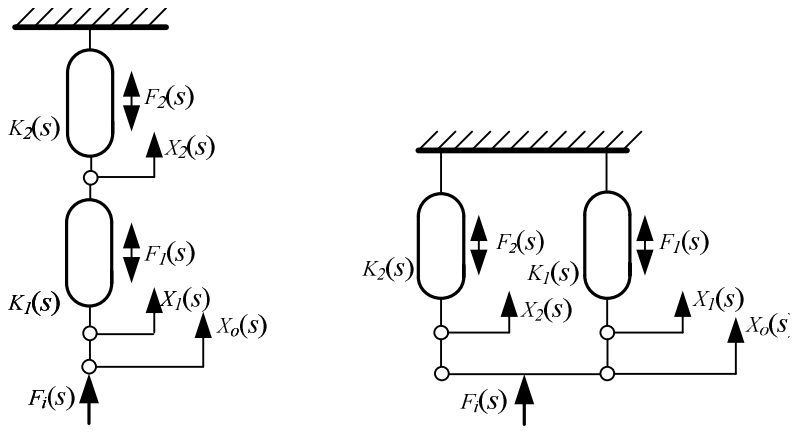

Fig. 1 (a) complex stiffness elements in series and (b) complex stiffness elements in parallel

Applying the Complex Stiffness to Model the Mass-Spring-Damper System

Applying Example 1. As shown in Fig. 2 (a), there is a spring-damper system whose input and output are x_i and x_o respectively. According to Newton's third law and complex stiffness concept there gets:

$$[X_i(s)-X_o(s)]K_{1e}(s)=X_o(s)K_{2e}(s), \tag{17}$$

where

$$K_{1e}(s)=\frac{k_1 f_1 s}{k_1+f_1 s},\ K_{2e}(s)=k_2+f_2 s, \tag{18}$$

so system transfer function $G_1(s)$ can be modeled directly as follows:

$$G_1(s)=\frac{X_o(s)}{X_i(s)}=\frac{K_{1e}(s)}{K_{1e}(s)+K_{2e}(s)}=\frac{k_1 f_1 s}{f_1 f_2 s^2+(k_1 f_1+k_1 f_2+k_2 f_1)s+k_1 k_2}. \tag{19}$$

Applying Example 2. As shown in Fig. 2 (b), there is a mass-spring-damper system whose input and output are F_i and x_o respectively. According to Newton's third law and complex stiffness concept there gets:

$$[X_i(s)-X_o(s)]K_{1e}(s)=X_o(s)K_{2e}(s),\ F_i(s)=X_i(s)K_{1e}(s), \tag{20}$$

where

$$K_{1e}(s)=\frac{k_1 m s^2}{k_1+ms^2},\ K_{2e}(s)=k_2+fs, \tag{21}$$

so system transfer function $G_2(s)$ can be modeled directly as follows:

$$G_2(s)=\frac{X_o(s)}{F_i(s)}=\frac{1}{K_{1e}(s)+K_{2e}(s)}=\frac{k_1+ms^2}{mfs^3+m(k_1+k_2)s^2+k_1 fs+k_1 k_2}. \tag{22}$$

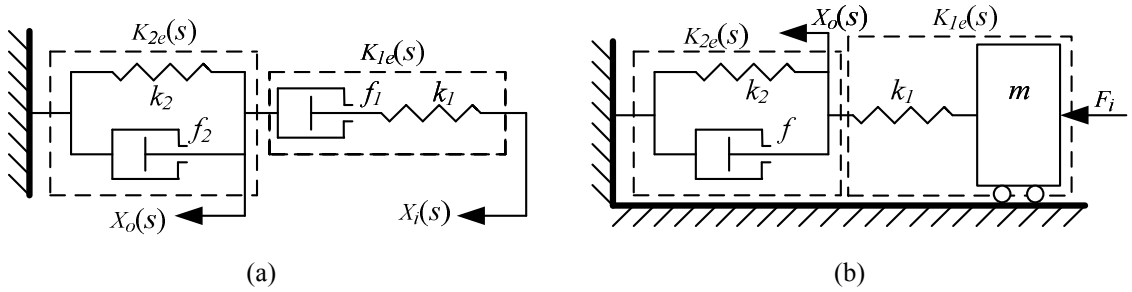

Fig. 2 (a) spring-damper complex stiffness system and (b) mass-spring-damper complex stiffness system

Conclusions

This paper focused on modeling of the mass-spring-damper system quickly.

By using complex stiffness method instead of using Laplace transformation of differential equation, the transfer functions of the mass-spring-damper systems are modeled directly. This facilitates the modeling of the complicated mechanical system very much.

Acknowledgements

This work was financially supported by the Fundamental Research Funds for the Central Universities (31920140082) and the Introduction Talent Research Project of Northwest University for Nationalities (XBMUYJRC201301).

References

[1] J.X. Dong, C.D. Zhao, Control Engineering Fundamentals, first ed., Tsinghua University Press, Beijing 1992.

[2] S.S. Hu, Automatic Control Principle, fifth ed., Science Press, Beijing 2007.

[3] T. Fang, P. Xue, Theory of Vibration with Applications, first ed., Northwestern Polytechnical University Press, Xi'an 1998.

[4] W.T. Thomson, M.D. Dahleh, Theory of Vibration with Applications, fifth ed., Tsinghua University Press, Beijing 2005.

Advanced Materials Research Vol. 983 (2014) pp 424-427

doi:10.4028/www.scientific.net/AMR.983.424

Study on Control Quality of Valve Outlet Blockage Fault

Yantao An [a*], Rujian Ma[b] and Dong Zhao[c]

School of Mechanical Engineering,University of Jinan, Jinan 250022, China

[a] me_anyt@ujn.edu.cn, [b] rjma@ujn.edu.cn, [c] me_zhaod@ujn.edu.cn

Keywords: Control valve, Flow characteristic, Blockage, Differential pressure

Abstract. The flow characteristic and differential pressure-flow of outlet blockage fault and trouble-free for control valve are simulated by CFD. The study shows that the vortex at the bottom of control valve outlet is main reason for the outlet blockage fault, relative gain of flow characteristic curve for outlet blockage is increased, the flow percentage of outlet blockage compared with trouble-free is maximum value at relative opening is 60% and 100%, the pressure - flow percentage reaches maximum value at differential pressure is 800 kPa.

Introduction

The welding slag after the inspection or maintenance regularly, the impurities of flow are easy to form a blockage [1-2], it can cause pressure pulsation and lower control quality of the valve, it especially on the flow characteristic of valve [3-5]. Therefore, the study the blockage fault of control valve becomes very important. In this paper, based on the study the causation of outlet blockage fault, applying CFD to simulate the internal flow field, and comparative analysis of flow characteristics and flow for outlet blockage fault and trouble-free, the results can provide theoretical foundation for further study on blockage fault of control valve.

Influence of Blockage Fault

Causation of Outlet Blockage

Fig.1 is the velocity contours of internal flow field for trouble-free, it shows that because of the circulation area of valve inlet is decreased, and it reduces pressure of fluid and increase speed of fluid. Fluid reaches the bottom of the valve core, and the circulation area increases suddenly, fluid is blocked by the wall at the bottom of valve core, and it stagnates at the bottom of the valve body, which makes the pressure rise sharply, the kinetic energy is converted to potential energy. When the fluid through the valve core, because the area is rapidly decreases, the pressure decline dramatically and speed increases, the potential energy is converted to kinetic energy. Because of the high speed of fluid flow, the maximum of velocity does not happen in the valve core, it in the outlet of valve core. Fluid through the orifice at high-speed, the high-speed fluid is mainly at the upper pipe, and the flow rate of upper pipe is higher, velocity is lower at bottom of pipe, velocity is non-uniform, it easy to form vortex in the bottom, as shown in Fig. 1 and Fig. 2. The vortex makes the solid particles of fluid subside and form a blockage.

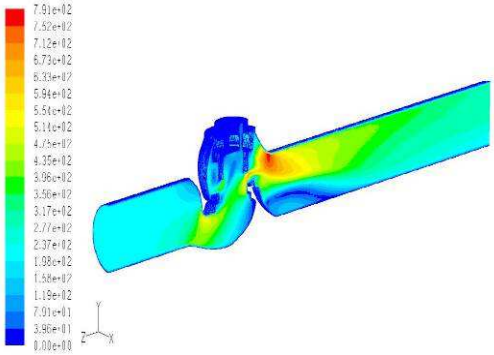

Fig. 1 Velocity contours

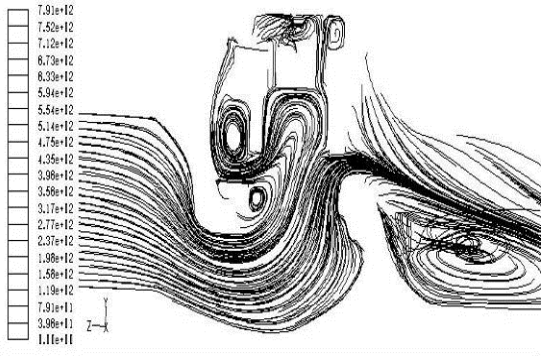

Fig. 2 Streamline

Flow Characteristic of Valve

Flow control of control valve can be done by changing the circulation area between the valve core and valve seat. But many factors can affect it. Such as when the throttling area changes, the differential pressure of valve before and valve after can change at the same time, and it causes the change of the flow. If differential pressure is constant, flow characteristic is ideal flow characteristic, otherwise the flow characteristic is actual flow characteristics. Fig.3 is the ideal flow characteristic curve, 1 is quick opening, 2 is linear, 3 is parabolic and 4 is equal percentage flow characteristic.

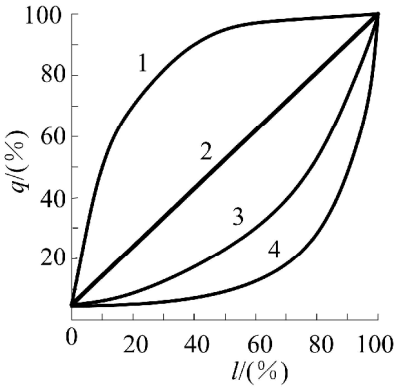

Fig. 3 Ideal flow characteristic curve

When the blockage fault is occurred at valve outlet, because of the existence of a blockage, it changes the flow area of outlet, and it make the differential pressure of valve before and valve after change and it changes the actual flow characteristics.

Blockage Fault Simulation Analysis

Simulation Settings

A block is designed at the interface section of valve and pipeline to simulate the outlet blockage fault, and on the basis of it, the flow channel model of outlet blockage is set up. When meshing the flow channel, according to the structure and fluid state to process grid and select unit, as shown in Table 1.

Table 1 Meshing

divided area	structure	fluid state	mesh processing	element type
valve inlet	simple	stable	sparsity	hexahedral
valve body	complex	unstable	refinement	unstructured tetrahedral
valve outlet	simple	unstable	refinement	unstructured tetrahedral

Mesh model of fully opening for outlet blockage is shown in Fig. 4.

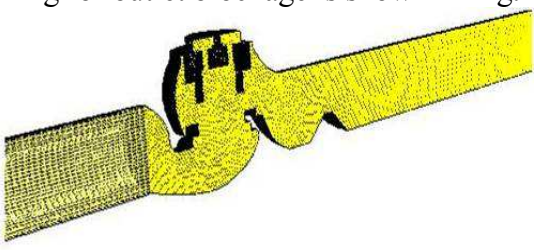

Fig. 4 Outlet blockage mesh model

Solver type, turbulence model, the fluid medium and boundary conditions are needed to set, as shown in Table 2.

Table 2 Simulation Settings

settings	solver	turbulence model	media	boundary conditions	differential pressure
parameters	separating	Standard k-ε equation	mixed gas	pressure inlet / outlet	0.4MPa

Analysis of Simulation Results

Analysis of Flow Characteristic

Fig.5 is the flow characteristic of trouble-free and outlet blockage. From the fitting curve, it shows that outlet blockage does not change flow characteristic as a whole, but it increase the relative gain of flow characteristic curve, especially at relative opening between 20% to 60%, it has a larger flow at small opening, with the increase of the opening, the flow can quickly achieve maximum, then, when adding the opening, the change of flow becomes very small.

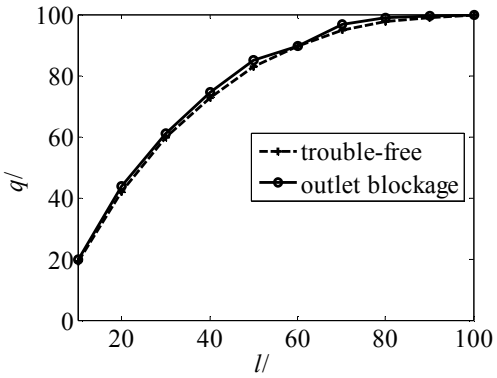

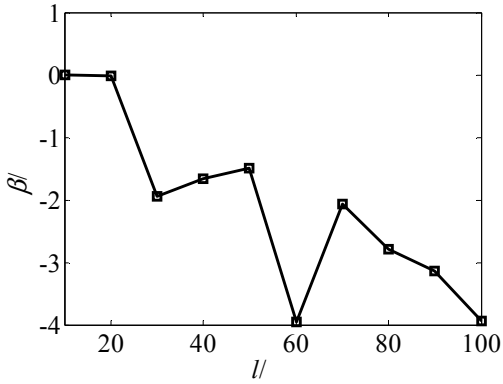

Fig.5 Flow characteristic of trouble-free and outlet blockage Fig.6 Relatively trouble-free flow

Fig.6 is the relatively trouble-free flow percentage, it shows that as a whole, with the increase of the opening, the percentage of outlet blockage relative to the trouble-free is decreasing, differential flow is increased gradually. At the main use of opening, due to the blocking, the flow is reduced, so comparing with trouble-free, outlet blockage need to increase the opening to meet the requirements of the same flow.

Through further analysis of Fig.6, it shows that the flow percentage is not a linear decline, and it appears the trend of increase about 30% to 50% and about 60% to 70%. By the analysis, it has to do with the open flow characteristic of valve, when the relative opening is 30%, the relative flow rate reached more than 60%, then it changes slow. The relative opening 60% can get the same percentage with the fully opening.

Data Analysis of Differential Pressure - Flow

Fig.7 is the differential pressure-flow of trouble-free and outlet blockage, Fig.8 is relatively differential pressure - flow diagram of outlet blockage and trouble-free. Relative opening degree is 40% and differential pressure is 100kPa~1000kPa,

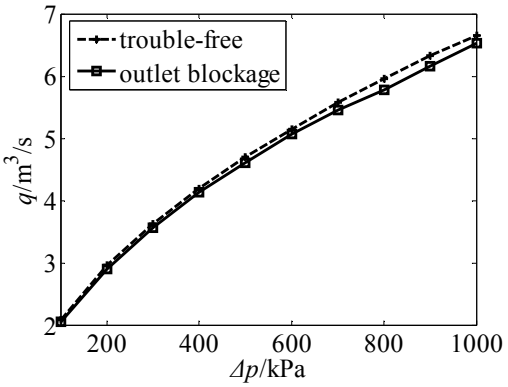

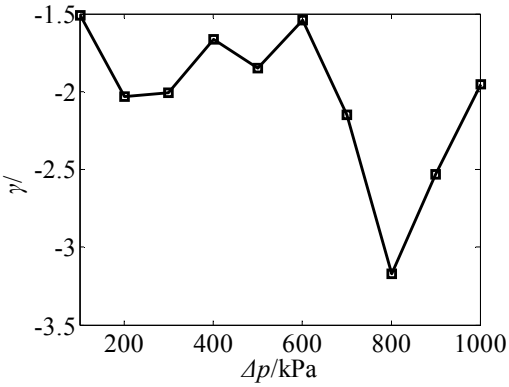

Fig.7 Differential pressure - flow Fig.8 Relatively differential pressure - flow

Fig.7 and Fig.8 show that at the outlet blockage fault, flow can increase with the increase of the pressure difference, but because of the influence of blocking, the flow of outlet blockage is less than trouble-free at the same pressure difference, and with the increase of pressure differential, differential

flow of outlet blockage and trouble-free is increases gradually. The flow percentage can reach a maximum at the differential pressure is 800 kPa.

Conclusion

Establishing the valve trouble-free and outlet blockage flow model, and applying the CFD numerical simulation of flow characteristic and differential pressure-flow, obtained the following conclusions.

(1) The vortex at the bottom of control valve outlet is main reason for the outlet blockage fault, and it changes the actual flow characteristics.

(2) Outlet blockage does not change flow characteristic as a whole, but it increase the relative gain of flow characteristic curve, the relative opening 60% can get the same percentage with the fully opening.

(3) The flow of outlet blockage is less than trouble-free at the same pressure difference, and with the increase of pressure differential, differential flow of outlet blockage and trouble-free is increases gradually. The flow percentage can reach a maximum at the differential pressure is 800 kPa.

Acknowledgements

This project is supported by Doctoral Fundation of University of Jinan (XBS1303) and Scientific Research Foundation of University of Jinan (XKY1312).

References

[1] Yantao An, Rujian Ma, Yong Wang, Simulation and Analysis the Internal Flow Field of Control Valve Bonnet Leakage, Applied Mechanics and Materials [J], 2013, 425, 2078-2081.

[2] Yantao An, Rujian Ma , Yong Wang, Research the Internal Flow Field of Valve Stem Leakage, Applied Mechanics and Materials[J], 2013,397, 257-260.

[3] D. Huang, Z.L. He, X.L. Yuan. Dynamic characteristics of an air-to-water heat pump under frosting/defrosting conditions [J].Applied Thermal Engineering,2007, 27(11-12):1996-2002.

[4] Zhang Deshegn，Zhao Juyun，Liulibao, etc. Analysis on electric and hydraulic valve jam problem of valve controlled hydraulic filling type hydraulic coupling [J]. COAL ENGINEERING, 2010(8: 81-82.

[5] Tang Yanchun. Study on Blocking Problem of Control Valve[J]. Process Equipment & piping, 2009, 46(2): 47-51.

Advanced Materials Research Vol. 983 (2014) pp 428-435

doi:10.4028/www.scientific.net/AMR.983.428

Development of Digital Filter Software in Auto Safety Components Test

Chang Jiang Du[1,a], Tian Qiang Du[2,b], Wei Liu[3,c]

[1]CATARC No.68,East Xianfeng Road, Dongli District, Tianjin, China

[2]CATARC No.68,East Xianfeng Road, Dongli District, Tianjin, China

[3]CATARC No.68,East Xianfeng Road, Dongli District, Tianjin, China

[a]duchangjiang@catarc.ac.cn, [b]dutianqiang@catarc.ac.cn, [c]liuwei01@catarc.ac.cn

Keywords: Safety Components, Auto Crash Test, Digital Filters, Software Development

Abstract. In auto safety components crash test, noise and interference signals is inevitable in the collected physical data, which will seriously affect the accuracy of the data. In this paper, the advantages and disadvantages are compared between IIR filters and FIR filters, a Butterworth filter is designed using the impulse response invariant method, and a filtering software is developed to meet the need of data processing for different measurement projects. The results showed that: according to different test data, the filter can achieve CFC filtering of different frequency levels, exclude interference data, preserve useful information, which ensures data accuracy and reliability, provides a convenient for the following data processing.

Introduction

Date filtering is to eliminate the unwanted signals mixed in the useful ones as much as possible according to certain requirements, and try to obtain useful signals completely. Filtering is based on the principle of the different characteristics between the useful and noise signals to achieve the separation of them, then eliminate or weaken the noise, and extract the useful ones [1].

During the car safety components crash tests, physical data such as speed, acceleration, pressure, displacement and so on is needed, in the process of data collection, transmission and conversion, because of the internal and external noise, there will be more or less interference signals in the obtained data. Therefore, various ways(excluding the singular value, filtering, etc.) must be tried to maximize the elimination of noise mixed in the data, and to ensure the data accuracy and test(car crash or component test) success rate [2,3].

The digital filter is a signal processing device with certain transfer characteristics, the input and output are digital signal. With the help of digital devices and some numerical methods, the waveform or spectrum of the input signal is processed, then the useless ingredients are removed while the useful ones are retained. The digital filter has many advantages, such as high accuracy, good reliability and flexibility, ease of large-scale integration, etc., so, it has been widely used in networking and filtering areas [4].

In ISO and SAE regulations [5,6], filtering characteristics of different measurement objects are described by Channel Frequency Class (CFC), for different test items, there are specific filtering methods with different CFC level, which requires that the designed filter should have certain versatility and adaptability.

In order to achieve data filtering, eliminate interference data, avoid amplitude-frequency and phase-frequency distortion phenomena, meanwhile meet the treatment needs of different measurement projects and regulatory requirements, this paper has made an in-depth study of data filtering technology and digital filter according to the collected data in components test, a reasonable digital filter is designed, and an integrated software for data filtering is developed, which meets the data processing needs of many components tests.

1 Test data digital filtering analysis

CFC notes that the frequency response of the data channel should be within the prescribed limit frequency range, dynamic frequency response of data channel is different for different objects, there

are four data channel frequency levels CFC1000, CFC600, CFC180 and CFC60, the value of CFC indicates the maximum flat frequency. For different auto safety components test items, the CFC filtering levels requirements are shown in Table 1.

Table 1 CFC of different test items

Test Items		*CFC*
Car body acceleration	Vehicle Comparison	60
	Crash simulation input	60
	Component analysis	600
	Integral calculation of speed, displacement	180
	Collision Wall load	60
	Safety belt load	60
Passenger	Head acceleration	600
	Chest acceleration	180
	Chest compression deformation	180
	Thigh axial load	600
	Sled acceleration	60
	Steering wheel force	600

For different parts test, the sampling frequencies are different generally, as well as the CFC processing methods, therefore, it is necessary to explore and analyze the principle of digital filtering to meet the different processing needs. The characteristic frequency of four CFC levels required by GB 11551-2003 are shown in Table 2, requirement of frequency response curve is shown in Fig. 1.

Table 2 Characteristic frequency of four CFC levels

CFC	F_L[Hz]	F_H[Hz]	F_N[Hz]
1000	≤0.1	1000	1650
600	≤0.1	600	1000
180	≤0.1	180	300
60	≤0.1	60	100

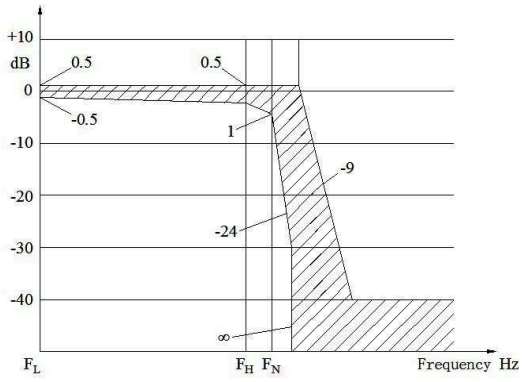

Fig. 1 Requirement of frequency response curve

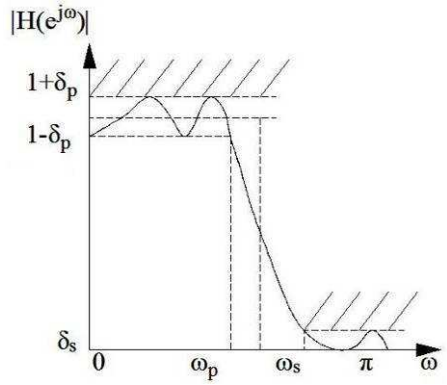

Fig. 2 Frequency limits of ideal low-pass filter

Typically, pretreatment of the obtained analog signal is mostly conducted by the hardware device when the data is collected, then, a frequency level filtering will be carried out through the digital filter, and at last, the final data meeting requirements is obtained.

An ideal filter, the frequency response within the required pass band needs to be a constant; the phase-frequency response is zero or a linear function of frequency. But it is impossible to get the ideal amplitude and phase-frequency an the same time for an actual filter. In order to meet the reasonable filtering characteristics, it is possible to approximate the ideal situation in a right tolerance condition. For the approximate of the ideal low-pass filter, the frequency limits diagram [7] will always be given first. Fig. 2 shows the frequency limits diagram for a low-pass filter, solid curve represents the amplitude-frequency response meeting the predetermined technical indicators,

in the pass band, the error requirement is $\pm\delta_p$, the frequency response of system approximate 1, that is: $1-\delta_p \le |H(e^{jw})| \le 1+\delta_p$, when $|w| \le w_p$; In the stop band, the frequency response of system approximate 0, error is less than δ_σ, that is: $|H(e^{jw})| \le \delta_\sigma$, when $w_s \le |w| \le \pi$. Among then, pass-band cutoff frequency w_p and stop-band cutoff frequency w_s are all digital frequencies. Between them, it is the transition zone, where the amplitude-frequency characteristic is monotonically decreasing.

2 Digital Filter Design and Comparison

The digital filter theory is derived and developed from analog filter theory, there are a variety of designing methods, the goal of which is to get the differential equations suitable for computer calculating.

The differential equation of general digital filter [8] is:

$$Y_n = \sum_{q=1}^{Q} b_q X_{n-q} - \sum_{p=1}^{Q} a_p Y_{n-q} \tag{1}$$

Among it: a_p and b_q is linear operator; X is sequence function before filtering; Y is sequence function after filtering. If for all the P, there is $a_p = 0$, then:

$$Y_n = \sum_{q=1}^{Q} b_q X_{n-q} \tag{2}$$

Such filter is called finite impulse response (FIR) filter, the output value is the weighted average of the input value; If $a_p \neq 0$, it is called infinite impulse response (IIR) filter, digital filtering is achieved using recursive method, that is, calculate the weighted value of the past output value and feedback it, then superimpose it on the weighted sum of the previous and current input values.

2.1 IIR Digital Filter

The most topical design approach of this filter is the same impulse response, the design criteria is to make the unit impulse response of the digital filter equal to the sample value of the unit impulse response for the analog filter, that is:

$$h(n) = h(t)|_{t=nT} \tag{3}$$

Specifically, the analog filter $H(s)$ is determined according to the technical specifications, the unit impulse response $h(t)$ is calculated after Laplace inverse transform, then by the principle of the same impulse response, $h(n)$ is obtained through sampling, do Z transformation to $h(n)$, and at last we can get the digital filter $H(z)$. The differential equation of the filter can be obtained according to the transfer function. Supposing that the system transfer function of the analog filter has N single poles:

$$H(s) = \sum_{i=1}^{N} \frac{K_i}{s - p_i} \tag{4}$$

Where: $K_i = (s - p_i)H(s)|_{s=p_i}$. Taking the Laplace inverse transform of Eq. 4:

$$h(t) = \sum_{i=1}^{N} K_i e^{p_i t} u(t) \tag{5}$$

Sampling to $h(t)$, there is:

$$h(n) = h(t)|_{t=nT} = \sum_{i=1}^{N} K_i e^{p_i nT} u(n) \tag{6}$$

So, getting the pulse transfer function of digital filter as follows:

$$H(z)=\sum_{n=0}^{\infty}(\sum_{i=1}^{N}K_i e^{p_i nT})z^{-n}=\sum_{i=1}^{N}\frac{K_i}{1-e^{p_i T}z^{-1}} \tag{7}$$

For automotive crash test or safety component test, second-order or third-order Butterworth filter can meet the requirement. The standard transfer function of second-order Butterworth filter can be expressed as:

$$H(S)=\frac{1}{S^2+\sqrt{2}S+1} \tag{8}$$

After bipolar transformation, that is let $S=\frac{Z+1}{Z-1}$, get the transfer function of the second-order digital filter:

$$H(Z)=\frac{b_0+b_1Z^{-1}+b_2Z^{-2}}{1-a_1Z^{-1}-a_2Z^{-2}} \tag{9}$$

The differential equation of the corresponding second-order filter is:

$$Y_n=b_0X(n)+b_1X(n-1)+b_2X(n-2)+a_1X(n-1)+a_2X(n-2) \tag{10}$$

The difference coefficients are shown in Table 3.

Table 3 Differential coefficient

Differential coefficient	Second-order
b_0	$\frac{\Omega_c^2}{\Omega_c^2+\sqrt{2}\Omega_c+1}$
b_1	$2b_0$
b_2	b_0
a_1	$\frac{2-2\Omega_c^2}{\Omega_c^2+\sqrt{2}\Omega_c+1}$
a_2	$\frac{-1+\sqrt{2}\Omega_c-\Omega_c^2}{\Omega_c^2+\sqrt{2}\Omega_c+1}$

In the table,

$$\Omega_c=\tan(\frac{\pi}{Q}),\quad Q=\frac{F_s}{F_N} \tag{11}$$

Where: F_s is sampling frequency; F_N is characteristic frequency f_N specified in CFC.

For IIR filter, its calculation is small, just need four multiplications, has a good processing speed; also, the designing is simple and convenient, and has good amplitude-frequency characteristics. But the transfer function of IIR digital filter is a rational function with zero point and extreme point, IIR system has stability problem, and under normal circumstances, its phase-frequency characteristics is nonlinear, there is a delay or phase shift, see Fig. 3, the red curve is the original data, the blue curve is the filtered data by IIR filter, we can see that, there is an obvious phase shift in the filtered data. Of course, we can use the positive and negative secondary filtering technique [9] to eliminate the phase shift problem of this filter, also see Fig. 3, the green curve is the secondary filtered data, and its phase is consistent with the original data.

2.2 FIR Digital Filter

There is no correspondence between the system transfer function of FIR digital filter and analog filter, a direct design method can only be used, that is, based on the technical indicators, the system pulse transfer function physically realizable is calculated directly. Among them, the window function method is the most commonly used one with linear phase-frequency characteristics.

Window function method is also known as the Fourier series method, the given design specifications are generally frequency domain indicators, such as frequency response $H_d(\Omega)$ of the filter. According to DTFT, there is:

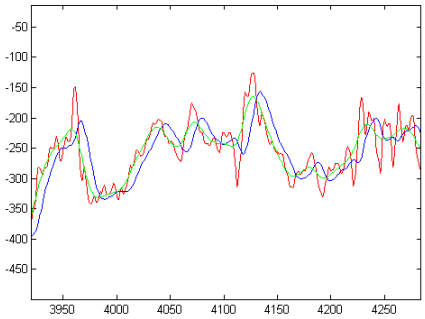

Fig. 3 Phase displacement of IIR filter

$$h_d(n)=\frac{1}{2\pi}\int_{-\pi}^{\pi}H_d(\Omega)e^{j\Omega n}d\Omega \tag{12}$$

$$H_d(\Omega)=\sum_{n=-\infty}^{\infty}h_d(n)e^{-j\Omega n} \tag{13}$$

Window function method is that, to multiply window function $\omega(n)$ in time-domain by infinite unit impulse response $h_d(n)$, cut off the infinite unit impulse response sequence, constitute $h(n)$ of FIR digital filter. That is:

$$h(n)=h_d(n)\omega(n) \tag{14}$$

Frequency response of FIR digital filter is:

$$H(\Omega)=\sum_{n=0}^{N-1}h(n)e^{-j\Omega n}=\sum_{n=0}^{N-1}h_d(n)e^{-j\Omega n} \tag{15}$$

From the above equation, the actual designed frequency response $H(\Omega)$ is different from the frequency response $H_d(\Omega)$ required by technical specifications, the former one is the approximation of the latter one. For window function method, cut off the infinite sequence $h_d(n)$ using the window function $\omega(n)$ to get a finite sequence $h(n)$, $h(n)$ is the approximation of $h_d(n)$, so, the shape and length of the window function have a great effect on the system performance. The commonly used window functions are shown in Table 4.

Kaiser window function is to approximate an ideal window using Bessel function. Where, a is independent parameter, I_o is the first zero order variant Bessel function, with the following rapid convergence formula, accuracy of any need can be calculated:

$$I_o(x)=1+\sum_{k=1}^{\infty}\left[\frac{1}{k!}\left(\frac{x}{2}\right)^k\right]^2 \tag{16}$$

General procedure for design of linear phase FIR filter using window function method is [10] :

(1) Determine the characteristics $H_d(\Omega)$ of ideal filter according to needs;

(2) Based on DTFT, calculate $h_d(n)$ from $H_d(\Omega)$;

(3) Choose right window function, and determine the window width N according to transitional bandwidth;

(4) By $h(n)=h_d(n)\omega(n),0\le n\le N-1$, obtain the unit impulse response $H(z)$ of the filter;

(5) Make a Z transform to $h(n)$, acquire the pulse transfer function $H(z)$ of the linear phase FIR filter.

Transfer function of FIR digital filter is a linear function of frequency, which ensures the signal distortion to be minimum during transmission, also there is no stability problem, and it is easy to achieve strict linear phase, without phase shift. But to get a better filter, it needs a higher order, and a long time to be calculated.

Table 4 Window function introduction

Name	Time domain expression $\omega(n)$, $0 \le n \le N-1$
Rectangular window	$r_N(n)$
Hanning window	$\frac{1}{2}(1-\cos\frac{2\pi n}{N-1})$
Harmming window	$0.54-0.46\cos(\frac{2\pi n}{N-1})$
Blackman window	$0.42-0.5\cos\frac{2\pi n}{N-1}+0.08\cos\frac{4\pi n}{N-1}$
Bartlett window	$1-\frac{2(n-\frac{N-1}{2})}{N-1}$
Kaiser window	$\frac{I_0[a\sqrt{(\frac{N-1}{2})^2-(n-\frac{N-1}{2})^2}]}{I_0[a(\frac{N-1}{2})]}$

3 Digital Filter Software Development and Application

From the above analysis it is known that, FIR filter has no phase shift, but the computation is large, IIR filter has simple calculation, and good amplitude-frequency characteristic, a secondary filter can be used to eliminate the phase shift problem. Therefore, the regulation in SAEJ211 and ISO6487:2002 is, Butterworth filter should be used in CFC digital filter. For automotive crash tests or safety components tests, a second-order or third-order filter can meet the data processing requirements. As to safety components, the related test projects needing filtering process are seat belt dynamic test, chest impact, seat dynamic, luggage impact, steering wheel impact, door locks dynamic, HIC calculation etc. To meet the requirements of national regulations, according to different filtering needs, a large number of design improvements and practical test verifications are carried out, a digital filter and integrated software is developed which can meet the regulatory requirements and test data processing needs.

3.1 Integrated Software Development

In this paper, based on the Visual Basic 6.0 software, according to the design method of second-order Butterworth filter, using the positive and negative secondary filtering technology, a digital filter is developed. Depending on different filtering levels and test requirements, a friendly simple interactive interface is designed, which can do digital filtering to test data, edit test manufacturer informations, generate PDF format test reports etc. By compiling an executable file, the data processing software can run and be used under different test equipments and environment.

As shown in Fig. 4, it is the running interface of data processing software, in this screen you can select different test projects, set up CFC filtering frequency level and sampling frequency parameters. Then, click on the 'Test Parameters' button, the main test parameters and informations can be set. After that, click on 'OK' button to return to the main interface. At that time, the 'Filtering' button will become to a selectable item, see Fig. 5, click on this button, an 'Open' dialog box will pop up, select the original data, click on the 'Open' button, the filtering process will be completed. Then a 'Save' dialog box will pop up, which tell you to save the filtered data and report, enter the file name, and click on the button to complete the filtering.

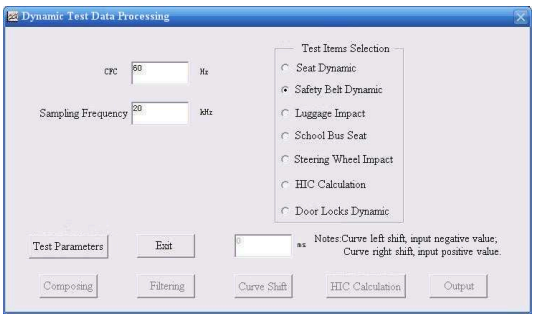

Fig. 4 Main interface of data processing software

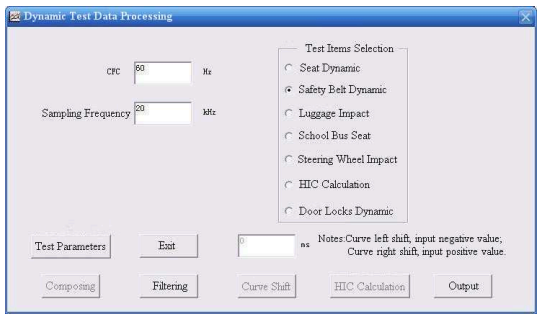

Fig. 5 Filtering operation interface

3.2 The Practical Application of Digital Filtering

Sled impact test is a real car crash simulation test, the platform sled is used to generate deceleration near actual car crash, then the performance of occupant protection device and inertial force resistance performance of the components are tested. According to national standards, a dynamic test should be done to seat belt, this test is carried out on the crash sled, a 50 percentile US or Europe dummy should be settled on the seat, and set the seat belt according to real car environment, the deceleration waveform of the sled must be located within the standard required scope. Therefore, this paper use the simulated crash test sled device, carry out a safety belt dynamic test, the installation is shown in Fig. 6, and two acceleration sensors are arranged on the platform, which collect the parking deceleration data to analysis, research and adjust the deceleration performance of the sled.

The original collected data is shown in Fig. 7(a), it can be seen, there are a large number of noise and interference data, which affect the data accuracy and processing efficiency. Sled acceleration data requires CFC 60 level filtering. After a positive second-order Butterworth filtering, the data is shown in Fig. 7(b), the interference data is eliminated clearly; Then, the designed positive and negative secondary filter is used to process the original data, see Fig. 7(c), the interference and noise data are significantly eliminated, the data has better smoothness, and the phase shift is substantially eliminated.

When there is a vehicle front collision, the driver's chest will collide with the steering mechanism, the chest model impact test is a method using to evaluate the impact energy absorbing performance of steering mechanism. In the GB 11557-2011, the human chest model must hit the steering wheel with a horizontal velocity 24.1km/h~25.3km/h, the horizontal force acting on the steering wheel must not more than 11123N. So, during this test, the impact force data needs to be measured accurately. The steering mechanism is mounted according to the manner shown in Fig. 8, the test is carried out, and the impact force data during the experiment is collected to evaluate the energy absorbing performance.

Fig. 6 Seat belt dynamic tes

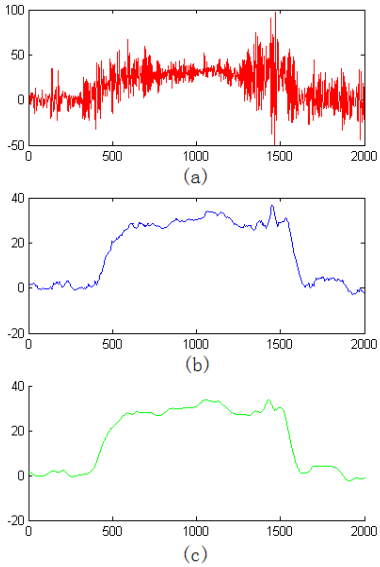

Fig. 7 Filtering of seat-belt dynamic test data

Steering wheel impact force data requires CFC 600 level filtering. The measured data is shown in Fig. 9(a), there are much interference and noise data; Fig. 9(b) shows the prior filtering process results, Fig. 9(c) shows the filtered test data using our designed filter, as it can be seen, the filtered data has good smoothness, and the interference data is eliminated.

Fig. 8 Chest block impact test

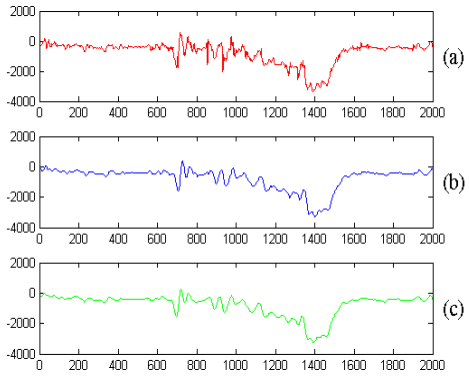

Fig. 9 Filtering of chest block impact test data

Summary

In auto safety components crash test, noise and interference signals is inevitable in the collected physical data, such as force, speed and acceleration etc., which will seriously affect the accuracy of the data. Then, in order to ensure the accuracy and reliability of the measured data, necessary filtering needs to be done. For digital filters, IIR filter has simple calculation, and good amplitude-frequency characteristic, which is superior to FIR filter. In this paper, according to the CFC frequency level requirements in ISO and SAE regulations, dynamic test data processing software is developed, which can meet different CFC frequency level filtering requirements for different projects. The second-order Butterworth filter with positive and negative secondary filtering function is used, which simplifies the designing, meets the regulation requirement, avoids the phase shift, and improves the accuracy and reliability of the data. Data acquisition and processing has important significance for the accuracy and reliability of the test data, is an important basis for automotive safety parts and vehicle test evaluation & improvement, researching data process technology has a profound significance.

References

[1] Zhao Guangzhou. *Signal Analysis and Processing*. Second edition, Beijing: Machinery Industry Press, (2006)

[2] Yan Yan. *Study on Crash Test for Motor Vehicle and Data Processing Method*. Changchun: Jilin University [Master's degree], (2008)

[3] Hua Xiang. *Data acquisition and processing in automobile collision test*. Shanghai Automotive, Vol. 12 (2000), p.14-16

[4] Zhang Jinhuan, Du Huiliang, Ma Chunsheng. *Automotive Design for Crash Safety*. Beijing: Tsinghua University Press, (2010)

[5] International Standard. *Road vehicles - Measurement techniques in impact tests – Instrumentation*. ISO 6487, (2002)

[6] SAE. *Instrumentation for impact test*. SAE Handbook J211, (1984)

[7] Bai Zhonghao, Cao Libo, Liu Chenghua. *Research on Test Data Processing for Automotive Crash*. Bus Technology and Research, Vol. 26 (2004), p. 5-7

[8] Louis Litwin. *FIR and IIR digital filters*. IEEE POTENTIALS,(2000), p.28-31.

[9] Chen Hong. *Achievement of Analog and Digital Filter in Automotive Crash Test*. Automotive Engineering, Vol. 20 (1998), p. 84-89

[10] Bai Zhonghao, Cao Libo,etc. *Research on the Application of Digital Filter Technology in Auto Crash Test*. Journal of Hunan University (Natural Sciences), Vol. 32(2005), p.13-16

Advanced Materials Research Vol. 983 (2014) pp 436-439

doi:10.4028/www.scientific.net/AMR.983.436

A New Type of Adjusting Coaxiality Structure Design

Sun baorui[1], Zheng yan[1,2,a], Zhang yong[1] and Fan xiaowang[1]

[1.] Changchun mechanical science research institute co., LTD

[2.] Jilin university mechanical science and engineering college

[a]435562852@qq.com

Key Words: tester; coaxiality, detector

Abstract: This paper analyzes the factors that cause axial fatigue testing machine not coaxiality and influence on test results, put forward the axial fatigue testing machine alignment inspection, and designed a new type concentric structure to adjust not coaxiality.

Introduction

Generally speaking, general specimens of component fatigue testing machine are bigger, demand of concentricity is not strict. Even if the concentricity is requested, it can be resolved by increasing the ball hinge. For the material and property test, the specimen is small, smaller additional partial load can influence the test result, and even some composite has more higher requirement for concentricity[1-4]. The attempt of increasing the coaxial regulating mechanism on the component fatigue test machine is of great significance.

The Influence for Test Results Caused by Coaxiality

Figure 1 is fatigue testing machine, the upper and lower clamp coaxiality not only influences the accuracy of test force, but also influences the material pull, pressure fatigue test result, especially for low strain test effect is more bigger[5]. Upper and lower clamp's not coaxial will introduce additional bending stress and superimposed to the mean stress, and lead to local stress concentration, reduce material fatigue life.

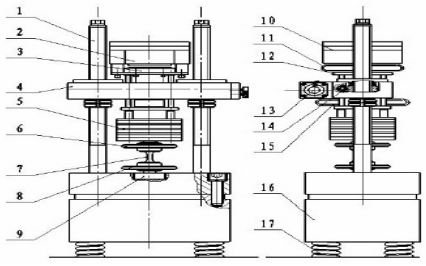

1.Screw 2.Magnet 3.Armature 4.The beam 5.Farmar 6.The up jig 7.Sample 8.The down jig 9.The sensor 10.Encourage quality 11.Incentive spring 12.The tray 13.The motor 14.The turbine worm 15.Arch ring 16.The base 17.Damping spring

Fig. 1 Fatigue Testing Machine

Concentric Deviation Classification and Adjustable Concentric Mechanism Design

Generally speaking, different heart deviation can be summed up the following two kinds, they are angle deviation and level of the deviation respectively. Namely according to the result of measuring to corresponding adjust, it can complete the task of adjusting concentric. As shown in Fig 2:

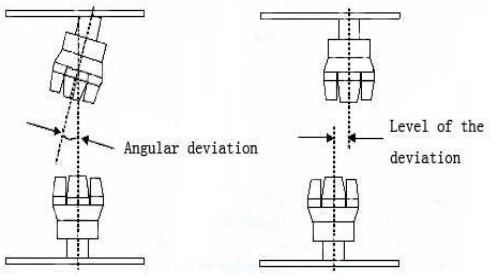

Fig. 2 Two Concentric Deviation

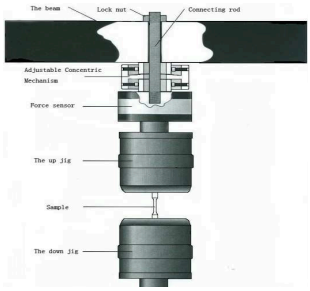

Fig.3 Adjustable Concentric Institutions and Installation Position

Adjustable concentric institutions and installation position as shown in Fig 3:

Adjustable Concentric Institutions Detection System Design

Geometric Detection

It can be adjusted manually by dial indicator (relatively simple). Fig.4 is coaxiality measurement method of upper and lower clamping head. When measuring coaxiality, using low pressure to clamp concentric rods, the reference plate is put on the clamp head upper plane. Two columns by chuck side rotating one round, it can get dial indicator reading lines of concentric rods A, at the same time, it can get B readings. According to dial indicator readings, it can get eccentric value by formula:

$$e_A = \frac{|X_{\max} - X_{\min}|}{2} \tag{1}$$

$$\Delta_{A-B} = e_A - e_B \tag{2}$$

In the formula: e_A - eccentric value of A place; $X_{\max}$, $X_{\min}$ - maximum and minimum readings of dial indicator; Δ_{A-B} - the difference eccentric value between A and B.

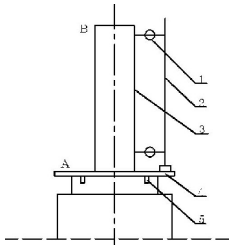

1. Dial indicator; 2.The magnetic table; 3.Concentric rods; 4.The base plate; 5.Cylindrical

Fig. 4 Coaxiality Detection Method

Strain Gauge Testing

In this method, it pastes strain gauge standard samples on different positions of sample to check up machine and fixture system coaxiality. The shape, size and strain gauge paste position of standard circular sample as shown in Fig. 5. Strain gauge is symmetric pasted along the sample axial, and is located in the center of the sample range. It should ensure the strain gauge paste firm, the strain values measured stability and have good repeatability. Test steps are as follows:

a) Installing one end of the test specimen on the upper grip, and adjusting the strain gauge reading to zero on multipoint strain gauge.

b) Installing the other end of the test specimen on the lower grid, measuring the strain gauge reading under zero loading;

c) The sample is stretched up to 0.4% of the biggest variable, or imposing on the sample of the test force should make the sample have the corresponding maximum dependent variable. Record each point of strain gauge readings;

d) The sample is turned 180°, and repeat b, c step;

e) The strain values at various points are generated into the formula to calculate. If calculated value is greater than 5%, adjusting the dynamometer or fixture, repeating above steps until the bending strain value on sample is meet requirements. Computation formula is as follows:

The average bending strain:

$$\varepsilon_M = \left[\left(\varepsilon_1 + \varepsilon_2 + \varepsilon_3 + \varepsilon_4 \right)_0 + \left(\varepsilon_1 + \varepsilon_2 + \varepsilon_3 + \varepsilon_4 \right)_{180} \right] / 8 \tag{3}$$

The average bending strain of 1 and 2 points:

$$\varepsilon_{1,2} = \left[\left(\varepsilon_{1,0} - \varepsilon_{1,180} \right) + \left(\varepsilon_{2,180} - \varepsilon_{2,0} \right) \right] / 4 \tag{4}$$

The average bending strain of 3 and 4 points:

$$\varepsilon_{3,4} = \left[\left(\varepsilon_{3,0} - \varepsilon_{3,180} \right) + \varepsilon_{4,0} \right] / 4 \tag{5}$$

The relative bending strain:

$$\varepsilon_R = \left[\sqrt{\left(\varepsilon^2_{1,2} - \varepsilon^2_{3,4} \right)} / \varepsilon_M \right] \times 100\% \tag{6}$$

In the formula: $\varepsilon_{1,0}$ to $\varepsilon_{4,0}$ represents 1 to 4 strain value when the sample at initial position. $\varepsilon_{1,180}$ to $\varepsilon_{4,180}$ represents 1 to 4 strain value when the sample rotating 180°.

The position of strain gauge should corresponding to the position of governing mechanism regulating bolt （namely corresponding coordinate direction）, as shown in Fig. 6.

Fig.5 Position of Standard Specimen Strain Gauge

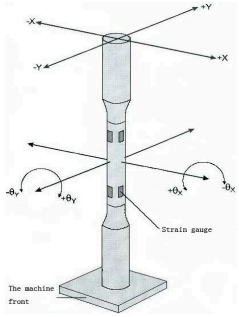

Fig. 6 Axis Definition

The Principle of the Concentric Institutions

When it has angular deviation, strain polarity distribution as shown in Fig. 7 left, If it is horizontal deflection, strain polarity distribution as shown in Fig.7 right. Through the software to draw the strain distribution and indicate the bolt that needs adjust (It can be considered judgment). Angle adjustment principle is shown in Fig. 8, horizontal adjustment principle is shown in Fig. 9. After each strain value is adjusted to a certain range, it can be considered that it meets a certain standard requirement. And then concluded specific scope of numerical that conform to the precision requirements, As the later testing standard of "virtual", as long as in the standard range, even if using the standard test, it also should comply with the request. Then this standard can be put into formal standards.

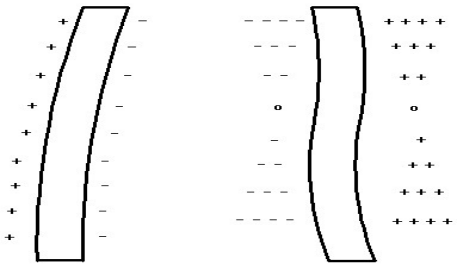

Fig. 7 Different Heart Strain Distribution

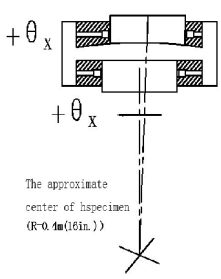

Fig. 8 Angle Adjustment Principle

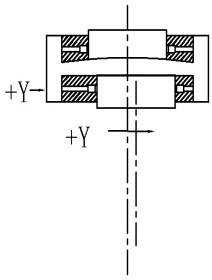

Fig.9 Level Adjustment Principle

Conclusion

Alignment test is an important content in the project of fatigue testing machine performance, it is the premise that obtains real test data. With the development of materials science research, the requirements of tester force value accuracy, coaxiality and controlling are improving. This paper also designs a new type of coaxial structure, when the coaxial deviation obtained by detecting, base on the test results, it can correct sample by the coaxial agency, maintaining the interest of the lab and the customers better.

Reference

[1]FEI Ming-hui. Universal Testing Machine Alignment Test Method of Analysis[J]. Advanced Measurement and Laboratory Management,2013,02,7-9.

[2]CHEN Yi-ming. Fatigue Testing Machine Alignment Detector Design Based on The LabVIEW[J]. Automation & Instrumentation, 2012,01,106-107.

[3]LIANG Xinbang. The Calculation of Alignment[J]. Physical Testing and Chemical Analysis Part A :Physical Testing,1992(5),46-48.

[4]Zhang Jinwei, Guo Jian. Concentricity Test for Testing Machine of Tensile and Compressive[J].Te-
st Technology and Testing Machine, 2008,03,17-19.

[5]Zheng Wenlong, Wang Chunhua. Discussion on Testing Machine Proper Alignment[J]. Test Technology and Testing Machine, 2011, S1,14-17.

Advanced Materials Research Vol. 983 (2014) pp 440-443

doi:10.4028/www.scientific.net/AMR.983.440

Design of A PLC-based Engineering Training Unit

Han JianBing

Hebei Technology University, Shijiazhuang Hebei

15836687@qq.com

Key Words: unit ; training; Programmable Logic Controller

Abstract: The handling unit based on PLC is composed of seven motors, Programmable Logic Controller, touch panel, sensor and so on, The unit controls the bucket to move up and down, left and right with seven motors, and back and forth and regulates the speed of motor movement with speed regulators, complete the material transport, the touch panel help realize the manual and full-automatic control of motor and the switching between manual and automatic modes. The handling unit based on PLC for strengthening the operating ability in college or junior technical personnel are of great help.

Graduates-to-be or junior technicians are required to have the training of practical projects, so as to strengthen their ability of practice and accordingly lay a firm foundation for their career before they are about to enter the society or take the work positions. To this end, the author designs a handling unit based on Programmable Logic Controller (PLC) for engineering training. The handling unit utilizes PLC control technology and combines with sensors, relays and other components to complete the operation of bucket-type handling unit. The unit controls the bucket to move up and down, left and right with seven motors, and back and forth and regulates the speed of motor movement with speed regulators. When the motor moves to the ends of unit, the sensors will stop the movement of motor and the touch panel help realize the manual and full-automatic control of motor and the switching between manual and automatic modes.

1. Unit Composition

Motor #1 and Motor #4 in the unit control the leftwards/rightwards movement of bucket, with four sensors are installed at front-left (above), front-right (above), back-left (above) and back-right (above) of unit as left and right limits; Motor #2 and Motor #5 the upwards/downwards movement of bucket; Motor #3 and Motor 6# the back-and-forth movement of bucket to adjust the position of bucket; and Motor #7 realizes the transfer of handling, with every one sensor installed on front and back (below) ends as front and back limits.

2. Hardware Model Selection

2.1 PLC model selection

PLC is the core of entire unit and the most important component to realize tension control and what selected is Siemens S7-200 CPU224 PLC, which has a high share in enterprises or various workplaces. Siemens S7-200 PLC is strong in functions and can realize good effects either alone or online to realize complicated control. Siemens S7-200 boasts the extremely high price-performance ratio, sufficient order sets, high reliability, rich built-in functions, powerful real-time communication ability and abundant extension modules for use, simple to operate and easy to master[1].

2.2 Motor model selection

The unit demands for good regulation of bucket speed and a small DC motor will be OK. The small DC motor possesses the following advantages: smooth speed regulation characteristics, wide speed regulation range; strong overload ability, large heat and brake torque; and good potential

wave form, with little impact on electromagnetic interference. After comprehensive consideration with references of related materials, Taiwan OPG 05SGN DC motor is selected.

2.3 Sensor model selection

Proximity switch is a kind of position switch that can operate without mechanical contact with moving parts. When an object approaches the sensing surface of switch and reaches the action distance, the switch will act without mechanical contact or any pressure applied, so as to drive AC or DC electric appliances or send control orders to computer devices[2]. Regardless of great varieties, Youtai LJA12M-5P1 sensor is selected for price-performance ratio.

2.4 Touch panel model selection

Nowadays with soaring development of electronic times, touch panel becomes more and more important in the industrial control sector for its safety, stability and reliability[3]. With science and technology advancing by leaps and bounds, the performance of electronic products is improved greatly, but the prices are cheaper. For this unit, i Series TM6100i touch panel made by WEINVIEW CO., LTD. is selected.

3. I/O port distribution

The unit needs six limits to control the stop positions of motor, so there are six input points; seven motors are designed to move in two directions, so there are 14 output points. See Table 1 for I/O port distribution.

Table 1 I/O Port Distribution Table

Input Point	Name	Output Point	Name
I0.0	Motor #1 Right Limit	Q0.0	Motor #1 in Forward Rotation
I0.1	Motor #1 Left Limit	Q0.1	Motor #1 in Reverse Rotation
I0.2	Motor #4 Right Limit	Q0.2	Motor #2 in Forward Rotation
I0.3	Motor #4 Left Limit	Q0.3	Motor #2 in Reverse Rotation
I0.4	Motor #7 Right Limit	Q0.4	Motor #3 in Forward Rotation
I0.5	Motor #7 Left Limit	Q0.5	Motor #3 in Reverse Rotation
		Q0.6	Motor #4 in Forward Rotation
		Q0.7	Motor #4 in Reverse Rotation
		Q1.0	Motor #5 in Forward Rotation
		Q1.1	Motor #5 in Reverse Rotation
		Q2.0	Motor #6 in Forward Rotation
		Q2.1	Motor #6 in Reverse Rotation
		Q2.2	Motor #7 in Forward Rotation
		Q2.3	Motor #7 in Reverse Rotation

4. System Wiring

Unit wiring mainly includes connection of PLC and relay, connection of extension module and relay, wiring of touch panel and speed regulator, wiring of electric appliances and the power supply.

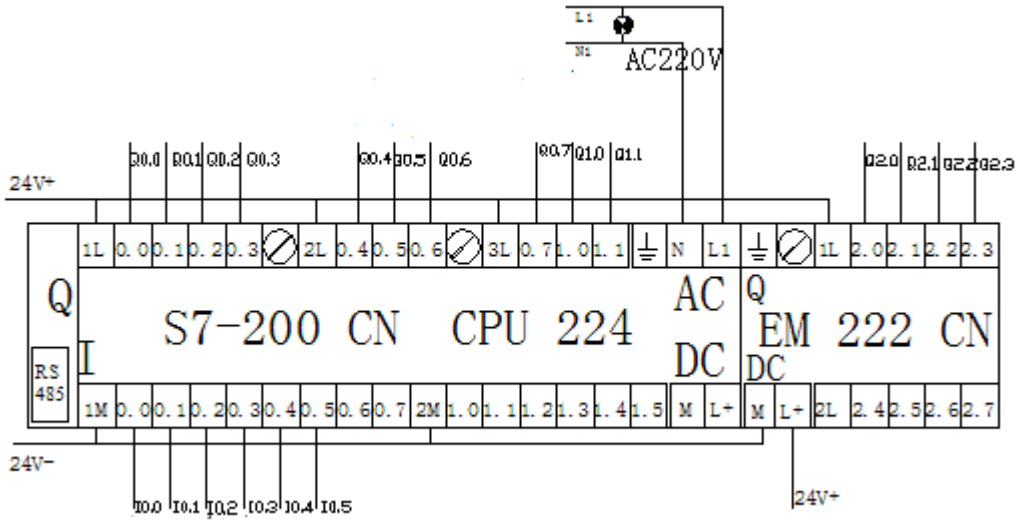

Fig.1 Wiring Diagram of PLC and Extension Module

5. Software Design

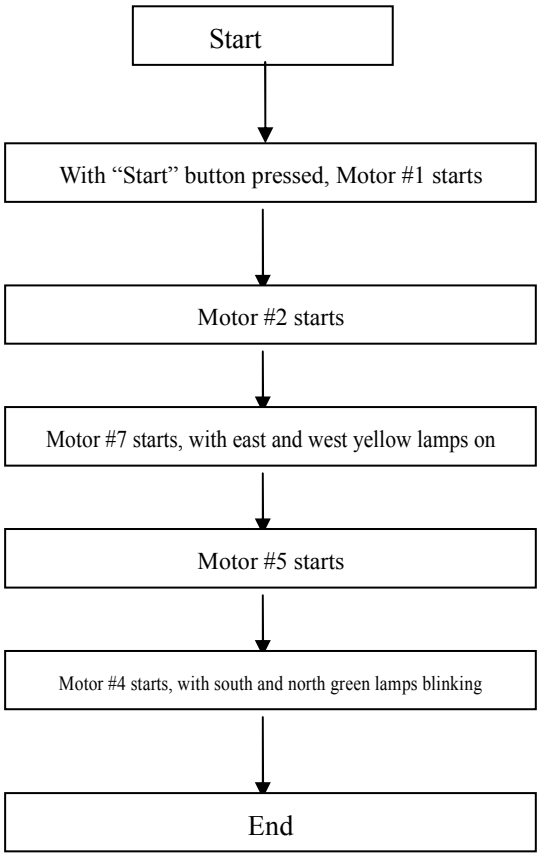

Fig.2 System Flow Chart

References:

[1]Wang Yonghua. Modern Electric Control and PLC Application Technology. Beijing: BEIHANG UNIVERSITY PRESS.p. 120-121(2008)

[2] Song Huan. Analysis on Proximity Switch Model Selection and Performance Determination. Inner Mongolia Petrochemical Industry.Vol. 18(2008),p.54-56

[3] Estevez.M.Marcos.Graphical Modeling of PLC-based Industrial Control Applications[C]. Proceedings of the 2007 American Control Conference.New York City.USA, p.220(2007)

Advanced Materials Research Vol. 983 (2014) pp 444-449

doi:10.4028/www.scientific.net/AMR.983.444

Flexible Thermosetting Pipe

Zahiraniza Bt Mustaffa[a], and Thar M. Badri Albarody[b]*

Civil Engineering Department, Universiti Teknologi PETRONAS, Bandar Seri Iskandar,

31750 Tronoh, Perak, Malaysia

[a]zahiraniza@petronas.com.my, [b]t.albarody@ymail.com,

Keywords: Thermosetting material, Laminated composite, Dual-helical wrapping of tape stacks process, Flexible Pipe.

Abstract. The typified as flexible thermosetting pipe, is a new product, developed initially in response to the need for a non-metallic replacement for steel pipe used for oil and gas productions. This product may use for high pressure down-hole applications in which the pipe could repeatedly transported onto a drum. The proposed pipe comprise an internal thermoplastic layer play as liner and a fluid-tight cover, and one or more dual-helical wounding tape stacks applied to the internal liner for absorbing axial and bending loads. The tape stacks are wrapped helically onto the pipe structure with adjacent gaps between wrappings tape to reduce the pressure integrity of the tubular pipe structure. The composite tape stacks are formed from a plurality of thin tape strips and are bonded to each other within a stack. All the layers are manufactured from composite material consisting of highly noncorrosive epoxied matrix reinforced by long continuous fibers. Thus, the proposed flexible pipe designed to be stand alone with thermoplastic liner over-wound with one or more of an epoxy-based structural thermosetting laminate. To this aim, a straightforward simulations of thermosetting pipe is developed via using ANSYS software. Apart from possessing an accurate operational condition, on account of its simplicity the proposed simulation seems also very suitable for further developing and prototyping purposes. Finally, it has been shown that the proposed thermosetting pipe, which partially attains some classical characteristic of both offshore and onshore pipeline by a different line of reasoning, is may serve as a reference in designing flexible pipe.

Introduction

Fiber reinforced thermosetting comes into the categories of “composites” materials and have few applicable standards such as ASTM and AWWA, which is standard for fibreglass pressure pipes. The reinforcement “fibers” are responsible for the mechanical characteristics of the product, minimizing the chance of defects and so the material comes close to its theoretical strength such as glass fibers that have a tensile strength of about 18.000 Kg/cm^2, which is higher than that of the best steels [1, 2].

Furthermore, the reinforcing material can be arranged with any desired density and orientation, allowing the technical and economic characteristics of the structure to be optimized [3].

There are several technologies for manufacturing thermosetting pipes or sometimes called composite pipework such as; filament winding, continuous winding of composite tape, etc.[4]. The said tapes stacks should composed from several layers for absorbing the desired axial loads but extremely bendable.

In this paper a flexible thermosetting pipe is proposed achieved its flexibility by virtue of the fact that the tape stacks that form pipe layers are free to move relative to one another. The said flexible pipe comprise one or more thermosetting layer formed by applying a dual-helical wounding and wrapping of tape stacks to a plastic internal liner and perfectly connected one to the other. Such system will describe in next section.

Geometry Description

As mentioned earlier, the tape stacks in the pipe are design to accommodate the flexural strain by sliding on each other, during pipe coiling, without damaging either the load-bearing capability of the fibers or the fluid containment capability of the thermoplastic liner. The said flexible has minimum bending radius equal to 0.9m per each 3 foot of its length. Such flexible can have a high pressure rating, typically 350 bar, and could fabricate with large diameters (250-550)mm. The reinforcement is typically E-glass, but carbon may also be employed, according to the application and economic factors. The liner material may also be tailored to the application, but would normally be polyethylene, cross-linked polyethylene, nylon 11 or PVDF. The key components of this flexible that displayed in Fig. 1, are:

1. An inner polyethylene liner, to prevent collapse under external compressive load that applied during the hoop-wound of thermosetting layer at highly tension. As well as, to be in direct contact with the fluid, provides the highest chemical resistance and impermeability.
2. An intermediate "thermoplastic" layers, to prevent corrosive product from coming into contact with the outer components of the flexible.
3. Near-hoop, pressure resisting thermosetting tapes stacks.

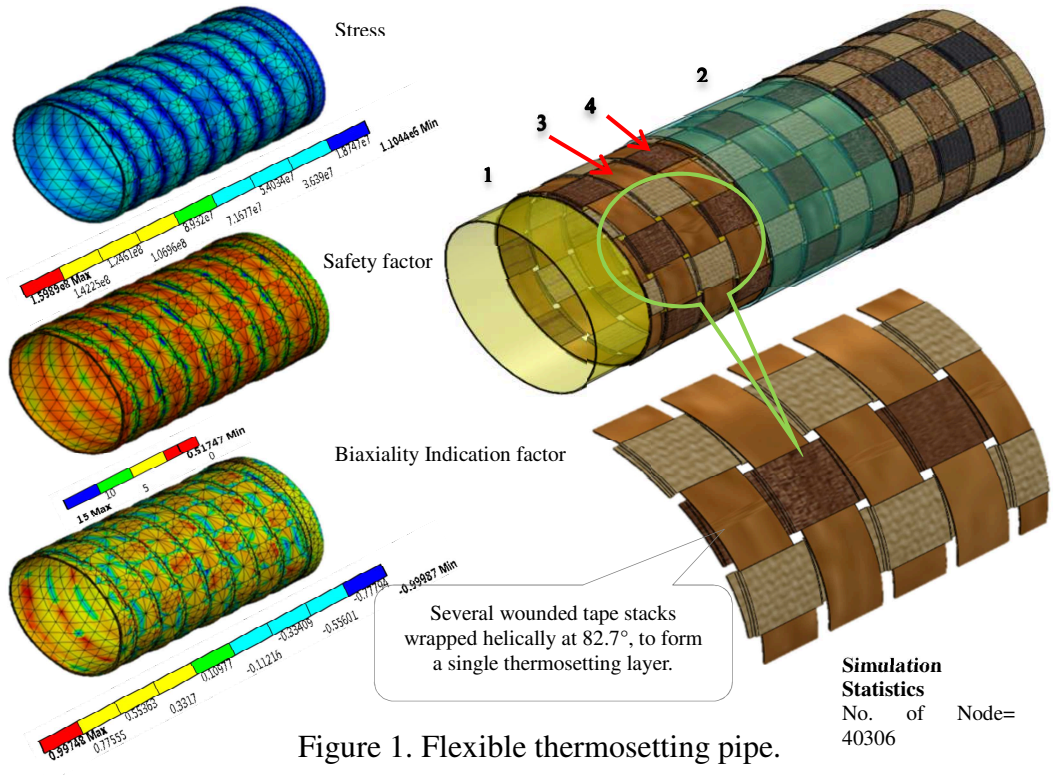

Figure 1. Flexible thermosetting pipe.

4. Near-axial thermosetting tapes stacks.

After repeating the layers construction to reach the desired characteristic, an outer polymeric casing could apply for external protection or other (gel-coat) protects the fibers externally from abrasion and atmospheric agents.

Material Selections

In order to develop flexible pipe ideal for petrochemical industry, and for transporting oil, aqueous fluids and other fluids, a composite material should select to have had a high specific strength and corrosion resistance, such as those explained in Fig. 2. The maximum temperature of

the fluid being handled, of course, may limit the selections of resin system. For example, amine-cured epoxy systems could be used at temperatures up to 115ºC.

Risen can suffer rapid hydrolysis damage in steam, which must therefore be avoided. Although, epoxy and vinyl-ester systems are relatively immune to attack by CO2 and H2S, as well as the main organic components of crude oil, the care needs to be taken, however, when volatile aromatic fractions such as toluene or xylene are present. Therefore, the characteristics shown in the Table 1 are those commonly required for the proposed flexible thermosetting pipe.

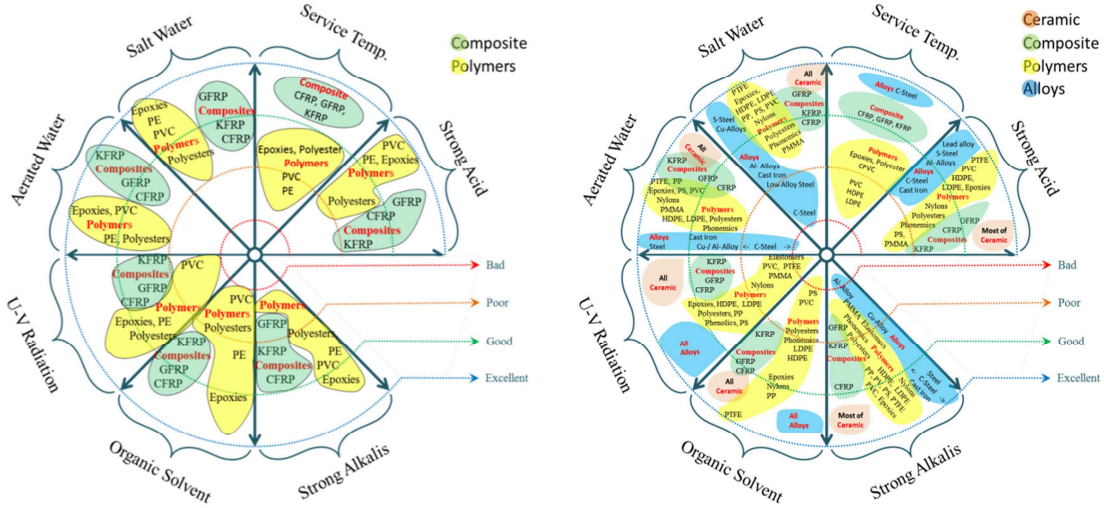

FIGURE 2. All main characteristics of all the alternative materials that could use in construction of pipeline[5, 6].

TABLE 1. The characteristics commonly required for current proposed flexible thermosetting pipe.

Properties		Flexible Thermosetting Pipe	Stainless Steel
Tensile Strength (N/mm^2)		382	340
Flexural Strength (N/mm^2)		468.3	380
Flexural Modulaus (N/mm^2)		22489	196000
Izod Impact (Kg.m/cm)		2.15	0.53
Specific Gravity		1.8	1.8
Thermal Conductivity (Kcal/hr/m^2/° C)		24.4	732.00
Coeff. of Linear Expansion (cm/cm° C) x 10-6		5.2	10
Safe Working Temp. (° C)		130	600
Flame Resistance		Good	
Corrosion Resistance	a. Acidic	Excellent	Excellent
	b. Alkaline	Good	Excellent
	c. Solvents	Fair	Excellent
	d. Coastal Environment	Excellent	Excellent
	e. Outdoor Exposure	Excellent	Excellent
	f. Effluent Water	Excellent	Excellent
	g. Steam	Good	Excellent

Parametric Analysis

An example is shown in Table 2, for a thermosetting pipe made of Gl-Ep composite material. Gl-Ep properties are found in [7-9]. Thus, the characteristics of that proposed flexible are given in Table 3. Although, Gl-Ep not cheaper than polymer according to the relative cost estimation attached in Table 3, thermosetting material still best choice for pipeline construction than steel. However, Gr-Ep material gives similar characteristics to those shown in the Table 3, which are commonly required in both onshore and offshore pipeline. As clearly seen in Table 3, the proposed flexible has a weight when full of seawater and submerged in seawater equal to 37.5624 kg/m which is less than its empty weight in air, result in small negative buoyancy force, shall minimize the pipe high self-weight when is suspended. In Table 4, 5 and 6 the proposed flexible was examined under varied external and internal pressure conditions and when subjected to wide range

of applied tension. Table 4, 5 and 6 shows that flexible made of Gl-Ep could emulate the Gr-Ep and steel pipe and expect to be a good non-metallic replacement for steel pipe that would be used for conveying oil and gas. Although, Gl-Ep is slightly less flexible but shows good load bearing capability than Gr-Ep, especially when under internal pressure or when subjected to tension. In fact, this is due to large orthotropic-ratio in Gl-Ep composite result in loss in hop stiffness on account of longitudinal stiffness. Therefore, Gr-Ep could be the best choice for preventing collapse in pipeline. In other word, a hybrid composite pipe comprising both Gl-Ep and Gr-Ep expect to behave as steel pipe.

Table 2. Following give an example for flexible pipe comprising of two thermosetting mats each are form of 20 wrapped tape stacks (i.e., first mat is wrapped at (0°, −82.7°) and the second mat is wrapped at (+82.7°, 0°)), the tape layers are assumed made of Gl-Ep.

Description†	T_m (MPa)	Kg/m	D_i (mm)	H (mm)
First layer				
Carcass	250	11.047	480	5
Tape stacks made of 10 composite layer each 0.2 mm thick	420	0.030325× 16 tape stacks	485±20	2.00
The warped tape stacks made of 10 composite layer each 0.2 mm thick	420	3.7652 kg × 8 tape stacks	485	2.00
Second layer				
An intermediate Polyamide 11	250	11.047	500	5
Tape stacks made of 10 composite layer each 0.2 mm thick	420	0.030325× 16 tape stacks	505±20	2.00
The warped tape stacks made of 10 composite layer each 0.2 mm thick	420	3.7652 kg × 8 tape stacks	505	2.00

† Tm= maximum tensile strength in MPa at elasticity limit of 0.2% extension, Kg/m=weight in kg per meter of pipe, Di=internal diameter in mm, and H=thickness.

Table 3. The characteristics of the proposed Flexible pipe made of Gl-Ep.

Characteristics	Metric	Unit
Internal diameter	480	mm
Composite layer volume	0.013144	mm
Internal volume	0.18095	m³
External volume	0.21647	m³
Empty weight in air	72.3720	kg/m
Weight full of sea water in air	249.856	kg/m
Empty weight in sea water	-139.768	kg/m
Weight full of sea water in sea water	37.5624	kg/m
Floatability factor empty in sea water†	0.33412	
Bursting pressure	≈350	bars
Collapse pressure	≈150	bars

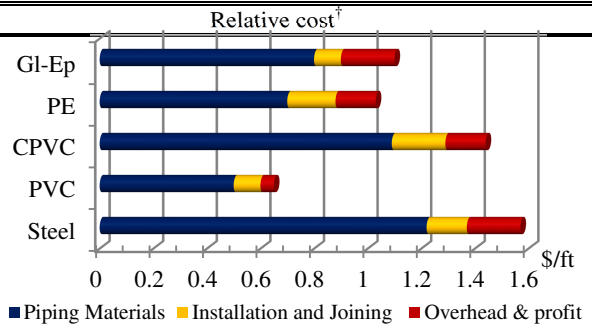

†Floatability factor= Empty weight in air / (External volume×1.02×Density of sea water), and cost data are adopted by Means 2012 Mechanical Cost Data.

Table 4. Stress, Strain, Deformation at flexible thermosetting pipe its tapes stacks made of Gl-EP, Gr-Ep(AS), and Steel, under different internal pressure scenarios.

Internal Pressure (bar)	Gl-EP			Gr-Ep(AS)			Steel		
	Stress Pa×10^8	Strain m/m ×10^{-2}	Deformation m×10^{-3}	Stress Pa×10^8	Strain m/m ×10^{-2}	Deformation m×10^{-3}	Stress Pa×10^8	Strain m/m ×10^{-2}	Deformation m×10^{-3}
25	1.62	1.25	1.29	3.42	1.24	1.98	1.11	9.60	1.21
30	1.95	1.50	1.54	4.10	1.49	2.38	1.34	1.15	1.45
35	2.27	1.74	1.80	4.79	1.73	2.78	1.56	1.34	1.69
40	2.59	1.99	2.06	5.47	1.98	3.18	1.78	1.54	1.94
45	2.92	2.24	2.32	6.15	2.23	3.57	2.00	1.73	2.18
50	3.24	2.49	2.57	6.84	2.48	3.97	2.23	1.92	2.42

Table 5. Stress, Strain, Deformation at flexible thermosetting pipe its tapes stacks made of Gl-EP, Gr-Ep(AS), and Steel, under different external pressure scenarios.

External Collapse Pressure (bar)	Gl-EP			Gr-Ep$^{(AS)}$			Steel		
	Stress Pa×10^8	Strain m/m ×10^{-2}	Deformation m×10^{-3}	Stress Pa×10^8	Strain m/m ×10^{-2}	Deformation m×10^{-3}	Stress Pa×10^8	Strain m/m ×10^{-2}	Deformation m×10^{-3}
5	3.4043	2.5138	2.6933	7.1299	2.5434	4.1808	2.2992	1.9328	2.5337
6	4.0853	3.0166	3.2322	8.5564	3.0521	5.0173	2.7591	2.3194	3.0414
7	4.7664	3.5193	3.7711	9.9829	3.5609	5.8538	3.2190	2.7061	3.5491
8	5.4474	4.0221	4.3100	1.1409	4.0696	6.6904	3.6790	3.0927	4.0568
9	6.1284	4.5249	4.8489	1.2836	4.5783	7.5269	4.1389	3.4793	4.5645
10	6.8094	5.0276	5.3879	1.4262	5.0870	8.3634	4.5988	3.8660	5.0723

Table 6. Stress, Strain, Deformation at flexible thermosetting pipe its tapes stacks made of Gl-EP, Gr-Ep(AS), and Steel, under different tension scenarios.

Tension (ton)	Gl-EP			Gr-Ep$^{(AS)}$			Steel		
	Stress Pa×10^8	Strain m/m ×10^{-2}	Deformation m×10^{-3}	Stress Pa×10^8	Strain m/m ×10^{-2}	Deformation m×10^{-3}	Stress Pa×10^8	Strain m/m ×10^{-2}	Deformation m×10^{-3}
0.5	4.5733	2.8693	1.6105	6.4276	5.5893	3.1663	4.4969	2.2539	1.3875
1	9.1491	5.7398	3.2266	1.2857	1.1181	6.3409	9.0038	4.5127	2.7944
2	1.8301	1.1481	6.4587	2.5716	2.2363	1.2690	1.8018	9.0304	5.6082
3	2.7452	1.7222	9.6908	3.8574	3.3545	1.9039	2.7031	1.3548	8.4221
4	3.6603	2.2963	1.2923	5.1433	4.4728	2.5389	3.6045	1.8066	1.1236
5	4.5755	2.8704	1.6155	6.4292	5.5910	3.1738	4.5059	2.2584	1.4050

Conclusions

The present invention relates to a flexible composite pipe, intended to be used for the transport of fluids and in particular hydrocarbons. The pipe may also be used as a flexible riser, adapted for transportation of fluids from/to a floating production unit to/from a subsea wellhead etc. The flexible composite line according to the present invention is expected being a high performance device developed to serve the above purposes at high temperatures (up to 135 °C) , high pressures (up to 350 bars), and for shallow water dynamic applications. Although, the proposed flexible pipe is lighter in weight than prior art pipes it expect maintaining correct performances, particularly mechanical performances.

Acknowledgments

Authors would like to acknowledge Universiti Teknologi PETRONAS, for sponsoring this research.

References

[1] T. M. Badri, Z. Mustaffa, M. B. Taufiq, in *Materials and Diverse Technologies in Industry and Manufacture,* M. Yahaya, Ed. (Trans Tech Publications Inc, 2013).
[2] T. M. Badri, Z. Mustaffa, M. B. Taufiq, in *Materials and Diverse Technologies in Industry and Manufacture,* M. Yahaya, Ed. (Trans Tech Publications Inc., 2013).
[3] T. M. Badri, Z. B. Mustaffa, M. B. Taufiq, paper presented at the The Offshore Technology Conference, 2013.
[4] T. M. Badri, Z. B. Mustaffa, M. B. Taufiq, paper presented at the The Offshore Technology Conference, 2013.
[5] Z. Mustaffa, M. B. Taufiq, T. M. Badri, *Applied Mechanics and Materials* **353-356**, 3280 (2013).
[6] Z. Mustaffa, M. B. Taufiq, T. M. Badri, *Applied Mechanics and Materials* **353-356**, 3316 (2013).

[7] T. M. B. Albarody, H. H. Al-Kayiem, M. B. Taufiq, *The Theory of Functional and Adaptive Shell Structures*. Mschmoeltz, Ed., (LAP LAMBERT Academic Publishing GmbH & Co., ISBN: 978-3-8465-2175-5, Saarbrücken, Germany., 2013), pp. 212 Pages.
[8] Reddy J.N., *Mechanics of Laminated Composite Plates and Shells*. (CRC Press, New York, 2004).
[9] Qatu M.S., *Vibration of Laminated Shells and Plates*. (Elsevier, London, 2004).

M

N

O

P

R

S

T

U

W

Y